

Final Report

High Strength Steel Welding Research

Submitted to:

Dr. Julie Christodoulou
Office of Naval Research
Arlington, Virginia 22217

Submitted by

Profs. Stephen Liu and Glen Edwards
Center for Welding, Joining and Coatings Research
Colorado School of Mines
Golden, Colorado 80401

20050602 002

Research Performed under Contract:

N00014-04-1-0156

DISTRIBUTION STATEMENT A

Approved for Public Release
Distribution Unlimited

May 27, 2005

CSM



**CENTER FOR WELDING, JOINING
AND COATINGS RESEARCH**

Colorado School of Mines
Golden, Colorado 80401

REPORT DOCUMENTATION PAGE

Form Approved
OMB No. 0704-0188

The public reporting burden for this collection of information is estimated to average 1 hour per response, including the time for reviewing instructions, searching existing data sources, gathering and maintaining the data needed, and completing and reviewing the collection of information. Send comments regarding this burden estimate or any other aspect of this collection of information, including suggestions for reducing the burden, to Department of Defense, Washington Headquarters Services, Directorate for Information Operations and Reports (0704-0188), 1215 Jefferson Davis Highway, Suite 1204, Arlington, VA 22202-4302. Respondents should be aware that notwithstanding any other provision of law, no person shall be subject to any penalty for failing to comply with a collection of information if it does not display a currently valid OMB control number.

PLEASE DO NOT RETURN YOUR FORM TO THE ABOVE ADDRESS.

1. REPORT DATE (DD-MM-YYYY) 05-27-2005		2. REPORT TYPE Technical Report		3. DATES COVERED (From - To) 12/1/2003 - 12/31/2004	
4. TITLE AND SUBTITLE HIGH STRENGTH STEEL WELDING RESEARCH: Integration of Yttrium and Fluoride Additions in a Flux-Cored Arc Welding Consumable & Spectroscopic Monitoring of Hydrogen in Welding Arcs				5a. CONTRACT NUMBER N00014-04-1-0156	
				5b. GRANT NUMBER	
				5c. PROGRAM ELEMENT NUMBER	
				5d. PROJECT NUMBER	
6. AUTHOR(S) Prof. Stephen Liu and Glen R. Edwards				5e. TASK NUMBER	
				5f. WORK UNIT NUMBER	
7. PERFORMING ORGANIZATION NAME(S) AND ADDRESS(ES) Center for Welding, Joining and Coatings Research Colorado School of Mines Golden, Colorado 80401				8. PERFORMING ORGANIZATION REPORT NUMBER MT-CWJCR-005-006	
9. SPONSORING/MONITORING AGENCY NAME(S) AND ADDRESS(ES) Dr. Julie Christodoulou Office of Naval Research Arlington, Virginia 22217				10. SPONSOR/MONITOR'S ACRONYM(S) ONR 332	
				11. SPONSOR/MONITOR'S REPORT NUMBER(S)	
12. DISTRIBUTION/AVAILABILITY STATEMENT DISTRIBUTION STATEMENT A Approved for Public Release Distribution Unlimited					
13. SUPPLEMENTARY NOTES					
14. ABSTRACT The application of high strength low alloy (HSLA) steels has been limited by the availability of suitable filler metals. Specifically, as the weld metal strength increases, the susceptibility to hydrogen-assisted cracking increases. To take full advantage of the developments in HSLA steel base metals, weld filler metals which minimize the effects of diffusible hydrogen and develop tough microstructures must be designed. The benefit of yttrium-containing inclusions to provide effective hydrogen traps and reduce diffusible hydrogen levels, as well as, to act as intragranular nucleation sites to produce tough microstructures has been demonstrated. Furthermore, fluoride-containing consumables have been demonstrated to reduce weld metal diffusible hydrogen levels through reactions within the arc atmosphere. The current research was undertaken to study the effects on welding characteristics and weld metal properties when these two concepts are integrated into a single welding consumable. Additionally, current methods of quantifying the amount of diffusible hydrogen in a steel weldment are destructive and are performed only after the weldment has been deposited. There is a need of real time, in situ, and non-intrusive method for diffusible hydrogen.					
15. SUBJECT TERMS High Strength Steel Welding, Flux-Cored Arc Welding consumables, Diffusible Hydrogen, Residual Hydrogen, Hydrogen Traps, Weld metal inclusions, Microstructural Optimization, Arc Emission Spectroscopy, Arc Temperature, Hydrogen Distribution in Arc					
16. SECURITY CLASSIFICATION OF:			17. LIMITATION OF ABSTRACT	18. NUMBER OF PAGES 471	19a. NAME OF RESPONSIBLE PERSON Prof. Stephen Liu
a. REPORT	b. ABSTRACT	c. THIS PAGE			19b. TELEPHONE NUMBER (Include area code) 303 273-3796

Final Report

High Strength Steel Welding Research

Submitted to:
Dr. Julie Christodoulou
Office of Naval Research
Arlington, Virginia 22217

Submitted by
Profs. Stephen Liu and Glen Edwards
Center for Welding, Joining and Coatings Research
Colorado School of Mines
Golden, Colorado 80401

Research Performed under Contract:
N00014-04-1-0156

May 27, 2005

THIS DOCUMENT CONTAINED
BLANK PAGES THAT HAVE
BEEN DELETED

EXECUTIVE SUMMARY

This is the final report submitted to ONR on the High Strength Steel Welding Research Program conducted at the Colorado School of Mines. Since the submission of the last report on June 29, 2004, the two graduate students, Justin Chandler (M.Sc.) and Craig Clasper (M.Sc.) have completed their degree at CSM. As such, this report is a compilation of the two M.Sc. theses.

Despite the many measures proposed to minimize hydrogen-assisted cracking (HAC) in high-strength steel weld metal, cold cracking or delayed cracking still remains one of the major challenges that welding engineers face. Since HAC is due to diffusible hydrogen in the metal matrix, filler metals that incorporate mechanisms that reduce diffusible hydrogen must be developed to minimize their effect. Optimal weld metal chemical composition containing yttrium to form hydrogen traps will also be able to create inclusions with proper size and spatial distribution for nucleation of tough microstructures such as acicular ferrite. High-yttrium deposits (up to 2800 ppm) exhibited approximately 3.5 times the surface area of oxides formed in deposits with lower yttrium contents and were extremely efficient in diffusible hydrogen reduction (to below 2 ml/100g deposited metal). The microstructure that resulted was predominately coarse ferrite with high volume fraction of nonmetallic inclusions. With yttrium-to-oxygen ratio controlled to between 1.3 and 0.3, the inclusion density and size distribution were optimal to produce high amounts of acicular ferrite. As an individual addition, KF was effective in decreasing the partial pressure of hydrogen in the arc and the amount of diffusible hydrogen in the weld metal.

When fluoride was mixed with yttrium, the partial pressures of fluorine and hydrogen in the arc changed significantly, result of perturbation of the multiple O-F-X equilibria, with X being the alloying elements. With that, the amount of hydrogen and oxygen pickup in the weld metal also changed substantially. The presence of fluoride in excess of 10 percent created serious arc instability and weld porosity. High amounts of fluorides also jeopardized base metal wetting that required formulation modification (1% silicon addition) to restore good weld metal fluidity and bead morphology. With concurrent fluoride and yttrium additions, alloying element recovery became different from the earlier concept systems, affecting the composition of the key alloying elements in the weld metal. Manganese content decreased from 1.47 to 0.89 wt. pct., titanium from 150 to 50 ppm, and nickel increased from 2.85 to 3.78 wt. pct. Understandably, from an alloy strengthening point of view, these welds yielded mechanical properties inferior to those expected from a 100-ksi level steel welds. By adjusting the key alloying elements to the following values, 1.2Mn, 2.84Ni, 0.26Mo, 480ppm Y, and 210 ppm Ti, the resulting welds performed close to the properties specified by the U.S. Navy. With carbon equivalent around 0.17, the weld contained about 60% acicular ferrite, 25% ferrite with second phase, 10% polygonal ferrite, and 5% martensite.

Current methods of quantifying the amount of diffusible hydrogen in a steel weldment are destructive and are performed only after the weldment has been deposited. Thus, a second objective of this research was to examine the viability of arc emission spectroscopy as a non-destructive, in-situ method of hydrogen determination in high strength steel weldments. GMAW processes, with varying levels of hydrogen in the welding arc and from different sources, were monitored using emission spectroscopy and

the findings were correlated to weld metal hydrogen content. Hydrogen additions were made to argon shielding gas in the amounts of 220 parts-per-million, 1-vol. percent, and 3-vol. percent. The ion-neutral line ratio method was utilized to calculate the temperature of the welding arcs. A summation of hydrogen concentration in the welding arcs out to 3.25 millimeters was measured and correlated to the hydrogen content of the weldments. Diffusible hydrogen content of the weld metal was found to increase linearly as a function of hydrogen observed in the arc using emission spectroscopy. Diffusible hydrogen content of steel weldments was also found to exhibit a Sievert's law type of relationship with the hydrogen additions in argon shielding gas.

In addition, the spectroscopy system was able to detect hydrogen in the arc resulting from moisture in the shielding gas as well as rust on a steel wire consumable. Moisture additions, even at 220 ppm level, were found to be a very potent source of hydrogen. After exposing HSLA wire consumable to atmosphere at 33°C and 85% relative humidity for four days, the contamination on the consumable introduced hydrogen into the welding arc at a level greater than that provided by 220 ppm hydrogen additions in argon shielding gas.

Findings in this ONR research program showed that this tool has great potential for application to real fabrication environment. Once refined for application to an industrial setting, emission spectroscopy can serve as a warning device to alert fabricators when dangerous levels of diffusible hydrogen may be present.

In addition to Justin Chandler and Craig Clasper, three other Ph.D. graduate students (Chad Lensing, Marshall Clark, Muneo Matsushita) benefited from this ONR sponsored research program. Beginning 2001, more than 10 technical papers based on

this program's findings had been published. Amongst those, a paper titled, "Alloying and Microstructural Management in Developing SMAW Electrodes for HSLA-100 Steel" was selected for the AWS McKay-Helm Award as the best paper on steel welding published in the Welding Journal in 2002. In addition, Craig Clasper and Justin Chandler submitted posters for competition in the 2004 AWS Welding Convention and were awarded first and second prize in the Graduate Students category.

The PI's (Profs. Stephen Liu and Glen Edwards, and Prof. David Olson – early stages of the program) are very grateful for the support received from Dr. George Yoder, a long time ONR monitor of this program and from Dr. Julie Christodoulou during the last one year and a half of this work.

INTEGRATION OF YTTRIUM AND FLUORIDE ADDITIONS IN A FLUX-CORED
ARC WELDING CONSUMABLE FOR HIGH STRENGTH STEEL WELDING

by
Craig Matthew Clasper

A thesis submitted to the Faculty and the Board of Trustees of the Colorado School of Mines in partial fulfillment of the requirements for the degree of Master of Science (Metallurgical and Materials Engineering).

Golden, Colorado

Date: _____

Signed: _____
Craig M. Clasper

Approved: _____
Dr. Stephen Liu
Thesis Advisor

Golden, Colorado

Date: _____

Dr. John J. Moore
Professor and Head,
Metallurgical and Materials
Engineering Department

ABSTRACT

The application of high strength low alloy (HSLA) steels has been limited by the availability of suitable filler metals. Specifically, as the weld metal strength increases, the susceptibility to hydrogen-assisted cracking increases. Therefore, to take full advantage of the developments in HSLA steel base metals, weld filler metals which minimize the effects of diffusible hydrogen develop tough microstructures must be designed. The benefit of yttrium-containing inclusions to provide effective hydrogen traps and reduce diffusible hydrogen levels, as well as, to act as intragranular nucleation sites to produce tough microstructures has been demonstrated. Furthermore, fluoride-containing consumables have been demonstrated to reduce weld metal diffusible hydrogen levels through reactions within the arc atmosphere. The current research was undertaken to study the effects on welding characteristics and weld metal properties when these two concepts are integrated into a single welding consumable.

To study the effects of integrating fluoride additions to yttrium-containing consumables, flux-cored arc welding (FCAW) consumables were manufactured. A total of twenty-one wires of varying compositions were fabricated and used to produce bead-on-plate welds and bead-on-bead chem-pads. A target weld metal composition of 2.5 weight percent nickel, 1.1 weight percent manganese, 0.2 weight percent molybdenum, 280 ppm titanium, and 300 to 900 ppm yttrium was selected because it has been observed to produce a fine-grained microstructure with low diffusible hydrogen content.

Characterization of these welds included arc stability, weld bead morphology, microstructural development, chemical composition, and inclusion development. Consumables that produced welds with good characteristics were then selected for multiple-pass welds so evaluations of impact toughness, tensile strength, and

microhardness could be performed. In addition, diffusible hydrogen analysis was performed with these consumables.

Potassium fluoride additions were found to be detrimental to weld metal characteristics compared to welds produced with metal-cored, yttrium-containing consumables. Powder fills containing an excess of ten percent potassium fluoride produced welds with significant amounts of porosity due to an increase in arc stability. Up to ten percent, good quality welds were produced but had poor wetting characteristics and an insufficient volume of fine-grained, acicular ferrite.

To improve wetting characteristics, ferrosilicon and other flux ingredients such as calcium fluoride, calcium oxide, silica, and alumina were integrated into the welding process. These additions not only improved wetting characteristics, but also improved alloy recovery and microstructure.

Evaluation of mechanical properties was performed on welds produced with the metal-cored, yttrium-containing consumables, consumables with the powder fill containing five and ten percent potassium fluoride, and consumables integrating the additional ingredients. Consumables that produced welds with microstructures containing a fraction of acicular ferrite of 65 percent or more met the requirements for impact toughness and tensile strength, but only had about 18 percent elongation. Welds with microstructures containing between 45 and 60 percent acicular ferrite were within fifteen percent of the minimum toughness standards. The U.S. Navy set minimum requirements of 35 and 60 foot-pounds (48 and 81 J) at -60 and 0°F, respectively, 88 to 115 ksi (607 to 793 MPa) yield strength with 20 percent elongation for high strength steel weld metals.

TABLE OF CONTENTS

ABSTRACT.....	iii
LIST OF FIGURES	ix
LIST OF TABLES	xvii
ACKNOWLEDGEMENTS	xx
 CHAPTER 1: INTRODUCTION	 1
 CHAPTER 2: LITERATURE REVIEW	 5
2.1 Welding of High Strength Steels	6
2.2 Effect of Alloying Weldments	10
2.3 Weld Metal Microstructural Development	13
2.3.1 Weld Metal Solidification.....	13
2.3.2 Inclusion Characteristics and Development.....	21
2.3.3 Austenite Decomposition and Microstructural Constituents	40
2.3.3.1 Grain Boundary Ferrite	42
2.3.3.2 Widmanstätten Ferrite.....	43
2.3.3.3 Bainite	44
2.3.3.4 Acicular Ferrite	45
2.3.3.5 MA Constituent.....	47
2.3.4 Influence of Weld Metal Inclusions on Microstructural Development	47
2.3.5 Effects of Microstructure on Mechanical Properties	54
2.4 Hydrogen Assisted Cracking	56
2.4.1 General Features of HAC.....	57
2.4.1.1 Macroscopic Observations	57
2.4.1.2 Microscopic Observations	58

2.4.2 Factors Responsible for HAC and their Control.....	60
2.4.2.1 Hydrogen Level.....	61
2.4.2.2 Stress Level.....	62
2.4.2.3 Types of Microstructure.....	63
2.4.2.4 Temperature	64
2.5 Hydrogen Pickup in Weldments	65
2.5.1 Hydrogen Sources.....	65
2.5.2 Forms of Hydrogen in the Flux Covered and Cored Electrodes.....	65
2.5.3 Influence of Hydrogen in the Flux of Weld Metal Diffusible Hydrogen	67
2.5.4 Influence of the Atmosphere and Surrounding Environment on Steel Weld Metal Diffusible Hydrogen.....	69
2.6 Hydrogen Management in Low Carbon and Low Alloy Steel Weldments	71
2.6.1 Modification of Flux Ingredients	71
2.6.2 Control of Oxygen Content in the Steel Weld Metal.....	72
2.6.3 Hydrogen Trapping in the Steel Weld Metal.....	72
2.6.4 Dilution of Hydrogen in the Arc with Inert Gas	73
2.6.5 Addition of Fluorides	74
2.7 Yttrium.....	77
2.7.1 Effects on Inclusion and Microstructural Development	85
2.7.2 Effects on Hydrogen Management	88
2.8 Effective Fluorides and their Effects on Hydrogen Management	89
2.8.1 Consideration of Mechanism of Reduction of Hydrogen Pickup	89
2.8.2 Thermodynamic Behavior of Species Involved in HF Formation.....	92
2.8.2.1 Forms of Hydrogen.....	92
2.8.2.2 Vaporization of Fluorides	94
2.8.3 Model of HF Formation Effect	97
2.8.3.1 Reaction Occurring in the Surroundings of the Molten Pool and Molten Droplet	97
2.8.3.2 Concerns for Hydrogen Absorption from the Arc Atmosphere to the Weld Pool.....	99

2.8.4 Model of HF Transport Effect	100
2.8.5 Model of Dilution Effect.....	104
CHAPTER 3: OBJECTIVES OF RESARCH.....	107
CHAPTER 4: EXPERIMENTAL METHODS	109
4.1 Electrode Formulation.....	109
4.2 Materials Used	113
4.2.0 Fabrication of Ferroyttrium.....	115
4.3 Fabrication of Experimental Electrodes.....	115
4.3.1 Tubular Wire Making Facility at Colorado School of Mines	116
4.3.2 Forming and Closing the Strip and Adding Flux in the Wire	117
4.3.3 Concerns for Flux-Cored Wire Making.....	119
4.4 Welding Procedures	121
4.5 Macroscopic Analysis	124
4.6 Weld Bead Chemical Analysis	124
4.6.1 Inductively Coupled Plasma	126
4.6.2 Diffusible Hydrogen Analysis	126
4.6.2.1 Weld Test Assembly.....	127
4.6.2.2 Welding Fixture	127
4.6.2.3 Welding Analysis.....	128
4.6.2.4 Diffusible Hydrogen Measurements	129
4.7 Light Optical Microscopy.....	130
4.8 Mechanical Properties Evaluation.....	131
4.8.1 Charpy V-Notch Impact Testing.....	131
4.8.2 Tensile Testing.....	134
4.8.3 Hardness Measurements	136

CHAPTER 5: RESULTS AND DISCUSSION.....	137
5.1 Integrating Fluoride Additions to Yttrium-Containing Consumables	137
5.1.1 Welding Characteristics	137
5.1.2 Weld Bead Morphology Analysis.....	140
5.1.3 Microstructural Analysis.....	143
5.1.4 Chemical Analysis	151
5.1.5 Inclusion Analysis.....	156
5.1.6 Summary of the Integration of Fluorides to Yttrium-Containing Consumables.....	164
5.2 Integrating Additional Flux Ingredients to Yttrium-Containing Consumables ...	164
5.2.1 Improving Molten Weld Metal Fluidity with Ferrosilicon.....	165
5.2.2 Addition of Other Flux Ingredients to Yttrium-Containing Consumables .	168
5.3 Integration of Flux Ingredients Through the Use of a Paste.....	171
5.3.1 Welding Characteristics	171
5.3.2 Weld Bead Morphology.....	172
5.3.3 Microstructural Analysis.....	173
5.3.4 Chemical Analysis	175
5.3.5 Inclusion Analysis.....	177
5.4 Summary of Consumables Selected for Further Observations	178
5.5 Diffusible Hydrogen Measurements	186
5.6 Comparisons of Mechanical Properties	188
CHAPTER 6: CONCLUSIONS	197
CHAPTER 7: RECOMMENDATIONS FOR FUTURE WORK	199
CHAPTER 8: REFERENCES CITED	201

LIST OF FIGURES

Figure 1: The weldability diagram illustrating HY- and HSLA-series steels.....	8
Figure 2: Different solidification principles in an iron-based alloy.....	15
Figure 3: Two dimensional appearance of the weld pool showing the columnar development in (a) an elliptical weld pool where the progressive change in direction of the maximum thermal gradient is reflected by the survival of many more columnar grains, and (b) a tear drop shaped weld pool where the direction of the maximum thermal gradient is almost invariant along the edge of the pool.	16
Figure 4: Schematic diagram showing the location of inclusion in the microstructure of a weld for solidification as (a) δ -ferrite and (b) austenite, assuming that the inclusions locate themselves preferentially at the cell boundaries and austenite boundaries diverge, because in arc welding, the heat source is not stationary.	19
Figure 5: Effect of deoxidation practice on the δ -ferrite to austenite transformation in Al-Ti-Si-Mn deoxidized steel welds. (a) Growth of austenite along the boundaries of the primary δ -ferrite phase, and (b) growth of austenite across the boundaries of the primary δ -ferrite phase.....	20
Figure 6: Schematic diagrams showing the sequence of reactions occurring during weld metal deoxidation and their relationship to the hot and cold regions of the weld pool; (a) longitudinal section of section of weld pool, and (b) cross section of weld pool along A-A.	23
Figure 7: Schematic illustration of composition profile ahead of inclusion during growth.	31
Figure 8: Welding geometry coordinate system for temperature profile model developed by Ion et al.	34
Figure 9: Flow chart of integrated inclusion model showing calculation steps.....	35

Figure 10: (a) Schematic representation of microstructural constituents as defined by IIW Subcommittee IX-J methodology. (b) Representative photomicrographs showing the IIW scheme for the classification of microstructures in low alloy steel weld metal.	41
Figure 11: Variation in the energy barrier to nucleation, ΔG , normalized to that corresponding to unfaceted homogeneous nucleation in an austenite matrix, for unfaceted ferrite formed on an inclusion ($\Delta G^*_{inc. unf.}$), as a function of inclusion radius, I . Constant values of the volume of free energy change ($\Delta G_V = -300 \text{ J/mol}$) and surface free-energy of both austenite-austenite and austenite-ferrite boundaries ($\sigma = 0.75 \text{ J/m}^2$) are assumed. The equivalent energy barrier for austenite grain-boundary nucleation is also shown ($\Delta G^*_{gb unf.}$).	49
Figure 12: Schematic illustration showing the presence of primary and secondary phases in weld metal inclusions.	52
Figure 13: HAC in heat-affected zones of (a) fillet and (b) butt welds.	58
Figure 14: HAZ in C-Mn steel (a) HAC at root of single-pass fillet weld, and (b) HAC at toe of multiple-pass fillet weld.	59
Figure 15: HAC in steel weld metal of (a) single-pass SMA weld, (b) root bead of a Y-groove welding test, and (c) SA weld.	59
Figure 16: Typical fractographic modes of HAC, (a) intergranular fracture (IG), (b) quasicleavage fracture (QC), and (c) microvoid coalescence (MVC).	59
Figure 17: Beacham diagram on interrelationship between stress intensity factor and dissolved hydrogen content.	60
Figure 18: Solubility of hydrogen in low carbon steel weld metal as a function of temperature.	62
Figure 19: Relationship between diffusible hydrogen and total hydrogen content in the coatings.	68
Figure 20: Vapor pressure/diffusible hydrogen content (PH ₂ O1/2-HDM) diagram for redried basic-type SMAW electrodes; average value diagram.	70
Figure 21: Effect of primer thickness, primer type, and fluoride additions on weld metal diffusible hydrogen content.	70

Figure 22: Effect of CO ₂ in fluxes on diffusible hydrogen content in weld metal.	74
Figure 23: Influence of fluorine content in fluxes on diffusible hydrogen content in weld metal and slag.	75
Figure 24: Plot of diffusible hydrogen content in deposited weld metal as a function of the amount of fluorides in the wire core.	76
Figure 25: Binary phase diagram of iron-yttrium system.	78
Figure 26: The temperature dependences of the isobaric-isothermic potential of formation of specific oxides.	80
Figure 27: Crystal structure of Y ₂ O ₃ . Three quarters of cations are in cubes in which the missing oxygens are along a face diagonal. One quarter of cations are in cubes in which the missing oxygens are along a body diagonal.	81
Figure 28: The phase stability diagram for the Fe-Y-S-O system at 1600°C.	82
Figure 29: (a) Phase diagram for the Y ₂ O ₃ -Al ₂ O ₃ system. (b) Phase diagram for the Y ₂ O ₃ -TiO ₂ system. (c) Phase diagram for Y ₂ O ₃ -SiO ₂ system. Oxide ratios of compounds are given as Y ₂ O ₃ :SiO ₂	83
Figure 30: STEM image of a representative oxide from a hypostoichiometric weld with EDS dot maps showing the distribution of aluminum, yttrium, titanium, manganese, sulfur, and iron.	86
Figure 31: Representative photomicrographs of (a) yttrium-free welds, (b) hyperstoichiometric welds, and (c) hypostoichiometric welds.	87
Figure 32: Effect of trap additions to the amount of diffusible hydrogen in Armco iron samples welded with GMA welding processes at three levels of hydrogen contamination in the shielding gas and at nominal heat input of 1.5 kJ/mm.	88
Figure 33: Illustration of the low temperature regions in the arc system.	90
Figure 34: Illustration of dilution effect in the arc system.	91
Figure 35: Equilibrium constant of reaction, $\frac{1}{2} \text{H}_2 = \text{H}$	93
Figure 36: Reduction in weight at elevated temperatures for various fluorides.	94

Figure 37: Equilibrium constants of vaporization of fluorides.....	95
Figure 38: Illustration of reactions between fluoride and hydrogen in thermal layer surrounding molten pool or droplet.	98
Figure 39: Illustration of reactions between fluoride and hydrogen at periphery of the arc.....	101
Figure 40: Illustration of mass flow between two systems with pressure difference.	102
Figure 41: Equilibrium constants of HF formation reactions of MnF_2 , KF , and CaF_2 between 2,900 and 4,400 K.....	105
Figure 42: Photograph of powder V-blender.	116
Figure 43: (a) Photograph of tubular wire making mill at CSM. (b) Representative illustration of a tubular wire making facility.	118
Figure 44: Schematic diagram of tubular wire fabrication, (a) flat strip, (b) U-forming dyes, (c), U-shaped sheath, (d) powder filling of U-shaped sheath, (e) filled U-shaped sheath, (f) U-closing dyes, and (g) Closed tubular wire with flux.....	119
Figure 45: Schematic illustration of bead-on-bead weld sample used for chemical analysis, microstructural assessment, and inclusion characterization.	123
Figure 46: Schematic illustration of V-groove plate preparations for multiple-pass welding.....	123
Figure 47: Schematic illustration of macroscopic measurements of bead-on-plate weld deposits.....	124
Figure 48: Schematic representation of locations where chemical analysis was performed for (a) bead-on-bead welds, and (b) multiple-pass V-groove welds.	125
Figure 49: Representative illustration of the locations where photomicrographs were taken in (a) bead-on-bead welds, and (b) multiple-pass V-groove welds.....	131
Figure 50: Representative locations of sample extraction from multiple-pass V-groove weld deposits.....	132

Figure 51: (a) Illustration of the dimensions of a CVN sample, and (b) representative location of the extraction of the CVN sample	134
Figure 52: (a) Representative location of the extraction of tensile bar samples, and (b) "dimensions" of tensile bar specimens where the actual dimensions are shown in Table 15.	135
Figure 53: Schematic illustration of the locations where Vicker's microhardness measurements were taken.	136
Figure 54: Plot showing the average voltage and change in voltage as additions of potassium fluoride to the powder fill increase.	139
Figure 55: Plot showing the average currents and change in current as additions of potassium fluoride to the powder fill increase.	139
Figure 56: Representative photographs of cross sections of bead-on-plate welds produced with the metal-cored, yttrium-containing consumables (a) 0-1-C, (b) 0-1-D, and (c) 0-2, and welds produced with (d) 1-1-C, (e) 1-1-D, (f) 1-2-C, (g) 1-2-D, (h) 1-3, (i) 1-4, (j) 1-5, and (k) 1-6 showing significant increases in porosity and contact angles with increasing fluoride additions.	142
Figure 57: Photograph showing the trapping of gases in the solidified weld metal prior to before the gases could escape the molten weld metal.....	143
Figure 58: Representative photomicrograph of welds produced with the 0-1-C consumable, consisting of about 60 percent ferrite with second phases (aligned and non-aligned combined), 30 percent acicular ferrite, and 10 percent grain boundary ferrite.....	145
Figure 59: Representative photomicrograph of welds produced with the 0-1-D consumable, consisting of 50 percent acicular ferrite, 29 percent ferrite with second phases, and 20 percent grain boundary ferrite.	145
Figure 60: Representative photomicrograph of welds produced with consumable 0-2, consisting of 72 percent acicular ferrite, 22 percent ferrite with second phases, and 3 percent grain boundary ferrite.	146
Figure 61: Representative photomicrograph of welds produced with consumable 1-1-C, consisting of 44 percent acicular ferrite, 47 percent ferrite with second phases, and 9 percent grain boundary ferrite.	146

Figure 62: Representative photomicrograph of welds produced with consumable 1-1-D, consisting of 47 percent acicular ferrite, 46 percent ferrite with second phases, and 7 percent primary ferrite.	147
Figure 63: Representative photomicrograph of welds produced with consumable 1-2-C, consisting of 45 percent acicular ferrite, 43 percent ferrite with the second phases, and 12 percent primary ferrite.	147
Figure 64: Representative photomicrograph of welds produced with consumable 1-2-D, consisting of 48 percent acicular ferrite, 41 percent ferrite with the second phases, and 11 percent primary ferrite.	148
Figure 65: Representative photomicrograph of welds produced with consumable 1-3, consisting of 54 percent ferrite with the second phases, 38 percent acicular ferrite, and 8 percent primary ferrite.	148
Figure 66: Representative photomicrograph of welds produced with consumable 1-4, consisting of 54 percent ferrite with the second phases, 29 percent acicular ferrite, and 17 percent primary ferrite.	149
Figure 67: Representative photomicrograph of welds produced with consumable 1-5, consisting of 68 percent ferrite with the second phases, 20 percent acicular ferrite, and 12 percent primary ferrite.	149
Figure 68: Representative photomicrograph of welds produced with consumable 1-6, consisting of 73 percent ferrite with the second phases, 15 percent acicular ferrite, and 11 percent primary ferrite.	150
Figure 69: Elemental recoveries with changing potassium fluoride additions. (a) nickel, (b) manganese, (c) molybdenum, (d) yttrium, (e) titanium, and (f) aluminum.	155
Figure 70: Representative photomicrographs of the unetched weld samples used in the inclusion characteristics study for the metal-cored yttrium-containing consumables (a) 0-1-C, (b) 0-1-D, and (c) 0-2.	159
Figure 71: Representative photomicrographs of the unetched weld samples used in the inclusion characteristics study for the potassium fluoride to yttrium-containing consumables (a) 1-1-C, (b) 1-1-D, (c) 1-2-C, (d) 1-2-C, (e) 1-3, (f) 1-4, (g) 1-5, and (h) 1-6.	160

Figure 72: Distribution of the diameters of inclusions found in welds produced with (a) the metal-cored-yttrium containing consumables, and (b) the potassium fluoride additions to yttrium-containing consumables.	163
Figure 73: Longitudinal cross-section showing the decrease in porosity achieved when ferrosilicon paste was applied in combination with the 1-2-C consumable. Weld metal (a) was made without ferrosilicon and weld metal (b) was made with ferrosilicon	166
Figure 74: Representative photomicrographs of welds produced with the (a) 0-2 and (b) 0-3 consumables, where the microstructure constituents are listed in Table 24.....	167
Figure 75: Representative photomicrographs of welds produced using the 0-1-D consumable and the (a) 3-1 or (b) 3-2 flux pastes, where the constituent contents are shown in Table 31.....	174
Figure 76: Representative photomicrographs of the unetched weld samples produced with the 0-1-D consumable using the (a) 3-1 and (b) 3-2 flux pastes.....	178
Figure 77: The amount of microstructural constituents of welds with increasing yttrium-to-oxygen ratio.....	179
Figure 78: The change in each microstructural constituent with carbon equivalent, where the shaded regions result in poor microstructures. The unshaded region resulted in a high amount of acicular ferrite in the microstructure.....	180
Figure 79: Elemental recoveries compared to the yttrium-to-oxygen ratio for (a) nickel, (b) manganese, (c) molybdenum, (d) yttrium, (e) titanium, and (f) aluminum.	183
Figure 80: Elemental recoveries compared to carbon equivalent for (a) nickel, (b) manganese, (c) molybdenum, (d) yttrium, (e) titanium, and (f) aluminum. ...	184
Figure 81: Elemental recoveries compared to heat input for (a) nickel, (b) manganese, (c) molybdenum, (d) yttrium, (e) titanium, and (f) aluminum. ...	185
Figure 82: Diffusible hydrogen content shown as a function of potassium fluoride additions present in the consumable powder fill.....	188
Figure 83: Charpy V-Notch impact toughness results of the selected consumables with the target impact toughness values labeled with the two horizontal lines.	190

Figure 84: Stress-strain curves of the welds produced with the selected consumables with the target yield strength labeled with the horizontal line.....	192
Figure 85: Hardness profiles of multiple-pass welds produced with consumables (a) 0-1-C, (b) 0-1-D, (c) 0-2, (d) 0-3, (e) 1-1-C, (f) 1-2-C, (g) 3-1, and (h) 3- 2.....	193

LIST OF TABLES

Table 1: The Chemical Composition of HY- and HSLA-Series Steels.....	8
Table 2: The influence of microstructural features on ductile fracture, cleavage fracture, and hydrogen induced cracking resistance.....	56
Table 3: Thermodynamic Parameters for the Deoxidation, Desulfurization and Deoxysulfurization of Yttrium in Liquid Iron.	81
Table 4: Potential Compounds Between Y_2O_3 and Oxides of Aluminum, Titanium, Manganese, and Silicon.	82
Table 5: Law of mass action for dissociation of H_2	93
Table 6: Dissociation Potential and 90 Percent Dissociation Temperature for Various Multi-Atomic Gases.....	93
Table 7: Powder Compositions of Metal-Cored Yttrium-Containing Consumables.....	110
Table 8: Powder Compositions of Potassium Fluoride Additions to Yttrium-Containing Consumables.	111
Table 9: Powder Compositions of KF and Other "Flux Ingredients" to Yttrium-Containing Consumables.	112
Table 10: Powder Compositions of the "Flux Paste" used with the 0-1-D Consumable.	113
Table 11: Compositions of Metallic Powders Used as Filler Metals (wt. %).	114
Table 12: Composition of the AISI 1008 Low Carbon Steel Strip Used as Tubular Sheath.	114
Table 13: Sieve Analysis for Metallic Powders Used as Tubular Wire Filler Metals (Percent Retained).	114
Table 14: Welding Parameters Used During Experimental Welding.	122

Table 15: Dimensions of the Sub-Sized Tensile Samples.	135
Table 16: Measured Arc Parameters of the Metal-Cored, Yttrium-Containing Consumables and the Potassium Fluoride Additions to Yttrium-Containing Consumables.....	138
Table 17: Representative Measurements of Weld Bead Macrostructures of the Metal-Cored, Yttrium-Containing Consumables and the Potassium Fluoride Additions to Yttrium-Containing Consumables.....	141
Table 18: Microstructural Constituent Fractions Present in Welds Produced with the Metal-Cored, Yttrium Containing Consumables and the Potassium Fluoride Additions to Yttrium-Containing Consumables.	144
Table 19: Top-bead Chemical Composition for Welds Produced with the Metal-Cored, Yttrium-Containing Consumables and the Potassium Fluoride Additions to Yttrium-Containing Consumables.....	152
Table 20: Elemental Recoveries of the Welds Produced with the Metal-Cored, Yttrium-Containing Consumables and the Potassium Fluoride Additions to Yttrium-Containing Consumables.....	154
Table 21: Comparison of the Yttrium-to-Oxygen Ratio of Welds Produces with the Metal-Cored, Yttrium-Containing Consumables and the Potassium Fluoride Additions to Yttrium-Containing Consumables.	154
Table 22: Results of Inclusion Characterization for Welds Produced with the Metal-Cored, Yttrium-Containing Consumables and Potassium Fluoride Additions to Yttrium-Containing Consumables.....	157
Table 23: Measurements of the Weld Beads Produced with Consumables 0-2 and 0-3. Consumable 0-3 Contained One Weight Percent Ferrosilicon.	166
Table 24: Microstructural Constituent Fractions for Welds Produced with Consumables 0-2 and 0-3.....	166
Table 25: Top-Bead Chemical Analysis of Welds Produced with Consumables 0-2 and 0-3.....	168
Table 26: Inclusion Characteristics of Inclusions Contained in Welds Produced with Consumables 0-2 and 0-3.....	168

Table 27: Measurements of the Weld Beads Produced with Consumables 2-2, 2-3, 2-4, and 2-5.	170
Table 28: Measurements of the Weld Beads Produced with Consumables 1-1-C, 1-2-C, and 2-1.	170
Table 29: Measured Current, Voltage, and the Variations During Welding with Consumables 3-1, 3-2, 3-3, and 3-4.	172
Table 30: Measurements of the Weld Beads Produced with Consumables 3-1, 3-2, 3-3, and 3-4.	173
Table 31: Microstructural Constituent Fractions for Welds Produced Using the 3-1 and 3-2 Flux Pastes.	175
Table 32: Top-Bead Chemical Analysis of Welds Produce with the 0-1-D Consumable Using the 3-1 and 3-2 Flux Pastes.	176
Table 33: Elemental Recoveries of Welds Produced with the 0-1-D Consumable Using the 3-1 and 3-2 Flux Pastes.	176
Table 34: Yttrium-to-Oxygen Ratios of the Welds Produced with the 0-1-D Consumable Using the 3-1 and 3-2 Flux Pastes.	176
Table 35: Characteristics of Inclusions Studied in the Welds Produced with the 0-1-D Consumable Using the 3-1 and 3-2 Pastes.	177
Table 36: Microstructural Constituent Fractions for Welds Produced with Consumables Selected for Further Observations.	179
Table 37: Top-Bead Chemical Analysis of Welds Produced with the Consumables Selected for Further Observations.	182
Table 38: Characteristics of Inclusions Studied in Welds Produced with Consumables Selected for Further Study.	186
Table 39: Diffusible Hydrogen Measurements of the Selected Consumables	187
Table 40: Measured Mechanical Properties of the Selected Consumables	190

ACKNOWLEDGEMENTS

I would like to acknowledge the financial support of the U.S. Office of Naval Research and the direction of Dr. Julie Christodoulou for this work,

I would like to express my gratitude to my advisor, Dr. Stephen Liu, for his continuous support and guidance during the course of this investigation and during my graduate studies.

I would like to thank my committee members Dr. Glen Edwards and Dr. David Olson for their support and suggestions throughout my work at Mines.

I would also like to thank my colleagues in the Center for Joining, Welding, and Coatings Research, particularly Dr. Fernando Martinez, Faustino Perez, Jeff Major, and Justin Chandler for their assistance during my research and demonstrating the use of much of the equipment used during the investigation.

I would also like to acknowledge the efforts of Scott Lemoine for his assistance with metallography and lending a hand when needed.

Finally, but not least, I would like to thank my family and friends for their support and encouragement through the course of my research. Most of all, I would like to thank Trinity Sipma for her continued support, encouragement, love, patience, and understanding through the strenuous and trying times during my research and graduate studies.

CHAPTER 1

INTRODUCTION

The application of advanced high strength low alloy (HSLA) steels has been limited by the availability of suitable welding consumables. Specifically, as the weld metal strength increases, its susceptibility to hydrogen cracking increases. To take full advantage of the higher strength HSLA steels, welding consumables that minimize the effect of diffusible hydrogen and develop tough microstructures must be designed. The Center for Welding, Joining, and Coatings Research at the Colorado School of Mines has conducted research for the Office of Naval Research to study improved methods for reducing the effect of diffusible hydrogen in high strength steel welding through innovative consumable design for these materials.

Researchers at the Colorado School of Mines have developed two independent concepts for high strength steel welding that are effective in the reduction of diffusible hydrogen. The first dealt with the minimization of hydrogen in the welding arc, while the second dealt with the immobilization of hydrogen through trapping and microstructural modification. Through the use of arc emission spectroscopy, Matsushita and Liu [1, 2, 3] initially characterized the behavior of fluoride-type flux ingredients in the welding arc and confirmed the effectiveness of potassium fluoride, manganese fluoride, and sodium fluoride in displacing hydrogen from the arc plasma. They then proposed three models for the mechanisms by which weld metal hydrogen is reduced. The fluorides primarily reduce the amount of diffusible hydrogen in steel through the formation of hydrogen fluoride. In fact, thermodynamic calculations predict HF formation near the cathode or electrode tip. In addition to HF formation, two other mechanisms of hydrogen reduction

were identified: through the sluggish HF transport and through dilution of the arc atmosphere.

Once hydrogen enters the steel weld pool, its elimination can only occur as part of the cooling cycle when hydrogen solubility drastically decreases with decreasing temperature. The large effusion of hydrogen in a high strength microstructure such as martensite or bainite will likely lead to hydrogen-assisted cracking (HAC). One method to diminish HAC is to render the hydrogen atoms immobile through trap-forming element additions. Lensing [4], Maroef and Olson [5, 6, 7], and Lensing et al. [8] demonstrated that rare earth metal (REM) and REM-type additions such as neodymium (Nd) and yttrium (Y) form strong hydrogen traps when added to a steel weld pool. Stronger than typical hydrogen traps, Nd and Y form bonds with hydrogen that are stable to temperatures in excess of 600°C. By thermal desorption experiments, Maroef [5] characterized the hydrogen-REM bonds and determined the hydrogen trapping mechanism. Ferroalloys of these elements, for example ferroyttrium, are the preferred forms of additions.

Clark and Edwards [9-12] continued the research of yttrium additions and reported that yttrium-containing oxide inclusions were effective hydrogen traps, reducing diffusible hydrogen levels in low alloy steels. The microstructural development and resulting toughness of HSLA steel weld metals are dependent upon the composition, size, and distribution of oxides and non-metallic inclusions. Weld deposits with yttrium levels near the stoichiometric limit of yttria (Y_2O_3) produced Y_2O_3 and Y_2O_2S clusters that contained a few to hundreds of individual oxide particles. Weld deposits with low-to-moderate levels of yttrium produced primarily discrete, randomly distributed, spherical inclusions of yttrium aluminum garnet (YAG, $Y_3Al_5O_{12}$) with a uniform distribution of titanium. The inclusions present in yttrium-free weld deposits were complex, spherical and discrete, containing aluminum, titanium, manganese, sulfur, and silicon. When compared to low-to-moderate yttrium and yttrium-free deposits with comparable heat inputs, the surface area of the oxide clusters in the high-yttrium deposits was on the order

of 3.5 times greater. This finding indicates that a significant portion of the diffusible hydrogen reduction observed with the high-yttrium welds was the result of the increase inclusion surface area rather than composition. Moderate levels of yttrium displaced silicon and manganese from the inclusions, leading to the development of tough microstructures consisting of high percentages of acicular ferrite.

The two independently successful additions were combined in an effort to design a welding filler metal that can simultaneously decrease hydrogen levels in both the welding arc and in the high strength steel weld deposits. When fluoride and yttrium are mixed together, the final oxygen and hydrogen concentration reached will depend on the multiple equilibria of the system. The proper amount of yttrium and fluoride additions must be determined to remove the maximum amount of hydrogen, but at the same time, to produce weld deposits with a tough microstructure.

CHAPTER 2

LITERATURE REVIEW

The microstructural development in ferritic steel weld metals is dependent upon the alloy composition, deoxidation practice, and thermal history. The allotropic behavior of iron adds a degree of complexity not typically seen in other metallic materials. The limited solubility of carbon in body centered cubic (bcc) iron and the resultant formation of metastable carbides upon cooling further increases this complexity. The range of microstructural morphologies, which develop in low alloy steel weld metals as a result of the relative relationship between ferrite and these carbides, provides similar diversity in mechanical properties and structural performance.

This review begins with a discussion of high strength steel welding through the development of high strength low alloy steels and the development of welding consumables. In this discussion, the effects of alloying additions are covered. The review continues with a discussion of the solidification structure of ferritic steel weld metal. The characterization of the resulting room temperature microstructure and associated properties are strongly influenced by the development of the solidification structure.

Following the discussion of the solidification structure, a review of inclusion formation will be provided. While base metal inclusions contribute to the anisotropy of mechanical properties, the volume fraction and number density of weld metal inclusions are much higher than those of typical base metals. As a result, these weld metal inclusions play a pivotal role in microstructural development and impact toughness.

The most direct correlations between structure and properties are based upon the observed room temperature microstructures; therefore, a discussion of the various microstructural constituents and their development is provided. This analysis is followed

by a review of nonmetallic inclusions in the formation of acicular ferrite, a fine-grained, interwoven microstructure that promotes high impact toughness and high strengths in many low alloy steel weld deposits.

Hydrogen-assisted cracking is a major concern when welding high strength steels. The general features of hydrogen-assisted cracking are discussed, along with the factors responsible for hydrogen-assisted cracking and ways to control these factors. In addition, there is a discussion of how hydrogen is picked up in the weld deposits.

Following the discussion of hydrogen-assisted cracking and weld-metal hydrogen pickup; techniques for hydrogen management are discussed, particularly, hydrogen trapping and removal of hydrogen from the arc. In addition to their role as heterogeneous nucleation sites for acicular ferrite, weld metal inclusions have been proposed as potential trap sites for hydrogen to reduce the propensity of hydrogen cracking in the high strength weld metals. Additions of fluorides have been found to be effective in reducing or removing hydrogen from the arc atmosphere.

Additions of yttrium and fluorides have been proposed to manage diffusible hydrogen. Since yttrium-rich inclusions have been proposed as potent hydrogen traps, a review of yttrium and yttrium-rich inclusions in ferrite steel weld metals, as well as their effects on weld metal properties, is included. Finally, since fluoride additions have been shown to effectively reduce diffusible hydrogen content, a discussion of the proposed models is also included in this review.

2.1 Welding of High Strength Steels

High strength low alloy (HSLA), or microalloyed steels, can be defined as steels having a yield strength of greater than 45 ksi (300MPa), which is achieved by thermomechanical processing such as quench and tempering, or by way of microalloying. Alloying elements are purposely introduced to the steels to enhance their mechanical properties. Typically, manganese, chromium, molybdenum, nickel, vanadium, niobium,

nitrogen, boron, titanium, and copper are alloying elements used in HSLA steels. Since these alloying elements can increase the hardenability of HSLA steels, precautions must be taken to achieve quality welds. Both thermomechanical processing and alloying elements can work together to strengthen HSLA steels to yield strengths in excess of 130 ksi (860MPa) and Charpy V-notch impact toughness superior to those of low carbon structural steels.

Economically welding steels without cracking while producing acceptable weld metal and heat-affected zone (HAZ) toughness has been the main priority. In other words, the challenge became the reduction of carbon equivalent (CE) values while attaining the required strength levels.

During the 1980's, the U.S. Navy developed microalloyed steels classified as HSLA-80 and HSLA-100 with the goal of reducing shipbuilding costs [13]. The purpose for the development of these HSLA-series steels was to achieve higher weldability without cracking and meet the performance required for the HY-series quenched and tempered steels, steels with improved strengths through the use of grain refining elements, such as niobium, vanadium, and titanium, and process controls. The chemical compositions of the HY- and HSLA-series steels are shown in Table 1. The most notable features of the HSLA-series are the reduction of carbon to 0.04 weight percent and sulfur to 0.005 weight percent and the increase of copper content to between 1.20 and 1.60 weight percent. Since carbon is the most influential element on the weldability of steels, the lower carbon contents of the HSLA-series steels makes them very weldable although the CE values are as high as those of the HY-series steels. The weldability diagram illustrating both HY- and HSLA-series steels is shown in Figure 1. As can be seen in this diagram, the HY-series steels are located in the "Difficult to Weld" Zone III; whereas the HSLA-series steels were shifted to the "Easily Weldable" Zone I due to the lower carbon content. The mechanical properties of the HSLA-series steel weldments are comparable to those of the HY-series weldments, primarily because copper precipitation

Table 1: The Chemical Composition of HY- and HSLA-Series Steels [13].

Steel	HY-80	HY-100	HSLA-80	HSLA-100
C	0.15	0.17	0.04	0.04
Mn	0.25	0.25	0.55	0.90
P	0.01	0.01	0.01	0.01
S	0.01	0.01	0.01	0.01
Si	0.25	0.25	0.30	0.25
Cr	1.40	1.40	0.70	0.60
Ni	2.70	2.90	0.90	3.50
Mo	0.40	0.40	0.20	0.60
Cu	0.01	0.05	1.20	1.60
Nb	—	—	0.04	0.03
V	0.01	0.01	—	—
B	—	—	—	—
CE	0.78	0.81	0.50	0.81

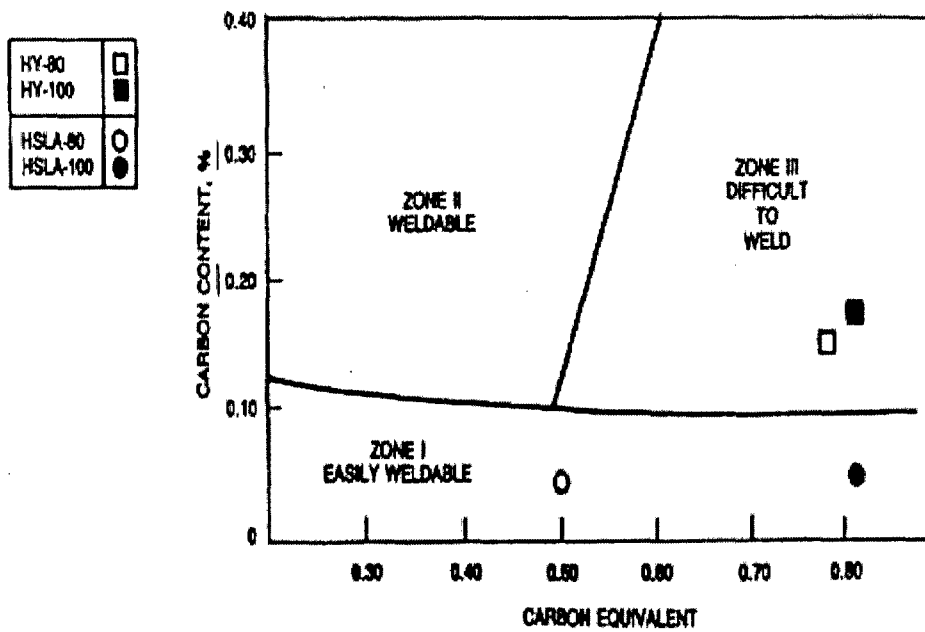


Figure 1: The weldability diagram illustrating HY- and HSLA-series steels [13].

strengthening in HSLA-steels increases strength to the level commonly found in HY-steels.

As the use of modern high strength steels increases in fabrication and manufacturing, the demands for consumables that produce higher strength and higher toughness weld metals also greatly increase. To obtain improved mechanical properties, the cleanliness, or low inclusion count, of the weld metal and the reduction of hydrogen content in the weld metal are important factors.

Inclusions are introduced into a weld metal primarily through reactions with oxygen from the atmosphere, and tend to deteriorate the toughness of the weld metal. It is well recognized that oxygen pickup in the steel weld metal can be controlled by adjustments of slag basicity [14, 15, 16]. Some early shielded metal arc welding (SMAW) steel electrodes developed during the 1920's already had highly basic coverings consisting of lime (CaO) and fluorspar (CaF_2), which continue to be used as base ingredients in low-hydrogen electrodes of modern manufacturing to produce welds with excellent mechanical properties [17].

The reduction of weld metal hydrogen content is another concern because an excess amount of hydrogen in the weld metal can result in cold cracking, or hydrogen-assisted cracking (HAC), a phenomenon that will be discussed more in depth in a later section. Since the HAC susceptibility of a steel increases as its strength increases, shielded metal arc welding (SMAW) steel electrodes designed to provide lower weld metal hydrogen levels, i.e. low hydrogen type electrodes have been developed since the 1940's [17]. The interesting feature of these electrodes is the addition of calcium carbonate (CaCO_3) instead of lime to the coatings. Calcium carbonate decomposes to CaO and CO_2 gas in the arc during welding so that the CaO produces a basic slag and the CO_2 gas dilutes the moisture in the arc atmosphere and shields the molten droplets, which results in lower hydrogen content in the weld metal.

Low hydrogen electrodes with iron powder added to the coatings have been successfully designed and commercialized. The E7018- and E7028-type steel electrodes,

for example, include approximately 30 and 50 percent iron powder, respectively. These electrodes exhibited excellent welding characteristics with six to eight percent higher efficiency than the conventional E7016 steel electrodes with lime and fluorspar. These electrodes also produced weld metal with satisfactory notch toughness to prevent crack propagation in ship structures at low temperatures so that they could be used for quenched and tempered steels such as T-1 and HY-80 grade. However, moisture pickup in these low-hydrogen electrodes caused porosity in weld metal. Therefore, electrode baking to remove any absorbed moisture from the atmosphere during storage and manufacturing became a necessary part of the welding process.

In addition to the microstructure and mechanical properties, improved weldability is also essential for better welding efficiency and reduced production costs. To avoid HAC, preheat may be required for high strength steel welding; however, because of its extra expense, fabricators and manufacturers demand crack-free welding with minimal or no preheat. One alternative to preheat would be the reduction of the weld metal diffusible hydrogen content. Current and recent research and development efforts have been focused on reducing weld metal hydrogen, and these effects will be discussed in later sections.

2.2 Effect of Alloying Elements

Carbon is a powerful strengthening agent in steel weld metal [18, 19]. However, excess carbon has a deleterious effect on notch ductility and toughness [19]. Carbon increases hardenability by stabilizing austenite. Work by Enis and Telford [20] found a linear relationship between carbon content and yield strength and a power function relationship between carbon content and toughness. They concluded that at higher strength levels, increasing the carbon content above 0.10 weight percent will further increase the strength only moderately while causing a severe decrease in toughness.

Manganese has been shown to increase the tensile strength and hardness [18-24]. In high strength steels, manganese additions up to 1.8 weight percent improve toughness; but further additions degrade toughness [22, 23] and have little effect on the yield strength. Dorsch and Stout [19] reported rapid degradation in toughness at manganese levels in excess of 1.6 weight percent. Some controversy exists concerning the optimal manganese content for high strength steel weld metal.

Silicon is added to weld metal primarily as a deoxidant for the control of porosity. Silicon, like oxygen, produces non-metallic inclusions in the weld metal and thus decreases hardenability due to the nucleation of ferrite. Silicon increases strength and decreases toughness [18, 19, 21]. Although the optimal silicon content will vary from one steel to another, it is generally agreed that contents in excess of 0.50 weight percent degrade toughness in the weld metal. Silicon increases the fluidity of the molten weld metal and improves weld bead characteristics [25].

Nickel is not a strong hardenability agent [19] and results in moderate increases in strength and hardness [25, 26]. Nickel is primarily added to steel weld metal to improve toughness [18-21, 26]. It has been reported [22] that nickel contents in excess of 2.5 weight percent can cause hot cracking for steel containing sulfur and phosphorus with yield strengths greater than 150 ksi (1030 MPa). Careful control of sulfur and phosphorus levels will help to minimize the likelihood of hot cracking, and steel weld metals with nickel contents of ten weight percent [18] have been successfully made. On the other hand, a loss of toughness can occur when the nickel content drops to below 1.5 weight percent. Nickel is especially effective in maintaining toughness at low temperatures.

Chromium is generally added to steel weld metal to increase hardenability and yield strength while decreasing toughness [27, 28]. It has been reported that chromium additions up to six weight percent increase strength [18]. Chromium promotes the formation of bainite and reduces softening during multiple-pass welding, and it is detrimental to weld metal toughness [27, 28]. General agreement exists that toughness is severely decreased in weld metal containing chromium concentrations of ten weight

percent or more [18, 25, 28]. Steels containing bainite, martensite, and small amounts of ferrite will experience a severe loss of toughness due to chromium [20] while in steels that are martensite, chromium has little effect on toughness [29].

Molybdenum is a more potent strengthener than manganese, silicon, nickel, or chromium [18, 19, 22, 29]. Molybdenum is similar to chromium in that it favors the formation of bainite and minimizes softening due to tempering during multiple-pass welding operations. Molybdenum is detrimental to toughness; however, the level at which it degrades toughness is not agreed upon in the literature. Heaschkel [18] found all additions of molybdenum to be detrimental to toughness. Others [30] report additions up to 0.6 weight percent will increase strength without impairing toughness. This data is close in agreement with Shackelton [25] who suggested the optimal molybdenum content to be 0.5 weight percent. The reason for these conflicting results is microstructurally based. Like chromium, molybdenum has a strong detrimental effect on toughness in steels containing ferrite, bainite, and martensite and has little or no effect on strength and toughness on fully martensitic steels.

Titanium is added for its strong deoxidation capability and for grain refinement [31-34]. In small amounts, approximately 0.01 to 0.025 weight percent, titanium is beneficial to both strength and toughness [19]. Recent work [35-37] has shown that titanium is associated with intragranular nucleation of acicular ferrite, and thus improves toughness. Titanium in excess of 0.030 weight percent has been shown to degrade toughness by grain boundary embrittlement. Careful control of the weld metal titanium content is necessary to take advantage of strength and toughness improvements while avoiding grain boundary embrittlement [37].

Aluminum has been used as a deoxidant in steel production and in steel welding electrodes [25, 38, 39]. Aluminum has been shown to increase strength and decrease toughness in high strength steel weld metal [23]. Because the effects of aluminum on strength and impact toughness are less consistent than those of titanium, titanium is a preferable addition to high strength steel weld metal [25].

2.3 Weld Metal Microstructural Development

Steel weld metal microstructures develop through solidification and subsequent austenite decomposition. Compositional variation of a weld metal is a result of solidification which affects the local hardenability and may result in a cored microstructure. This section will discuss weld metal solidification and the subsequent solid-state decomposition of austenite leading to microstructural development.

2.3.1 Weld Metal Solidification

The development of the weld metal microstructure begins with solidification. Reviews by Davies and Garland [40] and David and Vitek [41] provide a comprehensive overview of the microstructural development in fusion welding. Much of the knowledge base regarding weld metal solidification was developed through studies on solidification in castings; however, there are significant differences that are expected to modify the behavior of weld deposits. For example, the welding process involves very rapid localized melting and cooling. The cooling rates experienced by weld deposits of conventional welding processes such as SMAW, GMAW, and SAW are on the order of 10 to 10^3 degree Celsius per second as compared to the 10^{-2} to 10^2 degrees Celsius per second experienced by castings. Fluid flow behavior is also expected to be different. Unless artificial stirring occurs, fluid flow in casting is primarily controlled only by buoyancy effects, whereas fluid flow behavior in the weld metal is controlled by buoyancy effects as well as by electromagnetic and surface tension forces. Variations of temperature across either the weld pool or the casting result in variation in liquid density, which cause convective fluid flow, i.e. the buoyancy effect. In addition to convective fluid flow, the molten weld pool is subjected to electromagnetic effects from the welding arc that result from the interaction between the divergent current path and resultant magnetic fields. Electromagnetic forces are approximately opposite of those due to the

buoyancy forces. The surface tension of the molten weld metal is dependent upon temperature and composition. The temperature variation across the weld pool surface results in gradients in surface tension. The compositional variations across the surface of the weld pool also affect the surface tension. In pure iron, the surface tension decreases as temperature increases, which results in an outward flow away from the arc, tending to promote a broad weld pool with low penetration. Surface active impurities such as oxygen and sulfur result in a positive temperature coefficient of surface tension, such that surface tension increases as temperature increases. This reversal in the temperature coefficient of surface tension promotes an inward flow along the surface, toward the center of the arc, promoting deeper penetration.

The grain structure of the fusion zone is largely dependent on that of the base metal heat-affected zone. Since melting of the base metal occurs during the welding process, there is always a region of solid in contact with the molten weld pool. In most welding applications, the base metal and molten weld pool have similar compositions, and epitaxial growth from the partially melted grains at the fusion line occurs. Thus a coarse-grained HAZ will promote a coarse-grained structure in the weld metal, and a fine-grained HAZ will promote a fine-grained structure.

Low-carbon and low-alloyed steel weld deposits will begin to solidify as bcc δ -ferrite at temperatures around 1500 degrees Celsius. In more highly alloyed weld deposits, or during an extremely high cooling rate, as may be experienced with electron beam or laser welding, the liquid may solidify directly as austenite. The solidifying grains tend to grow in the direction of the maximum thermal gradient; although both bcc δ -ferrite and fcc austenite have preferential growth along the $\langle 100 \rangle$ directions, so solidification tends to proceed along the easy-growth direction that is most favorably oriented with the thermal gradient. The grains that are most favorably oriented will grow rapidly, and will eventually inhibit the growth of less favorably oriented grains. Upon further cooling, austenite will form either within the δ -ferrite grains or at the δ -

ferrite/liquid interface as schematically shown in Figure 2. Figure 2(a) illustrates the case in which the material solidifies completely to δ -ferrite, then transforms to austenite in the solid state. In Figure 2(b) and (c), austenite forms in the boundaries between the δ -ferrite and liquid iron. Figure 2(d) illustrates the case in which the material solidifies initially as austenite.

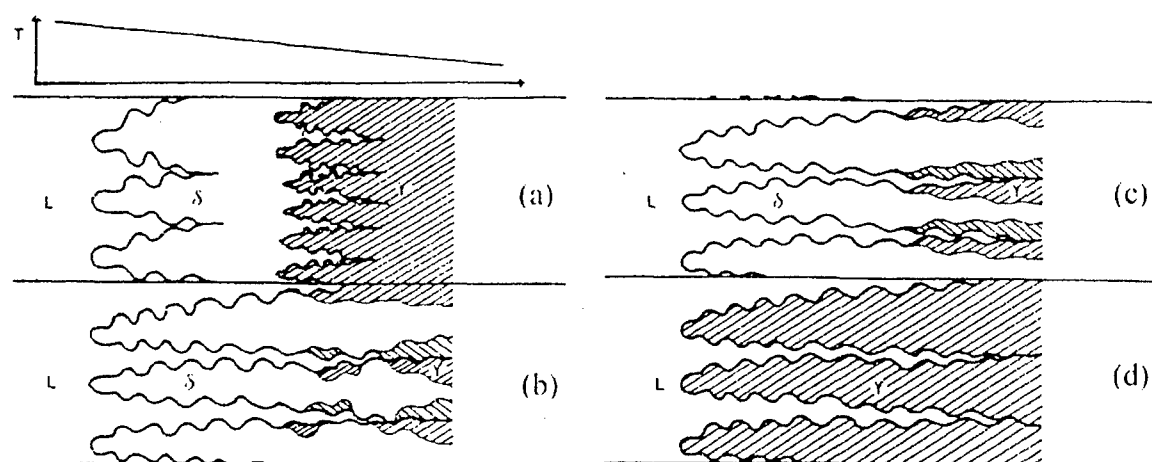


Figure 2: Different solidification principles in an iron-based alloy [42].

For welds made at low-to-moderate speeds, the two-dimensional appearance of the weld pool forms an ellipse, as illustrated in Figure 3(a) and the corresponding isotherms are elliptically shaped. Under these conditions, no one grain experiences a favored growth throughout solidification, so more of the fusion-line-nucleated grains survive to reach the center of the weld. Furthermore, any grain that survives over any great distance in an elliptical weld pool exhibits significant curvature. While the crystallographic orientation of the curved grain does not change, the curvature is generated by repeated side-branching of the solidification substructure. As for welds made at higher travel speeds, a tear drop shape weld pool forms as shown in Figure 3(b).

The direction of the thermal gradient means that those grains growing in the most favorable orientation will continue to grow and widen, at an optimal speed across the weld deposit. This growth behavior results in fewer grains surviving to reach the centerline of the weld.

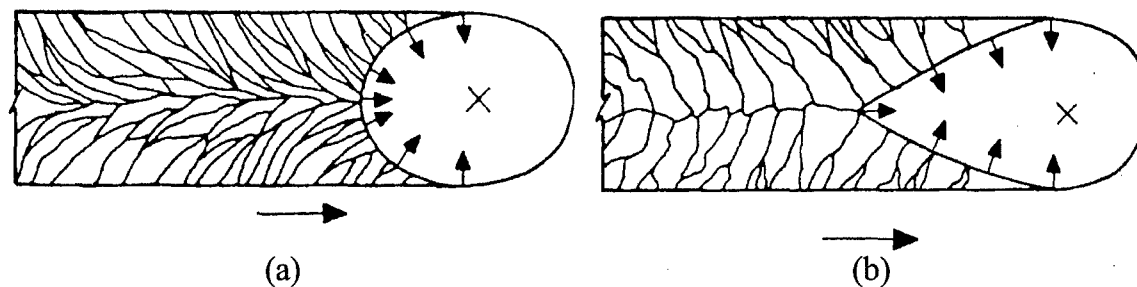


Figure 3: Two dimensional appearance of the weld pool showing the columnar development in (a) an elliptical weld pool where the progressive change in direction of the maximum thermal gradient is reflected by the survival of many more columnar grains, and (b) a tear drop shaped weld pool where the direction of the maximum thermal gradient is almost invariant along the edge of the pool [40].

The change in the weld pool shape from elliptical to tear drop occurs due to the minimal thermal gradient along the weld centerline. The growth rate, or solidification rate, along the edge of the weld is related to the travel speed of the heat source by Equation 1:

$$|R_s| = |R_H| \cos \theta, \quad (1)$$

where R_s is the growth rate of the solidification front, R_H is the travel speed of the heat source, and θ is the angle between the surface normal on the edge of the weld pool and the welding direction. From Equation 1, the maximum solidification rate occurs along the weld center line; and correspondingly, the maximum rate of dissipation of latent heat also

occurs along the weld centerline. The maximum heat input and peak temperatures are associated with the welding arc; therefore, the higher temperatures, located along the centerline in the solid immediately behind the weld pool, cause less efficient heat transfer and minimal thermal gradient. A critical growth rate exists beyond which the minimal thermal gradient cannot dissipate the generated heat of fusion rapidly enough, so the weld pool takes on an elongated, tear drop shape.

Within the primary columnar-shaped grains of the weld structure, there is a substructure divided by small-angle grains [43]. The mode of substructure development is dependent upon the extent of undercooling, which is the difference between the liquidus temperature based on the nominal composition of the weld pool and its actual temperature. The total undercooling is given by Equation 2 [44]:

$$\Delta T = \Delta T_{TH} + \Delta T_C + \Delta T_R + \Delta T_K, \quad (2)$$

where ΔT_{TH} is the thermal undercooling, ΔT_C is the constitutional undercooling, ΔT_K is the kinetic undercooling, and ΔT_R is the undercooling due to the curvature at the solid/liquid interface. Since weld metal microstructures generally grow epitaxially from the partially melted base metal microstructure, thermal undercooling in welds, which is associated with the barrier to nucleation, is small and is generally ignored. The effect of kinetic undercooling, which is associated with the rate at which atoms become attached to the solid forming, is small and normally ignored in welding processes. The increased surface area and associated increase in surface energy associated with the curved interface locally suppresses the liquid-to-solid transformation temperature. The effects of undercooling due to curvature, which is related to the increase in surface area associated with the formation of solidification front, can be significant in weld solidification. As the δ -ferrite forms, solute atoms are rejected into the remaining liquid in advance of the solidification front. Since this material is higher in alloy content, the solid and liquid at

the interface will have a lower melting point than the bulk weld pool, a phenomenon referred to as constitutional undercooling, and is normally the most significant form of undercooling in weld deposits. The extent of undercooling determines the morphology of the solidification front. With a small degree of undercooling, cellular growth is expected, whereas, a high degree of undercooling is expected to form a dendritic solidification front.

The effect of the primary solidification mode on inclusion distribution has been investigated by Sudgen and Bhadeshia [45] and Kluken et al. [46]. Sudgen and Bhadeshia proposed that since the distribution of inclusions is determined during solidification while they are mobile, they may be pushed by the solid/liquid interface, perhaps to the columnar grain boundaries. For steels solidifying completely as δ -ferrite, the subsequent austenite transformation would cause the inclusions to end up near the center of the columnar grains, as seen Figure 4(a). In the center of the grains, the inclusions serve as potential nucleation sites for intragranularly nucleated acicular ferrite. In contrast, if solidification occurs such that austenite is the primary phase, then the inclusions would tend to remain at the austenite grain boundaries, as seen in Figure 4(b). Not only would these inclusions no longer be effective heterogeneous nucleation sites for acicular ferrite, but they would coincide with the formation of grain boundary ferrite. These grain boundary inclusions could potentially initiate fracture, and the grain boundary ferrite would offer minimal fracture propagation resistance. Sudgen and Bhadeshia produced a series of carbon-manganese SMA welds designed to produce welds with primary δ -ferrite and welds with primary austenite solidification. They observed that inclusions one to three microns in diameter tended to concentrate along the grain boundaries of the initial solidification phase and attributed this to either the surface tension effect at the solidification front, the Marangoni effect, or the pushing of the inclusions by the solid-liquid interface.

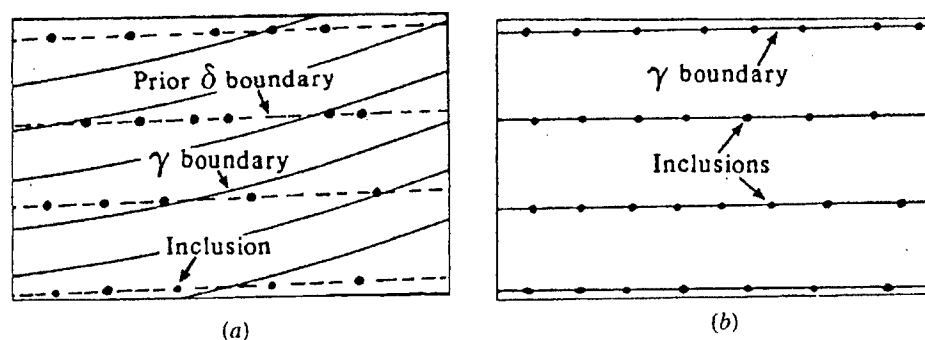


Figure 4: Schematic diagram showing the location of inclusion in the microstructure of a weld for solidification as (a) δ -ferrite and (b) austenite, assuming that the inclusions locate themselves preferentially at the cell boundaries and austenite boundaries diverge, because in arc welding, the heat source is not stationary [45].

Kluken et al. [46] proposed that inclusions influence the primary solidification structure by serving as heterogeneous nucleation sites for austenite ahead of δ -ferrite solidification front. In welds with low aluminum-to-oxygen ratios, $[Al]/[O]$, austenite was observed to experience epitaxial growth at the boundaries of the primary δ -ferrite, as shown in Figure 5(a). As the $[Al]/[O]$ ratios increase, nucleation of austenite on the inclusions becomes more favorable. When the chemical composition for precipitation of pure Al_2O_3 occurs at an $[Al]/[O]$ ratio of 1.13, primary nucleation of austenite in the interdendritic liquid was observed, as shown in Figure 5(b). Under these conditions, the austenite is not bound by an orientation relationship with the δ -ferrite, which facilitates growth of the austenite grains across the primary δ -ferrite phase. Kluken, et al. [46] proposed that this change in the peritectic reaction is related to the nucleation potency of the oxides. The nucleation potency of the oxides increases in the order of SiO_2 - MnO , Al_2O_3 - Ti_2O_3 - SiO_2 - MnO , Al_2O_3 , reflecting a corresponding increase in the inclusion/liquid interfacial energy. It was proposed that this change in the peritectic reaction may alter the subsequent solid-state transformation reactions by promoting growth of Widmanstätten ferrite sideplates at the expense of intragranularly nucleated

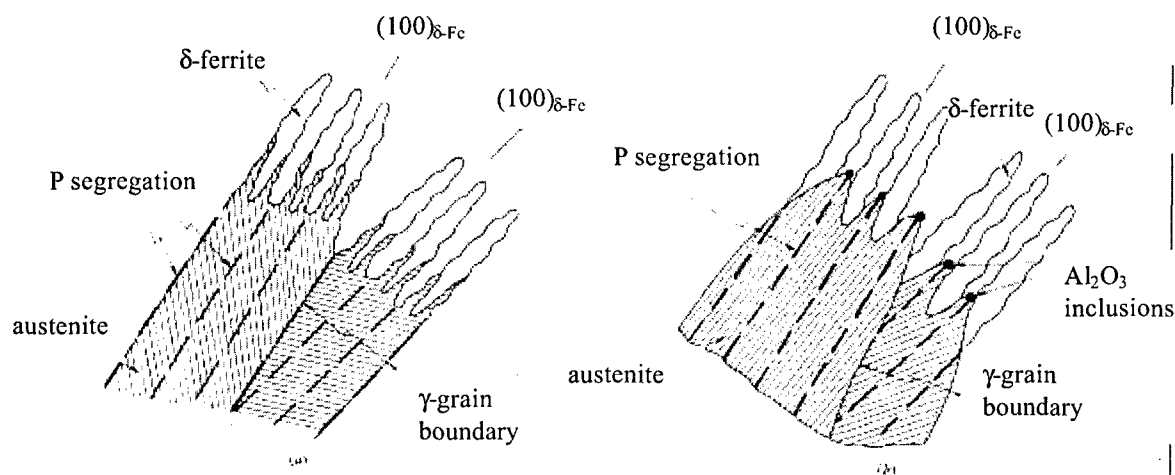


Figure 5: Effect of deoxidation practice on the δ -ferrite to austenite transformation in Al-Ti-Si-Mn deoxidized steel welds. (a) Growth of austenite along the boundaries of the primary δ -ferrite phase, and (b) growth of austenite across the boundaries of the primary δ -ferrite phase [46].

acicular ferrite. Heterogeneous nucleation of austenite on inclusions promotes the growth of austenite grains across phosphorus-rich boundaries of the primary δ -ferrite because phosphorus has been shown to raise the local A_{c3} temperature. In the absence of phosphorus, sideplates nucleate directly from the grain boundaries and grow rapidly across the austenite grains, inhibiting acicular ferrite formation.

The distribution of inclusions, particularly those forming at temperatures above the liquidus, may be influenced by their interaction with the solid/liquid interface. When the solidification front intercepts an insoluble particle, it either pushes or engulfs it. In many studies of the interaction of foreign particles with advancing planar solidification fronts in water and organic materials, it has been shown that particles are pushed at low growth velocities [47-50]. Uhlmann, et al. [50], Omenyi, et al. [51], and Neumann, et al. [52] explained the pushing based upon short-range repulsive forces occurring when the particle/solid interfacial free energy is greater than the sum of the particle/liquid and liquid/solid interfacial energies. Ciccè and Bolling [48] developed a theory where the

trapping of inert particles by the advancing solidification front was primarily due to viscous drag. Both theories conclude that there is a critical growth velocity of the solidification front below which particles are rejected.

In summary, it is apparent that the microstructural development of the weld metal is influenced by a number of important variables affecting solidification including complex fluid flow due to natural convection, variations in surface tension, electromagnetic forces, and arc pressure forces.

2.3.2 Inclusion Characteristics and Development

During arc welding processes, the high arc plasma temperatures in excess of 10,000°C results in the dissociation of oxygen in the shielding gas or arc atmosphere. The dissociated oxygen is absorbed into the weld pool. As the welding arc passes and the weld pool cools, from an initial molten state then a solid state, the solubility of oxygen decreases and is removed as oxygen-rich phases and compounds. Oxygen is expected to react with a variety of elemental species present in the weld metal: carbon, iron, silicon, manganese, titanium, aluminum, and yttrium in this study. To reduce weld metal porosity, deoxidizing elements such as silicon, manganese, titanium, aluminum, and yttrium are added to the filler metal to react with oxygen.

The presence of nonmetallic inclusions can have a profound effect on weld metal microstructure and properties. Tweed and Knott [53] and Almond, et al. [54] have demonstrated that oxides may be detrimental to weld metal toughness through the initiation of brittle fracture. In contrast, the optimal weld metal toughness is not associated with very low oxygen levels. The presence of significant volume fractions of intragranularly nucleated acicular ferrite has been demonstrated by numerous researchers to significantly improve the toughness of low alloy steel weld deposits. It is generally agreed that the development of acicular ferrite is promoted by heterogeneous nucleation on nonmetallic inclusions. Inclusions may also promote acicular ferrite formation through

Zener pinning of prior austenite grain boundaries, where larger prior austenite grains promote a larger content of acicular ferrite.

The solubility of oxygen in pure liquid iron is 1600 ppm at 1527°C, the eutectic temperature [55], and approximately 8000 ppm at 2200°C [56]. This solubility decreases to 82 ppm in δ -ferrite upon solidification and the maximum solubility of oxygen in γ -iron is 28 ppm at the peritectic invariant at 1390°C. In the presence of deoxidizing elements such as silicon, manganese, and aluminum, the equilibrium level of oxygen in liquid iron at the melting point is reduced to very low levels, and upon cooling, a supersaturation with respect to the products of various oxidation reactions occurs, providing the driving force for the nucleation of oxides. Typical GMA and FCA steel weld metals contain 200 to 400 ppm of oxygen, primarily in the form of micron-sized oxide inclusions, with oxide densities in the range of 10^7 to 10^8 oxides per cubic millimeter. The remainder of the dissolved oxygen from the molten weld pool will have been removed as slag.

Kluken and Gröng [57] modeled inclusion formation in Al-Ti-Si-Mn deoxidized steel weld metals. They considered the weld pool to be divided into two regions: hot and cold, as illustrated in Figure 6, where they proposed that inclusions form in the hot region under the arc and growth occurs in the cold region at a temperature near the liquidus. Inclusion nucleation occurs homogeneously as a result of supersaturation established during cooling. Deoxidation proceeds by a diffusion-controlled process in the molten weld metal and is essentially complete when the liquid metal temperature attains a relatively constant value, near the melting point of the steel, in the trailing edge of the weld pool.

Based upon a simplified model of Turpin and Elliot [59], the required temperature difference ($T_1 - T_2$) necessary to achieve spontaneous precipitation of an oxide (M_xO_y) is approximately given by Equation 3:

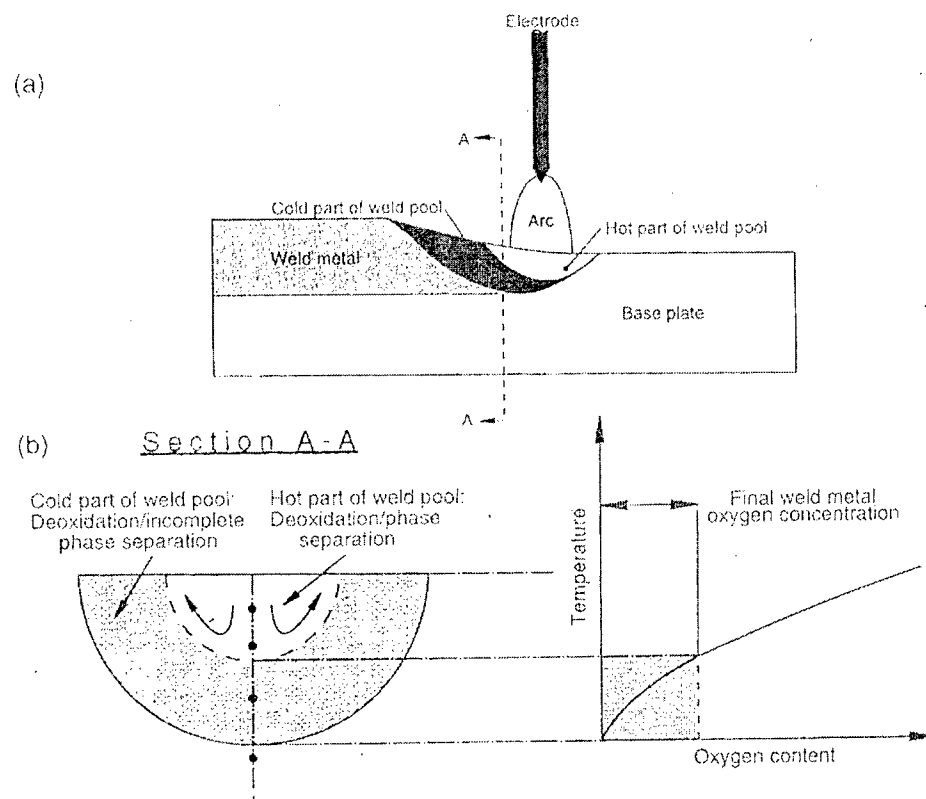


Figure 6: Schematic diagrams showing the sequence of reactions occurring during weld metal deoxidation and their relationship to the hot and cold regions of the weld pool; (a) longitudinal section of section of weld pool, and (b) cross section of weld pool along A-A [58].

$$T_1 \approx \frac{T_2^{1.5} \Delta H^o}{\left(T_2^{0.5} \Delta H^o\right) - \left(1.48 \times 10^{11} \gamma^{1.5} V_m\right)}, \quad (3)$$

where ΔH^o is the standard enthalpy of reaction; γ is the oxide-steel interfacial energy, assumed to be constant and independent of temperature; and V_m is the molar volume of the nuclei. Using Equation 3, Klukun and Gröng [57] estimated the undercooling required for homogeneous nucleation of $\text{FeO}_{(l)}$, $\text{SiO}_{2(s)}$, and $\text{Al}_2\text{O}_{3(s)}$ is on the order of 200°C to 300°C. It is reasonable to assume the actual temperature interval of undercooling required for spontaneous oxide precipitation in a weld metal is less than 200°C. Based upon these estimated undercoolings, the authors concluded it is reasonable for nucleation of oxide inclusions to occur readily during cooling, since the liquid weld metal spans a temperature range of about 2200°C to 1500°C.

Klukun and Gröng [57] considered three major growth processes: collision, diffusion, and Ostwald ripening. They excluded particle growth by collision, since there is a low probability of inclusion collision while ascending in the molten steel within the regime of Stokes' law. They also excluded particle growth by diffusion since the diffusion-controlled deoxidation process is expected to be complete within a fraction of a second when the number of nuclei is greater than $10^8/\text{mm}^3$. Therefore, they concluded that the primary growth mechanism is Ostwald ripening, which occurs in the cold portion of the weld pool where inclusion growth can be treated as an essentially isothermal process. Under these conditions, the time dependence of the mean particle diameter (\bar{d}) is approximately given by Wagner Equation 4:

$$\bar{d}^3 = \bar{d}_o^3 + \frac{64\gamma DCV_n^2}{9RT} t \approx kt, \quad (4)$$

where \bar{d}_o is the initial particle diameter, γ is the oxide-steel interfacial energy, D is the element diffusivity, C is the bulk concentration of the diffusing species, V_n is the molar volume of the oxide per mole of diffusate, and t is the retention time. Kluken and Gröng [57] showed that the three-dimensional inclusion diameters of several experimental Al-Ti-Si-Mn deoxidized steel weld metals versus the cube root of the retention time could be represented by a straight line, supporting their supposition that oxide growth occurs by Ostwald ripening.

Using data obtained by Widgery [71] and Terashima and Hart [72], Gröng and Matlock [31] showed that, as the average inclusion diameter of a weld increases, the total number of inclusions tends to decrease indicating that once deoxidation is complete, weld metal oxides may continue to grow through a coagulation of smaller particles into larger ones. Kluken and Gröng [57] attributed this growth to Ostwald ripening, and excluded particle growth by collision and diffusional growth.

Hsieh et al. [44] evaluated inclusion formation in low alloy steel welds using equilibrium thermodynamic calculations to predict the sequential formation of inclusions. Unlike earlier models, their model considered the effects of depletion of alloying elements due to inclusion formation on oxide stability. Thermodynamic relationships between complex oxides were determined by use of ThermCalc™ software, which can be used for calculating multi-phase equilibria in a multi-component system. The methodology developed by Scheil [60] was used to model progressive changes in weld metal composition as oxidation proceeds. This approach assumed no diffusion in the solid and perfect mixing in the liquid. At any given temperature, T_l , the mass balance for a given species is given by Equation 5:

$$\bar{C}_l = f_s^l C_s^l + (1 - f_s^l) C_L^l, \quad (5)$$

where \bar{C}_1 is the bulk elemental concentration, f_s^1 is the mass fraction of solid oxide formed, C_s^1 is the composition of the element in the oxide which forms at T_1 , and C_L^1 is the composition of the liquid in equilibrium with the oxide at the temperature of interest.

Hsieh, et al. [44] adapted the mass balance given in Equation 5 to the case of continuous cooling by considering the composition of the liquid remaining at a given temperature, T_1 , and using this composition to determine the thermodynamic considerations at the next temperature step, T_2 . The overall composition at T_2 is thus given by Equation 6:

$$\bar{C}_2 = C_L^1 \text{ at } T=T_2 \text{ where } T_2 < T_1, \quad (6)$$

and the mass balance at T_2 is given by Equation 7:

$$\bar{C}_2 = f_s^2 C_s^2 + (1 - f_s^2) C_L^2, \quad (7)$$

where f_s^2 is the fraction of oxide formed at T_2 from the residual liquid present after oxide formation at T_1 , and \bar{C}_2 is the overall composition of the liquid prior to oxide formation at T_2 . Hsieh, et al. found reasonably good correlation between predicted average inclusion composition and measured values, and they attribute the difference to several potential factors. The calculation methods do not consider the kinetics of inclusion formation and, while complex oxides may be thermodynamically favorable, the kinetics of formation of the oxides may be sluggish. The model also did not include precipitation of MnS or TiN below the liquidus.

Babu, et al. [56, 61, 62] considered the kinetic aspects of inclusion formation and growth by using the theories of transformation kinetics described by Christian [63]. Christian addressed transformations with parabolic growth laws, and his concepts have

been extended to continuous weld metal cooling by using incremental time steps, assuming that the overall extent of reaction is represented by the summation of the incremental steps. The model has been coupled with computer determination of thermodynamic phase stability to predict the kinetics of oxide formation.

Nucleation of oxides may occur homogeneously in the melt or heterogeneously on pre-existing surfaces. For simplicity, Babu considered homogeneous nucleation for the first oxides to form. Following the methodology used by Turpin and Elliot [59], the nucleation rate of an oxide is given by Equation 8:

$$I_{\text{hom}} = A \exp \left(\frac{-\Delta G_{\text{hom}}^*}{kT} \right), \quad (8)$$

where ΔG_{hom}^* is the activation energy for formation of the oxide nucleus, which is the free energy of activation for short range diffusion of atoms or molecules moving a fraction of an atomic distance across an interface to join a new lattice; T is the temperature in Kelvin; k is the Boltzmann's constant; and A is the pre-exponent factor, which is related to the number of surface atoms in the critical nucleus [64]. The value of A is generally taken to be $10^{33} \text{ m}^{-3} \text{ s}^{-1}$ [65].

The activation energy for homogeneous nucleation is derived from the work to form a nucleus of a second phase and is given by Equation 10 [59]:

$$w = 4\pi r^2 \gamma + \frac{4}{3}\pi r^3 \left(\frac{\Delta G}{V} \right), \quad (9)$$

where r is the particle radius, V is the molar volume, γ is the surface energy between the liquid and inclusion, and ΔG is the bulk free energy change between the liquid and the oxide. There is an energy balance between the decrease in free energy associated with the

precipitation of the oxide and the increase in free energy due to the formation of a new surface. The critical radius, r^* , occurs when $dw/dr = 0$ and is given by Equation 10:

$$r^* = \frac{-2\gamma V}{\Delta G} \quad (10)$$

The activation energy for the formation of an oxide nucleus, ΔG_{hom}^* , is the work to form a nucleus of a second phase particle with the critical radius r^* and is given by Equation 11:

$$\Delta G_{\text{hom}}^* = \frac{16\pi\gamma^3 V^2}{3(\Delta G)^2} \quad (11)$$

ΔG_{hom}^* is actually the Helmholtz free energy; however, Turpin and Elliot [59] indicate that for the processes involved, the difference between Gibbs and Helmholtz free energy is negligible. Since the Gibbs free energy is more easily calculated from available thermodynamic data, it is used rather than the Helmholtz free energy. Babu, et al. [62] assumed a constant value of 0.5 Joules per square meter for the surface energy of the various oxides in liquid steel.

Following nucleation of the initial oxide, subsequent nucleation is assumed to occur heterogeneously, with a rate of nucleation given by Equation 12:

$$I_{\text{het}} = Bf(\theta)^{1/6} \exp\left(\frac{-\Delta G_{\text{het}}^*}{kT}\right), \quad (12)$$

where B is a frequency factor, ΔG_{het}^* is the activation energy of heterogeneous nucleation, and $f(\theta)$ is a function of the contact angle of the nucleus on the substrate. The value of ΔG_{het}^* determined by Equation 13:

$$\Delta G_{het}^* = \Delta G_{hom}^* f(\theta), \quad (13)$$

And Equation 14:

$$f(\theta) = \frac{1}{4}(2 + \cos \theta)(1 - \cos \theta)^2. \quad (14)$$

Babu, et al. [62] considered the growth of inclusions based upon the diffusion of oxygen, assuming that the model developed by Zener [66] for the growth of spherical precipitates from solid solution is applicable to diffusion controlled growth of inclusions in liquid steel. For this, the following assumptions are required:

1. At the start of growth, oxygen and deoxidizers are assumed to be in solution homogeneously.
2. The nuclei that form are spherical, uniform size, and growing without interaction between other oxides. This requires that the bulk concentration of the liquid remains constant and that there is no overlapping of diffusion fields.
3. There is local equilibrium at the precipitate/matrix interface.
4. The interface growth rate can be determined by the oxygen flux alone. This requires pseudo-steady-state conditions where the ratio of the flux of the deoxidizing element to that of oxygen is given by stoichiometric ratio of these components in the oxide.

Under the above conditions, the relationship between the velocity of the growing interface and thickening rate is given by Equation 15:

$$v = \frac{dr}{dt} = \frac{d}{dt} (\alpha_3^* D_o \sqrt{t}), \quad (15)$$

where α_3^* is the parabolic thickening rate constant, D_o is the diffusivity of oxygen in liquid iron, and t is time. Zener [66] developed an approximate solution, represented by Figure 7, for the three-dimensional thickening rate constant corresponding to the conditions in Equation 16:

$$(C_M^l - C_M^{il}) / (C_M^i - C_M^{il}) \ll 1, \quad (16)$$

where the depletion of the solute atoms extends to a large distance compared to the radius of the precipitate. Under these conditions, the thickening rate constant is given by Equation 17:

$$\alpha_3^* = \left[2 \left(\frac{C_M^l - C_M^{il}}{C_M^i - C_M^{il}} \right) \right]^{1/2}, \quad (17)$$

where C_M^l is the nominal concentration of deoxidizer element in the liquid far away from the inclusion/liquid interface, C_M^i is the concentration of deoxidizer element in the inclusion, and C_M^{il} is the equilibrium concentration of the deoxidizer at the inclusion/liquid interface.

Babu, et al. [62] coupled the nucleation and growth rate equations by applying the theory of overall kinetics for precipitation from a supersaturated solution as described by

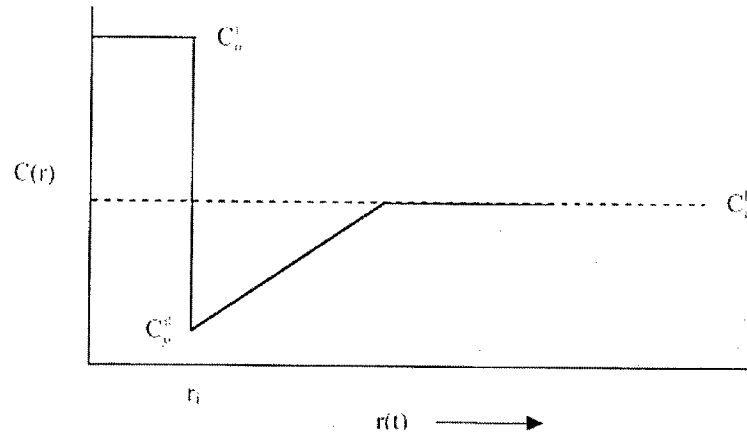


Figure 7: Schematic illustration of composition profile ahead of inclusion during growth [9].

Christian [63] where the growth rate is controlled by long-range diffusion. For a spherical particle that is nucleated at time τ , the volume at time t is given by Equation 18:

$$v(t) = \frac{4\pi}{3} (\alpha_3^*) D^{\frac{3}{2}} (t - \tau)^{\frac{3}{2}}. \quad (18)$$

For a linear growth process in which the nucleation is effectively randomly distributed throughout the assembly, the fraction transformed is assumed to be Equation 19:

$$\xi = 1 - \exp \left[- \int_0^t v(t) I^{vol} d\tau \right]. \quad (19)$$

However, for a diffusion-controlled process, ξ cannot be defined as the fraction of the whole assembly that has transformed. If the equilibrium volume of the oxide phase is given by V^f in an assembly of volume V , conservation of solute atoms requires Equation 20:

$$\frac{V^i}{V} = \left(\frac{C_M^i - C_M^{il}}{C_M^i - C_M^{il}} \right). \quad (20)$$

The total volume of precipitate can be written as $V^i(t)$, and the volume fraction transformed is given by Equation 21:

$$\xi = \frac{V^i(t)}{V^i} = \frac{V^i(t)}{V} \left(\frac{C_M^i - C_M^{il}}{C_M^i - C_M^{il}} \right), \quad (21)$$

which for the case of impingement through nucleation results in Equation 22:

$$\xi = 1 - \exp \left[- \left(\frac{C_M^i - C_M^{il}}{C_M^i - C_M^{il}} \right) \int_0^t v(t) I^{vol} d\tau \right], \quad (22)$$

where ξ is the extent of oxide formation at a given temperature, and I^{vol} is given by Equation 8. If τ is assumed to be negligible and a constant nucleation rate is assumed, Equation 22 can be integrated to give Equation 23:

$$\xi = 1 - \exp \left[- \left(\frac{C_M^i - C_M^{il}}{C_M^i - C_M^{il}} \right) I^{vol} \left(\frac{8\pi}{15} \right) D^{\frac{3}{2}} (\alpha_3^*) t^{\frac{5}{2}} \right]. \quad (23)$$

To calculate the overall kinetics during weld cooling, an estimate of the cooling curve is required. Ion, et al. [67] developed an analytical equation to describe the temperature profile based upon the Rosenthal equations [68], but modified them by assuming a circular disk heat source of radius r_B . The temperature variation in a weld as a

function of welding parameters, location in the transverse section (y,z) , and time is given by Equation 24:

$$T = T_o + \frac{\eta \left(\frac{q}{v} \right)}{2\pi\lambda [t(t+t_o)]^{0.5}} \exp \left\{ -\frac{1}{4a} \left[\frac{(z+z_o)^2}{t} + \frac{y^2}{(t+t_o)} \right] \right\}, \quad (24)$$

where

$$t_o = \frac{(r_B)^2}{4a}, \quad (25)$$

and

$$(z_o)^2 = \left[\frac{r_B}{e} \left(\frac{\pi a r_B}{v} \right)^{0.5} \right]. \quad (26)$$

The coordinate system is as defined in Figure 8. The radius of the heat source is r_B , a is the thermal diffusivity, λ is the thermal conductivity, $\eta(q/v)$ is the heat input, and T_o is the preheat temperature.

Figure 9 outlines the calculation steps of the overall inclusion model. To apply Equation 19 to continuous cooling conditions, the extent of the reaction given by Equation 16 is assumed to be additive. The calculation starts with the development of a cooling curve for the welding variable using Equations 24, 25, and 26. Even though the expression developed by Ion, et al. [67] is not valid for the liquid weld metal, this cooling rate equation reasonably approximates the liquid weld metal cooling curve above the liquidus. Furthermore, since Equation 24 considers only conductive heat transfer, the

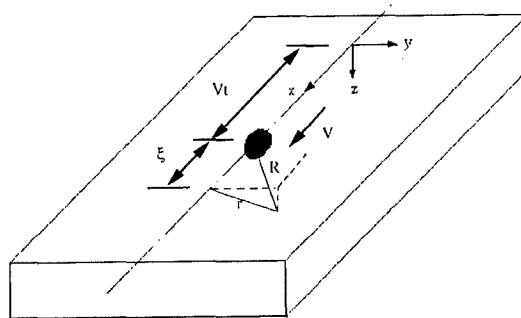


Figure 8: Welding geometry coordinate system for temperature profile model developed by Ion, et al. [67].

convective heat transfer was considered by including an enhanced thermal conductivity. A time step, Δt , and corresponding temperature interval, ΔT , are set. For each time step/temperature interval, the following values are calculated: 1) the mole fraction and activities of the various constituents; 2) the free energy of formation of potential compounds and equilibrium concentrations for the various constituents in equilibrium with the compounds; 3) the nucleation rate, Equation 8, the growth rate, Equation 18, and the extent of reaction, Equation 23, for each phase. This procedure is repeated for each time/temperature step, using the cumulative volume fraction formed, until a particular oxide reaction reaches ninety percent completion. Once the most stable phase reaches ninety percent completion, the final number density of oxides is set to the integrated nucleation rate for the first forming phase, given by Equation 27:

$$\text{Number Density} = \sum_{i=T_{start}}^{i=T_{end}} I_{oxide}^{vol} t_i \quad (27)$$

The liquid phase concentrations are then reset to new levels, taking the completion of the first oxide reaction into account. The extent of reaction of other phases is then calculated based upon heterogeneous nucleation, Equation 12. As each new phase reaches

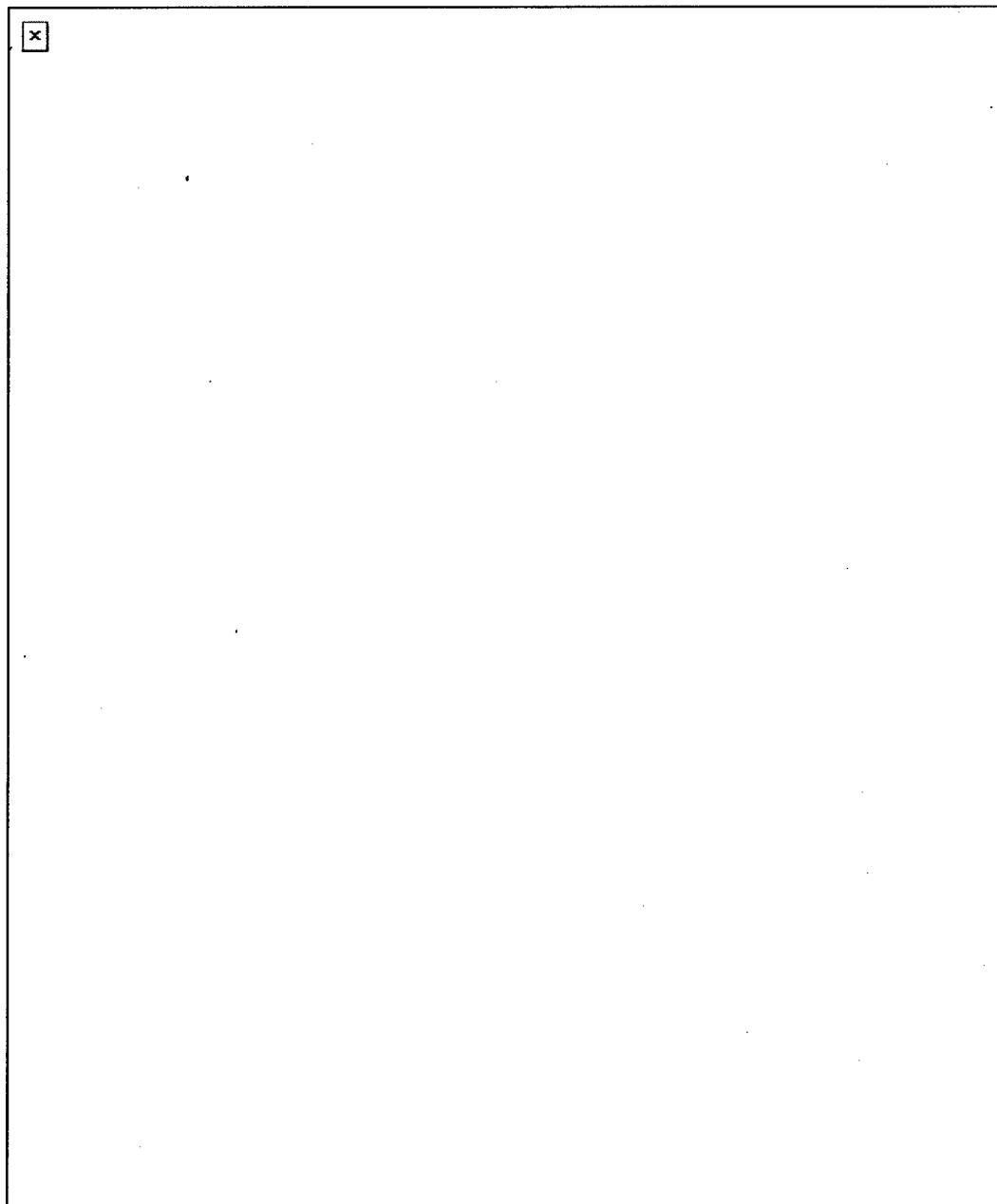


Figure 9: Flow chart of integrated inclusion model showing calculation steps [62].

completion, the liquid concentrations are reset to new levels. The procedure is then repeated until the temperature reaches 1800K.

Olson, et al. [69] and Frost, et al. [70] considered the effects of partition behavior of solute elements on inclusion formation during solidification. During alloy solidification, a compositional profile develops in the liquid ahead of the solid-liquid interface. This segregation is expected to influence inclusion formation, particularly during cellular/dendritic solidification. For alloy solidification, it is useful to define the equilibrium partition coefficient, κ , of a specific solute element as the ratio of the solute concentration of the solid, C_s , to that of the liquid at the solid-liquid interface, C_l , given in Equation 28:

$$\kappa = \frac{C_s}{C_l} \quad (28)$$

For the case of no diffusion in the solid and complete mixing in the liquid, the solute accumulation ahead of the solid-liquid interface is given by Equation 29:

$$C_l = C_o f_L^{\kappa-1}, \quad (29)$$

where C_o is the bulk solute concentration of the weld pool and f_L is the fraction of liquid remaining. Since κ is less than one for most solutes, the interdendritic liquid will have a higher solute content than the bulk material resulting in segregation of typical inclusion forming species to the interdendritic regions.

Frost, et al. [70] considered the deoxidation process for a carbon steel weld metal containing titanium and boron as well as other common deoxidizers such as aluminum, silicon, and manganese. They considered the deoxidation equilibrium as represented by the reaction in Equation 30:

$$M_x N_y O_z = x M_l + y N_l + z O_l, \quad (30)$$

where M_l and N_l are the concentration of deoxidizing elements in the liquid weld metal, O_l is the dissolved oxygen concentrations, and $M_x N_y O_z$ is the formula of the oxide product. The free energy change associated with Equation 26 is given by Equation 31:

$$\Delta G = \Delta G^o + RT \ln \left(\frac{a_{M_x N_y O_z}}{a_M^x a_N^y a_O^z} \right), \quad (31)$$

where a_M , a_N , and a_O are the solute activities in the liquid, and $a_{M,N,O}$ is the activity of the oxide product, assumed to be one. Using Equation 25 to represent the extent of segregation, the solute activities of each solute in the interdendritic liquid are written as:

$$a_M = \gamma_M [\% M] f_L^{\kappa_M - 1}, \quad (32)$$

$$a_N = \gamma_N [\% N] f_L^{\kappa_N - 1}, \quad (33)$$

$$a_O = \gamma_O [\% O] f_L^{\kappa_O - 1}, \quad (34)$$

where γ_M , γ_N , and γ_O are the activity coefficients, and $[\% M]$, $[\% N]$, and $[\% O]$ are the bulk concentrations of the various solute species in the melt.

Comparing the equilibrium data for the dissolution of various potential oxides, Frost, et al. [70] showed that Al_2O_3 is the strongest deoxidant. They suggested the deoxidation sequence during solidification could be predicted assuming the weld pool comes to equilibrium with the strongest deoxidant, Al_2O_3 , and the concentrations of oxygen and deoxidants are increased by microsegregation during solidification. For an

aluminum addition of 0.04 weight percent (400 ppm), the soluble oxygen content at the start of solidification will be reduced to 0.0006 weight percent (6 ppm). They then calculated the increase in composition during solidification as a function of the liquid fraction showing a dramatic increase in the oxygen concentration as solidification progresses. Furthermore, by considering the equilibrium ratio, given by Equation 35:

$$\text{Equilibrium Ratio} = \frac{a_M^x a_N^y a_O^z}{[\% M]^x [\% N]^y [\% O]^z}, \quad (35)$$

To be a function of the liquid fraction, they predicted a deoxidation sequence of $\text{Al}_2\text{O}_3 \rightarrow \text{Ti}_2\text{O}_3/\text{Ti}_2\text{O}_5 \rightarrow \text{SiO}_2 \rightarrow \text{MnO}$.

In contrast, Babu, et al. [73] consider collision and coalescence a more appropriate explanation of the rapid growth of inclusions observed in steel melts, and suggested that this collision and coalescence is promoted by the fluid velocity gradients in the weld pool. Also, the velocity gradients in the weld pool may transport inclusions to regions of varying temperature [74], resulting in the partial dissolution and growth of inclusions. Babu, et al. [75] reviewed the mechanism of Ostwald ripening proposed by Kluken and Gröng [57] and discounted it since their model assumed variations in heat input do not affect the nucleation and growth conditions, and interaction of the weld pool fluid flow with inclusion growth in the hot part of the weld is unnecessary.

Lindborg and Torsell [76] investigated the kinetics of precipitation deoxidation in steel melts, and showed that the kinetics of Ostwald ripening are expected to be very sluggish at the low levels of dissolved oxygen present near the liquidus. Their analysis also showed that rapid growth of inclusions occurs as a result of collision and coalescence in steel melts with convective flow. Similar to the work performed by Kluken and Gröng [57], Babu, et al. [73] observed that the average inclusion diameter increased with the cube root of holding time, as would be expected for Ostwald ripening.

However, the maximum inclusion diameter did not vary linearly with the cube root of time and, instead of a gradual shift of the inclusion size distribution to coarser sizes, the size distributions were progressively skewed, showing a rapid increase in the diameter of coarser inclusions. The latter observations do not support Ostwald ripening as a potential mechanism.

Babu, et al. [73] observed that instances of partially coalesced oxides and elemental maps for these inclusions showed that the elements were uniformly distributed. They considered these microstructural observations, as well as the size distribution analysis, to suggest that collision and growth is a better explanation for the observed changes in inclusion size distributions. Following the methods of Lindborg and Torsell [76] and Iyengar and Philbrook [77], Babu, et al. developed the following equation to relate the change in oxide size distribution with time, $(dn(r)/dt)$:

$$\frac{dn(r)}{dt} = \frac{1}{2} \int_0^r n(r_1) n(r_2) \frac{4}{3} (r_1 + r_2)^3 \left(\frac{r_1^3 + r_2^3}{r_2} \right)^2 \nabla V dr_1 - \int_0^\infty n(r_1) n(r_2) \frac{4}{3} (r_1 + r_2)^3 \nabla V dr_2 \quad (37)$$

Assuming a collision efficiency of one and a velocity gradient of $3 \times 10^{-3} \text{ s}^{-1}$, reasonable agreement between the experimental and predicted values was achieved and the calculations indicated that the change in inclusion size distribution occurred rapidly in the early stages.

A significant limitation to current models is the assumption that the thermodynamics of weld metal oxide formation can be determined based upon as-deposited compositions. While this assumption is reasonable for weaker deoxidizing species such as manganese and silicon, it is likely less valid for stronger deoxidizers that have greater thermodynamic stability, such as aluminum, titanium, and yttrium.

2.3.3 Austenite Decomposition and Microstructural Constituents

Low carbon and low alloyed steel weld deposits begin to solidify as bcc δ -ferrite at temperatures around 1500 to 1550°C. Upon further cooling, austenite forms either within the δ -ferrite grains or at the δ -ferrite/liquid interface. Finally, upon cooling below the A_{c3} temperature, the austenite decomposes to initially form α -ferrite and eventually, as the carbon level of the remaining austenite exceeds the saturation limit for α -ferrite, a two-phase mixture of α -ferrite and iron carbides. Alpha-ferrite exists in a number of morphologies: grain boundary ferrite, Widmanstätten sideplates, intragranular idiomorphs, and intragranular plates. The structural relationships between the iron-carbides and α -ferrite result in a number of additional morphologies or microstructural constituents with distinctly different properties: pearlite, bainite, and martensite.

Sub-commission IX-J of the IIW developed guidelines for the identification and quantification of microstructural constituents in ferritic weld metals [78]. The IIW system has been directed toward international agreement on terminology for the description of constituents as well as a standardization of methodologies for its application. The IIW system is less complicated than those based solely upon transformation behavior, and tends to group constituents together based upon morphological similarities. A schematic diagram of the major constituents as identified by the IIW system is shown in Figure 10(a) and representative photomicrographs are presented in Figure 10(b). Despite the simplification of the IIW system, considerable variability of results in the application of this system during round robin testing has been observed [79]. Where more definitive identification of a microstructural constituent is necessary, transmission electron microscopy may be required in lieu of optical methods; however, these processes require extensive sample preparation and are limited to small regions of material limiting their application in characterization of the entire weld deposit.

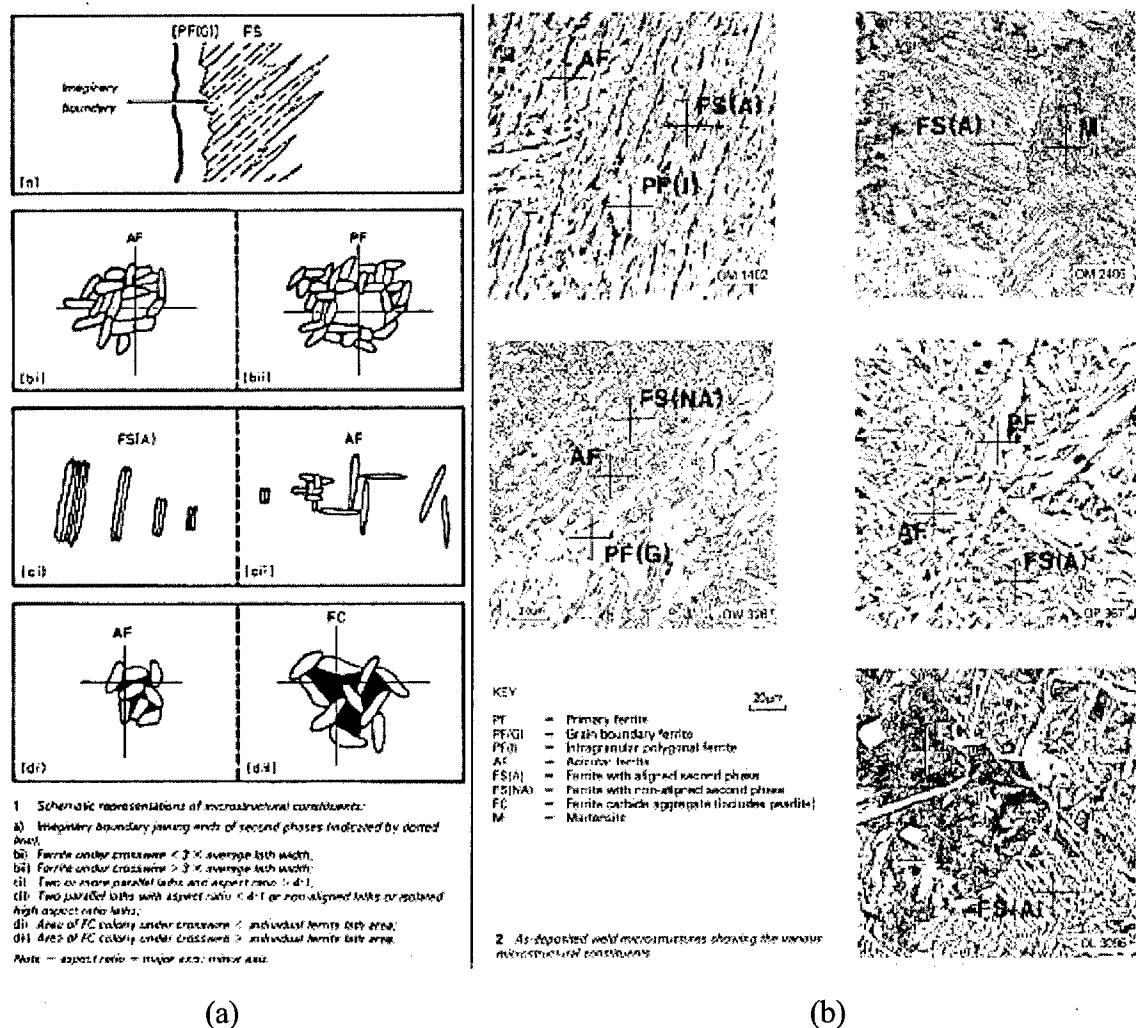


Figure 10: (a) Schematic representation of microstructural constituents as defined by IIW Subcommission IX-J methodology [78]. (b) Representative photomicrographs showing the IIW scheme for the classification of microstructures in low alloy steel weld metal [78].

The following subsections are brief descriptions of the various microstructural constituents expected in ferritic steel weld deposits. Typically, the microstructure of a steel weld deposit will be comprised of two or more of these constituents, the relative proportions of which will be dependent upon deposit composition and thermal cycle, primarily cooling rate. The distribution and percentages of these various microstructural constituents are a predominant factor in determining the properties and performance of welds. Several excellent reviews [27,31, 80-82] have been prepared on the development of microstructures in C-Mn and low alloy steel welds and their influence on as-deposited strength and toughness.

2.3.3.1 Grain Boundary Ferrite

This constituent is identified as grain boundary ferrite (PF(G)), one of two forms of primary ferrite (PF), under the IIW system. Grain boundary allotriomorphs are crystals that nucleate at the austenite grain boundaries. Typically, these crystals are equiaxed or lenticular in shape; the first to form upon cooling; and can have either curved, incoherent or faceted, semicoherent interfaces with the austenite.

Nucleation of grain boundary ferrite occurs along the austenite grain boundaries. To minimize the energy required for nucleation, it is likely the ferrite nuclei will develop with a crystallographic relationship with one of the austenite grains resulting in an interface with a high degree of coherency between the ferrite and one of the two austenite grains. With small undercooling, both the semicoherent and incoherent interfaces are expected to migrate at similar rates, resulting in the equiaxed morphology observed with grain boundary ferrite.

Since ferrite offers little resistance to cleavage crack propagation, grain boundary ferrite is generally said to be detrimental to weld metal toughness. However, Bhadeshia and Svensson [83] have proposed that because the formation of grain boundary ferrite is reconstructive transformation involving the diffusion of all atoms, grains of α -ferrite can

grow across the austenite grain boundary, completely disrupting the original austenite grains. Segregation of impurities, such as phosphorus, to austenite grain boundaries will be less detrimental to the final structure because it will be moved towards the interior of the grain boundary ferrite.

2.3.3.2 Widmanstätten Ferrite

With greater undercooling the blocky structure of grain boundary allotriomorphic ferrite is replaced by a needle- or plate-like morphology referred to as Widmanstätten ferrite. This constituent is identified as ferrite with aligned second phase, FS(A), or ferrite with non-aligned second phase or side plate, FS(NA) under the IIW system.

With greater undercooling, the diffusional transformation of the iron atoms across the semicoherent interfaces is restricted and the ferrite will grow into the adjacent austenite more rapidly along the incoherent interface. However, the temperature at which Widmanstätten ferrite forms is sufficiently high such that carbon diffusion is still quite rapid, and the carbon is able to diffuse away from the tip of a growing side plate. The lateral growth of Widmanstätten ferrite occurs by the movement of ledges along a relatively low-energy, semicoherent interface. It has been shown that the ferritic product is related to the austenite into which it is growing by the Kurdjumow-Sachs orientation relationship, and that the broad faces of the Widmanstätten plates are close in crystallographic indices to the $(111)_\gamma/(110)_\alpha$ planes.

Howell, et al. [84] observed the formation of interphase precipitation in association with the lateral movement of ledges along the low-energy interfaces of Widmanstätten ferrite. The orientation of these interphase precipitates were observed to be crystallographically related to the Widmanstätten plates by the Kurdjumow-Sachs or Baker-Nutting orientation relationship with the specific relationship dependent upon the steel composition studied. The observed orientation relationships suggest these interphase precipitates nucleated on the low-energy immobile austenite/ferrite interfaces.

Once nucleated, the ferrite sideplates grow very rapidly across the incoherent interface resulting in a parallel array of ferrite laths of high aspect ratio. Primary Widmanstätten sideplates may nucleate directly from the austenite grain boundary or secondary Widmanstätten ferrite may nucleate at the grain boundary ferrite/austenite grain boundaries.

2.3.3.3 Bainite

At even larger undercoolings than those required for the formation of Widmanstätten ferrite, bainite forms. This constituent is also identified as ferrite with aligned second phase (FS(A)) or ferrite with second phase, under the IIW system. Bainite exists in two forms, upper and lower, and may be classified as FS(UB) and FS(LB) under the IIW system when the operator is confident of the distinction, which is not normally possible with light optical microscopy.

In the classical definition, bainite is a mixture of ferrite and carbide [85]. During ferrite formation, carbon is continuously rejected from the ferrite phase enriching the remaining austenite. At transformation temperatures above which bainite forms, carbon can diffuse considerable distances from the transformation front. However, at the lower temperatures at which bainite forms, carbon diffusion is limited, resulting in the formation of a structure consisting of ferrite and cementite in nonlamellar arrays.

As with martensite, the ferrite laths of bainite contain a significant dislocation substructure, suggesting the mechanism of bainite formation involves shear as well as diffusion, although the exact mechanism of bainite formation is uncertain. As with Widmanstätten ferrite, the aligned structure of bainite may promote cleavage fracture and lower weld metal toughness. Cleavage cracks may propagate along the interlath boundaries with minimal resistance until they encounter the next packet boundary. Therefore, it is generally considered desirable to limit the percentage of aligned structures in ferritic steel weld deposits.

2.3.3.4 Acicular Ferrite

Acicular ferrite or intragranularly nucleated ferrite forms at temperatures intermediate to those of Widmanstätten ferrite and bainitic ferrite. Unlike grain boundary, Widmanstätten or bainitic ferrite, acicular ferrite is formed within the prior austenite grains. It is generally accepted that the presence of nonmetallic inclusions of an appropriate size and composition promote the formation of acicular ferrite through heterogeneous nucleation. In two dimensions, acicular ferrite appears to consist of very fine-grained interlocking needles with a “basket weave” appearance. In three dimensions, acicular ferrite has the morphology of thin, non-parallel, lenticular plates approximately five to ten microns long and one micron thick with a corresponding aspect ratio on the order of 0.2 to 0.1. The individual plates have a relatively high dislocation density on the order of 10^{10} cm^{-2} [86] and are separated by high angle grain boundaries. The very fine grain size and interweaving nature of acicular ferrite has been shown to enhance toughness of ferritic steel weld deposits. It is widely accepted that deposits containing significant percentages of acicular ferrite are desirable. The chaotic nature of the structure and the large number of intersecting high angle grain boundaries tends to deflect a propagating cleavage crack, enhancing weld metal toughness.

While there is reasonable agreement among researchers concerning the microstructural form and crystallographic nature of acicular ferrite, growth characteristics of AF are still debated. Acicular ferrite may in fact be intragranularly nucleated bainite or Widmanstätten ferrite. A number of review papers discussing the nature of acicular ferrite in C-Mn and low alloy steel welds have been written [87, 88]. Following a study of C-Mn SMAW weld deposits, Ricks, et al. [89] concluded that acicular ferrite is likely intragranularly nucleated Widmanstätten ferrite. This conclusion was supported by the observation of both retained austenite and twinned martensite between the acicular laths. They concluded that the carbon partitioning, indicated by the presence of these interlath phases was evidence of a proeutectoid reaction. In addition, stepped-growth interfaces

were observed between the acicular ferrite and the austenite or martensite regions, implying a ledge mechanism analogous to that documented for the lateral growth of Widmanstätten ferrite.

In contrast, Bhadeshia [88], Kluken, et al. [90], and others have concluded that acicular ferrite is intragranularly nucleated bainite. The formation of acicular ferrite is accompanied by a surface relief when developed at a pre-polished free surface. Bhadeshia concluded that this surface relief is indicative of a shear mechanism resulting in an invariant-plane strain similar to those associated with the martensitic transformation. Based upon diffraction pattern analyses, Yang and Bhadeshia [86] have shown that acicular ferrite plates have an orientation relationship with the parent austenite grain. This relationship lies within the Bain orientation region, which is also consistent with an invariant-plane strain deformation. Work by Kluken, et al. [90] confirmed this relationship by using an electron backscattering pattern technique and further indicated the acicular ferrite laths exhibit an orientation relationship with the prior δ -ferrite grains as well.

Although the initial acicular ferrite is generally accepted to form heterogeneously on nonmetallic inclusions, subsequent acicular ferrite may form autocatalytically through sympathetic nucleation. Evidence of sympathetic nucleation of acicular ferrite has been observed by Court and Pollard [91] and Ricks, et al. [89] in C-Mn steel weld deposits. The nature and nucleation characteristics of the sympathetic nucleation of ferrite in plain carbon steels has been considered by Aaronson and Wells [92] and Aaronson, et al. [93]. Aaronson and Wells showed that the nucleation of new ferrite crystals at the interphase boundaries of previously formed ferrite increased with decreasing transformation temperature. Although the higher specific interfacial free energy of the nucleus-nucleation site interface at the austenite/ferrite boundaries, and the lower supersaturation of the austenite at these boundaries, act against sympathetic nucleation, Aaronson and Wells concluded that the much larger total area of austenite/ferrite boundaries is

sufficient to allow for sympathetic nucleation. Coarser austenitic grain size promotes this effect.

2.3.3.5 MA Constituent

In addition to the various forms of ferrite described above, the microstructure of low carbon steel weld deposits may contain a small percentage of martensite and retained austenite. Due to the difficulty distinguishing these minor phases from each other they are often grouped together and referred to as MA, MC or MAC.

2.3.4 Influence of Weld Metal Inclusions on Microstructural Development

The development of weld metal microstructures is a competitive process between lower toughness grain-boundary nucleated constituents, such as grain boundary ferrite, Widmanstätten ferrite, or bainite; and intragranularly nucleated acicular ferrite. Due to the random orientations of intragranularly nucleated acicular ferrite, this microstructure constituent has been associated with higher weld metal toughness compared to the weld metal toughness of aligned sideplates and bainitic microstructures.

There are a number of ways in which inclusions promote the nucleation of ferrite [89]:

1. Inclusions may serve as inert, heterogeneous nucleation sites for acicular ferrite.
2. Thermal strains around an inclusion due to the difference in thermal expansion coefficients of the particle relative to the austenitic matrix may stimulate nucleation.
3. By pinning the prior austenite grain boundaries and inhibiting growth of the austenite grains during cooling, small inclusions promote large austenite grain

boundary surface area which enhance the formation of grain boundary nucleated phases and limit the formation of acicular ferrite.

4. Inclusions of specific composition and crystallographic structure may lower the barrier to heterogeneous nucleation further by offering a low lattice mismatch.
5. Depletion of austenite stabilizing elements such as manganese and carbon around the inclusions may promote nucleation of ferrite.

The effectiveness of inclusions as inert substrates for heterogeneous nucleation has been considered by Ricks, et al. [89] using classical nucleation theory. For this analysis, the authors assumed that the inclusions were inert, had an incoherent interface with the matrix, and were non-deformable. The findings of this work are summarized in Figure 11. For a given driving force, inclusion nucleation is always less energetically favorable than grain boundary nucleation. For the assumptions used in their model, Ricks, et al. found that the effectiveness of inclusion as heterogeneous nucleation sites decreased rapidly at inclusion diameters less than approximately 0.2 microns.

Tessellated stresses, generated around inclusions due to differences in thermal expansion between the inclusion and the austenite matrix, have been proposed by Dallum and Olson [94] to favor the nucleation of acicular ferrite by contributing to the total free energy of austenite decomposition. The thermal expansion coefficient of the austenitic matrix is much higher than that of the oxide inclusions; therefore, the austenite matrix surrounding the inclusions may be strained during cooling. The additional strain energy favors the nucleation of acicular ferrite by increasing the overall free energy change associated with the austenite to ferrite transformation. Liu [95] investigated the impact of the increase in strain energy on the nucleation of acicular ferrite in submerged arc welding (SAW) deposits of niobium microalloyed steels, concluding that the strain energy effect associated with the differences in thermal expansion coefficients was insignificant when compared to the overall free energy change associated with the austenite to ferrite transformation.

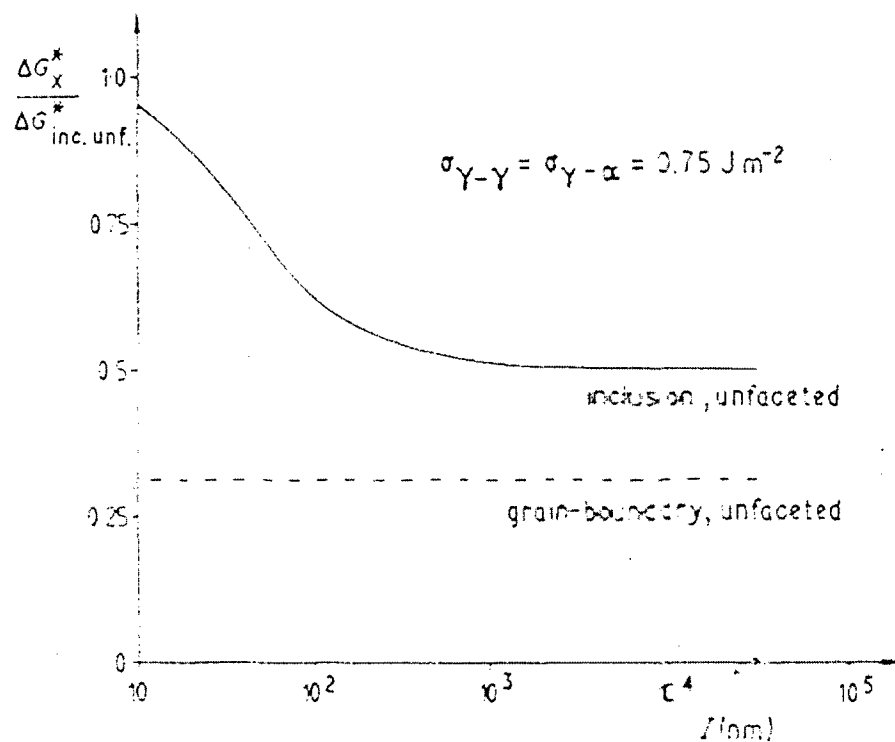


Figure 11: Variation in the energy barrier to nucleation, ΔG , normalized to that corresponding to unfaceted homogeneous nucleation in an austenite matrix, for unfaceted ferrite formed on an inclusion ($\Delta G_{inc. unf.}^*$), as a function of inclusion radius, I . Constant values of the volume of free energy change ($\Delta G_V = -300 \text{ J/mol}$) and surface free-energy of both austenite-austenite and austenite-ferrite boundaries ($\sigma = 0.75 \text{ J/m}^2$) are assumed. The equivalent energy barrier for austenite grain-boundary nucleation is also shown ($\Delta G_{gb unf.}^*$) [89].

Inclusions may also play a role in the austenite-to-ferrite transformation kinetics through their effect on the austenite grain size, as investigated by Ferrante and Farrar [96]. A high density of fine inclusions pin the austenite grain boundaries, limiting the growth, resulting in a large grain-boundary-surface-area-to-volume ratio. The large austenite grain boundary surface area promotes the nucleation of grain boundary ferrite, Widmanstätten ferrite, and bainite. On the other hand, a large austenite grain size increases the hardenability of the weld metal promoting the formation of acicular ferrite. This phenomenon was investigated by Liu and Olson [97], who found good correlation between the prior austenite grain size and the inclusion number density. However, the effectiveness of inclusions pinning the austenite grain boundaries will also be related to inclusion size. Following the model proposed by Zener [66], the limiting grain size is given by Equation 38:

$$D_{\text{lim}} = k \frac{r}{f}, \quad (38)$$

where r is the radius of the pinning particles, f is the volume fraction of particles, and k is a constant evaluated by Zener to have a value of $4/3$.

The interfacial free energy at the nucleating interface is the controlling factor of heterogeneous nucleation behavior. The total interfacial free energy is composed of several contributing factors: the chemical nature of the substrate, the topographic features of the substrate surface, the lattice strain, or disregistry between two phases at the interface. A number of researchers proposed that certain inclusions promote acicular ferrite formation through more favorable lattice matching. Turnbull and Vonnegut [98] theorized that the effectiveness of a substrate in promoting heterogeneous nucleation depends on the crystallographic disregistry between the substrate and the nucleated solid given by Equation 39:

$$\delta = \frac{\Delta a_0}{a_0}, \quad (39)$$

where Δa_0 is the difference between the lattice parameter of the substrate and the nucleated solid for a low index plane, a_0 is the lattice parameter for the nucleated phase. The Turnbull and Vonnegut model, however, is limited because it is restricted to linear geometry. Bramfitt [99] modified the relationship for planar systems to more accurately describe the crystallographic relationships at the interface during heterogeneous nucleation. Bramfitt's planar lattice disregistry model is given by Equation 40:

$$\delta_{(hkl)_n}^{(hkl)_s} = \sum \frac{1}{3} \left\{ \frac{\left| (d_{[uvw]_s} \cos \gamma) - d_{[uvw]_n} \right|}{d_{[uvw]_n}} \right\} \times 100\% \quad (40)$$

where:

- $(hkl)_s$ is a low-index plane of the substrate;
- $[uvw]_s$ is a low-index direction in $(hkl)_s$;
- $(hkl)_n$ is a low-index plane in the nucleated solid;
- $[uvw]_n$ is a low-index direction in $(hkl)_n$;
- $d_{[uvw]_n}$ is the interatomic spacing along $[uvw]_n$;
- $d_{[uvw]_s}$ is the interatomic spacing along $[uvw]_s$; and
- γ is the angle between the $[uvw]_n$ and the $[uvw]_s$.

Turnbull and Vonnegut [98] postulated that the degree of supercooling required to heterogeneously nucleate a phase was parabolically related to the disregistry factor, and was confirmed by Bramfitt for the heterogeneous nucleation behavior in liquid iron. This means that the most potent catalyst particles are those that provide a good epitaxial fit between the substrate and nuclei.

From the above discussion, the composition and crystallographic structure of weld metal inclusions are expected to be a significant factor in promoting heterogeneous nucleation of acicular ferrite and this in fact has been observed by a large number of researchers. It is generally accepted that nonmetallic inclusions in steel weld metals are complex; of heterogeneous chemical nature [36, 100, 101]; and, depending on alloy deposit composition, comprised of a wide variety of elemental species including aluminum, silicon, manganese, titanium, copper, calcium, magnesium, sulfur, and iron. As schematically illustrated in Figure 12 [58], Kluken and Gröng [57] proposed that inclusions will have a heterogeneous structure comprised of an oxide core that is formed during the primary deoxidation stage. The composition of the oxide core will vary depending on the specific deoxidizing species present and the resulting thermochemistry. In addition, the oxide core will be partly covered by secondary reaction products, such as TiN and MnS that will precipitate after completion of the weld metal deoxidation. If the oxides act in a manner other than as inert sites for heterogeneous nucleation, it is likely that the outer character of the oxide core or the secondary reaction products present on the oxide surface will have the greatest influence on acicular ferrite nucleation.

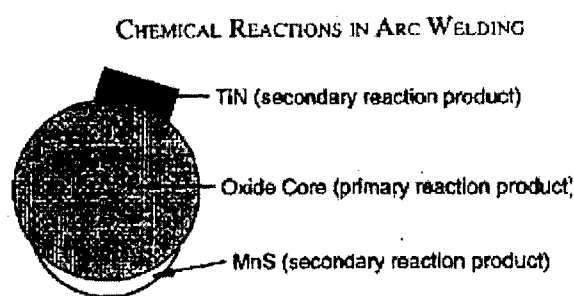


Figure 12: Schematic illustration showing the presence of primary and secondary phases in weld metal inclusions [58].

Dowling et al. [101] evaluated the microstructural development in a series of HSLA steel submerged arc welds made with three different fluxes and metallic additions of titanium, molybdenum, and chromium. Their work showed that the inclusions contained a number of compounds, with the relative amounts of the compounds depending on both the flux and metallic additions. Six inclusion phases were specifically identified: galaxite ($\text{Al}_2\text{O}_3 \cdot \text{MnO}$), an unidentified titanium-rich compound, copper sulfide, manganese sulfide, a silica-rich phase, and an aluminum-rich phase. Dowling, et al. did not observe any correlation between the amount of acicular ferrite in the weld metal and the inclusion composition or phases. They concluded that inclusions nucleate acicular ferrite by acting as inert substrates according to classical nucleation theory or heterogeneous nucleation. This theory was supported by Zhang and Farrar [102], who observed a similar behavior in a series of low carbon, low alloy C-Mn-Ni welds produced by SMA or gas tungsten arc (GTA) welds.

In contrast, numerous studies have concluded that the chemical composition of inclusions is the primary factor in promoting the formation of acicular ferrite. Based upon analysis of inclusions associated with the formation of acicular ferrite in C-Mn SMA welds containing titanium, Court and Pollard [103, 104] concluded that acicular ferrite formation was promoted by the formation of globular sulfides, such as CuS or $(\text{Cu}, \text{Mn})\text{S}$, on the surface of oxide inclusions. Several other researchers [32, 36, 101, 105, 106] have identified titanium-rich phases associated with the formation of acicular ferrite; however, the exact nature of the phase or phases is still in debate. A study by St. Laurent and L'Esperance [107] indicated that even with the presence of a titanium-rich phase in the inclusion, the effectiveness of titanium-containing inclusions to nucleate acicular ferrite may be related to the total external surface area of the titanium-rich phase covering the inclusions. Inclusions of galaxite [108], and MnTi_2O_4 [109], among others have also been proposed to promote acicular ferrite formation.

To study the effects of various crystalline materials on the formation of bainite, Gregg and Bhadeshia [110, 111] performed experiments where pure minerals were

pressure bonded to steels and, also added to molten steel [112]. The samples were heat treated to induce transformation so that the transformation behavior around the ceramic/steel interface could be compared to that of the bulk steel. These studies showed TiO_2 , TiO , and Ti_2O_3 were potent catalysts for bainite nucleation, while TiN , galaxite, $\alpha\text{-Al}_2\text{O}_3$, and $\gamma\text{-Al}_2\text{O}_3$, among others, were ineffective as catalysts for bainite nucleation. TiO_2 appeared to induce the nucleation of ferrite and bainite by causing diffusion of oxygen into the surrounding steel. It is suggested that the presence of oxygen may induce decarburization, promoting ferrite formation. In contrast, SEM EDS analysis of substitutional element concentrations around Ti_2O_3 revealed a significant depletion in the manganese concentration in the adjacent steel. Since manganese stabilizes austenite, it is speculated that this manganese-depleted zone (MDZ) would stimulate ferrite formation. The SEM EDS analysis also showed that the manganese diffused into the Ti_2O_3 , which acted as a manganese sink. SEM EDS analysis of the steel adjacent to TiO showed little difference in substitutional element concentrations. Nevertheless, the bonding experiments demonstrated that TiO may promote nucleation of bainite from its surface.

Supporting the observations of Gregg and Bhadeshia [110-112], a number of researchers [113-115] observed that Ti_2O_3 promotes the formation of acicular ferrite in the HAZ and base metal microstructures of carbon and low alloy steels. Mabuchi, et al. [115] and Shim, et al. [114] attributed the catalytic effect of Ti_2O_3 to the formation of an MDZ around the oxide. Since manganese is an austenite stabilizer, the formation of the MDZ locally promotes the nucleation of ferrite, allowing intragranularly nucleated laths to grow prior to being overwhelmed by grain boundary nucleated Widmanstätten ferrite or bainite.

2.3.5 Effects of Microstructure on Mechanical Properties

Cleavage fracture can initiate through the cracking of brittle second phase particles [116], such as carbides [117] or inclusions [118]. The crack formed by a

fractured particle will only propagate into the adjacent ferrite matrix if the stress intensity factor at a newly formed crack tip is large enough to initiate cleavage in the ferrite. Larger particles are more likely to initiate cleavage since the crack formed by their fracture will be longer and hence the stress intensity factor at the crack tip will be higher. It has been observed that cleavage in weld metal is initiated by inclusions at the uppermost end of the inclusion size distribution ($>1\text{ }\mu\text{m}$) despite the small number of inclusions of this size [118, 119]. In contrast, the propagation of a cleavage fracture is unlikely to be affected by inclusions.

Since ductile fracture occurs by the growth and coalescence of microvoids nucleated at inclusions, ductile crack growth will be promoted by an increased size and decreased separation of inclusions, which to a first approximation, will be given by the volume fraction of inclusions [27, 120, 121].

A finer grain size improves the resistance to cleavage initiation [122, 54] through the influence of dislocation pile-up stresses on the fracture stress [123, 118]. A finer grain size also improves the resistance to cleavage propagation. Since cleavage fracture in ferrite occurs along the $\{100\}$ planes, a fracture must change direction when it crosses a high angle boundary between adjacent grains of acicular ferrite. The smaller the grain size, the more tortuous the fracture path and the greater the resistance to cleavage fracture propagation [27].

Although the effect of a grain size on the resistance to ductile fracture has not been investigated explicitly, a finer grain size will increase the strength of the weld metal, which in turn is believed to reduce the longitudinal strain needed to cause microvoids to coalesce [124].

The presence of grain boundary ferrite is considered to be detrimental to cleavage fracture initiation and propagation and has been implicated as a contributing factor in intergranular HAC. Tweed and Knott [118] showed that in a C-Mn steel weld containing acicular ferrite and grain boundary ferrite, strain will be localized in the grain boundary ferrite until the bulk specimen strain reaches approximately seven percent. They suggest

that this localization of strain may promote cleavage initiation in non-metallic inclusions. They also noted a slight tendency for the cleavage fracture to preferentially follow the grain boundary ferrite.

The influence of these three microstructural features: second-phases, grain boundary ferrite, and acicular ferrite, on ductile fracture, cleavage fracture, and HAC resistance is summarized in Table 2. Although each fracture mode is affected by each of the microstructural features listed, the physical processes by which each fracture mode is affected is different. Cleavage initiation is affected most by the largest inclusions, ductile fracture is controlled by the volume fraction of inclusions, and HAC resistance is affected by the number of inclusions on prior-austenite grain boundaries and the trapping effects of the inclusions. It is evident from Table 2, that HAC resistance, toughness, and strength are indirectly related through the mutual dependence on microstructural features.

Table 2: The influence of microstructural features on ductile fracture, cleavage fracture, and hydrogen induced cracking resistance [125].

Parameter	Intergranular HIC Resistance	Ductile Fracture Resistance	Cleavage Fracture Resistance
Inclusions	Number on prior-austenite grain boundaries [121] Hydrogen trapping effects	Volume fraction [120, 27]	Largest inclusion ($>1\mu\text{m}$) [118, 119]
Ferrite grain size	Hydrogen trapping effects	Indirect relationship through dependence on strength	Inversely proportional to $d^{1/2}$ [28]
Grain boundary ferrite	Increase of grain boundary carbon		Localized strain causes cracked inclusions [118]

2.4 Hydrogen-Assisted Cracking

Service failures due to fatigue and brittle fracture of welded steel components usually originate at small pre-existing cracks in the HAZ. The most common HAZ defects result from the presence of diffusible hydrogen in the weld metal, known as

hydrogen-assisted cracking (HAC). This type of cracking occurs within minutes to several days after weld completion and is difficult to detect despite extensive inspection. The conditions that collectively result in HAC can be determined as “sufficient hydrogen and sufficient stress in a hard microstructure at a temperature below 150°C” [126]. It is difficult to avoid exceeding the critical stress and even impossible to keep a weld at a temperature greater than 150°C when in service. Therefore, HAC prevention must largely rely on control of hydrogen level and control of microstructure.

2.4.1 General Features of HAC

Prior to World War II, delayed HAZ cracking frequently occurred in the welding of armor plates and other alloy steels. Even though the cracking could be prevented through the use of Cr-Ni electrodes, it could not be prevented when ferritic electrodes were used. Furthermore, it was found that the cracking was caused by the hydrogen introduced from the flux of the electrodes. As low hydrogen electrodes were developed, the cracking occurred less frequently.

2.4.1.1 Macroscopic Observation of HAC

Cracks in the HAZ are usually located either at the weld toe, the weld root, or in an underbead position, which are schematically illustrated for fillet welds and butt welds in Figure 13 [126]. In fillet welds, HAZ cracks are usually oriented along the weld length, whereas, in butt welds, subsurface cracks can be transverse to the weld. The cracks vary in length from microns to several millimeters. Representative photographs of typical HAZ cracks are shown in Figure 14 [126].

In some cases, HAC can occur in the weld metal. As the alloy contents of both base and weld metals are increased, cracking in the weld metal becomes more significant. Weld metal hydrogen cracks may be within the weld or exposed on the surface and may

be transverse to the weld. Cracks that originate at the weld root are often longitudinal to the weld. Figure 15 [126] shows representative photographs of typical weld metal cracks.

2.4.1.2 Microscopic Observation of HAC

Microscopic observations of HAC fracture surface are important for understanding hydrogen embrittlement and for determining the cause of cracking. The fracture modes of HAC include microvoid coalescence (MVC) or dimple rupture, quasicleavage (QC), and intergranular fracture (IG). Figure 16 [127] shows representative SEM micrographs of each fracture mode. The Beacham diagram shown in Figure 17 [128] illustrates the interrelationship between the stress intensity factor, dissolved hydrogen content, and HAC fracture mode in a microscopically small volume near the crack tip. The threshold stress intensity factor to initiate cracking is lower at higher hydrogen concentration. Among the three modes, the IG mode predominates when the stress intensity factor is low. This mode is the most energetically favorable process because it involves the least amount of plastic deformation compared with the other

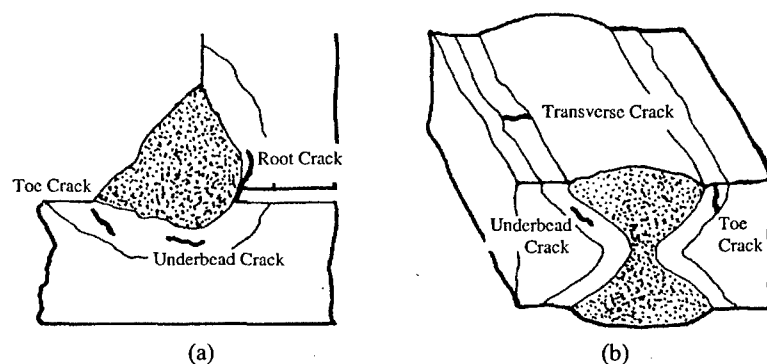


Figure 13: HAC in heat-affected zones of (a) fillet and (b) butt welds [126].

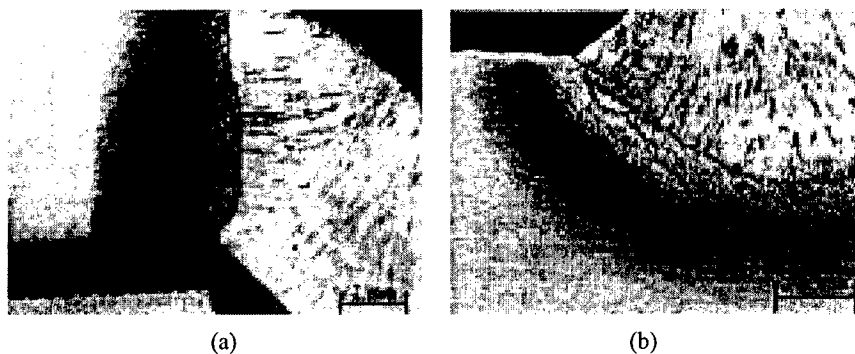


Figure 14: HAZ in C-Mn steel (a) HAC at root of single-pass fillet weld, and (b) HAC at toe of multiple-pass fillet weld [126].

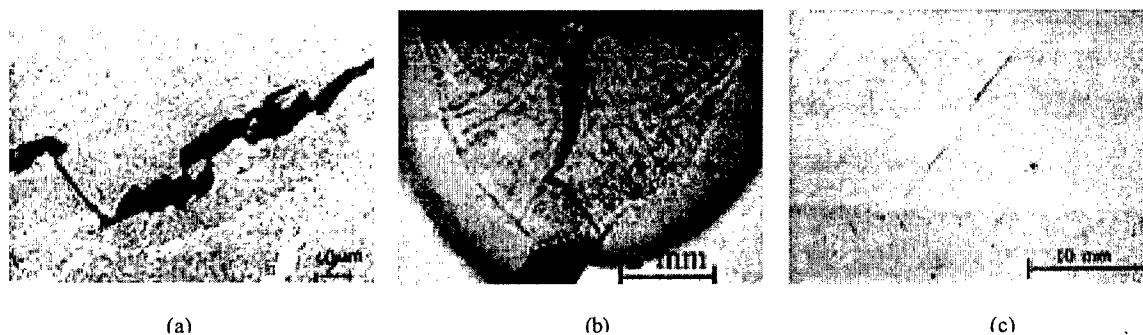


Figure 15: HAC in steel weld metal of (a) single-pass SMA weld, (b) root bead of a Y-groove welding test, and (c) SA weld [126].

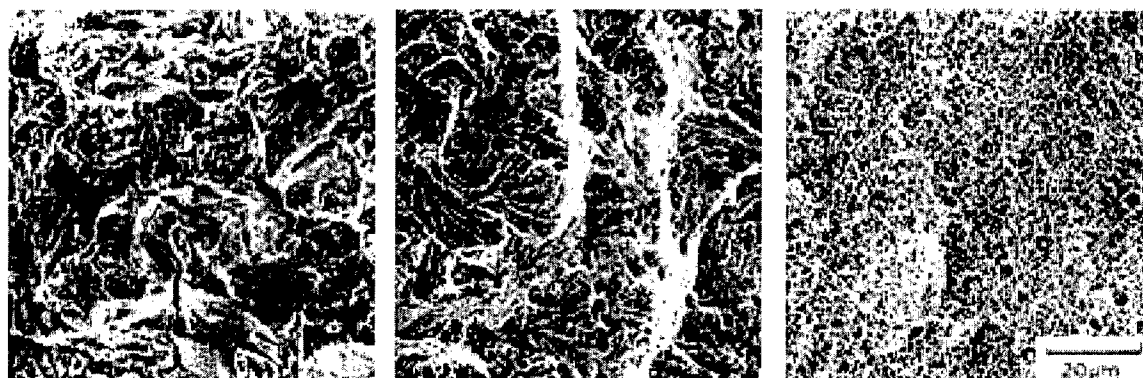


Figure 16: Typical fractographic modes of HAC, (a) intergranular fracture (IG), (b) quasicleavage fracture (QC), and (c) microvoid coalescence (MVC) [127].

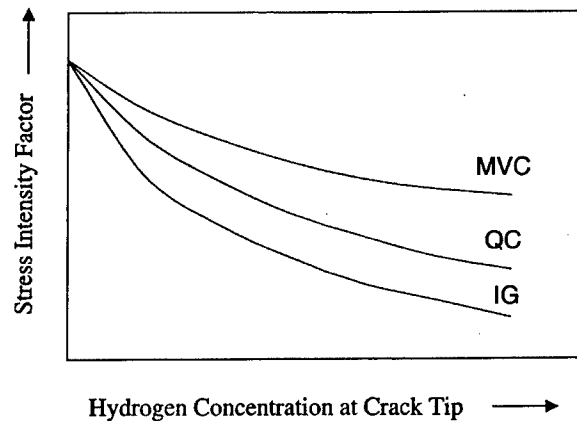


Figure 17: Beacham diagram on interrelationship between stress intensity factor and dissolved hydrogen content [128].

modes. At higher stress intensity, the fracture process involves plastic deformation, so the fracture mode shifts from IG to QC or MVC. The kinetics and morphology of growth of HAC is influenced by microstructural features and other factors including hydrogen content, strain rate, temperature, and stress intensity [129].

2.4.2 Factors Responsible for HAC and Their Control

It is well recognized that HAC may occur in both the HAZ and the solidified weld metal if the following four conditions are present [127]: 1) critical concentration of diffusible hydrogen at a crack tip, 2) stress intensity of sufficient magnitude, 3) a microstructure susceptible to hydrogen, and 4) temperatures lower than about 150°C.

HAC can be prevented if the simultaneous presence of the four conditions is avoided. Management of these conditions becomes more critical as the requirements for high strength steel welding become more stringent. The occurrence of HAC in the HAZ and weld metal has increased because of the higher strength in both the HAZ and weld

metal, and became minimal or no preheat is applied in attempts to reduce the production cost. To overcome these problems, one of the research and development focal points is the development of quality electrodes that provide lower levels of weld metal diffusible hydrogen. The previous limit of five milliliters of diffusible hydrogen per 100 grams of weld metal level is no longer acceptable for modern high strength steel welding. The challenge has become to further reduce the diffusible hydrogen level to as low as one milliliter per 100 grams.

2.4.2.1 Hydrogen Level

During welding, hydrogen is absorbed by the weld pool from the arc atmosphere. Much of this hydrogen escapes from the solidified weld metal by diffusion, but some diffuses into the HAZ and the base metal. Upon cooling, hydrogen solubility in steel diminishes, most drastically during the transformation from austenite to ferrite as shown in Figure 18 [126]. Hydrogen rejected by ferrite tends to be distributed on lower energy sites such as dislocations, grain boundaries, and inclusions. The final amount of diffusible hydrogen at ambient temperature depends on several factors: the originally absorbed amount, the size of the weld, the decreasing solubility, and the cooling rate. In general, the more hydrogen present in the weld, the greater the risk of cracking. The critical concentration of diffusible hydrogen at a crack tip can be avoided by reducing the diffusible hydrogen level of the entire weld metal. The specific technologies to reduce the diffusible hydrogen will be discussed later.

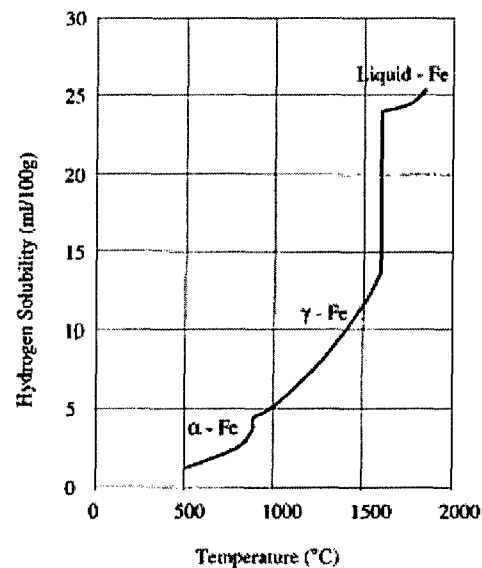


Figure 18: Solubility of hydrogen in low carbon steel weld metal as a function of temperature [126].

2.4.2.2 Stress Level

When a stress intensity factor reaches the critical level, a brittle crack initiates and propagates rapidly. On the other hand, HAC typically propagates discontinuously. It requires some time before the hydrogen concentration at a notch reaches the critical level, at which time cracking initiates. HAC eventually stops as it leaves the vicinity of critical hydrogen concentration. Every time a crack propagates, an incubation period for hydrogen accumulation is necessary. The extent of hydrogen accumulation at the crack tip can be predicted if the chemical potential of hydrogen is known, since both the gradient of the chemical potential of hydrogen is known, and the gradient of the chemical potential determines the flux of a solute. The potential of hydrogen in terms of stress Φ_H is given by the specific molar volume of hydrogen in a steel, V_H (mm³/mol), and the triaxial stress as shown in Equation 41 [127]:

$$\Phi_H = -\frac{(\sigma_1 + \sigma_2 + \sigma_3)V_H}{3} \quad (41)$$

When the triaxial stress is tensile, the potential becomes negative and a potential well of hydrogen arises with hydrogen flowing into the well. Stresses in a weld are developed by thermal contraction during cooling. The presence of hydrogen appears to relieve the stress level by causing cracking. The higher degree of strain produces higher risk of cracking for a given microstructure and hardness.

The stress acting on a weld is a function of weld size, joint geometry, fixturing, external restraint, and the yield strengths of the base and weld metals. Hydrogen embrittlement is strain-rate dependent, where the risk of cracking is greatest at slow strain rates.

2.4.2.3 Type of Microstructure

The HAZ can be clearly seen on the polished and etched cross-section of a steel weld. This zone is raised to a temperature above the A_{c3} temperature during welding. Subsequent rapid cooling by the surrounding base metal causes hardening. Near the fusion line, the HAZ is subjected to a temperature causing grain coarsening. This temperature region, because of its coarse grain size, is not only more hardenable but also less ductile. As a general rule, the harder and less ductile the microstructure the greater the risk of HAC.

Hard microstructures such as bainite and martensite are high in dislocation density, so their stress concentrations are also high. Therefore, diffusible hydrogen tends to accumulate in these microstructures, and microcracks may initiate. Hard microstructures in HAZ can be avoided by using steel plates with low contents of carbon and alloying elements; i.e., low hardenability. As an alloy parameter, hardenability is

useful since it assesses the total contribution of all the elements, using empirical formulas such as the IIW carbon equivalent (CE) shown in Equation 42:

$$CE = C + \frac{Mn}{6} + \frac{Cu + Ni}{15} + \frac{Cr + Mo + V}{5}. \quad (42)$$

Among the elements included in the formula, carbon is the most influential element to produce hard microstructures. Research conducted by Czyryca [13] found that the weldability is remarkably improved with steel plates containing a carbon content less than 0.1 weight percent, even when the carbon equivalent is considerably high. Slow cooling of a large weld deposit, thin plate, and preheat will also reduce the formation of hard microstructures. After a bead has been deposited, the HAZ can be softened by tempering either as a result of subsequent welds or by postheating, including the stress relief treatment.

2.4.2.4 Temperature

Hydrogen embrittlement of ferritic steels only occurs at low temperatures. Therefore, it is possible to avoid cracking in a susceptible microstructure by maintaining it at a sufficiently high temperature, either until hydrogen has diffused away or until the microstructure is softened by tempering. This is the principle used in multipass welding and in postweld heat treatments. Raising the temperature increases the rate of hydrogen diffusion, thus accelerating its removal from the weld. Hydrogen diffusion is particularly sluggish in the temperature range between 20 and 150°C [126]. Therefore, any means to slow down the cooling rate in a weld will help to reduce the hydrogen level in the weld. On the other hand, this higher temperature leads to discomfort for the welders, therefore they would prefer to have the hydrogen control performed at lower temperatures.

2.5 Hydrogen Pickup in Weldments

This section discusses the manners of which hydrogen enters the steel weld metal.

2.5.1 Hydrogen Sources

Before discussing the techniques established for weld metal hydrogen reduction, it is important to understand where hydrogen exists in the welding environment and how it is introduced into the weld metal. There are six known weld metal hydrogen sources: 1) various forms of hydrogen in the flux covering or the core of an electrode, 2) oil or organic lubricant on the surface of GMAW, FCAW, or SAW electrodes, 3) oil, primer, and oxide layers on the base metal surface, 4) residual hydrogen in the base metal, 5) moisture from the atmosphere, and 6) residual water vapor in GMAW or GTAW shielding gas. Among these, assuming non-faulty equipment, 4) and 6) are minor, while 1) and 2) are the major hydrogen sources.

2.5.2 Forms of Hydrogen in Flux-Covered and Cored Electrodes

It is impossible to completely eliminate hydrogen from the coatings of shielded metal arc welding electrodes because of the flux composition and production process, thus importance to understand how hydrogen incorporates in these coatings. Hydrogen may exist as: 1) hydrogen in the flux ingredients such as organic compounds like cellulose ($C_6H_{12}O_5 \cdot nH_2O$), 2) water of crystallization such as talc or mica, 3) water in the binder (50% aqueous solution), and 4) water absorbed because of hygroscopicity. Cellulosic electrodes rely on organic compounds in the flux to provide better arc force and greater arc stability. However, these carbon and hydrogen-rich compounds decompose readily in the arc introducing large quantities of hydrogen to the weld pool.

Some slag ingredients such as talc ($3\text{MgO} \cdot 4\text{SiO}_2 \cdot \text{H}_2\text{O}$) and mica ($\text{K}_2\text{O} \cdot 3\text{Al}_2\text{O}_3 \cdot 6\text{SiO}_2 \cdot 2\text{H}_2\text{O}$) contain molecules of water of crystallization in their formulae. Since these ingredients are important to the electrode extrusion process and arc stability, they are added despite the possibility of moisture and hydrogen pickup in the weld pool. It is generally difficult to remove chemically bonded water from minerals, where it is believed that water of crystallization may be stable at temperatures as high as 800 to 900°C. However, in actual production circumstances, the baking temperature is often limited to below 350°C because of the decomposition of organic ingredients and some carbides, and the oxidation of metal ingredients for alloying. Therefore, minerals containing water of crystallization will break down in the arc, potentially providing hydrogen to the weld pool.

The coverings for shielded metal arc welding electrodes include not only flux ingredients but also binding agents. Sodium silicate, potassium silicate, lithium silicate, or mixtures of these silicates are added to the flux as binders for the covering. These silicates are viscous, colloidal solutions that contain up to 50% water by weight.

The last consideration of hydrogen in the covering is water absorbed by the covering. The surface of the covering is generally porous with fine crevices continuing into the interior of the flux coating. Therefore, physical adsorption and capillary action of water are significant to affect the moisture content in the coating. The physically adsorbed water can be eliminated at relatively lower temperatures, around 100°C; however, the water of hydrolysis requires higher temperatures for removal, believed to be around 350°C.

The forms of hydrogen in the flux of FCAW steel wires are similar to that of SMAW except for the fact that a binder is not used for the manufacturing of FCAW steel wires. Also, commercial FCAW consumables do not contain organic compounds such as cellulose. On the other hand, oil or organic lubricant from the surface of an electrode can be considered as a hydrogen source. The lubricant is present because of the wire drawing process. Therefore, the different forms of hydrogen in consideration are: 1) water of

crystallization, 2) water absorbed because of hygroscopicity, and 3) oil or organic lubricant from the surface of an electrode. Since there is no need to use binder for FCAW wire production, the removal of water from the fluxes is easier than in SMAW electrode manufacturing. Flux ingredients can be baked separately prior to the wire production process, at the appropriate temperature for each ingredient without requiring any additional baking process. Instead, the removal of the lubricant is critical in FCAW wire production. The lubricant has to be carefully wiped off and baked out. Again, the baking temperature is typically less than 350°C because of the decomposition of some flux ingredients and the oxidation of metal ingredients for alloying.

2.5.3 Influence of Hydrogen in the Flux on Weld Metal Diffusible Hydrogen

Godai, et al. [130] quantified the total water content in the covering of shielded metal arc welding electrodes. Figure 19 shows the relationship between the total hydrogen content in the coating and diffusible hydrogen level in weld metal deposited with high cellulose, rutile, lime-rutile, lime-rutile-fillet weld, and low hydrogen type electrodes. It is clear from this figure that the lower total hydrogen in the covering resulted in lower diffusible hydrogen. Moreover, the diffusible hydrogen content tends to vary linearly with the square root of the total hydrogen content in the covering. This observation may be attributed to Sievert's law, Equation 43,

$$[H]_{steel} = \alpha \sqrt{p_{H_2}}, \quad (43)$$

where $[H]_{steel}$ is the concentration of hydrogen in steel, p_{H_2} is the partial pressure of hydrogen in the atmosphere, and α is a temperature dependent coefficient; indicating that diffusible hydrogen is proportional to the square root of partial pressure of hydrogen in the atmosphere.

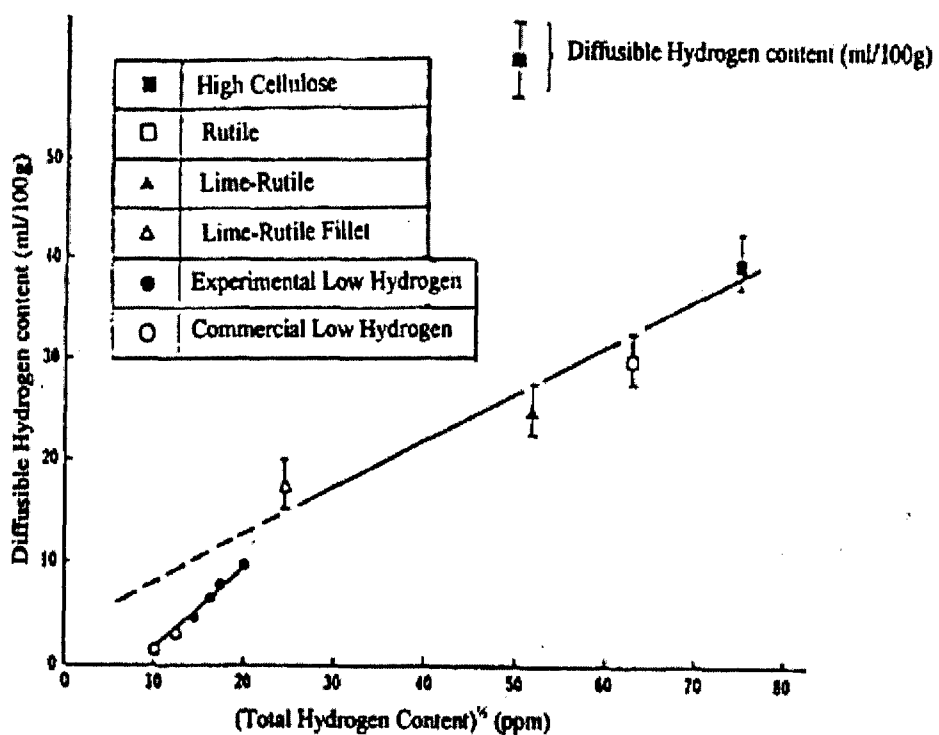


Figure 19: Relationship between diffusible hydrogen and total hydrogen content in the coatings [130].

2.5.4 Influence of the Atmosphere and Surrounding Environment on Steel Weld Metal Diffusible Hydrogen

It is known that the moisture in the atmosphere influences weld metal diffusible hydrogen pickup. Dickehut, et al. [131] modeled the hydrogen pickup in the weld metal as described by Sievert's law, Equation 43. Therefore higher vapor pressure will lead to a higher level of weld metal diffusible hydrogen.

Temperature and relative humidity are commonly used to describe atmospheric conditions. However, since dew point, or 100% relative humidity, is dependent on temperature, relative humidity does not correspond to absolute vapor pressure. The plot on the left of Figure 20 [131] illustrates the effect of vapor pressure as a function of temperature and relative humidity. As shown in the figure, the vapor pressure for the same relative humidity changes widely with temperature. For example, the vapor pressure at 30% RH changed from 0.03 to 2.21 kilopascals. The plot on the right of Figure 20 shows the relationship between vapor pressure and weld metal diffusible hydrogen content. It shows that the diffusible hydrogen content is a function of the vapor pressure. For instance, when the vapor pressure is 2.21 kilopascals, as indicated by points 4, 5, and 6 in the figure, the diffusible hydrogen content is 4.4 milliliters per 100 grams weld metal, independent of the relative humidity changes with temperature.

The contaminants on the base plate also influences the weld metal diffusible hydrogen level. If the surface of a base plate is wet and rusted, hydrogen may be introduced to the welding arc plasma and the weld metal. Iron oxides are hygroscopic, absorbing water as $-OH$ radicals [132], so that the rust on the surface of the plate must be removed and the plate kept dry. To avoid rusting during storage, the plate can be coated with a primer. However, the primer coating can also be a source of hydrogen during welding because it often contains organic compounds. Figure 21 [133] illustrates the weld metal diffusible hydrogen content as a function of primer coating thickness in welds performed with flux cored arc welding. It is obvious that the diffusible hydrogen level

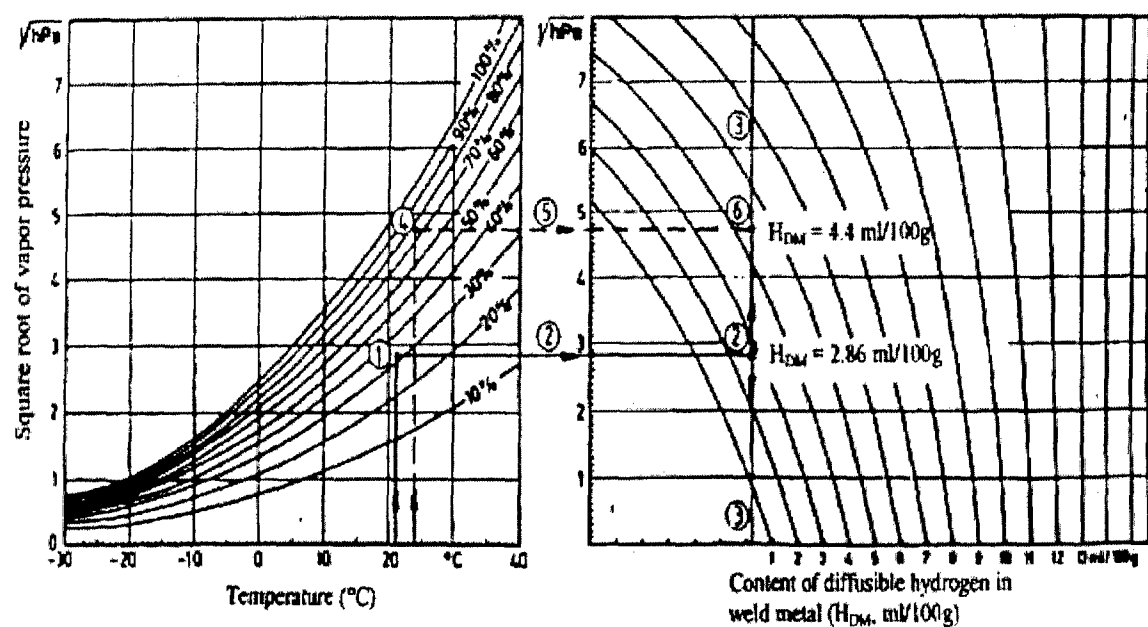


Figure 20: Vapor pressure/diffusible hydrogen content (PH₂O_{1/2}-HDM) diagram for redried basic-type SMAW electrodes; average value diagram [131].

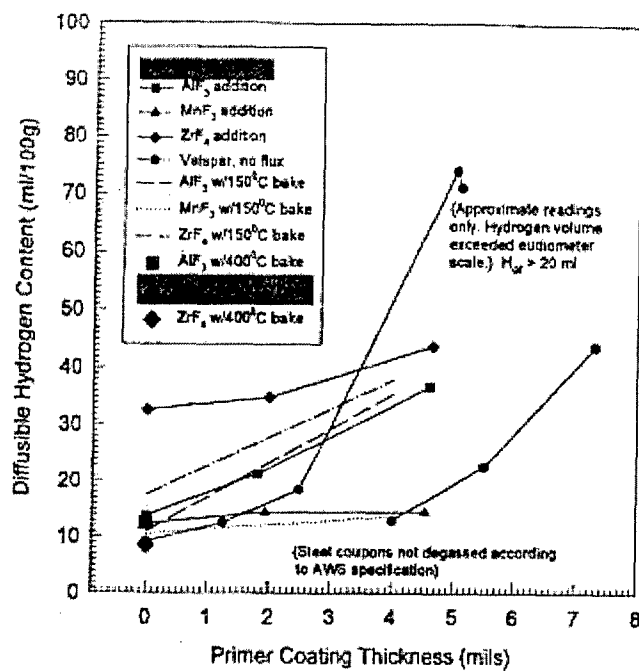


Figure 21: Effect of primer thickness, primer type, and fluoride additions on weld metal diffusible hydrogen content [133].

increases as the primer coatings become thicker. For the curve with no flux, the hydrogen level increased from ten to 73 milliliters per 100 grams weld metal while the primer thickness changed from 0 to 0.11 millimeters.

2.6 Hydrogen Management in Low Carbon and Low Alloy Steel Weldments

Mitigation of diffusible hydrogen in welds is one approach to prevent HAC in welds. These methodologies can be categorized as three groups: process-control, material-cleanliness-control, and metallurgical. The process-control approach includes preheating, control of interpass temperature, and postweld heating. Material cleanliness must be carefully controlled to assure minimizing hydrogen pickup. These process and cleanliness controls are effective only when performed precisely, and are also time-consuming, which lowers the convenience and productivity. Therefore, they must be made more efficient or simplified. Alternatively, high performance welding materials have been developed for low-hydrogen characteristics. The methods of reducing hydrogen for these welding materials are based on the metallurgical principles.

2.6.1 Modification of Flux Ingredients

Terashima et al. [134] and DeRissone et al. [135] investigated the effect of basicity of welding slags on diffusible hydrogen content in weld metal. In both cases, weld metal diffusible hydrogen level decreased with increasing basicity index. Basicity index is commonly represented by the one introduced by Tuliani et al. [14], Equation 44:

$$BI = \frac{CaO + MgO + BaO + SrO + Na_2O + Li_2O + CaF_2 + \frac{1}{2}(MnO + FeO)}{SiO_2 + \frac{1}{2}(Al_2O_3 + TiO_2 + ZrO_2)}, \quad (44)$$

where the basicity index is most likely acting as an indicator of the oxygen potential in the flux.

2.6.2 Control of Oxygen Content in the Steel Weld Metal

The effect of oxygen on diffusible hydrogen has been investigated by several researchers to establish a better understanding of the relationship between oxidizing electrodes and diffusible hydrogen [136-141]. It was shown that oxidizing electrodes are able to deposit welds with lower hydrogen content but with higher oxygen content, when compared to rutile electrodes [141]. This effect can be attributed to the following equilibrium reaction shown in Equation 45:



Based on the law of mass action, if the oxygen level on the right side of the equation is increased, the reaction will be forced to proceed to the left, resulting in a decrease in the hydrogen level in the system. Thus, the diffusible hydrogen level can be controlled by adjusting the oxygen level in weld metal.

2.6.3 Hydrogen Trapping in the Steel Weld Metal

Another method to reduce diffusible hydrogen is the use of hydrogen getters to trap hydrogen [142]. The introduction of trapping sites partitions the absorbed hydrogen between lattice sites and trap sites, forcing a redistribution of absorbed hydrogen, thus reducing diffusible hydrogen although the total hydrogen content of the weld is unchanged.

Based on theoretical predictions, Maroef et al. [142] investigated the effect of oxides and carbides of titanium, vanadium, neodymium, and yttrium. According to experimental data, a decrease of more than fifty percent of diffusible hydrogen, from 4.5 milliliters per 100 grams to 1.5 milliliters per 100 grams, resulted from an addition of 680 ppm of yttrium to the weld metal.

2.6.4 Dilution of Hydrogen in the Arc

Most industrial arc welding processes use inert gas to protect the arc from the surrounding atmosphere to avoid oxidation or nitriding of the molten metal. Argon, helium, and carbon dioxide shielding gases are good examples. The gases displace oxygen and nitrogen from the weld zone resulting in the low partial pressures of oxygen and nitrogen in the arc. For SMAW, self-shielded FCAW (FCAW-S), or SAW, calcium carbonate, CaCO_3 , is often added to the fluxes to have a similar shielding effect as carbon dioxide gas due to the decomposition of calcium carbonate in the arc, which generates CO_2 , as shown in Equation 46:



The dilution effect reduces the partial pressure of hydrogen that is originated by the decomposition of water. Weld metal diffusible hydrogen content is observed to linearly increase with the square root of the partial pressure of hydrogen in the atmosphere, according to Sievert's law [131], Equation 43. This relationship exists because moisture in the atmosphere goes into the arc and the hydrogen originated from the dissociation of water may find its way to the weld pool. Therefore, the reduction of partial pressure of hydrogen in the arc directly influences the hydrogen content in the weld metal.

In 1973, Tsuboi [143-145] conducted investigations to lower the diffusible hydrogen by adding calcium carbonate to agglomerated fluxes of SAW. Figure 22 [143] shows the result of diffusible hydrogen measurement when lime, CaO, was replaced with calcium carbonate. The diffusible hydrogen level was reduced from thirteen to one milliliter per 100 grams as the CO₂ content in the flux increased from zero to eight percent.

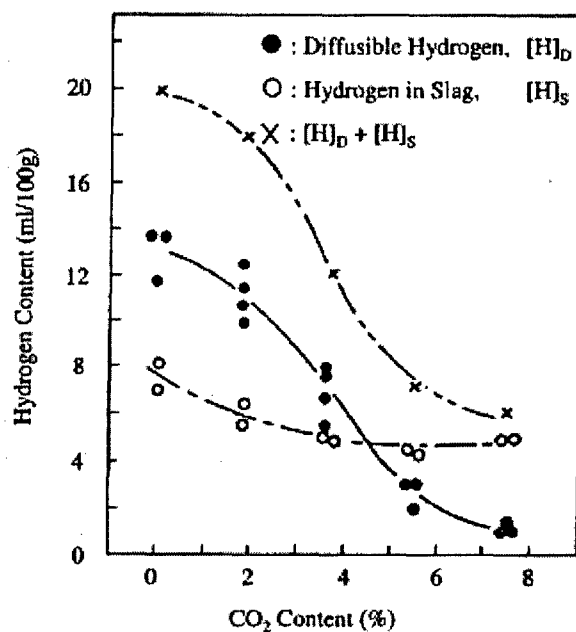


Figure 22: Effect of CO₂ in fluxes on diffusible hydrogen content in weld metal [143].

2.6.5 Addition of Fluorides

Another method to reduce the partial pressure of hydrogen is to add ingredients to the flux coating to react with hydrogen and form hydrogen-containing products that are insoluble in liquid iron. For example, fluorspar, CaF₂, is commercially added to the

fluxes of low hydrogen electrodes. It is believed that CaF_2 partially dissociates at high temperatures to produce fluorine and the increase of fluorine shifts the reaction occurring in the arc in Equation 47 to the right, resulting in reduced hydrogen in the arc [134, 146]:



where fluorine and hydrogen are assumed to be in the dissociated state.

Several studies have been undertaken to identifying more effective fluorides than CaF_2 , since CaF_2 is not particularly efficient in hydrogen removal. For instance, Tsuboi et al. [143-145] observed a greater reduction of diffusible hydrogen with the addition of Na_3AlF_6 to the welding flux as shown in Figure 23. The diffusible hydrogen level was four milliliters per 100 grams of the deposited weld metal which was thirty percent lower than that obtained by using CaF_2 .

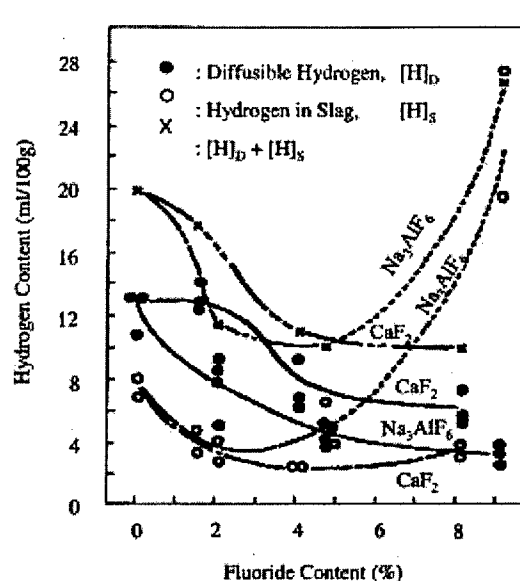


Figure 23: Influence of fluoride content in fluxes on diffusible hydrogen content in weld metal and slag [143].

This line of research received little attention during the 1980's while the optimization of CE in high strength steels and their weld metals were being studied to reduce their HAC susceptibility. However, as further reduction of diffusible hydrogen content was demanded, the approach of adding fluorides to reduce hydrogen gained new interests in the 1990's. Pokhodnya, et al. [147] reported the effectiveness of complex fluorides such as Na_2SiF_6 , Na_2TiF_6 , K_2SiF_6 , and K_2TiF_6 . Their FCAW experiments demonstrated that these complex fluorides produced welds with diffusible hydrogen levels between 3.5 and 6.5 milliliters per 100 grams as compared to the ten milliliters per 100 grams of weld metal deposited with CaF_2 consumables, as shown in Figure 24.

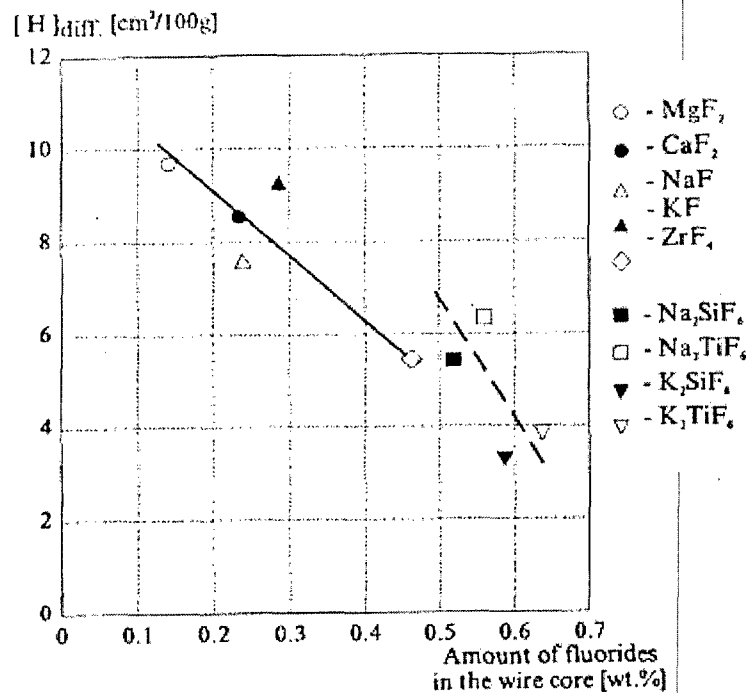


Figure 24: Plot of diffusible hydrogen content in deposited weld metal as a function of the amount of fluorides in the wire core [147].

2.7 Yttrium

Yttrium, element 39 on the periodic table, is the first of the second transition group, and thus is in Group IIIB along with scandium, lanthanum and actinium. Although it is not a rare earth element, due to its similarity in both chemical and metallurgical respects [148], it is often classified as a rare earth. Unlike many of the rare earth elements, yttrium only exists in the trivalent, Y^{3+} , state. The similarity in behavior in solutions between Y^{3+} ion and ions of the rare earth elements is largely due to the lanthanide contraction, which reduces the size of the heavier rare earths so that they are similar to that of Y^{3+} [148, 149].

Yttrium is a large atom compared to most metals, and can form substitutional solid solutions with only a few metals [149]. Yttrium will form nearly complete solid solutions with the rare earths and thorium, and has significant solid solubility in magnesium; however, the solubility of yttrium in iron is quite low and this element forms several intermetallic compounds: Fe_9Y , Fe_4Y , Fe_3Y , and Fe_2Y , as can be seen in the iron-yttrium phase diagram shown in Figure 25. Li, et al. [150] studied the solubility of cerium, neodymium, and yttrium in α -iron at room temperature. Based upon thermodynamic data, and by assuming that dilute solutions of yttrium in α -iron are Henrian, Li, et al. calculated the solubility of yttrium in α -iron as a function of temperature:

$$\ln X_Y^\alpha = -5.892 - 2362.7T \quad (48)$$

where X_Y^α is the solubility of yttrium in α -iron in atomic percent and T is the absolute temperature. Taking room temperature to be 293 K, the calculated solubility of yttrium in α -iron is 0.0001 weight percent, whereas, the solubilities of neodymium and cesium in room temperature α -iron were found to be 0.0032 weight percent and 0.0048 weight

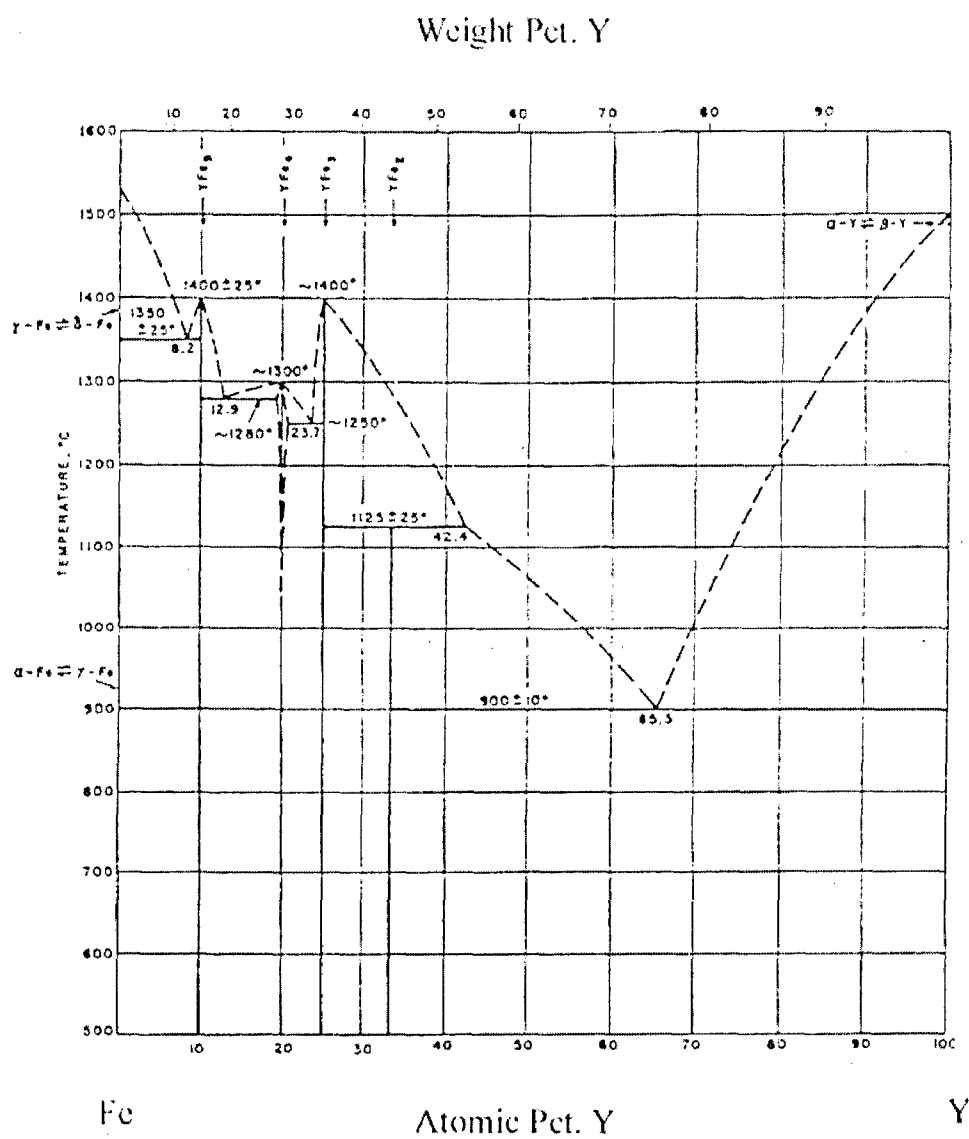


Figure 25: Binary phase diagram of iron-yttrium system [152].

percent, respectively. Since intermetallic compounds are often brittle, their presence in a ferritic weld is likely to be detrimental to weld metal toughness, so that any filler metal designed to contribute yttrium to the weld metal will need to be carefully balanced to limit yttrium levels to below those required for deoxidation and desulfurization.

Like the rare earths, yttrium has a strong affinity for oxygen and sulfur. The free energy diagram of oxide formation, shown in Figure 26, shows that yttrium has a considerably higher affinity for oxygen than other traditional steel weld metal deoxidizers such as aluminum, titanium, manganese, and silicon. Only zirconium, beryllium, calcium, and the rare earths compete with the deoxidizing behavior of yttrium. Yttrium forms a single oxide, yttria, with the composition Y_2O_3 ; which has a reported melting point of $2680^\circ C$ [151], a density of 4.84 g-cm^{-3} [151], and a coefficient of thermal expansion of $9.3 \times 10^{-6} \text{ }^\circ C^{-1}$ from room temperature to $1400^\circ C$ [149]. The crystal structure of yttria is reported to be cubic with a lattice parameter of 10.605 \AA . The structure of yttria is shown in Figure 27, where one-quarter of the anion sites are empty. The vacancies on the oxygen sublattice allows for rapid diffusion of oxygen, while yttrium diffusion is restricted to interstitial diffusion. In addition to the cubic structure, a hexagonal close packed structure has been reported above $2310^\circ C$ [153].

The thermodynamics of the Fe-Y-S, Fe-Y-O and Fe-Y-S-O system have been studied by Wing and Longmei [154-156]. They considered the formation of Y_2O_3 , Y_2O_2S , Y_2S_3 , and YS in liquid iron at 1575 , 1600 , $1625^\circ C$ and obtained relationships for the standard Gibbs free energy and equilibrium constants provided in Table 3. A phase stability diagram for the Fe-Y-S-O systems is shown in Figure 28.

With the presence of titanium, aluminum, manganese, silicon, and yttrium, complex interactions between these species and oxygen are expected. A number of compounds between Y_2O_3 and oxides of aluminum, titanium, manganese, and silicon have been identified and are listed in Table 4. Figure 29(a), (b), and (c) are the phase diagrams for $Y_2O_3\text{-}Al_2O_3$ [153], $Y_2O_3\text{-}TiO_2$ [159], and $Y_2O_3\text{-}SiO_2$ [160], respectively.

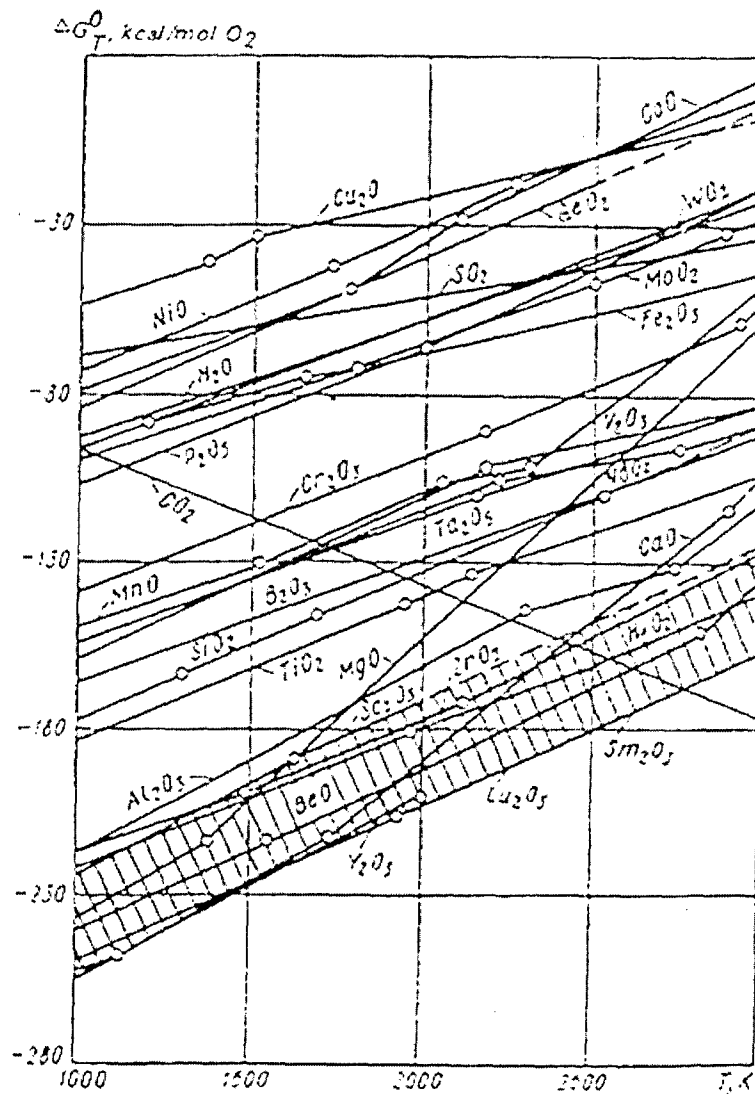


Figure 26: The temperature dependences of the isobaric-isothermic potential of formation of specific oxides [157].

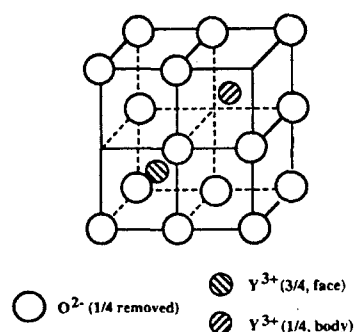


Figure 27: Crystal structure of Y_2O_3 . Three quarters of cations are in cubes in which the missing oxygens are along a face diagonal. One quarter of cations are in cubes in which the missing oxygens are along a body diagonal [158].

Table 3: Thermodynamic Parameters for the Deoxidation, Desulfurization and Deoxysulfurization of Yttrium in Liquid Iron.

Reactions	$\Delta G^\circ = C + DT$ (J/mol)		$\log K = -(A/T) + B$	
	$10^{-6} \times C$	$10^{-3} \times D$	$10^{-4} \times D$	B
$Y_2O_{3(s)} = 2[Y] + 3[O]$	1.793	-0.658	9.365	34.4
$Y_2O_2S_{(s)} = 2[Y] + 2[O] + [S]$	1.521	-0.536	7.949	28
$Y_2S_{3(s)} = 2[Y] + 3[S]$	1.171	-0.441	6.119	23.1
$YS = [Y] + [O]$	0.321	-0.091	1.677	4.7

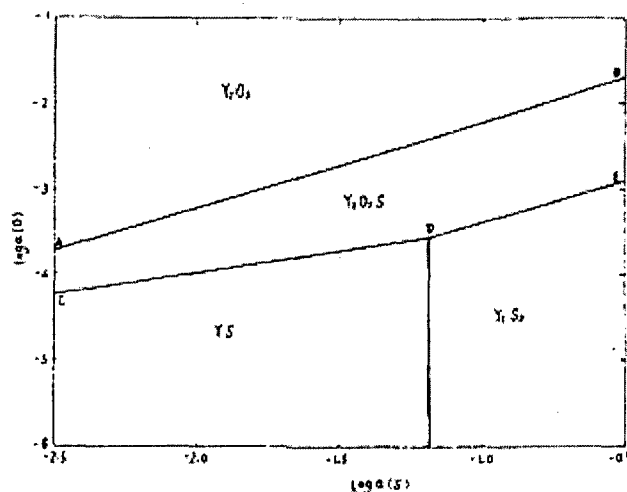


Figure 28: The phase stability diagram for the Fe-Y-S-O system at 1600°C [156].

Table 4: Potential Compounds Between Y_2O_3 and Oxides of Aluminum, Titanium, Manganese, and Silicon.

Compound	Reference
$Y_4Al_2O_9$	153
$YAlO_3$	153
$Y_3Al_5O_{12}$	153
$Y_2Ti_2O_7$	159
Y_2TiO_5	159
$YTiO_3$	162
Y_2SiO_5	160
$Y_4Si_3O_{12}$	160
$Y_2Si_2O_7$	160
YMn_2O_5	163
$YMnO_3$	164

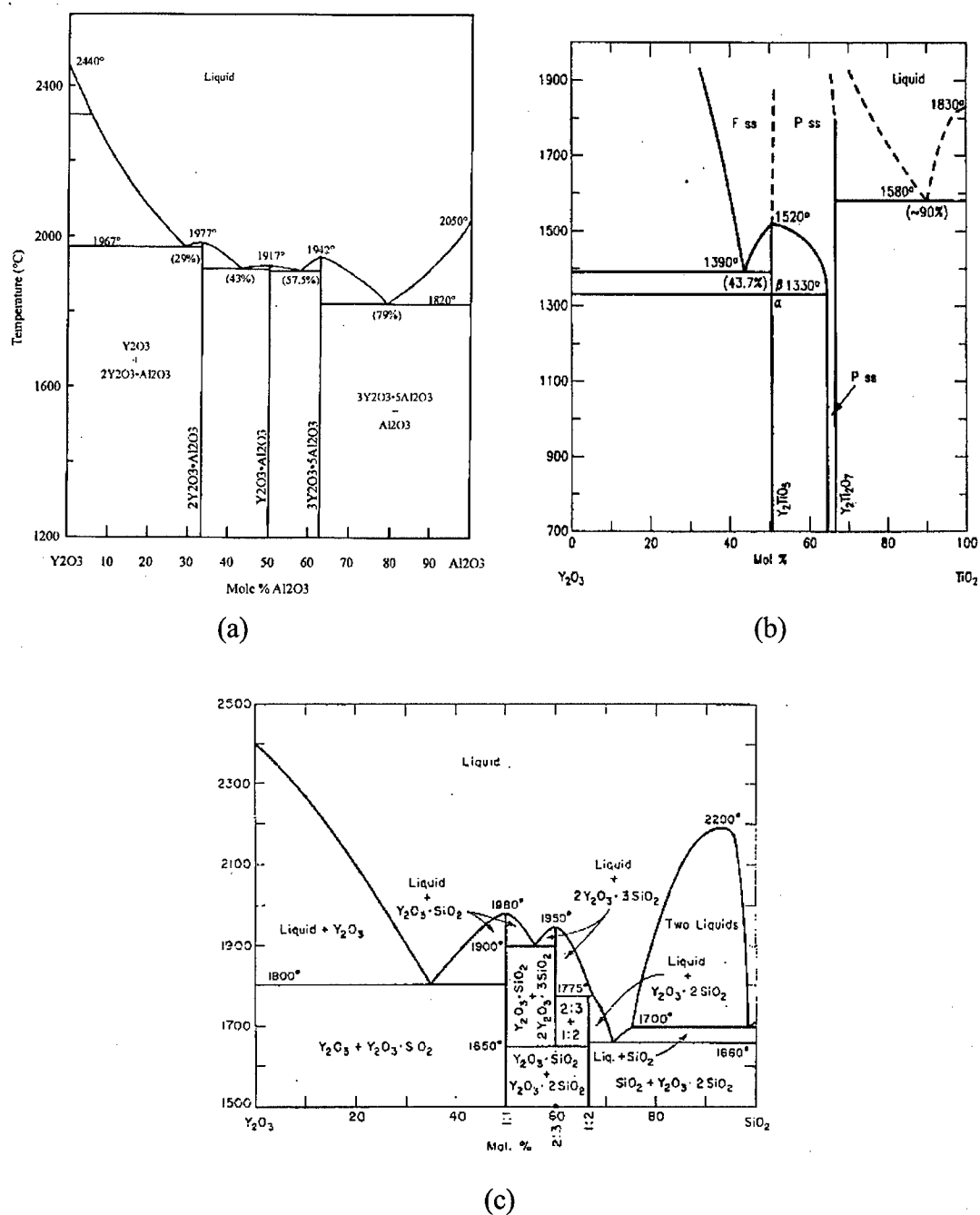


Figure 29: (a) Phase diagram for the Y_2O_3 - Al_2O_3 system [153]. (b) Phase diagram for the Y_2O_3 - TiO_2 system [159]. (c) Phase diagram for Y_2O_3 - SiO_2 system. Oxide ratios of compounds are given as Y_2O_3 : SiO_2 [160].

Shiliang, et al. [161] studied the effects of yttrium additions to flux coatings of SMAW electrodes employing a $\text{CaCO}_3\text{-SiO}_2$ high basic slag system on the mechanical properties and inclusion development in a low alloy steel weld deposit. Yttrium additions were made as pure yttrium and as yttrium-containing ferrosilicon. In the weld metal incorporating yttrium, Shiliang, et al. observed that the inclusions were mainly complex silicates containing yttrium, titanium, and manganese. The inclusions were spherical with diameters on the order of one micron. No change in tensile or room temperature impact properties were observed with weld metal yttrium contents up to 16 ppm; however, low temperature (-40°C) impact properties increased with increasing weld metal yttrium contents up to ten ppm and decreased thereafter. Efimenko [165] also considered small additions of yttrium on the mechanical properties of basic carbon steel SMAW electrodes. Efimenko reported the optimal improvements in weld metal impact properties was obtained with a yttrium content in the coating to be in the range of 0.2 to 0.4 weight percent.

Aleksandrov, et al. [166] evaluated the effects of calcium, yttrium, and cerium in the electrode coating, at levels higher than those used by Shiliang, et al. and Efimenko, on the microstructure and impact properties of a 0.1 weight percent carbon, 0.7 weight percent manganese ferritic steel deposit. They used a 4-mm-dia. electrode with a rutile-type coating containing 41 to 45 weight percent rutile, 23 weight percent mica, fifteen weight percent magnetite, fifteen weight percent ferromanganese, two weight percent cellulose, and zero to four weight percent AlY . The impact properties were observed to be optimal at a two percent AlY addition to the coating, which was reported to produce a weld deposit of 500 ppm yttrium. Inoculating the deposit with yttrium was shown to reduce the grain size and the amount of nonmetallic inclusions, and the inclusion morphology changed from irregular-shaped chains of inclusions to globular shaped uniformly distributed, discrete inclusions.

2.7.1 Effects of Inclusion and Microstructural Development

Clark [9] studied the effects of yttrium on the development of inclusions and microstructure in low carbon, low alloy steel welds. He characterized the weld deposits into three categories: yttrium-free welds, high-yttrium welds, and low-to-moderate yttrium welds, where the division between each category is based upon the ratio of yttrium to oxygen. A yttrium-to-oxygen ratio of 3.7 represents the stoichiometric balance to produce yttria. Welds with a ratio greater than 3.7 have excessive yttrium content and were referred to as high-yttrium or hyperstoichiometric welds, whereas, those with a ratio less than 3.7 have an excess of oxygen and are referred to as low-to-moderate or hypostoichiometric welds.

Clark and Edwards [11, 12] characterized inclusions using light optical microscopy and transmission and scanning transmission electron microscopy. During light optical microscopy, they noticed that inclusions in hyperstoichiometric welds were clustered and possibly sintered together. The inclusions present in hypostoichiometric welds were not clustered, but did begin to cluster as the yttrium-to-oxygen ratio increased towards 3.7.

Using electron microscopy, they further characterized the inclusions with morphological, compositional, and crystallographic considerations. Yttrium-free welds contained complex inclusions that contained aluminum, manganese, silicon, iron, and sulfur, as well as titanium when present in the weld deposit. These inclusions were discrete, randomly distributed, and spherical in shape. Based on electron dispersive spectroscopy (EDS) and SAD analysis, these inclusions possessed manganese sulfide caps, and complex, multiple-phased bulk composition. Hyperstoichiometric welds contained inclusions comprised of yttrium, sulfur, and oxygen with only minor amounts of other constituents. These inclusions contained no manganese or silicon, and limited amounts of aluminum, iron, and titanium. Clark and Edwards [11, 12] reported that the aluminum was present only infrequently and the titanium was present in large cuboidal

shaped particles, most likely TiN. Morphologically, these inclusions were clustered, often producing extensive networks of coalesced oxides, where each cluster contained up to a hundred or more individual members. In hypostoichiometric welds, inclusions were found to be compositionally complex, containing aluminum, yttrium, titanium, and sulfur. Based on EDS and SAD analysis, they reported that the inclusions contained manganese sulfide caps, similar to the yttrium-free welds, and that the bulk of the inclusions were yttrium aluminum garnet (YAG - $Y_3Al_5O_{12}$) with titanium distributed throughout the inclusion, suggesting that the titanium may substitute for the aluminum. These inclusions were reported to be discrete, randomly distributed, and spherical in shape. Figure 30 shows the STEM image of a representative inclusion from a hypostoichiometric weld, as well as the EDS dot mapping showing the distribution of aluminum, yttrium, titanium, manganese, sulfur, and iron. The most notable features of this figure are the spherical shape of the oxide and the uniform distribution of aluminum, yttrium, and titanium. Another feature that can be noticed is the displacement of the manganese and sulfur to the one spot forming a manganese sulfide cap.

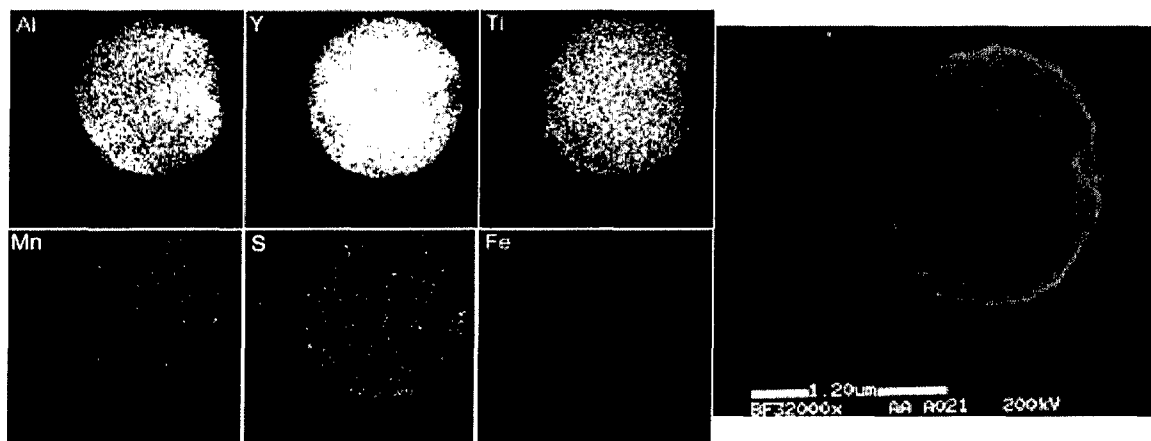


Figure 30: STEM image of a representative oxide from a hypostoichiometric weld with EDS dot maps showing the distribution of aluminum, yttrium, titanium, manganese, sulfur, and iron [9].

Clark and Edwards [11, 12] characterized microstructures of weld deposits using the same three categories. Figure 31 show representative photomicrographs of welds of each category. Yttrium-free welds were reported to produce welds comprised of ten percent acicular ferrite, 85 percent ferrite with aligned second phase, and five percent grain boundary ferrite. The low acicular ferrite content was attributed to the formation of MnSiO_3 , which has been reported to produce a glassy slag that covers the oxides and inhibits acicular ferrite formation. The hyperstoichiometric welds consisted of a microstructure similar to the yttrium-free welds, where ferrite with aligned second phase is the primary constituent. In these welds, yttria was expected to be present in significant levels, and the oxygen was expected to react completely with yttrium and aluminum before the formation of any titanium-containing oxides. The hypostoichiometric welds consisted of nearly seventy percent acicular ferrite, 25 percent ferrite with aligned second phase, and five percent grain boundary ferrite. This was reported to be due to the distribution of titanium in the YAG inclusions.

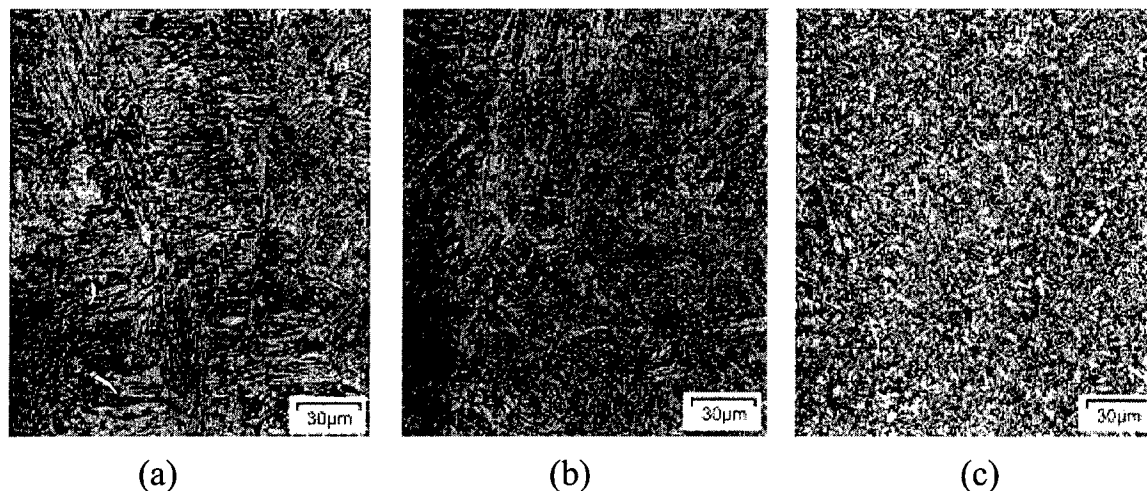


Figure 31: Representative photomicrographs of (a) yttrium-free welds, (b) hyperstoichiometric welds, and (c) hypostoichiometric welds [9].

2.7.2 Effects on Hydrogen Management

In a recent study, Maroef [5] investigated the benefits and effectiveness of strong irreversible hydrogen traps in reducing diffusible hydrogen content of GMA and GTA welds on Armco iron. Based on the theoretical calculations by Olson, et al. [167], which suggests yttria inclusions may be effective hydrogen traps, Maroef conducted diffusible hydrogen measurements on a series of GMA welds made with a mild steel filler metal containing yttrium. Figure 32 shows the results of these studies. Reductions in weld metal diffusible hydrogen levels of about fifty percent were observed with increasing yttrium additions in the range of 0 to 680 ppm yttrium in the Armco iron deposits.

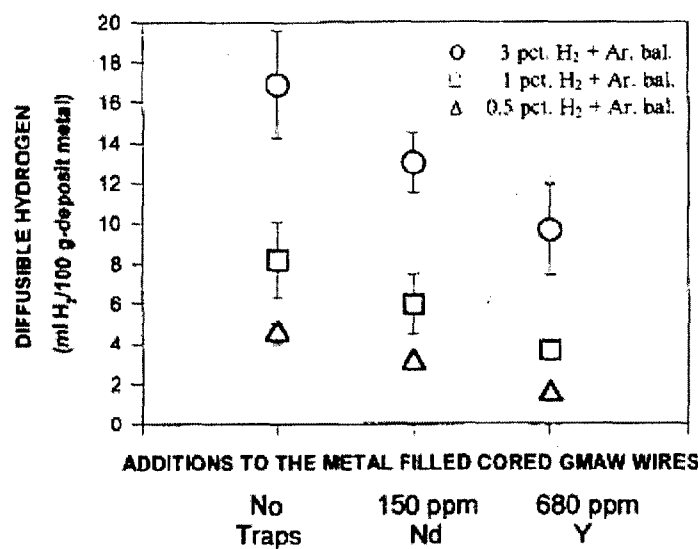


Figure 32: Effect of trap additions to the amount of diffusible hydrogen in Armco iron samples welded with GMA welding processes at three levels of hydrogen contamination in the shielding gas and at nominal heat input of 1.5 kJ/mm [5].

The work of Maroef [5] was extended by Lensing [4] to consider the effectiveness of yttrium additions to produce hydrogen traps in C-Mn and low alloy steel welds. Similar to the work performed by Maroef, Lensing used diffusible hydrogen measurements and hydrogen thermal desorption analyses to study trapping behavior in yttrium containing C-Mn and low alloy steel GMA weld deposits. Lensing identified two potential irreversible traps; one with a binding energy of seventy kilojoules per mole of hydrogen, which he attributed to yttria; and a second with a binding energy of 96 kilojoules per mole of hydrogen, which was attributed to yttrium oxysulfides.

The work of Maroef, Lensing, and Olson [4-8, 167] has demonstrated that Y_2O_3 and Y_2O_2S inclusions are potential irreversible hydrogen traps for ferritic steel weld deposits resulting in a reduction of diffusible hydrogen to less than 1.5 ml H_2 /100g weld metal. They showed that yttrium additions clearly result in diffusible hydrogen reduction. Clark [9] verified their work, and attributed the decrease to an increase in oxide inclusion surface area and not to any specific oxide composition.

2.8 Effective Fluoride Additions and Their Effects on Hydrogen Management

The use of effective fluoride additions, their effects on hydrogen management, and the mechanisms of hydrogen reduction are discussed in this section.

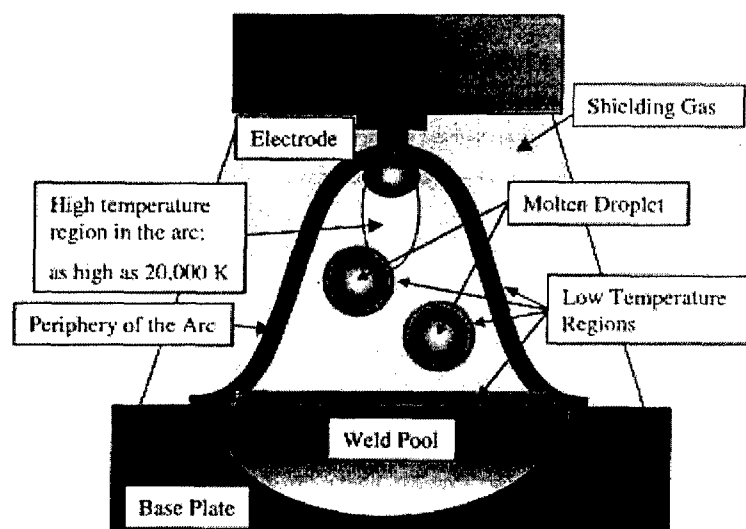
2.8.1 Consideration of Mechanism of Reduction of Hydrogen Pickup

The reduction of partial pressure of hydrogen with fluoride additions is generally considered a result of the formation of HF in the welding arc. The reaction does not occur homogeneously in the welding arc because of its high temperature. The temperatures observed near the electrode tip can be as high as 20,000K [168-175]. At this temperature, the arc constituent elements are expected to be monatomic or ionized, instead of molecular. Therefore, the HF formation must occur in the low temperature regions in the

arc such as the periphery of the arc and the surroundings of the molten metal droplet as illustrated in Figure 33.

Weld metal hydrogen absorption in the arc atmosphere is considered to occur on the surface of the molten droplet and molten pool during welding, where the resulting hydrogen concentration in the weld metal is assumed to follow Sievert's Law, Equation 43. Subsequently, the HF will be ejected to the outer atmosphere due to the mass flow from the electrode tip to the weld pool. This sequence is designated as the mechanism of "HF formation effect."

On the other hand, HF formation is also considered to occur at the periphery of the arc, which causes changes in the hydrogen mass transport. The presence of HF varies the mass transport of hydrogen atoms from the periphery to the cathode region. The reduction of hydrogen pickup as a consequence of this mechanism is different from the HF formation effect and was designated as the "HF transport effect."



* HF formation occurs at low temperature regions illustrated above

Figure 33: Illustration of the low temperature regions in the arc system [2].

Calcium carbonate is added to the welding flux to dilute the arc atmosphere with CO_2 and therefore protect weld metal from the surrounding atmosphere. Similarly, the dilution of the arc atmosphere by vaporized fluoride is also possible, and, as a result, hydrogen pickup from the surrounding atmosphere can be minimized. This mechanism of hydrogen reduction is not related to the formation of HF. The chemical species contained in the fluoride, either compound form of the fluoride; e.g., CaF_2 , or atomic or ionic form; e.g., Ca or Ca^{2+} and F or F^- , displace the arc atmosphere, resulting in a reduction of hydrogen partial pressure. This designated "dilution effect" is illustrated in Figure 34.

The three mechanisms will be discussed with simplified models in the following sections, and the behavior of hydrogen and its interaction with other chemical species with respect to these mechanisms will be predicted.

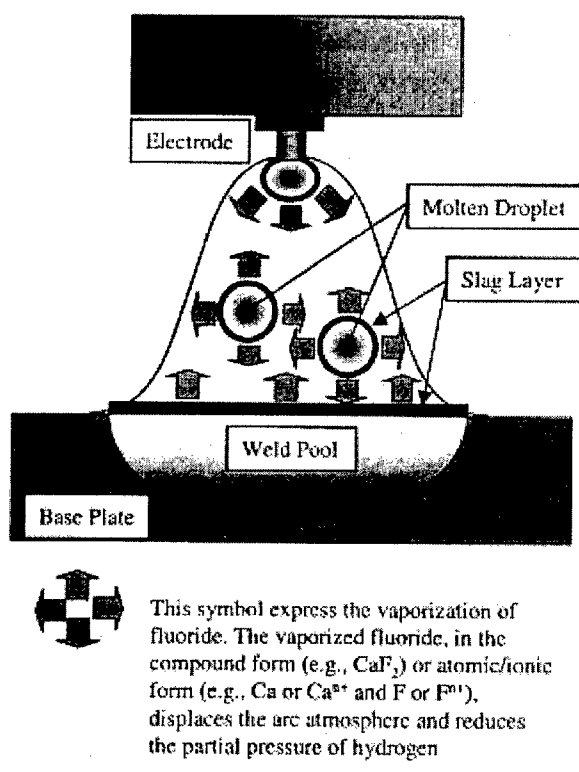


Figure 34: Illustration of dilution effect in the arc system [2].

2.8.2 Thermodynamic Behavior of Species Involved in HF Formation

A review of the thermodynamic behavior of the species that are involved in the formation of potassium fluoride is discussed in the following sections.

2.8.2.1 Forms of Hydrogen

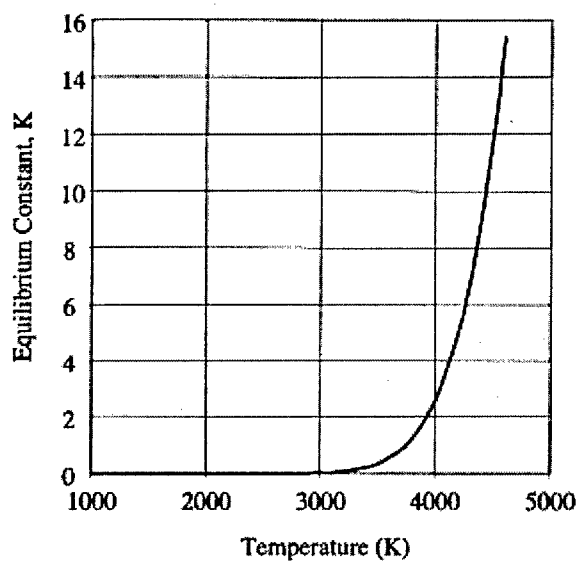
Hydrogen molecules dissociate to single atoms at high temperatures. The dissociation temperature of diatomic hydrogen can be predicted with the thermodynamic calculations. From the standard free energy change of the dissociation of diatomic hydrogen, the standard free energy as a function of temperature can be described as:

$$\Delta G^{\circ} = a + bT \ln T + cT^2 + dT^{-1} + eT. \quad (49)$$

where the constants, a , b , c , d , and e for chemicals or minerals are found in thermodynamic tables [176, 177]. Once the standard free energy is obtained, the equilibrium constant can be calculated as a function of temperature. According to the law of mass action, changes in the partial pressure of H_2 and H due to dissociation is shown in Table 5. Ten and ninety percent dissociations of hydrogen, where α in Table 5 is 0.1 and 0.9, respectively, can be established when the equilibrium constants, K , are 0.011 and 8.1, respectively. Figure 35 shows the calculated result. Below 2,900K, K is less than 0.011 and more than 8.1 above 4,400K. The ninety percent dissociation temperature of hydrogen calculated here is close to that reported by Milner, et al. [178] shown in Table 6. Therefore, hydrogen can be present in mostly diatomic form below 2,900K, in both monatomic and diatomic form in the temperatures between 2,900 and 4,400K and mostly in monatomic form above 4,400K.

Table 5: Law of mass action for dissociation of H_2 [2].

	H_2	H
P_{H_2} (atm)	N	0
P_H (atm)	$(1-\alpha)n$	$2\alpha n$



$$K = \frac{P_H^2}{P_{H_2}}$$

Figure 35: Equilibrium constant of reaction, $\frac{1}{2} H_2 = H$ [2].

Table 6: Dissociation Potential and 90 Percent Dissociation Temperature for Various Multi-Atomic Gases [178].

Gas	CO_2	O_2	H_2	N_2
Dissociation Potential	4.3	5.084	4.477	9.762
90% Dissociation Temperature (K)	3800	5110	4575	8300

2.8.2.2 Vaporization of Fluorides

Since fluorine introduced to the arc is initially provided in the form of fluorides, the stability of fluorine must influence the formation of HF. Figure 36 shows the weight loss of MnF_3 , KF , LiF , K_3AlF_6 , and CaF_2 when subjected to high temperatures. MnF_3 lost weight significantly below 600°C due to the dissociation to MnF_2 and F . KF is hygroscopic; therefore, the weight loss shown below 400°C must be due to the release of water. KF , LiF , K_3AlF_6 , and CaF_2 began to lose their weight at their melting points due to the vaporization. Melting of MnF_2 was not observed. MnF_2 is considered to sublime at higher temperatures [177]; therefore, it begins to lose weight at its sublimation temperature due to vaporization.

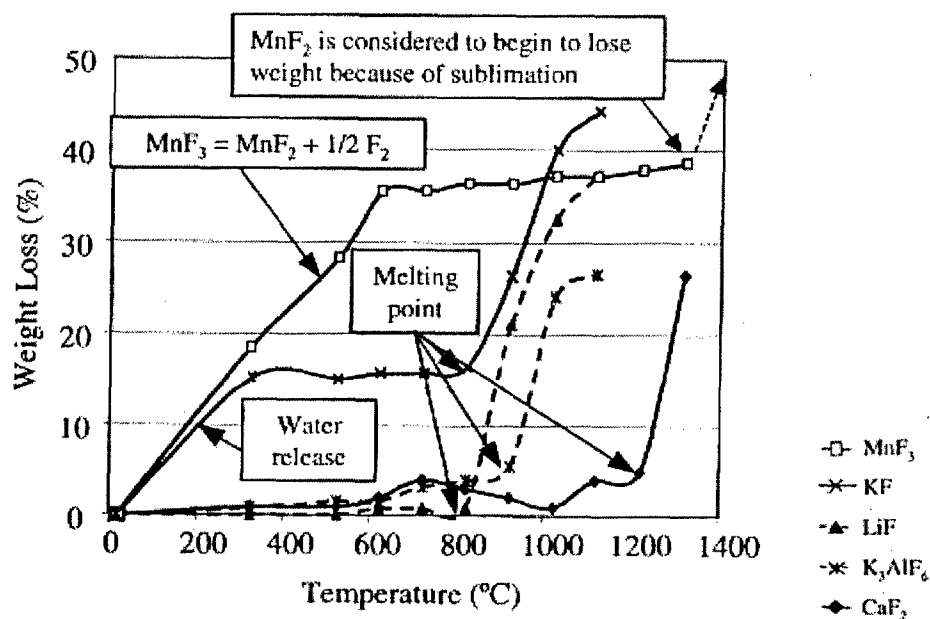


Figure 36: Reduction in weight at elevated temperatures for various fluorides [2].

The equilibrium constants of vaporization of CaF_2 , KF , and MnF_2 were calculated and shown in Figure 37. Johnson [133] reported the effectiveness of MnF_3 on reducing diffusible hydrogen in weld metal deposited on primer coated steel plates. Also, Liu, et al. [1] reported the effectiveness of MnF_3 and KF based on thermodynamic calculations. MnF_3 dissociates to MnF_2 and F at relatively low temperatures; consequently, MnF_2 instead of MnF_3 was considered in this calculation. CaF_2 and KF melt at their respective melting points as shown in Figure 36, while MnF_2 stays solid form below its sublimation temperature. The equilibrium constant of vaporization is expressed as Equation 50:

$$K = \frac{P_{MF(\text{gas})}}{a_{MF(\text{solid/liquid})}}, \quad (50)$$

where the MF in subscripted letters represents any fluoride, p is vapor pressure of MF in gas state, and a is activity of MF in solid or liquid state. Considering pure MF , the

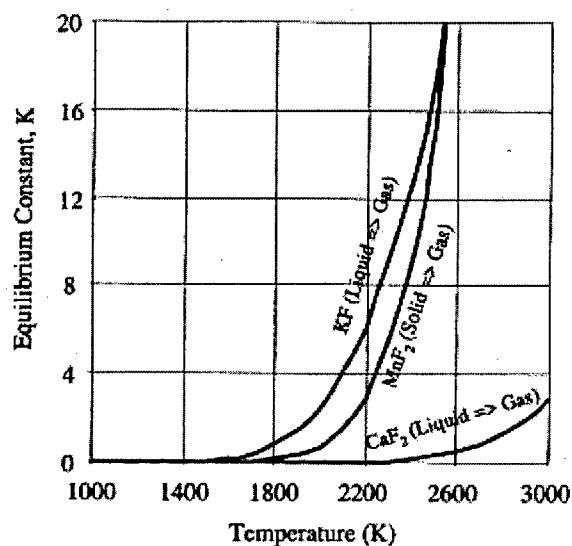


Figure 37: Equilibrium constants of vaporization of fluorides [2].

activity is unity. Therefore, when the equilibrium constant is unity, the vapor pressure is one atmosphere, so boiling occurs under ambient pressure in the case of transition from liquid to gas, and sublimation in the case of transition from solid to gas. The equilibrium constants of CaF_2 , KF , and MnF_2 are unity at 2750, 1830, and 2040K, respectively. These temperatures are the boiling points of the CaF_2 and KF and the sublimation point for MnF_2 . Vaporization of these fluorides occurs below their boiling or sublimation points but not at high rates. Since the equilibrium constants of KF and MnF_2 , which are also related to rate of these reactions, exponentially increase above their boiling points, the vaporization of these fluorides occurs rapidly above this temperature. On the other hand, CaF_2 has a higher boiling point than the others, and its equilibrium constant is far lower. Therefore, the vaporization of CaF_2 can be considered to be lower than the others.

Summarizing all the temperature ranges, MnF_3 is the most active fluoride to form HF ; in other words, the most effective in reducing the partial pressure of hydrogen. Contrarily, CaF_2 would be the least effective among these three fluorides. Moreover, taking into account the reacted fraction of reactants according to the law of mass action, the most effective temperature region to produce HF must be Region 2.

Even though the thermodynamic calculation predicted the effectiveness of MnF_3 and KF , the addition of MnF_3 and KF to the welding flux must involve limitations or cautions. The amount of the additions must be minimized because HF , which is a hazardous substance, is more actively formed by the reaction between hydrogen and MnF_3 and KF rather than CaF_2 . Careful ventilation and respiratory equipment for the welder are recommended when fluxes containing these fluorides are being used. Also, these fluorides are unstable even at ambient temperature that it may react with other substance in the flux.

2.8.3 Model of HF Formation Effect

A description of the model for potassium fluoride formation is present in this section.

2.8.3.1 Reaction Occurring in the Surroundings of Molten Pool and Molten Droplet

The gas temperature drops rapidly at the surroundings of the molten pool or molten droplet due to deprivation of heat from the arc atmosphere caused by the vaporization of metal or slag from their surfaces. The temperature of the molten steel is no more than the boiling temperature of iron, 2862°C. Taking into account the heat deprivation caused by vaporization of the molten steel and slag, the surface of the molten pool or molten droplet may be stabilized at approximately 2,500°C [179]. The region with a large temperature gradient is considered to be a very thin layer, less than a millimeter because of convection heat [180]. The reaction between fluoride and hydrogen to form HF must occur within this thermal layer between the surface temperature of the molten pool or droplet and the temperature of the HF formation limit.

According to thermodynamic calculations, the reactions between fluoride and hydrogen in the thermal layer are modeled as shown in Figure 38. The highest temperature of Region 1 (2,900K) is very close to the surface temperature of molten pool or molten droplet (2,773K) so that Region 1 is neglected in this model [2]. Therefore, the surface of molten pool or molten droplet is considered to be adjacent to the Region 2, which is the most effective range to form HF for the three fluorides: CaF_2 , KF and MnF_2 . Also, the thermodynamic calculations predicted the greatest effectiveness for MnF_2 , while CaF_2 was the least effective.

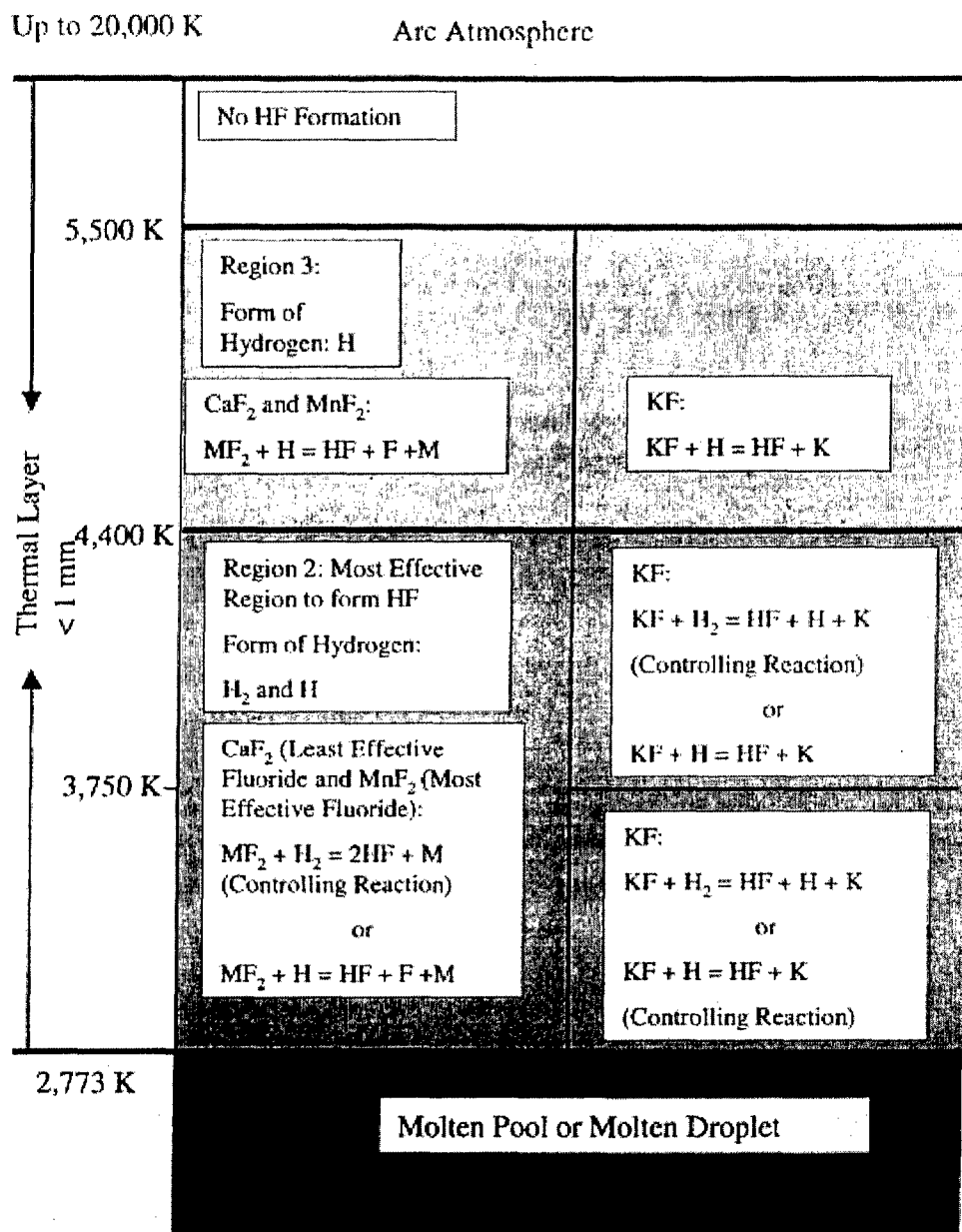


Figure 38: Illustration of reactions between fluoride and hydrogen in thermal layer surrounding molten pool or droplet [2].

2.8.3.2 Concerns for Hydrogen Absorption from the Arc Atmosphere to Weld Pool

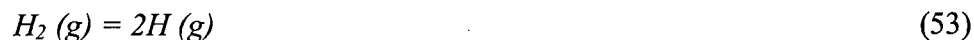
The absorption of hydrogen during welding is also an issue. There are two methods of hydrogen absorption in a molten pool of steel, such as monatomic hydrogen absorption,



and diatomic hydrogen absorption,



In these equations, \underline{H} is dissolved hydrogen in molten steel. Some researchers have applied Sievert's law, Equation 43, which only considers the reaction in Equation 52 at equilibrium, to the absorption of hydrogen during welding. However, monatomic (H) and diatomic (H₂) hydrogen coexist in Region 2, adjacent to the molten surface. Therefore, Sievert's law alone, as derived from classical thermodynamics, does not completely explain the hydrogen absorption phenomena. Gedeon, et al. [180] suggested that the absorption of hydrogen occurs through both reactions in Equations 51 and 52 during welding. The partial pressure of either H or H₂ is reduced by the controlling reaction in Region 2 dependent on the cases of CaF₂, KF and MnF₂. However, the reduction of either of them quickly responds to the reduction of the other due to the equilibrium reaction of Equation 53:



Therefore, the fluorides in the thermal layer are considered to reduce partial pressures of both H and H₂, preventing their absorption into the molten pool or molten droplet.

2.8.4 Model of HF Transport Effect

Hydrogen fluoride formation is considered to occur at the periphery of an arc, which causes a change in the hydrogen mass transport. Figure 39 shows the illustration of the temperature regions of HF formations and reactions considered to take place in the respective temperature region. HF must be formed in the periphery of the arc below 5,500K, and is partitioned within the three regions depending on the form of hydrogen and the controlling reaction to form HF. Region 2 between 2,900 and 4,400K is considered to be the most effective range to form HF.

There is a high temperature gradient from the cathode center to the anode center in the arc, varying from approximately 20,000 to 10,000K. The mass velocity varies from 2×10^2 meters per second at the cathode region to about one to ten meters per second near the anode. Hiraoka [174] observed the accumulation of small atoms such as hydrogen and helium at the arc center when the gases of those small atoms were mixed with argon shielding gas. He attributed this phenomenon to the large temperature and pressure gradients at the cathode region. He also pointed out that a change in hydrogen diffusivity might occur due to the dissociation of hydrogen molecule or some reactions of hydrogen with other species. Therefore, it is possible to consider the change in diffusivity of hydrogen due to HF formed in the temperature regions shown in Figure 39, which may vary the mass transport of hydrogen atoms from the periphery to the cathode region. Figure 40 illustrates the accumulation of small atoms in the arc center mixed with argon shielding gas by isotherms and mass flow lines. This mass flow is considered to occur due to the pressure increase originated by a self-induced magnetic field and the temperature increase and the ionization of the gas species. An increase of the temperature, which accelerates the mean velocity of particles (atoms and ions), results in an increase of the pressure. The relationship between kinetic energy of a particle and temperature is given as Equation 54:

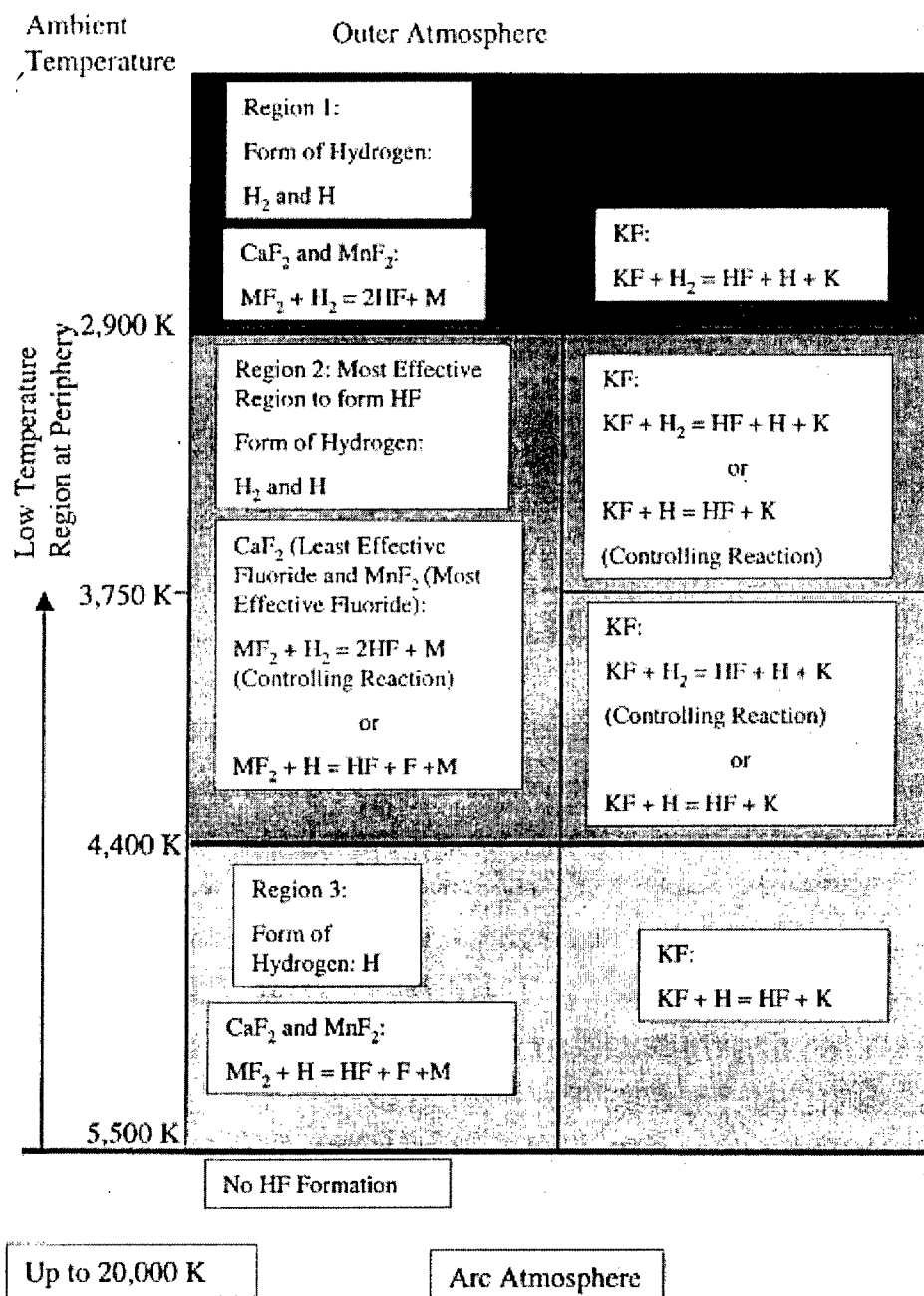


Figure 39: Illustration of reactions between fluoride and hydrogen at periphery of the arc [2].

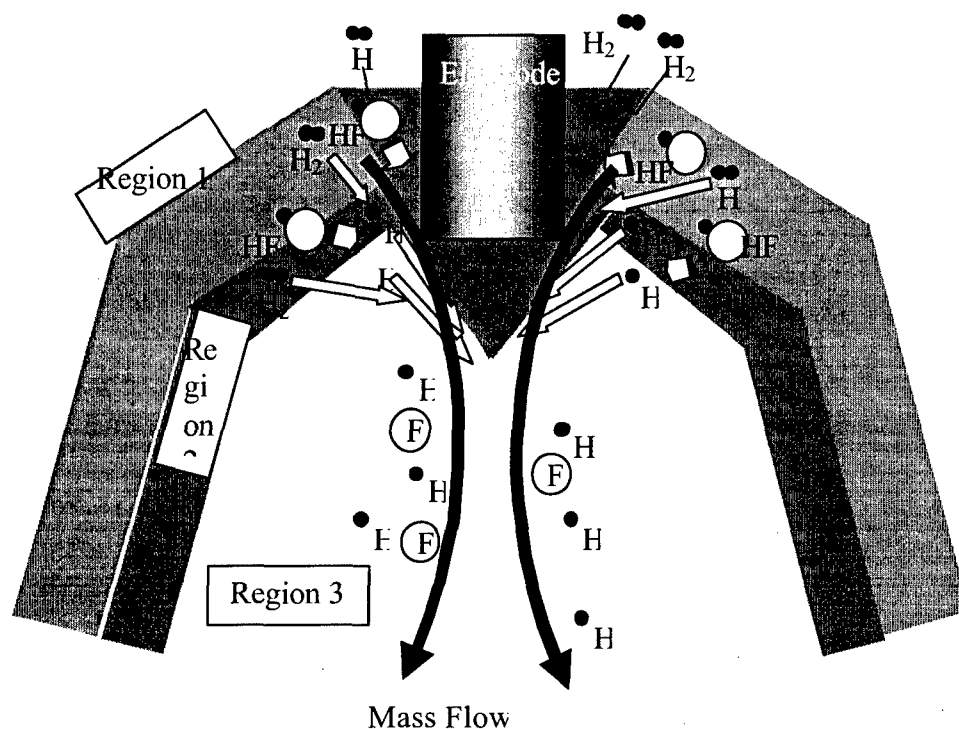


Figure 40: Illustration of mass flow between two systems with pressure difference [2].

$$\frac{1}{2} m_i v_i^2 = \frac{3}{2} k T_i. \quad (54)$$

This equation shows that the mean velocity of a particle is dependent on its mass at a constant temperature. Since the atomic masses of hydrogen and argon are 1.00 and 39.9, respectively, the mean velocity of hydrogen is 6.32 times as large as that of argon. In a closed system where pressure and temperature are uniform, the distribution of their particle population would not be different although the mean velocities between these species are different; however, the arc is an open system involving temperature and pressure gradients. Those gradients are extremely large, especially in the cathode region.

The phenomena continuously occurring in this region is modeled as follows. When two closed systems with the same volume but different temperature contain the

same numbers of dissimilar particles in terms of mass are combined, there will be a pressure difference between them, which creates the mass flow. During this dynamic process, the smaller particles must be transported more rapidly than the larger because of its larger mean velocity. Thus, the higher mass transport of lighter particles is possible if there are temperature and pressure gradients. Moreover, the kinetic energy of heavy particles such as molecules and atoms is transmitted by elastic collision with electrons. The fraction of energy K , transferred from one particle of mass m to another of mass M averaged over all angles is expressed in Equation 55:

$$K = \frac{2mM}{(m+M)^2} \approx \frac{2m}{M} \quad \text{Since } m \ll M \quad (55)$$

According to this equation, the larger the mass of the particle, the less fraction of energy transferred at one elastic collision with an electron. Therefore, argon atoms will require 40 times more collisions than hydrogen atoms to acquire the same level of kinetic energy as that of hydrogen. Near the cathode and anode, T_e , electron temperature, is generally greater than T_h , temperature of heavier particles (photons, ions, or atoms), since the collisions between electrons and heavy atoms are not enough to equilibrate these temperatures, which indicates that the state of these regions are not in complete local thermodynamic equilibrium. In the state out of complete local thermodynamic equilibrium, the temperature difference (in other words, difference in kinetic energy) may also be present among the heavy atoms, depending on their mass. Among the heavy atoms, the smaller atoms such as hydrogen would have larger kinetic energy than the larger atoms such as argon. As a result, the mean velocity of smaller atoms is further greater than that of the larger, which may be another reason of the higher mass transport at the cathode region.

H_2 molecules will be transported from the outskirts of the cathode tip to the arc column through the temperature regions. In Region 1, H_2 molecules could react with

fluoride to form HF. Both H_2 and H will be present in Region 2, while only H will exist in Region 3. Once HF molecules pass through the temperature regions, they tend to dissociate to H and F.

The mass of the molecule of H_2 and HF is 2.00 and 20.0, respectively. According to Equation 6, the velocity of HF molecule is 3.3 or 4.5 times slower than those of H_2 or H, respectively, when they are subjected to the same temperatures. In other words, they have the same kinetic energy. Therefore, if the hydrogen transported to the temperature regions is associated with the fluorine provided by fluoride, the mass transport of hydrogen into the arc column would be less because of lower mean mass velocity of HF in the temperature regions as shown in Figure 40, compared with those of diatomic or monatomic hydrogen. Furthermore, the thermodynamic state in the cathode region is out of complete local thermodynamic equilibrium. Therefore, there is a difference between T_e and T_h . Even among heavy particles, the temperature, i.e., kinetic energy, of smaller particles may possibly be larger than larger particles. Therefore, the kinetic energy of HF molecules could be lower than those of H atoms or H_2 molecules, which would further retard the mass transport of hydrogen into the arc column.

Since thermodynamic calculations predicted that MnF_2 is the most active fluoride to react with hydrogen, the most effective fluoride for the HF transport effect is considered to be MnF_2 ; on the other hand, the least effective one must be CaF_2 .

2.8.5 Model of Dilution Effect

The dilution of arc atmosphere with fluoride component elements can reduce the partial pressure of hydrogen in the arc. This process of hydrogen reduction is not related to the formation of HF. The component elements in either molecular form of the fluoride (e.g., CaF_2), or atomic or ionic form (e.g., Ca or Ca^{n+} and F or F^{n+}) displace the arc atmosphere, resulting in reduced partial pressure of hydrogen as illustrated in Figure 34. The dilution of arc atmosphere with fluoride may be related to the vaporization

characteristics of fluoride. Vaporization of fluoride starts at its melting temperature. The rate of vaporization corresponds to the equilibrium constant of the transition from liquid (or solid for sublimation) to gas. When the equilibrium constant is larger, the vaporization must proceed more rapidly. Figure 41 shows the equilibrium constant of vaporization for CaF_2 , KF and MnF_2 . KF showed the highest value between 1,500 and 2,600K and MnF_2 displays the second highest. Above 2,600K, the equilibrium constants of KF and MnF_2 increased sharply, which indicates a very high rate of vaporization above the temperature.

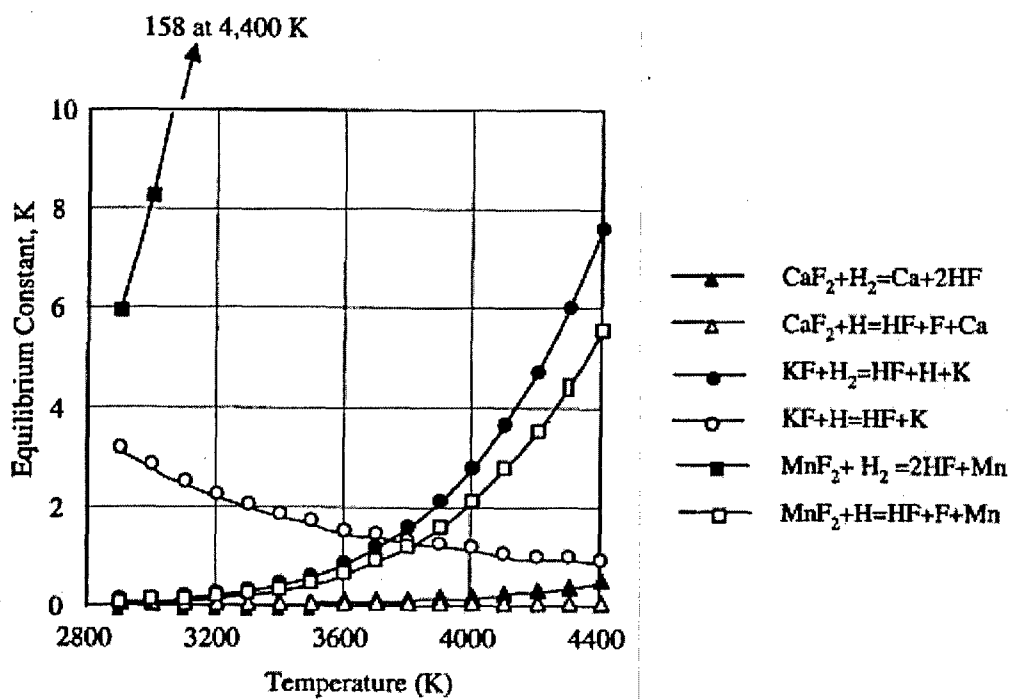


Figure 41: Equilibrium constants of HF formation reactions of MnF_2 , KF , and CaF_2 between 2,900 and 4,400 K [2].

On the other hand, the equilibrium constants of CaF_2 are very small compared with the other two. The boiling points of CaF_2 , KF and MnF_2 were identified as 2,750, 1,830 and 2,040K. According to this discussion, KF must be the most effective fluoride; on the other hand, CaF_2 would be the least effective one among these three. If the temperature range of vaporization of the fluoride is too low, there is a concern that the vaporization occurs before the component elements cover the welding arc and displace the arc atmosphere. It is known that the decomposition temperature range of CaCO_3 to CaO and CO_2 is between 450 and 890°C [181]. The vaporization of KF starts at its melting temperature around 800°C, and must finish below its boiling temperature at 1,557°C (1,830 K). Therefore, the vaporization temperature range of KF is not critically low.

CHAPTER 3

OBJECTIVES OF RESEARCH

The objective of the current research has been to develop a metal-and-flux-cored gas metal arc welding consumable that integrates the concept of both yttrium additions and fluoride additions. Yttrium additions are effective in forming inclusions in the weld metal which act as both hydrogen traps, reducing diffusible hydrogen, and as potent intragranular nucleation sites for the nucleation of acicular ferrite. Fluoride additions are effective in reducing diffusible hydrogen by reducing the partial pressure of hydrogen in the arc atmosphere, thus reducing weld metal hydrogen pickup.

Both concepts have been previously studied as independent studies. The addition of yttrium was initially studied with the additions of rare earth metals to metal-cored welding consumables to reduce diffusible hydrogen by forming rare earth metal inclusions within the weld that would act as strong hydrogen traps, immobilizing hydrogen atoms. Yttrium was found to be one of the most effective in reducing diffusible hydrogen to less than 1.0 milliliters per 100 grams weld metal with as little 0.6 weight percent yttrium added to the metal-cored consumable. Additional studies of yttrium additions found that the yttrium additions can be optimized to form inclusions that are potent nucleation sites for acicular ferrite.

A separate study focused on the use of fluorides to reduce weld metal hydrogen pickup. In this study, potassium fluoride or manganese fluoride, among others, was substituted into a base electrode which was similar to a fluorspar-lime type electrode in place of part of the calcium fluoride. This study found that five percent potassium fluoride additions in place of some calcium fluoride was effective in reducing diffusible

hydrogen to less than 1.5 milliliters per 100 grams weld metal. Using arc spectroscopy, three models of hydrogen reduction were developed, as explained in the previous chapter.

The integration of the two concepts requires several steps to develop an optimized consumable. The first step was to produce an yttrium-containing consumable that produced welds with similar characteristics as those developed by the previous researcher. The second step was to study the effects of fluoride additions to these yttrium-containing consumables. The addition of potassium fluoride was expected to alter everything from oxygen potential to arc stability. The next step was to study the changes in microstructural development of welds made with and without fluoride additions. Then additional iterations were made once the most effective consumable-fluoride content was determined to adjust the resulting weld metal composition so that the best microstructure could be produced. Finally, the mechanical properties of the deposited weld metal were determined and compared to the Navy minimum standards.

CHAPTER 4

EXPERIMENTAL METHODS

To study the effects of the addition of fluoride fluxes to yttrium-containing consumables for the arc welding of HSLA steels, carefully formulated gas-metal arc (GMA) and flux-cored arc (FCA) weld consumables were manufactured. Of particular concern were the welding characteristics and arc stability, the weld metal chemical composition and alloy recovery, the weld metal microstructure and inclusion development, the diffusible hydrogen content, and the mechanical performance of the deposited weld metals. A total of twenty-one experimental consumables were fabricated and divided into four categories: 1) metal-cored yttrium-containing consumables, 2) potassium fluoride additions to yttrium-containing consumables, 3) addition of other flux ingredients to yttrium-containing consumables, and 4) flux paste with metal-cored yttrium-containing consumable.

4.1 Electrode Formulation

1. Metal-Cored Yttrium-Containing Consumables:

Four experimental consumables (0-series) were manufactured to create welds with chemical compositions, microstructures, and diffusible hydrogen contents similar to that of the consumable produced by Clark [9]. Table 7 shows the powder composition of each of the four experimental consumables. The target weld metal composition was 2.5 wt% nickel, 0.25 wt% molybdenum, 1.25 wt% manganese, 200 to 400 ppm titanium, and 300 to 1000 ppm yttrium. This nominal composition, with the exception of the yttrium

content, has been shown to produce robust shielded metal arc welds [182]. The target yttrium composition was found to be effective in reducing diffusible hydrogen content [4] and promoting the formation of acicular ferrite [9]. Nickel and molybdenum were added as pure metal powder, whereas titanium was added as ferrotitanium, manganese as ferromanganese, and yttrium as ferroyttrium.

Table 7: Powder Compositions of Metal-Cored Yttrium-Containing Consumables.

Consumable	0-1-C	0-1-D	0-2	0-3
Ni (wt%)	14.00	14.00	10.00	10.00
Fe-Mn (wt%)	7.67	7.67	7.30	7.30
Mo (wt%)	1.70	1.70	1.50	1.50
Fe-Ti (wt%)	0.88	0.88	2.64	2.64
Fe-Y (wt%)	8.57	8.57	10.00	10.00
Fe-Si (wt%)	----	----	----	1.00
Fe (wt%)	Bal	bal	bal	bal

Three of these consumables were produced at CSM: 0-1-C, 0-2, 0-3. The fourth consumable, identified as 0-1-D, was manufactured at Devasco International, Inc. (from a powder blend prepared at CSM) to have the same composition as wire 0-1-C. Wires 0-1-C and -D contained lower titanium and yttrium concentrations, but higher nickel, manganese, and molybdenum contents. Wire 0-2 contained lower nickel, manganese, and molybdenum contents, but higher titanium and yttrium contents. The composition of wire 0-3 was similar to that of wire 0-2; however, an addition of one weight percent ferrosilicon was added to improve molten weld metal fluidity.

2. Potassium Fluoride Additions to Yttrium-Containing Consumables:

Eight consumables (1-series) were manufactured where potassium fluoride was added to the metal-cored yttrium-containing consumable that produced welds most

similar to the target chemical composition and microstructure. The fluoride additions ranged from five to thirty weight percent of the powder blend. The compositions of the powders used for these consumables are shown in Table 8. These consumables were produced so that the effect of potassium fluoride additions on welding characteristics and weld metal properties could be studied without drastically altering the oxygen content and oxygen potential, inclusion characteristics, yttrium-to-oxygen ratio, and the microstructure.

Table 8: Powder Compositions of Potassium Fluoride Additions to Yttrium-Containing Consumables.

Consumable	1-1-C	1-1-D	1-2-C	1-2-D	1-3	1-4	1-5	1-6
Ni (wt%)	10.00	10.00	10.00	10.00	10.00	10.00	10.00	10.00
Fe-Mn (wt%)	7.30	7.30	7.30	7.30	7.30	7.30	7.30	7.30
Mo (wt%)	1.50	1.50	1.50	1.50	1.50	1.50	1.50	1.50
Fe-Ti (wt%)	2.64	2.64	2.64	2.64	2.64	2.64	2.64	2.64
Fe-Y (wt%)	10.00	10.00	10.00	10.00	10.00	10.00	10.00	10.00
KF (wt%)	5.00	5.00	10.00	10.00	15.00	20.00	25.00	30.00
Fe (wt%)	Bal	bal	bal	bal	bal	bal	bal	Bal

3. Fluoride and Other Flux Ingredient Additions to Yttrium-Containing Consumables:

Five consumables (2-series) were fabricated in this series. Consumable 2-1 was similar in composition to consumables 1-1-C and -D, but had the addition of one weight percent ferrosilicon to improve molten weld metal fluidity. In addition to KF, calcium carbonate, silica, alumina, potassium oxide, and calcium fluoride were blended with the alloying elements used in the yttrium-containing consumable that produced welds most similar to the target chemical composition and microstructure for consumables 2-2, -3, -4, and -5. The latter powders were blended such that the ratio of KF, CaF_2 , SiO_2 , Al_2O_3 , and CaCO_3 relative to each other remained constant, and the ratio of alloying elements relative to each other remained constant. The "flux ingredients" were blended with

powders similar in composition to consumables 0-2 and 0-3, where consumables 2-2 and 2-3 contain the "flux ingredients" and consumables 2-4 and 2-5 contain 1 wt% ferrosilicon in addition to the "flux ingredients." Also, the "flux ingredients" were added to the yttrium-containing consumables in five (2-2 and 2-4) and ten (2-3 and 2-5) weight percent additions. The powder compositions are shown in Table 9.

Table 9: Powder Compositions of KF and Other "Flux Ingredients" to Yttrium-Containing Consumables.

Consumable	2-1	2-2	2-3	2-4	2-5
Ni (wt%)	10.00	10.00	9.62	10.00	10.00
Fe-Mn (wt%)	7.30	7.30	7.02	7.30	7.30
Mo (wt%)	1.50	1.50	1.45	1.50	1.50
Fe-Ti (wt%)	2.64	2.64	2.53	2.64	2.64
Fe-Y (wt%)	10.00	10.00	9.62	10.00	10.00
Fe-Si (wt%)	1.00	----	----	1.00	1.00
KF (wt%)	5.00	0.37	0.74	0.37	0.74
CaF ₂ (wt%)	----	0.78	1.55	0.78	1.55
CaCO ₃ (wt%)	----	0.29	0.57	0.29	5.70
Al ₂ O ₃ (wt%)	----	0.05	0.10	0.05	0.10
SiO ₂ (wt%)	----	0.38	0.75	0.38	0.75
K ₂ O (wt%)	----	0.05	0.10	0.05	0.10
Fe (wt%)	bal	bal	bal	bal	bal

4. "Flux Paste" with Metal-Cored Yttrium-Containing Consumables

In this matrix of research, four powders were blended (3-X series) to produce a paste that was layered over each weld pass just prior to welding using the 0-1-D consumable. These four powder compositions, shown in Table 10, were made because of difficulties that were encountered during the welding of the 2-X series consumables. In the so-called pastes, calcium carbonate was replaced with calcium oxide so that the formation of carbon dioxide is limited.

Table 10: Powder Compositions of the "Flux Paste" used with the 0-1-D Consumable

Consumable	3-1	3-2	3-3	3-4
"Flux Paste" Composition				
Fe-Si (wt%)	----	2.56	----	2.72
KF (wt%)	19.70	18.90	----	----
CaF ₂ (wt%)	40.70	39.60	57.40	55.80
CaO (wt%)	15.00	14.60	16.00	15.50
Al ₂ O ₃ (wt%)	2.62	2.56	2.84	2.72
SiO ₂ (wt%)	19.70	19.20	21.00	20.40
K ₂ O (wt%)	2.62	2.56	2.84	2.72

4.2 Materials Used

The composition of the various metallic powder additions used in the steel filler metals are provided in Table 11. The ferroyttrium powder was fabricated at CSM. The remaining powders were obtained commercially. The strip used in the manufacturing of the consumables was AISI 1008 low carbon steel with a composition shown in Table 12, a width of 0.500 inches and a thickness of 0.015 inches.

Powder size analysis was performed for all of the metallic powders and these results are reported in Table 13. The nickel powder was reported to pass between 60 and 325 mesh. The molybdenum was reported to be between 70 and 325 mesh. The iron powder was reported to be less than 100 mesh.

Since only the properties of the weld metal are of concern in this study, all welding experiments for weld metal composition, microstructural properties, oxide characteristics and mechanical testing were performed on ASTM A36 low carbon structural steel plates. This type of steel is recognized as a common structural steel including low carbon content and low manganese content.

Table 11: Compositions of Metallic Powders Used as Filler Metals (wt. %).

Element	Ni	Mo	Fe-Mn	Fe-Ti	Fe-Y
Mn	----	----	88.95	----	----
Ti	----	----	----	38.14	----
Y	----	----	----	----	20.5
Ni	98.0 min	----	----	----	----
Mo	----	99.8	----	----	----
Fe	1 max	----	bal	bal	bal
Al	----	----	----	2.93	1.0
Si	----	----	0.75	0.61	----
S	0.05 max	----	0.008	0.027	----
P	0.02 max	----	0.186	0.012	----
C	0.2 max	----	0.145	0.17	----
Co	1 max	----	----	----	----

Table 12: Composition of the AISI 1008 Low Carbon Steel Strip Used as Tubular Sheath.

Element	C	S	P	Si	Cr	Ni	Mn	Cu	Mo	Al	Fe
Wt.%	0.064	0.01	0.017	0.02	0.03	0.04	0.34	0.05	0.01	0.032	bal

Table 13: Sieve Analysis for Metallic Powders Used as Tubular Wire Filler Metals (Percent Retained).

Screen Size	Fe-Ti	Fe-Mn	Fe-Y	Ni	Mo	Fe
>40	0	0	0	0	0	0
40-70	0	20.3	24.8	42.6	0	0
70-150	79.0	43.9	31.4	47.7	45.6	-100
150-200	21.0	16.6	14.1	7.3	39.7	
200-325	0	19.2	29.7	1.6	14.7	
<325	0	0	0	1.1	0	

4.2.0 Fabrication of Ferroyttrium

The ferroyttrium powder was fabricated at CSM. Iron powder and yttrium powder were mixed in a ratio of approximately 58 wt% iron to 42 wt% yttrium in an yttria crucible. The powders were melted in a vacuum furnace heated to a temperature of 1750°C. There were five stages in the furnace heat cycle. First, the furnace was heated to and held at 100°C for 1 hour while the system was evacuated. Next, the furnace was heated up to 1750°C in 6 hours, then held at temperature for approximately 22 hours. Finally, the furnace was allowed to cool to room temperature in five hours, then held at room temperature under vacuum until the ferroyttrium was removed.

After the solidified ingot is removed from the furnace, it was crushed into powder form in a shatter box. The powders were then sieved to collect only the appropriate size range of powders with the powder sizes presented in Table 13. The composition of the powder was then verified using energy dispersive spectroscopy (EDS) to determine the composition of the ferroyttrium formed. The composition of the powder is provided above in Table 11.

4.3 Fabrication of Experimental Electrodes

The first step in manufacturing the experimental electrodes was preparing the powders for blending. All of the powder ingredients, with the exception of potassium fluoride, were baked at 150°C for 6 hours in an inert atmosphere to remove any moisture present in the powders. This temperature allows for the removal of any moisture present in the powder without causing additional reactions such as oxidation. The potassium fluoride was dried at 600°C for 24 hours in air to remove moisture. Since KF is hygroscopic, such a high temperature is necessary. According to Matsushita [2], potassium fluoride will lose approximately 16 percent of its weight due to water release as can be seen in Figure 36. After drying, the powders were then blended using a V-

blender shown in Figure 42. The blender was run for approximately 6 hours to thoroughly mix the powders. After blending the powders, the powders were again dried at 150°C for 6 hours in an inert atmosphere just prior to the manufacturing of the consumable.

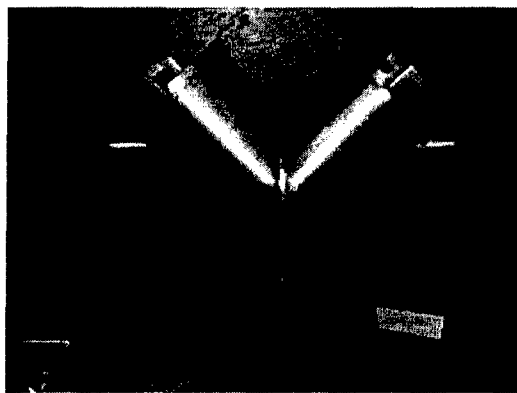


Figure 42: Photograph of powder V-blender.

4.3.1 Tubular Wire Making Facility at Colorado School of Mines

All of the experimental electrodes used in this research were initially fabricated with the tubular wire mill at the Colorado School of Mines using the AISI 1008 low carbon steel strip previously described. The facility is designed so that it is feasible to produce small batches of a wire. This is appropriate for the production of experimental welding electrodes. The weld metals made from selected consumables were selected for mechanical property testing, as will be discussed later. For three of those consumables (0-1, 1-1, and 1-2), the flux additions for the tubular wires were mixed and blended at CSM, then shipped to Devasco International for manufacturing of larger quantities of the consumables.

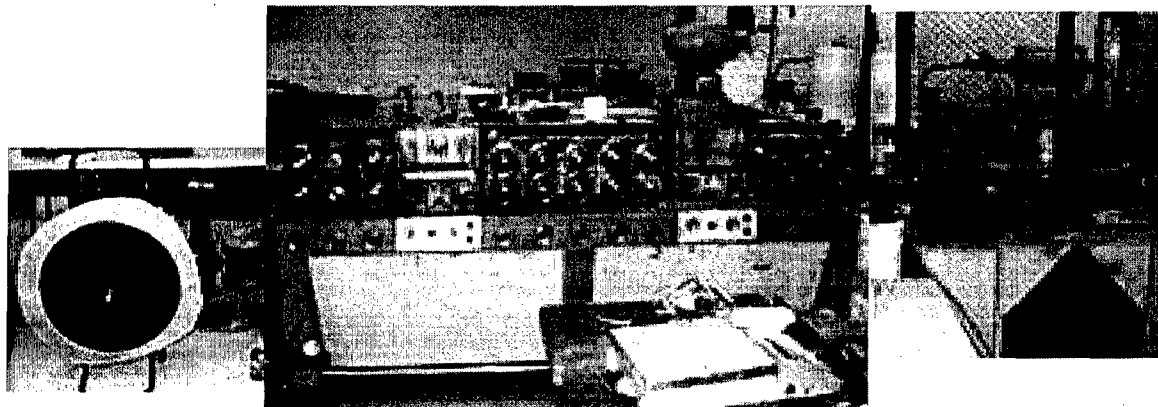
Figure 43 (a) is a photograph of the tubular wire mill, and is schematically illustrated in Figure 43(b). The final reel that coils the formed electrode is connected to a motor so that a tubular wire is processed as that reel rotates. The speed at which the strip is drawn through the forming dies is controlled by the rotational speed of the final reel, and is measured by a sensor within the motor. The flow of the powders from the hopper is measured using an electric scale connected to a data acquisition system that measures the change in weight with time in grams per second. With the known powder flow rate and the desired fill ratio, the speed at which the wire is drawn is then calculated using Equation 56:

$$s = \frac{x}{w}(1 - f), \quad (56)$$

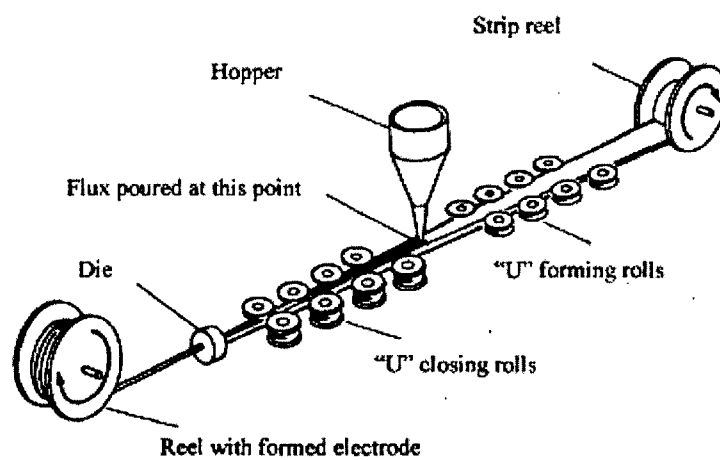
where x is the weight of flux added in grams per second, s is the speed of the strip going through the dies in centimeters per second, w is the weight of the strip in grams per centimeter, and f is the desired fill ratio. For fabrication of the consumables, a target fill ratio of thirty percent was desired to match the fill ratios proposed by Devasco International.

4.3.2 Forming and Closing the Strip and Adding Flux in the Wire

The strip in the strip reel from Figure 43 is initially flat. As the strip is drawn through the forming dies, it is formed into a shape of a "U" as shown in Figure 44(a) - 44(c). As the "U" shaped strip is drawn further across the mill, a vibrating flux hopper pours the flux into the "U" as seen in Figure 44(d). The open end of the strip is then closed by the remaining three roller dies into a tubular wire as seen in Figure 44(e) - 44(g). Finally, the closed tube is drawn through reducing dies to tighten and reduce the diameter of the wire to its final size, approximately 0.060 inches (1.5 millimeter).



(a)



(b)

Figure 43: (a) Photograph of tubular wire making mill at CSM. (b) Representative illustration of a tubular wire making facility [183].

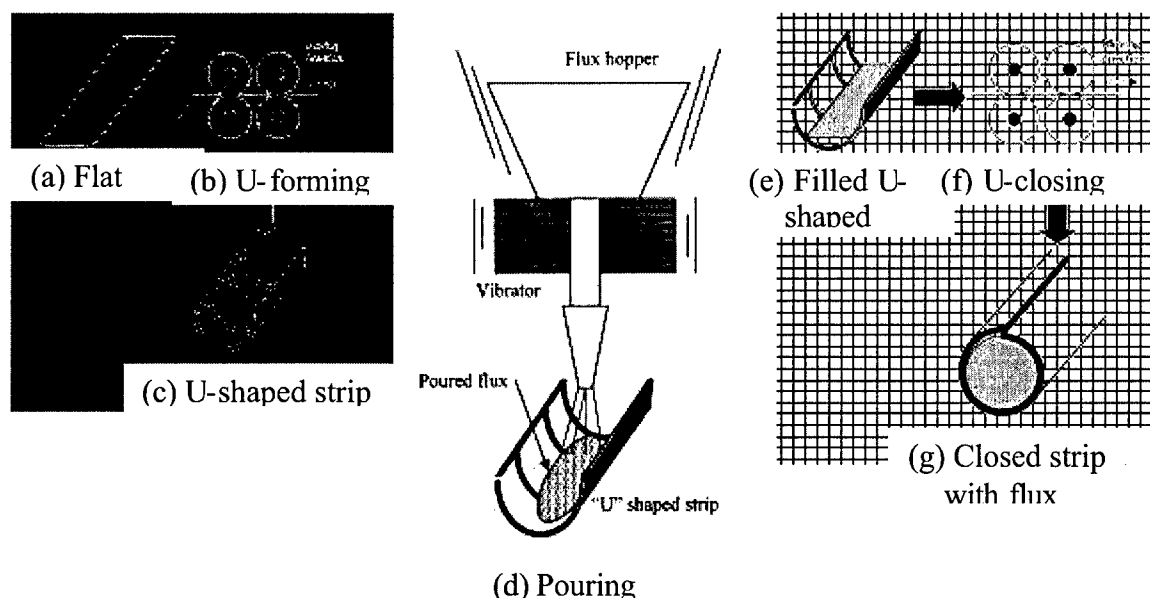


Figure 44: Schematic diagram of tubular wire fabrication, (a) flat strip, (b) U-forming dies, (c), U-shaped sheath, (d) powder filling of U-shaped sheath, (e) filled U-shaped sheath, (f) U-closing dies, and (g) Closed tubular wire with flux [184].

4.3.3 Concerns for Flux Cored Wire Making

There are three major concerns regarding industrial metal/flux-cored wire manufacturing. The first is the control of the flux flow from the nozzle of the flux hopper into the “U” shaped strip. The flux flows from the nozzle of the hopper by gravity and is helped by the vibration of the hopper. With this, if the flow of the flux is not constant, the fraction of the flux in the wire will fluctuate along the wire, which may cause instability in the welding current and arc. One possible reason for this is that larger particles create less friction, both with each other, and with the wall of the hopper (larger particles create less particle-to-particle contact) [184]. Also, smaller particles create a larger surface area per volume, and would be more prone to absorb moisture and become adhesive. Therefore, larger particle sizes, mesh sizes between 60 and 200, were used for most of the ingredients. A second factor is the density of the material. For instance, iron and

ferromanganese powders demonstrated excellent fluidity [184]. Since these materials are quite dense, the force of gravity can be much greater than the frictional force caused by the surroundings, facilitating the free fall of the particles. Since some of the flux powders could absorb moisture and become adhesive, the powders were all baked at 150°C to eliminate moisture prior to the wire fabrication.

The second concern is the segregation of the flux ingredients. It is well established that welding fluxes generally contain multiple ingredients and that the fraction of each ingredient performs specific functions in the weld system. Therefore, the fraction of each addition must be maintained during the wire electrode production. It is possible that segregation begins when the flux is mixed with a V-blender, as seen in Figure 42, or poured from the hopper to the strip during the wire fabrication process. These compositional fluctuations are of great concern because they may influence the performance of the electrodes from location to location within the same coil.

According to Williams and Khan [185], segregation occurs when particles of different physical properties such as size, density, shape, surface roughness, and resilience are handled in hoppers, conveyors, ball mills, and in filling containers. Although any of these properties may yield segregation under any circumstances, most industrial segregation problems are due to different particle size. The mechanisms caused by size segregation can be considered as follows [185]:

- (i) If particles are projected horizontally, the distance that they travel is proportional to the square of the particle diameter. The differential projection may cause segregation. For instance, if particles are projected from a mixer to spread them over the surface of a bed of powder, it is possible that this type of segregation may occur.
- (ii) When a bed of powder is distributed and rearrangement of particles takes place, the possibility of a particle falling into a void is dependent on the size. Therefore, smaller particles tend to move downwards and larger particles remain in place.

The most common situations to yield this type of segregation are considered to be pouring heaps, stirring and vibrating.

The particle size must be homogenous to avoid the size segregation. To obtain the uniform particle size for each ingredient, the ingredients were sieved and the particle size was selected from 60 mesh and 200 mesh. The particles in this range were sufficiently coarse to maintain powder flow.

A third concern is the removal of the lubricant used during the wire drawing process. To minimize friction and heat generation between the wire and the dies, powdered soap is used for lubrication. If a significant amount of lubricant remains on the surface of the wire, hydrogen pickup in the weld may increase. Therefore, the lubricant must be carefully removed, especially from the seam of the wire, to eliminate it as a potential hydrogen source. The lubricant can be removed by simply wiping the wire with a cloth or sponge saturated with acetone or ethanol, or the wire can be scoured with a scouring pad. In addition, baking the wire to burn out the hydrogen contained in the lubricant is effective. The baking temperature of 300°C for six hours is believed to be high enough to burn the lubricant, but still low enough to avoid the oxidation of alloying elements or other chemical reactions involving the flux ingredients in the wire.

4.4 Welding Procedures

Welding was performed by semi-automatic GMA or FCA welding using a Miller Nirvana constant potential power supply with direct current electrode positive mode. Initial welding consisted of bead-on-plate welds using a range of welding parameters, as shown in Table 14. The welds were shielded with 2% O₂ + 98% Ar shielding gas. Electrical characteristics were measured and a qualitative assessment of weldability was performed based upon porosity, spatter, arc stability, penetration, reinforcement, contact angle, and weld bead appearance.

Table 14: Welding Parameters Used During Experimental Welding

Parameter	Value or Range
Voltage	26 V - 30 V, DCEP
Electrode Extension	18-22 mm (0.71-0.87 in.)
Wire Feed	127 mm/s (300 ipm)
Travel Speed	5.74-12.23 mm/s (13.5-28.9 ipm)
Shielding Gas	98% Ar + 2% O ₂
Shielding Gas Flow Rate	18.9-21.2 l/min (40-45 cfh)
Preheat Temperature	None
Interpass Temperature	177°C maximum
Heat Input	1.0 to 4.0 kJ/mm

In addition to single pass bead-on-plate welds used to study welding characteristics, bead-on-bead chem-pads were produced on ASTM A36 steel for each consumable using the welding parameters that produced the best overall weld appearance. A minimum of three weld layers was deposited, as schematically shown in Figure 45, and subsequent microstructural, chemical, and inclusion analyses were performed on the top layer to minimize the effects of base metal dilution.

Multiple pass welds were produced with selected experimental consumables. Figure 46 shows a schematic representation of the single V-groove, multiple-pass weld specimen. The multiple-pass welds were made in a single V-groove with a 12.7-to-25.4-mm (0.5-to-1.0-in.) root opening. The plates were machined so that the V-groove would make a 45-degree angle. The plates were 19-mm-thick (0.75-in.) ASTM A36 structural steel. Twelve to twenty passes were made to fill the groove. The same analyses that were performed on the bead-on-bead chem-pads were also performed on the multiple-pass welds in addition to mechanical performance testing.

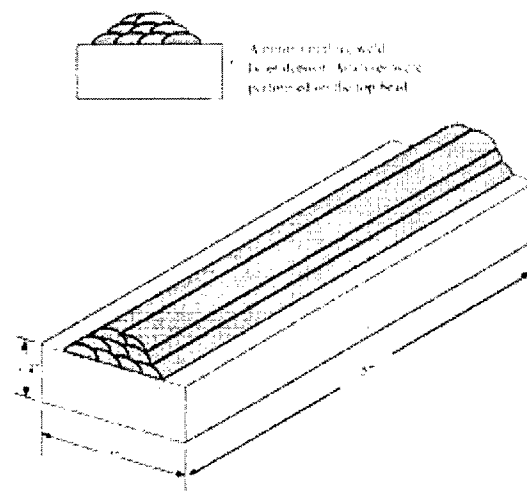


Figure 45: Schematic illustration of bead-on-bead weld sample used for chemical analysis, microstructural assessment, and inclusion characterization [9].

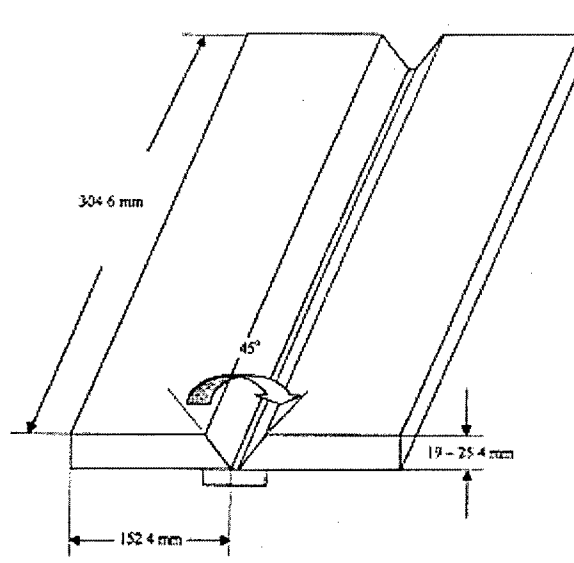


Figure 46: Schematic illustration of V-groove plate preparations for multiple-pass welding.

4.5 Macroscopic Analysis

Macroscopic analysis was performed on all bead-on-plate welds. Samples were prepared mechanically by grinding down through 600 grit, then polishing with 6-micron, 1-micron, and 0.25-micron diamond compounds. The samples were then lightly etched with 2 percent nital (2 percent nitric acid in ethano l) so as to reveal the heat-affected zone and weld metal. The samples were then rinsed and dried. Photomacrographs were made by scanning each etched sample on a flatbed scanner using at least 1200 dpi resolution so that suitable digital enlargements could be made for further analysis. From the digital enlargements, penetration, reinforcement, weld bead width, and contact angle were measured as described in Figure 47. In addition to the quantitative measurements, qualitative measurements of porosity could be analyzed.

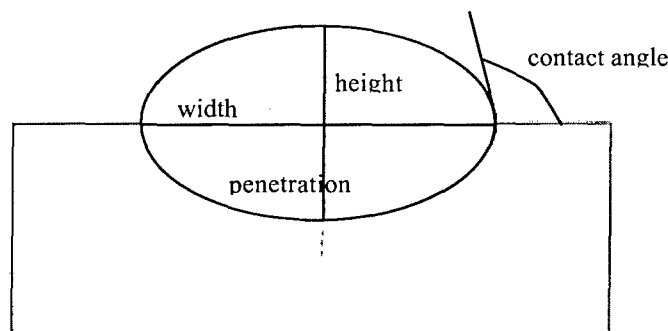


Figure 47: Schematic illustration of macroscopic measurements of bead-on-plate weld deposits.

4.6 Weld Bead Chemical Analysis

Chemical analysis was performed on the bead-on-bead chem-pads and on the multiple pass, V-groove welds. For the chem-pads, top bead bulk chemical analysis was

performed as shown in Figure 48(a). For the multiple pass groove welds, the bulk chemical analysis was performed near the locations schematically shown in Figure 48(b). Bulk analyses were performed at CSM by glow discharge spectrum (GDS), using a Leco SA-2000 glow discharge spectrometer. Carbon, sulfur, oxygen and nitrogen analyses also were performed at CSM using a Leco TC-436 analyzer. Total hydrogen analyses were also performed at CSM.

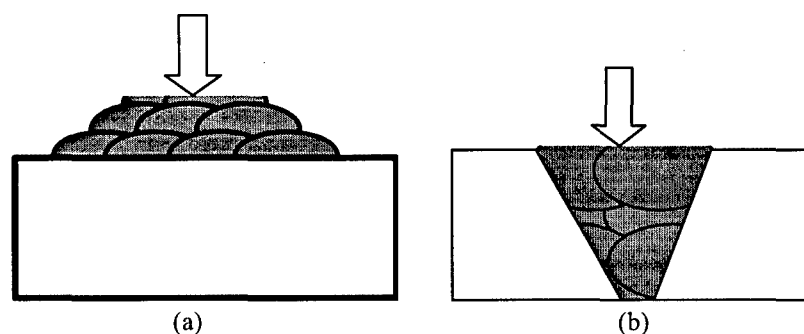


Figure 48: Schematic representation of locations where chemical analysis was performed for (a) bead-on-bead welds, and (b) multiple-pass V-groove welds.

At the present time, there are no standards for yttrium measurements using the glow discharge spectrum. To measure yttrium content, there are only a couple of methods. Inductively coupled plasma (ICP) analysis was selected for yttrium analysis. Initially, ICP analysis was performed at CSM using the method for digestion described in the following section. Due to the amount of time necessary to complete the digestion procedure, all samples, including those measured at CSM for verification purposes, were sent to a nationally certified lab for ICP analysis of yttrium content in the weld metal.

4.6.1 Inductively Coupled Plasma

To perform ICP analysis, small samples of top bead weld metal were digested in a 4:1 ratio of nitric acid to perchloric acid, called ashing acid, heated to 120°C. The digestion procedure follows that suggested by Method 7300, Issue 2 from the NIOSH Manual of Analytical Methods [186]. This method suggests that 5 milliliters of the ashing acid is added to a beaker containing the weld metal, which is then covered with a watch glass, and held at room temperature for 30 minutes. After 30 minutes, the beaker is then heated until ca. 0.5 milliliters of the solution remains. Then 2 milliliters of ashing acid is added to the beaker and held at temperature until ca. 0.5 milliliters of solution remains. This step is repeated until the solution becomes clear, after which it is heated to near dryness. The residue is then dissolved in 2 to 3 milliliters of dilution acid (50 milliliters of ashing acid diluted to 1 liter). The solution is then transferred to centrifuge tubes and further diluted to 10 milliliters. The ICP analysis is then performed.

The results of ICP are given in milligrams per liter and must be converted to weight percent. This is done by multiplying the measured result by the volume of the solution made, then dividing by the weight of the original sample piece, and finally multiplying by 100. This calculation determines the amount of yttrium that was recovered in the weld deposit. A minimum of five sample pieces were digested for each experimental consumable.

4.6.2 Diffusible Hydrogen Analysis

Diffusible hydrogen was measured using the ANSI/AWS A4.3-93 standard [187]. This standard prescribes a standard weld test assembly, a standard method of test sample preparation, and two standard methods of analysis for determination of diffusible hydrogen from martensitic, bainitic, and ferritic steel weld metals. These methods are suitable for shielded metal arc, gas metal arc, flux cored arc, and submerged arc welding

processes. In the current research, the standard method for determination of diffusible hydrogen using gas chromatography was used.

4.6.2.1 Weld Test Assembly

Each test assembly was ASTM A36 grade steel consisting of a starting weld tab, a test specimen at the center, and a run-off weld tab. The three pieces from each test assembly are held in a copper clamping fixture. All three pieces of the test assembly had a cross section of 25 mm wide by 12 mm thick. The length of the center test specimen was eighty millimeters in length. The start tabs and run-off tabs were forty millimeters in length. Four such test assemblies constitute a complete test for each filler composition developed in the research.

The pieces for the test assemblies were heat-treated six hours at 600°C to remove any hydrogen present in the material. The rate of heating and cooling is not important during this degassing procedure.

The test assembly pieces were then dry-shot blasted to remove any scaling that was formed during the degassing procedure. The pieces were then labeled by stamping one of the unwelded surfaces, usually the side opposite the weld bead to prevent any discontinuous contact with the copper fixture. Then the test assembly pieces were weighed to the nearest 0.1 gram. From this point forward, the test pieces were handled with latex gloves to ensure no contamination. Immediately prior to welding, the stamped specimens were cleaned with acetone.

4.6.2.2 Welding Fixture

A copper-clamping fixture was used during welding to hold the weld test assembly in alignment, with the test specimen and weld tabs in firm contact, and to serve as a heat sink. The copper-clamping fixture allows clamping pressure from the sides of

the weld test assembly and also permits rapid release and removal of the test assembly. In addition to the copper fixture, two thin strips of copper foil were used to protect the copper fixture from errant arcs and to prevent discontinuous contact between the test assembly and the fixture.

4.6.2.3 Welding for Analysis

Prior to welding a set of four weld test assemblies, the welding parameters were adjusted to the optimal levels for each test. All four test assemblies for each of the experimental consumables were welded with no alterations of the parameters.

During the welding of the test assemblies, the arc was initiated on the starting weld tab so that the starting edge of the deposit was 25 millimeters from the edge of the test specimen. The welding was performed in a uniform, uninterrupted manner along the weld test assembly to the run-off tab. Welding was terminated on the run-off tab at a position so that the back edge of the crater is on the run-off tab and within 25 millimeter of the edge of the test specimen.

Immediately upon completion of welding each test assembly, the test assembly was released from the clamping fixture and submerged into an iced water bath within five seconds of the extinguishing of the arc. The welded test assembly was vigorously agitated in the iced water bath for twenty to thirty seconds and then quickly transferred to a dry ice and acetone bath for storage. All four test assemblies were welded within one hour of each other for each experimental consumable.

After completion of welding and placing the test assemblies into the storage bath, the test pieces are prepared for analysis. First, the start tabs and run-off tabs were removed from the test pieces. Then the test pieces were placed back into the storage bath for at least two minutes. The longest period of time each test piece was allowed to remain out of the storage bath was 55 seconds. Next the weld tabs were measured to ensure that

the bead lengths were within in the 25 millimeters specified distance, recorded, and then discarded.

The second step in preparation of the test pieces was the removal of any slag that was produced during welding. This was accomplished using 45-second intervals under a dry-shot blaster. After each interval, the test piece was placed back into the storage bath for a minimum of two minutes. The intervals were repeated until the slag was completely removed from each test specimen. After the slag was completely removed, the test pieces were returned to the storage bath during the set up and preparation of the analytical apparatus.

4.6.2.4 Diffusible Hydrogen Analysis

Diffusible hydrogen was measured using a gas chromatograph. Each test piece was placed into an air tight steel cylinder. Prior to placing the test pieces in the cylinders, the cylinders were flushed with high purity argon gas to evacuate any hydrogen in the cylinders. The test pieces were removed from the storage bath and cleaned with acetone to remove any residue that formed in the storage bath. Then the test pieces were placed in the cylinders and the cylinders were sealed with a copper paste that acted as a gasket. Next, the cylinders were pressurized to ten pounds per square inch with the high purity argon. Once the cylinders have been sealed and pressurized, one milliliter of ultra-high purity helium was injected into each cylinder to act as a standard using a syringe.

The test specimens then were placed into a furnace and were heated to and held at 150°C for 6.5 hours to allow hydrogen to evolve from the weld test pieces. This amount of time was sufficient to allow at least ninety percent of the diffusible hydrogen to diffuse out of the specimen.

4.7 Light Optical Microscopy

Top bead microstructures were characterized by light optical microscopy. Metallographic specimens were prepared using the same procedure for macroscopic analysis preparations.

Oxide statistics were determined on unetched, 1000x fields of view, using Leco 3001A image analysis software. A minimum of 1000 oxides were measured for each weld sample. The area fraction (A_A), number of particles per area (N_A), size distribution of oxides, and two-dimensional arithmetic mean diameter (D_A) were determined directly from each sample. The three-dimensional arithmetic mean oxide diameter (D_V) was calculated from the two-dimensional value assuming a spherical shape. Similarly, the three-dimensional number density (N_V) and oxide surface area (S_V) were calculated based on the assumption of spherical oxides. The number density of oxides per unit volume of weld metal was determined by the volume fraction divided by the average particle volume, and the calculated surface is determined from the number density of oxides multiplied by the average oxide surface area, assuming spherical particles.

A qualitative assessment of the microstructure of each bead-on-bead and multiple pass weld sample was performed, and representative photomicrographs were typically taken at 200x, 500x, and 750x. A schematic representation of the typical locations of the micrographs is shown in Figure 49(a) for the bead-on-bead and Figure 49(b) for the multiple-pass welds. Quantitative metallography was performed on all weld deposits. Classification of microstructures was performed in accordance with the guidelines of the International Institute of Welding (IIW) Sub-Commission IX-J [78]. The IIW guidelines identify five microstructural constituents: primary ferrite (PF), acicular ferrite (AF), ferrite with second phase (FS), ferrite carbide aggregates (FC), and martensite constituents (MA). A minimum of 1000 counts, on 500x fields of view was performed for each weld.

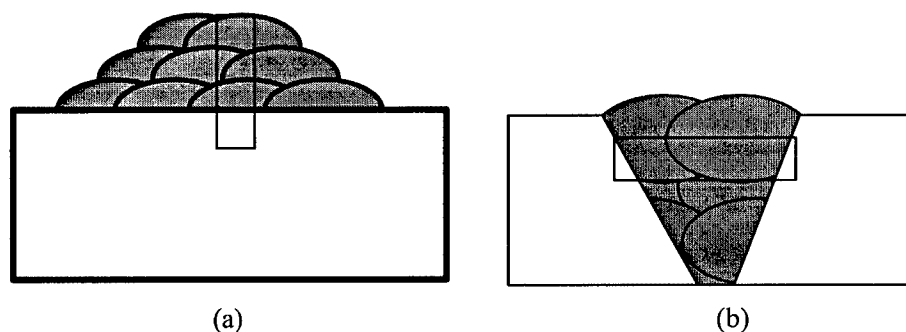


Figure 49: Representative illustration of the locations where photomicrographs were taken in (a) bead-on-bead welds, and (b) multiple-pass V-groove welds.

4.8 Mechanical Properties Evaluation

Mechanical properties of weld metal deposited by selected consumables were determined by use of Charpy V-notch impact testing, sub-size weld metal tensile testing, and weld metal hardness measurements. All testing was performed on multiple-pass, single V-groove welds produced at CSM. X-ray radiography was performed on these multiple-pass welds to ensure that weld metal defects were not encountered in the test specimens. All test specimens sampled for each experimental consumable were extracted from a single complete penetration welded test assembly. Figure 50 shows a schematic diagram of the welded test assembly and the location of test specimens.

4.8.1 Charpy V-Notch Impact Testing

A Charpy impact test is a dynamic test in which a selected specimen, machined or surface ground and notched, is struck and broken in a single blow in a specially designed testing machine, and the energy absorbed in breaking the specimen is measured. The energy values determined are qualitative comparisons on a selected specimen, and although frequently specified as an acceptance criterion, they cannot be used directly as

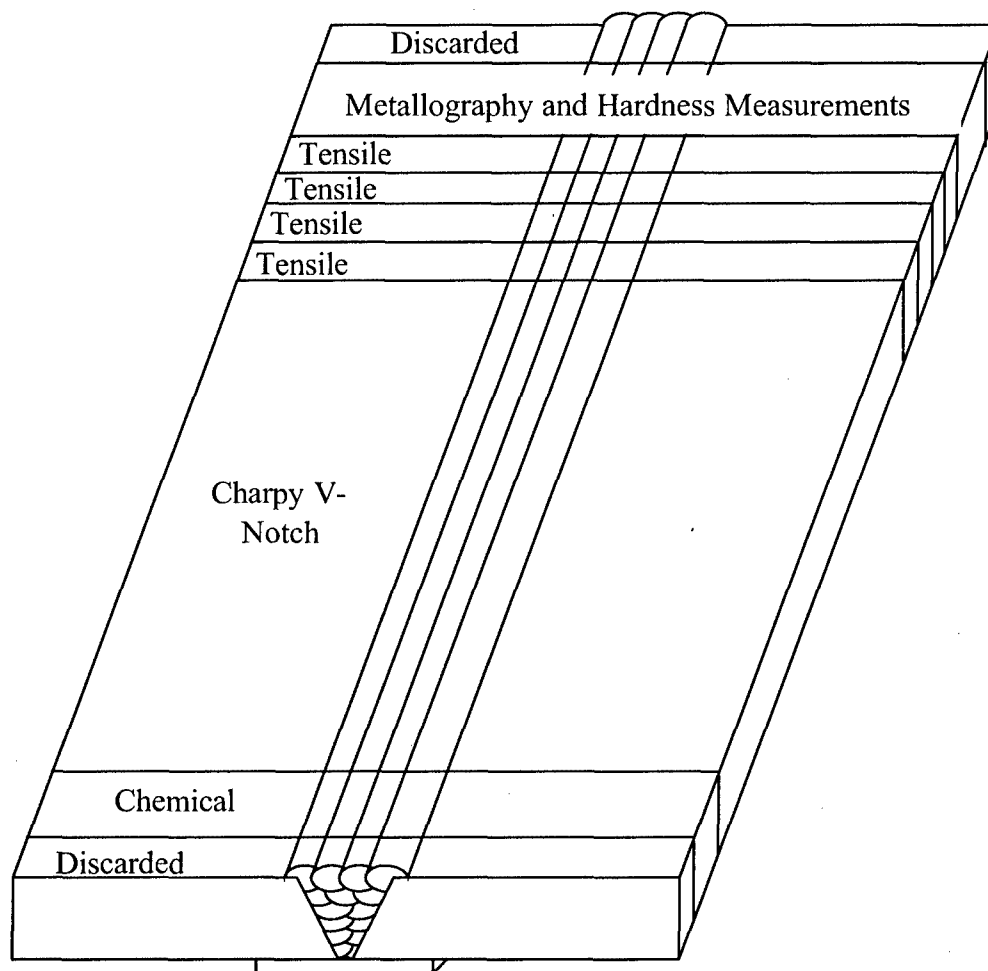


Figure 50: Representative locations of sample extraction from multiple-pass V-groove weld deposits.

energy figures that would serve for engineering calculations. The Charpy V-notch (CVN) impact test has been used extensively in mechanical testing of steel products and in research for over four decades. Moreover, failure analysis has, with few exceptions, shown service failures to be attended by low energy values, usually 15 foot-pounds or less, at the temperature of service failure. Most notable are the statistical studies of WWII Liberty ships and T2 tankers by the National Bureau of Standards where significant differences were found between plates in which fracture started and plates in which fracture arrested.

The test method relates specifically to the behavior of metal when subjected to a single overload of stress, applied at a high rate of loading and at specified testing temperature. The behavior of ferritic steels when notched cannot be reliably predicted from their properties as revealed by the tension test. Such materials may display normal ductility in the smooth tension test, but nevertheless break in brittle fashion when loaded in the notched condition.

Test specimens were prepared and tested according to ANSI/AWS D1.1-00 [187]. Figure 51(a) shows a schematic of the dimensions of the CVN specimen. It is a 10-mm by 10-mm square bar that is 5.5 centimeters in length with a notch that is 2 millimeters deep, machined along one side at the center of the length. Figure 51(b) is a schematic diagram of the location in the weld where the test specimens were extracted relative to the weld cross section. The positioning of the notch for the weld metal was completed by first machining 10-by-10-mm square bars out of the test weld at the depth shown in Figure 51(b). The longitudinal centerline of the specimens was located transverse to the weld axis. Next, the bars were etched with 2 percent nital to reveal the location of the weld fusion zone. Finally, the centerline of the notch was located at the center of the weld. The base of the notch was cut perpendicular to the weld surface. A minimum of three tests were performed at -60° , -30° , and 0°F and at room temperature.

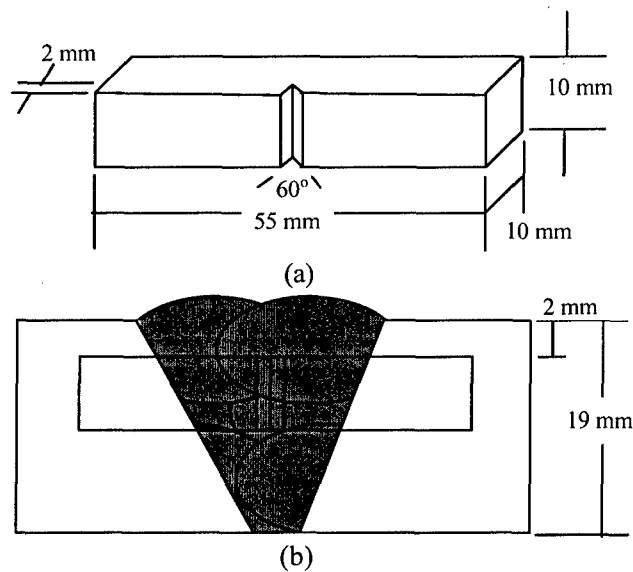


Figure 51: (a) Illustration of the dimensions of a CVN sample, and (b) representative location of the extraction of the CVN sample

4.8.2 Tensile Testing

Sub-size all-weld metal tensile specimens were extracted from a weld test assembly as shown in Figure 52(a). The specimens were then machined to match the dimensions specified in ANSI/AWS D1.1-00 [188] and shown in Figure 52(b). The dimensions of the tensile specimens are listed in Table 15. The tensile specimens had a reduced section of 4 millimeters (0.157 inches) in diameter and were tested on an MTS Alliance/RT 100 screw driven machine at the strain rate of 1.27 millimeter/minute (0.05 inches per minute). All tensile data were digitally recorded using a data acquisition system on a personal computer.

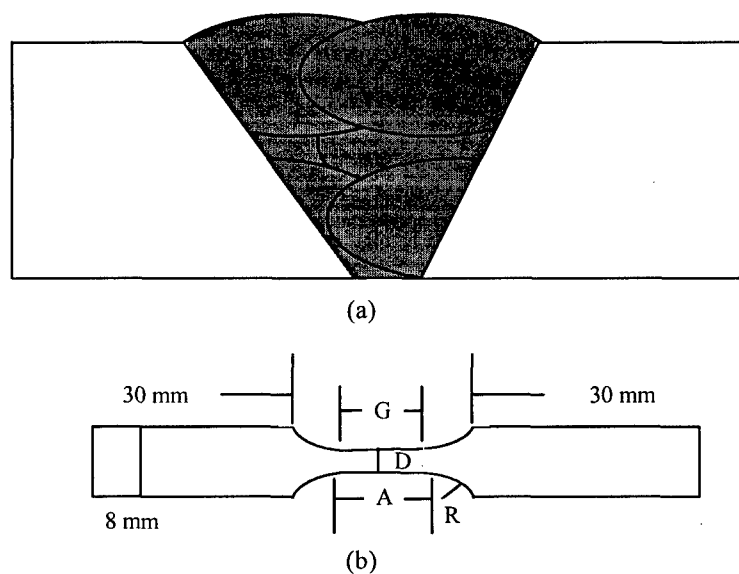


Figure 52: (a) Representative location of the extraction of tensile bar samples, and (b) “dimensions” of tensile bar specimens where the actual dimensions are shown in Table 15.

Table 15: Dimensions of the Sub-Sized Tensile Samples

Measurement	Dimension (mm)
G - Gage Length	12.5 ± 0.1
D - Diameter	4.0 ± 0.1
R - Radius	4 ± 0.1
A - Length of Reduced Section	20 ± 0.1

4.8.3 Hardness Measurements

Hardness measurements were performed on the multiple-pass, V-groove weld samples. Vickers hardness measurements were made on the cross section of the weld. Hardness measurements were made across the weld from the base metal, through the heat-affected zone and weld metal, then through the heat-affected zone on the opposite side of the weld and finishing in the base metal as schematically shown in Figure 53. These transverse measurements would determine the variations of hardness between the as-deposited weld metal, reheated weld metal, the heat affected zone, and the base metal. Measurements were taken at every hundredth of an inch across the weld.

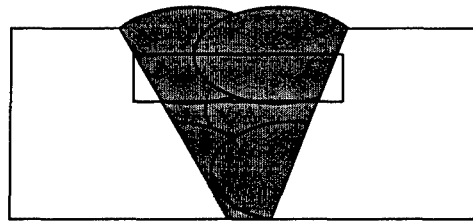


Figure 53: Schematic illustration of the locations where Vicker's microhardness measurements were taken.

CHAPTER 5

RESULTS AND DISCUSSION

5.1 Integrating Fluoride Additions to Yttrium-Containing Consumables

The first part of this study was to determine the effects that fluoride additions would have on the welding behavior of consumables that contain yttrium. Initially, it was believed that the addition of ingredients normally associated with welding with fluorides: calcium carbonate, silica, alumina, potassium oxide, etc. would have detrimental effects on oxygen potential and pickup, the yttrium-to-oxygen ratio, alloy recovery, inclusion characteristics, and microstructural development. For this initial study, fluorides were added entirely as potassium fluoride and varied from zero to thirty weight percent of the powder fill.

5.1.1 Welding Characteristics

To study the effects of fluoride additions on the welding behavior, the first step was to look at the stability of the welding arc. Voltage and current were measured directly with a data acquisition program on a personal computer during the welding of bead-on-plate welds, using the welding parameters presented in Table 14 in the experimental procedures section. The voltages and currents measured for the metal-cored, yttrium-containing consumables and the potassium fluoride additions to yttrium-containing consumables are presented in Table 16.

All welds made in this portion of the study were made using identical process settings: voltage, wire-feed rate, travel speed, gas and gas flow, and electrode

Table 16: Measured Arc Parameters of the Metal-Cored, Yttrium-Containing Consumables and the Potassium Fluoride Additions to Yttrium-Containing Consumables.

Consumable ID	KF Additions	ΔI	Current (A)	Voltage (V)	ΔV	Heat Input (kJ/mm)
Metal-Cored Yttrium-Containing Consumables						
0-1-C	0	26.3	545	25.69	0.47	2.4
0-1-D	0	66.4	526	25.91	0.54	2.4
0-2	0	23.8	528	25.62	0.68	2.4
Potassium Fluoride Additions to Yttrium-Containing Consumables						
1-1-C	5	27.8	448	26.79	1.27	2.1
1-1-D	5	53.2	422	25.61	2.31	1.9
1-2-C	10	30.6	445	26.16	1.38	2.0
1-2-D	10	39.5	437	25.93	1.54	2.0
1-3	15	38.2	341	26.03	1.00	1.6
1-4	20	47.2	328	26.37	1.52	1.5
1-5	25	39.8	344	26.61	1.61	1.6
1-6	30	26.2	343	26.13	1.43	1.6

extension. Figure 54 compares the average voltages and variations in voltage as the fluoride additions increase from zero to thirty weight percent of the powder fill. It can be seen from this plot that the average voltage remained constant over the entire range of fluoride additions as expected. The variation in voltage, ΔV , was seen to increase as the additions of fluoride increased. Thus, the addition of potassium fluoride decreased arc stability, and as the additions increased further, the arc became more unstable with a ΔV in excess of 1.5 volts. This decrease in arc stability resulted in difficulties during the welding process. This change was expected to: 1) adversely affect weld bead morphology, weld metal compositions and recoveries, 2) increase weld metal oxygen, hydrogen, and nitrogen content, 3) increase porosity, and 4) reduce weld metal strength and toughness.

Figure 55 compares the average current and the variation in current as the fluoride additions increase. As the amount of potassium fluoride in the consumable increased, the

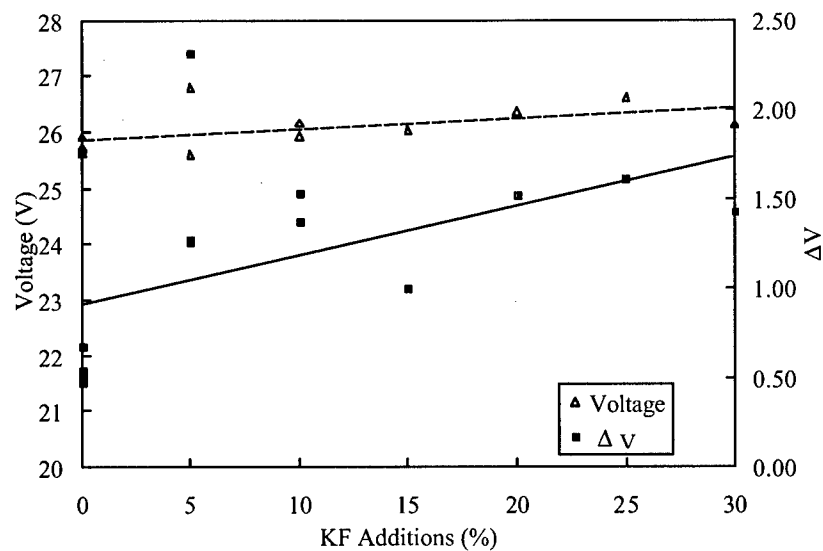


Figure 54: Plot showing the average voltage and change in voltage as additions of potassium fluoride to the powder fill increase.

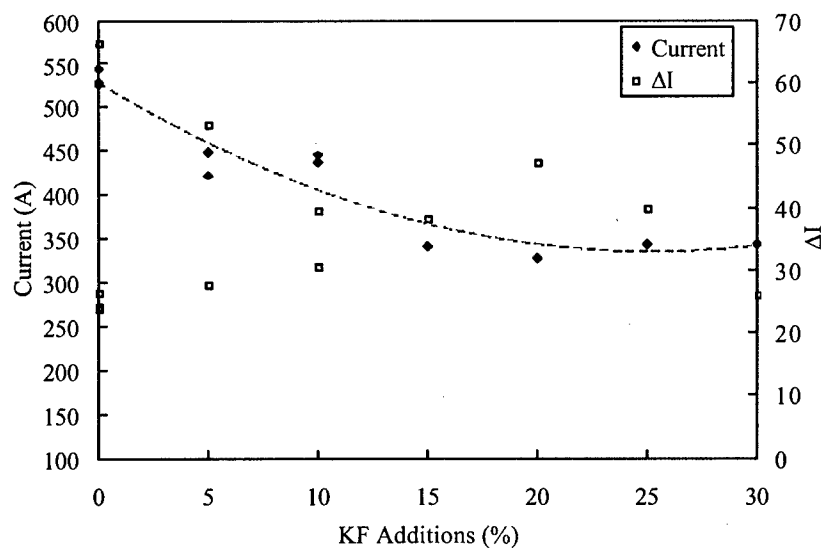


Figure 55: Plot showing the average currents and change in current as additions of potassium fluoride to the powder fill increase.

current was observed to decrease while the average change in current, ΔI , remained relatively constant at approximately 38 amperes. The presence of potassium fluoride in the welding consumable decreased the current measured during welding as expected, because the current carried through the electrode is dependent upon the conductivity of the electrode. An electrode that contains a fully metal core should carry the largest amount of current through the electrode. When a material that is nonconductive, such as potassium fluoride in this case, is added to an electrode, the current carried through that electrode should be less than the current carried through the metal-cored electrode. Consequently, when the amount of potassium fluoride is increased, the conductivity of the electrode should decrease. Since the additions of fluorides reduced the current during welding, heat input decreased, altering the cooling rate and resulting microstructures.

5.1.2 Weld Bead Morphology Analysis

Following the analysis of the welding characteristics, the bead-on-plate welds produced were examined for porosity and the weld bead contact angles, penetrations, widths, and reinforcements. Table 17 shows the results of these measurements for the welds produced with the metal-cored, yttrium-containing consumables and the potassium fluoride additions to yttrium-containing consumables. Clark [9] reported that the addition of yttrium-containing materials also reduced wetting and fluidity of the molten weld metal. The metal-cored, yttrium-containing consumables produced at CSM have contact angles in excess of 50° . It can be seen that the addition of fluorides further increased the contact angle to greater than 100° , showing that the potassium fluoride also reduced wetting and molten metal fluidity. Furthermore, the addition of fluorides also decreased the width and penetration of the weld beads. Since both the yttrium additions and fluoride additions reduce wetting and fluidity, the presence of porosity was expected to become more significant as the addition of fluorides increased. Figure 56 shows the transverse cross sections of representative bead-on-plate

Table 17: Representative Measurements of Weld Bead Macrostructures of the Metal-Cored, Yttrium-Containing Consumables and the Potassium Fluoride Additions to Yttrium-Containing Consumables.

Consumable ID	Contact Angle	Penetration (mm)	Width (mm)	Reinforcement (mm)
Metal-Cored Yttrium-Containing Consumables				
0-1-C	68.5	4.1	12.8	3.7
0-1-D	44.0	4.0	15.6	4.3
0-2	47.5	4.5	12.0	4.8
Potassium Fluoride Additions to Yttrium-Containing Consumables				
1-1-C	99.6	3.5	11.8	4.4
1-1-D	86.0	3.7	14.3	4.6
1-2-C	108.0	2.7	9.7	4.4
1-2-D	97.0	3.1	12.2	4.3
1-3	109.6	2.9	10.2	4.5
1-4	110.1	2.7	11.1	4.4
1-5	112.5	2.6	12.6	4.7
1-6	112.5	2.3	11.1	4.5

welds, showing the significant increase of porosity as the fluoride additions increased from zero to thirty weight percent powder fill.

The significant increase in porosity shown in Figure 56 was attributed to two possibilities. The first possibility is that potassium fluoride is hygroscopic. As such, there is a high probability that moisture may be present within the welding consumable. To minimize this problem, the potassium fluoride was baked at approximately 600°C to release any moisture contained within the KF for wires manufactured at CSM. Supporting this assumption, the consumables containing potassium fluoride that were manufactured by Devasco International (which is located in Houston, Texas, where the average humidity is around eighty percent, compared to the twenty percent or less experienced in Golden) produced welds with a much greater amount of porosity compared to their counterparts manufactured at CSM, as can be seen

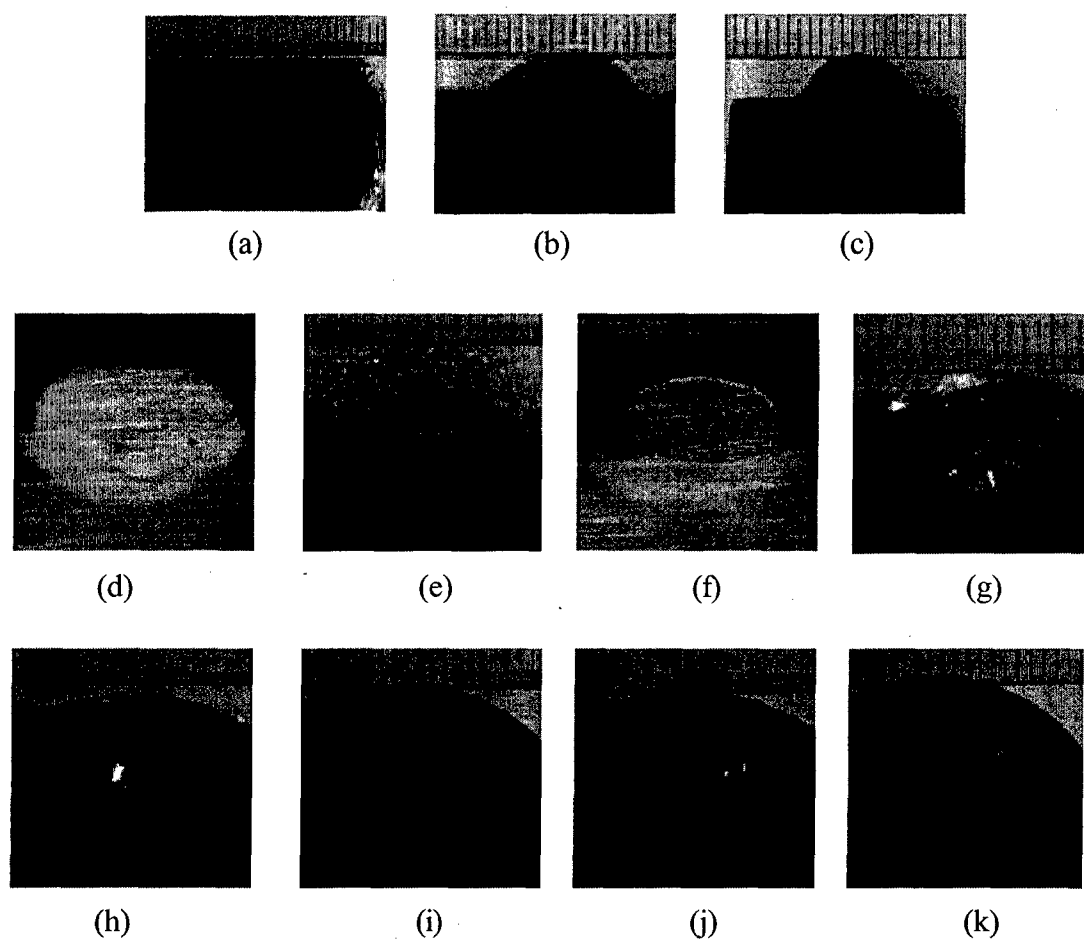


Figure 56: Representative photographs of cross sections of bead-on-plate welds produced with the metal-cored, yttrium-containing consumables (a) 0-1-C, (b) 0-1-D, and (c) 0-2, and welds produced with (d) 1-1-C, (e) 1-1-D, (f) 1-2-C, (g) 1-2-D, (h) 1-3, (i) 1-4, (j) 1-5, and (k) 1-6 showing significant increases in porosity and contact angles with increasing fluoride additions.

Figure 56(d) and (e), and Figures 56(f) and (g). The second possibility is due to the reduced fluidity of the molten weld metal. In this case, gases that form through reactions occurring in the molten weld metal become trapped under or within the solidified weld metal. This phenomenon occurs because the weld metal solidifies before the gases are able to escape out of the molten weld metal or into the slag layer. Evidence of this can be seen in Figure 57, which shows a longitudinal cross section of a bead-on-plate weld. In the figure, it can be seen that the gases that formed in the molten weld are rising to the top of the weld, but become trapped by the solidified weld metal before they escape the weld metal.

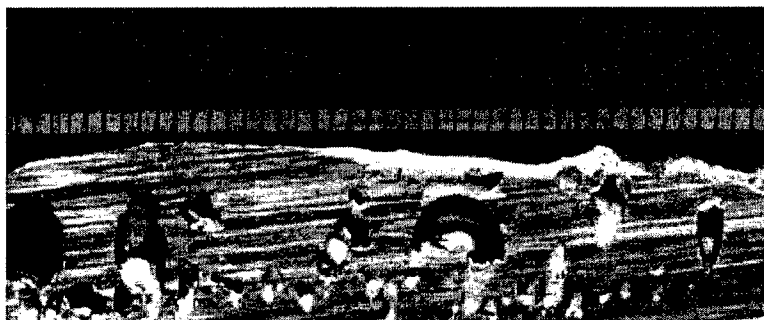


Figure 57: Photograph showing the trapping of gases in the solidified weld metal prior to before the gases could escape the molten weld metal.

5.1.3 Microstructural Analysis

After examining the weld bead morphology of the bead-on-plate welds for the metal-cored, yttrium-containing consumables and the potassium additions to yttrium-containing consumables, bead-on-bead welds were produced to examine the top-bead microstructures and inclusion characteristics. This section covers the microstructural analysis and the following section covers the analysis of the inclusion characteristics.

The microstructural constituents of interest were primary or grain boundary ferrite (PF), acicular ferrite (AF), ferrite with second phases aligned (FS(A)) and non-aligned (FS(NA)), and martensite (M). Figures 58 through 68 shows representative photomicrographs of the top bead microstructures of welds produced with the metal-cored, yttrium and potassium fluoride containing consumables. Table 18 presents the microstructural statistics of these welds.

Table 18: Microstructural Constituent Fractions Present in Welds Produced with the Metal-Cored, Yttrium Containing Consumables and the Potassium Fluoride Additions to Yttrium-Containing Consumables

Weld ID	KF Additions	Heat Input (kJ/mm)	PF(G)	FS(A)	FS(NA)	AF	M
Metal-Cored Yttrium Containing Consumables							
0-1-C	0	2.4	10	57	4	29	0.3
0-1-D	0	2.4	20	14	15	50	1.3
0-2	0	2.4	3	14	8	72	3.2
Potassium Fluoride Additions to Yttrium Containing Consumables							
1-1-C	5	2.1	9	42	5	44	0.2
1-1-D	5	1.9	8	40	6	47	0.3
1-2-C	10	2.0	12	36	7	45	0.4
1-2-D	10	2.0	12	32	9	48	0.3
1-3	15	1.6	8	44	10	38	0.4
1-4	20	1.5	17	41	13	29	0.4
1-5	25	1.6	11	59	9	20	0.5
1-6	30	1.6	11	65	9	15	0.5

The addition of potassium fluoride was detrimental to the microstructural development of the weld metal. Welds produced with consumable 0-2, Figure 60, exhibited excellent microstructures, containing an excess of seventy percent acicular ferrite. This was an improvement from the first metal-cored, yttrium-containing

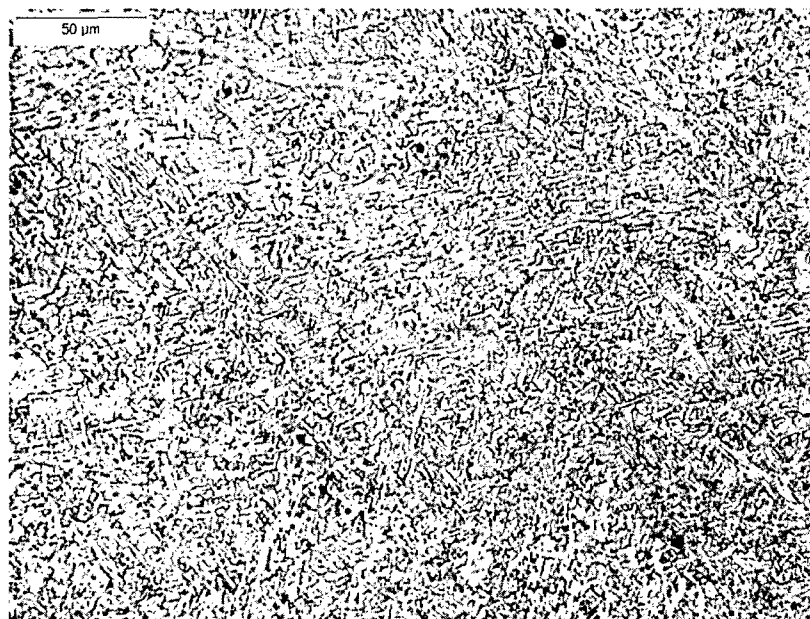


Figure 58: Representative photomicrograph of welds produced with the 0-1-C consumable, consisting of about 60 percent ferrite with second phases (aligned and non-aligned combined), 30 percent acicular ferrite, and 10 percent grain boundary ferrite.



Figure 59: Representative photomicrograph of welds produced with the 0-1-D consumable, consisting of 50 percent acicular ferrite, 29 percent ferrite with second phases, and 20 percent grain boundary ferrite.

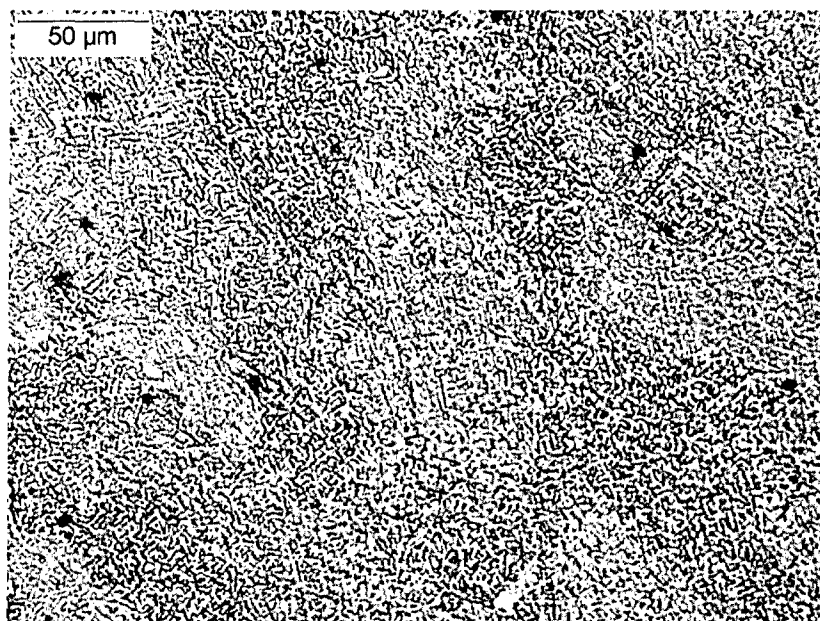


Figure 60: Representative photomicrograph of welds produced with consumable 0-2, consisting of 72 percent acicular ferrite, 22 percent ferrite with second phases, and 3 percent grain boundary ferrite.

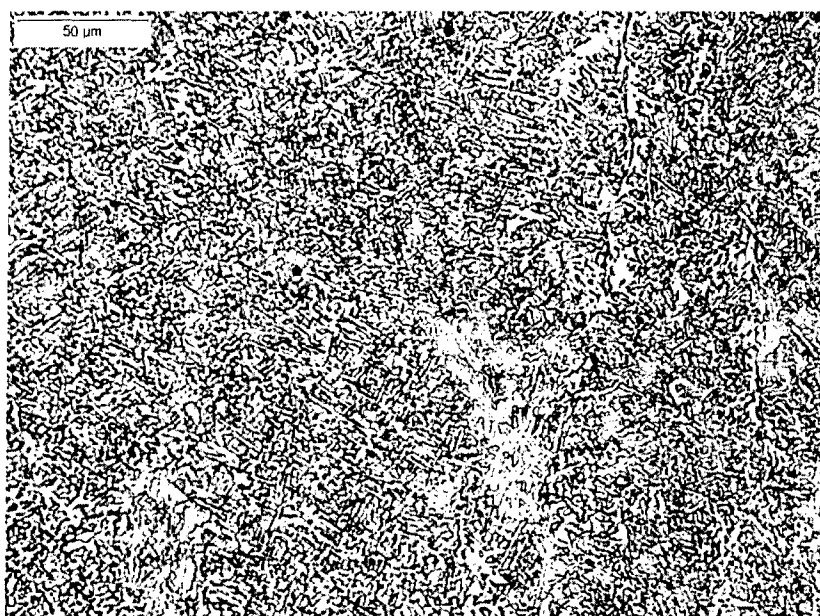


Figure 61: Representative photomicrograph of welds produced with consumable 1-1-C, consisting of 44 percent acicular ferrite, 47 percent ferrite with second phases, and 9 percent grain boundary ferrite.

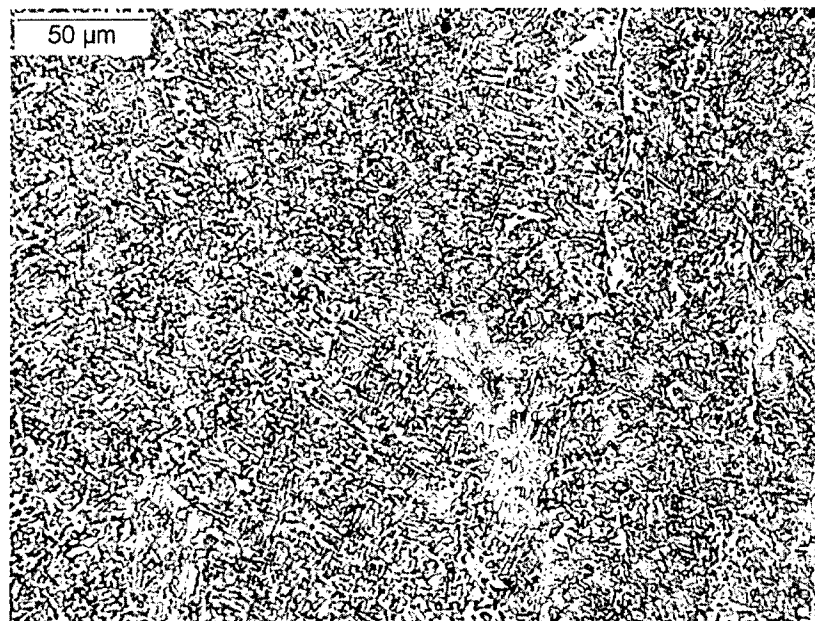


Figure 62: Representative photomicrograph of welds produced with consumable 1-1-D, consisting of 47 percent acicular ferrite, 46 percent ferrite with second phases, and 7 percent primary ferrite.

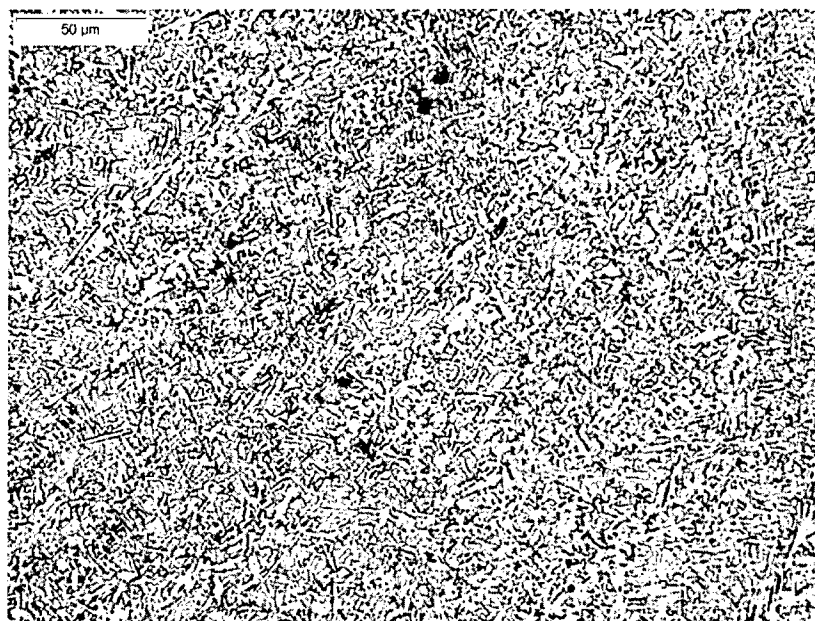


Figure 63: Representative photomicrograph of welds produced with consumable 1-2-C, consisting of 45 percent acicular ferrite, 43 percent ferrite with the second phases, and 12 percent primary ferrite.

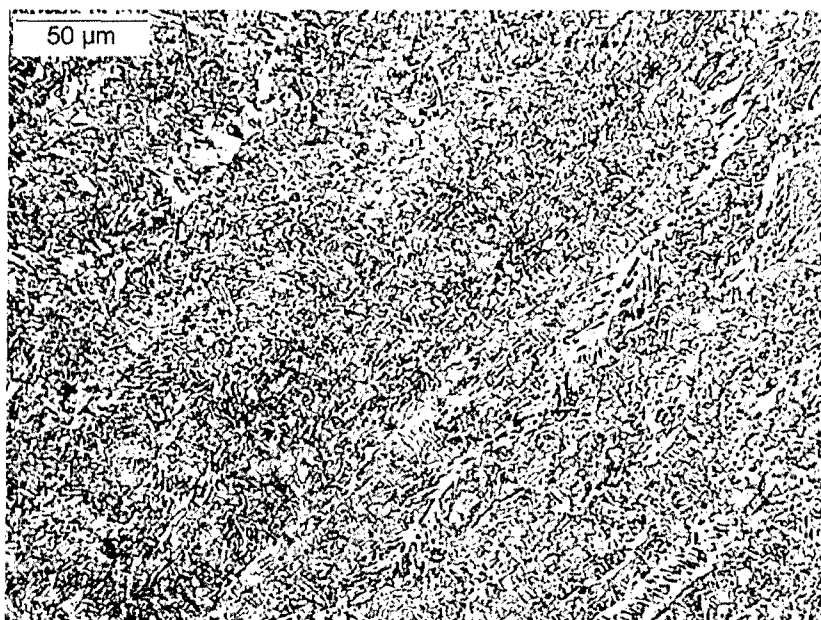


Figure 64: Representative photomicrograph of welds produced with consumable 1-2-D, consisting of 48 percent acicular ferrite, 41 percent ferrite with the second phases, and 11 percent primary ferrite.



Figure 65: Representative photomicrograph of welds produced with consumable 1-3, consisting of 54 percent ferrite with the second phases, 38 percent acicular ferrite, and 8 percent primary ferrite.

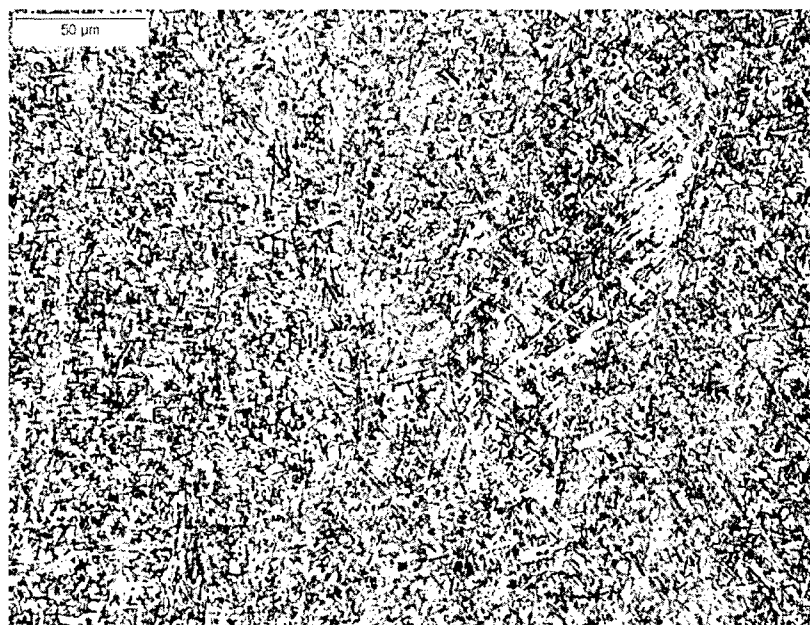


Figure 66: Representative photomicrograph of welds produced with consumable 1-4, consisting of 54 percent ferrite with the second phases, 29 percent acicular ferrite, and 17 percent primary ferrite.

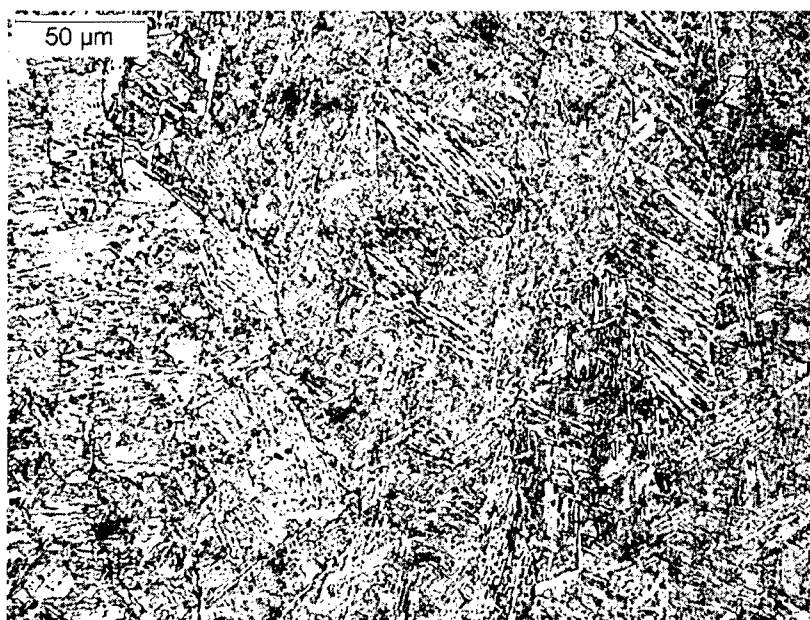


Figure 67: Representative photomicrograph of welds produced with consumable 1-5, consisting of 68 percent ferrite with the second phases, 20 percent acicular ferrite, and 12 percent primary ferrite.

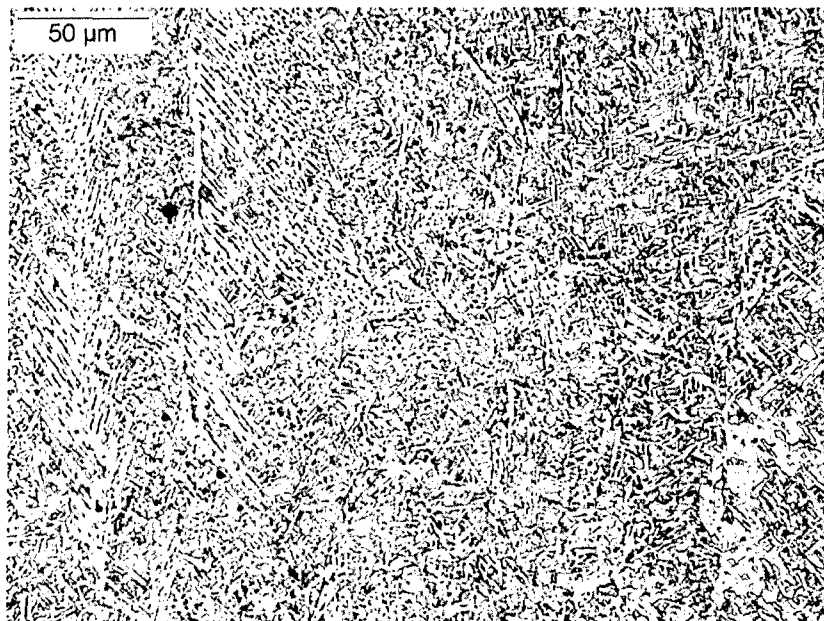


Figure 68: Representative photomicrograph of welds produced with consumable 1-6, consisting of 73 percent ferrite with the second phases, 15 percent acicular ferrite, and 11 percent primary ferrite.

consumables, 0-1 series, Figures 58 and 59, due to the changes in alloying additions. The 0-2 consumable was designed to have a lower nickel and manganese concentrations and higher titanium and yttrium concentrations. These alterations showed to be beneficial, increasing acicular ferrite content from less than fifty percent to greater than seventy percent, and decreasing ferrite with second phases from greater than sixty percent to less than 25 percent. The resulting chemical compositions are discussed in the following section. The addition of potassium fluoride, however, reduced the fraction of acicular ferrite from the seventy percent exhibited by the 0-2 consumable to about 45 percent with five percent, Figures 61 and 62, and ten percent, Figures 63 and 64, potassium fluoride additions, and to less than 35 percent with potassium fluoride additions in excess of ten weight percent, Figures 65 through 68.

The analysis of the microstructures shows that the addition of fluorides increases the amount of bainitic phases, apparently at the expense of acicular ferrite. These results

suggests that the addition of fluorides not only reduce current and heat input as seen in Table 16, which changed the cooling rates of the weld metal and the resulting microstructures, but also change the recovery of alloying elements and gas pickup, as will be discussed in a later section. The results also suggest that the characteristics of the inclusions are also affected by the fluoride additions, which may also be a result of elemental recoveries and gas pickup.

5.1.4 Chemical Analysis

Clark [9] reported that a weld metal composition of 2.5 weight percent nickel, 1.1 weight percent manganese, 0.2 weight percent molybdenum, 300 ppm titanium, and 300 to 900 ppm yttrium (depending on oxygen content) produced welds that contained approximately seventy percent acicular ferrite and 25 percent ferrite with second phases. The dependency of yttrium on oxygen was used to group welds through the yttrium-to-oxygen ratio, where an yttrium-to-oxygen ratio less than 1.3 resulted in a fine-grained, acicular ferrite microstructure. An additional characterization was made using the carbon equivalent of each type of weld metal. The carbon equivalent was calculated using the P_{cm} equation shown in Equation 57:

$$P_{CM} = C + \frac{Si}{30} + \frac{Mn}{20} + \frac{Cu}{20} + \frac{Ni}{60} + \frac{Cr}{20} + \frac{Mo}{15} + \frac{V}{10} + 5B. \quad (57)$$

The carbon equivalent varies from one weld to another, and it may influence the steel weld metal microstructure and mechanical properties.

To determine the chemical composition of the welds produced with the metal-cored, yttrium-containing consumables and the potassium fluoride additions to yttrium-containing consumables, top bead chemical analysis was performed on the bead-on-bead welds. The results of these analyses are shown in Table 19. From these results, it can be

Table 19: Top-bead Chemical Composition for Welds Produced with the Metal-Cored, Yttrium-Containing Consumables and the Potassium Fluoride Additions to Yttrium-Containing Consumables.

	Metal-Cored Yttrium-Containing Consumable			Fluoride Additions to Yttrium-Containing Consumables							
	0-1-C	0-1-D	0-2	1-1-C	1-1-D	1-2-C	1-2-D	1-3	1-4	1-5	1-6
C (%)	0.05	0.05	0.05	0.05	0.05	0.05	0.05	0.06	0.05	0.04	0.05
S (%)	0.01	0.01	0.01	0.01	0.01	0.01	0.01	0.01	0.01	0.01	0.02
Si (%)	0.02	0.02	0.02	0.02	0.02	0.02	0.02	0.02	0.02	0.02	0.02
Mn (%)	1.47	1.42	1.14	1.41	1.40	1.40	1.41	0.74	0.44	0.63	0.69
Cu (%)	0.017	0.017	0.017	0.035	0.041	0.006	0.006	0.006	0.020	0.014	0.010
Cr (%)	0.05	0.05	0.05	0.03	0.03	0.03	0.03	0.03	0.03	0.03	0.03
Ni (%)	3.78	3.65	2.55	2.85	2.75	3.70	3.51	1.53	1.17	0.86	0.64
Mo (%)	0.42	0.38	0.24	0.19	0.24	0.35	0.33	0.01	0.18	0.10	0.07
V (%)	0.005	0.005	0.005	0.004	0.004	0.002	0.002	0.003	0.005	0.002	0.003
Al (ppm)	170	170	180	120	110	90	110	60	60	70	60
Y (ppm)	320	330	650	800	770	310	480	110	290	170	120
Ti (ppm)	150	180	280	170	220	60	80	20	50	60	70
O (ppm)	680	630	610	980	800	740	760	1120	1160	1190	1530
N (%)	0.11	0.10	0.11	0.05	0.05	0.07	0.07	0.07	0.07	0.08	0.10
Retained H (ppm)	4.2	4.5	5.2	2.1	3.2	2.0	3.1	1.6	1.5	1.6	1.6
Carbon Equivalent (P_{CM})	0.22	0.21	0.17	0.19	0.19	0.21	0.20	0.13	0.11	0.10	0.10
Heat Input (kJ/mm)	2.4	2.4	2.4	2.1	1.9	2.0	2.0	1.6	1.5	1.6	1.6

seen that only consumable 0-2 was similar to the target composition mentioned above, which is also the weld that contained the highest acicular ferrite fraction. Consumables 0-1-C and 0-1-D contained excessive nickel, manganese, and molybdenum contents and were deficient in titanium. Consumables 1-1-C and 1-1-D were similar in nickel and molybdenum content, but contained excessive manganese and deficient titanium concentrations. Consumables 1-2-C and 1-2-D were similar in composition to the 0-1-X consumables. The other four consumables, 1-3, 1-4, 1-5, and 1-6, produced welds with compositions that were deficient in all the alloying elements listed in the target composition.

Due to the reduction in alloying elements as the potassium fluoride additions increased, the elemental recoveries were examined. The recoveries that resulted are shown in Table 20. Figure 69 shows the recoveries of the six highly influential alloying elements in this study: (a) nickel, (b) manganese, (c) molybdenum, (d) yttrium, (e) titanium, and (f) aluminum, as they were affected by the addition of fluorides. As can be seen in the plots, elemental recovery was drastically reduced when powder-fill potassium fluoride content exceeded ten percent. This is expected to be a result of the arc instability experienced. The other five consumables had similar recoveries for all of the elements.

Another notable occurrence was the increase in oxygen with increasing fluoride additions. This increase can also be attributed to the increase in arc instability experienced with increasing fluoride additions. To further characterize the welds produced, a comparison of yttrium and oxygen was performed. Table 21 shows the yttrium-to-oxygen ratios of welds produced with each of the consumables. Clark [9] had suggested that an upper limit of 1.3 for this ratio would produce suitable inclusions for nucleation of acicular ferrite. From this study, it can be suggested that 0.4 should be the lower limit, because welds that had a ratio less than that consisted of microstructures similar to those present by Clark as "yttrium-free" welds, which consisted of high amounts of ferrite with second phases.

Table 20: Elemental Recoveries of the Welds Produced with the Metal-Cored, Yttrium-Containing Consumables and the Potassium Fluoride Additions to Yttrium-Containing Consumables.

Weld ID	KF Additions	Y/O ratio	Carbon Equivalent (P_{CM})	Heat Input (kJ/mm)	Y	Ti	Al	Mn	Ni	Mo
Metal-Cored Yttrium Containing Consumables										
0-1-C	0	0.47	0.22	2.4	6.1	14.9	30.4	64.3	91.2	81.4
0-1-D	0	0.52	0.21	2.4	6.3	17.9	30.4	62.2	88.1	73.7
0-2	0	1.07	0.17	2.4	10.6	9.3	23.8	52.2	85.9	52.6
Potassium Fluoride Additions to Yttrium Containing Consumables										
1-1-C	5	0.82	0.19	2.1	13.0	5.6	15.9	64.5	96.0	41.7
1-1-D	5	0.96	0.19	1.9	12.5	7.3	14.6	64.0	92.7	52.6
1-2-C	10	0.42	0.21	2.0	5.0	2.0	11.9	64.0	89.3	76.7
1-2-D	10	0.63	0.20	2.0	7.8	2.7	14.6	64.5	84.7	72.4
1-3	15	0.10	0.13	1.6	1.8	0.7	7.9	33.9	51.6	1.3
1-4	20	0.25	0.11	1.5	4.7	1.7	7.9	20.1	39.4	39.5
1-5	25	0.14	0.10	1.6	2.8	2.0	9.3	28.8	29.0	21.9
1-6	30	0.08	0.10	1.6	2.0	2.3	7.9	31.6	21.6	15.4

Table 21: Comparison of the Yttrium-to-Oxygen Ratio of Welds Produces with the Metal-Cored, Yttrium-Containing Consumables and the Potassium Fluoride Additions to Yttrium-Containing Consumables

Consumable ID	Y (ppm)	O (ppm)	[Y]/[O] ratio
Metal-Cored Yttrium Containing Consumables			
0-1-C	320	680	0.47
0-1-D	330	630	0.52
0-2	650	610	1.07
Potassium Fluoride Additions to Yttrium Containing Consumables			
1-1-C	800	980	0.82
1-1-D	770	800	0.96
1-2-C	310	740	0.42
1-2-D	480	760	0.63
1-3	110	1120	0.10
1-4	290	1160	0.25
1-5	170	1190	0.14
1-6	120	1530	0.08

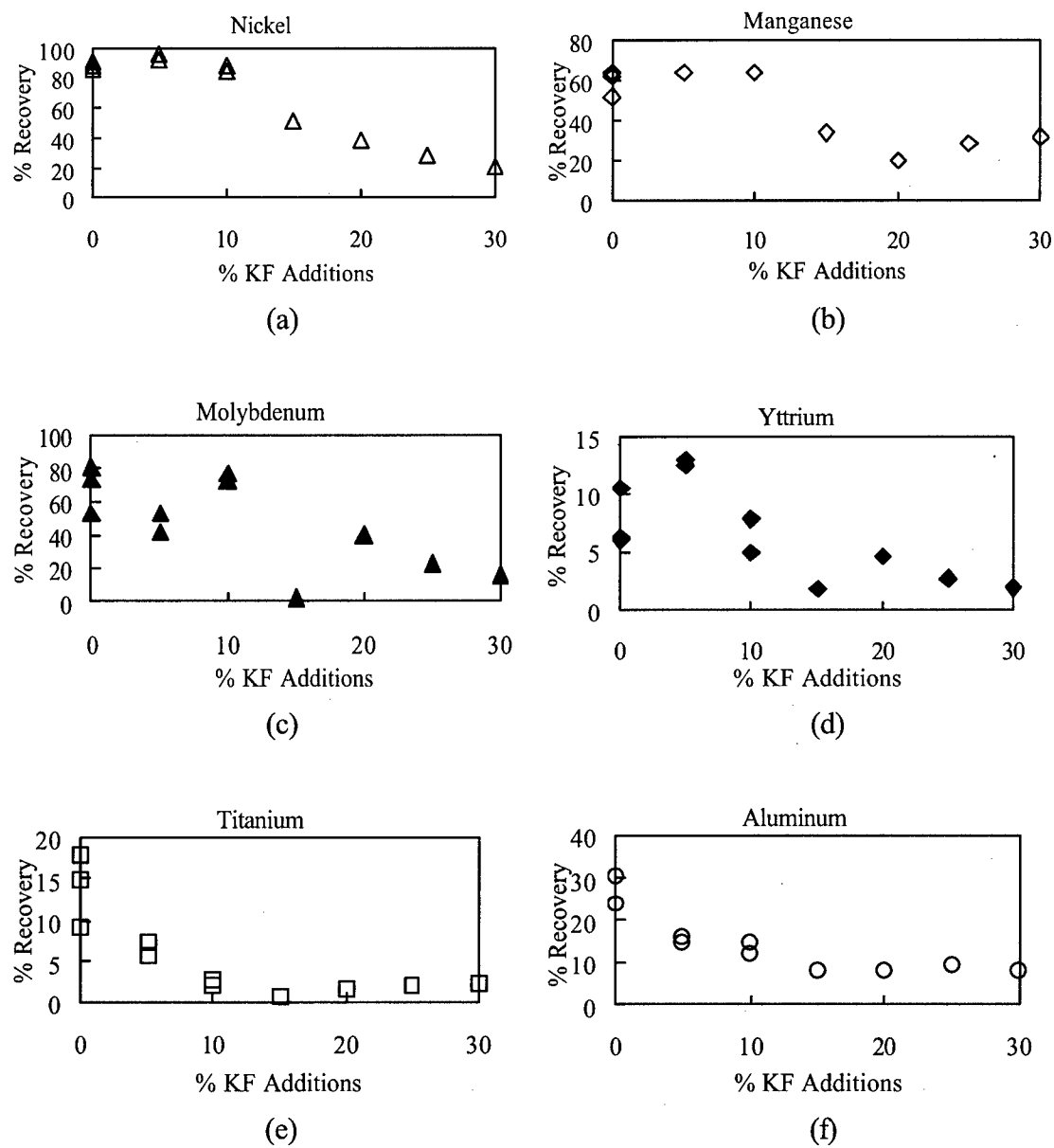


Figure 69: Elemental recoveries with changing potassium fluoride additions. (a) nickel, (b) manganese, (c) molybdenum, (d) yttrium, (e) titanium, and (f) aluminum.

5.1.5 Inclusion Analysis

Inclusion-assisted microstructural control has been intensely studied and applied to improve the toughness of carbon-manganese and low-alloy steels over the past thirty years. The microstructure of weld metals is refined by different inclusions, some of which work as nucleation sites for acicular ferrite. Another effect of the inclusions is the pinning of prior austenite grains from grain growth. The effect of a particular inclusion is based on several characteristics: 1) number density, 2) volume fraction, 3) diameter, 4) surface area, and 5) chemical composition.

The inclusions in the weldments produced during this study were characterized using light microscopy. The results of inclusion characterizations for welds produced with the metal-cored, yttrium-containing consumables and the yttrium-potassium fluoride consumables, with the exception of chemical composition, are shown in Table 22. The three-dimensional diameter was calculated as the characteristic diameter using Equation 58:

$$d_c = \left(\frac{3V}{4\pi} \right)^{1/3}, \quad (58)$$

where V is the average volume of the inclusions. The three-dimensional characteristics were calculated from two-dimensional measurements assuming all of the inclusions were spherical and randomly distributed throughout the weld metal. According to Clark [9], this assumption is suitable if the yttrium-to-oxygen ratio is less than 3.7.

Clark [9] characterized inclusions and summarized the results into three categories: yttrium-free welds, high-yttrium welds, and low-to-moderate-yttrium welds. The division between these categories was based on the yttrium-to-oxygen ratio, where a ratio of 3.7 represents the stoichiometric balance of yttria (Y_2O_3). The high-yttrium welds

Table 22: Results of Inclusion Characterization for Welds Produced with the Metal-Cored, Yttrium-Containing Consumables and Potassium Fluoride Additions to Yttrium-Containing Consumables.

Consumable ID	Volume Percent	3D Characteristic Diameter (μm)	Density ($10^7/\text{mm}^3$)	Surface Area ($10^7 \mu\text{m}^2/\text{mm}^3$)	Heat Input (kJ/mm)
Metal-Cored Yttrium-Containing Consumables					
0-1-C	0.38	0.37	1.85	3.11	2.4
0-1-D	0.56	0.40	2.13	4.23	2.4
0-2	1.02	0.53	1.68	5.82	2.4
Potassium Fluoride Additions to Yttrium-Containing Consumables					
1-1-C	1.12	0.59	1.31	5.70	2.1
1-1-D	1.14	0.60	1.34	5.89	1.9
1-2-C	1.33	0.60	1.45	6.63	2.0
1-2-D	1.28	0.59	1.43	6.42	2.0
1-3	1.23	0.59	1.41	6.20	1.6
1-4	1.48	0.59	1.70	7.49	1.5
1-5	1.05	0.58	1.26	5.40	1.6
1-6	1.02	0.58	1.28	5.33	1.6

produced welds with inclusions that are clustered and non-spherical, whereas the yttrium-free and low-to-moderate yttrium welds were reported to form spherical and randomly distributed inclusions. The yttrium-free welds from Clark and Edwards' [10, 11, 12] studies formed complex inclusions containing aluminum, titanium, manganese, silicon, iron, and sulfur. Welds with an yttrium-to-oxygen ratio of up to 1.3 formed complex inclusions containing aluminum, yttrium, titanium, sulfur, and in some cases, manganese and silicon; and allowed for the formation of yttrium-containing inclusions such as yttrium-aluminum garnet with evenly distributed titanium content throughout the inclusions, possibly substituting for aluminum.

The metal-cored, yttrium-containing consumables developed in this study produced inclusion characteristics similar to those determined by Clark [9]. Clark reported the inclusion volume percent to be between 0.30 and 1.0 percent for welds

containing a low-to-moderate yttrium content. The number density reported by Clark was between 1.55×10^7 and 4.80×10^7 inclusions per cubic millimeter and an inclusion surface area between 2.85×10^7 and 7.86×10^7 square microns per cubic millimeter of weld metal. Figure 70 shows representative photomicrographs of the unetched weld samples used in the inclusion characteristics study for the metal-cored yttrium-containing consumables. In these micrographs, the inclusions can be seen to be predominately spherical in shape and randomly distributed throughout the weld metal.

The addition of potassium fluoride altered the formation of the weld metal inclusions. The first noticeable effect was the slight reduction in the inclusion number density. The addition of potassium fluoride increased the diameter from approximately 0.5 microns to 0.6 microns. It also caused a slight increase in volume percent from less than one percent for the potassium-free welds to 1.1 volume percent or greater. Total surface area also increased from the addition of fluorides. Figure 71 shows representative photomicrographs of unetched weld samples produced with the potassium fluoride additions to yttrium-containing consumables. In these micrographs, fewer inclusions exist as compared to the welds made with the metal-cored yttrium-containing consumables.

Control of the inclusion size is important to develop an optimized microstructure. For instance, if there is a large density of the small inclusions in the weld metal, the prior austenite grains are pinned and prevented from growing, resulting in a large number of small grains, but a large area of grain boundaries. Grain boundary ferrite and ferrite with second phases nucleate from the prior austenite grain boundaries and grow into the grain. The larger inclusions that act as intragranular nucleation sites can nucleate acicular ferrite but this phase is limited in growth. Less intragranular area for transformation is available, and the phases that nucleate from the grain boundaries grow into the grain, consuming a major fraction of the intragranular area.

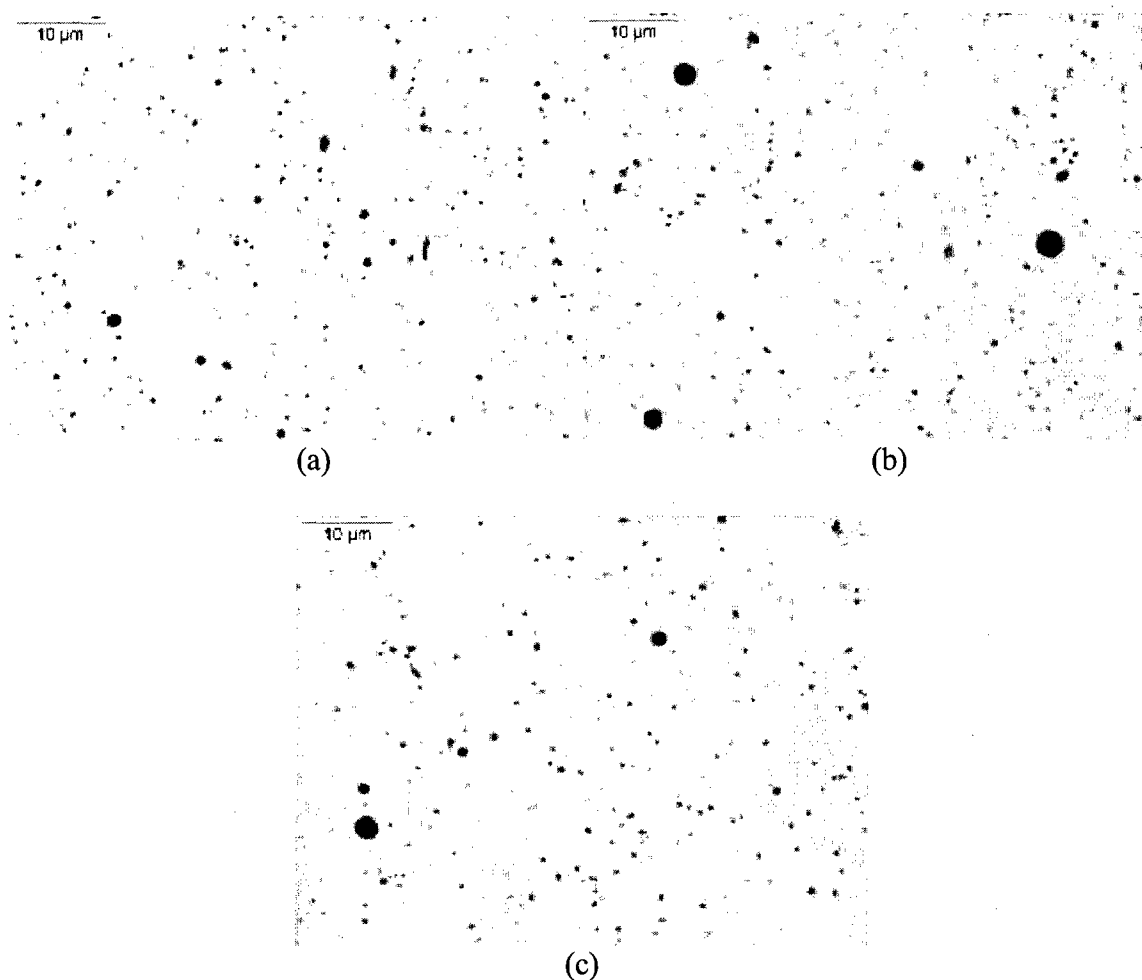


Figure 70: Representative photomicrographs of the unetched weld samples used in the inclusion characteristics study for the metal-cored yttrium-containing consumables (a) 0-1-C, (b) 0-1-D, and (c) 0-2.

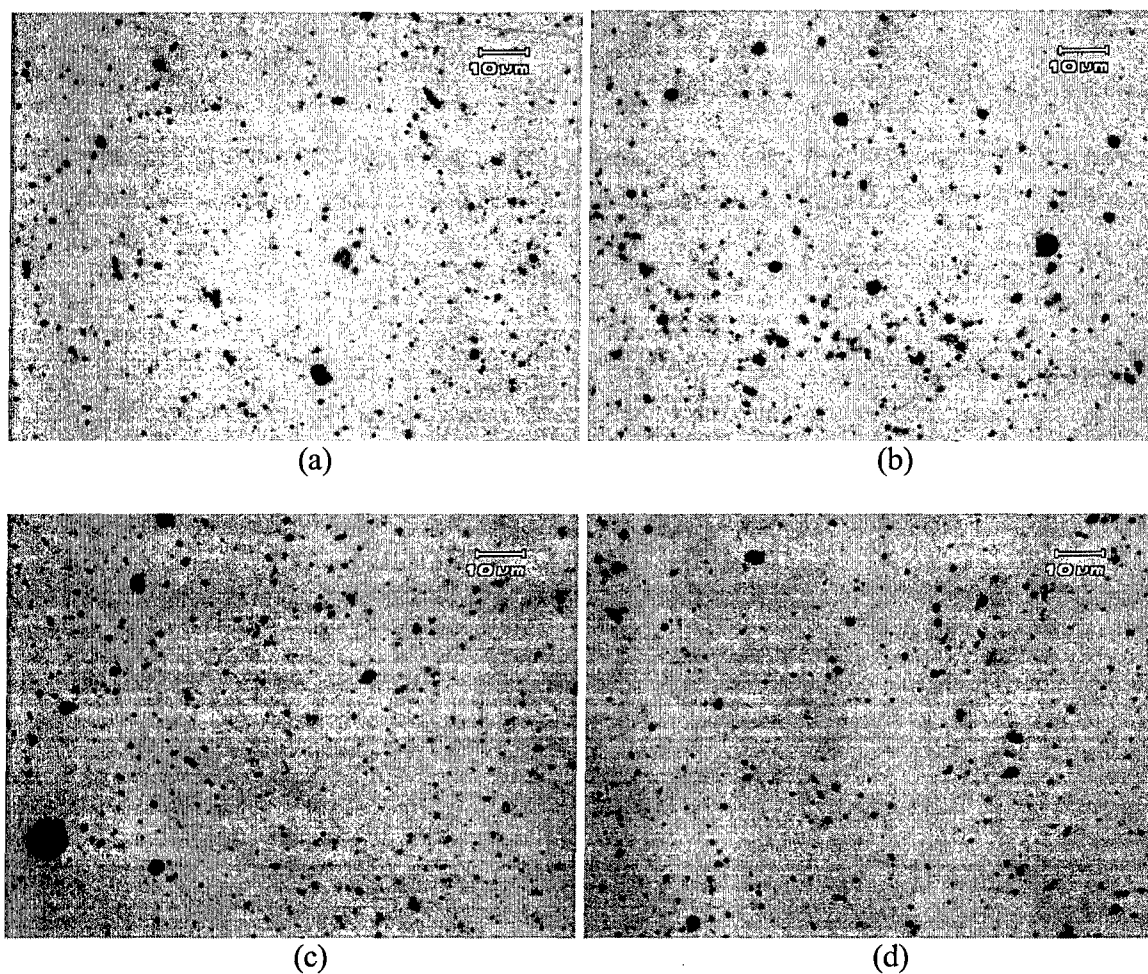


Figure 71: Representative photomicrographs of the unetched weld samples used in the inclusion characteristics study for the potassium fluoride to yttrium-containing consumables (a) 1-1-C, (b) 1-1-D, (c) 1-2-C, (d) 1-2-C, (e) 1-3, (f) 1-4, (g) 1-5, and (h) 1-6.

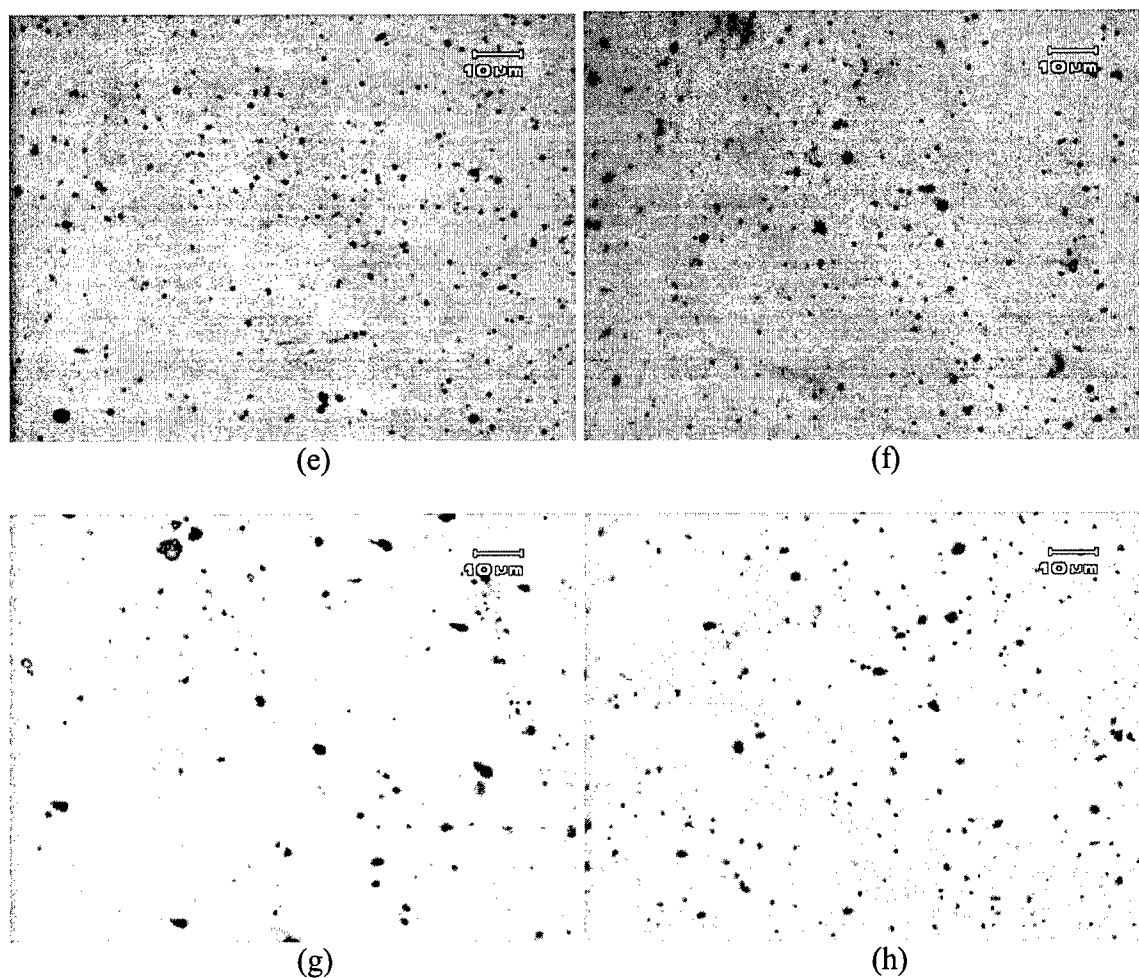
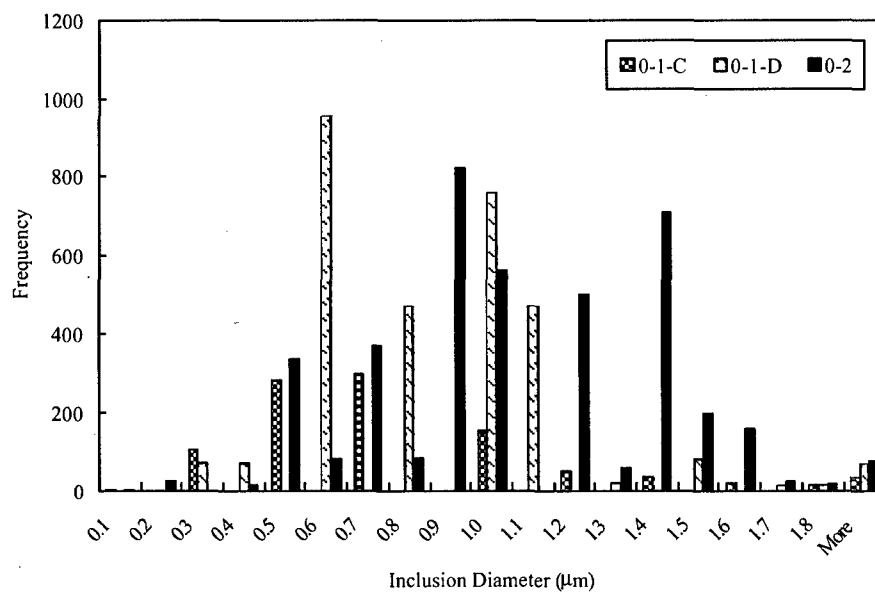


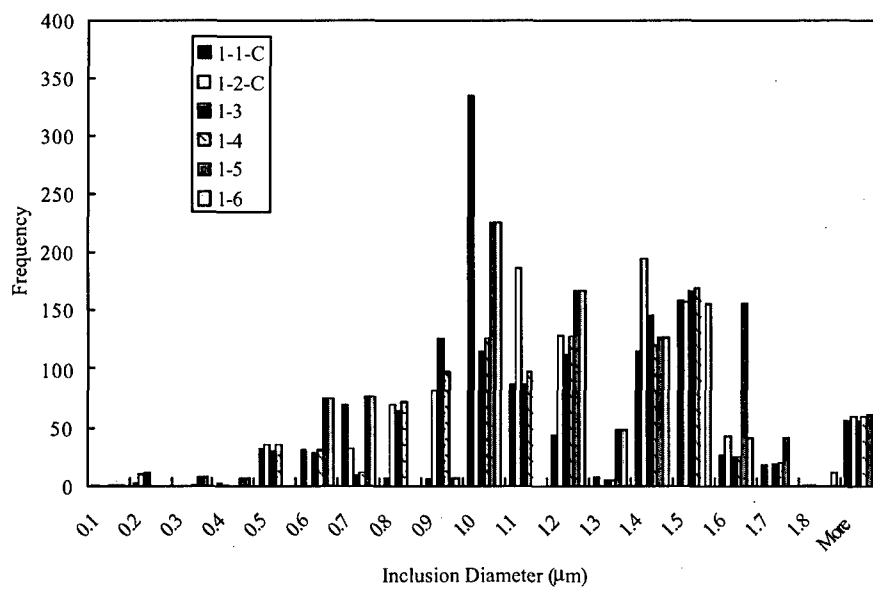
Figure 71(cont.): Representative photomicrographs of the unetched weld samples used in the inclusion characteristics study for the potassium fluoride additions to yttrium-containing consumables (a) 1-1-C, (b) 1-1-D, (c) 1-2-C, (d) 1-2-C, (e) 1-3, (f) 1-4, (g) 1-5, and (h) 1-6.

The optimal condition to develop a microstructure consisting primarily of acicular ferrite is to have a high density of inclusions with a diameter greater than 0.4 micron and a small density of smaller inclusions randomly distributed throughout the weld metal. This type of distribution would allow for prior austenite grains to be pinned, but with a much larger grain size so that the intragranular inclusions can nucleate acicular ferrite before the phases nucleated at the grain boundary impinge. Figure 72 shows the size distributions for the welds produced with the metal-cored, yttrium-containing and the potassium-fluoride-and-yttrium-containing consumables, where a majority of the consumables were larger than 0.4 microns and a noticeable shift in inclusion diameter with the addition of potassium fluoride can be seen.

The descriptions mentioned above would suggest that all of the welds should consist of a high acicular ferrite, which contradicts what was observed. This observation suggests that the chemical composition of the weld metal altered the microstructures. The target chemical composition of 2.5 weight percent nickel, 1.1 weight percent manganese, 0.2 weight percent molybdenum, 300 ppm titanium, and 300 to 900 ppm yttrium was shown by Clark [9] to produce welds with large fractions of acicular ferrite when the yttrium-to-oxygen ratio was between 0.4 and 1.3. Increased oxygen pickup with larger amounts of potassium fluoride, as well as the decreased titanium, yttrium and aluminum recoveries, suggests that undesired inclusion types that do not promote the formation of acicular ferrite formed. For the welds produced without potassium fluoride, there was an insufficient amount of titanium and aluminum, leading to a similar lack of desired inclusion types. Furthermore, according to Liu and Olson [97] and Fleck [38], who correlated the effect of weld metal oxygen content on austenite grain size, prior austenite grain size decreases with increasing oxygen content. This dependency on oxygen content suggests that the excessive oxygen content (greater than 1100 ppm) observed in welds made with a consumable containing more than ten percent potassium fluoride, was expected to result in smaller prior austenite grains, and therefore, provide for the



(a)



(b)

Figure 72: Distribution of the diameters of inclusions found in welds produced with (a) the metal-cored-yttrium containing consumables, and (b) the potassium fluoride additions to yttrium-containing consumables.

formation of grain boundary ferrite or ferrite with second phases rather than acicular ferrite.

5.1.6 Summary of the Integration of Fluorides to Yttrium-Containing Consumables

From the above results, excessive additions of potassium fluoride to the yttrium-containing consumables is detrimental to welding characteristics, alloying element recovery, inclusion development, and thus microstructural development. Potassium fluoride additions of more than ten percent of the powder fill produce welds with poor properties; i.e., significant porosity, minimal fine-grained microstructures, high oxygen content, etc. For these reasons, the potassium fluoride additions to yttrium-containing consumables 1-3, 1-4, 1-5, and 1-6 were eliminated from further study.

5.2 Integrating Additional Flux Ingredients to Yttrium-Containing Consumables

Continuing the study of the integration of fluoride additions and yttrium additions to a single FCAW consumable required two major parts: the improvement of molten weld metal fluidity, and the addition of other ingredients associated with fluoride-containing consumables. In this part of the study, attempts to improve molten weld metal fluidity through the addition of ferrosilicon were performed. In addition, potassium fluoride, calcium fluoride, calcium carbonate, silica, alumina, and potassium oxide were integrated with metal-cored, yttrium-containing consumable 0-2, which had produced the best characteristics in the first part of the study.

5.2.1 Improving Molten Weld Metal Fluidity with Ferrosilicon

Improvement of molten weld metal fluidity was necessary to minimize porosity and improve weld metal contact angle. A quick experiment was performed using consumable 1-2-C. In this experiment, a 2-mm-thick layer of ferrosilicon, blended with acetone to form a paste, was placed onto a steel plate, then welded over using the same arc parameters as before. Figure 73 compares the longitudinal cross section of welds made with this consumable before and after the use of ferrosilicon. In addition, the contact angles of the same welds were 108 degrees before and 43 degrees after the addition of ferrosilicon, obviously improving the weld bead morphology. The metal-cored, yttrium-containing consumable 0-3 was then designed to have identical alloying element additions as consumable 0-2, but to also incorporate one weight percent ferrosilicon. The comparison of the resulting macroscopic measurements is shown in Table 23, demonstrating the improved wetting, decreasing from nearly 50 degrees without ferrosilicon to less than 40 degrees with the addition of ferrosilicon.

Further comparison of welds produced with consumables 0-2 and 0-3 included microstructural development, inclusion characteristics, and chemical analysis. Figure 74 compares representative photomicrographs of each consumable. The fractions of each microstructural constituent are shown in Table 24. There was a minor decrease in acicular ferrite content from about 72 percent to 67 percent, a minor decrease in ferrite with second phases, a slight increase in martensite, and an increase of five percent in grain boundary ferrite. Table 25 compares the top-bead chemical analysis of these welds, showing minor changes in composition, carbon equivalents, and yttrium-to-oxygen ratios. In terms of inclusion characteristics, there was a decrease of about 0.15 volume percent while the diameters, number density, and surface areas were similar as can be seen in Table 26.

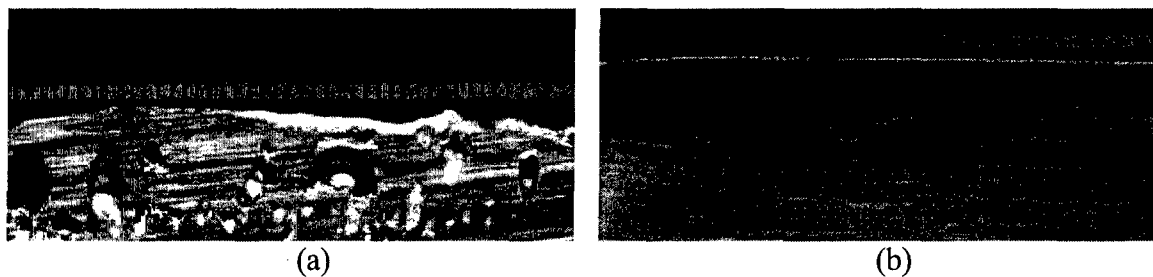


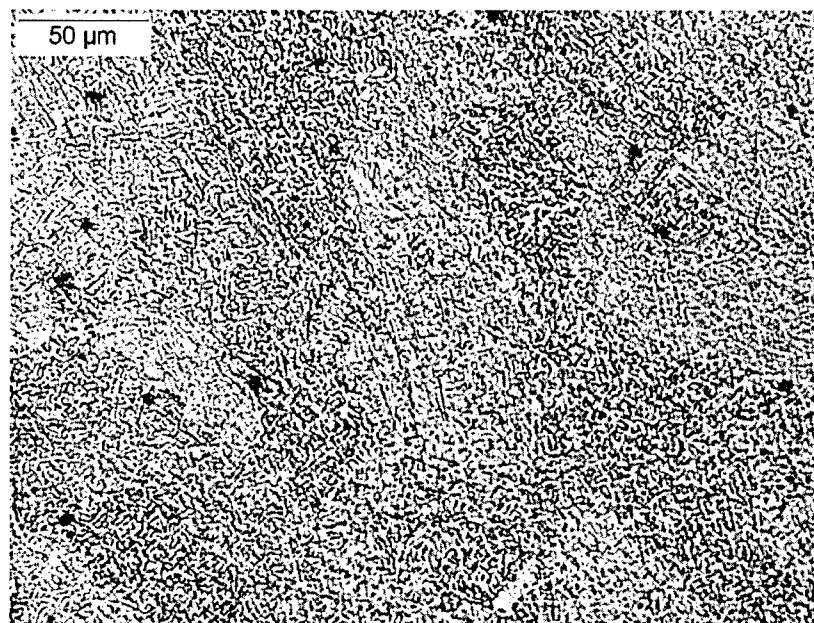
Figure 73: Longitudinal cross-section showing the decrease in porosity achieved when ferrosilicon paste was applied in combination with the 1-2-C consumable. Weld metal (a) was made without ferrosilicon and weld metal (b) was made with ferrosilicon.

Table 23: Measurements of the Weld Beads Produced with Consumables 0-2 and 0-3. Consumable 0-3 Contained One Weight Percent Ferrosilicon.

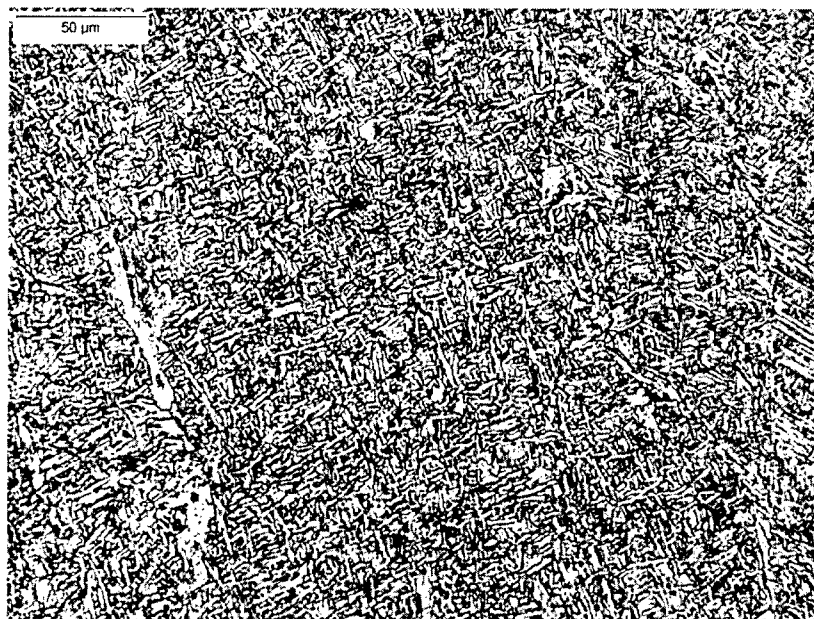
Consumable ID	Contact Angle	Penetration (mm)	Width (mm)	Reinforcement (mm)
0-2	47.5	4.5	12.0	4.8
0-3	39.5	3.9	17.1	5.1

Table 24: Microstructural Constituent Fractions for Welds Produced with Consumables 0-2 and 0-3.

Consumable ID	Y/O ratio	Carbon Equivalent (P_{CM})	Heat Input (kJ/mm)	Constituent Fractions				
				PF(G)	FS(A)	FS(NA)	AF	M
0-2	1.07	0.17	2.4	3	14	8	72	3
0-3	0.98	0.16	2.4	8	13	7	67	5



(a)



(b)

Figure 74: Representative photomicrographs of welds produced with the (a) 0-2 and (b) 0-3 consumables, where the microstructure constituents are listed in Table 24.

Table 25: Top-Bead Chemical Analysis of Welds Produced with Consumables 0-2 and 0-3.

	C (%)	S (%)	Si (%)	Mn (%)	Cu (%)	Cr (%)	Ni (%)	Mo (%)	
0-2	0.05	0.01	0.02	1.14	0.017	0.05	2.55	0.24	
0-3	0.04	0.01	0.09	1.11	0.024	0.05	2.49	0.28	
	V (%)	Al (ppm)	Y (ppm)	Ti (ppm)	O (ppm)	N (%)	Retained H (ppm)	Carbon Equivalent (PCM)	Heat Input (kJ/mm)
0-2	0.005	180	650	280	610	0.11	5.2	0.17	2.4
0-3	0.005	180	610	240	620	0.10	5.2	0.16	2.4

Table 26: Inclusion Characteristics of Inclusions Contained in Welds Produced with Consumables 0-2 and 0-3.

ID	Volume %	3D Characteristic Diameter (μm)	Density ($10^7/\text{mm}^3$)	Surface Area ($10^7 \mu\text{m}^2/\text{mm}^3$)	[%Y]/[%O] Ratio	Carbon Equivalent (PCM)	Heat Input (kJ/mm)
0-2	1.02	0.525	1.7	5.8	1.07	0.17	2.4
0-3	0.88	0.51	1.6	5.2	0.98	0.16	2.4

5.2.2 Addition of Other Flux Ingredients to Yttrium-Containing Consumables

From the experiments studying the addition of ferrosilicon, five additional consumables were designed to study and compare welding characteristics and weld bead morphology. These consumables were designed such that consumable 2-1 was similar to consumable 1-1-C and -D, except for the addition of one weight percent ferrosilicon. Consumables 2-2 and 2-3 were designed such that a flux blend consisting of calcium fluoride, potassium fluoride, calcium carbonate, silica, alumina, and potassium oxide was added to the powder composition used in consumable 0-2 at five and ten weight percent, respectively. Consumables 2-4 and 2-5 were designed similarly to 2-2 and 2-3, except

that the flux blend was added to the powder fill used for consumable 0-3 at five and ten weight percent, respectively, so that the effect of ferrosilicon could be studied.

There was considerable difficulty in welding with these consumables. During welding, these consumables produced a very unstable arc, with standard deviations of voltage as high as two volts. The four consumables containing calcium carbonate were difficult to produce weld lengths greater than three inches. This was attributed to the fact that calcium carbonate decomposes to calcium oxide and carbon dioxide at approximately 900°C, which is estimated to be located at one inch from the electrode tip. In FCAW processes, this distance is located within the contact tip, which is only slightly wider than the electrode. As the calcium carbonate decomposes and forms carbon dioxide gas, the electrode either will form a bulge and cause excessive friction in the contact tip, or it will cause a "bullet-in-a-gun-barrel" type action and eject the parts of the electrode. This effect led to an unstable arc where the electrode would stick in the contact tip because the formation of carbon dioxide would cause the electrode to expand, fracture and expel the piece of electrode that broke off, and possibly melt the copper contact tip.

Due to the difficulties encountered during welding with these consumables, only bead-on-plate welds were produced. The measurements of the contact angles, penetrations, widths, and reinforcements are shown in Table 27. Compared to the welds produced with consumables 0-2 and 0-3, the contact angle increased, as well as the weld bead widths and reinforcements, but the penetrations were seen to decrease. Also, due to the arc instability, porosity became significant in these welds. With these observations, consumables 2-2, 2-3, 2-4, and 2-5 were eliminated from further study, primarily due to the difficulties caused by the calcium carbonate decomposition.

Consumable 2-1 was studied more in depth because welding was a little more stable, although it still had a ΔV in excess of 1.25 volts. Comparing the macrostructure measurements of welds produced with this consumable and consumable 1-1-C and -D, shown in Table 28, showed that the ferrosilicon addition was effective in reducing the contact angle, although the penetration, width, and reinforcement were decreased. In

Table 27: Measurements of the Weld Beads Produced with Consumables 2-2, 2-3, 2-4, and 2-5.

Consumable ID	Contact Angle	Penetration (mm)	Width (mm)	Reinforcement (mm)
2-2	60.2	4.0	17.1	5.1
2-3	61	3.4	18.2	4.8
2-4	55	3.8	20.1	5.2
2-5	57	3.5	20.5	5.1

Table 28: Measurements of the Weld Beads Produced with Consumables 1-1-C, 1-2-C, and 2-1.

Consumable ID	Contact Angle	Penetration (mm)	Width (mm)	Reinforcement (mm)
1-1-C	99.6	3.5	11.8	4.4
1-1-D	86	3.7	14.3	4.6
2-1	55	1.2	11.4	4.3

bead-on-bead welds, a significant amount of porosity developed, which made obtaining the chemical composition impossible. Furthermore, it showed that either the amount of ferrosilicon was insufficient to counteract the detrimental effects of the potassium fluoride, the potassium fluoride hydrated, or a combination of both. Due to a shortage of material, particularly ferroyttrium, further iterations using this consumable composition (or variations of it) were not possible.

This section of the study touched on the possible benefits of using ferrosilicon as a flux/metal core ingredient, but still needs further study. With the shortage of material encountered during this study, designing and manufacturing additional FCAW consumables to further study ferrosilicon effects and the addition of the other flux ingredients to a yttrium-containing consumable was not possible. As an alternative procedure, the flux ingredients were introduced to the welding process as a paste.

5.3 Integration of Flux Ingredients Through the Use of a Paste

In this part of the study, four flux paste blends were prepared so that the flux ingredients that were used in the previous section (with calcium oxide substituted for calcium carbonate) could be evaluated. The consumable that was used during the welding was the 0-1-D consumable because it was the only metal-cored, yttrium-containing consumable with a sufficient amount remaining to make comparable welds. The compositions of the flux pastes can be found in Table 10. The same analytical methods were performed in this part of the study as were used in the first part.

5.3.1 Welding Characteristics

The measured voltages and currents, and their variations, are shown in Table 29. Comparing these values to those of the previously studied consumables, current was seen to decrease for each "paste" and the average voltage had increased to nearly thirty volts. Welds produced with fluxes 3-1 and 3-2 were very stable with ΔV 's of 0.25 and 0.35 respectively, and similar stability was experienced with current. On the other hand, welds produced with fluxes 3-3 and 3-4 had variations in voltage approaching one volt and less stability in the current. The pastes were blended such that blends 3-1 and 3-2 contained the equivalent of five percent potassium fluoride if it were blended with the metal powder additions, with the latter containing the equivalent of one percent ferrosilicon. Blends 3-3 and 3-4 did not contain potassium fluoride additions, but 3-4 contained the equivalent of one percent ferrosilicon. Since the fluxes were added in the form of a paste, it was unclear what caused the variations between the four fluxes other than the presence of potassium fluoride in the first two.

Table 29: Measured Current, Voltage, and the Variations During Welding with Consumables 3-1, 3-2, 3-3, and 3-4.

Consumable ID	ΔI	Current (A)	Voltage (V)	ΔV	Heat Input (kJ/mm)
3-1	42	258	29.9	0.25	2.4
3-2	38	258	29.6	0.35	2.4
3-3	62	264	31.2	0.81	2.6
3-4	66	266	30.5	0.92	2.5

5.3.2 Weld Bead Morphology

In this part of the study, the bead-on-plate welds were examined for porosity and the weld bead contact angles, penetrations, widths, and reinforcements were measured. Table 30 shows the results of these measurements for the welds produced with these flux pastes. Comparing these results to those of the previously reported, it can be seen that the contact angles were greater than the welds produced with the metal-cored, yttrium-containing consumables, but were less than those containing potassium fluoride. This suggests that addition of potassium fluoride alone is detrimental to the weld bead morphology, but incorporating the other ingredients with potassium fluoride improves wetting and molten weld metal fluidity. The other fluoride additions apparently produce wider welds with greater reinforcement. Penetration was reduced, but this may be due to the fact that the flux was pasted onto the plate rather than incorporated into the consumable.

Pastes 3-1 and 3-2, which improved molten weld metal fluidity better than the flux pastes 3-3 and 3-4, did not produce significant porosity in the weld metal. Welds produced with pastes 3-3 and 3-4 produced welds with porosity that was visible in the transverse cross-section, suggesting possible contamination or moisture in the paste. This was unexpected because the latter two pastes did not contain potassium fluoride, unlike the pastes 3-1 and 3-2.

Table 30: Measurements of the Weld Beads Produced with Consumables 3-1, 3-2, 3-3, and 3-4.

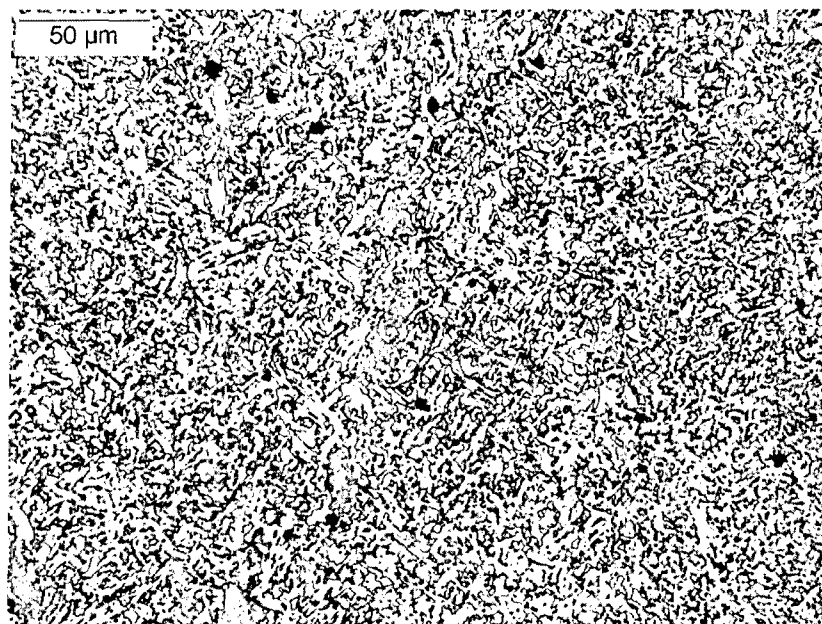
Consumable ID	Contact Angle	Penetration (mm)	Width (mm)	Reinforcement (mm)
3-1	55	2.5	23.5	6.1
3-2	65	3.0	21.3	8.2
3-3	85	1.8	19.5	5.9
3-4	74	2.7	20.1	7.6

Due to the porosity that was present in the bead-on-plate welds produced with the 3-3 and 3-4 flux pastes, the bead-on-bead welds were expected to multiply the amount of porosity from one pass to the next. This occurrence was observed and proved to make microstructural characterization and chemical analysis difficult. Consequently, these consumables were eliminated from further analysis.

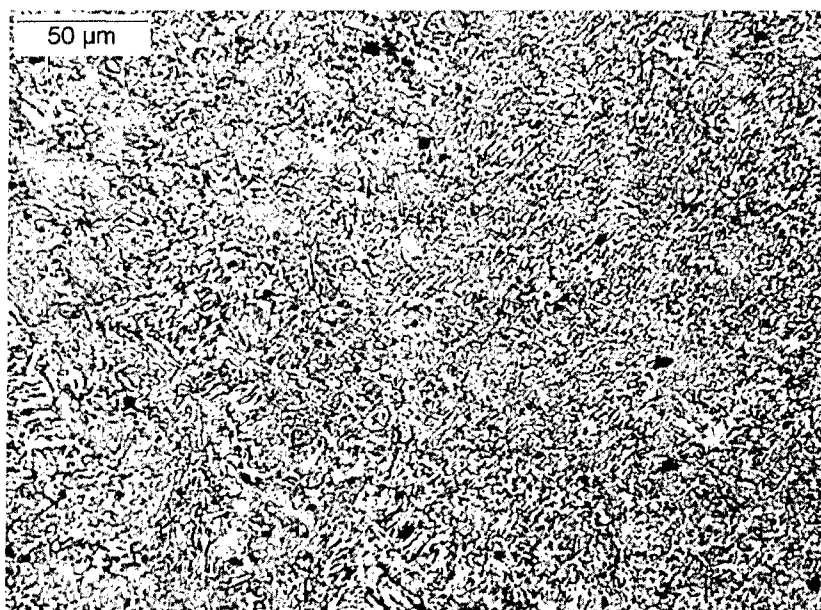
5.3.3 Microstructural Analysis

After examining the weld bead morphology of the bead-on-plate welds for the flux-paste consumables 3-1 and 3-2, bead-on-bead welds were produced to examine the top-bead microstructures and inclusion characteristics. This section covers the microstructural analysis, and the following section covers the analysis of the inclusion characteristics.

Representative photomicrographs of the top-bead microstructures of welds produced with paste fluxes 3-1 and 3-2 are shown in Figure 75. The microstructural constituent fractions are shown in Table 31. Both pastes produced welds with similar microstructures consisting of approximately sixty percent acicular ferrite, thirty percent ferrite with second phases, five percent martensite, and five to ten percent grain boundary ferrite. Compared to consumables 0-2 and 0-3, there was a decrease in acicular ferrite



(a)



(b)

Figure 75: Representative photomicrographs of welds produced using the 0-1-D consumable and the (a) 3-1 or (b) 3-2 flux pastes, where the constituent contents are shown in Table 31.

Table 31: Microstructural Constituent Fractions for Welds Produced Using the 3-1 and 3-2 Flux Pastes.

Consumable ID	Y/O ratio	Carbon Equivalent (P_{CM})	Heat Input (kJ/mm)	Constituent Fractions				
				PF(G)	FS(A)	FS(NA)	AF	M
3-1	0.71	0.17	2.4	9	16	12	58	5
3-2	0.74	0.17	2.4	7	16	14	57	5

content, but they contained more than the welds produced with the potassium-fluoride-containing consumables.

5.3.4 Chemical Analysis

The welds were made with the expectation of maintaining a target composition of 2.5 weight percent nickel, 1.1 weight percent manganese, 0.2 weight percent molybdenum, 300 ppm titanium, and 300 to 900 ppm yttrium (depending on oxygen content). The top-bead chemical composition is given in Table 32. Both of these consumables produced weld metals with compositions slightly high in nickel and insufficient in titanium, but the appropriate concentrations of yttrium, manganese, and molybdenum. Both weld metal microstructures contained a fraction of about sixty percent acicular ferrite, suggesting high impact toughness and high strength. The elemental recoveries are given in Table 33. The recoveries of nickel, manganese, molybdenum, yttrium, and titanium were similar to those of the welds produced with consumable 0-2 and 0-3. The recoveries of silicon and aluminum are larger due to the presence of these elements in the paste flux. The comparison of the yttrium-to-oxygen ratios are given in Table 34. The yttrium-to-oxygen ratios are within the desired range for improved weld metal characteristics.

Table 32: Top-Bead Chemical Analysis of Welds Produced with the 0-1-D Consumable Using the 3-1 and 3-2 Flux Pastes.

	C (%)	S (%)	Si (%)	Mn (%)	Cu (%)	Cr (%)	Ni (%)	Mo (%)	
3-1	0.04	0.02	0.06	1.20	0.015	0.04	2.84	0.26	
3-2	0.04	0.01	0.12	1.17	0.016	0.05	2.88	0.22	
	V (%)	Al (ppm)	Y (ppm)	Ti (ppm)	O (ppm)	N (%)	Retained H (ppm)	Carbon Equivalent (PCM)	Heat Input (kJ/mm)
3-1	0.005	250	480	210	680	0.11	5.7	0.17	2.4
3-2	0.004	240	490	220	660	0.12	5.3	0.16	2.4

Table 33: Elemental Recoveries of Welds Produced with the 0-1-D Consumable Using the 3-1 and 3-2 Flux Pastes.

Consumable ID	Y/O ratio	Carbon Equivalent (P _{CM})	Heat Input (kJ/mm)	Y	Ti	Al	Si*	Mn	Ni	Mo
3-1	0.71	0.17	2.4	9.1	20.9	44.8	183	52.5	68.5	50.4
3-2	0.74	0.16	2.4	9.3	21.9	43.0	365	51.2	69.5	42.6

* Silicon values present in flux paste blend were not accounted for during the calculation of recovery.

Table 34: Yttrium-to-Oxygen Ratios of the Welds Produced with the 0-1-D Consumable Using the 3-1 and 3-2 Flux Pastes.

Consumable ID	Y (ppm)	O (ppm)	[Y]/[O] ratio
3-1	480	680	0.71
3-2	490	660	0.74

5.3.5 Inclusion Analysis

The results of inclusion characterizations for welds produced with these flux paste consumables, with the exception of chemical composition, are shown in Table 35. These consumables produced welds contained inclusion with larger diameters than those found in the previously studied welds. Paste 3-1 produced welds with a larger volume percent, smaller number density, and similar total surface area when these results are compared to those of other welds. Paste 3-2 produced welds with a similar volume percent, much lower number density, and about half the total surface area. Figure 76 shows representative photomicrographs of the unetched weld samples used in the inclusion characteristics for this part of the study. In these micrographs, the inclusions can still be seen to be predominately spherical in shape and randomly distributed throughout the weld metal.

Since there is an even smaller number density than that found in the analysis reported for the first part of the study, larger prior austenite grains are expected, leading to a fine-grained, acicular ferrite microstructure, which was observed as mentioned above. Furthermore, since the optimal condition to develop a microstructure consisting primarily of acicular ferrite is to have a high density of inclusions with a diameter greater than 0.4 micron and a small density of smaller inclusions randomly distributed throughout the weld metal, which occurs in these welds, the fine-grained, acicular ferrite microstructure was expected.

Table 35: Characteristics of Inclusions Studied in the Welds Produced with the 0-1-D Consumable Using the 3-1 and 3-2 Pastes.

Consumable ID	Volume %	3D Characteristic Diameter (μm)	Density ($10^7/\text{mm}^3$)	Surface Area ($10^7 \mu\text{m}^2/\text{mm}^3$)	[%Y]/[%O] Ratio	Carbon Equivalent (P_{CM})	Heat Input (kJ/mm)
3-1	1.37	0.84	0.56	4.93	0.71	0.17	2.4
3-2	0.70	0.78	0.35	2.67	0.74	0.17	2.4

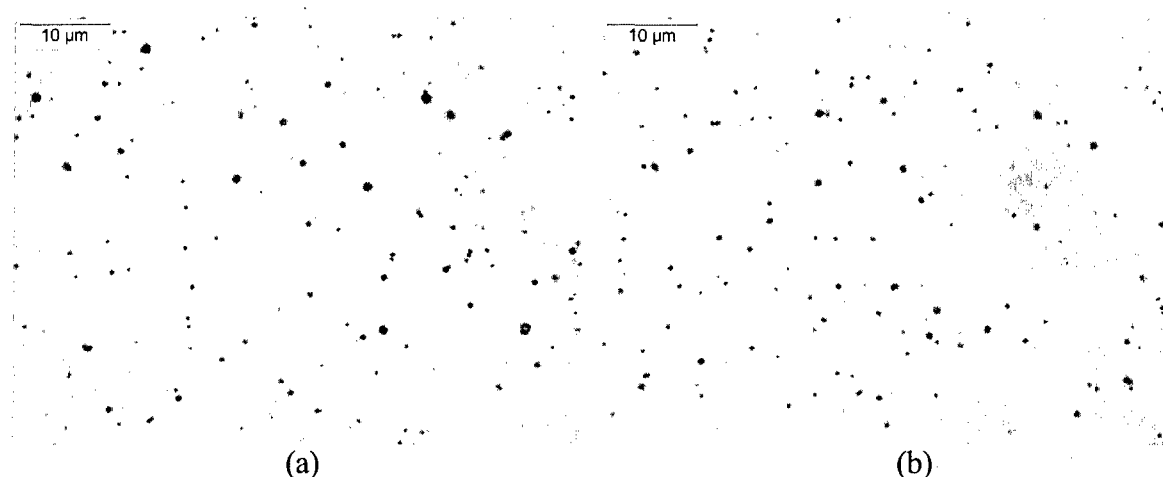


Figure 76: Representative photomicrographs of the unetched weld samples produced with the 0-1-D consumable using the (a) 3-1 and (b) 3-2 flux pastes.

5.4 Summary of Consumables Selected for Further Observation

The consumables that were selected for further observations were the four metal-cored, yttrium-containing consumables, and consumables 1-1-C, 1-2-C, 3-1, and 3-2. These consumables were selected because they produced the most stable arcs during welding, had an yttrium-to-oxygen ratio between 0.4 and 1.3, produced welds consisting of at 45 percent acicular ferrite or more, and had welds with no significant porosity.

There are several ways to compare these welds in terms of microstructure, inclusion development, chemical composition, and element recoveries using the yttrium-to-oxygen ratio, carbon equivalent, and heat input as comparison references. Table 36 compares the microstructural constituents present in the welds produced with the consumables selected for further observations. Figure 77 shows the changes in the microstructures as the yttrium-to-oxygen ratio changes. In this plot, it can be seen that the amount of acicular ferrite present increases with increasing $[\%Y]/[\%O]$ and the amount of the other constituents decrease. Figure 78 shows the variation of each individual

Table 36: Microstructural Constituent Fraction for Welds Produced with Consumables Selected for Further Observations.

Weld ID	KF Additions	Y/O ratio	Carbon Equivalent (P_{CM})	Heat Input (kJ/mm)	PF(G)	FS(A)	FS(NA)	AF	M
Metal-Cored Yttrium Containing Consumables									
0-1-C	0	0.47	0.22	2.4	10	57	4	29	0.3
0-1-D	0	0.52	0.21	2.4	20	14	15	50	1
0-2	0	1.07	0.17	2.4	3	14	8	72	3
0-3	0	0.98	0.16	2.4	8	13	7	67	5
Potassium Fluoride Additions to Yttrium Containing Consumables									
1-1-C	5	0.82	0.19	2.1	9	42	5	44	0.2
1-2-C	10	0.42	0.21	2.0	12	36	7	45	0.4
Flux Paste with Yttrium-Containing Consumable									
3-1		0.71	0.17	2.4	9	16	12	58	5
3-2		0.74	0.17	2.4	7	16	14	57	5

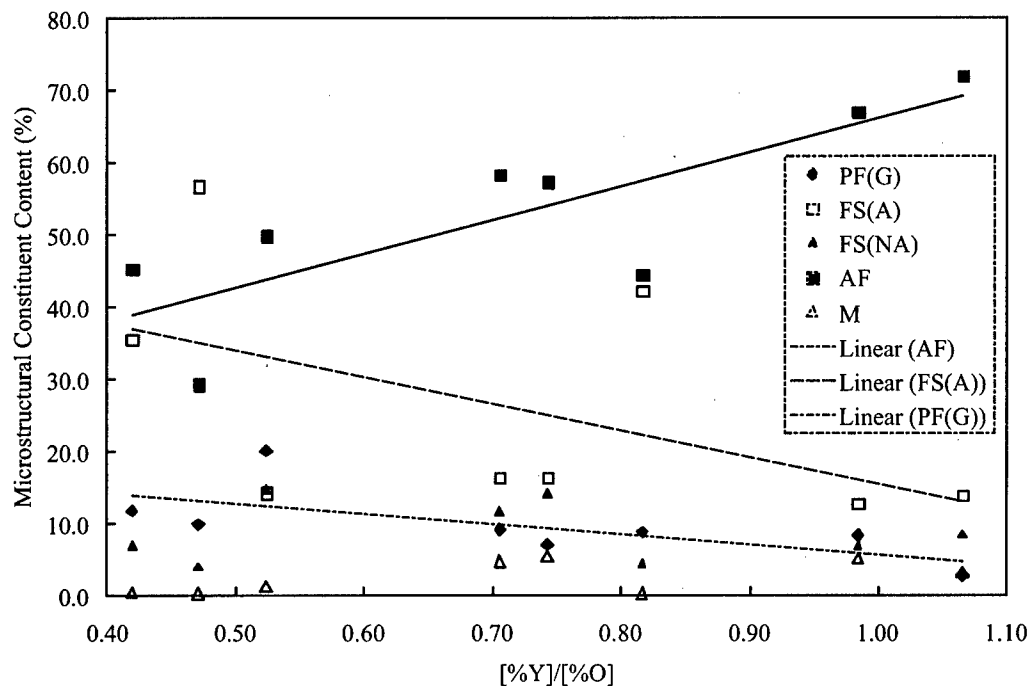


Figure 77: The microstructural constituents of experimental welds, shown as a function of yttrium-to-oxygen ratio.

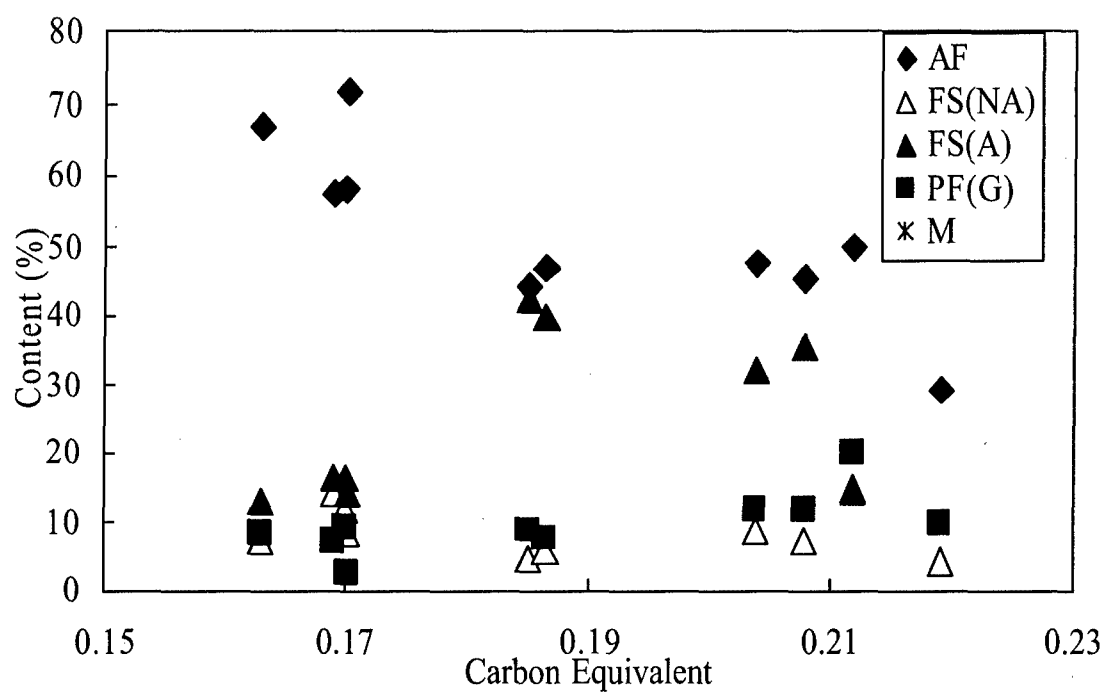


Figure 78: The change in each microstructural constituent with carbon equivalent, where the shaded regions result in poor microstructures. The unshaded region resulted in a high amount of acicular ferrite in the microstructure.

constituent with carbon equivalent. From these figures, it can be seen that the optimal carbon equivalent is between 0.16 and 0.17 weight percent. With CE values between 0.16 and 0.17, the microstructures consist of sixty percent or more acicular ferrite. These results suggest that the welds with CE values between 0.16 and 0.17 weight percent would result in tough weld metals due to the significant amount of acicular ferrite.

In addition to the comparison of microstructures, the top-bead chemical compositions were compared. Table 37 compares the chemical compositions of the welds produced with the selected consumables. Figure 79 compares the elemental recoveries of the alloying elements with the yttrium-to-oxygen ratio of the welds produced with the selected consumables. Within the yttrium-to-oxygen ratios selected, most of the recoveries were consistent, with the exception of yttrium, which should increase as the ratio increases. Figure 80 compares the same recoveries with the carbon equivalent values. As seen with microstructural development, a CE value between 0.16 and 0.17 weight percent resulted in chemical compositions most similar to the target composition. Figure 81 compares the same recoveries as a result of heat input. Higher heat inputs tended to result in higher alloy element recoveries.

Comparisons of the inclusion characteristics were also studied. Table 38 compares the inclusion characteristics of the welds produced with the selected consumables. The most notable results are the increase in the characteristic diameters and the decrease in inclusion density as non-metallic ingredients are added to the welds. The most drastic changes can be seen during the study of the welds produced using the flux-paste blends in association with a metal-cored, yttrium-containing consumable. The increase in inclusion diameter and the decrease in inclusion number density would lead to fewer intragranular nucleation sites and result in a coarser grain structure. The coarser grain structure could limit the potential of improving the mechanical properties of the welds that were produced with the consumables containing fluorides and other flux ingredients.

Table 37: Top-Bead Chemical Analysis of Welds Produced with the Consumables Selected for Further Observations.

	Metal-Cored Yttrium-Containing Consumable				Fluoride Additions to Yttrium-Containing Consumables		Flux Paste with Yttrium-Containing Consumable	
	0-1-C	0-1-D	0-2	0-3	1-1-C	1-2-C	3-1	3-2
C (%)	0.05	0.05	0.05	0.04	0.05	0.05	0.04	0.04
S (%)	0.01	0.01	0.01	0.01	0.01	0.01	0.02	0.01
Si (%)	0.02	0.02	0.02	0.09	0.02	0.02	0.06	0.12
Mn (%)	1.47	1.42	1.14	1.11	1.41	1.40	1.20	1.17
Cu (%)	0.017	0.017	0.017	0.024	0.035	0.006	0.015	0.016
Cr (%)	0.05	0.05	0.05	0.05	0.03	0.03	0.04	0.05
Ni (%)	3.78	3.65	2.55	2.49	2.85	3.70	2.84	2.88
Mo (%)	0.42	0.38	0.24	0.28	0.19	0.35	0.26	0.22
V (%)	0.005	0.005	0.005	0.005	0.004	0.002	0.005	0.004
Al (ppm)	170	170	180	180	120	90	250	240
Y (ppm)	320	330	650	610	800	310	480	490
Ti (ppm)	150	180	280	240	170	60	210	220
O (ppm)	680	630	610	620	980	740	680	660
N (%)	0.11	0.10	0.11	0.10	0.05	0.07	0.11	0.12
Retained H (ppm)	4.2	4.5	5.2	5.2	2.1	2.0	5.7	5.3
Carbon Equivalent (P_{CM})	0.22	0.21	0.17	0.16	0.19	0.21	0.17	0.17
Heat Input (kJ/mm)	2.4	2.4	2.4	2.4	2.1	2.1	2.4	2.4

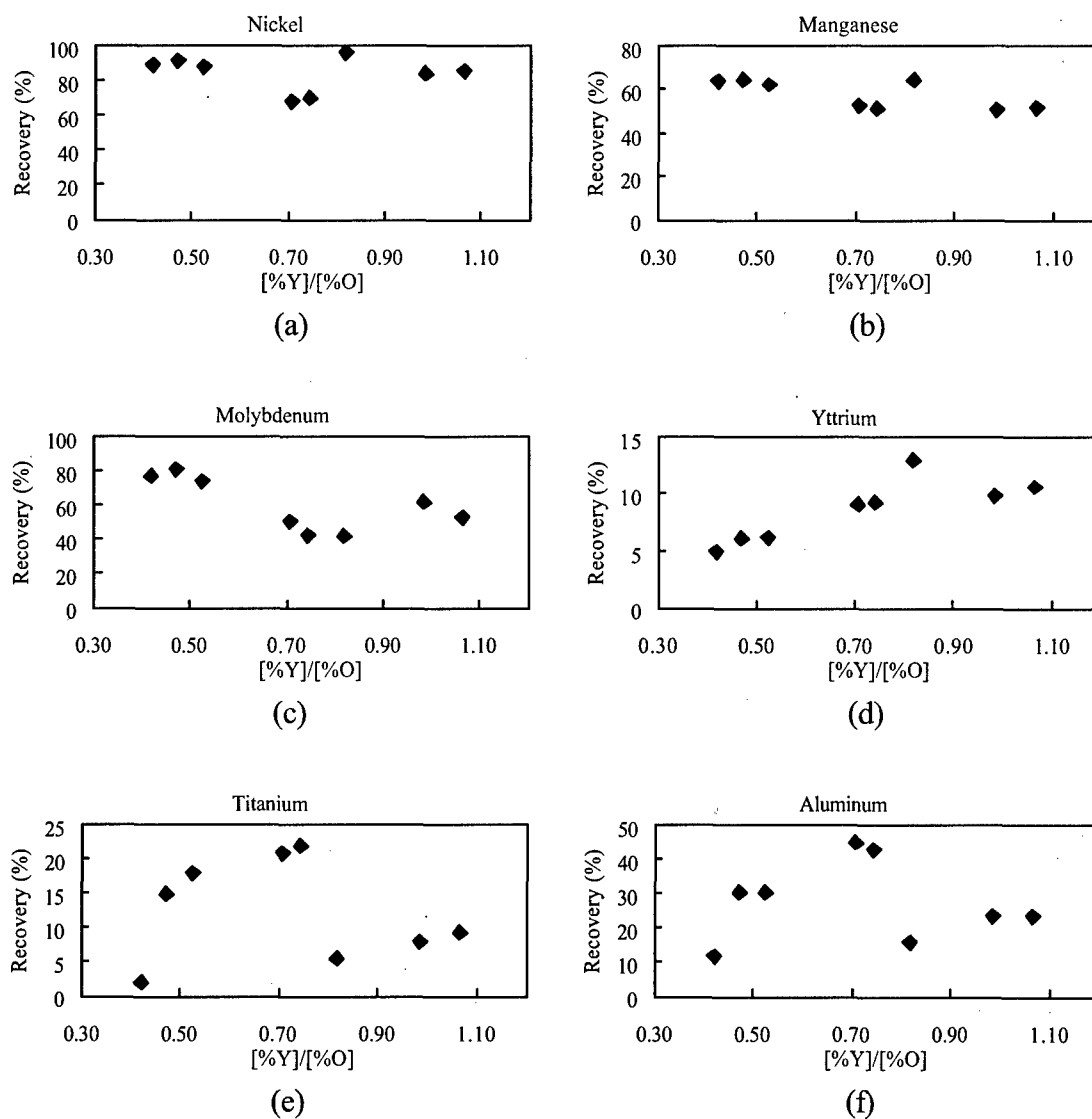


Figure 79: Elemental recoveries compared to the yttrium-to-oxygen ratio for (a) nickel, (b) manganese, (c) molybdenum, (d) yttrium, (e) titanium, and (f) aluminum.

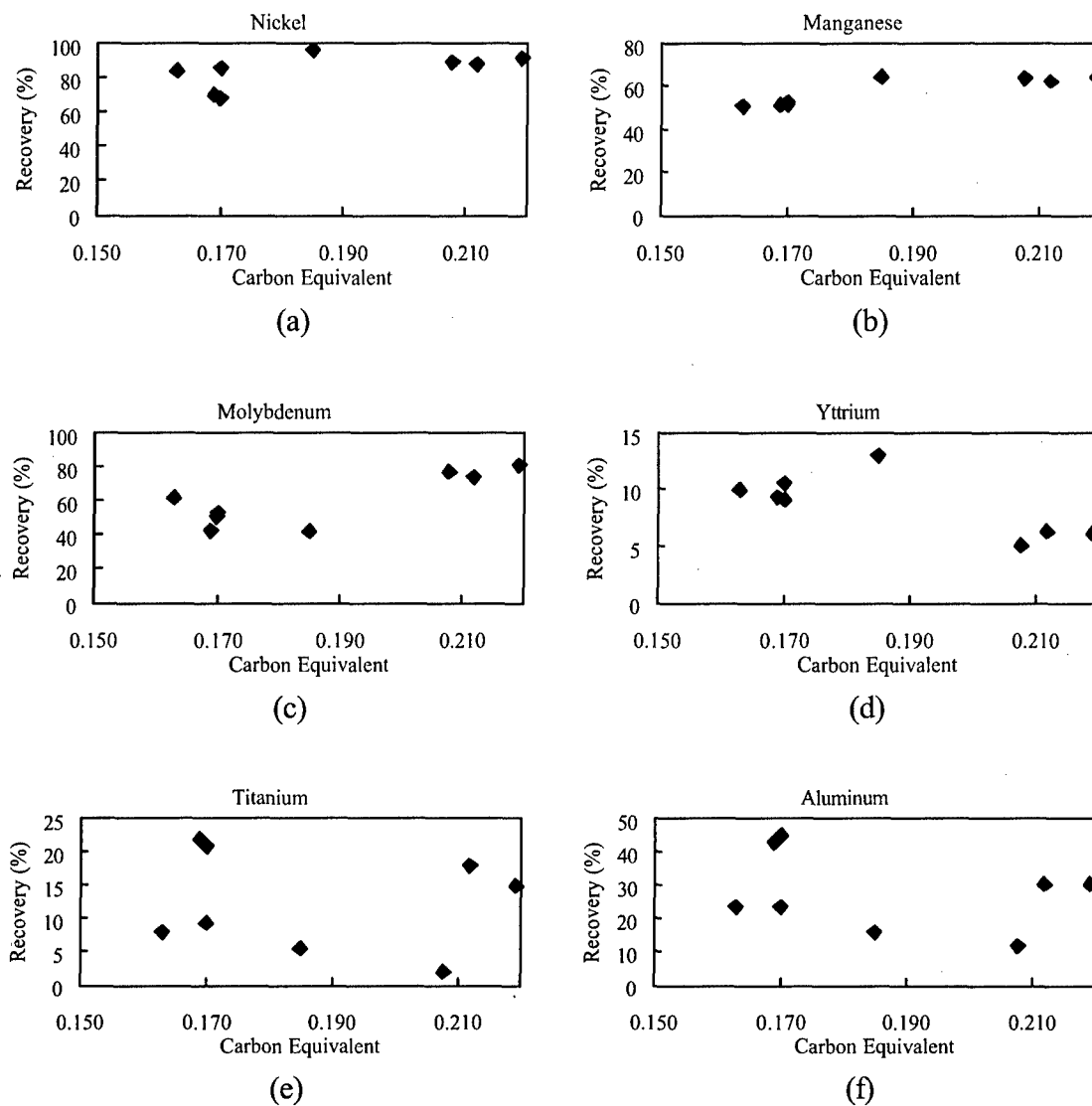


Figure 80: Elemental recoveries compared to carbon equivalent for (a) nickel, (b) manganese, (c) molybdenum, (d) yttrium, (e) titanium, and (f) aluminum.

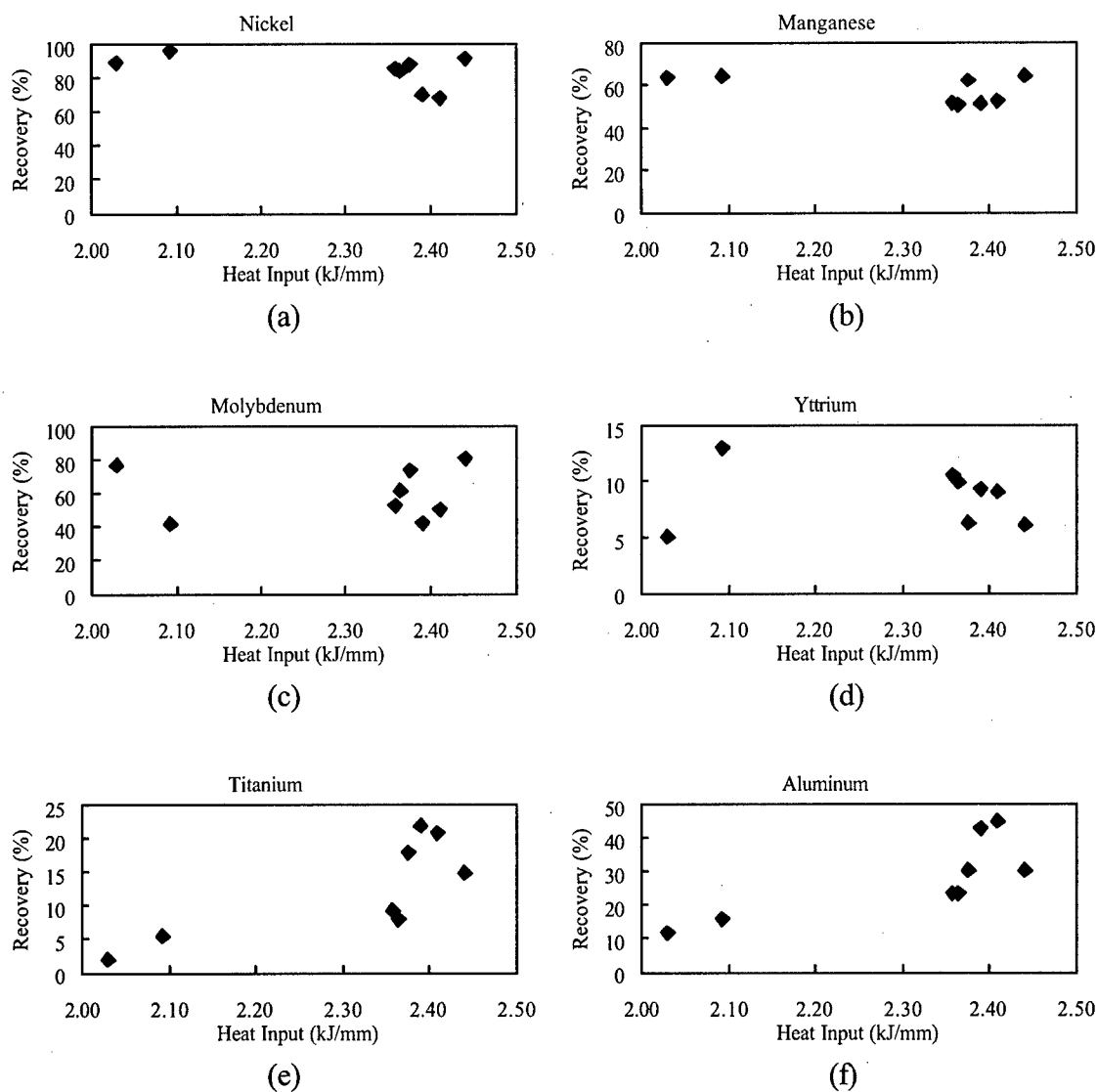


Figure 81: Elemental recoveries compared to heat input for (a) nickel, (b) manganese, (c) molybdenum, (d) yttrium, (e) titanium, and (f) aluminum.

Table 38: Characteristics of Inclusions Studied in Welds Produced with Consumables Selected for Further Study.

ID	Volume %	3D Characteristic Diameter (μm)	Density ($10^7/\text{mm}^3$)	Surface Area ($10^7 \mu\text{m}^2/\text{mm}^3$)	KF Additions (%)	[%Y]/[%O] Ratio	Carbon Equivalent (P_{CM})
Metal-Cored Yttrium Containing Consumables							
0-1-C	0.38	0.37	1.85	3.11	0	0.47	0.22
0-1-D	0.56	0.40	2.13	4.23	0	0.52	0.21
0-2	1.02	0.53	1.68	5.82	0	1.07	0.17
0-3	0.88	0.51	1.58	5.16	0	0.98	0.16
Potassium Fluoride Additions to Yttrium Containing Consumables							
1-1-C	1.12	0.59	1.31	5.70	5	0.82	0.19
1-2-C	1.33	0.60	1.45	6.63	10	0.42	0.21
1-2-D	1.28	0.59	1.43	6.42	10	0.63	0.20
Flux Paste with Yttrium-Containing Consumable							
3-1	1.37	0.84	0.56	4.93	----	0.71	0.17
3-2	0.70	0.78	0.35	2.67	----	0.74	0.17

After comparing the consumables selected for further study (0-1-C, 0-1-D, 0-2, 0-3, 1-1-C, 1-2-C, 3-1, and 3-2) diffusible hydrogen and mechanical properties analyses were performed. The results of these analyses will be discussed in the final two sections of this study.

5.5 Diffusible Hydrogen Measurements

Only a limited number of diffusible hydrogen analyses were performed. The primary purpose was to analyze the effect of potassium fluoride additions in combination with yttrium additions. Diffusible hydrogen tests were performed with consumables 0-1-C, 0-1-D, 0-2, 1-1-C, 1-2-C, 2-1, 3-1, and 3-2. The results are reported in Table 39. Yttrium has been reported to have the potential to reduce diffusible hydrogen to below two milliliters per 100 grams weld metal when in the form of yttria or yttrium oxysulfide

inclusions in the weld metal [4]. For these inclusions to form so that yttrium is most effective, the yttrium-to-oxygen ratio needs to exceed 3.7. At the lower levels of yttrium, the weld deposits are not expected to contain significant amounts of Y_2O_3 or Y_2O_2S , but the inclusions are expected to be primarily yttrium aluminum garnet. It is apparent that when using yttrium to reduce diffusible hydrogen to very low levels, it will be at the expense of weld metal toughness through the loss of effective nucleation sites for acicular ferrite.

Table 39: Diffusible Hydrogen Measurements of the Selected Consumables

	KF Additions	Yttrium Content (ppm)	Y/O Ratio	Diffusible Hydrogen Content (mL/100g weld metal)
0-1-C	0	320	0.47	15.3
0-1-D	0	330	0.52	10.6
0-2	0	650	1.07	16.7
0-3	0	610	0.98	13.2
1-1-D	5	800	0.82	5.2
1-2-D	10	310	0.42	4.2
3-1	2.3**	480	0.71	6.0
3-2	2.2**	490	0.74	6.8
2-1	5	Not Measured	Not Measured	11.8

** KF additions were calculated based on the weight fraction added to the flux paste blend that would be incorporated to the FCAW consumable at a thirty weight percent fill ratio.

Incorporating fluorides, which have been reported to reduce weld metal hydrogen pickup and, thus diffusible hydrogen, it was seen that diffusible hydrogen could be reduced from greater than ten milliliters per 100 grams to around four milliliters per 100 grams with ten percent potassium fluoride additions to the yttrium-containing consumable powder fill. Figure 82 shows this reduction in diffusible hydrogen with the addition of potassium fluoride. In this plot, the diffusible hydrogen contents of welds produced with consumables 3-1 and 3-2 are plotted only in terms of hydrogen content

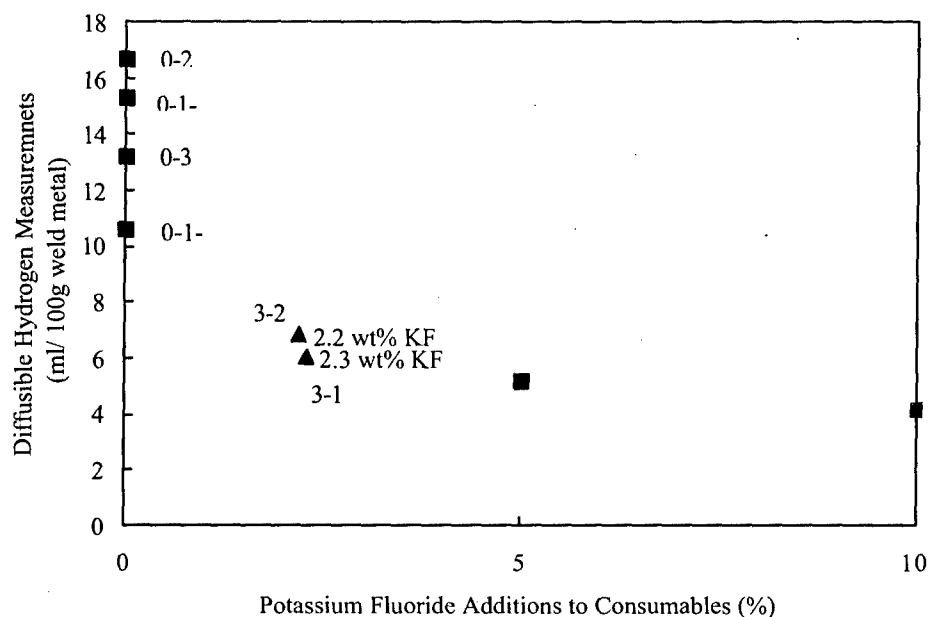


Figure 82: Diffusible hydrogen content shown as a function of potassium fluoride additions present in the consumable powder fill.

and not as a function of KF additions for comparison reasons only. These consumable contain potassium fluoride, but since it is incorporated to the welding process as a paste, the actual KF content is unknown. The results suggest that the ingredients in the flux, KF, CaF_2 , CaO , etc., are effective in further reducing the weld metal diffusible hydrogen content when incorporated with yttrium additions, but not as effective of potassium fluoride additions alone.

5.6 Comparisons of Mechanical Properties

The evaluation of mechanical properties was performed on all of the welds produced with the metal-cored, yttrium-containing consumables, consumable 1-1-C and 1-2-C, and flux-pastes blends 3-1 and 3-2. The specific goal of the study was to develop a

GMAW/FCAW consumable that is capable of producing as-deposited, multiple-pass weld metal with a yield strength in the range of 88 to 115 ksi (607 to 793 MPa), a minimum of twenty percent elongation, and a minimum Charpy V-notch impact toughness of sixty foot-pounds (81 Joules) at 0°F and 35 foot-pounds (48 Joules) at -60°F.

The multiple-pass welds that were produced in this part of the study were sent to a certified non-destructive testing lab for X-ray radiography. The resulting X-ray films were then compared to the welds, and the welds were then marked so that the test specimens were absent of defects when extracted from the welds. All the test specimens for each consumable were extracted from a single multiple-pass weld. A minimum of one sub-size tensile specimen and three full-size CVN samples for each testing temperature were extracted, for a minimum of six. If there was sufficient material, additional CVN samples were extracted for testing at additional temperatures. Microhardness measurements were made across the transverse cross section of each multiple-pass weld so that a hardness profile of each weld was produced.

Table 40 presents the measured values of impact toughness, tensile strengths, elongation, and average hardness for welds produced with each consumable. Figure 83 compares the impact toughness of the welds and how these values compare with the target impact toughness values. It can be seen in the plot that welds produced with consumables 0-2 and 0-3, which both contained fractions of acicular ferrite between 65 and 70 percent, exceeded the minimum required impact toughness values at both of the temperatures. With the exceptions of welds produced with consumables 1-2-C, 3-1 and 3-2, which encountered a large amount of microporosity on the fracture surfaces, weld metals that contained a fraction of acicular ferrite of at least 45 percent were within fifteen percent of the minimum required values. Efimenko [154] reported that the optimal weld metal impact properties occurred when 0.2 to 0.4 weight percent yttrium was present in SMAW electrode coatings. The consumables used in this study contained between 0.5 and 0.65 weight percent yttrium in the powder fill. The increase in yttrium

Table 40: Measured Mechanical Properties of the Selected Consumables

Target	35	47	60	81	88	607			20%		
ID	CVN		CVN		Yield Strength		Tensile Strength		Elon-gation	Average Hardness	
	(-60°F) (ft-lb)	(-51°C) (J)	(0°F) (ft-lb)	(-18°C) (J)	(ksi)	(Mpa)	(ksi)	(Mpa)	(%)	(HV)	
Metal-Cored Yttrium Containing Consumables											
0-1-C	21	29	28	38	78	538	94	648	14.5	285	
0-1-D	31	42	53	72	85	586	103	710	14.5	356	
0-2	41	55	67	90	105	724	120	827	17.2	278	
0-3	37	51	63	85	110	758	129	889	18.0	314	
Potassium Fluoride Additions to Yttrium Containing Consumables											
1-1-C	31	42	52	71	64	441	77	531	13.5	197	
1-2-C	21	29	24	33	----	----	----	----	----	313	*
Flux Paste with Yttrium-Containing Consumable											
3-1	24	32	36	49	----	----	----	----	----	363	*
3-2	25	34	48	65	----	----	----	----	----	343	*

* Encountered large amounts of microporosity in weld metals

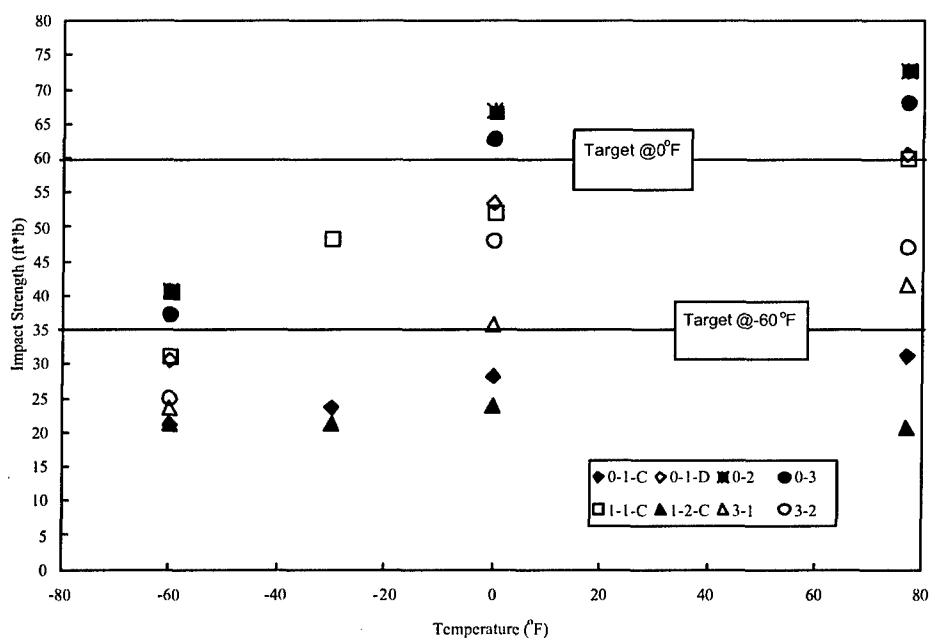


Figure 83: Charpy V-Notch impact toughness results of the selected consumables with the target impact toughness values labeled with the two horizontal lines.

content was necessary due to low weld metal yttrium recovery (less than fifteen percent). Aleksandrov, et al. [166] evaluated the effects of yttrium in the electrode coating, at levels higher than those used by Efimenko, on the microstructure and impact properties, and report that the impact properties were observed to be optimal with 500 ppm yttrium. Inoculating the deposit with yttrium was shown to reduce the grain size and the amount of nonmetallic inclusions, and the inclusion morphology changed from irregular-shaped chains of inclusions to globular shaped uniformly distributed, discrete inclusions. The welds that performed the best in this study, 0-2 and 0-3, contained between 600 and 650 ppm yttrium. Other weld metals tested contained less than 400 ppm or greater than 800 ppm yttrium, suggesting that the optimal range of yttrium is between the 500 ppm reported by Aleksandrov, et al. and the 650 ppm determined in this study.

Figure 84 presents the stress-strain curves for the multiple pass welds that did not contain the large amounts of microporosity experienced during the impact toughness tests and compares them to the minimum desired tensile strength. Again, the welds produced with 0-2 and 0-3 exceeded the minimum strength requirements, with tensile strengths of 105 and 110 ksi, respectively, but all of the weld metals were insufficient in the desired elongation. Figure 85 shows the hardness profiles of the multiple-pass welds produced with the selected consumables. As can be seen in the profiles, the weld metal hardness is greater than that of the A36 base metal in all cases. With the exception of the welds produced with consumable 1-1-C, which revealed an average hardness of about 200 H_v, the microhardness of the welds ranged between 260 and 370 H_v.

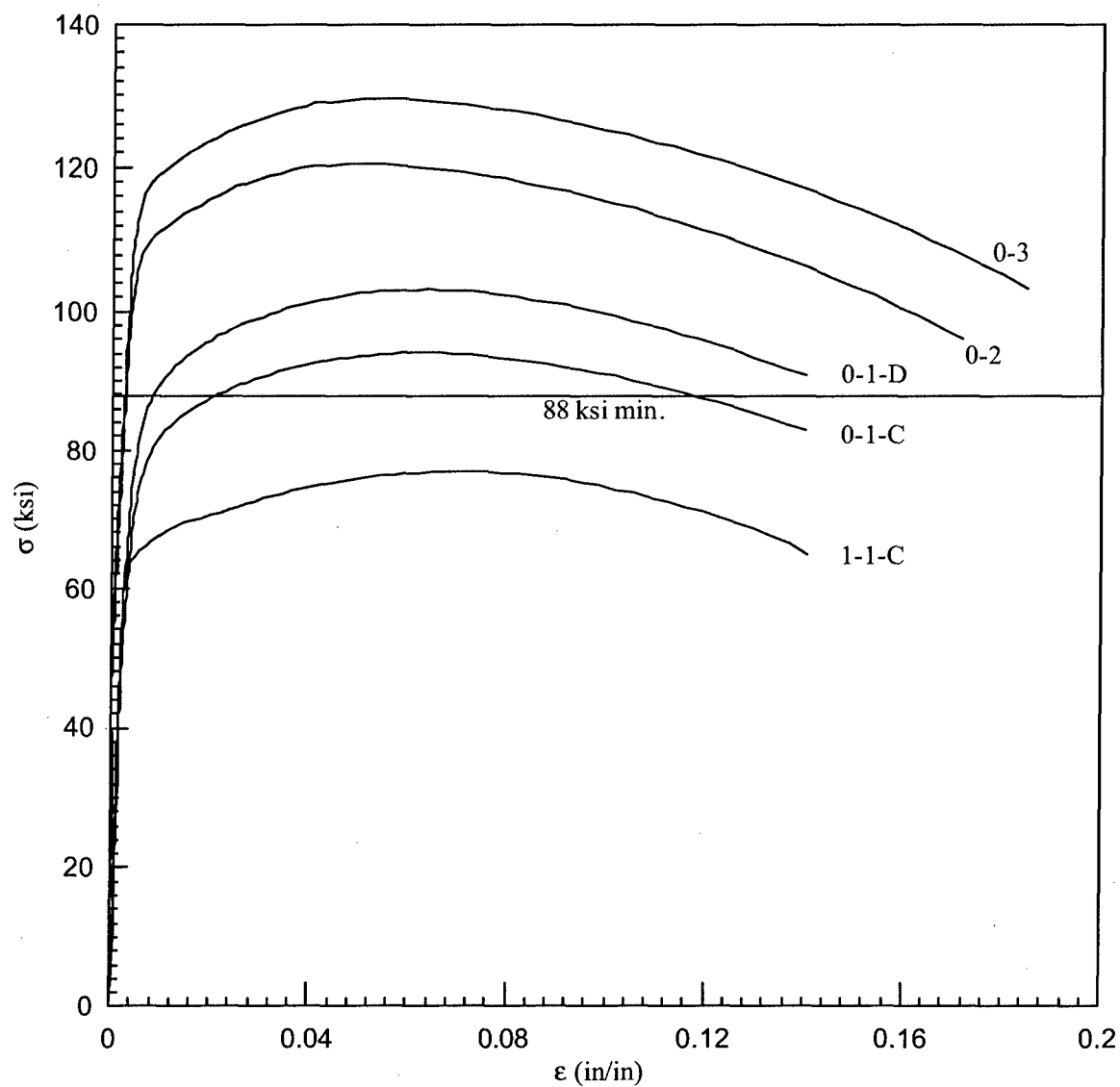
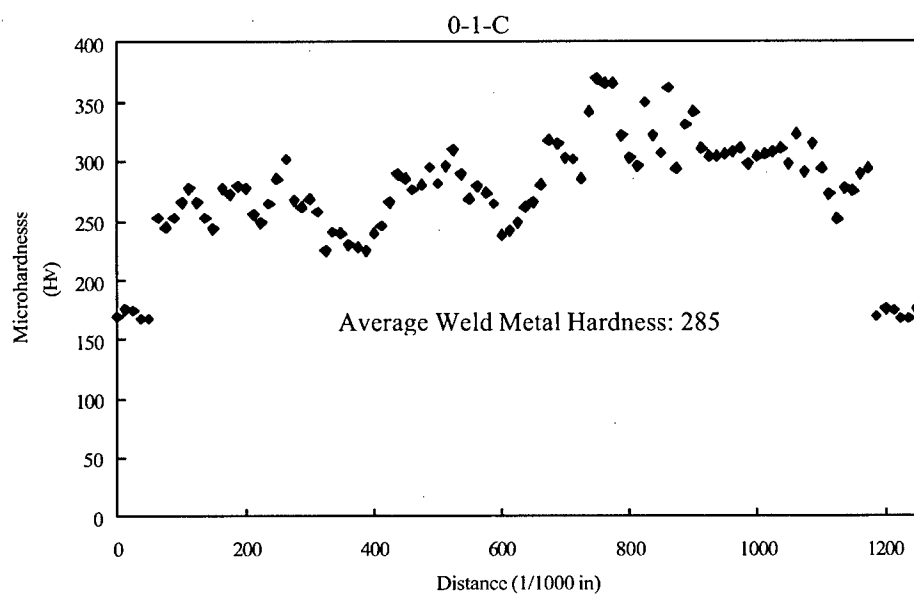
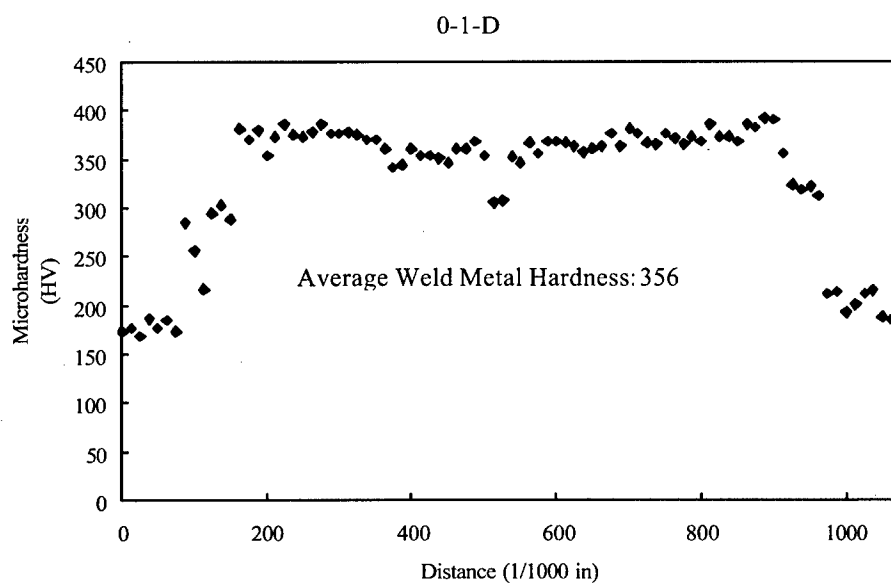


Figure 84: Stress-strain curves of the welds produced with the selected consumables with the target yield strength labeled with the horizontal line.

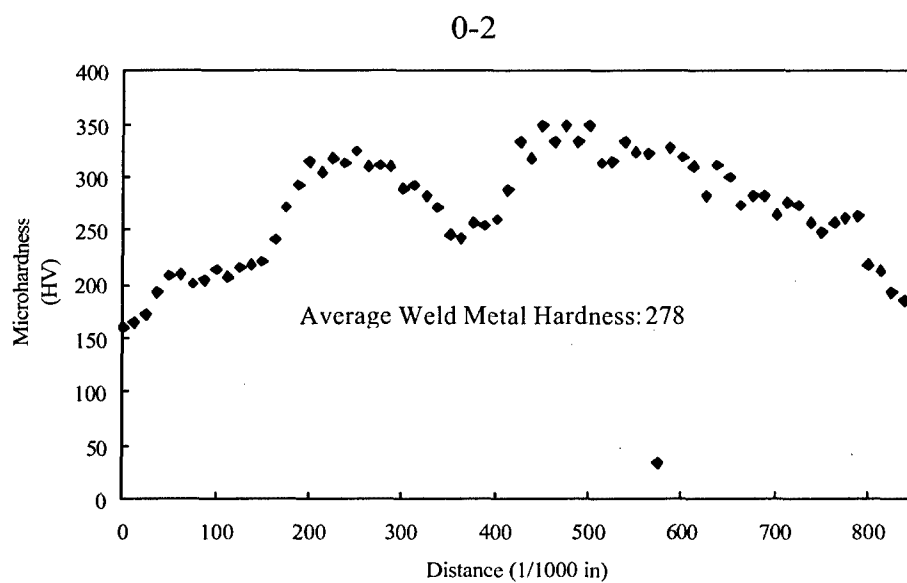


(a)

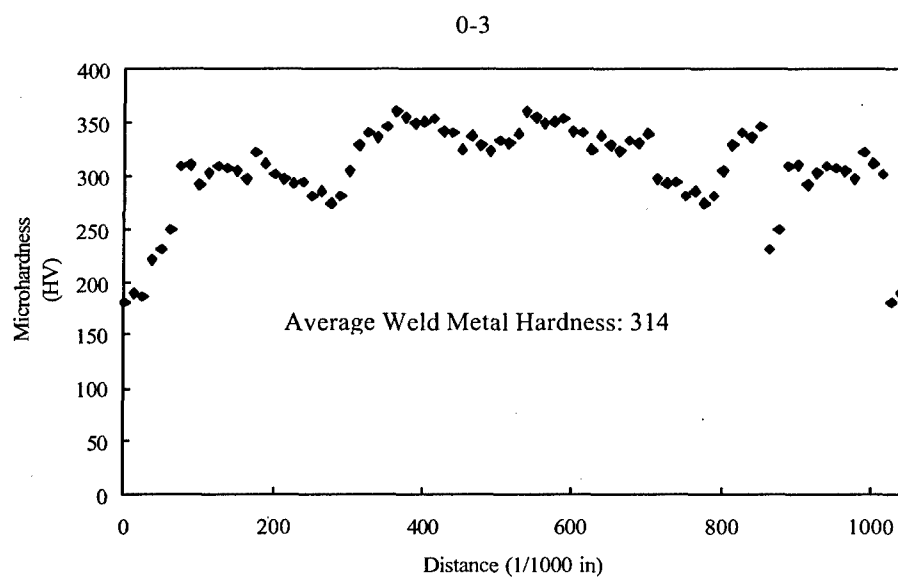


(b)

Figure 85: Hardness profiles of multiple-pass welds produced with consumables (a) 0-1-C, (b) 0-1-D, (c) 0-2, (d) 0-3, (e) 1-1-C, (f) 1-2-C, (g) 3-1, and (h) 3-2.

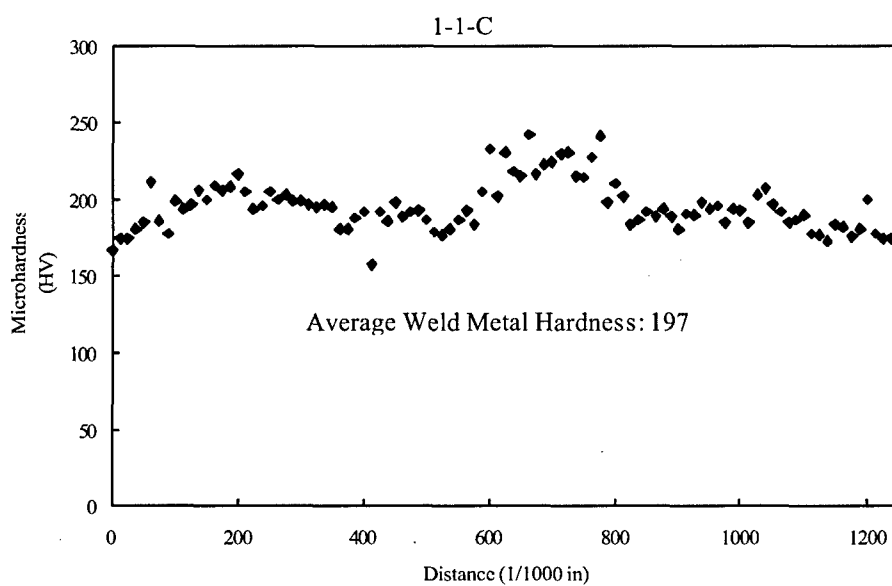


(c)

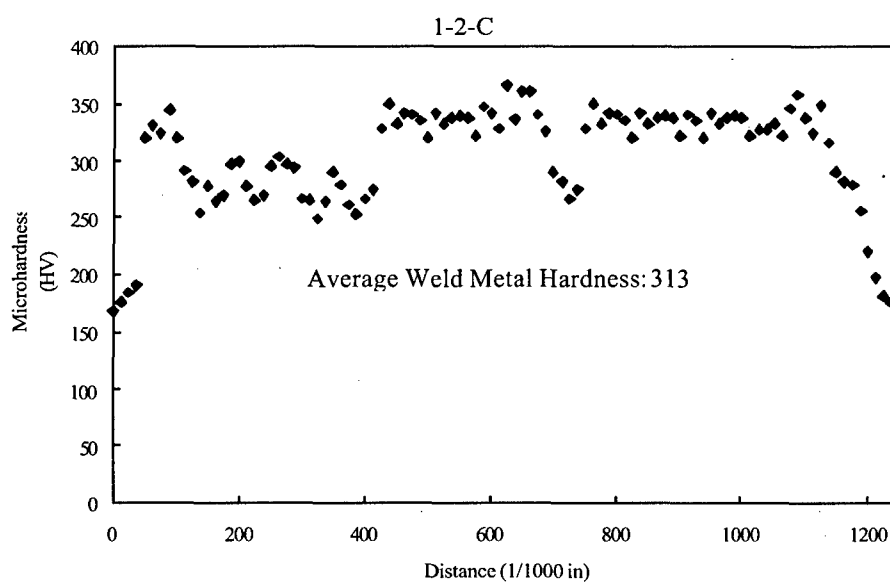


(d)

Figure 85 (cont.): Hardness profiles of multiple-pass welds produced with consumables (a) 0-1-C, (b) 0-1-D, (c) 0-2, (d) 0-3, (e) 1-1-C, (f) 1-2-C, (g) 3-1, and (h) 3-2.

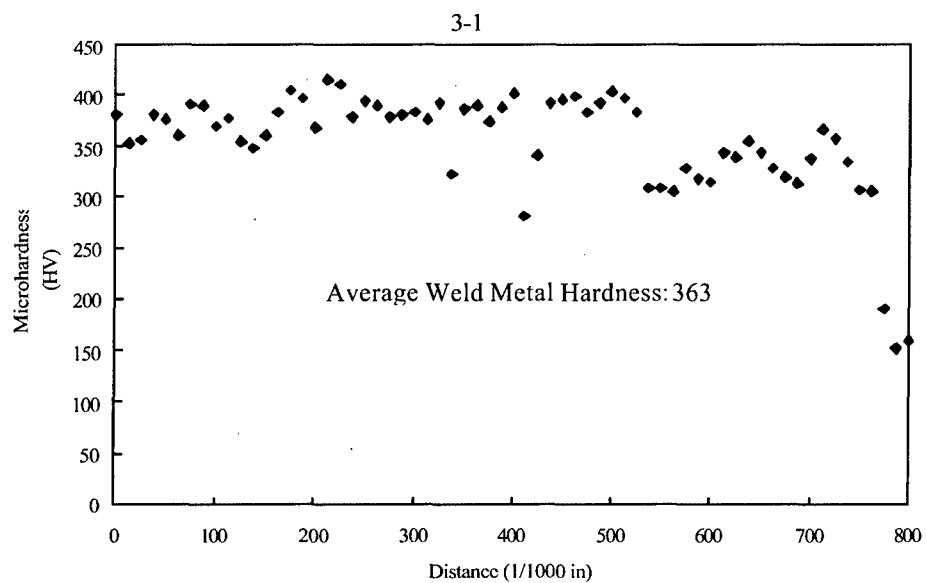


(e)

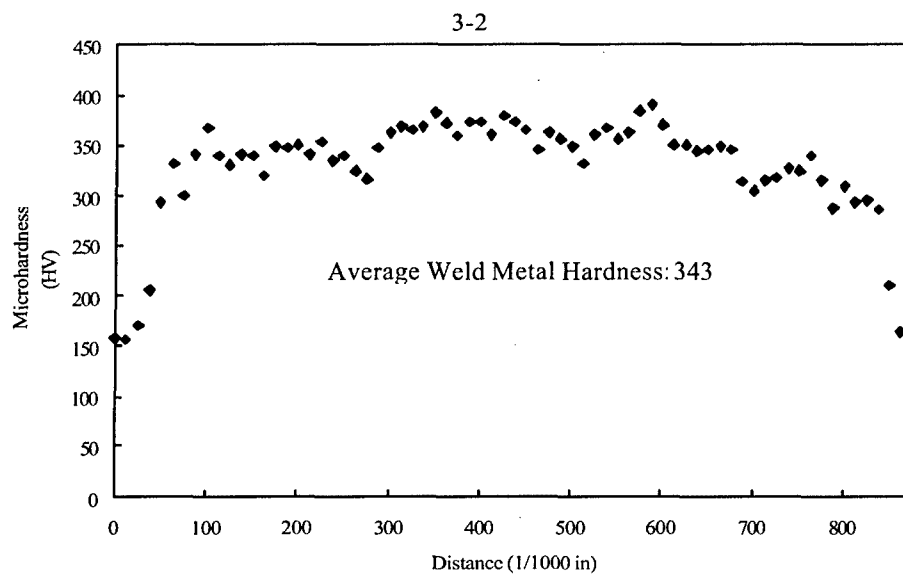


(f)

Figure 85 (cont.): Hardness profiles of multiple-pass welds produced with consumables (a) 0-1-C, (b) 0-1-D, (c) 0-2, (d) 0-3, (e) 1-1-C, (f) 1-2-C, (g) 3-1, and (h) 3-2.



(g)



(h)

Figure 85 (cont.): Hardness profiles of multiple-pass welds produced with consumables (a) 0-1-C, (b) 0-1-D, (c) 0-2, (d) 0-3, (e) 1-1-C, (f) 1-2-C, (g) 3-1, and (h) 3-2.

CHAPTER 6

CONCLUSIONS

1. Both yttrium and potassium fluoride additions reduce molten weld metal fluidity and produce contact angles in excess of sixty degrees, causing difficulty in producing multiple-pass welds. The addition of ferrosilicon improved molten weld metal fluidity, allowing for improved wetting conditions.
2. Potassium fluoride additions are effective in reducing diffusible hydrogen when integrated into an yttrium-containing consumable, but can be detrimental to weld metal properties. Fluorides affected the recovery of potent alloying elements and oxygen potential. The alloying elements and oxygen potential are important for the control of the developing microstructure. The carbon equivalent is a way of determining the effectiveness of the alloying elements, and appears to be optimized when the CE is around 0.17 weight percent. Above or below a CE of 0.17 weight percent, the developing microstructures became coarsened.
3. Potassium fluoride additions of more than 10 weight percent to the consumable powder fill were detrimental to weld metal properties, and were considered to be excessive. These consumables did not produce quality welds. Poor arc stability and inadequate molten weld metal fluidity resulted in porous weld beads with high contact angles.
4. Although the mechanical properties of welds produced with the experimental consumables integrating fluoride and yttrium additions used in this study are lower

than the minimum Navy requirements for welding of steels with strength in excess of 80ksi, these consumables have yet to be optimized.

5. Metal-cored yttrium-containing consumables that produce welds with improved microstructures and improved welding behaviors have been developed. The mechanical properties of these welds were found to exceed the minimum required impact toughness and tensile strengths, but were insufficient in terms of elongation.
6. The consumables evaluated suggest that an addition of 5 weight percent potassium fluoride is the optimal amount. The composition of this consumable requires adjustment to: 1) improve the recovery of potent alloying elements, such as titanium and yttrium, 2) improve the fluidity of the molten weld metal to eliminate porosity, 3) improve bead morphology, 4) further reduce weld metal diffusible hydrogen, and 5) improve weld metal mechanical properties.
7. The incorporation of the additional flux ingredients was also effective in improving weld metal characteristics, but needs to be further studied and adjusted for FCAW consumable manufacturing for the same reasons presented in conclusion six.

CHAPTER 7

RECOMMENDATIONS FOR FUTURE WORK

In the progress of this research, several difficulties were encountered when potassium fluoride was added to the welding consumables. The major cause of the difficulties was the hygroscopicity of the potassium fluoride. Even after extensive preparation of the KF, there were continual opportunities for the pickup of moisture so that it would be present within the consumable. This moisture pickup was particularly noticeable in the two wires that contained KF prepared by Devasco International, 1-1-D and 1-2-D. Due to the potential presence of moisture from the beginning of consumable fabrication, this study suggests that research of additional fluorides, such as manganese MnF_3 and K_3AlF_6 , to yttrium-containing consumables is needed.

In addition to the study of the fluoride additions mentioned above, a fundamental study of the effectiveness of yttrium fluoride, YF_3 , on the reduction of diffusible hydrogen would be valuable. The potential of this fluoride addition is two-fold. First, it will decompose into three fluorine ions in the arc atmosphere, allowing for three possible reactions with hydrogen. Second, it provides for a source of yttrium that is commercially available, unlike ferroyttrium, and this compound is less likely to oxidize during consumable manufacturing. This fluoride would allow for a more consistent wire fabrication; because it is not a hygroscopic compound, and it provides a consistent source to add yttrium to the weld pool.

The ingredients added to the welding process as pastes (3-1 and 3-2) were effective in forming a slag and were not very detrimental to the weld characteristics. These compositions need to be incorporated into a FCAW consumable and studied in a more complete manner.

CHAPTER 8

REFERENCES CITED

1. M. Matsushita and S. Liu, "Hydrogen Control in Steel Weld Metal by Means of Fluoride Additions in Welding Flux," *The Welding Journal*, vol. 79, no. 10, pp. 295s-303s, October, 2000.
2. M. Matsushita, "Clarification of Hydrogen Reduction Mechanisms in Steel Weld Metal by Means of Fluoride Additions in Welding Flux," PhD. Thesis, Colorado School of Mines, Golden, CO, 2001.
3. M. Matsushita and S. Liu, "Plasma Arc Diagnostics to Clarify Hydrogen Reduction Mechanisms Due to Fluoride Addition in Welding Arc," *ASM International Conference on Trends in Welding Research, Pine Mountain, Georgia, April 15-19, 2002*, ASM International, April, 2002.
4. C.A. Lensing, "The Utilization of Yttrium Hydrogen Trap and Welding Parameters in Managing Hydrogen Content in Welding High Strength Low Alloy (HSLA) Steel," PhD Thesis, T-5459, Colorado School of Mines, Golden, CO, 2001.
5. I.S. Maroef, "Fundamental Study of Hydrogen Trapping in Steel Weld Metal," PhD Thesis, T-5274, Colorado School of Mines, Golden, CO, 1999.
6. I.S. Maroef and D.L. Olson, "Fundamental Aspects of Hydrogen Trapping in Steel Weld Metal," *Proceedings from Materials Solutions Conference '99 on Joining of Advanced and Specialty Materials, 1-4 November 1999, Cincinnati, Ohio*, November, 1999.
7. I.S. Maroef and D.L. Olson, "The Effect of Composition and Hydrogen Traps on Hydrogen and Distribution in Steel," *19th ASM Heat Treating Society Conference Proceedings Including Steel Heat Treating in the New Millennium*, 2000.
8. C. Lensing, I. Maroef, and D.L. Olson, "Hydrogen Trapping in Hydrogen Management of Steel Welding," presented at the *78th Annual AWS Convention*, Los Angeles, CA, April 13-17, 1997.
9. M.D. Clark, "The Effects of Yttrium on the Microstructural and Inclusion Development in Low Alloy Steel Weld Metal," PhD Thesis, T-5507, Colorado School of Mines, Golden, CO, 2001.

10. M.D. Clark and G.R. Edwards, "Microstructural and Fractographic Characterization of SMAW Filler Metal for HSLA-100 Steel," presented at the 79th Annual AWS Convention, Detroit, MI, April 26-29, 1998.
11. M.D. Clark and G.R. Edwards, "Inclusion Growth in Yttrium Containing Low Alloy Steel Welds through Liquid Phase Sintering," *ASM International Conference on Trends in Welding Research, Pine Mountain, Georgia, April 15-19, 2002*.
12. M.D. Clark and G.R. Edwards, "Characterization of Weld Metal Oxides in Low Alloy Steel Welds Containing Yttrium," *Proceedings from Joining of Advanced and Specialty Materials, 9-11 October 2000, St. Louis, MO, 2000*.
13. E.J. Czyryca, "Development, Qualification, and Certification of HSLA-80 and HSLA-100 Steels for U.S. Navy Ship Construction," *Proceedings of the International Conference on The Metallurgy, Welding, and Qualification of Microalloyed (HSLA) Steel Weldments*, pp. 553-572, Houston, Texas, November 6-8, 1990.
14. S.S. Tuliani, T. Boniszewski, and N.F. Eaton, "Notch Toughness of Commercial Submerged Arc Weld Metal," *Welding and Metal Fabrication*, vol. 37, p. 327, 1969.
15. T.W. Eagar, "Sources of Weld Metal Oxygen Contamination During Submerged Arc Welding," *The Welding Journal*, pp. 76s-80s, March, 1978.
16. N.N. Potapov and S.A. Kurlanov, "A Quantitative Evaluation of the Basicity of Welding Fluxes," *Welding Production*, vol. 25, no. 9, pp. 39-42, 1978.
17. S. Liu, "Arc Welding Consumables – Covered and Cored Electrodes A Century of Evolution," 5th *International Conference on Trends in Welding Research, Callaway Gardens Resort – Pine Mountain, Georgia, ASM, Materials Park, Ohio*, pp. 1-5, June, 1998.
18. J. Heaschkel, "Weld Metal Property Selection and Control," *The Welding Journal*, vol. 50, pp. 1s-25, 1973.
19. K.E. Dorschu and R.D. Stout, "Some Factors Affecting the Notch Toughness of Steel Weld Metal," *The Welding Journal*, vol. 40, pp. 97s-105s, 1961.
20. A. Enis and R.T. Telford, "Gas Metal Arc Welding of HY-130(T) Steel," *The Welding Journal*, vol. 47, pp. 271s-278s, 1968.
21. J.H. Gross, "The New Development of Steel Weldments," *The Welding Journal*, vol. 47, pp. 241s-270s, 1968.
22. H. Suzuki, "Carbon Equivalent and Maximum Hardness," *IIW Doc. IX-1279-83*, 1983.

23. K.E. Dorschu and S. Lesnewich, "Development of a Filler Material for a High-Toughness Alloy Plate Steel with a Minimum Yield Strength of 140 ksi," *The Welding Journal*, vol. 43, pp. 564s-576s, 1964.
24. E. Surian, J. Trotti, A.N. Casanelli, and L.A. deVedia, "Influence of Mn Content on Mechanical Properties and Microstructure of a High Strength M.M.A. Electrode Weld Wire," *IIW Doc. II-A-724-87*, 1987.
25. D.N. Shakleton, *Welding HY-100 and HY-130 Steels: A Literature Review*, The Welding Institute, Cambridge, England, p. 40, 1973.
26. G.G. Saunders, "Effect of Major Alloying Elements on the Toughness of High Strength Weld Metal," *Welding Research International*, vol. 7, pp. 91-117, 1977.
27. D.J. Abson and R.J. Pargeter, "Factors Influencing As-Deposited Strength, Microstructure, and Toughness of Manual Metal Arc Weld Suitable for C-Mn Steel Fabricators," *International Metals Reviews*, vol. 31, no. 4, pp. 141-194, 1986.
28. A.M. Makara, V.F. Grabin, and V. Denisenko, "Effects of Alloying Elements on the Structure and Properties of Low Alloy Steel Welds," *Avt. Svarka*, vol. 6, pp. 6-11, 1968.
29. P.J. Konkol, A.M. Rathbone, and J.H. Gross, "Development of 170/200 ksi Yield Strength Ni-Cr-Mo-Co Weld Metals for Construction Steels," *The Welding Journal*, vol. 45, pp. 525s-539s, 1966.
30. G. Krauss, *Principles of Heat Treatment of Steel*, ASM International, Metals Park, Ohio, p. 44, 1980.
31. O. Gröng and D.K. Matlock, "Microstructural Developments in Mild and Low Alloy Steel Weld Metals," *International Metals Review*, vol. 31, no. 1, pp. 27-48, 1986.
32. N. Bailey, "Titanium Flux Additions During Submerged Arc Welding of Ferritic Steels," *The Welding Institute Research Report*, No. 221/1983, pp. 1-5, July, 1983.
33. A.H. Koukabi, T.H. North, and H.B. Bell, "Properties of Submerged Arc Deposits - Effects of Zirconium, Vanadium, and Titanium/Boron," *Metal Construction*, vol. 11, pp. 639-644, 1979.
34. N. Mori, H. Homma, S. Okita, and M. Wakabayashi, "Mechanism of Notch Toughness Improvement in Ti-B Bearing Weld Metals," *IIW Doc. IX-1196-81*, 1981.

35. C.W. Ramsay, D.L. Olson, and D.K. Matlock, "The Influence of Inclusions on the Microstructures and Properties of a High Strength Steel Weld," *Conference Proceedings of the Second International Conference on Trends in Welding Research*, ASM-AWS, 1989.
36. A.R. Mills, G. Thewlis, and J.A. Whiteman, "Nature of Inclusions in Steel Weld Metals and Their Influence on Formation of Acicular Ferrite," *Materials Science and Technology*, vol.3, pp 1051-1062, 1987.
37. D.W. Oh, "The Influence of Boron and Titanium on Low Carbon Microalloyed Steel Weld Metal," M.S. Thesis, T-3415, Colorado School of Mines, Golden, CO, 1987.
38. N.A. Fleck, "The Effect of Filler Wire and Flux Compositions on the Microstructure of Microalloyed Steel Weld Metal," M.S. Thesis, T-2923, Colorado School of Mines, Golden, CO, 1984.
39. H. Terashima and P.H.M. Hart, "Effect of Aluminum on C-Mn-Nb Steel Submerged Arc Weld Metal Properties," *The Welding Journal*, vol. 63, pp. 173s-184s, 1984.
40. G.J. Davies and J.G. Garland, "Solidification Structures and Properties of Fusion Welds," *International Metallurgical Reviews*, vol. 20, no. 6, pp. 83-106, 1975.
41. S.A. David and J.M. Vitek, "Correlation Between Solidification Parameters and Weld Microstructures," *International Materials Reviews*, vol. 34, no. 5, pp 213-245, 1989.
42. H. Fredriksson and J. Stjern Dahl, "The Influence of Ferrite to Austenite Transformation on the Formation of Sulfides," *Metallurgical and Materials Transactions A*, vol. 8A, pp. 1107-1115, July, 1977.
43. L.E. Svensson, *Control of Microstructures and Properties in Steel Arc Welds*, CRC Press, Boca Raton, FL, 1994.
44. K.C. Hsieh, S.S. Babu, J.M. Vitek, and S.A. David, "Calculation of Inclusion Formation in Low-Alloy-Steel Welds," *Materials Science and Engineering A, Structural Materials: Properties, Microstructure, and Processing*, A215, pp. 84-91, 1996.
45. A.A.B. Sudgen and H.K.D.H. Bhadeshia, "The Nonuniform Distribution of Inclusions in Low Alloy Steel Weld Deposits," *Metallurgical and Materials Transactions A*, vol. 19A, pp. 669-674, March, 1988.
46. A.O. Kluken, O. Gröng, and G. Rorvick, "Solidification Microstructures and Phase Transformations in Al-Ti-Si-Mn Deoxidized Steel Weld Metals," *Metallurgical and Materials Transactions A*, vol. 21A, pp. 2047-2058, July, 1990.

47. J. Cissé and G.F. Bolling, "A Study of the Trapping and Rejection of Insoluble Particles During Freezing of Water," *Journal of Crystal Growth*, vol. 10, pp 67-76, 1971.
48. G.F. Bolling and J. Cissé, "A Theory for the Interaction of Particles with a Solidifying Front," *Journal of Crystal Growth*, vol. 10, pp 56-66, 1971.
49. J. Cissé and G.F. Bolling, "The Steady State Rejection of Insoluble Particles by a Solid Grown from the Melt," *Journal of Crystal Growth*, vol. 11, pp 25-28, 1971.
50. D.R. Uhlmann, B. Chalmers, and K.A. Jackson, "Interaction Between Particles and a Solid-Liquid Interface," *Journal of Applied Physics*, vol. 35, no. 10, pp. 2986-2993, October, 1964.
51. S.N. Omenyi and A.W. Neumann, "Thermodynamic Aspects of Particle Engulfment by Solidifying Melts," *Journal of Applied Physics*, vol. 47, no. 9, pp. 3956-3962, September, 1976.
52. A.W. Neumann, J. Szekely, and E.J. Rabenda, Jr., "Thermodynamics of Particle Engulfment by Solidifying Melts," *Journal of Colloid and Interface Science*, vol. 43, no. 3, pp. 727-732, June, 1973.
53. J.H. Tweed and J.F. Knott, "Effect of Reheating on Microstructure and Toughness of C-Mn Weld Metal," *Metal Science*, vol. 17, no. 2, pp. 45-54, February, 1983.
54. E.A. Almond, D.H. Timbres, and J.D. Embury, "Influence of Second Phase Particles on Brittle Fracture," *Proceedings of the Second International Conference on Fracture*, pp. 253-264, April, 1969.
55. *Making, Shaping, and Treating of Steel*, 10th ed. (ed. W.T. Lankford, Jr., N.L. Samways, R.F. Craven, and H.E. McGannon), Pittsburgh: United States Steel, 1985.
56. S.S. Babu, S.A. David, J.M. Vitek, K. Mundra, and T. DebRoy, "Development of Macro- and Microstructure of Carbon-Manganese Low Alloy Steel Welds: Inclusion Formation," *Materials Science and Technology*, vol. 11, no. 2, pp. 186-199, 1995.
57. A.O. Kluken and O. Gröng, "Mechanism of Inclusion Formation in Al-Ti-Si-Mn Deoxidized Steel Weld Metals," *Metallurgical and Materials Transactions A*, vol. 20A, pp. 1335-1349, August, 1989.
58. O. Gröng, *Metallurgical Modeling of Welding*, London: Institute of Metals, 1994.
59. M.L. Turpin and J.F. Elliot, "Nucleation of Oxide Inclusions in Iron Melts," *Iron and Steel Institute, London Journal*, pp. 217-225, March, 1966.
60. E. Scheil, *Z. Metallkd*, vol. 34, p. 70, 1942.

61. S.S. Babu, S.A. David, J.M. Vitek, K. Mundra, and T. DebRoy, "Model for Inclusion Formation in Low Alloy Steel Welds," *Science and Technology of Welding and Joining*, vol. 4, no. 5, pp. 276-284, 1999.
62. S.S. Babu, S.A. David, J.M. Vitek, K. Mundra, and T. DebRoy, "Modeling the Formation of Oxide Inclusions in Low-Alloy Steel," *4th International Conference on Trends in Welding Research, Gatlinburg, TN, USA*, pp. 135-140, 1995.
63. J.W. Christian, *Theory of Transformations in Metals and Alloys -Part 1, Equilibrium and General Kinetic Theory*, 2nd ed., Oxford, Pergamon Press, p. 534, 1981.
64. D. Turnbull and J.C. Fisher, "Rate of Nucleation in Condensed Systems," *Journal of Chemical Physics*, vol. 17, no. 1, pp. 71-73, January, 1949.
65. E.T. Turkdogan and C. Edgar, Bain Laboratory for Fundamental Research, United States Steel Corporation Research Centre, Montroeville, PA, pp. 153-170.
66. C. Zener, "Theory of Growth of Spherical Precipitates from Solid Solution," *Journal of Applied Physics*, vol. 20, pp. 950-953, October, 1949.
67. J.C. Ion, K.E. Easterling, and M.F. Ashby, "A Second Report on Diagrams of Microstructure and Hardness for Heat-Affected Zones in Welds," *Acta Metallurgica*, vol. 32, no. 11, pp 1949-1962, 1984.
68. D. Rosenthal, *Transactions of the American Society of Metals*, vol. 68, p. 849, 1946.
69. D.L. Olson, S. Liu, and G.R. Edwards, *Mathematical Modeling of Weld Phenomena*, (ed. H. Cerjak and K. E. Easterling), Institute of Materials, pp. 89-108, 1993.
70. R.H. Frost, D.L. Olson, S. Liu, "International Trends in Welding Science and Technology," (ed. S.A. David and J.M. Vitek), *International Conference Proceedings on Trends in Welding Research*, ASM International, pp. 205-209, 1992.
71. D.J. Widgery, "Deoxidation Practice for Mild Steel Weld Metal," *The Welding Journal*, vol. 55, pp. 57s-68s, 1976.
72. H. Terashima and P.M.H. Hart, "Effect of Residual, Impurity and Microalloying Elements on Weldability and Weld Properties," *Proceedings of the International Conferences*, London, The Welding Institute, Paper 27, November, 1983.
73. S.S. Babu, S.A. David, and T. DebRoy, "Inclusion Formation in Low-Alloy Steel Welds," *Proceedings of the International Conference on Trends in Welding Research*, Pine Mountain, Georgia, 1-5 June 1999, ASM International, pp. 179, 1999.

74. T. Hong, W. Pitscheneder, and T. DebRoy, "Quantitative Modeling of Motion, Temperature Gyration, and Growth of Inclusions in Weld Pool," *Science and Technology of Welding and Joining*, vol. 3, no. 1, pp 33-41, 1998.
75. S.S. Babu, S.A. David, and T. DebRoy, "Coarsening of Oxide Inclusions in Low Alloy Steels Welds," *Science and Technology of Welding and Joining*, vol. 1, no. 1, pp. 17-27, 1996.
76. U. Lindborg and K. Torssell, "A Collision Model for the Growth and Separation of Deoxidation Products," *Transactions of the Metallurgical Society of AIME*, vol. 242, pp. 94-102, January, 1968.
77. R.K. Iyengar and W.O. Philbrook, "A Mathematical Model to Predict the Growth and Elimination of Inclusions in Liquid Steel Stirred by Natural Convection," *Metallurgical and Materials Transactions*, vol. 3, pp. 1823-1830, July, 1972.
78. *Guide to the Light Microscope Examination of Ferritic Steel Weld Metals*, IIW Doc. No. IX-1533-38, IXJ-123-87, rev. 2, June, 1988.
79. T. Kojima, N. Yurioka, T. Kasuya, and C. Shiga, IX 1865-97, Round Robin Test Results in "HAZ Microstructure."
80. O. Gröng and A.O. Kluken, "Microstructure and Properties of Steel Weld Metals," *Key Engineering Materials*, vols. 69 & 70, pp. 21-46, 1992.
81. G. Thewis, "Transformation Kinetics of Ferrous Weld Metals," *Materials Science and Technology*, vol. 10, no. 2, pp. 110-125, February, 1994.
82. R.C. Cochrane, "Weld Metal Microstructures – A State-of-the-Art Review," *Welding in the World*, vol. 21, nos. 1-2, pp. 16-24, 1983.
83. H.K.D.H. Bhadeshia and L.E. Svensson, *Mathematical Modeling of Weld Phenomena* (ed. H. Cerjak and K.E. Easterling), Institute of Materials, pp. 109-180, 1993.
84. P.R. Howell, P.A. Ricks, and R.W.K. Honeycombe, "The Observation of Interphase Precipitation in Association with the Lateral Growth of Widmanstätten Ferrite," *Journal of Materials Science*, vol. 15, pp. 376-380, 1980.
85. H.K.D.H. Bhadeshia and J.W. Christian, "Bainite in Steels," *Metallurgical and Materials Transactions A*, vol. 21A, pp. 767-797, April, 1990.
86. J.R. Yang and H.K.D.H. Bhadeshia, "The Dislocation Density of Acicular Ferrite in Steel Welds," *The Welding Journal*, vol. 69, pp. 305s-307s, 1990.
87. R.A. Farrar and P.L. Harrison, "Acicular Ferrite in Carbon-Manganese Weld Metals: An Overview," *Journal of Materials Science*, vol. 22, no. 11, pp. 3812-3820, 1987.

88. H.K.D.H. Bhadeshia, "International Trends in Welding Science and Technology," (ed. S.A. David and J.M. Vitek), *International Conference Proceedings on Trends in Welding Research*, ASM International, pp. 213-222, 1992.
89. R.A. Ricks, P.R. Howell, and G.S. Barritte, "The Nature of Acicular Ferrite in HSLA Steel Weld Metals," *Journal of Materials Science*, vol. 17, no. 3, pp. 732-740, 1982.
90. A.O. Kluken, O. Gröng, and J. Hjelen, "The Origin of Transformation Textures in Steel Weld Metals Containing Acicular Ferrite," *Metallurgical and Materials Transactions A*, vol. 22A, pp. 657-663, March, 1991.
91. S.A. Court and G. Pollard, "The Development of Microstructure in C-Mn Steel Weld Deposits," *Conference: Welding Metallurgy of Structural Steels*, Denver, Colorado, USA, 22-26 February 1987, Metallurgical Society /AIME, pp. 505-516, 1987.
92. H.I. Aaronson and C. Wells, "Sympathetic Nucleation of Ferrite," *Journal of Metals*, Transactions AIME, pp. 1216-1223, October, 1956.
93. H.I. Aaronson, G. Spanos, R.A. Masamura, R.G. Vardiman, D.W. Moon, E.S.K. Menon, and M.G. Hall, "Sympathetic Nucleation: An Overview," *Materials Science and Engineering B, Solid State Materials for Advanced Technology*, B32, pp. 107-123, 1995.
94. C.B. Dallum and D.L. Olson, "Stress and Grain Size Effects on Weld Metal Ferrite Formation," *Welding Journal*, vol. 68, no. 5, pp. 198s-205s, 1989.
95. S. Liu, "The Role of Non-Metallic Inclusions in Controlling Weld Metal Microstructures in Niobium Microalloyed Steels," Ph.D. Thesis, T-2923, Colorado School of Mines, Golden, CO, 1984.
96. M. Ferrante and R.A. Farrar, "The Role of Oxygen-Rich Inclusions in Determining the Microstructure of Weld Metal Deposits," *Journal of Materials Science*, vol. 17, no. 11, pp. 3293-3298, 1982.
97. S. Liu and D.L. Olson, "The Role of Inclusions in Controlling Steel Weld Microstructures," *The Welding Journal*, vol. 65, no. 6, pp. 139s-149s, 1986.
98. D. Turnbull and R. Vonnegut, "Nucleation Catalysis," *Industrial and Engineering Chemistry*, vol. 44, p. 1292, 1952.
99. B.L. Bramfit, "The Effect of Carbide and Nitride Additions on the Heterogeneous Nucleation Behavior of Liquid Iron," *Metallurgical and Materials Transactions*, vol. 1, pp. 1987-1995, July, 1970.

100. B.R. Keville, "Preliminary Observations of the Type, Shape, and Distribution of Inclusions Found in Submerged Arc Weldments," *The Welding Journal*, vol. 62, no. 9, pp. 253s-260s, 1983.
101. J.M. Dowling, J.M. Corbett, and H.W. Kerr, "Inclusion Phases and Nucleation of Acicular Ferrite in Submerged Arc Welds in High Strength Low Alloy Steels," *Metallurgical and Materials Transactions A*, vol. 17A, pp. 1611-1623, September, 1986.
102. Z. Zhang and R.A. Farrar, "Role of Non-Metallic Inclusions in Formation of Acicular Ferrite in Low Alloy Weld Metals," *Materials Science and Technology*, vol. 12, no. 3, pp. 237-260, March, 1996.
103. S.A. Court and G. Pollard, "Microanalysis of Weld Metal Inclusions," *Journal of Materials Science Letters*, vol. 4, no. 5, pp. 427-430, 1985.
104. S.A. Court and G. Pollard, "Inclusion Chemistry and Morphology in Shielded Metal Arc (SMA) Steel Weld Deposits," *Metallography*, vol. 22, no. 3, pp. 219-243, 1989.
105. Y. Ito and M. Nakanishi, "Study of Charpy Impact Properties of Weld Metal with Submerged Arc Welding," *Sumitomo Search*, no. 15, pp. 42-62, May, 1976.
106. G. Thewlis, "Pipeline Welds – Effects of Pipe Material and Consumables Composition. Part 1: Experimental Investigation and Results. Part 2: Discussion and Conclusions.," *Joining & Materials*, vol. 2, no. 1, pp. 125-129, 1989.
107. S. St. Laurent and G. L'Esperance, "Effects of Chemistry, Density, and Size Distribution of Inclusions on the Nucleation of Acicular Ferrite of C-Mn Shielded-Metal-Arc Welding Weldments," *Materials Science and Engineering A, Structural Materials: Properties, Microstructure, and Processing*, A149, pp. 203-216, 1992.
108. T. Kosecki, S. Ohkita, and N. Yurioka, "Thermodynamic Study of Inclusion Formation in Low Alloy Steel Weld Metals," *Science and Technology of Welding and Joining*, vol. 2, no. 2, pp. 65-69, 1997.
109. C. Blais, G. L'Esperance, and G.M. Evans, "Characterisation of Inclusions Found in C-Mn Steel Welds Containing Titanium," *Science and Technology of Welding and Joining*, vol. 4, no. 3, pp. 143-150, 1999.
110. J.M. Gregg and H.K.D.H. Bhadeshia, "Bainite Nucleation from Mineral Surfaces," *Acta Metallurgica et Materialia*, vol. 42, no. 10, pp. 3321-3330, 1994.
111. J.M. Gregg and H.K.D.H. Bhadeshia, "Titanium-Rich Mineral Phases and the Nucleation of Bainite," *Metallurgical and Materials Transactions A*, vol. 25A, pp. 1603-1611, 1994.

112. J.M. Gregg and H.K.D.H. Bhadeshia, "Solid State Nucleation of Acicular Ferrite on Minerals Added to Molten Steel," *Acta Materialia*, vol. 45, pp. 739-748, 1997.
113. H. Homma, S. Ohkita, S. Matsuda, and K. Yamamoto, "Improvement of HAZ Toughness in HSLA Steel by Introducing Finely Dispersed Ti-Oxide," *The Welding Journal*, pp. 301s-309s, October, 1987.
114. J.H. Shim, Y.W. Cho, S.H. Chung, J.D. Shim, and D.N. Lee, "Nucleation of Intragranular Ferrite at Ti_2O_3 Particle in Low Carbon Steel," *Acta Materialia*, vol. 47, no. 9, pp. 2751-2760, 1999.
115. H. Mabuchi, R. Uemori, and M. Fujioka, "The Role of Mn Depletion in Intra-Granular Ferrite Transformation in the Heat-Affected Zone of Welded Joints with Large Heat Input in Structural Steels," *ISIJ International*, vol. 36, no. 11, pp. 1406-1412, 1996.
116. N.P. Allen, W.P. Rees, B.E. Hopkins, and H.R. Tipler, "Tensile and Impact Properties of High-Purity Iron-Carbon and Iron-Carbon-Manganese Alloys of Low Carbon Content," *Iron and Steel Institute, London Journal*, vol. 174, p. 108, 1953.
117. C.J. McMahon, Jr. and M. Cohen, "Initiation of Cleavage in Polycrystalline Iron," *Acta Metallurgica*, vol. 13, p. 591, 1965.
118. J.H. Tweed and J.F. Knott, "Micromechanisms of Failure in C-Mn Weld Metals," *Acta Metallurgica*, vol. 35, p. 1401, 1987.
119. R.K. Hughes and J.C. Ritter, "Cleavage Fracture Properties of High Strength Steel Weldments," *Proceedings of the 4th International Conference on Trends in Welding, 5-8 June, 1995, Gatlinburg, TN, 1995*.
120. L.L.J. Chin, "A Model for Toughness Studies of Welds," *The Welding Journal*, vol. 48, no. 7, p. 290s, 1969.
121. R.H. Van Stone, T.B. Cox, J.R. Low, Jr, and J.A. Psioda, "Microstructural Aspects of Fracture by Dimpled Rupture," *International Metallurgical Review*, vol. 30, p. 157, 1985.
122. R.E. Dolby, "Factors Controlling Weld Toughness-The Present Position, Part 2-Weld Metals: Research Report 14/1976/M," TWI, Abington, May 1976.
123. A.H. Cottrell, "Theory of Brittle Fracture in Steel and Similar Metals," *Transactions of the Metallurgical Society of the AIME*, p. 192, 1958.
124. J.F. Knott, *The Effect of Second-Phase Particles on the Mechanical Properties of Steel*, *Conference Proceedings of the Iron and Steel Institute*, p. 44, March, 1977.

125. J.L. Davidson and S.P. Lynch, "Hydrogen Management for Welding Applications," *Proceedings of the International Workshop, October 6-8, 1998, Ottawa, Ontario, Canada*, (ed. J.E.M. Braid, C.V. Hyatt, D.L. Olson, and G.N. Vigilante), pp. 9-36, 1998.
126. *Welding Steels without Hydrogen Cracking*, 2nd Edition, ed. N. Nailey, F.R. Coe, T.G. Gooch, P.H.M. Hart, N.Jenkins, and R.J. Pargeter, ASM International, The Materials Information Society.
127. N. Yurioka and H. Suzuki, "Hydrogen Assisted Cracking in C-Mn and Low Alloy Steel Weldments," *International Materials Reviews*, vol. 35, no. 4, pp. 217-249, 1990.
128. C.D. Beachem, "A New Model for Hydrogen-Assisted Cracking (Hydrogen 'Embrittlement')," *Metallurgical Transactions*, 1972, vol. 3, pp. 437-451.
129. R. Vasudevan, R.D. Stout, and A.W. Pense, "Hydrogen-Assisted Cracking in HSLA Pipeline Steel," *The Welding Journal*, vol. 60, no. 9, 155s-168s, September, 1981.
130. T. Godai and M. Sugino, "The Hydrogen Sources in Covered Arc Welding," *The Welding Journal of Japan*, vol. 45, pp. 14-20, 1976.
131. G. Dickehut and U. Hotz, "The Effect of Atmospheric Condition on Weld Metal Diffusible Hydrogen Content," IIW – Commission II (Arc Welding), Subcommittee A (The Metallurgy of Weld Metal), II-A-764-89.
132. R.V. Gaines, H.C.W. Skinner, E.E. Foord, B. Mason, and A. Rosenzweig, *Dana's New Mineralogy*, 8th Edition, John Wiley & Sons Inc., 1997.
133. K. S. Johnson, "Diffusible Hydrogen Control and Microstructure Refinement in FCA Welds Performed over Primer-Coated Steels," Graduate Thesis, T-5098, 1998.
134. H. Terashima and J. Tsuboi, "Hydrogen in Submerged Arc Weld Metal Produced with Agglomerated Flux," *Welding Journal of Japan*, 45, 28-33, 1976.
135. N. DeRissone, I. Bolt, J. Jorge, P. Corvalan, and E. Surian, "ANSI/AWS A5.1-91 E6013 Rutile Electrodes: The effect of Wollastonite," *The Welding Journal*, vol. 76, no. 11, pp. 498s-507s, 1997.
136. S. Liu, D.L. Olson, and S. Ibarra, "Underwater Welding," *Welding, Brazing, and Soldering – ASM Handbook*, vol. 6, 9th Edition, pp. 1010-1015, Materials Park, Ohio, 1993.
137. A. Sanchez-Osio, S. Liu, D.L. Olson, "The Effect of Solidification on the Formation and Growth of Inclusions in Low Carbon Steel Welds," *Materials Science and Engineering*, pp. 122-133, 1996.

138. L. Reeve, "The Relation between the Hydrogen Content of Weld Metal and its Oxygen Content," *The Journal of the Iron and Steel Institute*, ccII, vol. II, pp. 385-396, 1945.
139. T.G. Gooch, "Properties of Underwater Welds, Part 1 – Procedural Trials," *Metal Construction*, pp. 164-167, March, 1983.
140. T.G. Gooch, "Properties of Underwater Welds, Part 1 – Procedural Trials," *Metal Construction*, pp. 206-216, April, 1983.
141. A. Pope and S. Liu, "Hydrogen Content of Underwater Wet Welds Deposited by Rutile and Oxidizing Electrodes," *OMAE – Vol. III, Materials Engineering*, ASME, 1996.
142. I. Maroef, C. Lensing, and D.L. Olson, "Evaluation of Hydrogen Trapping for Hydrogen Management in Ferrous Alloy Welding," presented at the 79th Annual AWS Convention, Detroit, MI, April 25-31, 1998.
143. J. Tsuboi, S. Nakano and K. Sato, "The Behavior of Hydrogen in Arc Welding," *The Welding Journal of Japan*, 42-3, 189-201, 1973.
144. J. Tsuboi and S. Nishiuma, "The Behavior of Hydrogen in Arc Welding (Report 2)," *The Welding Journal of Japan*, 42-4, 324-332, 1973.
145. J. Tsuboi, Y. Hirai and T. Hiro, "The Behavior of Hydrogen in Arc Welding (Report 3)," *The Welding Journal of Japan*, 42-5, 477-489, 1973.
146. D. McKeown, "Hydrogen and Its Control in Weld Metal," *Metal Construction*, V.17 pp.655-661, October, 1985.
147. I. K. Pokhodnya, "Hydrogen Behavior in Welded Joints," E. O. Paton Electric Welding Institute, National Academy of Sciences of Ukraine, Ukraine, Kiev, 1996.
148. A.H. Daane, Rare Metals Handbook, Chapter 33, 653-665, Wiley, New York, 1961.
149. C.E. Curtis, "Properties of Yttrium Oxide Ceramics," *Journal of the American Ceramic Society*, vol. 40, no. 8, pp. 274-278, August, 1957.
150. L. Li, Z. Xing, B. Zhao, "Solid Solubility of Ce, Nd, and Y in α -Fe at Room Temperature," *Transaction of Non-Ferrous Metals Society of China*, vol. 3, no. 3, pp. 48-51, August, 1993.
151. J.A. Gibson, J.F. Miller, P.S. Kennedy, and G.W.P. Rengstorff, Battelle Memorial Institute, Columbus, OH, May, 1959.
152. R.P. Elliot, *Constitution of Binary Alloys, First Supplement*, New York, McGraw Hill, 1965.

153. G.T. Adylov, G.V. Voronov, E.P. Mansurova, L.M. Sigalov, and E.M. Urazaeva, *Zh. Neorg. Khim*, vol. 33, no. 7, pp. 1867-1869, 1988. (English Translation) *Journal of Inorganic Chemistry*, vol. 33, no. 7, pp. 1062-1063, 1988.
154. D. Wing and W. Longmei, *Journal of the Chinese Rare Earth Society*, vol. 7, no. 1, pp. 12-18, March, 1989.
155. W. Longmei and D. Wing, *Iron and Steel*, vol. 20, no. 8, pp. 9-15, August, 1985.
156. D. Wing and W. Longmei, *Journal of the Less-Common Metals*, vol. 110, pp. 179-185, 1985.
157. N.G. Efimenko and N.A. Kalin, "The Deoxidising Ability of Rare Earth Metals in Comparison with Known Deoxidising Agents," *Svar. Proizvod.*, no. 10, pp. 1-2, 1978.
158. P.L. Chen and I.W. Chen, "Grain Boundary Mobility in Y_2O_3 : Defect Mechanism and Dopant Effects," *Journal of the American Ceramic Society*, vol. 79, no. 7, pp. 1801-1809, 1996.
159. O. Monnereau, F. Remy, and A. Casalot, *C.R. Academic Science*, Ser. 2, vol. 301, no. 6, pp. 375-378, 1985.
160. N.A. Toropov and I.A. Bondar, *Izv. Akad. Nauk SSSR, Otd. Khim. Nauk*, vol. 4, p. 547, 1961. (English Translation) N.A. Toropov, *Transactions of the International Ceramics Congress*, 7th, London, p. 438, 1960.
161. S.L. Wang, W.P. Hu, and B.G. Tang, "Improving the Toughness of Weld Metal by Adding Rare Earth Elements [Yttrium]," *Welding International*, vol. 1, no. 3, pp. 284-287, 1987.
162. B. Shveiken, *Journal of Inorganic Chemistry*, vol. 18, p. 155, 1973.
163. S. Prokudina, et al., *Inorganic Materials*, vol. 12, p. 598, 1976.
164. C.R. Waintal, *Seances Academy of Science.*, Ser. B, vol. 264, p. 168, 1967.
165. N.G. Efimenko, "The Use of Rare Earth Metals in the Coatings of Welding Electrodes," *Welding Production*, vol. 27, no. 7, pp. 47-49, 1980.
166. A.G. Aleksandrov, I.P. Volchok, M.V. Lutov, V.D. Tishchenko, and S.S. Milichenko, "The Effects of Calcium, Yttrium, and Cerium on the Structure and Properties of Deposited Metal," *Automatic Welding*, vol. 30, no. 1, pp. 40-42, 1977.
167. D.L. Olson, I. Maroef, C. Lensing, D. Smith, T. Wildeman, and M. Eberhart, "Hydrogen Management in High Strength Steel Weldments," *Hydrogen Management in Steel Weldments*, (ed. J.L. Davidson and D.L. Olson), pp. 1-19, Melbourne, Australia, DSTO and WTIA, 1996.

168. W. Petrie and E. Pfender, "*The Influence of the Cathode Tip on Temperature and Velocity Fields in a Gas-Tungsten Arc*," The Welding Journal, vol. 49, no. 12, pp.588s-596s December, 1970.
169. C.B. Shaw, JR, "*Diagnostic Studies of the GTAW Arc, Part 1 and Part 2*," The Welding Journal, vol. 54, nos. 2 and 3, pp.33s-44s February (Part 1), pp.81s-86s March (Part 2), 1975.
170. S.S. Glickestein, "*Temperature Measurements in a Free Burning Arc*," The Welding Journal, vol. 55, no. 8, pp. 222s-229s August, 1976.
171. J.F. Key, J.W. Chan and M.E. McIlwain, "*Process Variable Influence on Arc Temperature Distribution*," The Welding Journal, vol. 62, no. 7, pp.179s-184s July, 1983.
172. S. Albrecht, G. Forster, A. Koch, K. Landes, G. Seeger and W. Tiller, "*Gas Tungsten Arc Diagnostics-A Review*," IIW Doc. 212-824-93.
173. K. Hiraoka, "*Monitoring of Argon-Hydrogen Mixed Gas Arc Plasma*," NRIM Research Activities, pp.15-17, 1997.
174. K. Hiraoka, "*Characteristics of Plasma under Mixed Gas Atmosphere of Gas Tungsten Arc Welding and Its Spectroscopic Research*," NRIM thesis, November (Japanese), 1996.
175. S.A. Wutzke, C.J. Cremers and E. R.G. Eckert, "*The Thermal Analysis of Anode and Cathode Regimes in an Electric Arc Column*," University of Minnesota HTL TR 56, 1963.
176. JANAF Thermochemical Table, 3rd Edition, M.W. Chase, Jr., C.A. Davis, J.R. Downey, Jr., D.J. Frurip, R.A. McDonald, and N. Syverud, American Institute of Physics for the National Bureau of Standards, New York, 1986.
177. L.B. Pankratz, "Thermodynamic Properties of Halides," United States Department of the Interior, Bureau of Mines, Washington, D.C., 1984.
178. D.R. Milner, G.R. Salter, and J.B. Wilkinson, "Arc Characteristics and their Significance in Welding," *British Welding Journal*, pp. 73-88, February, 1960.
179. A. Block-Bolten and T.W. Eager, "*Selective Evaporation of Metal from Weld Pools*," American Society for Metal, Metals Park, Ohio 44073, 1982.
180. S.A. Gedeon and T.W. Eager, "*Thermochemical Analysis of Hydrogen Absorption in welding*," The Welding Journal, pp.264s-271s July, 1990.
181. A.Q. Bracarense, "Shielded Metal Arc Welding Electrode Heating Control by Flux Ingredients Substitution," PhD Thesis, T-5098, Colorado School of Mines, Golden, CO, 1994.

182. M.Q. Johnson, "Microstructure-Property Relationships in Titanium-Bearing High Strength Multipass Shielded Metal Arc Weldments," PhD. Thesis, F-4769, Colorado School of Mines, Golden, CO, 1996.
183. "Welding, Brazing, and Soldering," *ASM Handbook*, vol. 6, ASM International, Materials Park, OH, 1993.
184. M. Matsushita, "Hydrogen Control in Steel Weld Metal by Means of Fluoride Additions in Welding Flux," M.S. Thesis, T-5218, Colorado School of Mines, Golden, CO, 1999.
185. J.C. Williams and M.I. Khan, "The Mixing and Segregation of Particulate Solids of Different Particle Size," *The Chemical Engineer*, January, 1973, pp 19-24.
186. NIOSH Manual of Analytical Methods (NMAM, Method 7300, Issue 2, Fourth Edition, 1994.
187. American Welding Society, AWS A-4.3-93, American Welding Society, Miami, 1993.
188. ANSI/AWS D1.1-00, American Welding Society, Miami, 2000.
189. Brownlee, J.K., "Effects of Aluminum and Titanium on the Microstructure and Properties of Microalloyed Steel Weld Metal," M.S. Thesis, T- 3064, Colorado School of Mines, Golden, CO, 1985.

SPECTROSCOPIC MONITORING OF HYDROGEN
IN WELDING ARCS

by

Justin H. Chandler

A thesis submitted to the Faculty and Board of Trustees of the Colorado School of Mines in partial fulfillment of the requirements for the degree of *Master of Science Metallurgical and Materials Engineering*.

Golden, Colorado

Date _____

Signed: _____
Justin Chandler

Approved: _____
Dr. Stephen Liu
Thesis Advisor

Golden, Colorado

Date _____

Dr. John J. Moore
Professor and Head
Metallurgical and Materials
Engineering Department

ABSTRACT

Despite the measures proposed to counteract hydrogen-assisted cracking (HAC) in high-strength steel weld metal, it still remains as one of the major challenges that welding scientists and engineers face. HAC is due to diffusible hydrogen in the metal matrix. Current methods of quantifying the amount of diffusible hydrogen in a steel weldment are destructive and are performed only after the weldment has been deposited. In this research, the viability of arc emission spectroscopy as a non-destructive, in-situ method of hydrogen determination in high strength steel weldments was investigated.

Spectroscopy of gas-metal arc welding (GMAW) process was performed to correlate the amount of hydrogen detected in the arc to the hydrogen content measured in the weld deposit. Hydrogen additions were made to argon shielding gas in the amounts of 220 parts-per-million, 1-vol. percent, and 3-vol. percent. The ion-neutral line ratio method was utilized to calculate the temperature of the welding arcs. A summation of hydrogen concentration in the welding arcs out to 3.25 millimeters was measured and correlated to the hydrogen content of the weldments. Diffusible hydrogen content of steel weldments was found to exhibit a Sievert's law type of relationship with the hydrogen additions in argon shielding gas. The findings of this research proved that arc emission spectroscopy of GMAW was able to provide a reliable indicator of hydrogen content in the weld metal.

In addition, the spectroscopy system used in this research was able to detect hydrogen in the arc resulting from moisture in the shielding gas and rust on the wire consumable. However, a discrepancy was found between the amount of hydrogen detected in the arc due to moisture and the stoichiometric predictions of hydrogen content. Further work must be conducted to clarify this difference.

TABLE OF CONTENTS

ABSTRACT	ii
LIST OF FIGURES	vii
LIST OF TABLES	xi
ACKNOWLEDGEMENTS	xii
Chapter 1 INTRODUCTION	1
1.1 Need for Hydrogen Determination	1
1.1.1 High-Strength Steels	1
1.2 Conditions for HAC	3
1.2.1 Presence of Hydrogen	3
1.2.2 Tensile Stresses on Weldment	3
1.2.3 Susceptible Microstructures	4
1.2.4 Temperature	4
1.3 Embrittlement Models	6
1.3.1 Internal Pressure Theory	6
1.3.2 Hydride Formation Theory	6
1.3.3 Surface Energy Theory	7
1.3.4 Decohesion Theory	9
1.3.5 Slip Softening Theory	10
1.4 Hydrogen Absorption into Weld Metal	11
1.5 Methods of Hydrogen Measurement	15
1.5.1 Fluid Displacement Methods	16
1.5.2 Gas Chromatography	17
1.5.3 Hydrogen Sensor	20
1.5.4 Reporting of Results	22
1.6 Spectroscopy of Welding Processes	22

1.6.1	Basis for Spectroscopy	23
1.6.2	Quantification of Elements in Welding Arc	25
1.6.3	Quantification of Temperature in Welding Arc	27
1.6.3.1	The Boltzmann-Plot Method	29
1.6.3.2	The Off-Axis Peaking (Fowler-Milne) Method	30
1.6.3.3	The Ion-Neutral Line Ratio Method	31
1.6.4	Temperature Measurements of Welding Arcs	32
Chapter 2 RESEARCH OBJECTIVES		41
Chapter 3 EXPERIMENTAL METHODS		43
3.1	Arc Generation System – Power Supply and Consumables	43
3.2	Spectroscopy Process	45
3.2.1	Spectroscopy Equipment	45
3.2.2	Spectrometer Details	48
3.3	Shielding Gases	49
3.4	Analytical Methods	49
3.4.1	Diffusible Hydrogen Measurement	49
3.4.2	Residual Hydrogen Content	51
3.5	Data Processing	53
3.5.1	Data Acquisition	53
3.5.2	Identification of Spectra for Arc Elements	55
3.5.3	Smoothing Measured Intensity	55
3.5.4	Cubic Spline Curve	57
3.6	Temperature Determination	57
3.6.1	The Boltzmann-Plot Method	58
3.6.2	Off-Axis Peaking Method	59
3.6.3	Ion-Neutral Line Ratio Method	60

3.7	Concentration Determination	63
Chapter 4 RESULTS AND DISCUSSION		67
4.1	Observations in GMAW	67
4.1.1	Metal Transfer Mode	67
4.1.2	Masking of Excitation Signals	70
4.2	Additions of Hydrogen to Argon Shielding Gas	72
4.2.1	Effect of Hydrogen Additions on Weldment Hydrogen Content	72
4.2.2	Spectroscopic Evaluation of Hydrogen Additions to Argon Shielding Gas	74
4.3	Moisture Additions to Argon Shielding Gas	83
4.3.1	Effect of Moisture Additions on Weldment Hydrogen Content	83
4.3.2	Spectroscopic Evaluation of Moisture Additions to Argon Shielding Gas	87
4.4	Ionization Behavior of Hydrogen	90
4.5	Study of Rust-Induced Hydrogen in the Arc	90
4.6	Study of Metal-Cored Wire Consumables	92
4.7	Sources of Uncertainty	95
Chapter 5 CONCLUSIONS		99
Chapter 6 SUGGESTIONS FOR FUTURE WORK		101
6.1	Suggestions for Future Work	101
6.1.1	Placement of Spectrometer Probe	101
6.1.2	Infrared Emission Spectroscopy	101

6.1.3	Further Study of Moisture-Induced Hydrogen in Welding Arc	102
	REFERENCES	103
	APPENDIX	108

LIST OF FIGURES

Figure 1.1 Photograph of HAC in steel weld metal.	2
Figure 1.2 Relationship between carbon equivalent (CE) and critical amount of diffusible hydrogen	5
Figure 1.3 Diffusion data for hydrogen in steel.	5
Figure 1.4 Model of fracture in surface energy theory.	8
Figure 1.5 Model of fracture in decohesion theory.	10
Figure 1.6 Model of fracture in slip softening theory.	11
Figure 1.7 Solubility of monatomic hydrogen in molten iron at various temperatures.	14
Figure 1.8 Calculation of diatomic and monatomic hydrogen absorption levels within a weld pool at 2500 °C and 0.01-atm. hydrogen.	14
Figure 1.9 Photograph of diffusible hydrogen collection eudiometers utilizing mercury as collection fluid at the Colorado School of Mines. Arrows indicate volumes displaced by hydrogen evolved from samples.	18
Figure 1.10 Schematic diagram of thermal conductivity detector assembly in a gas chromatograph.	19
Figure 1.11 Correlation of hydrogen readings measured by electrolytic sensor and gas chromatograph (GC).	21
Figure 1.12 Schematic representation of reactions occurring at the surfaces of electrolytic hydrogen sensor.	21
Figure 1.13 Schematic illustration of monochromatic light emitted when an electron decays.	24
Figure 1.14 Illustration of light data emitted from welding arc and its conversion to an emission coefficient.	28

Figure 1.15 Temperature distribution calculated for GTAW process: 100 amperes, 15 volts, and 6-mm arc gap.	33
Figure 1.16 Temperature distributions for GTAW process under 100% argon, 150 amperes, 30° vertex angle: (a) 0.25 mm, (b) 0.50 mm, (c) 1.00 mm, and (d) 1.50 mm from cathode.	35
Figure 1.17 a.)Radial temperature distribution of 100% argon shielded GTAW process and b.) hydrogen concentration in 90% argon - 10% hydrogen shielded GTAW process.	36
Figure 1.18 Temperature distribution in GTAW process - temperatures for 100% argon and 1% hydrogen-balance argon shielding gases: 3 mm arc gap, 56 amperes.	37
Figure 1.19 Hydrogen concentration in arc as function of radius for GTAW process: 0.45 mm from anode, 1% hydrogen-balance argon, 3 mm arc gap, 90 amperes, calcium fluoride addition.	38
Figure 3.1 Photograph of HSLA steel consumable after rust formation.	44
Figure 3.2 Schematic representation of spectroscopic data collection setup.	46
Figure 3.3 Photograph of spectroscopic data collection setup.	47
Figure 3.4 Photograph of spectrometer probe used in this research. Demarcations on ruler in photograph are millimeters.	48
Figure 3.5 Photograph of degassing vessel used in this research.	51
Figure 3.6 Photograph of LECO hydrogen determination equipment at the Colorado School of Mines used for residual hydrogen measurement in this research.	52
Figure 3.7 Photograph of milled sample (left) and sample in process of being milled for residual hydrogen analysis.	53
Figure 3.8 Photograph of spectrometer with probe attached.	54
Figure 3.9 Illustration depicting scan heights during experiments.	54

Figure 3.10 Depiction of acquired data and the smoothing operation performed for data analysis.	56
Figure 4.1 (a) Light intensity vs. lateral distance for a GMAW process in short-circuiting transfer and (b) schematic illustration of short-circuiting transfer.	68
Figure 4.2 (a) Light intensity vs. lateral distance for a GMAW process in spray transfer and (b) schematic illustration of spray transfer.	69
Figure 4.3 Map of metal transfer modes in GMAW processes as a function of voltage and wire feed rate.	70
Figure 4.4 Typical spectra emitted by a GMAW process during this research project.	71
Figure 4.5 Observed relationship between residual hydrogen content in steel weldments and hydrogen additions to argon shielding gas.	73
Figure 4.6 Relationship between diffusible hydrogen content of steel weldments and hydrogen content in an argon shielding gas.	75
Figure 4.7 Temperature profiles at indicated heights for a GMAW process with 220-ppm hydrogen addition in argon shielding gas.	77
Figure 4.8 Relationship between diffusible hydrogen concentration of weldments and the summations of hydrogen concentration in the welding arc out to 3.25-millimeters.	78
Figure 4.9 Hydrogen concentration profiles across welding arcs with indicated hydrogen additions to argon shielding gas.	80
Figure 4.10 Ionization behavior of argon as function of temperature. Initial particle density of 6×10^{23} particles per cubic meter.	81
Figure 4.11 Photograph of weldments made with moisture additions to shielding gas. Demarcations on ruler are millimeters.	84
Figure 4.12 Comparison of residual hydrogen content of weldments made with moisture and hydrogen additions to argon shielding gas.	86

Figure 4.13 Hydrogen concentration profiles at indicated heights in GMAW processes with 220-ppm moisture additions in argon shielding gas.	88
Figure 4.14 Hydrogen concentration profiles at indicated heights in GMAW processes with 220-ppm hydrogen additions in argon shielding gas.	89
Figure 4.15 Ionized and neutral hydrogen ratios for GMAW processes with 1-vol. percent and 3-vol. percent hydrogen additions to argon shielding gas.	91
Figure 4.16 Hydrogen concentration profiles at indicated heights in GMAW processes with rusty consumable.	93
Figure 4.17 Relationship between hydrogen concentration summations and scan height for spectroscopy of GMAW processes with rusty consumable.	94
Figure 4.18 Portion of spectra emitted from metal-cored wire arc welding process with manganese emission lines superimposed.	96
Figure 4.19 Portion of spectra emitted from metal-cored wire arc welding process with iron emission lines superimposed.	96

LIST OF TABLES

Table 3.1 Parameters for welding processes performed during this research project.	44
Table 3.2 Particle density changes due to ionization.	61

CHAPTER 1

INTRODUCTION

1.1 Need for Hydrogen Determination in High Strength Steels

In the middle of the 20th century, welded steel structures frequently exhibited cracking in the heat-affected-zone (HAZ) of the weldments, often times after the welding process was completed. Cracking was first prevented by utilizing chromium-nickel weld metals that provided steels with a primarily austenitic microstructure, which was relatively ductile and did not experience brittle fracture like metals with ferritic microstructures. It was later discovered that mobile hydrogen in the weld metal was the cause of the cracking. Thus, this phenomenon was termed hydrogen-assisted cracking (HAC) or, due to its delayed nature, cold cracking. As base metals were improved in their resistance to HAC, the problem then became an issue in the weld metal itself. An example of HAC in weld metal can be seen in Figure 1.1. With the advent of micro-alloyed steels the problem subsided somewhat. These steels used small additions of elements like niobium and vanadium to form carbides and carbo-nitrides which refined the grain structure. The low carbon equivalent values of these steels improved the resistance to cracking. However, with the increase in alloying content for increased strength, modern high-strength steels are still vulnerable to HAC, even up to sixty-four hours after completion of welding [1].

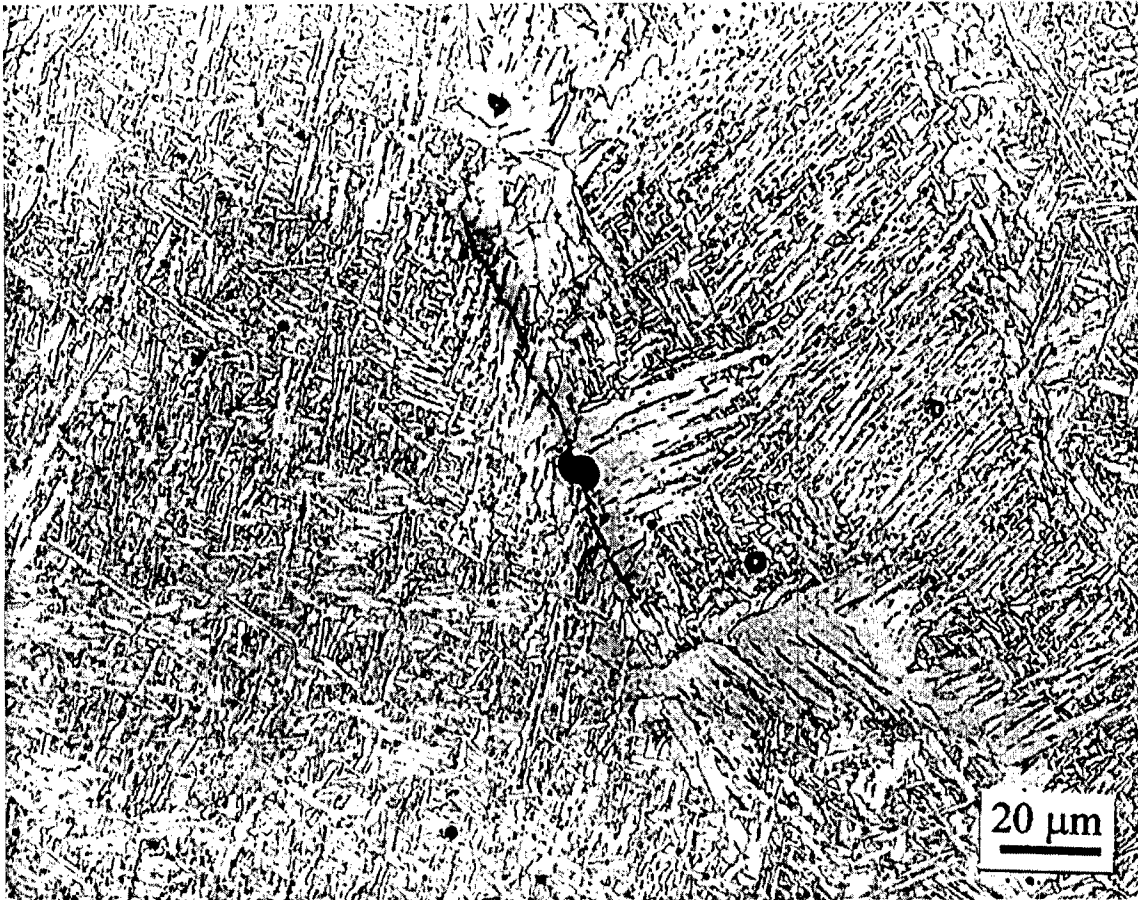


Figure 1.1 Photograph of HAC in steel [2].

1.2 Conditions for HAC

For HAC to occur, the following conditions must occur: 1) hydrogen is present, 2) tensile stresses act on the weldment, 3) a susceptible microstructure is present, and 4) a low temperature is reached.

1.2.1 Presence of Hydrogen

Hydrogen is inevitably present in most arc welding processes. Hydrogen originates from moisture in the flux, in the shielding gas, or in the atmosphere and from lubricants on the welding consumable, impurities on the workpiece, etc. Any hydrogenous compounds introduced into the arc will break down into hydrogen in the welding arc. Hydrogen present in the arc column is absorbed by the weld pool and moves through the weldment by diffusion. The amount of hydrogen absorbed by the weld pool is a function of the size of the weld, the decreasing solubility, and the thermal history of the weldment. Control of hydrogen absorption can be accomplished by reducing the amount of hydrogen in the arc atmosphere or by allowing the hydrogen to diffuse out of the weld metal before it cools.

1.2.2 Tensile Stresses on Weldment

The thermal contraction of a weldment produces stresses in a weldment, which is accommodated by strain. Thermal stresses in a weldment are exacerbated by external stresses imposed by the restraint of the joint. Stresses are concentrated at the root and toe of the weld, and at notches represented by inclusions and other defects such as undercutting. HAC is strain-rate dependent and the risk of cracking is most severe at low strain rates. The risk is highest during the final stages of cooling since this is when the strain rate is lowest.

1.2.3 Susceptible Microstructures

As a general rule, the harder a microstructure, the more susceptible it is to HAC [3]. During the welding process, the steel weld metal and HAZ are raised to a high temperature and rapidly cooled by the loss of heat to the surrounding workpiece. Fast cooling, combined with the hardenability of the metal, can produce hard, brittle microstructures such as martensite and bainite in the weldment. The microstructure in steel is a product of two factors: 1) the cooling rate through the transformation temperature range and 2) the composition, which determines the alloy hardenability. The cooling rate depends on the initial temperature of the steel (the preheat), the thickness of the steel, the joint geometry (including plate thickness, joint design and weld deposit size), and the heat supplied by the welding process. Hardenability depends on the composition and can be related to the contribution from all of the alloying elements. An empirical formula such as a carbon equivalent formula accounts for all the elements known to affect the hardenability of steel. A relationship between the carbon equivalent content and critical amount of diffusible hydrogen can be seen in Figure 1.2. Alloys with greater hardenability exhibit lower tolerance for diffusible hydrogen in crack origination.

1.2.4 Temperature

HAC occurs only at temperatures close to ambient, being particularly prevalent in the temperature range of 20 - 150° C. Temperatures above that range provide favorable kinetics that allow hydrogen to escape from the weldment altogether or migrate to internal defects such as porosity. Figure 1.3 shows the temperature dependency of hydrogen diffusion. Note that the y-axis is plotted in the form of a log scale. Hydrogen

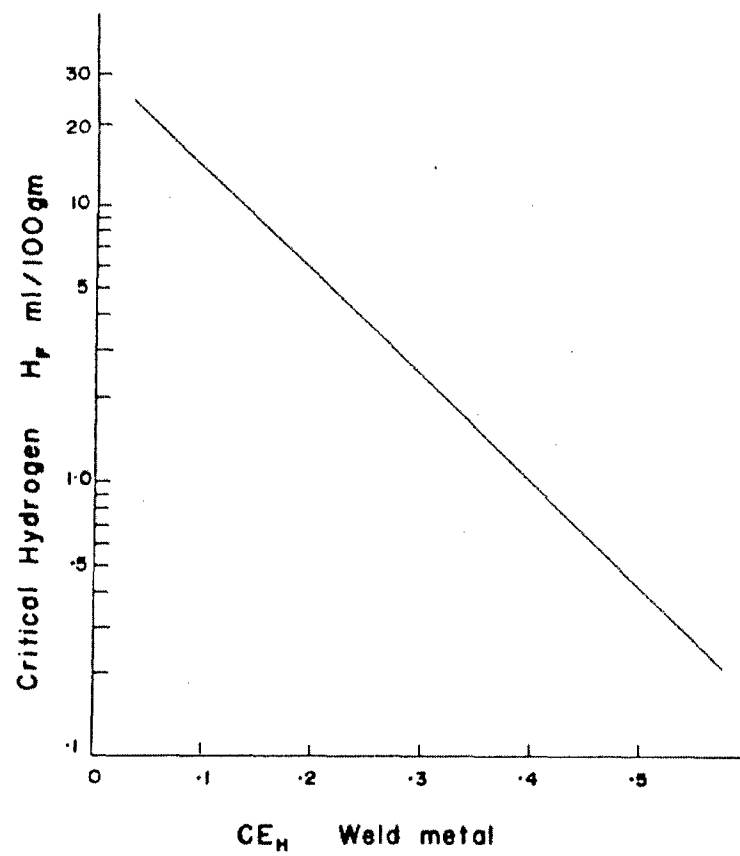


Figure 1.2. Relationship between carbon equivalent (CE) and critical amount of diffusible hydrogen [4].

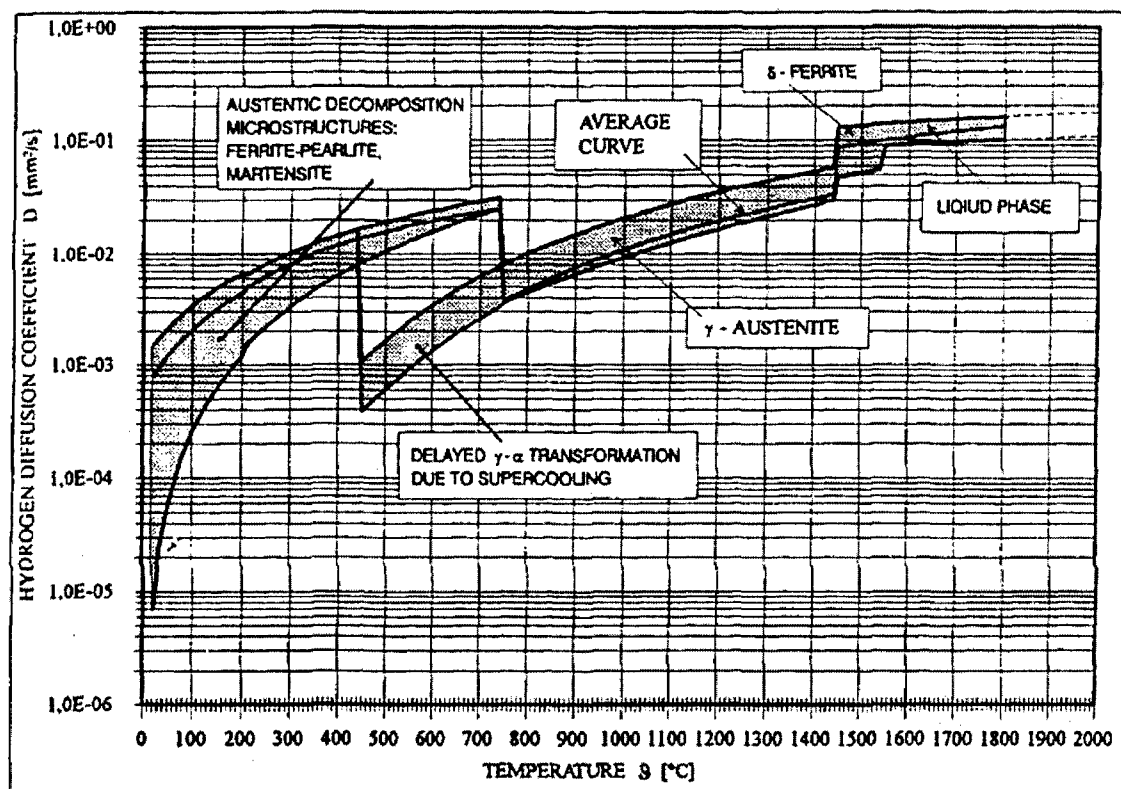


Figure 1.3. Diffusion data for hydrogen in steel [5].

diffusion is practically impossible below room temperature and will be trapped in the weld metal.

1.3 Embrittlement Models

While there is not a single theory that accounts for all the characteristics of hydrogen embrittlement, there are some generally accepted theories: 1) internal pressure theory, 2) hydride formation theory, 3) surface energy theory, 4) decohesion theory, and 5) slip softening theory.

1.3.1 Internal Pressure Theory

In this theory, Zapfe and Sims [6] suggested that hydrogen pressure in the weld metal is the source of embrittlement. Atomic hydrogen in the metal matrix diffuses to pre-existing microvoids and microcracks in the weld metal, where it recombines into molecular form. It is proposed that this collection of hydrogen creates enough pressure to propagate fracture in the weld metal. This theory is not without its critics. Hancock and Johnson [7] showed that crack propagation could occur in a subatmospheric hydrogen environment. Thus, it was shown that cracking occurred without the supersaturated solid solution supposedly required by the theory. Hirth [8] also discounted the theory on the basis of his studies showing that hydrogen supersaturation is greatly overstated in most cases. However, it is acknowledged that the theory can hold true for lower temperatures where supersaturation in voids is possible.

1.3.2 Hydride Formation Theory

Westlake [9] proposed that hydrogen enriches the metal ahead of a crack tip to the point of forming a phase with different mechanical properties than the metal matrix. It is

proposed that hydrogen causes a metal hydride to form ahead of the crack tip. The hydride is brittle compared to the matrix and fractures when subjected to the stress of a propagating crack tip. Gahr, et. al. [10] showed that hydride stabilization was possible due to the hydrostatic stress field at a crack tip, even when the hydride is unstable without stress. Hirth [8] performed computations regarding the Fermi-Dirac atmosphere of hydrogen at a stressed crack tip that somewhat validate the model. He found that saturation was possible at room temperature at a stressed crack tip. At lower temperatures, greater numbers of crack tips would be saturated, a trend generally inversely proportional to the absolute temperature. The localized hydrogen concentration it is essentially equivalent to the formation of a hydride with regard to mechanical property deterioration.

1.3.3 Surface Energy Theory

Petch and Stables [11] suggested that hydrogen embrittles through adsorption to crack surfaces. Hydrogen adsorption lowers the surface energy of surfaces created by cracking which lowers the work of fracture, thus promoting it. Lynch [12] further expounded on the theory, suggesting that hydrogen may even adsorb between the first and second atom layers at crack tips. The base for this model is Griffith's crack theory, which explains crack initiation as a method of releasing the energy of strain to create the new surfaces of a crack. Hydrogen adsorption lowers the surface energy, which reduces the amount of energy needed to create the new surfaces engendered by a crack, as portrayed in Figure 1.4. On an atomic level, it is believed that hydrogen atoms weaken the interatomic bonds at the crack tip, thus assisting the emission of dislocations. Small voids form around small particles and slip-band intersections ahead of the crack due to the localized dislocation activity. Thus, crack growth is sustained by dislocation emission from crack tips with assistance from void formation ahead of cracks [13].

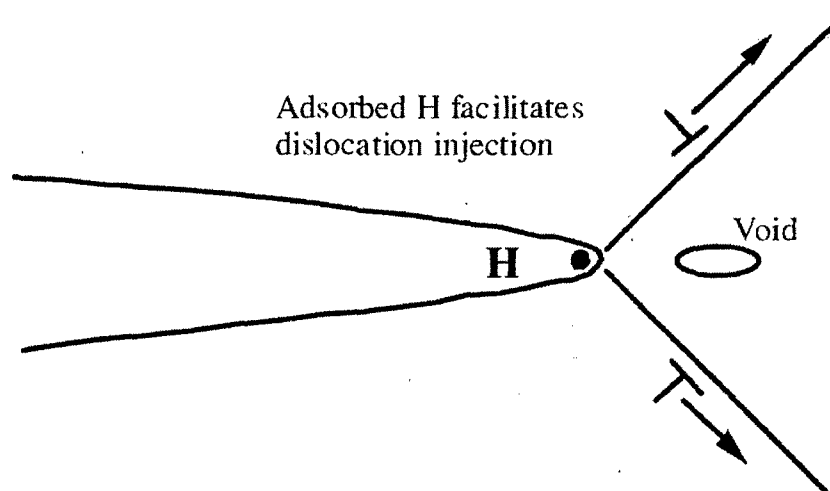


Figure 1.3 Model of fracture in surface energy theory [12].

Arguments contrary to this theory, as outlined by Hirth [8], are: 1) great underestimation of the work of fracture, 2) no accounting for discontinuous cracking as indicated by sonic emissions, 3) no explanation of why the tendency for delayed failure can be removed by stress relief, and 4) no explanation for why oxygen, with its greater heat of adsorption, does not promote cracking and actually stops the hydrogen effect. On the topic of the work of fracture, Thomson [13] showed that plastic flow can occur in such a manner as to screen the crack tip from severe stress concentrations while allowing the crack tip to advance in a brittle manner. Oxygen at the crack tip inhibits the adsorption of hydrogen probably because of its competitive adsorption rate, among other reasons [14,15]. Delayed failure reversibility is theorized to be a factor of crack nucleation [8]. Crack nucleation can involve not only surface energy reduction by hydrogen, but local stresses due to dislocation pileups and elastic incompatibility stresses as well. These can be relaxed or recovered during removal of external stresses.

1.3.4 Decohesion Theory

Originally put forth by Troiano [16], this theory involves the weakening of iron-iron bonds in the region of the crack tip to such a degree that a tensile separation of atoms (decohesion) occurs rather than deformation by slip. Dislocation activity on planes that do not intersect cracks, and discontinuous emission of dislocations from the crack tip could occur, as seen in Figure 1.5. Hydrogen concentration centers and decohesion sites have been proposed to include: 1) non-Hookean regions within a few atomic diameters of crack tips, 2) locations that are tens of nanometers ahead of cracks, where dislocation shielding effects result in a maximum tensile stress, and 3) positions of maximum hydrostatic stress at a distance on the order of twice the crack-tip-opening displacement [12]. Low-index crystallographic planes and grain boundaries are the avenues where decohesion may occur.

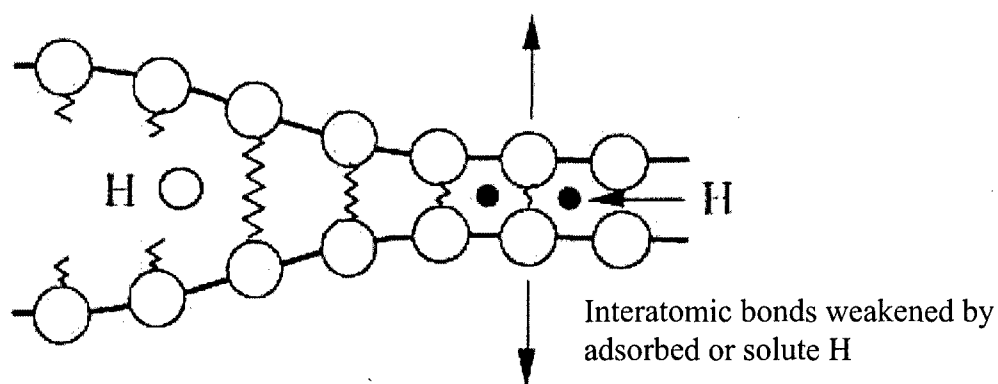


Figure 1.4 Model of fracture in decohesion theory [12].

1.3.5 Slip Softening Theory

Beachem [17] proposed this theory, which is based on hydrogen atmospheres around dislocations and obstacles to dislocations. Obstacles to dislocations can include other dislocations, solute atoms, and precipitates. These atmospheres distort in such a way that their repulsion is decreased when mobile dislocations approach. Deformation is localized near crack tips due to the concentration of hydrogen in that region, as seen in Figure 1.6. The localized deformation leads to a lower strain for fracture. However, it is acknowledged that enhanced dislocation motion is definitely established, considering the softening behavior associated with enhanced screw dislocation mobility, enhanced dislocation injection at surfaces, and the promotion of shear instabilities.

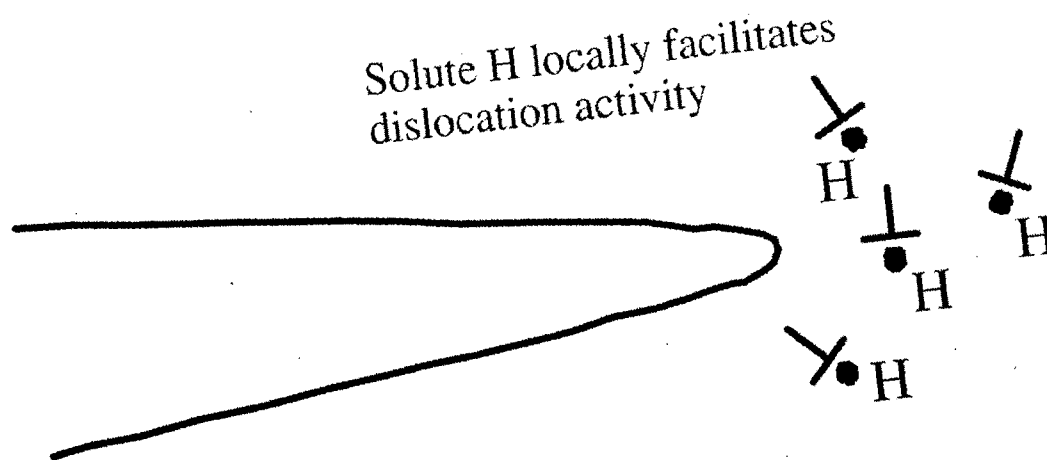
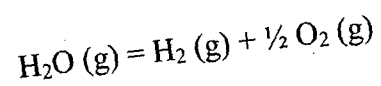


Figure 1.5 Model of fracture in slip softening theory [12].

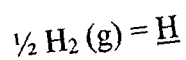
1.4 Hydrogen Absorption into Weld Metal

It is well established that moisture introduced into a welding arc will decompose into hydrogen in the following manner:



(1.1)

Hydrogen generated in the above reaction then exists in the arc, allowing for its absorption into the weld pool. The most common method of describing hydrogen absorption in weld pools is the relationship developed by Sievert. Sievert's law is based on the following reaction:



(1.2)

where \underline{H} is the amount of absorbed hydrogen. The free energy of the reaction in Eq. 1.2 can be described as:

$$G = 8720 - 11.02 \cdot T = -R \cdot T \ln K \text{ (kcal/mole)} \quad (1.3)$$

where G is the free energy of the reaction, R is the universal gas constant, T is the temperature, and K is defined as such:

$$K = \frac{\underline{H}}{(P_{H_2})^{\frac{1}{2}}} \quad (1.4)$$

where P_{H_2} is the partial pressure of hydrogen. Sievert's law states that:

$$\underline{H} = C \cdot \exp\left(\frac{-E_{abs}}{R \cdot T}\right) \cdot (P_{H_2})^{\frac{1}{2}} \quad (1.5)$$

where C is a constant independent of temperature and E_{abs} is the activation energy for absorption.

Hydrogen absorption in Sievert's law is considered to occur in diatomic form alone. However, calculations by Gedeon [18] predicted a higher solubility for monatomic hydrogen in the weld pool than hydrogen in diatomic form. Palmer and DebRoy [19] also noted nitrogen solubility in steel above that predicted by Sievert's law. In the high temperatures of a welding arc, monatomic hydrogen is the primary form of hydrogen present. Mundra et. al [20] pointed out that at an arc temperature of just 3600 K, 99 pct. of the diatomic hydrogen in a 1 pct. hydrogen-balance argon shielding gas would be dissociated. The series of reactions leading to hydrogen absorption, according to Gedeon, occurs first with the dissociation of diatomic hydrogen in the arc:



which, once completed, allowed for monatomic hydrogen absorption into the weld pool:



Utilizing the diffusible hydrogen data of previous researchers, Gedeon [18] calculated the effective reaction temperatures for hydrogen absorption implied in their studies. He determined that Sievert's law predicted unreasonably high temperatures for molten weld pools to allow for hydrogen absorption. Basis for this assertion stemmed from findings by Howden and Milner [21], which indicated that iron vaporization at such high temperatures, in excess of 2500 °C, would limit any contact hydrogen may have with the molten weld pool. According to Gedeon [18], analysis using the Sievert relationship would not result in a true hydrogen absorption temperature. Rather, the result would be an "effective" temperature where kinetics is such that hydrogen diffusion away from the weld would be lethargic.

It was also predicted by Gedeon and Eagar [22] that hydrogen absorption would occur primarily in the outer regions of the weld pool due to the solubility calculations shown in Figure 1.7. The calculated solubility of hydrogen in molten iron across a weld bead can be seen in Figure 1.8. This finding was in contrast to the belief held by other researchers, such as Li and North [23], that hydrogen absorption occurred primarily in the hottest portion of the weld pool, directly under the electrode. It was proposed by Gedeon and Eagar that the high temperature portions of the weld pool have a slow enough cooling rate to allow hydrogen escape. In the outer regions of the weld pool, the relatively quick rate of solidification would trap the hydrogen initially absorbed into the weld pool.

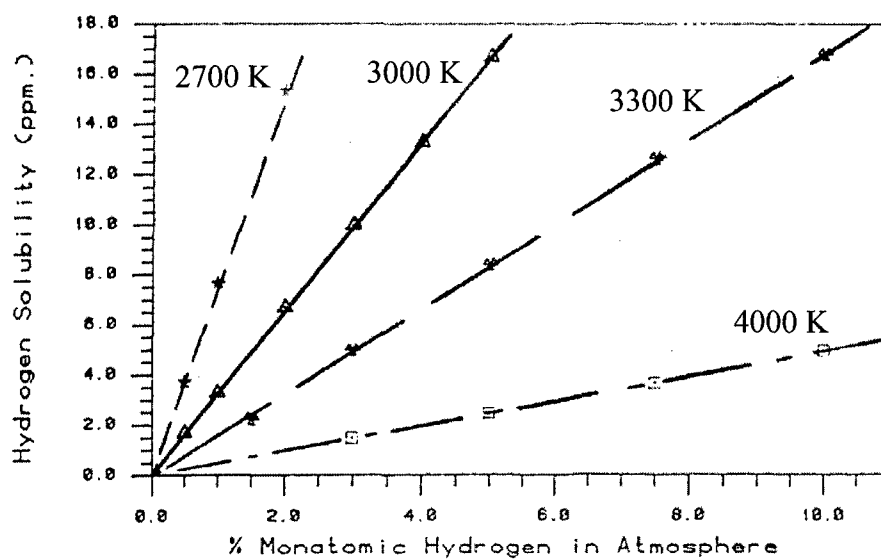


Figure 1.6 Solubility of monatomic hydrogen in molten iron at various temperatures [18].

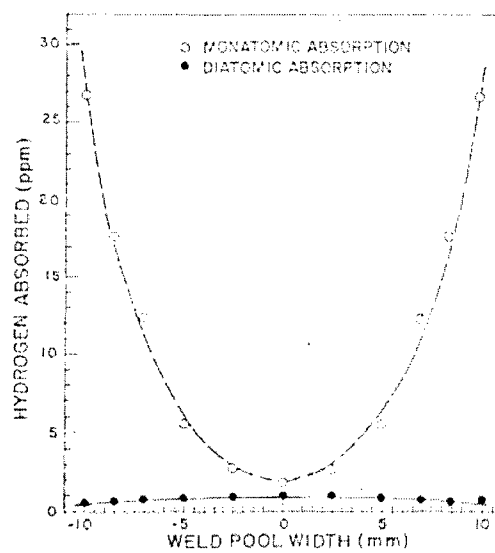


Figure 1.7 Calculation of diatomic and monatomic hydrogen absorption levels within a weld pool at 2500 °C and 0.01-atm. hydrogen [22].

Research by Mundra et. al [20] on GMAW processes supported their findings. Claims that rejection of hydrogen from solid weld metal into the weld pool as the source of hydrogen in weldments was discounted by Gedeon [18]. Steel weld metal does not typically exhibit the porosity that would be evident if hydrogen were rejected into the weld pool.

Hydrogen pickup by molten metal droplets as they cross the arc is another source of hydrogen in the weldment. Calculations by Mundra, et. al [20] estimated hydrogen pickup in a droplet to be 12 parts-per-million. In addition, Gedeon [18] found some correlation between metal transfer mode and diffusible hydrogen content of weldments. It was reported that weldments deposited with shielding gases containing greater than 0.5-vol. percent hydrogen exhibited an increase in diffusible hydrogen content of 3 parts-per-million.

1.5 Methods of Hydrogen Measurement

No matter the actual mechanism of HAC, it is the result of hydrogen that is mobile in the metal matrix of the weldment at or near room temperature. Thus, it is critical to be able to make reliable measurements of the amounts of mobile hydrogen in a weld metal. As such, it becomes necessary to examine the methods utilized to quantify the amount of mobile (diffusible) hydrogen in the weld metal. Samples for diffusible hydrogen analysis are produced by welding a test specimen and rapidly quenching it to prevent hydrogen loss. Removal of slag and oxides from the surface of the test specimen is required prior to analysis. Hydrogen is then evolved from the sample in a controlled environment, and the evolved gas is analyzed and/or measured. Test methods include all of the above factors but vary with respect to the specific sample sizes, sample configurations, degassing time, degassing temperature, measurements, and analyses.

1.5.1 Fluid Displacement Methods

Fluid displacement methods were the first type of tests used to quantify the diffusible hydrogen in a test sample. Ignoring the details of sample sizes and preparation methods, the methodology is common to all. A eudiometer is used to house a welded test sample and a collecting fluid. The sample is permitted to degas for a given time at a given temperature. Hydrogen that evolves from the test sample displaces the fluid at the top of the eudiometer. Gas volume is measured by the height of the fluid displaced at the top of the eudiometer. The earliest displacement fluid used was glycerin, which allowed for the observation of bubbles forming from the sample and floating to the top of the eudiometer. Concerns about the accuracy of measurements made with glycerin were soon raised due to the formation of foam at the meniscus. The foam made accurate measurement of the volume difficult using the graduations on the eudiometer. In addition, it was found that using the glycerin method allowed for recovery of only about half the hydrogen that was recovered from similar samples using more advanced methods.

Discrepancies in the amount of hydrogen recovered were believed to result from the solubility of hydrogen in glycerin. Moreover, only the fluid displacement was measured in this process, no chemical analysis of the displacing volume was required. It was found that the displacing volume in this method quite often contained gases other than hydrogen, namely oxygen and nitrogen [24]. Presence of these gases arose from the fact that glycerin is an exceptional solvent and quite hygroscopic. Unfortunately, the concentrations of the gases were not in constant ratios. Amounts of oxygen and nitrogen developing from the glycerin were a factor of the initial concentrations of those gases in the glycerin, which varied from laboratory to laboratory. Similar problems were found with other collecting fluids such as paraffin, alcohol, silicone oil, and demineralized water [24,25]. One proposed method of combating the hydrogen solubility problem was to bubble hydrogen through the glycerin prior to analysis in order to saturate it. This was not effective, however, as it created a large concentration gradient in the medium.

Hydrogen diffused down the gradient and increased the volume of the gas collected [18]. To avoid the problems associated with gas solubility, mercury was widely utilized as a collecting fluid, as seen in Figure 1.9. Arrows in the figure indicate where hydrogen evolved from the sample, has collected in the top of the eudiometer. The AWS method for determination of diffusible hydrogen, AWS A4.3-86, outlines degassing of the test sample at 45°C [26].

Degassing temperatures higher than 45°C are not desirable because vapor formation can occur, creating a health hazard. Safety precautions such as fume control and contact avoidance are necessary when working with mercury. It was even found that the dimensions of the glassware used for collection had an effect on the measurements [27]. It was found that the shape of the glassware affected the flow of hydrogen out of the collecting fluid. Neck size of the glassware, in particular, exerted influence on whether hydrogen evolved from the sample formed foam when exiting the collecting fluid, if the fluid was prone to foam formation.

1.5.2 Gas Chromatography

Due to the above concerns, a new method of measuring hydrogen was desired. Presently, gas chromatography is the preferred method of measuring hydrogen. In gas chromatography, a gas mixture is transported through stationary packing under the force of a carrier gas. Smaller gas molecules, like hydrogen, travel through the packing more quickly than larger gases. If the carrier gas flow rate, carrier gas composition, and column temperature are held constant, then each gas will pass through the system at a characteristic rate. Once the gas components are separated, the carrier gas transports them to a detection device, normally a thermal conductivity detector. A thermal conductivity detector is comprised of temperature sensitive resistors in two arms in a Wheatstone bridge as depicted in Figure 1.10. The temperatures of R_1 and R_2 increase with an increase in current, thus increasing their resistance. The bridge remains balanced because

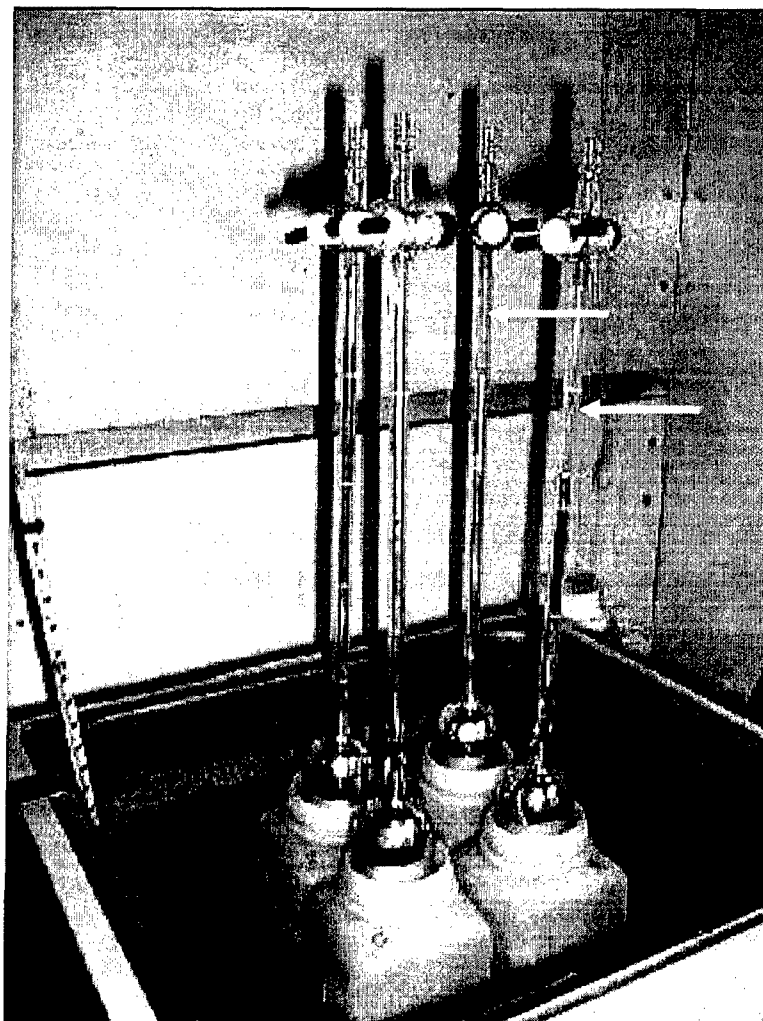


Figure 1.8 Photograph of diffusible hydrogen collection eudiometers utilizing mercury as collection fluid at the Colorado School of Mines. Arrows indicate volumes displaced by hydrogen evolved from samples.

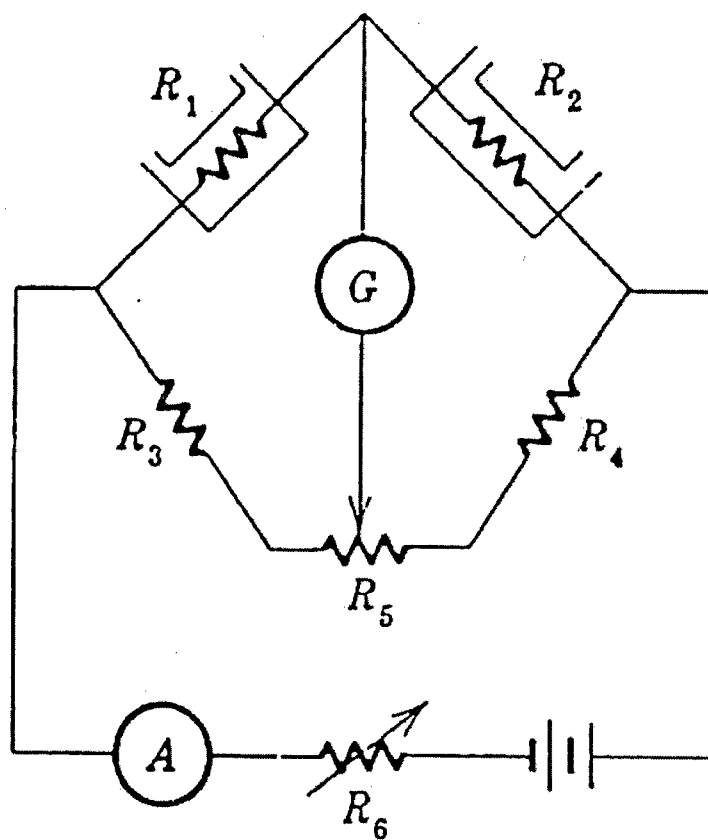


Figure 1.10 Schematic diagram of thermal conductivity detector assembly in a gas chromatograph [18].

the change is equal in both arms. Imbalance will occur if the temperatures of the resistors are not equal. Individual thermal conductivities of the gases in the mixture are different. Therefore, the heat created by the resistors will be conducted away at different rates depending on the gas present in the resistor's chamber at that time. Difference in temperatures of the resistors will cause an imbalance in the bridge. Readings in the thermal conductivity detector are zeroed as the same gas passes over both arms, or, different gases with known thermal conductivities. As the sample gas passes through the detector, the differences in the thermal conductivities of the gases will be revealed as imbalances in the Wheatstone bridge. Various components of the gas will arrive at the detector at their characteristic times. Amounts of component gases are calculated by integrating the signal with respect to time. The area under the curve is equal to the mass of the component detected. Calculations are performed by the electronics of the gas chromatography unit.

1.5.3 Hydrogen Sensor

Another method of measuring the hydrogen evolved from a weld sample involves the use of palladium-coated conducting polymer film. Albert, et. al [28] reported a nearly one-to-one correlation to gas chromatography hydrogen measurements using such a device down to sub-ppm levels of hydrogen, as demonstrated in Figure 1.11. In their research a weld specimen was placed in a chamber and degassed at 45° C for 72 hours in a pressurized argon atmosphere. Samples of gas from the chamber were inserted into a carrier gas stream and introduced to the sensor and a gas chromatography unit. The conducting polymer film was made using polyvinyl alcohol and phosphoric acid cast into a film that was then coated with palladium and connected to electrical leads. During testing, one side of the film was exposed to air and the other was in contact with the argon-hydrogen gas mixture sampled from the specimen chamber, as seen in Figure 1.12. The conducting polymer sandwiched between the two palladium films acted as a fuel

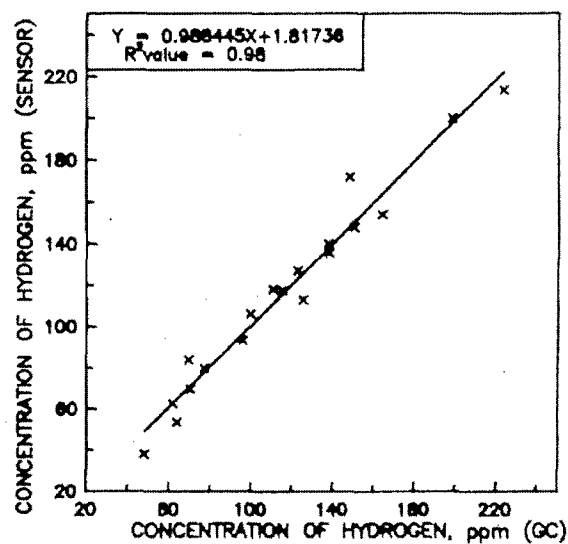


Figure 1.11 Correlation of hydrogen readings measured by electrolytic sensor and gas chromatograph (GC) [28].

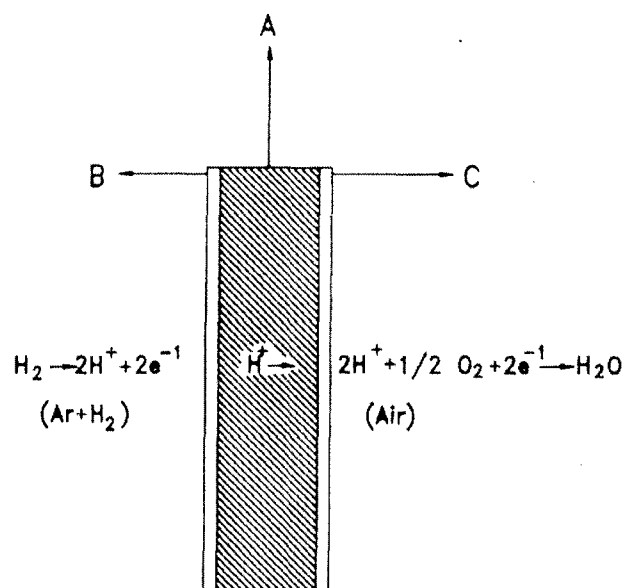


Figure 1.12 Schematic representation of reactions occurring at the surfaces of electrolytic hydrogen sensor [28].

cell. Measurements were taken of the short-circuit current and were found to be linearly dependent on the hydrogen concentration in the argon-hydrogen gas mixture. Although promising, this technology is not without limitations at the present time. Calibration of the sensor just prior to each measurement is recommended due to instability of the device over time [28]. Lifetime of the device and sensitivity to variations in measurement parameters are other issues as well.

1.5.4 Reporting of Results

Gas measurement results are reported as gas volume (typically milliliters) per 100 grams of deposited weld metal. With certain welding processes, it is more suitable to normalize the hydrogen volume to the amount of metal actually melted. In this case, the measurement would be reported in units of gas volume per 100 grams of fused weld metal [26].

1.6 Spectroscopy of Welding Processes

In all of the forms of hydrogen measurement just discussed, there is a common destructive nature to each. Also, each test requires time to allow for hydrogen evolution from the sample. Thus, at the present time, there is a destructive, after-the-fact nature to determination of diffusible hydrogen content of steel weldments. Additionally, due to its delayed nature, there is also a risk of weldments passing inspection and still being vulnerable to HAC. With these shortcomings in mind, spectroscopy of welding processes presents itself as an attractive means of in-situ, non-destructive determination of diffusible hydrogen concentration in steel weldments.

1.6.1 Basis for Spectroscopy

To correlate the activity of hydrogen in the arc to the hydrogen content of high-strength steel weld metal, spectroscopy was utilized as a method of non-intrusive monitoring of the arc. In the high temperature of the arc, electrons are excited to higher energy levels. As an electron decays back to a lower energy level, monochromatic light is emitted. A depiction of this process can be seen in Figure 1.13. The wavelength of that light is determined by the energy change undergone by the electron during its decay, as governed by the following equation:

$$E_1 - E_2 = \Delta E = h\nu \quad (1.8)$$

where E_1 is the energy level of the higher state, E_2 is the energy level of the lower state, ΔE is the change in energy, ν is the frequency of the emitted light, and h is Planck's constant. The frequency and wavelength of light are related by the following equation:

$$c = \nu\lambda \quad (1.9)$$

where c is the speed of light and λ is the wavelength. Light is more commonly described by its wavelength rather than frequency. Thus each decay event in a given atom has a characteristic wavelength of light associated with it. It is the unique spectra emitted by certain decay events that allow for detection of the elements within an arc.

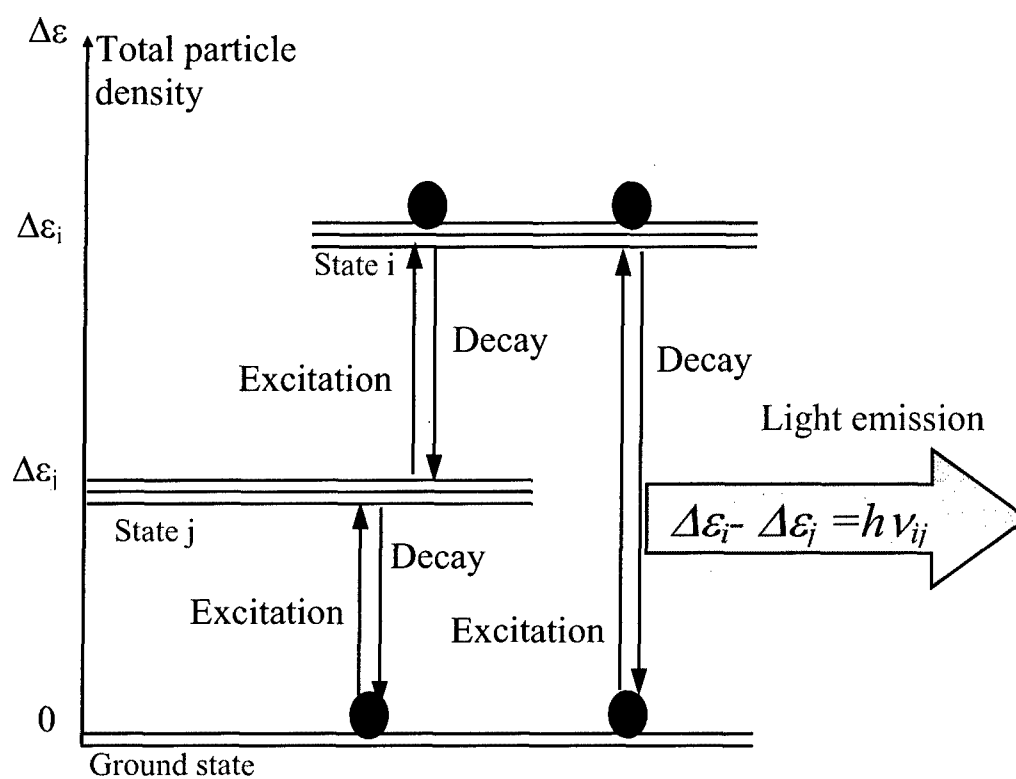


Figure 1.13 Schematic illustration of monochromatic light emitted when an electron decays [29].

Quantification of the light-emitting elements can be accomplished via the line emission coefficient of light emitted during a decay event:

$$i_{ij} = \frac{1}{4\pi} A_{ij} h \nu_{ij} \delta_i \quad (1.10)$$

where i_{ij} is the line emission coefficient of the light emitted during the decay of an electron from the i state to the j state in a given element, A_{ij} is the transition probability of the decay event, ν_{ij} is the frequency of the emitted light, and δ_i is the density of atoms in energy state i . Analysis of the above equation shows that all the terms are constant except for the atom density. Thus, the line emission coefficients emitted from a welding arc can be used to determine the density of atoms in a particular energy state.

1.6.2 Quantification of Elements in Welding Arc

Early research efforts into spectroscopic monitoring of welding arcs attempted to directly correlate the relative intensity of the spectrum from a given atom to its concentration in the arc. This method did not give accurate results because the particle density term describes only one energy state. For any given atom, there are a number of energy states in which an electron may reside. Thus, it is not reasonable to assume that one decay event is directly proportional to the concentration of the atom in which the event occurred. When determining the temperature of an arc using spectroscopy, it is a common treatment to make an assumption of "local thermodynamic equilibrium." Using this assumption, the distribution of particle density can be calculated with the Boltzmann distribution, which relates the particles in a certain energy state (N_i) to the total number of particles (N) in the following manner:

$$\frac{N_i}{g_i} = \frac{N}{q} \exp\left(-\frac{\varepsilon_i}{kT}\right) \quad (1.11)$$

In this equation, g_i is the statistical weight of state i , ε_i is the energy of state i from the ground level, k is Boltzmann's constant, and T is the temperature. The partition function is symbolized by q and is defined as:

$$q = \sum_i g_i \exp\left(-\frac{\varepsilon_i}{kT}\right) \quad (1.12)$$

which is a summation of the energy states in the system including their respective statistical weights. The particle density of an element is generally defined as:

$$\delta = \frac{N}{V} \quad (1.13)$$

where V is the volume of the system. Combining Eqs 1.10 and 1.11 results in the following equation:

$$I_{ij} = \frac{1}{4\pi} \frac{A_{ij} h \nu_{ij} g_i}{q} \frac{N}{V} \exp\left(-\frac{\varepsilon_i}{kT}\right) = \frac{1}{4\pi} \frac{A_{ij} h \nu_{ij} g_i}{q} \delta \exp\left(-\frac{\varepsilon_i}{kT}\right) \quad (1.14)$$

where δ is the density of particles in all energy states. Examination of the terms will show that the line emission coefficient is not only a factor of particle density, but also of temperature. Thus, to characterize the elemental concentrations, it is necessary to determine the temperature of a welding arc.

1.6.3 Quantification of Temperature in Welding Arc

Spectroscopic measurements to determine the temperature distribution of welding arcs were first performed on gas tungsten arc welding (GTAW) processes in the 1970's. In these research projects, a welding arc was produced on water-cooled copper anodes shielded by argon gas [30, 31]. Experiments were performed on GTAW processes to simplify the phenomena occurring in the plasma of the welding arc. The emission coefficient at certain wavelengths was measured and used to determine temperature in the arc. However, it was found that to obtain emission coefficients from a welding arc, one must assume a rotationally symmetric and optically thin welding arc plasma. Furthermore, it must be assumed that two-dimensional data can be extracted from a three-dimensional object, the welding arc. Operating under this second assumption, it was proposed that the Abel inversion equation could convert the lateral emission coefficient collected during experiments to the radial emission coefficient used for data analysis [32].

When a spectroscopic measurement is taken, an image of the welding arc plasma is projected onto the entrance slit of the spectrometer, and the portion of the spectrum falling on the exit plane is detected using photomultipliers, vidicon tubes, or photodiodes. What is observed is the intensity of light integrated along the line of sight. Plasma in a welding arc is an inhomogeneous and absorbing medium; thus, it is necessary to determine the line emission coefficients from the measurements.

Due to the axial symmetry of the welding arc, it is possible to represent the line emission coefficients as a function of the radius in the arc, as described in Figure 1.14. This operation is performed using the Abel inversion. An integrated line emission coefficient as a function of a lateral coordinate, x , can be stated as:

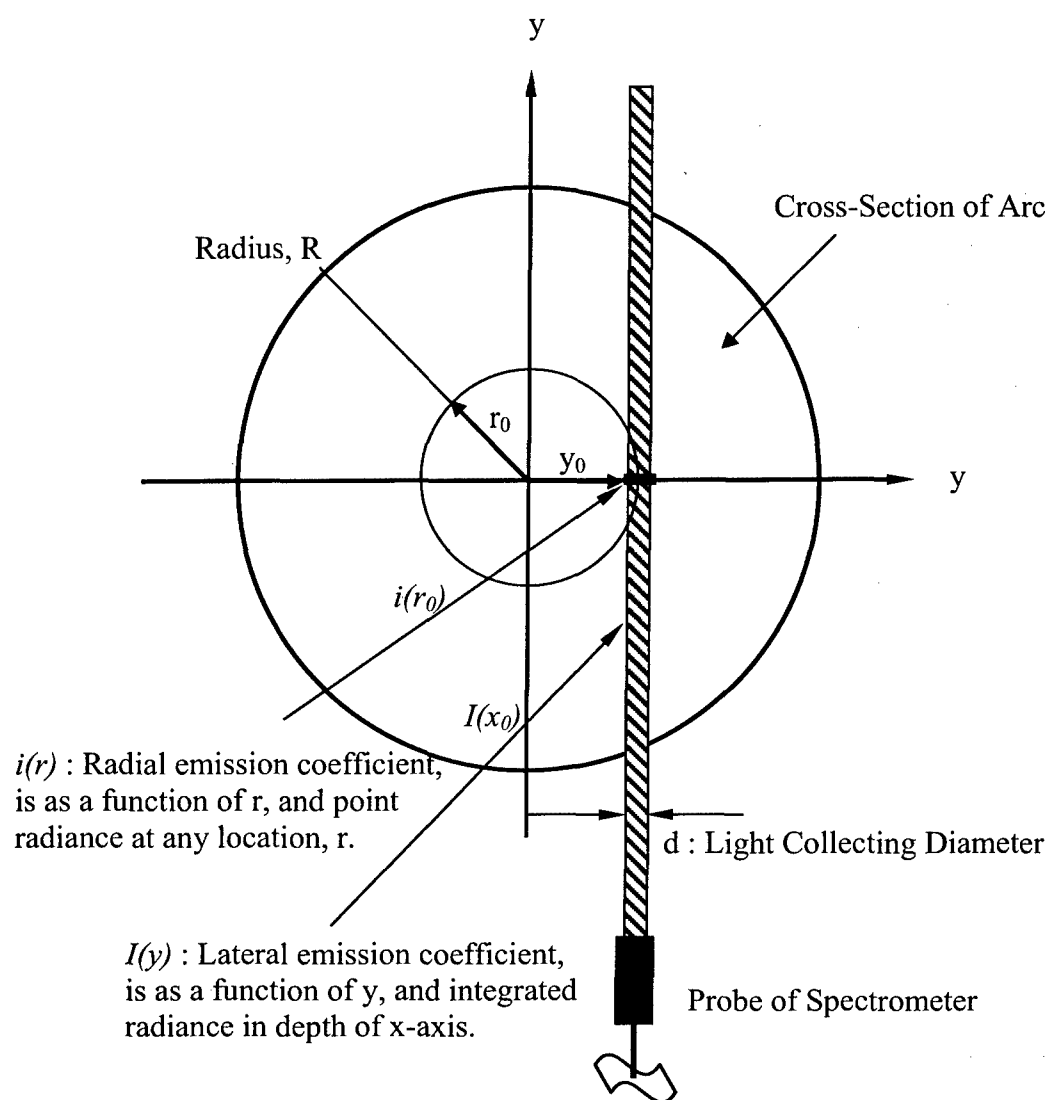


Figure 1.14 Illustration of light data emitted from welding arc and its conversion to an emission coefficient [29].

$$I(x) = 2 \int_x^R \frac{i(r) r dr}{(r^2 - x^2)^{1/2}} \quad (1.15)$$

where $i(r)$ is the line emission coefficient, r is the distance in the radial coordinate, and R is the overall radius of the welding arc. Inversion of the above equation allows for removal of the unknown function, resulting in:

$$i(r) = -\frac{1}{\pi} \int \frac{\left(\frac{dI(x)}{dx} \right)}{(x^2 - r^2)^{1/2}} dx \quad (1.16)$$

where $dI(x)/dx$ is the first derivative of the function describing the line emission coefficient in the lateral coordinate, x . Thus, $I(x)$ is the measured quantity, and its derivative can be calculated, so the result of the integral is the line emission coefficient.

With the assumption of partial local thermodynamic equilibrium, researchers attempted to determine the temperature of a welding arc using three methods: 1) Boltzmann-plot method, 2) off-axis peaking (Fowler-Milne) method, and 3) ion-neutral line ratio method [31, 33].

1.6.3.1 The Boltzmann-Plot Method

The ratio of the line emission coefficients emitted by the same type of particles (atoms or ions) is given by the following:

$$\frac{i_i^0}{i_j^0} = \frac{A_i^0 g_i^0 \nu_i^0}{A_j^0 g_j^0 \nu_j^0} \exp\left(-\frac{\Delta \varepsilon_i^0 - \Delta \varepsilon_j^0}{kT}\right) \quad (1.17)$$

In this method the partition function and particle density terms are removed. This equation is only a function of temperature, and no combination with other relationships, such as the Saha ionization equation, is required. This method is considered to be the least accurate of the three methods proposed [29]. Uncertainty in calculated temperatures may come from the exponential term; specifically, the small values associated with the energy difference ($\Delta\epsilon_i^0 - \Delta\epsilon_j^0$). This is due to the fact that particles in the same ionization state will have similar energy values.

1.6.3.2 The Off-Axis Peaking (Fowler-Milne) Method

This method utilizes the maximum volumetric emission coefficient seen at a temperature T^* . The maximum is due to the interaction of the increasing exponential in the volumetric emission coefficient equation and the decreasing particle density as temperature increases at constant pressure. The decrease in particle density is due to the ideal gas law and the decrease of r -times ionized particle ($r = 0$ signifies the neutral state) to $(r + 1)$ -times ionized states by ionization. Ionization fractions of species at temperatures of interest are calculated using the Saha ionization equation. The line emission coefficient ratio of neutral atoms at temperatures T and T^* can be derived from the volumetric emission coefficient equation:

$$\frac{i_j^0(T)}{i_j^0(T^*)} = \frac{\delta_0(T)q_0(T^*)}{\delta_0(T^*)q_0(T)} \exp\left(\frac{\Delta\epsilon_j^0}{k}\left(\frac{1}{T} - \frac{1}{T^*}\right)\right) \quad (1.18)$$

where i is the line emission coefficient calculated using the Abel inversion. There are no terms describing the transition probability or the statistical weight of the states in this equation. For this method to operate properly it is required that the line emission coefficients be measured on the same scale as the maximum line emission coefficient at

T^* . A limitation to this method is that it applies only to spectroscopic processes where the maximum line intensity is measured away from the center of the arc, hence the name.

1.6.3.3 The Ion-Neutral Line Ratio Method

In this method, the arc temperature is determined by taking the ratio of the line emission coefficient of a neutral atom to the line emission coefficient of first ionized atoms of the same element. Ionization fractions of the respective species are determined using the Saha ionization equation. Under the assumption of the Boltzmann distribution, the ratio is a function of the particle densities of the neutral atoms, δ^0 , and the singly ionized atoms, δ^+ , as well as the temperature, T , as can be seen in the following equation:

$$\frac{i_i^+}{i_j^0} = \frac{A_i^+ v_i^+ g_i^+ q^0}{A_j^0 v_j^0 g_j^0 q^+} \delta^+ / \delta^0 \exp\left(-\frac{\Delta\epsilon_i^+ - \Delta\epsilon_j^0}{kT}\right) \quad (1.19)$$

where the indices + and 0 refer to the ionized and neutral atoms, respectively. Indices i and j refer to certain energy states in the ionized and neutral atoms. The line emission coefficient, i , of the respective atoms is calculated using the Abel inversion. Particle densities are determined through use of the Saha [34] ionization equation:

$$\frac{\alpha^2}{1-\alpha^2} \frac{p}{p_0} = \left(\frac{2\pi m_e}{h^2}\right)^{3/2} \frac{(kT)^{5/2}}{P_0} \frac{2q^+}{q^0} \exp\left(-\frac{eV_i}{kT}\right) \quad (1.20)$$

This calculation is performed with the following relation between the particle density ratio of the ion-neutral line ratio method equation and ionization fraction ratio in the Saha ionization equation:

$$\frac{\delta^+}{\delta^0} = \frac{\alpha}{1-\alpha} \quad (1.21)$$

Temperature is determined by solving the combination of Eqs. 1.19 and 1.20. This method requires that the emission coefficients only be measured on the same scale. A relatively large difference in the energy of the states related in this method make this method more accurate than the Boltzmann-plot method.

1.6.4 Temperature Measurements of Welding Arcs

Emission spectroscopy of welding arcs has been performed by a number of researchers. The most common application of emission spectroscopy has been to measure the temperature of GTAW processes. Kobayashi and Suga [35] utilized the ion-neutral line intensity ratio method to determine temperature in their GTAW experiments and found the highest temperature to occur just under the cathode, as seen in Figure 1.15. They reported a maximum temperature of nearly 18,000 K with the welding conditions of 100 amperes, 15 volts, and a 6-mm arc gap. The relationships between arc temperature distribution and process parameters were also examined. It was found that the arc temperature was unaffected by the shielding gas flow rate, but increased proportionally with current, and inversely with voltage [35]. Petrie and Pfender [31] applied spectroscopic temperature determination methods for their study of a process similar to GTAW. Like Kobayashi and Suga, they found the highest temperatures directly under the cathode. Results from their study compared favorably with earlier findings by Wutze. Similar arc gaps were used in Petrie and Pfender's work as Kobayashi and Suga (5.5 mm to 6 mm). However, the peak temperature in their experiments was calculated to be 21,000 K due to the fact that their current was twice that of Kobayashi and Suga [35].

Glickstein [36] reported much lower peak temperatures near the cathode, approximately 11,000 K. Again, the discrepancy resulted from the parameters of the

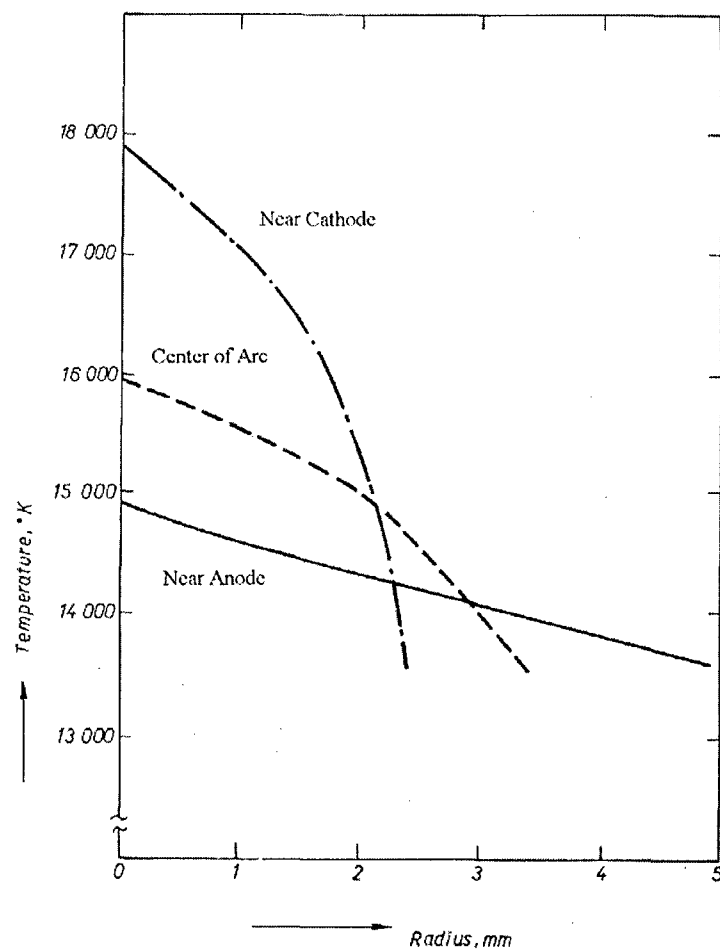


Figure 1.15 Temperature distribution calculated for GTAW process: 100 amperes, 15 volts, and 6-mm arc gap [35].

experiments. Namely, the current and arc gap were both smaller than those used in Petrie and Pfender's work. Glickstein [36] conducted experiments with a current of 100 amperes and an arc gap of 2 millimeters. Temperature distributions calculated by Key, et. al. [33] can be seen in Figure 1.16. An interesting feature of his results is the fact that the highest temperatures were found away from the cathode. This distribution is an unlikely event and was probably due to inaccuracies in his temperature determination method.

Hiraoka, et. al. [37] calculated temperatures of GTAW processes using the off-axis peaking method. They calculated a peak temperature of approximately 18,000 K for a process with 100-A current and a 5-mm arc gap as seen in Figure 1.17a. In addition, Hiraoka also performed hydrogen concentration analysis on argon – 10 pct. hydrogen shielded GTAW processes. He found that hydrogen concentration reached a peak near the cathode, as did the temperature [38]. As seen in Figure 1.17b, hydrogen concentrations reached 30 percent directly under the cathode. Matsushita [29] conducted spectroscopic studies on GTAW processes to analyze hydrogen mitigation by fluorides. Matsushita found similar results for argon-hydrogen shielding gas mixtures, as evidenced in Figures 1.18 and 1.19. In his studies, he found maximum temperatures of 17,000 K directly under the cathode. Hydrogen concentrations in his research were calculated to be as high as 10-percent when shielded with a 1-vol. percent hydrogen shielding gas, also directly under the cathode.

Mills [39] is alone in his suggestion of using different methods for various regions in the arc. He divided the arc into three regions: 1) pure argon plasma near the cathode, 2) metal vapor dominated plasma just above the weld pool, and 3) mixed argon and metal vapor plasma in between. For the pure argon plasma region, it was suggested that a maximum intensity method be used. Near the anode, too much metal vapor would be present. Since the proportions of the vapor mixture are not known, Mills' method can only be used in the pure argon plasma region. For the region in between, the Boltzmann-plot method was recommended. This approach was recommended because in this portion of the arc, the density of the emitting atoms or ions was not known. It is a feature of the

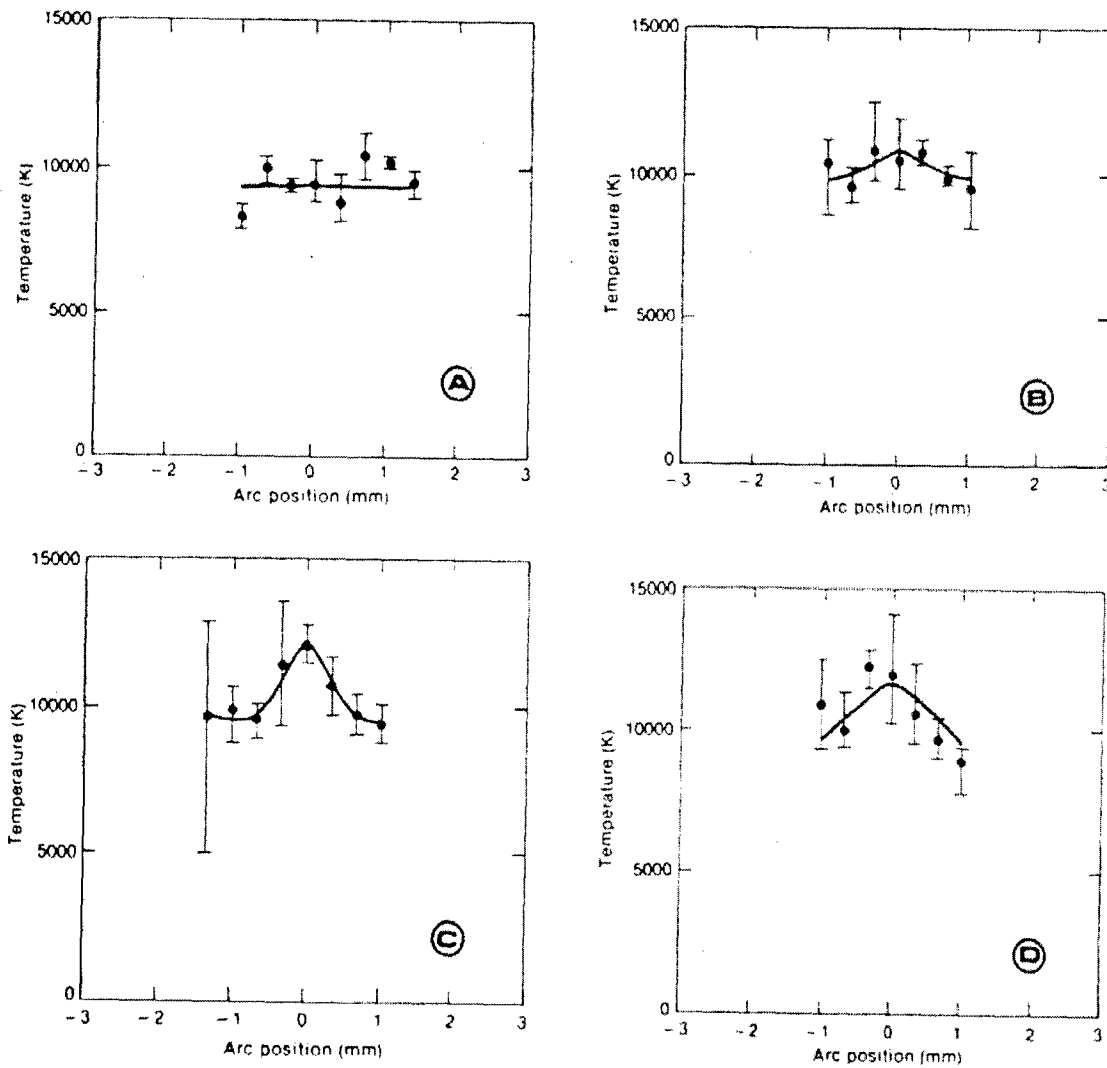
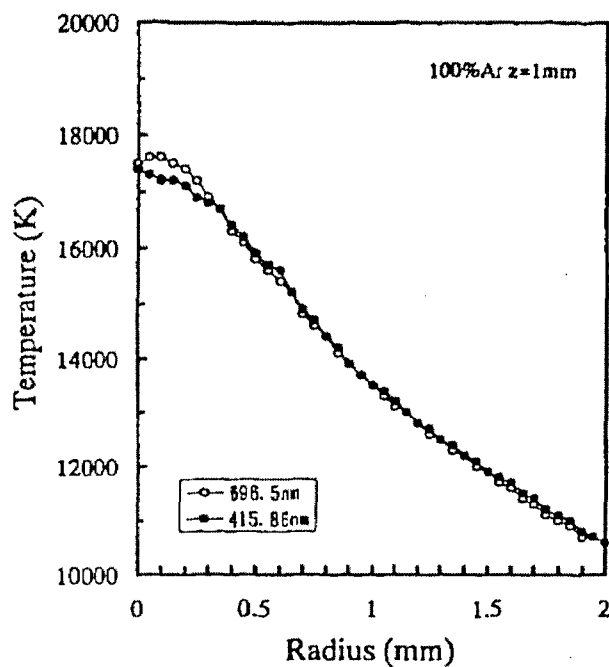
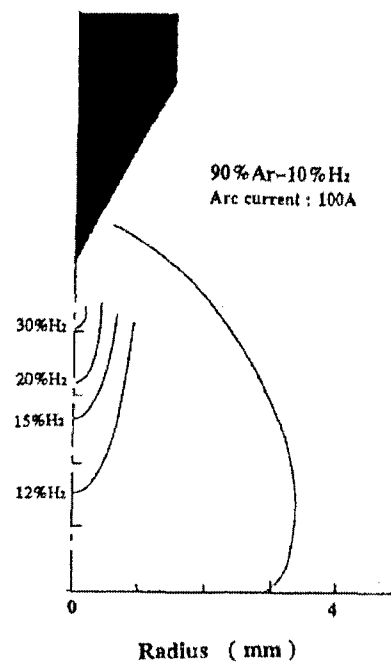


Figure 1.16 Temperature distributions for GTAW process under 100 pct. argon, 150 amperes, 30° vertex angle: (a) 0.25 mm, (b) 0.50 mm, (c) 1.00 mm, and (d) 1.50 mm from cathode [33].



a.)



b.)

Figure 1.17 a.)Radial temperature distribution of 100 pct. argon shielded GTAW process [37] and b.) hydrogen concentration in argon – 10 pct. hydrogen shielded GTAW process [38].

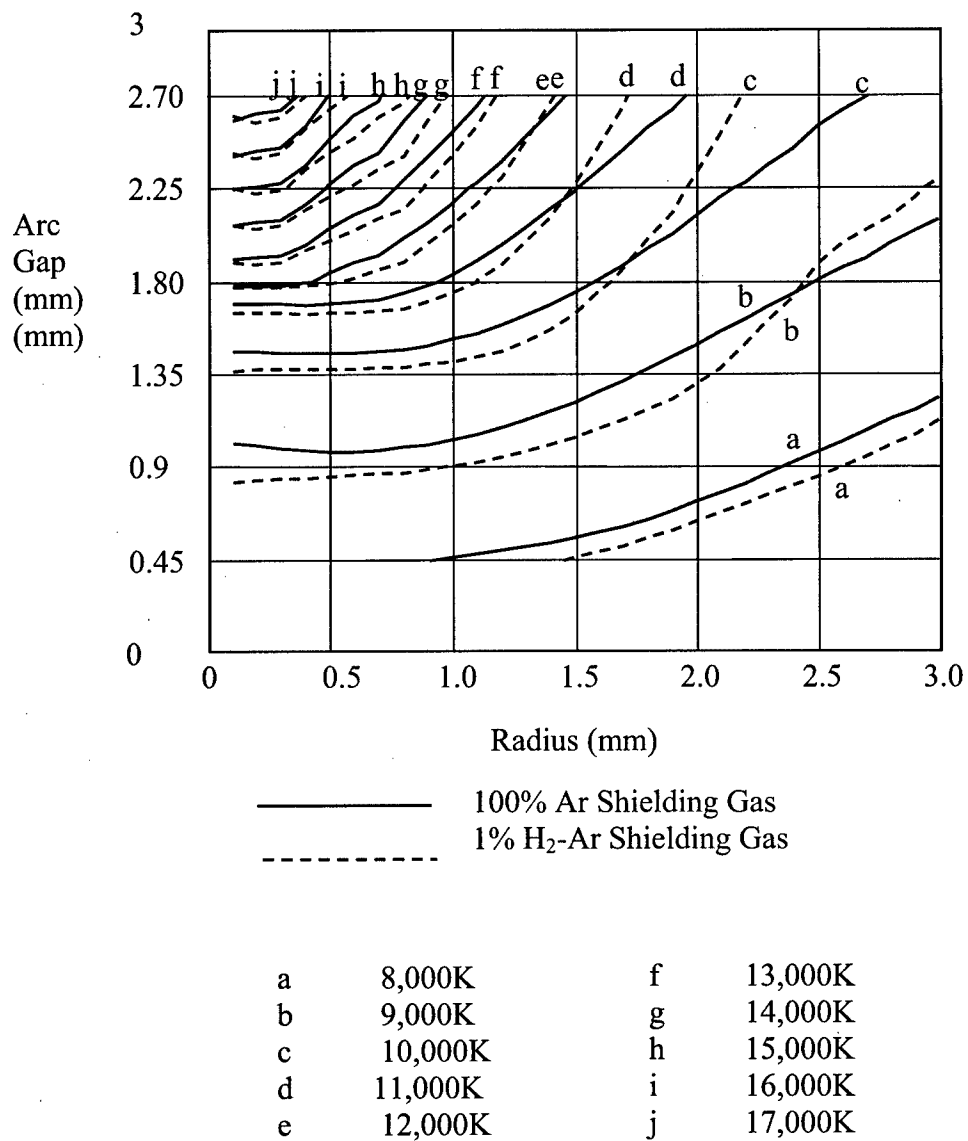


Figure 1.18 Temperature distribution in GTAW process - temperatures for 100 pct. argon and 1 pct. hydrogen-balance argon shielding gases: 3 mm arc gap, 56 amperes [29].

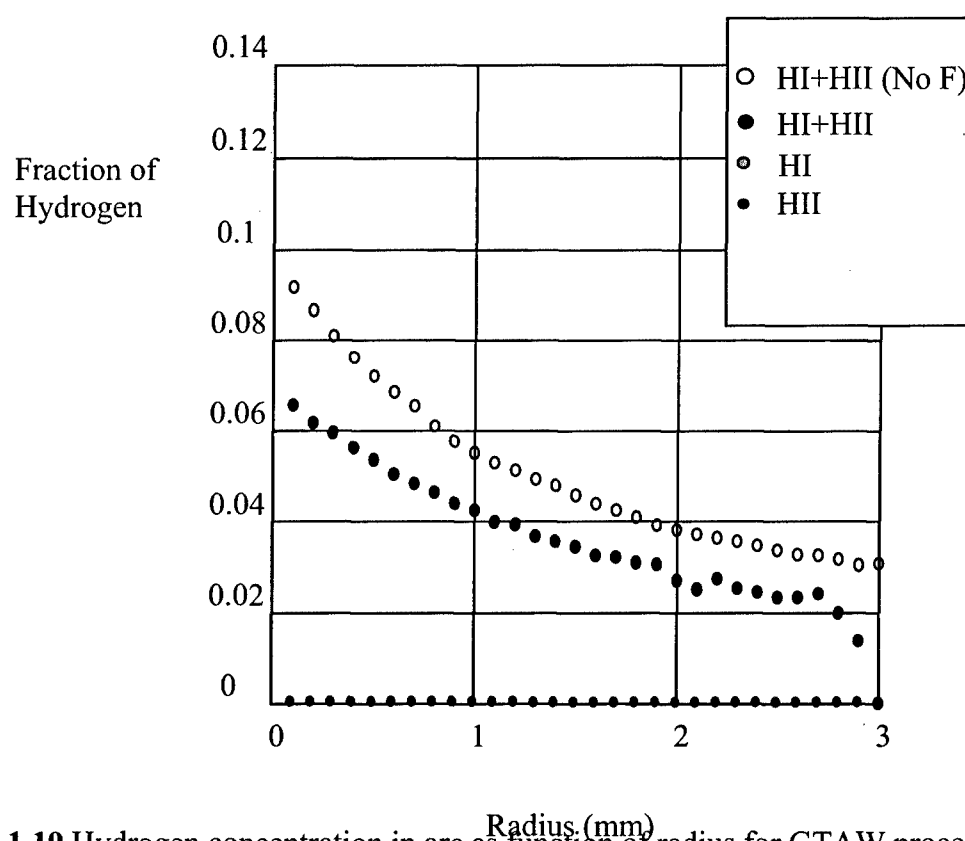


Figure 1.19 Hydrogen concentration in arc as function of radius for GTAW process: 0.45 mm from anode, 1% hydrogen-balance argon, 3 mm arc gap, 90 amperes, calcium fluoride addition [29].

Boltzmann-plot method that the density factors cancel out. Finally, in the metal vapor dominated region it was proposed that the Boltzmann-plot method be used again, since the vapor pressure of elements in the base metal are not known. Mills utilized the emission lines of manganese for his temperature calculations in this region [39].

Shea and Gardner [40] conducted emission spectroscopy analysis on GMAW processes in an effort to correlate hydrogen signal intensity to hydrogen content in the shielding gas. The line intensity of neutral argon at 696.5 nanometers was compared to the line intensity of neutral hydrogen at 656.3 nanometers. They found that hydrogen concentration in the arc could be measured with as little as 10 pct. error for hydrogen concentrations as low as 0.25 pct. by volume [40]. The neutral hydrogen emission line at 486.1 nanometers was disregarded for calculations due to interference of emission lines from the base metal [40]. Weber [41] also noted the same problem with the GMAW process. Weber correlated the intensity of the hydrogen signal to the hydrogen concentration in the arc by using a ratio method like that of Shea and Gardner. However, Weber's ratio included intensity terms for the background level of emission along with the same spectral lines for hydrogen and argon used by Shea and Gardner [40]. White [42] also performed arc emission spectroscopy on GMAW processes in an attempt to describe the behavior of hydrogen in a welding arc. Temperatures of welding arcs with up to two percent of hydrogen in an argon-oxygen shielding were calculated using the Boltzmann-plot method. It was found that the hydrogen additions significantly raised the arc temperature with a partial pressure of just 0.005, but additions beyond that did not further increase the arc temperature considerably. It should be noted that spectroscopy data collected from the welding arcs in this research was done so through a spectrometer probe focused on the entire arc. White [42] reasoned that emissions from the hottest part of the arc would be the most intense and thus dominate the readings collected by the spectrometer. In this manner, it was assumed that the temperatures calculated would tend to be a maximum temperature reached by the arc.

CHAPTER 2

GOAL OF RESEARCH

Despite the many methods available for the mitigation of hydrogen in arc welding of steel, HAC remains a problem. Currently practiced methods of measuring hydrogen content in steel weldments require destruction of the weldment and significant time consumption. A real-time, in-situ method of determining the hydrogen content of a steel weldment would drastically improve productivity in ventures where HAC is a possibility. Arc spectroscopy has been performed in the past to determine temperature and constituent concentration and was found to be a reliable indicator of those quantities. Much of the previous work, though, was performed on GTAW processes. In the pursuit of a process more germane to sponsor concerns, arc emission spectroscopy of GMAW processes was undertaken. The objective of this research project was to explore the capability of arc spectroscopy as a non-intrusive real-time method of hydrogen determination in high strength steel weldments. This involved spectroscopic evaluation of GMAW processes with hydrogen additions to argon shielding gas in concentrations of 220 parts-per-million, 1-vol. percent, and 3-vol. percent. The hydrogen content of the weldments deposited under those shielding gases were determined and correlated to hydrogen activity detected in the welding arc using spectroscopy. In addition, hydrogen activity in the arc due to moisture in the shielding gas and rust on the wire consumable was investigated.

CHAPTER 3

EXPERIMENTAL METHODS

3.1 Arc Generation System – Power Supply and Consumables

The welding arc studies were conducted using a Miller Nirvana welding machine; a 60M series CC/CV power supply. Within the course of this research project, four phases of experiments were performed to investigate the abilities of the spectroscopy system. In the first and second phase, the welding consumable held little importance on the goal of the research other than to provide weld metal for analysis. Thus, a general commercial wire consumable sufficed. An ESAB ER70S-3 consumable with a 0.045-inch (1.14 mm) diameter was used in that phase of research. The third phase of research investigated the ability of the spectroscopic equipment to detect alloying elements in the arc utilized experimental wires manufactured by another researcher in the Center for Welding, Joining, and Coatings Research. Flux-cored wires containing known amounts of ferromanganese (FeMn) were used. The sheath of the wire was composed of mild steel and the second core ingredient was iron powder. Manufacture of the wires was performed using the tube mill facilities in Hill Hall at the Colorado School of Mines. Diameter of the experimental wires was 0.060 inches (1.52 mm). The fourth and final phase of research was undertaken to determine the ability to detect hydrogen in the arc resulting from impurities on the wire, namely rust. For this portion of the research, a HSLA steel wire consumable with 0.0625-inch (1.59 mm) diameter was used. Prior to welding, the wire was cleaned of any oxidation using abrasive pads. Portions of wire were then placed in an environmental chamber for four days in air at 33 °C with 85-pct. relative humidity. The rust engendered on the consumable can be seen in Figure 3.1. Parameters for the welding processes can be seen in Table 3.1.

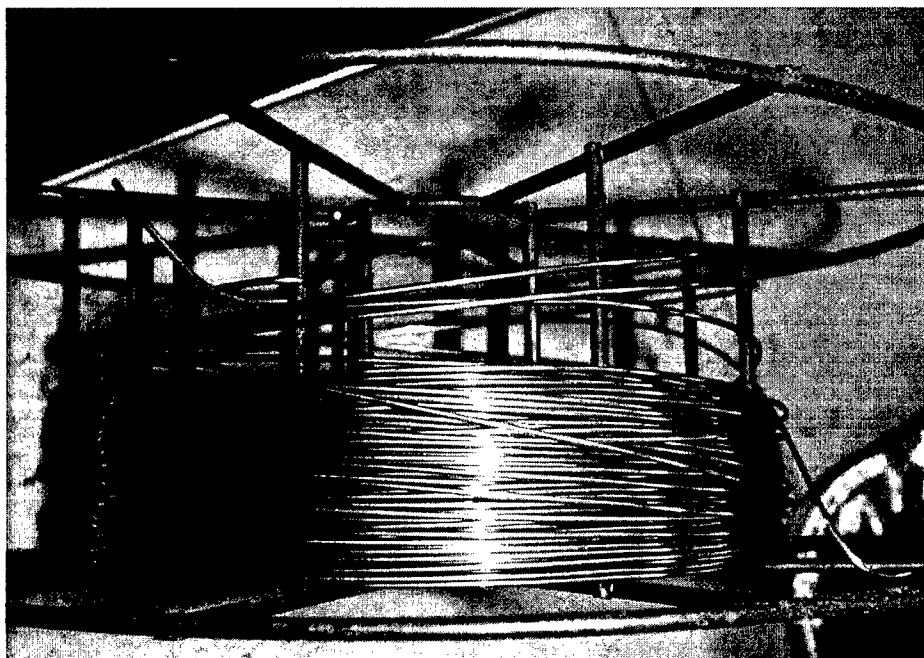


Figure 3.1 Photograph of HSLA steel consumable after rust formation.

Table 3.1. Parameters for welding processes performed during this research project.

Shielding Gas	Voltage (V)	Feed Rate (ipm)	Travel Speed (mm/s)	Gas Flow Rate (cfh)	Work Distance (mm)
Argon	27	250	6.25	40	22
Argon + 1 % Hydrogen	32.6	270	6.25	40	22
Argon + 3% Hydrogen	33	280	6.25	40	22
Argon + 220 ppm Hydrogen	30	300	6.25	40	22
Argon + 220 ppm Moisture	30.5	310	6.25	40	22
Argon	28	280	6	40	22
Argon	34.2	330	6.25	40	22

3.2 Spectroscopy Equipment

In order to make measurements of the light emitted from a welding arc, an apparatus was devised to magnify the arc and allow for discretion of the arc region studied. A schematic diagram of the equipment can be seen in Figure 3.2, and photographs of the setup can be seen in Figure 3.3. A shield constructed of sheet steel was placed next to the arc. An aperture was drilled into the shield to allow for the arc light to travel to the spectrometer probe. The shield served to limit the amount of light traveling to the spectrometer and also to protect the lens and filters from errant sparks and spatters emitted from the welding process. A high temperature polymer shield was placed between the steel shield and the lens/filter assembly. Its function was to protect the lens and filters from any sparks or spatters that went through the aperture in the steel shield. The lens used to magnify the arc was a 30 mm double convex polymer lens. Neutral density filters were utilized during this research for the purpose of attenuating the light signal emitted from the arc. A piece of plywood served as a screen onto which the image of the arc was projected. The probe of the spectrometer was situated into a hole drilled into the center of the screen. Slots were cut into the screen to allow for screen and probe height articulation. Since the image of the arc remained at a constant height, the probe height could be maneuvered to various regions of the arc. Thus, studies could be made of the light emitted from the various regions in the arc.

The welding process was performed on A36 steel diffusible hydrogen samples. In accordance with the standard AWS/ANSI A4.3-93: *Standard Methods for Determination*

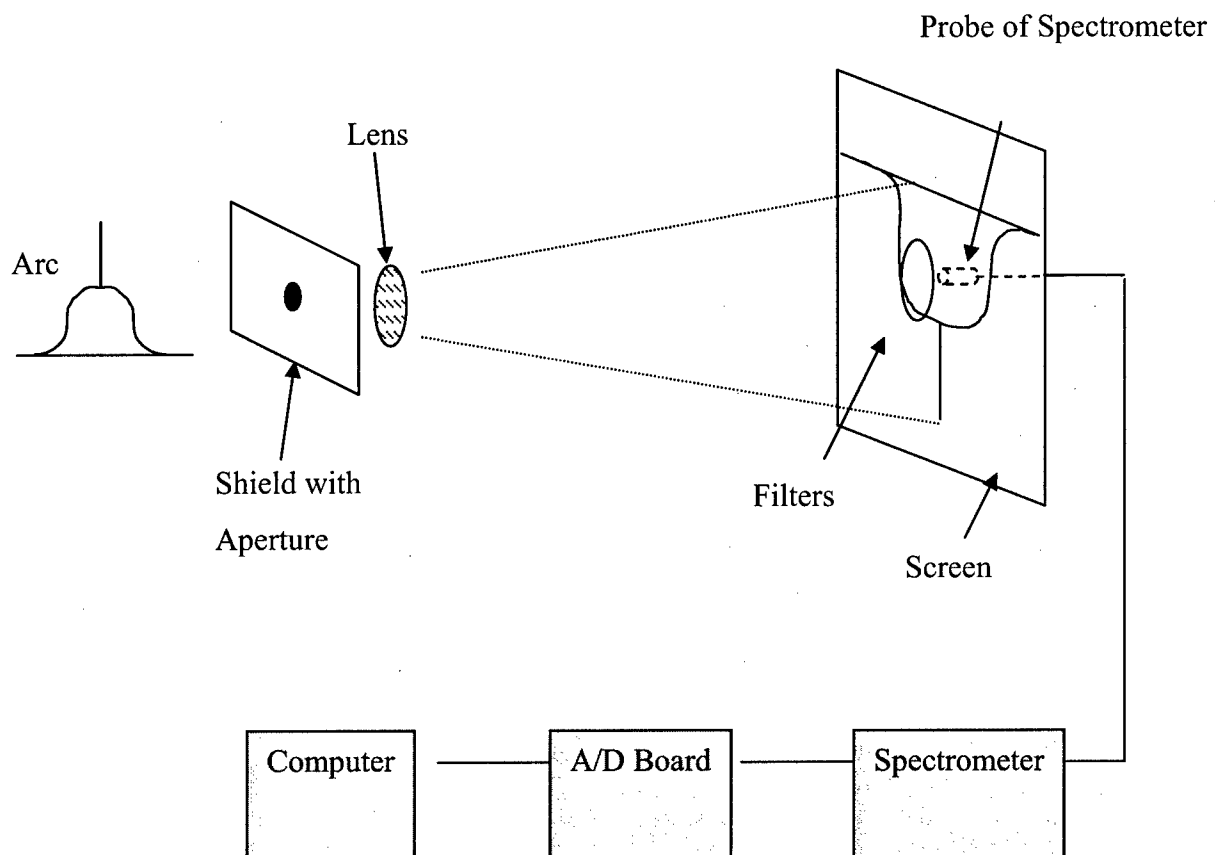


Figure 3.2 Schematic representation of spectroscopic data collection setup.

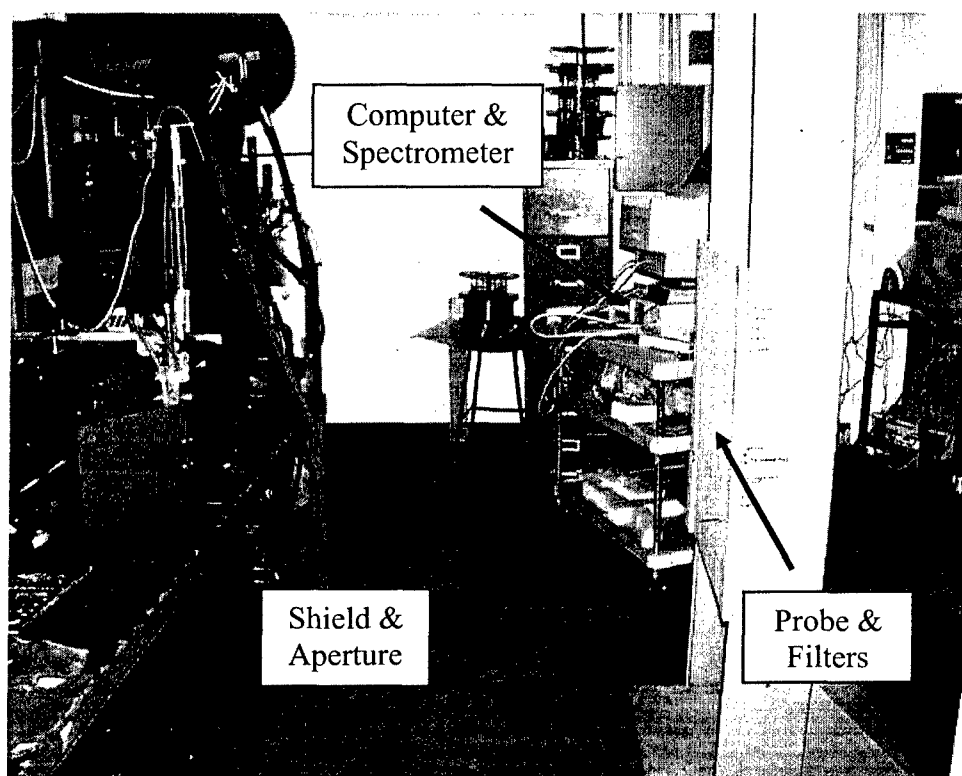


Figure 3.3 Photograph of spectroscopic data collection setup.

of the Diffusible Hydrogen Content of Martensitic, Bainitic, and Ferritic Steel Weld Metal Produced by Arc Welding [26], the diffusible hydrogen coupons were clamped in a machined copper block.

3.3 Spectrometer Details

The probe of the spectrometer used in this research can be seen in Figure 3.4. Within the probe was a collimating lens 5 millimeters in diameter. Light data were transmitted to the spectrometer via a fiber optic cable. Once it reached the spectrometer, the light was dispersed by a fixed grating and shone across a linear CCD array detector. The array detector contained 2048 elements reactive to light in the wavelength range of

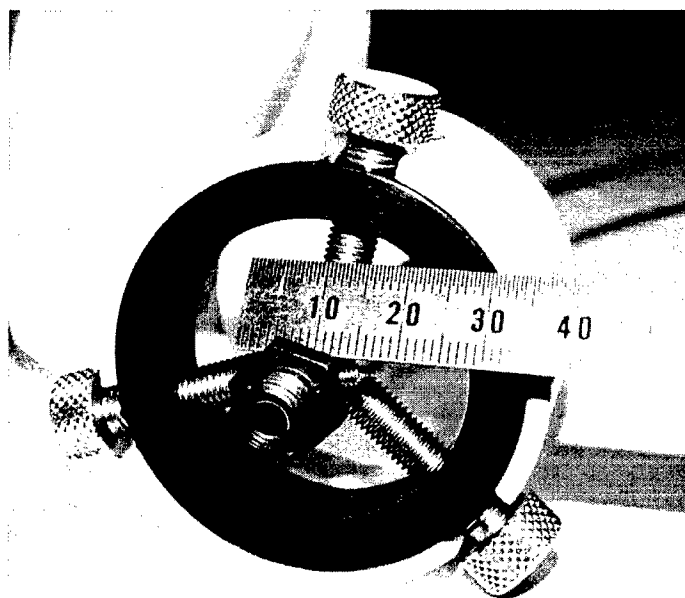


Figure 3.4 Photograph of spectrometer probe used in this research. Demarcations on ruler in photograph are millimeters.

200 nanometers to 1100 nanometers. Resolution in the spectrometer was about 0.5 nanometers. The spectrometer used for the light collection was a Model S2000 fabricated by Ocean Optics Inc. Information read by the spectrometer was converted by an analog-to-digital converter and then collected by a customized Labview application. Data was acquired every 100 milliseconds and stored on disk for later processing.

3.4 Shielding Gases

Shielding gases used for this research were chosen for the purpose of testing the ability of the spectroscopic equipment to determine the differences in the arc behavior. The parameters for the welding processes can be seen in Table 3.1. As the hydrogen content increased, the parameters needed adjustment to stay in spray metal transfer mode. This requirement will be discussed in more detail later in this report. Increasing the amount of hydrogen in the arc increased the arc resistance. This increase in resistance occurs because the arc must dissociate the hydrogen molecules before ionizing them to create the electric arc between the electrode and the workpiece. Shielding gases with 220 ppm each of hydrogen and moisture were ordered specially from a local gas distributor and each required their own sets of parameters for welding.

3.5 Diffusible Hydrogen Measurement

Measurement of the diffusible hydrogen content of the welded samples was performed in accordance with the AWS standard mentioned previously [26]. In this method, a weldment is produced across three steel tabs that have been degassed, cleaned, and weighed. The tabs are kept free of any contaminants until time of welding. A copper block is used to clamp the tabs together during welding and acts as a uniform chill block. Immediately upon termination of the welding process, the tabs are quenched in ice water

and then placed in a low-temperature bath to inhibit hydrogen release from the sample. It was mandated by the standard that the weldment be inserted into the ice bath within five seconds after the arc was extinguished. After thirty seconds of quenching, the weldment was placed in the low-temperature bath. Once in the low-temperature bath, the samples were not allowed to remain out of the bath for any longer than one minute until their placement in the degassing vessels. After post-weld cleaning and tab separation, the middle tab is degassed in a pressure vessel and the hydrogen content of the atmosphere in that vessel is measured. Degassing time-temperature combinations are prescribed by the standard to provide the same amount of diffusion. The time temperature combination used in this project was 150°C for six hours. The degassing vessel used in this project can be seen in Figure 3.5. A removable cap on one end of the vessel allowed for insertion of the sample into the vessel. Once the sample was placed into the vessel, a commercial silicone gasket sealer was used to seal the threads of the vessel's cap. Valves on each end allowed for pressurization of the vessel. On one end of each vessel was an assembly containing two rubber septums.

Samples of the gas in the vessel were taken using a syringe inserted through the septums. An atmosphere of argon was engendered in each vessel up to a gage pressure of ten psi. One milliliter of helium was introduced into each vessel with a syringe. Helium served as an internal standard when the gaseous contents of the vessel were measured with the gas chromatograph. The gas chromatograph was programmed to measure both the helium and hydrogen content of the sample gas inserted into the machine. It was assumed that the amount of helium lost in the degassing operation was directly proportional to the amount of hydrogen lost.

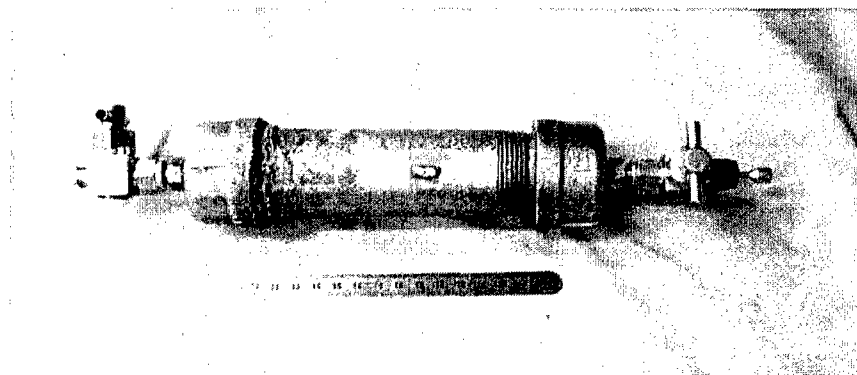


Figure 3.5 Photograph of degassing vessel used in this research.

3.6 Residual Hydrogen Content

The residual hydrogen content was measured using a hydrogen analyzer manufactured by LECO, which can be seen in Figure 3.6. Before an analysis, at least three calibration runs were performed. Steel sample standards with known hydrogen content were examined using the analyzer. The hydrogen content readings were then entered into the computer controller, which then calculated a new calibration factor. Analysis began by placing a graphite crucible on the lower electrode. The furnace was closed and the atmosphere was purged. A current was passed through the crucible to drive off any impurities or gases in the crucible, then, after a short cooling period, the sample was dropped into the crucible. High current was passed through the crucible to drive off the gases in the sample. Hydrogen emitted from the sample mixed with an argon gas stream and was passed through a series of filters that removed oxygen, carbon dioxide, water, and other undesirable materials. After filtering, the gas stream traveled through a molecular sieve where hydrogen was separated from the rest of the stream. Once the separation process was completed, the hydrogen content was detected using a thermal conductivity detector. An integration of the hydrogen level was taken over time resulting in a hydrogen reading for the sample.

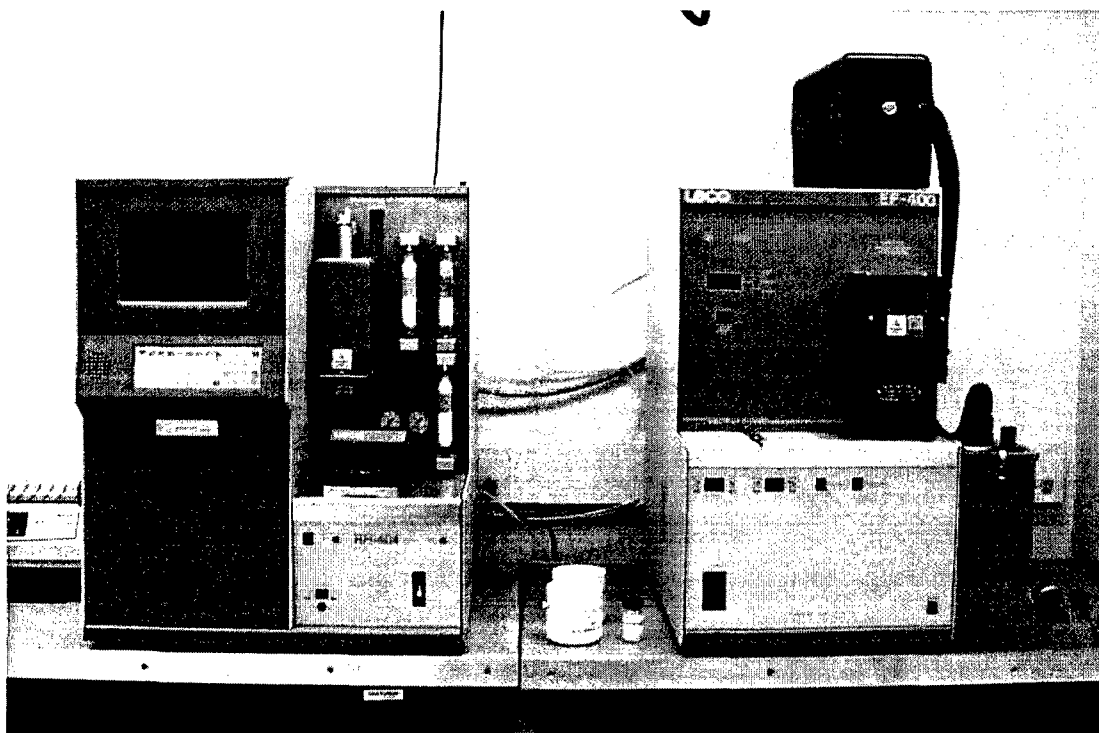


Figure 3.6 Photograph of LECO hydrogen determination equipment at the Colorado School of Mines used for residual hydrogen measurement in this research.

For all residual hydrogen measurements, samples of approximately one gram from the weldments were required. Milling the weldments down and collecting the machining chips to use for analysis accomplished this task. A picture of the samples after milling can be seen in Figure 3.7. Particular attention was paid to the speed of the milling process. Neither the travel speed of the milling tool nor its rotational speed was such that the friction of the process generated noticeable heat in the sample. This process was done to ensure that no hydrogen was introduced into the sample (nor desorption of hydrogen from the traps because of heating) during the process, which would result in spurious

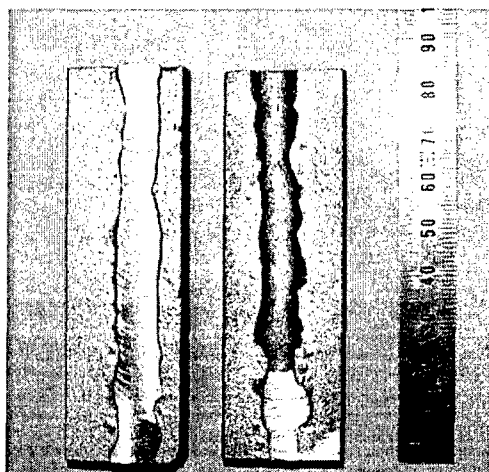


Figure 3.7 Photograph of milled sample (left) and sample in process of being milled for residual hydrogen analysis.

measurements during analysis. In addition, the machining chips were never handled with bare hands. Chips were collected with a clean brush and stored in polymer bags. To analyze the hydrogen content of the chips, the chips were placed into the analyzer crucible one gram at a time using forceps.

3.7 Data Acquisition

Spectroscopic data were obtained using the apparatus seen in Figure 3.8. Scans were taken at heights of 2, 4, and 6 millimeter above the baseplate, as illustrated in Figure 3.9. Radiation emitted from the welding arc was scanned in the lateral direction as the

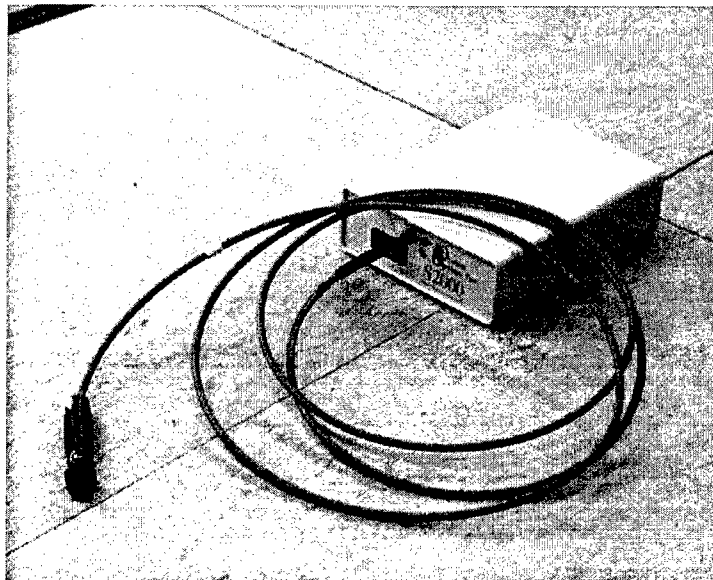


Figure 3.8 Photograph of spectrometer with probe attached.

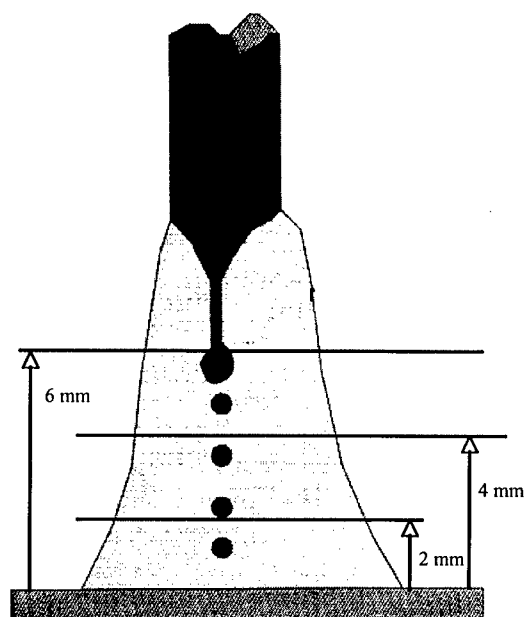


Figure 3.9 Illustration depicting scan heights during experiments.

welding torch passed the aperture. Typical arc lengths in this research were approximately eight millimeters. The spectrometer records 2048 data points every 100 milliseconds, and the data points cover the wavelength range of the spectrometer. Experimental data is put into a matrix form, whereby the 2048 data points are the rows and the columns are the time increments. A scan was initiated with the arc during each trial. During data analysis the peak of the intensity of a spectral line was considered to be the center of the arc. Thus, all spectroscopic measurements were calculated outward from the center. Since the cart carrying the torch traveled at a constant speed, the time increments can be considered distance increments as well.

3.8 Identification of Spectra for Arc Elements

Spectral lines of interest were found in the CRC Handbook of Chemistry and Physics 84th Annual Edition [43]. The degrees of the ionization of elements are indicated as I for the neutral species, II for the first ionized species, III for the second ionized species, etc., which follows the spectroscopic nomenclature. For example, emissions from neutral argon atoms are identified as ArI, emissions from singly ionized argon atoms are identified as ArII, emissions from doubly ionized argon atoms are identified as ArIII, etc.

3.9 Smoothing Measured Intensity

An example of acquired data and its smoothed form is shown in Figure 3.10. A graph of the line emission coefficient of a GMAW process under 100-pct. argon gas as a function of time is shown. To provide a better fit for later processing, the acquired data was smoothed. All data processing was performed using the computer program Mathcad 2000. The smoothing operation used an adaptive point averaging method. Data were

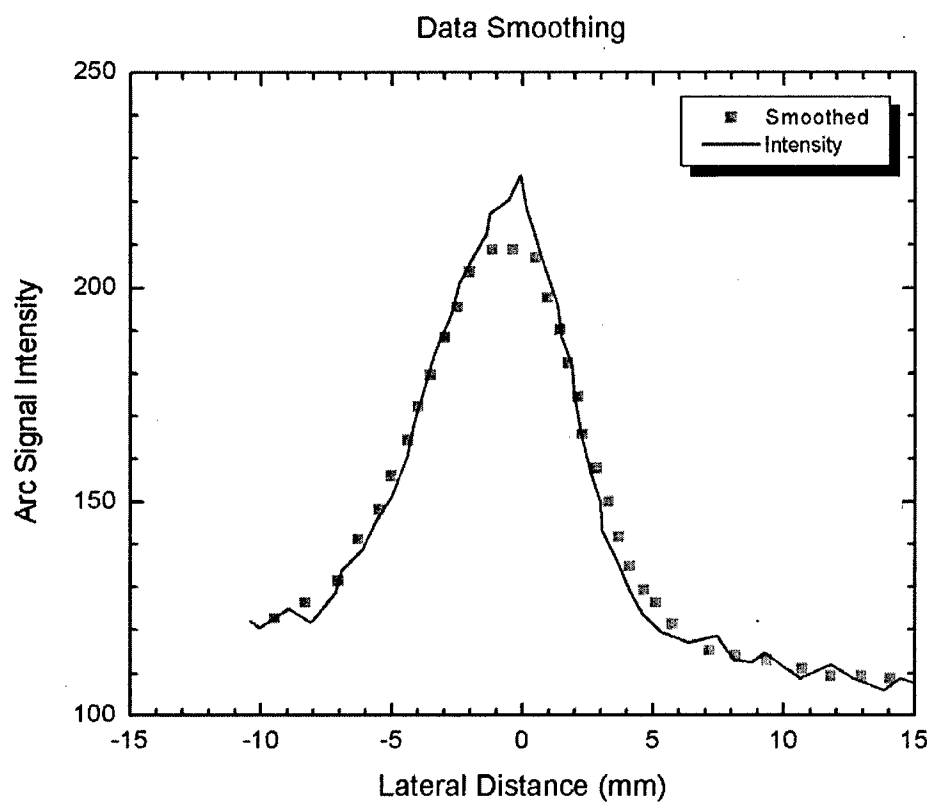


Figure 3.10 Depiction of acquired data and the smoothing operation performed for data analysis.

averaged over the number of points that provided the best fit to the acquired data. For example, in a six-point averaging method, a particular data point's value was the average of the three previous points and the following three points. In the method used in this research, the program ran iterations for each point to determine the optimal range of data points over which to average the value. The six-point averaging method was used by Matsushita, who studied spectroscopy of a GTAW process [29]. Due to the increased travel speed of the GMAW process studied in this research, fewer data points were gathered during each run, since the spectrometer sampling rate remained the same. The six-point averaging method was deemed to engender too large a deviation from the acquired data.

3.10 Cubic Spline Curve

To reconcile the fact that two-dimensional spectroscopic data were obtained from a three-dimensional object, the arc, the Abel inversion was used. This operation converts the line emission coefficient into the radial emission coefficient; expressed as:

$$i(r) = -\frac{1}{\pi} \int_r^{R_r} \frac{dI(y)/dy}{(y^2 - r^2)} dy \quad (1.9)$$

In the above equation, $dI(y)/dy$ is the first derivative of the function of the line emission coefficient in the lateral direction, y . To fit a function to the data, a Mathcad operation was performed that fitted a cubic spline curve to the data. This operation involved fitting a curve of cubic order between the individual points in the curve. The Mathcad program for this operation can be found in the Appendix.

3.11 Temperature Determination

Using the radial emission coefficient obtained with the previous methods, the temperature of the arc can be determined. Temperature calculations were determined as functions of the arc radius. Three methods were attempted to determine the temperature of the arc.

3.11.1 Boltzmann-Plot Method

As detailed in Section 1.6.3.1, the Boltzmann-Plot method utilizes the ratio between two line emission coefficients of the same species in the same ionization stage to the temperature. The relation is as follows:

$$\frac{i_i^0}{i_j^0} = \frac{A_i^0 g_i^0 \nu_i^0}{A_j^0 g_j^0 \nu_j^0} \exp\left(-\frac{\Delta \varepsilon_i^0 - \Delta \varepsilon_j^0}{kT}\right) \quad (1.10)$$

Missing are the coefficients of the neutral states and the partition function. Thus, in this method, the temperature can be directly determined from the above equation.

The temperatures resulting from this method were found to be unreasonably high and displayed significant statistical variance. A similar conclusion was reached by Matsushita regarding this method [29]. It was proposed that the energy difference between the excitation stages in the same species would be quite small, thereby allowing error in the other terms of the equation to predominate. With the ultimate goal of incorporating a real-time hydrogen content monitor into the welding process, this method was desirable due to its simplicity. However, the results it provided were not satisfactory. Since the determination of the concentration of elements in the arc relies on the temperature determination, a significant uncertainty in the temperature readings will lead

to significant uncertainty in the concentration determination. Thus, this method was deemed unsuitable for application to the process.

3.11.2 Off-Axis Peaking Method

This method utilizes the maximum of the line emission coefficient at a temperature T^* . In GTAW processes, a peak was exhibited due to the decrease in r -times ionized particle ($r = 0$ indicates neutral state) by ionization to $(r + 1)$ -times ionized states. The temperature for the maximum emission is determined through the following combination of the radial emission coefficient and the Saha equation:

$$i(T) = \frac{1}{4\pi} \frac{A_{ij} h \nu_{ij} g_i}{q} \delta \exp\left(-\frac{\Delta \varepsilon_i}{kT}\right) = \frac{1}{4\pi} \frac{A_{ij} h \nu_{ij} g_i}{q(T)} (1 - \alpha(T)) n \exp\left(-\frac{\Delta \varepsilon_i}{kT}\right) \quad (3.1)$$

The equation is only a function of temperature. Once the temperature at the maximum emission point is determined, the radial radiance and temperature at that point are substituted into the following equation to determine the temperature at other positions.

$$\frac{i_j^0(T)}{i_j^0(T^*)} = \frac{\delta_0(T) q_0(T^*)}{\delta_0(T^*) q_0(T)} \exp\left(\frac{\Delta \varepsilon_j^0}{k} \left(\frac{1}{T} - \frac{1}{T^*}\right)\right) \quad (1.11)$$

Previous GTAW spectroscopy research found this to be the most accurate method of determining temperature. However, during the course of this GMAW research, it was found that the line emission coefficient data did not exhibit a peak away from the center axis of the arc. The dynamics of the consumable electrode differentiated this research from the previous research projects. Transfer of metal droplets from the electrode to the

weld pool and the increased travel speed were the most likely reasons for not observing the offset peak.

3.11.3 Ion-Neutral Line Ratio Method

The ion-neutral line ratio method operates by comparing the ratio of radial emission coefficients of ionized atoms to neutral atoms of the same species, as seen in the following equation:

$$\frac{i_i^+}{i_j^0} = \frac{A_i^+ v_i^+ g_i^+ q^0}{A_j^0 v_j^0 g_j^0 q^+} \delta^+ / \delta^0 \exp\left(-\frac{\Delta\epsilon_i^+ - \Delta\epsilon_j^0}{kT}\right) \quad (1.12)$$

The ratio of first-ionized species to neutral species within the above equation is combined with the ratio calculated by the Saha equation:

$$\frac{\alpha^2}{1-\alpha^2} \frac{p}{p_0} = \left(\frac{2\pi m_e}{h^2}\right)^{3/2} \frac{(kT)^{5/2}}{P_0} \frac{2q^+}{q^0} \exp\left(-\frac{eV_i}{kT}\right) \quad (1.13)$$

Thus, the ratios between the two equations must be related to solve the combined equation for temperature. In the ion-neutral line ratio equation, the ratio between the two ionization states is described as a ratio of particle densities (δ^+ / δ^0); in the Saha equation the ratio is described as an ionization fraction (α). Assuming an initial neutral particle density of n and a fraction of first-ionized species of α compared to neutral species, then, according to the law of mass action, the particle densities of the first ionization products will be those seen in Table 3.2.

Table 3.1. Particle density changes due to ionization.

	δ^0	δ^+	δ^{++}	δ_e
Initial	n	0	0	0
First Ionization	$(1-\alpha) n$	αn	0	αn
Second Ionization	$(1-\alpha) n$	$\alpha (1 - \beta) n$	$\alpha \beta n$	$\alpha n + \alpha \beta n$

Where: δ^0 = Particle density of neutral species,
 δ^+ = Particle density of first-ionized species,
 δ^{++} = Particle density of second-ionized species,
 δ_e = Particle density of electron,

Assuming the fraction of second-ionized species is β with regard to the first-ionized species, the particle densities of the first and second ionization products are as follows:

$$\delta^0 = (1 - \alpha) n \quad (3.2)$$

$$\delta^+ = \alpha (1 - \beta) n \quad (3.3)$$

$$\delta^{++} = \alpha \beta n \quad (3.4)$$

where δ^0 , δ^+ and δ^{++} are the particle densities of the neutral, first-ionized and second-ionized species, respectively. With these relationships established, the ratios from the two equations can be related in the following manner:

$$\frac{\delta^+}{\delta^0} = \frac{\alpha(1-\beta)}{1-\alpha} \quad (3.5)$$

Ionization fractions α and β are determined using the Saha equation and related to the particle densities via the equations just described.

To solve the two equations for the temperature, the ion-neutral line ratio equation can be rearranged to isolate the particle density ratio:

$$\frac{\delta^+}{\delta^0} = \frac{i_i^+}{i_j^0} \frac{A_j^0 \nu_j^0 g_j^0 q^+}{A_i^+ \nu_i^+ g_i^+ q^0} \exp\left(-\frac{\Delta\epsilon_i^+ - \Delta\epsilon_j^0}{kT}\right) = f_{ion-neutral}(T) \quad (3.6)$$

Utilizing the relation between the ion-neutral line ratio equation and the Saha equation established in Eq. 3.5, it can be seen that the ionization fraction ratio is also a function of temperature:

$$\frac{\delta^+}{\delta^0} = \frac{\alpha(1-\beta)}{1-\alpha} = f_{Saha}(T) \quad (3.7)$$

Thus, the temperature can be found by solving the following equation:

$$f(T) = f_{ion-neutral}(T) - f_{Saha}(T) = 0 \quad (3.8)$$

This equation was solved by performing an iterative analysis in Mathcad. The program for this operation can be found in the Appendix. A temperature was achieved by: 1) programming a set of boundary temperatures within which the true temperature must reside, 2) directing the program to substitute a “guess” temperature, and 3) adjusting

its next iteration by the result produced. The final value was obtained once the two values, the “guess” and the “result” temperature, coincided. This method is known as the secant method.

Since argon constituted the major volume fraction of the shielding gases used in this research, the argon lines were used to calculate the temperature of the arc. In particular, the neutral argon line at 696.5 nanometers and the argon ionization line at 476.4 nanometers were used to calculate temperature. A disadvantage to this method of temperature determination is its accuracy. Matsushita found this temperature to be somewhat higher than that found by the off-axis peaking method [29]. Also, the noise in the spectrometer tends to cause the temperature readings to flatten out as the radius increases. In other words, the outer regions seem to have an unnaturally high temperature associated with them. Thus, temperature readings at the peripheries at the arc should be disregarded. A great advantage to this method, however, is that the intensity of the spectral lines need only be measured on the same scale. This method relies on the ratio of the spectral lines to one another, thus readings on an absolute scale are not required.

Due to the inapplicability of the off-axis peaking method and the scatter and inaccuracy of the Boltzmann-plot method, the ion-neutral line ratio method was chosen for temperature determination in this research. The Mathcad program for the temperature determination using the ion-neutral line ratio method can be viewed in the Appendix.

3.12 Concentration Determination

The concentration of the elements present in the welding arc was calculated using the ratio of the spectral intensity of the neutral species of a particular element to the spectral intensity of neutral argon. Concentrations were calculated with the following equation:

$$\frac{i_{i[M]}^0}{i_{j[Ar]}^0} = \frac{A_{i[M]}^0 \nu_{i[M]}^0 g_{i[M]}^0 q_{i[M]}^0}{A_{j[Ar]}^0 \nu_{j[Ar]}^0 g_{j[Ar]}^0 q_{j[Ar]}^0} \frac{\delta_{i[M]}^0}{\delta_{j[Ar]}^0} \exp\left(-\frac{\Delta \varepsilon_{i[M]}^0 - \Delta \varepsilon_{j[Ar]}^0}{kT}\right) \quad (3.9)$$

In the above equation, the superscripted 0 indicates a neutral ionization state, and subscripts i and j represent arbitrary excitation stages in respective species. The subscript [M] is the element of interest and [Ar] is neutral argon. Radial emission coefficients of the elements of interest were placed in the equation along with the temperatures calculated by the ion-neutral line ratio method. With these substitutions, particle density ratios with respect to neutral argon were obtained. The Saha equation was employed to find ionization fractions using the determined temperature. The ratios of the first and second-ionized species to that of the neutral species are as follows:

$$\frac{\delta_{i[M]}^+}{\delta_{i[M]}^0} = \frac{\alpha_{i[M]}(1 - \beta_{i[M]})}{1 - \alpha_{i[M]}} \quad (3.10)$$

$$\frac{\delta_{i[M]}^{++}}{\delta_{i[M]}^0} = \frac{\alpha_{i[M]} \beta_{i[M]}}{1 - \alpha_{i[M]}} \quad (3.11)$$

First and second-ionized argon could be calculated in the above manner. For the first and second-ionized species of other elements, modifications were needed. Particle density ratios from Eq 3.9 were combined and the first and second-ionized species are related to neutral argon in the following manner:

$$\frac{\delta_{i[M]}^+}{\delta_{j[Ar]}^0} = \frac{\alpha_{i[M]}(1 - \beta_{i[M]})}{1 - \alpha_{i[M]}} \frac{\delta_{i[M]}^0}{\delta_{j[Ar]}^0} \quad (3.12)$$

$$\frac{\delta_{[M]}^{++}}{\delta_{[Ar]}^0} = \frac{\alpha_{[M]} \beta_{[M]}}{1 - \alpha_{[M]}} \frac{\delta_{[M]}^0}{\delta_{[Ar]}^0} \quad (3.13)$$

Using these relationships between the various species, the particle densities of all the elements in the arc can be expressed as a ratio to the particle density of neutral argon. Concentrations of argon and the other elements in the arc can be conveyed as:

$$C_{[Ar]} = \frac{1 + R_{[Ar]}^+ + R_{[Ar]}^{++}}{1 + R_{[Ar]}^+ + R_{[Ar]}^{++} + R_{[M_1]}^o + R_{[M_1]}^+ + R_{[M_1]}^{++} + \cdots + R_{[e]}^{++}} \quad (3.14)$$

$$C_{[M_1]} = \frac{R_{[M_1]}^o + R_{[M_1]}^+ + R_{[M_1]}^{++}}{1 + R_{[Ar]}^+ + R_{[Ar]}^{++} + R_{[M_1]}^o + R_{[M_1]}^+ + R_{[M_1]}^{++} + \cdots + R_{[e]}^{++}} \quad (3.15)$$

In the above equations R is the ratio of particle density of the bracketed species to neutral argon, and M_1 and e are the constituent elements of the arc other than argon and electrons, respectively. As the number of elements in the arc increase, M_n will be added (where $n = 1, 2, 3 \dots$).

CHAPTER 4

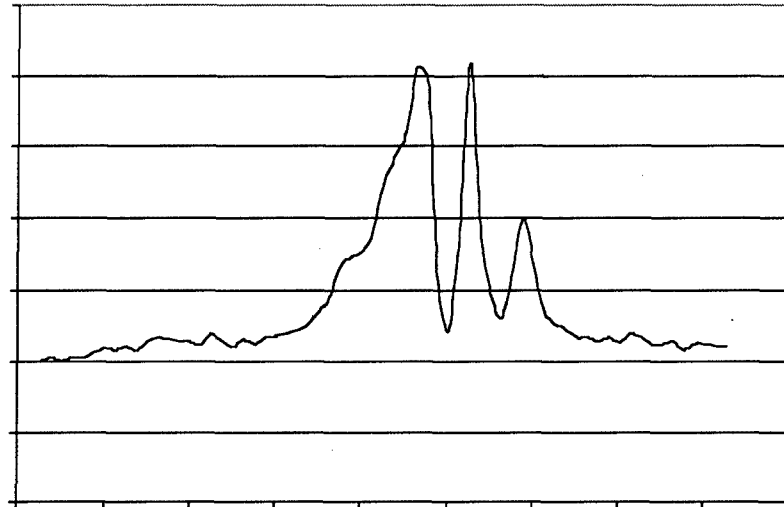
RESULTS AND DISCUSSION

4.1 Observations in GMAW

4.1.1 Metal Transfer Mode

During the initial stages of this research project, it was discovered that the metal transfer mode played a major role in the quality of the data collected. Accurate spectroscopic analysis of a welding arc in this research required a sustained observation of light emitted from the welding arc. Temperature and concentration determinations involved the integration of wavelengths of light over time. Thus, any significant perturbation in the intensity of emitted light over time renders the analysis unsuitable. A welding process that exhibits short-circuiting metal transfer mode is just such an example. As can be seen in Figure 4.1a, the light data collected from a welding process in short-circuiting transfer does not provide a continuous curve that would allow for the integration of an emission line. Figure 4.2a illustrates the light data collected from a welding process in spray metal transfer mode. It can be seen that the data lends itself to a more accurate analysis of the ionization behavior occurring in the welding arc. Prior to experimental analysis, parameter testing was performed for each condition to determine the voltage and wire feed rate that would place the process in spray mode transfer. A map of metal transfer modes as a function of voltage and wire feed rate can be seen in Figure 4.3. It is seen that for a given process, spray metal transfer mode typically occurs at relatively high voltages and wire feed rates. Higher voltages and wire feed rates increase the heat input into the weldment which would affect the diffusible hydrogen levels

a.)



b.)

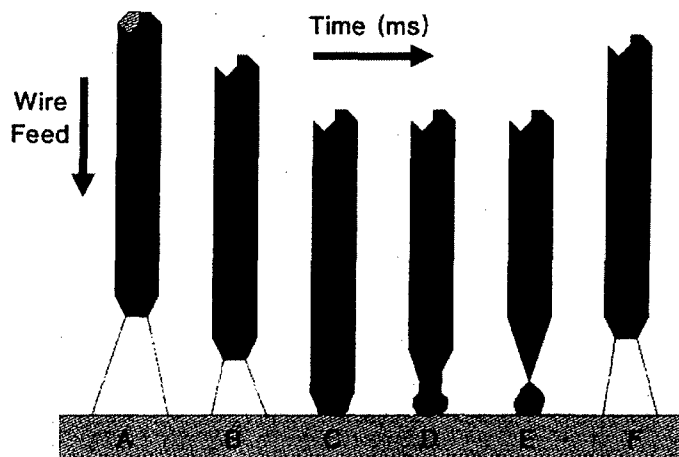
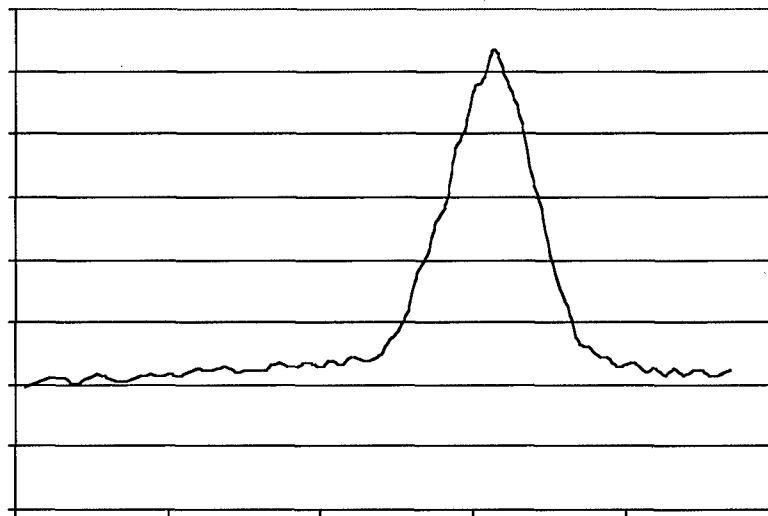


Figure 4.1 (a) Light intensity as a function of lateral distance for a GMAW process in short-circuiting transfer and (b) schematic illustration of short-circuiting transfer [44].

a.)



b.)

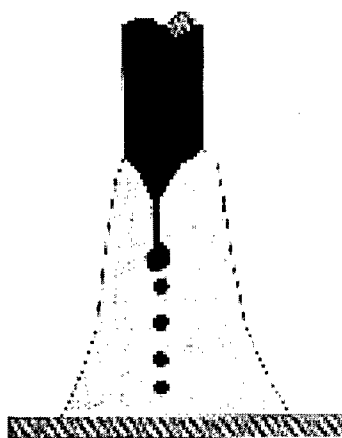


Figure 4.2 (a) Light intensity as a function of lateral distance for a GMAW process in spray transfer and (b) schematic illustration of spray transfer [44].

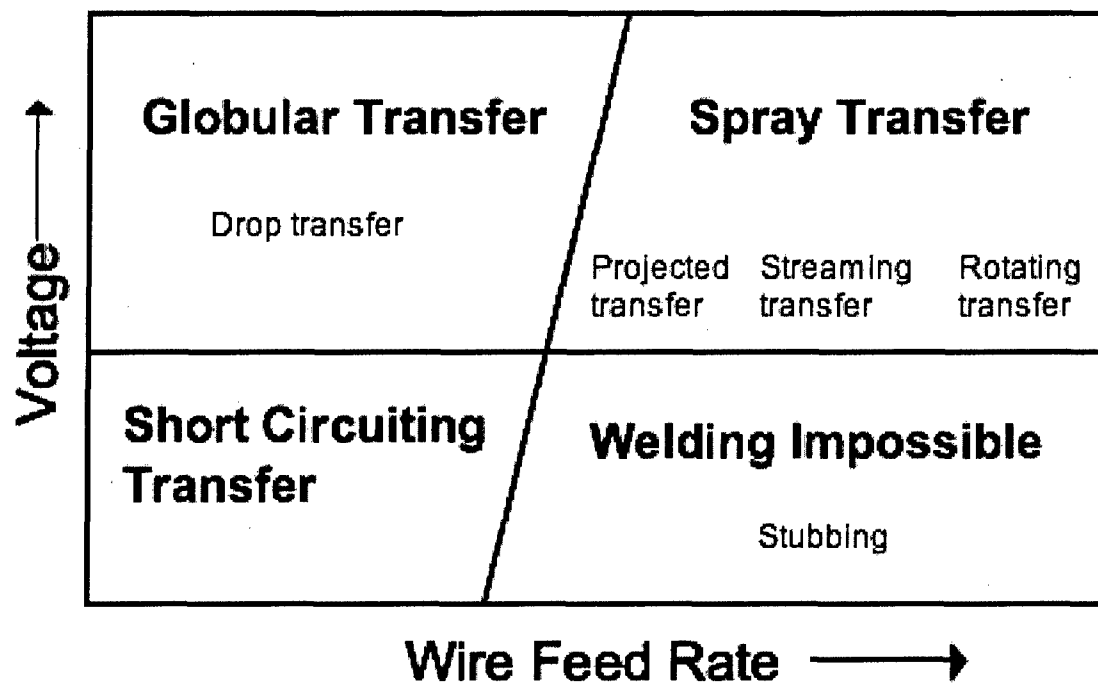


Figure 4.3 Map of metal transfer modes in GMAW processes as a function of voltage and wire feed rate [replotted from 45].

of the weldment. Thus, parameters were chosen so as to be just inside the operating window where spray metal transfer mode would operate.

4.1.2 Masking of Excitation Signals

A typical spectrum emitted by a GMAW process during this research project can be seen in Figure 4.4. Iron excitation signals dominate the middle portion of the

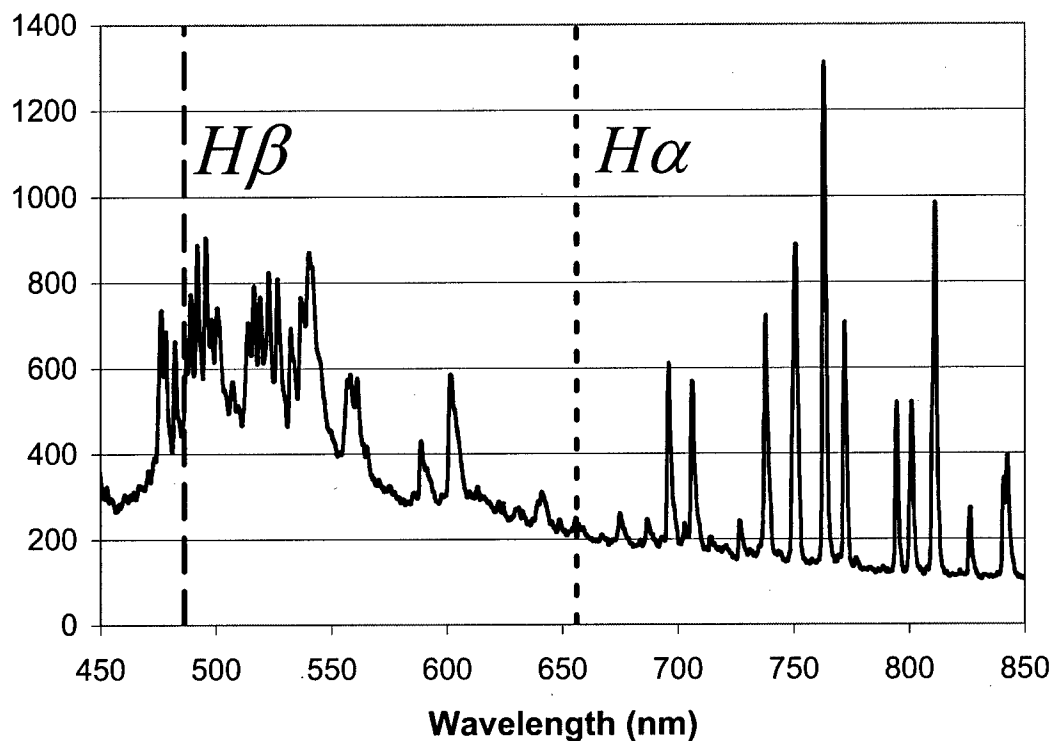


Figure 4.4 Typical spectra emitted by a GMAW process during this research project.

spectrum. Masked beneath those signals are excitation signals for other elements in the welding arc. Thus, the presence of metal droplets in the arc causes a loss of some information that may be available in a GTAW process. For instance, the hydrogen β emission line (electron decay from the fourth to second orbit) at 486.1 nanometers is masked by the iron excitation signals. This masking of signals was not an ideal situation

since detection of hydrogen was the main goal of this research project, and hydrogen does not contain many excitation levels due to its low atomic number. Hydrogen excitation behavior can still be observed, however, because the hydrogen α emission line (electron decay from the third to second orbit) at 656.3 nanometers is observable outside the range of the iron excitation signals. Thus, the concentration of hydrogen in the welding arc was calculated using the emission line at 656.3 nanometers.

4.2 Additions of Hydrogen to Argon Shielding Gas

GMAW processes with hydrogen additions to the argon shielding gas in the amounts of 220-ppm, 1-vol. percent, and 3-vol. percent were studied. The goal of the study was to observe the effect of the additions on the hydrogen content in the weldments and to test the ability of the spectroscopic system to observe hydrogen in the arc. The ultimate goal was to correlate the two activities.

4.2.1 Effect of Hydrogen Additions on Weldment Hydrogen Content

The residual hydrogen content of weldments was found to not vary significantly with hydrogen content of the shielding gas, as seen in Figure 4.5. This was the expected response since any residual hydrogen content in the weldment would be due to the population of trapping sites. The same consumable and base metal were used for all the welding in this phase of research, so the defect population (dislocations, inclusions, etc.) would remain essentially constant across the range of shielding gas additions. The scattering present at the upper hydrogen contents is characteristic of the hydrogen analyzer used for measurement. The relationship between diffusible hydrogen content of

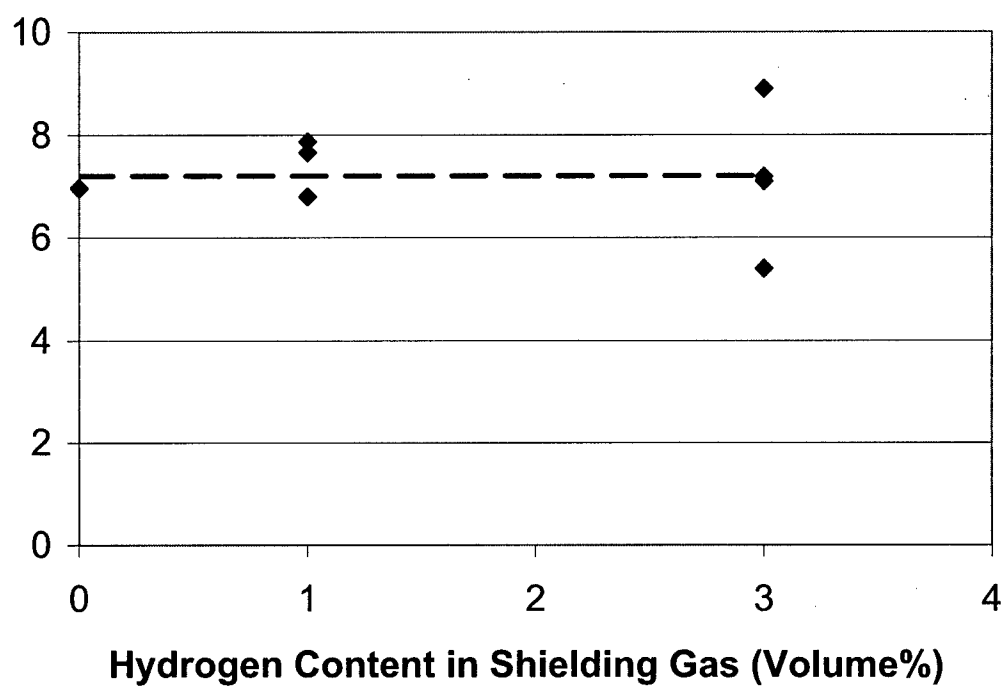


Figure 4.5 Observed relationship between residual hydrogen content in steel weldments and hydrogen additions to argon shielding gas.

steel weldments and hydrogen additions to an argon shielding gas can be observed in Figure 4.6. It is shown that the relationship is similar to that predicted by Sievert's law. As the hydrogen content of the shielding gas is increased, the diffusible hydrogen content of the weldments deposited under the shielding gases increased proportionally to the square root of the amount of hydrogen in the shielding gas. A regression line with a power of one-half is superimposed on the graphic for reference. The relationship suggests that absorption of diatomic hydrogen plays a role in the total amount of hydrogen absorbed during deposition. If hydrogen absorption were to occur only from monatomic hydrogen entering the weld metal, the relationship would be expected to exhibit a linear behavior.

4.2.2 Spectroscopic Evaluation of Hydrogen Additions to Argon Shielding Gas

As discussed in Section 3.6.3, the method of temperature determination chosen for this research project was the ion-neutral line ratio method. Compared to the off-axis peaking method, the ion-neutral line ratio method is considered to be somewhat inaccurate. In order to determine the concentration of constituents in the arc, the temperature had to be known. The temperature calculated with the ion-neutral line ratio method was inserted into the Saha equation to determine the ionization fractions of hydrogen and argon in the arc. Because of occasional inaccuracies in the temperature determined with the ion-neutral line ratio method, hydrogen concentration profiles were affected. Because of this situation, it was decided that a summation of the hydrogen concentrations at the various radii within the arc would be the best method of correlating the spectroscopic

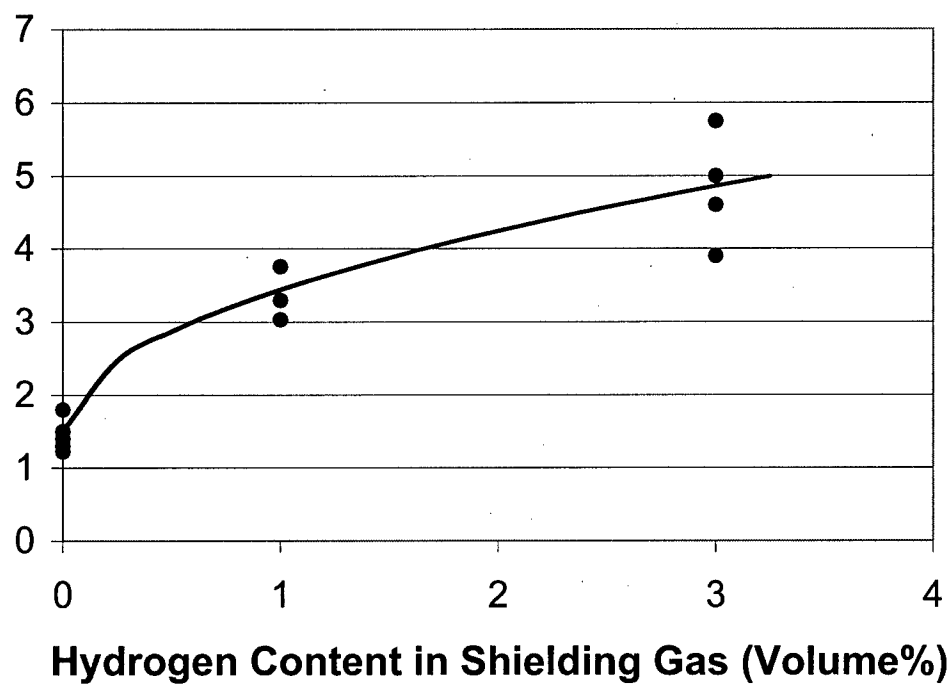


Figure 4.6 Relationship between diffusible hydrogen content of steel weldments and hydrogen content in an argon shielding gas.

concentration data to the hydrogen content of the weldments. In this manner, any point-to-point variations in the profile would be averaged out in the final concentration value. Concentration calculations were performed at every 0.25 millimeters from the center of the arc out to 3.25 millimeters. Measurements beyond 3.25 millimeters were not considered because readings beyond that width would most likely be spurious noise and not a true reading from the arc.

The calculated temperatures for GMAW processes with 220-ppm hydrogen additions can be seen in Figure 4.7. It is seen that the largest gradients occurred at the 6-mm scan height due to its relatively small width. Temperature profiles at 4 millimeters and 2 millimeters exhibited less severe gradients of temperature, due to the increased width of the arc at heights closer to the workpiece. The high temperatures at each scan height were calculated to be at the center axis of the arc, decreasing in value from approximately 25,500 K at 6-millimeters to 22,500 K at 2-millimeters. A similar relationship determined by an earlier researcher can be seen in Figure 1.15. The temperature values calculated in this research were somewhat higher than the temperatures calculated by White in GMAW processes. However, temperatures calculated by White were done so using the Boltzmann-plot method and with additions of oxygen to the shielding gas as well [42].

The relationship between the summation of hydrogen observed in the arc out to 3.25 millimeters and the diffusible hydrogen content of the weldments may be seen in Figure 4.8. An approximately linear correlation exists between the summations of observed hydrogen concentrations in the arc and diffusible hydrogen in the weldments. Though the relationship is not an exact correlation, it is proof that spectroscopy can be used as a diagnostic tool for determination of hydrogen concentration in the arc. With this tool, a manufacturer may designate a certain, unacceptable level of hydrogen content in the weldment and correlate that to an amount of arc-observed hydrogen. During fabrication of a structure this particular amount of hydrogen observed in the arc would act as a warning sign that the deposited weldment may be prone to HAC. In this manner, the

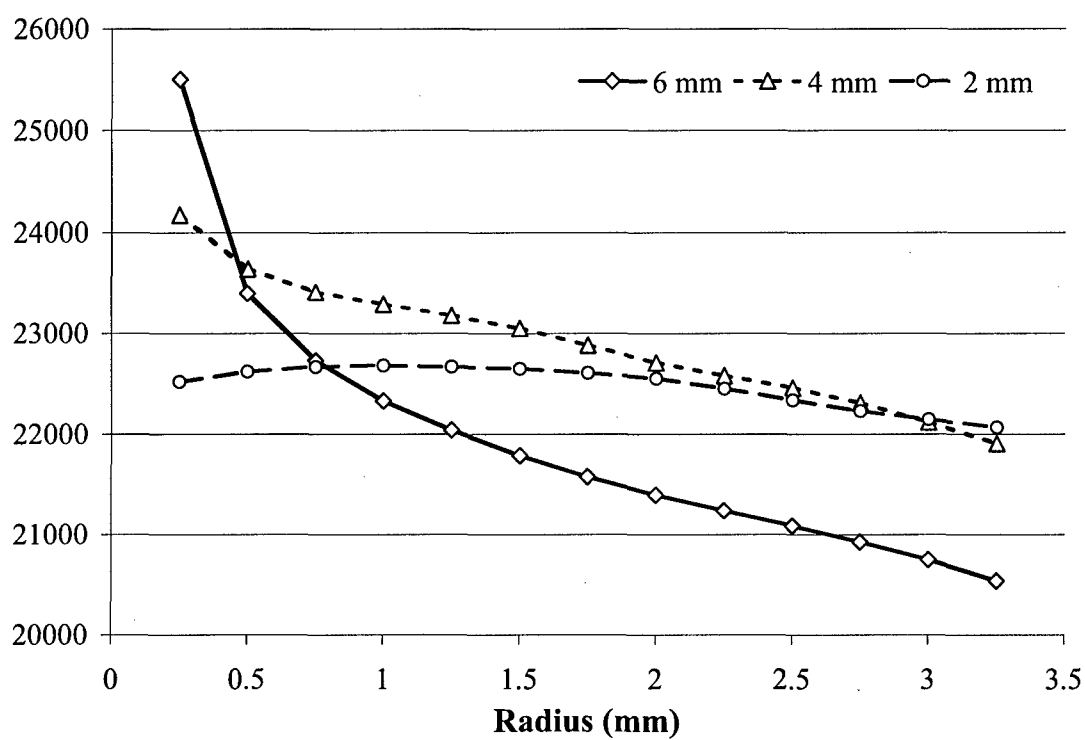


Figure 4.7 Temperature profiles at indicated heights for a GMAW process with 220-ppm hydrogen addition in argon shielding gas.

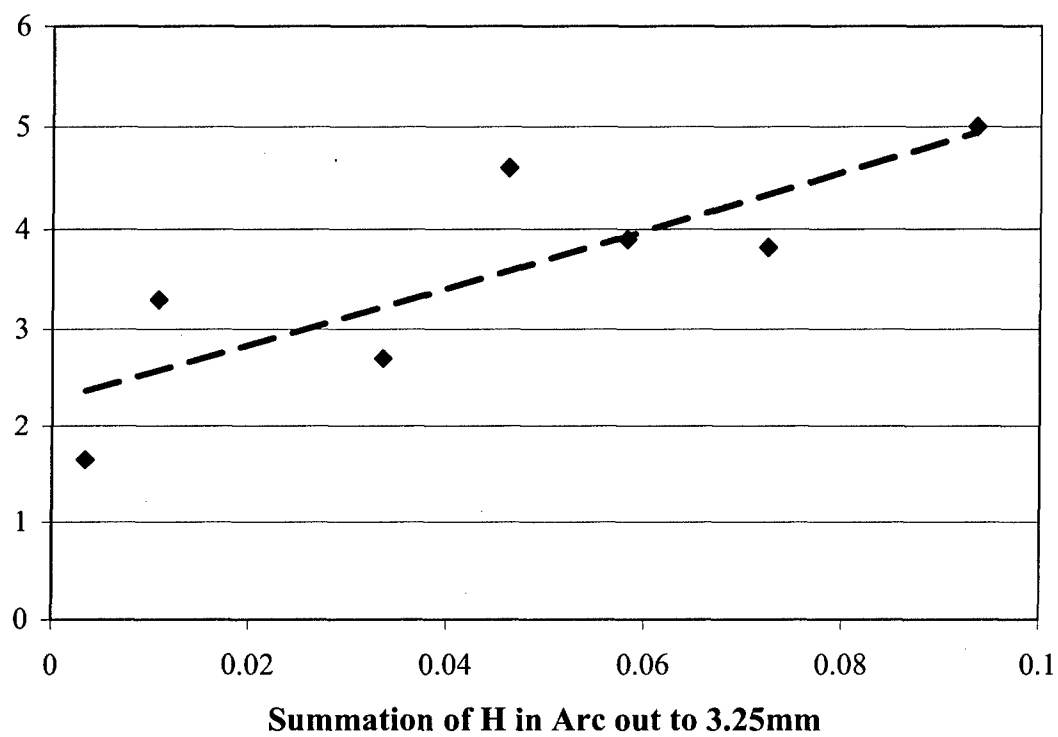


Figure 4.8 Relationship between diffusible hydrogen concentration of weldments and the summations of hydrogen concentration in the welding arc out to 3.25-millimeters.

time and expense associated with destructive testing of diffusible hydrogen analysis may be reduced or avoided altogether. Before final application to a fabrication process, similar sets of tests as was performed in this research should be done with the conditions that would be present at the time of welding. In other words, the testing in this research project was performed on steel with argon as the primary constituent of the shielding gas. As such, the results may not be directly applicable to a GMAW process that uses an argon-carbon dioxide, or another mixture, as a shielding gas.

Hydrogen concentration profiles for GMAW processes with 1-percent and 3-percent hydrogen additions at 6-millimeters above the workpiece can be seen in Figure 4.9. The hydrogen concentration profiles found in this study were found to exhibit a trend opposite that of previous researchers. In this research, hydrogen concentration was generally found to increase from the center of the arc outward. The minimum hydrogen concentrations were calculated to be in the center of the arc. This trend is a result of the temperatures found at the center of the arc. As expected, the maximum temperatures in the welding arcs examined usually occurred along the center axis of the arc because this is the region of highest energy density. As discussed in Section 3.7, the concentrations of the constituents in the arc were calculated by computing a ratio of their concentration in the arc to the concentration of neutral argon in the arc. The ratios of first and second ionized argon to neutral argon in the arc were calculated using the Saha ionization equation. The ionization behavior of argon with temperature can be seen in Figure 4.10. It is seen that the second ionization of argon begins to occur rapidly in the temperature range of the maximum temperatures calculated for the welding arcs in this research project. For each second ionized argon atom in the arc, there are two electrons present. They exert a significant influence near the center axis of the arc, but their influence diminishes as the radius in the arc increases. In other words, as the temperature decreases with increasing radius, the argon present tends to consist mainly of first ionized argon and neutral argon.

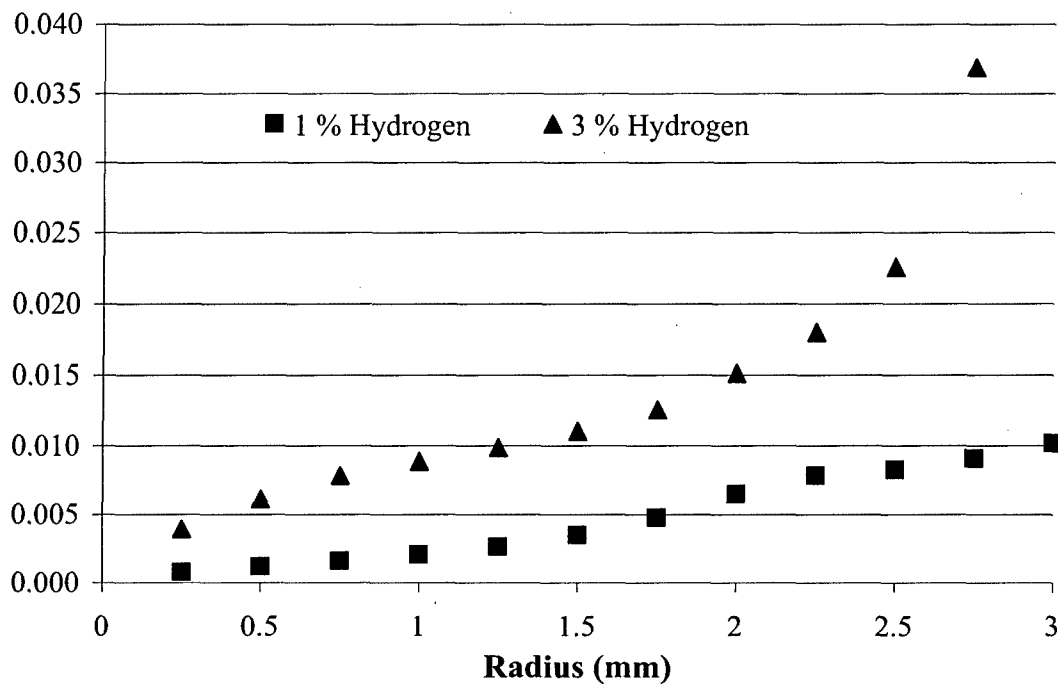


Figure 4.9 Hydrogen concentration profiles across welding arcs with indicated hydrogen additions to argon shielding gas.

Though this relationship has not been seen in the literature before, it should be noted that the temperatures reported in this research are somewhat higher than those reported previously. It is not the actual quantitative difference between previous reported temperatures and those being reported here, so much as it is the particular range of temperatures and the shielding gas being used. For instance, an increase in temperature

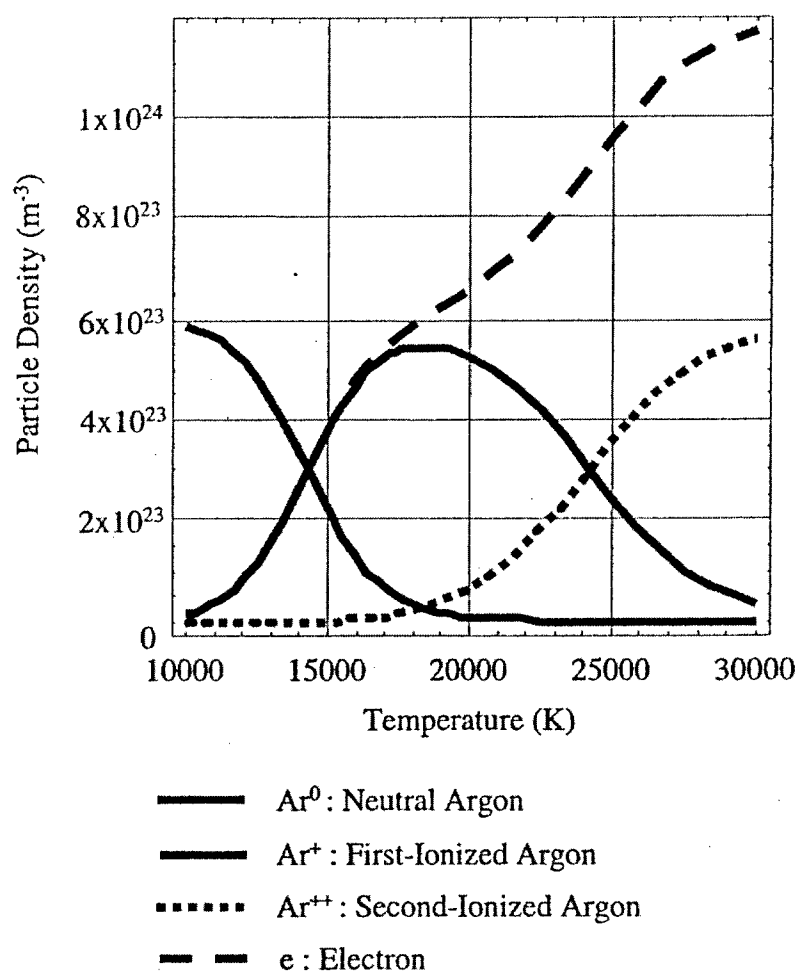


Figure 4.10 Ionization behavior of argon as function of temperature. Initial particle density of 6×10^{23} particles per cubic meter [28].

from 15,000 to 17,000 K would not have as significant an effect as does a change in temperature from 22,000 to 24,000 K, even though both differences are 2,000 K. That particular temperature range is critical only because argon is the primary constituent of the shielding gas. Another gas would have its own particular ionization behavior in that temperature range.

In previous spectroscopic research of hydrogen in GTAW processes it was postulated that hydrogen reaches a peak concentration near the cathode because of the diffusion behavior of monatomic hydrogen, reactions with other species in the arc, and variation of hydrogen mass transport due to the temperature and pressure gradients. The hydrogen concentration profiles calculated in this research suggests that the overwhelming presence of electrons in the core of the arc serve to displace hydrogen to the outer regions of the arc. The high temperature in the center of the arc causes a rapid expansion of the shielding gas which imparts kinetic energy to the particles in the arc. For a given kinetic energy, a smaller particle will experience a greater velocity than a relatively larger one. With regards to this particular research project, the hydrogen particles would move more quickly than the argon particles in the arc. Thus, it is not unreasonable to observe an increase in hydrogen content with increased distance from the center of the arc.

Another factor in the center of the arc is the presence of molten metal droplets traveling from the electrode to the weld pool. Calculations by Mundra, et. al [18] showed that molten iron droplets absorb as much as 12 ppm hydrogen while traversing the arc. The processes were performed primarily in spray mode, which would allow for maximum surface contact with the arc atmosphere and could have led to appreciable hydrogen absorption by the metal droplets on their journey to the weld pool.

4.3 Moisture Additions to Argon Shielding Gas

A study was undertaken to test the ability of the spectroscopy system to observe hydrogen in the arc resulting from moisture in the shielding gas. The impetus for this phase of research lies in the application of spectroscopy to a shipyard fabrication environment. Humidity in the atmosphere results in humidity in the shielding gas, which results in hydrogen in the weldment. Savage, et. al [46] found that moisture additions in a shielding gas are more potent than hydrogen additions with regards to hydrogen content of the weldment.

4.3.1 Effect of Moisture Additions on Weldment Hydrogen Content

Hydrogen and moisture additions were made to argon shielding gas in the amount of 220-parts-per-million. It was decided to specially order these gas mixtures from a distributor because of the compositional inaccuracy that would likely result from a custom built humidifying system. It was believed that losses of moisture in the shielding gas would occur through condensation on the metal fixtures controlling gas flow in the welding machine. Another source of uncertainty would have been inherent in the temperature control of the shielding gas. As the temperature of the shielding gas varies, so does its ability to hold moisture. Thus, control of the temperature of the shielding gas would have been critical to successful control of the experiments. In light of these arguments, it was deemed the appropriate course of action to specially order the shielding gas mixtures which exhibited a ± 3 -pct. variance according to manufacturer's specifications.

As expected, weldments made with the moisture-addition shielding gas exhibited considerable porosity, as evidenced in Figure 4.11. It was believed that the porosity was due to the moisture itself and not any instabilities in the arc that may have been caused by the additions to the shielding gas. The reason for this assumption is the fact that the



Figure 4.11 Photograph of weldments made with moisture additions to shielding gas.
Demarcations on ruler are millimeters.

welding arcs in this portion of the research, as in the previous phases, were operated in spray metal transfer mode. No porosity was evident in weldments made with the 220-ppm hydrogen addition shielding gas. This would suggest that the moisture engendered a considerable amount of hydrogen in the weldment. Low hydrogen levels in a weldment

would likely be in solution in the weld metal. Only when hydrogen levels exceed saturation in the weld metal would one expect to see porosity. Another possibility is the formation of carbon monoxide due to the increased oxygen potential in the weld metal. Diffusible hydrogen levels in the weldments generated with the two shielding gas mixtures did not support this reasoning, however. Diffusible hydrogen levels in weldments made with both shielding gas mixtures were very low, often times not evolving even enough hydrogen to register on the gas chromatograph.

When the hydrogen threshold was reached, the diffusible hydrogen levels were found to be 1.2 mL of hydrogen / 100 g of weld metal for the moisture-addition shielding gas and 1.5 mL of hydrogen / 100 g of weld metal for the 220-ppm hydrogen addition shielding gas. This was not a significant difference considering the drastic difference in weldment quality. However, the porosity of the moisture-addition weldments may be the reason for the low levels. Hydrogen in the molten weld metal exists in monatomic form until saturation. Once pores form, monatomic hydrogen will leave the weld metal to recombine in the energetically favorable diatomic form. As outlined in the AWS diffusible hydrogen standard [25], the weldments are quenched immediately after welding to retard hydrogen mobility. Upon degassing of the weldment samples it is entirely possible that hydrogen in the weld metal diffused into the pores instead of evolving from the sample. Once in diatomic form, hydrogen mobility in iron is severely limited. Thus, it is not necessarily a contradiction that the weldments made with the moisture-addition shielding gas exhibited lower diffusible hydrogen levels. Weldments made with the moisture-addition shielding gas did, however, contain higher levels of residual hydrogen, as seen in Figure 4.12. Higher levels of residual hydrogen would suggest that the moisture additions in the shielding gas were indeed more potent than hydrogen additions with regards to weldment hydrogen content.

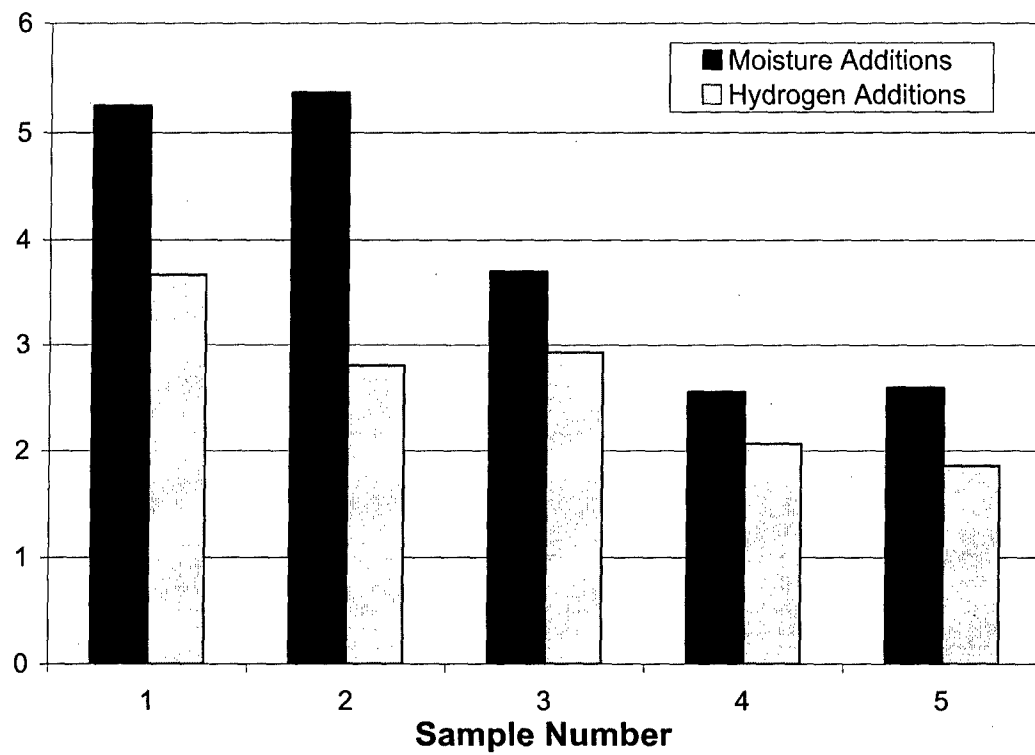


Figure 4.12 Comparison of residual hydrogen content of weldments made with moisture and hydrogen additions to argon shielding gas.

4.3.2 Spectroscopic Evaluation of Moisture Additions to Argon Shielding Gas

The spectroscopy system was able to detect hydrogen in the welding arcs resulting from moisture additions. Hydrogen concentration in the welding arcs with moisture additions followed the same general pattern as outlined in the previous section, i.e. increasing with increasing radius. The earlier discussion regarding the hydrogen concentration profiles is also valid in this case. High temperatures at the center of the arc cause an increase in the concentration of ionized argon, and thus, the concentration of electrons. A profile of the hydrogen concentration of GMAW processes with moisture additions to the shielding gas can be seen in Figure 4.13. The hydrogen concentrations shown further support the theory that moisture is a more potent means of hydrogen generation in the arc than hydrogen additions. A profile of the hydrogen concentration of GMAW processes with 220-ppm hydrogen additions can be seen in Figure 4.14.

Comparing the graphs it is observed that the concentration of hydrogen due to moisture is much greater than the hydrogen due to hydrogen additions, much greater, in fact. Both conditions follow the same trend of greater hydrogen concentration higher in the arc, but the maximum concentration of hydrogen resulting from the moisture additions is a magnitude greater than that of the hydrogen additions. Hydrogen concentration due to the hydrogen additions never exceed 220 parts-per-million contained in the shielding gas. Hydrogen concentrations in arcs with moisture additions exceed 2000 parts-per-million at their maximum. According to the law of mass action, this would seem to be an impossibility. Assuming complete dissociation of every water molecule in the welding arc, the maximum concentration should be 440 parts-per-million; because of the two hydrogen atoms in every water molecule. The variance quoted by the manufacturer, $\pm 3\%$, would not account for such a large difference. Thus, even though the spectroscopy system is able to detect moisture-induced hydrogen in the welding arc of a GMAW process. However, the large difference between observed hydrogen

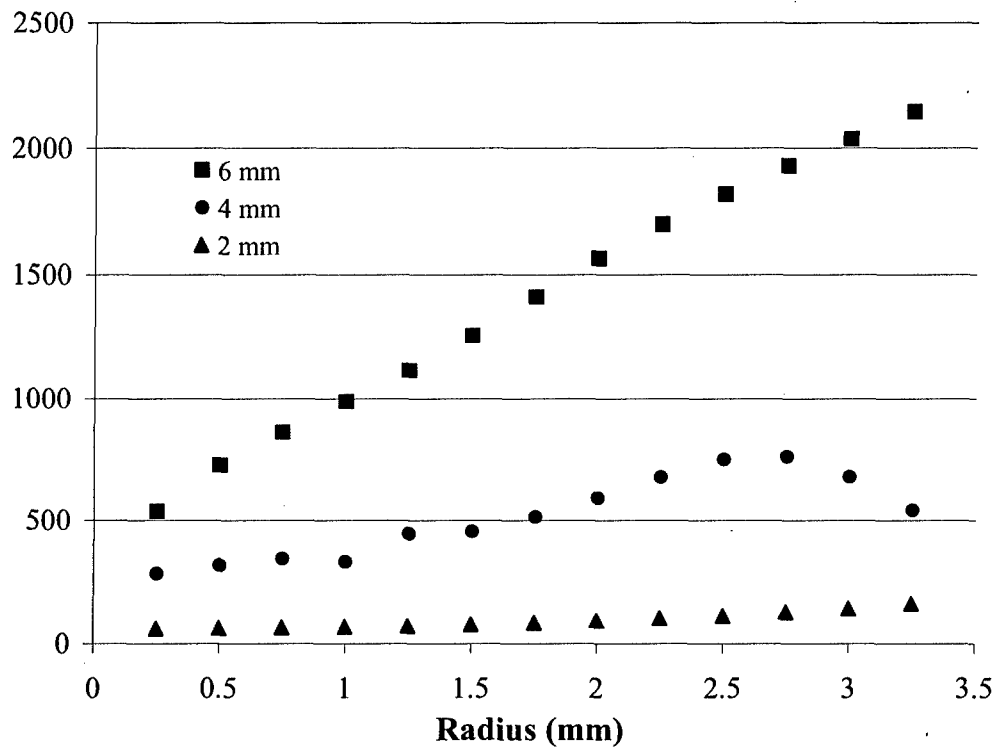


Figure 4.13 Hydrogen concentration profiles at indicated heights in GMAW processes with 220-ppm moisture additions in argon shielding gas.

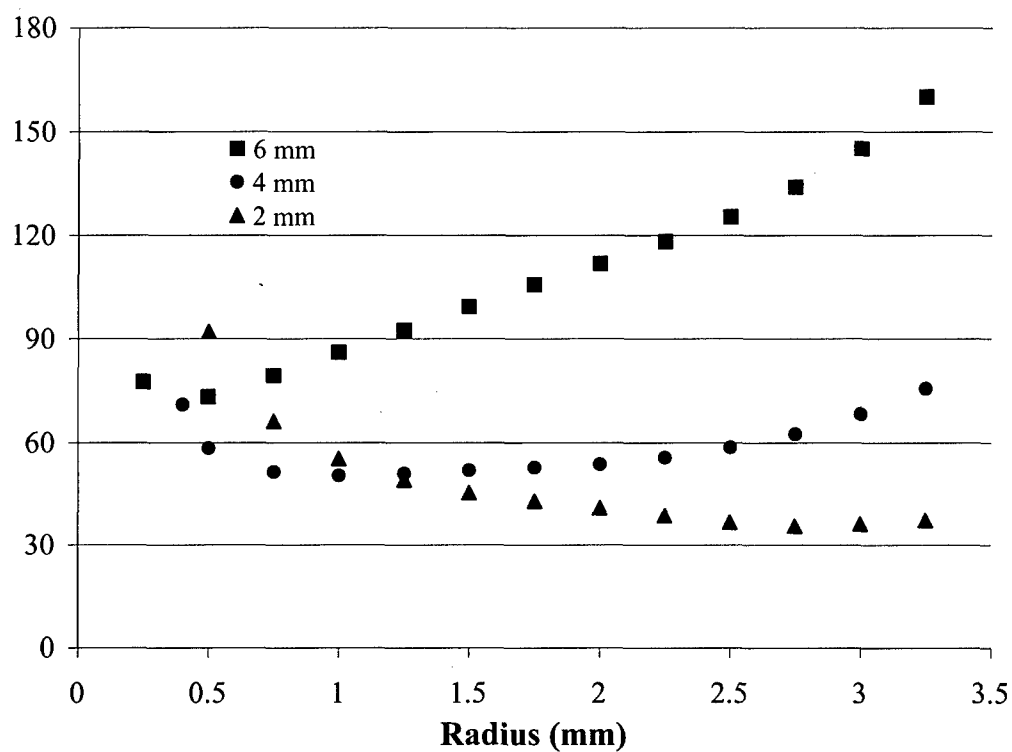


Figure 4.14 Hydrogen concentration profiles at indicated heights in GMAW processes with 220-ppm hydrogen additions in argon shielding gas.

concentration and actual concentration must be addressed in the near future. Possible reasons for this discrepancy may be the moisture in the shielding gas causing a process whereby hydrogen is brought into the welding arc from the atmosphere. Perhaps the hydrogen increase is due to the increased oxygen content in the welding arc.

4.4 Ionization behavior of Hydrogen

As discussed earlier, the reduction of hydrogen concentrations near the center of the arc resulted from the emergence of the second ionization of argon which occurs in the temperature ranges calculated. In this section, the behavior of neutral and ionized hydrogen in the arc will be discussed. The concentration of hydrogen in the arc was calculated utilizing the ratio of each to neutral argon. Ratios of neutral and ionized hydrogen to neutral argon for GMAW processes with 1-vol. percent and 3-vol. percent hydrogen additions at 6-millimeters above the workpiece are presented in Figure 4.15. It should be noted that although all sets of data are presented on the same scale, the neutral hydrogen (H_I / Ar_I) ratios were multiplied by a thousand to achieve this convenience. Ionized hydrogen ratios increased towards the center of the arc because of the high temperatures present in that region. As the radius increases, the temperatures decrease and the neutral hydrogen ratios begin to increase. The rise is not very dramatic because most hydrogen in the arc is ionized. In addition, as temperature decreases, the fraction of neutral argon in the arc will also increase. Both these factors combine to maintain the neutral hydrogen ratio at a relatively constant, and small, value across the width of the welding arc.

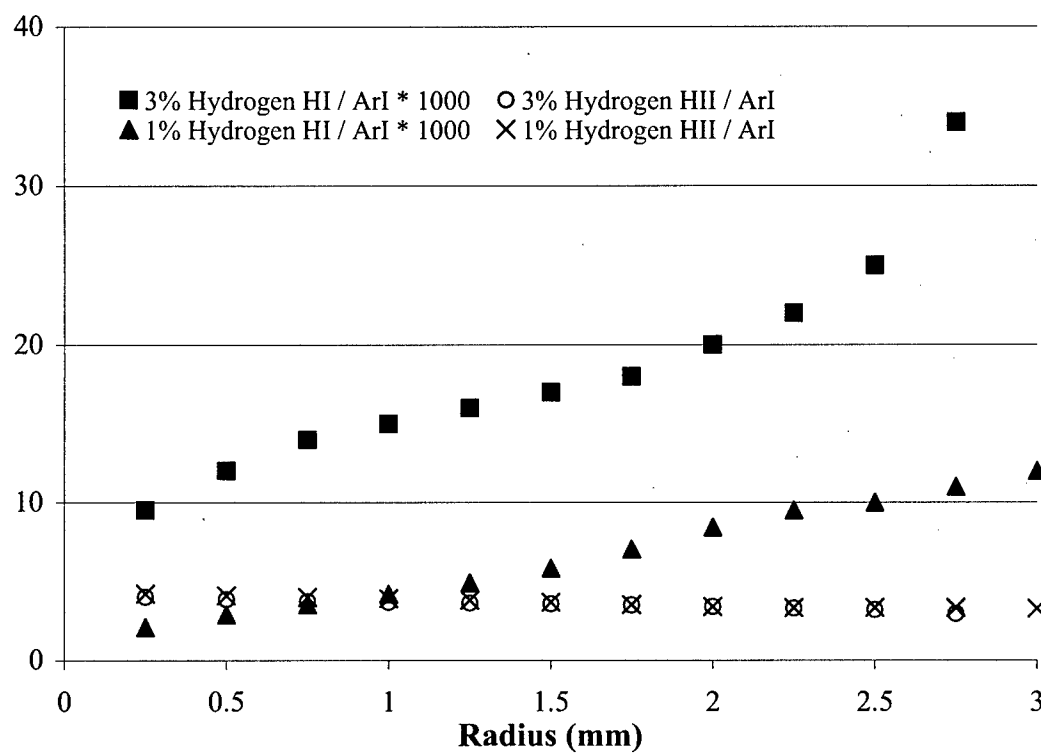


Figure 4.15 Ionized and neutral hydrogen ratios for GMAW processes with 1-vol. percent and 3-vol. percent hydrogen additions to argon shielding gas.

4.5 Study of Rust-Induced Hydrogen in the Arc

In this portion of the research project, rust was induced on solid steel wire in order to test the ability of the spectroscopy system to observe rust-induced hydrogen in a GMAW process. The purpose was to simulate a humid environment where consumables exposed to the atmosphere could pick up some oxide. The calculated hydrogen profiles at different scan heights for a GMAW process performed with a rusty wire consumable can be seen in Figure 4.16. Hydrogen profiles in this phase of the research exhibited a similar trend to the earlier phases with the exception of scans performed at 2-millimeters above the workpiece. It was calculated that the hydrogen concentration at 2-millimeters exhibited a gradual decrease as the radius increased. The reason for this opposite behavior was not immediately clear. One explanation may be the instability of the arc in this phase of research. The consumable used for this phase of research presented feeding problems due to the stiffness of the wire, leading to instability in the arc at times. It is believed that this instability may have contributed to the inaccurate readings. The unstable arcs emitted more flashes and sparks which may have caused some inaccuracies in the calculation process. However, using the summation of the hydrogen concentration in the arc out to 3.25-millimeters at each scan height provided the relationship seen in Figure 4.17. As the graphic demonstrates, the hydrogen concentration due to rust on the consumable increased proportionally with height in the arc.

4.6 Study of Metal-Cored Wire Consumables

In this phase of the research, spectroscopy was performed on metal-cored wire consumables. The core was composed of 60-wt. percent ferromanganese with the balance being iron powder. Scans performed at 6-millimeters and 4-millimeters above the workpiece revealed no discernable differences regarding emission lines between this

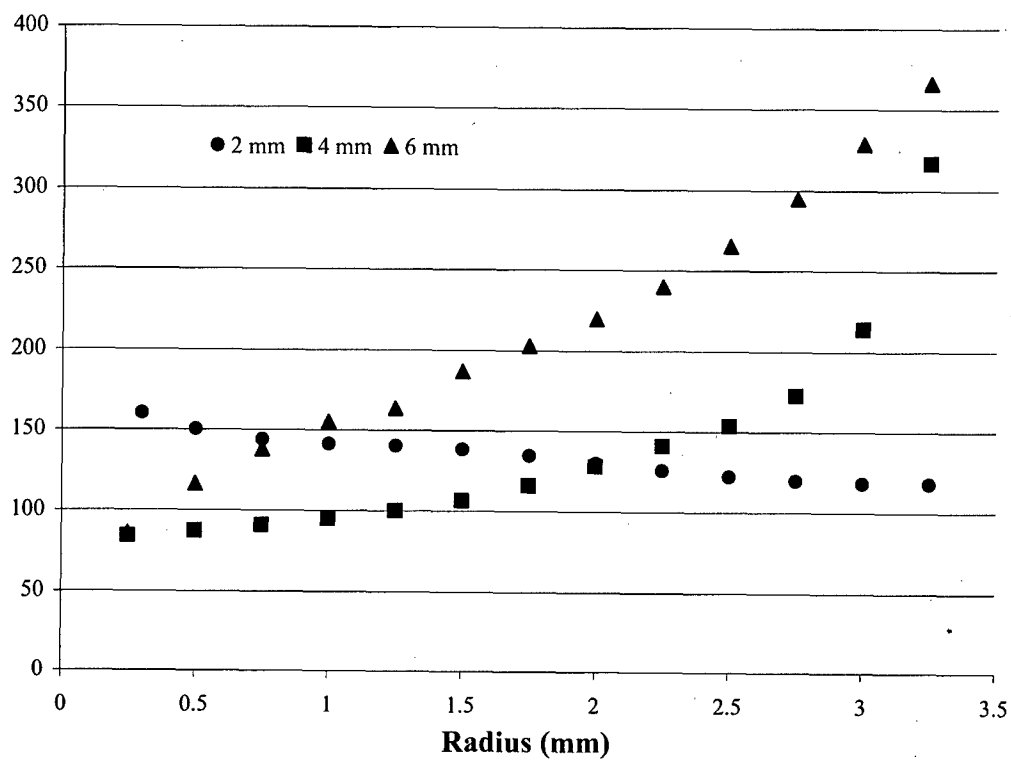


Figure 4.16 Hydrogen concentration profiles at indicated heights in GMAW processes with rusty consumable.

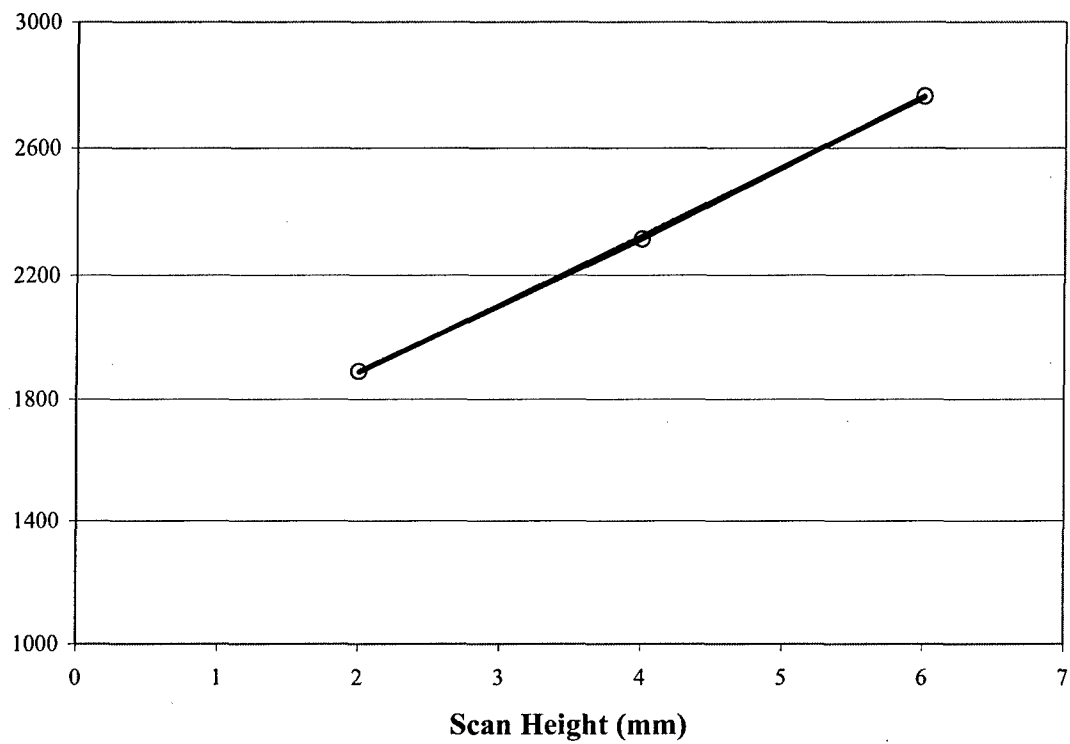


Figure 4.17 Relationship between hydrogen concentration summations and scan height for spectroscopy of GMAW processes with rusty consumable.

phase of research and the prior phases involving just argon shielding gas and a solid-wire consumable. A portion of the spectra emitted during a scan at 2-millimeters above the workpiece is provided in Figure 4.18. Superimposed on the spectra are the emission lines for neutral manganese. At first glance it would appear that the manganese emission lines are distinct and may be used to calculate the concentration of manganese in the arc. However, as seen in Figure 4.19, for each of the peaks that may be manganese emission lines, there exists iron emission lines as well. In addition, according to data in the CRC Handbook of Chemistry and Physics [43], the iron emission lines are just as strong, if not stronger, in their relative intensity than the manganese emission lines. Thus, it was concluded that this spectroscopy system and methodology was not immediately applicable to determination of the concentration of metals in the core of wire consumables. The reason for the absence of emission lines at the higher scan heights was postulated to occur because the elements in the core most likely melted in the arc and were deposited into the weld pool without much excitation occurring. Thus, the emission lines observed at 2-millimeters above the workpiece are likely the result of metal vapors from the weld pool becoming excited in the arc.

4.7 Sources of Uncertainty

Sources of uncertainty present in the results of this research project can be divided into uncertainty associated with the data collection and analysis of the data. The welding arc of a GMAW process is a complex physical and chemical phenomenon wherein extreme gradients of temperature, pressure, and composition are present. During the collection of data, precautions were taken to minimize the effect of ambient light on the measure of light intensity from the arc. A shield was used to limit the amount of arc-generated light that would strike the spectrometer probe. In addition, facility lights were extinguished during all experiments. In this manner, ambient light readings were believed to be of negligible intensity. A requirement of the ion-neutral line ratio method is that all

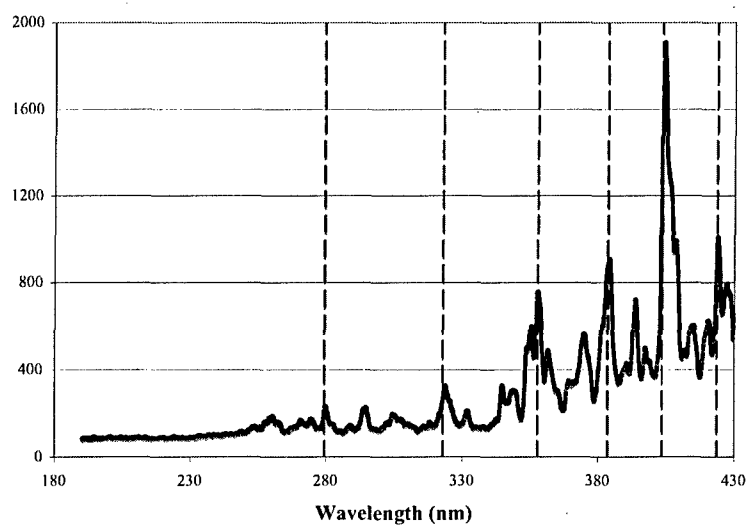


Figure 4.18 Portion of spectra emitted from metal-cored wire arc welding process with manganese emission lines superimposed.

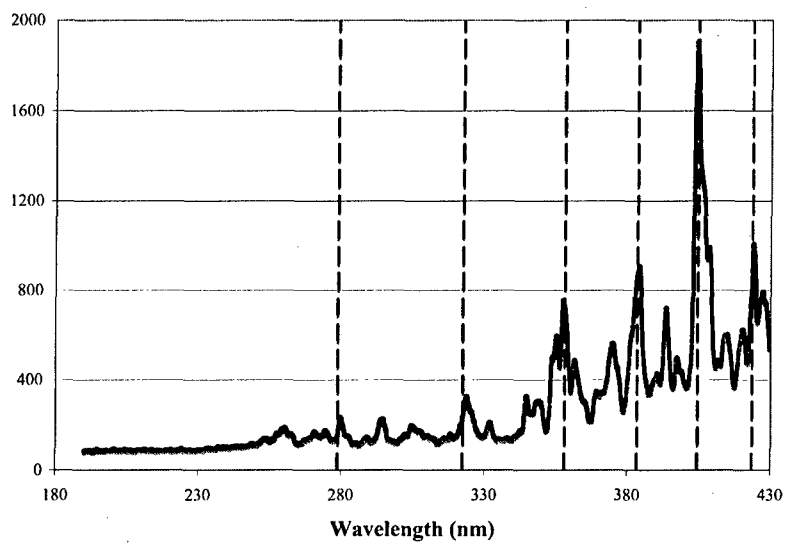


Figure 4.19 Portion of spectra emitted from metal-cored wire arc welding process with iron emission lines superimposed.

emission coefficients are measured on the same scale. Thus, any extraneous effects present during the data collection of each experiment were present in all the emission coefficients measured during the process. Measurement of hydrogen in the weldments was subject to the characteristic variation of the machine used. Diffusible hydrogen measurements using the gas chromatograph at the Colorado School of Mines exhibited a maximum variance of five percent at low concentrations (220-ppm hydrogen additions) and a minimum variance of below one percent at high concentrations (3-pct. hydrogen additions).

Residual hydrogen measurements from the hydrogen analyzer exhibited noticeable variance over the entire spectrum of samples tested, even with frequent calibration. A possible cause of the variation may be the fact that machining chips were used for the analysis. Though they are convenient to use and a relatively clean way of providing weld metal for analysis, it is possible that the form of chips may have led to incomplete melting at times. The shielding gases with the 220-ppm additions of hydrogen and moisture had a compositional variance of ± 3 percent according to distributor specifications. As discussed in Section 3.5.3, all spectroscopic data underwent a smoothing operation before calculations were performed. The correlation between the raw data and smoothed data was typically above 95 percent but was lower in cases where the arc momentarily left spray metal transfer mode or emitted a spark.

CHAPTER 5

CONCLUSIONS

5.1 Conclusions Reached During this Research Project

As a result of the research performed, the following conclusions were reached:

- 1.) The relationship between hydrogen additions to argon shielding gas and the diffusible hydrogen content of steel weldments resembles a Sievert's law type of relationship.
- 2.) No relationship was found to exist between hydrogen additions to an argon shielding gas and the residual hydrogen content of steel weldments.
- 3.) Calculations made using emission spectroscopy of a GMAW process was found to be a reliable indicator of the diffusible hydrogen content of a steel weldment.
- 4.) The spectroscopy setup used in this research was able to detect hydrogen present in the arc due to moisture in an argon shielding gas and rust on a steel wire consumable.
- 5.) Moisture additions were found to be somewhat more potent in causing hydrogen in a steel weldment than hydrogen additions of the same concentration.
- 6.) Spectroscopy of a FCAW process with manganese additions to the core did not provide the means required for core constituent concentration in the welding arc.



CHAPTER 6

SUGGESTIONS FOR FUTURE WORK

6.1 Design of Spectrometer System for Real-time Measurements

With the ultimate goal of applying the results of this research to a fabrication setting, the placement of the spectrometer probe should be considered. In this research, spectroscopy data was collected by taking a scan of the welding arc as it passed by an aperture. The data would be processed following welding, for temperature and hydrogen determination. It would not be practical to pause a welding process after every scan in order to calculate the hydrogen concentration. Instead, a study should be undertaken to determine the optimum placement of the spectrometer probe with regards to a welding process. The probe of the spectrometer in this research was small enough (5-mm diameter) to be placed on an actual welding torch assembly.

Equipment to perform the data analysis and computation could be placed away from the welding torch and connected to the probe through cables. Incorporating the spectrometer probe into the welding torch would allow for greater discretion of the hydrogen absorption processes occurring in the arc. More information could be gathered from the key regions of the arc with regard to hydrogen absorption, such as immediately above the weld pool. A more definitive point of observation within the arc would alleviate some of the inaccuracy that occurs from scans across different temperature regions in the arc. For example, hydrogen emissions from the arc may occur from monatomic hydrogen in the core of the arc and diatomic hydrogen in the outer regions of the arc. Focusing on a single location in the arc would allow for better determination of hydrogen activity. For example, hydrogen ionization processes could be detected in the core of the arc as well as hydrogen recombination occurring in the periphery of the arc.

6.2 Infrared Emission Spectroscopy

All the excitation signals collected in this research resided in the visible region of the electromagnetic spectrum. A welding arc emits much more than just visible light. Thus, it may be a rewarding venture to study the energy emitted in wavelengths beyond the visible spectrum. In particular, infrared detectors are fairly common and may provide further insight into the processes, other than just ionization, occurring in a welding arc. In particular, the vibrational and rotational spectra of many atoms and molecules, such as diatomic hydrogen, occur in the infrared region.

6.3 Further Study of Moisture-Induced Hydrogen in Welding Arc

The processes occurring in a welding arc with moisture additions in the shielding gas should be further investigated. In this research, the spectroscopy system detected an artificially high amount of hydrogen in a welding arc with moisture additions to an argon shielding gas. It is known that moisture is a more potent hydrogen producer as an addition to shielding gas than hydrogen itself, but the reasons why this is so could be investigated using arc emission spectroscopy. In addition, the amount of diffusible hydrogen evolved from the samples deposited with the moisture additions often did not reach the detection threshold of the gas chromatograph used in this research. If there are further studies undertaken with lower amounts of diffusible hydrogen, less than approximately one milliliter per hundred grams of weld metal, it would be wise to test the resolution of the gas chromatograph. At such low levels of hydrogen, it may be found that the gas chromatograph does not provide satisfactory precision.

Another topic of interest is the process of hydrogen absorption when moisture is present in the welding arc. Spectroscopy may be used to study the effect that oxygen has on the weld pool, more specifically, how hydrogen absorption is affected as well as oxide effects on the arc itself.

6.4 Investigation into Radial Distribution of Hydrogen

As outlined earlier in this document, the Abel inversion was performed on the data collected in order to reconcile the fact that two-dimensional data was being extracted from a three-dimensional welding arc. While it allowed for calculation of hydrogen profiles, it would be worth investigating to explore the intricacies of the mathematical treatments performed in this research. Specifically, the relationship between hydrogen density and radius in the arc could be explored. Each particular radius within the arc can be considered as describing a cylinder parallel to the electrode, assuming a constant arc height. An interesting topic of investigation would be to determine how the hydrogen density varies with the size of this theoretical cylinder. A higher hydrogen density can be viewed as either a function of increasing hydrogen content, or a reduction in the area of the theoretical cylinder. Analysis of the mathematics may reveal a more thorough understanding of the behavior of hydrogen in a welding arc.

ACKNOWLEDGEMENTS

I would like to express my appreciation to the Office of Naval Research for their research support.

My sincere gratitude goes to Dr. Liu for his guidance and counsel during the course of my graduate career.

In addition, I would like to thank Drs. Edwards and Olson for their advice and support.

I would also like to thank the other members of the Center for Welding, Joining, and Coatings Research as well as the Advanced Steel Processing and Products Research Center. Their help and friendship were greatly valued during the course of this research.

REFERENCES

- [1] R. Pargeter: *Welding Journal*, November 2003, vol. 82, pp. 321s-329s.
- [2] M. Rowe, "Effect of Ferro-Alloy Additions and Increasing Depth on the Quality of Underwater Wet Steel Welds," Master's Thesis at the Colorado School of Mines, November 1999.
- [3] N. Bailey, F.R. Coe, T.G. Gooch, P.H.M. Hart, N. Jenkins, and R.J. Pargeter. Welding Steels without Hydrogen Cracking – 2nd Edition. ASM International: Abington, UK, 1973.
- [4] B.A. Graville, "Cold Cracking in Welds in HSLA Steels." Welding of HSLA (Microalloyed) Structural Steels – Proceedings of an International Conference November 1976 – Rome, Italy. Eds. A.B. Rothwell and J. Malcolm Gray. American Society for Metals, 1978, 85-101.
- [5] T. Boellinghaus, H. Hoffmeister, and C. Schubert. Proceedings of the 4th International Conference on Trends in Welding Research – Gatlinburg, TN June 1995. ASM International, 25.
- [6] C. Zapffe and C. Sims: *Transactions of the AIME*, 1941, vol. 145, pp. 225-261.
- [7] G.G. Hancock and H.H. Johnson: *Transactions of the TMS/AIME*, 1965, vol. 236, pp. 513-516.
- [8] J.P. Hirth: *Metallurgical Transactions A*, 1980, vol. 11A, pp. 861-890.
- [9] D.G. Westlake: *Transactions of the ASM*, 1969, vol. 62, pp. 1000-1060.
- [10] S. Gahr, M.L. Grossbeck, and H.K. Birnbaum: *Acta Metallurgica*, 1977, vol. 25, pp. 125-133.
- [11] N.J. Petch: *Philosophy Magazine*, 1956, vol. 1, pp. 331-337.
- [12] S.P. Lynch. "Hydrogen Embrittlement of Steels: A Review of Mechanistic Aspects." Hydrogen Management for Welding Applications – Proceedings of International Workshop, October 6-8, 1998, Ottawa, Canada. Eds. J.E.M Braid, C.V. Hyatt, D.L. Olson, and G.N. Vigilante. Ottawa: CANMET, 1999. 53-64.

- [13] R. Thomson: *Journal of Materials Science*, 1978, vol. 13, pp. 128-142.
- [14] G.W. Simmons, P.S. Pao, and R.P. Wei: *Metallurgical Transactions A*, 1978, vol. 9A, pp. 1147-1158.
- [15] A.R. Troiano. "The Role of Hydrogen and Other Interstitials in the Mechanical Behavior of Metals." Hydrogen Damage. Ed. C.D. Beachem. Ohio: ASM, 1977, 151-177.
- [16] R.A. Oriani. "A Mechanistic Theory of Hydrogen Embrittlement of Steels." Hydrogen Damage. Ed. C.D. Beachem. Ohio: ASM, 1977, 301-310.
- [17] C.D. Beachem: *Metallurgical Transactions*, 1972, vol. 3, pp. 437-451.
- [18] T.A. Palmer and T. DebRoy: *Welding Journal*, July 1996, vol. 75, pp. 197s-207s.
- [19] K. Mundra, J.M. Blackburn, and T. Debroy: *Science and Technology of Welding and Joining*, 1997, vol. 2, no. 4, pp. 174-184.
- [20] D.G. Howden and D.R. Milner: *British Welding Journal*, June 1963, pp. 304-316.
- [21] S.A. Gedeon and T.W. Eagar: *Welding Journal*, July 1990, vol. 69, pp. 264s-271s.
- [22] H. Li and T.H. North, "Hydrogen Absorption and Hydrogen Cracking in High Strength Weld Metal." Key Engineering Materials Vols. 69 & 70. Eds. D. L. Olson and T. H. North. Trans Tech Publications, 1992, 95-112.
- [23] S.A. Gedeon, "Hydrogen Assisted Cracking of High Strength Steel Welds," Doctoral Thesis at Massachusetts Institute of Technology, May 1987.
- [24] M. A. Quintana, P. Cote, and L.G. Kvidahl. "Hydrogen Measurement Techniques." Hydrogen Management for Welding Applications – Proceedings of International Workshop, October 6-8, 1998, Ottawa, Canada. Eds. J.E.M Braid, C.V. Hyatt, D.L. Olson, and G.N. Vigilante. Ottawa: CANMET, 1999. 155-169
- [25] F.T. Fabling and B. Chew: *Welding Research International*, 1973, vol. 3, no. 4, pp. 81-87.
- [26] American Welding Society: AWS A4.3-93.

- [27] M.A. Quintana: *Welding Journal*, 1984, vol. 63, pp. 141s-149s.
- [28] S.K. Albert, C. Remash, N. Murugesan, T.P.S. Gill, G. Periaswami, and S.D. Kulkarni: *Welding Journal*, July 1997, vol. 76, pp. 251s-255s.
- [29] M. Matsushita, "Clarification of Hydrogen Reduction Mechanisms in Steel Weld Metal by Means of Fluoride Additions in Welding Flux," Doctoral Thesis at the Colorado School of Mines, September 2001.
- [30] C.B. Shaw, Jr.: *Welding Journal*, 1975, vol. 54, pp. 33s-44s (Part 1), pp. 81s-86s (Part 2).
- [31] W. Petrie and E. Pfender: *Welding Journal*, 1970, vol. 49, pp. 588s-596s.
- [32] C.J. Cremers and R.C. Birkebak: *Applied Optics*, 1966, vol. 5, pp. 1057-1064.
- [33] J.F. Key, J.W. Chan, and M.E. McIlwain: *Welding Journal*, 1983, vol. 62, pp. 179s-184s.
- [34] M.N. Saha and B.N. Srivastava, A Text Book of Heat. Indian Press, Ltd., Allahabad, India, 1931.
- [35] M. Kobayashi and T. Suga, "A Method for the Spectral Temperature Measurement of a Welding Arc." Arc Physics and Weld Pool Behaviour – International Conference Proceedings, London, May 8-10 1979. Ed. W. Lucas. Abington: The Welding Institute, 1980, 25-37.
- [36] S.S. Glickstein: *Welding Journal*, 1976, vol. 47, pp. 222s-229s.
- [37] K. Hiraoka, T. Shiwaku, and T. Ohji: *Welding International*, 1997, vol. 11, pp. 688-698.
- [38] K. Hiraoka: *Welding International*, 1998, vol. 12, pp. 186-194.
- [39] G.S. Mills: *Welding Journal*, 1977, vol. 56, pp. 93s-96s.
- [40] J.E. Shea and C.S. Gardner: *Journal of Applied Physics*, 1983, vol. 54, pp. 4928-4938.

- [41] R.A. Weber, "Detection of Hydrogen in the Welding Arc." Hydrogen Management in Steel Weldments – Proceedings of the Joint Seminar, October 23, 1996, Melbourne, Australia. Eds. J.L. Davidson and D.L. Olson. Defence Science and Technology Organisation, 1997, 113-123.
- [42] D. R. White, "In Process Measurement of Hydrogen in Welding." Technical Manuscript M-86/15, USA-CERL, September 1986.
- [43] CRC Handbook of Chemistry and Physics: 84th Edition. CRC Press, 2003.
- [44] J. Norrish. Advanced Welding Processes. Institute of Physics Publishing, New York, 1992.
- [45] M. Hermans, A Study of Short Circuiting Arc Welding. Delft University Press, Delft, The Netherlands, 1997.
- [46] W.F. Savage, E.F. Nippes, and E.I. Husa: *Welding Journal*, 1982, vol. 61, pp. 233s-242s.

List of Posters, Papers and Presentations Attached

1. Posters

- a. High Strength Steel Welding: Effects of Fluoride and Yttrium Additions on Weld Metal Properties - Craig Clasper – First Place Graduate Student Poster Award – 2004 AWS Technical Program
- b. Spectroscopic Monitoring of Welding Arcs - Justin Chandler – Second Place Graduate Student Poster Award – 2004 AWS Technical Program

2. Papers & Presentations

- a. Important Lessons Learnt in The Design of Consumables for Welding High Strength Steels - Stephen Liu – 2004 ASM International Materials Solutions Conference
- b. Spectroscopic Monitoring of Hydrogen in Welding Arcs - J. Chandler, G. Edwards, and S. Liu – 2005 Trends in Welding Research Conference
- c. Microstructural Design for High Strength Steel Welds: The Concept of Duplex Microstructure – 2005 OMAE Conference
- d. GTAW of Titanium Using Flux-Cored Wire with Magnesium Fluoride - Kook-Soo Bang, Greg Chirieleison, and Stephen Liu – Journal of Science and Technology of Welding and Joining, 2005

High Strength Steel Welding:

Effects of Fluoride and Yttrium Additions on Weld Metal Properties



by Craig Clasper

Colorado School of Mines, CWJCR, Golden, CO 80401

Research Motivation:

Develop an optimized flux cored arc welding consumable that improves weld metal microstructure and mechanical properties, limits the presence of diffusible hydrogen, and reduces the need for pre- and post weld heat treatments in high strength low alloy steels.

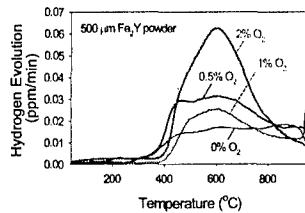
Methodology:

Starting with a previously studied consumable containing yttrium, a replicate of the consumable was fabricated along with six additional consumables containing a range of potassium fluoride additions from 5% to 30%. Microstructure, macrostructure, and chemical analysis were performed. Mechanical properties of multipass welds produced with the replicated consumable and the most promising consumable containing KF

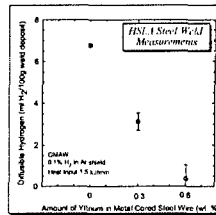
Background:

Effects of Yttrium Additions

Yttrium additions up to 600ppm in the weld metal reduced the diffusible hydrogen by fifty percent. Binding energies of yttrium-containing inclusions are greater than reversible traps such as microvoids. Hydrogen release temperature of yttrium-containing particles are higher than those of dislocations and voids.



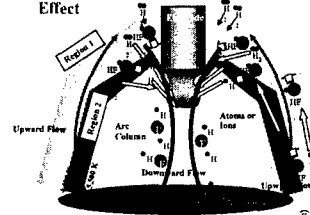
Yttrium has been found to create effective diffusible hydrogen traps. Previous research has allowed for the development of a methodology to optimize yttrium alloying to allow the formation of fine acicular ferrite microstructures.



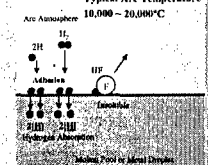
Effects of Fluoride Additions

Vaporized fluorides dilute the arc ingredients and decrease the partial pressure of hydrogen in the arc, P_{H_2} , thereby reducing the hydrogen pickup in the weld pool and combine with hydrogen to form HF, thus removing the hydrogen from the arc system

HF Transport Effect



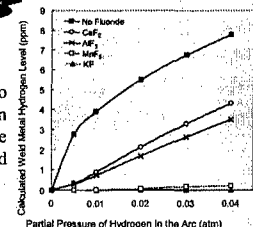
HF Formation



With CaF_2 Addition to the arc, H Accumulation at the Arc Center decreased

Retardation of H Transport due to HF Formation

HF Formation Effect



KF and K_2AlF_6 were found to exhibit excellent effectiveness in hydrogen control, reducing the diffusible hydrogen to around 1.5ml/100g weld metal.

M. Clark, 2001

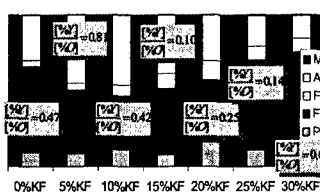
M. Matsushita, 2001

KF Additions to Yttrium Containing Consumable

Preliminary Matrix

Increasing additions of KF affected arc stability causing an increase in ΔV and was detrimental to weld metal properties. As-deposited microstructures of welds produced with consumables containing up to 15% KF contained 30-45% AF and 35-55% FS microstructures. Beyond 15% KF additions, AF content decreased and FS content increased.

Effect of KF Additions on Microstructure

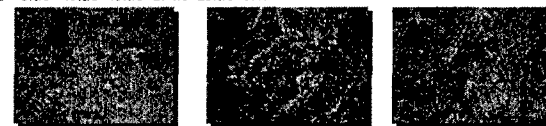


KF Additions (%)	Y (ppm)	O (ppm)	[Y]/[O] ratio
0%	317	680	0.47
5%	792	980	0.81
10%	308	740	0.42
15%	109	1117	0.10

Additions of KF proved to be effective in the reduction of weld metal hydrogen content from greater than 4ppm to as low as 1.5ppm. Weld metal oxygen content was increased from less than 700ppm to greater than 1500ppm partly due to the increase in arc instability with excessive KF additions. With the increased oxygen content, there is insufficient yttrium to form effective acicular ferrite nucleation sites and hydrogen traps.

Chemical Composition

KF Additions (%)	0%	5%	10%	15%
Ni	3.78	2.85	3.70	1.53
Mn	1.47	1.41	1.40	0.74
Mo	0.42	0.19	0.35	0.01
Ti (ppm)	150	164	52	20
V (ppm)	50	37	22	28
Al (ppm)	170	120	88	62
Y (ppm)	317	792	308	109



Excessive KF additions reduced pickup of alloying additions important for microstructural optimization and improved mechanical properties.

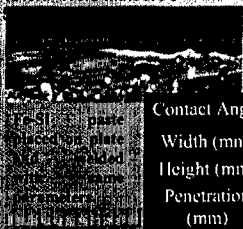
Mechanical properties were tested on welds produced with the 0%KF and 5%KF addition consumables. The 0%KF weld demonstrated a greater strength but, due to an insufficient content of AF, did not demonstrate improved impact toughness. Whereas, the 5%KF consisted of higher fractions of AF and resulted in greater impact toughness, but less than desired strength.

Mechanical Properties

	0%KF	5%KF
Microhardness, Hv	270	190
Yield Strength, ksi	78	64
UTS, ksi	94	77
Elongation	15%	14%
Impact Toughness @ -60°F, ft-lb	22	32
Impact Toughness @ 0°F, ft-lb	29	52

Improvement of Weld Metal Properties with Ferro-Silicon

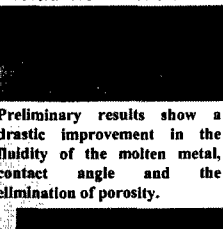
0%KF Weld without Fe-Si



Contact Angle
Width (mm)
Height (mm)
Penetration (mm)

	w/o FeSi	w/ FeSi
Contact Angle	108	43
Width (mm)	9.7	1.5
Height (mm)	4.4	5.0
Penetration (mm)	2.7	2.9

10%KF Weld with Fe-Si



Preliminary results show a drastic improvement in the fluidity of the molten metal, contact angle and the elimination of porosity.

Fabrication of consumables containing KF, Y, and Fe-Si additions is currently on-going to determine an optimized consumable.

Conclusions:

- The combination of KF and Y additions shows improvement in hydrogen management, but need improvement in molten and solidified weld metal characteristics.
- Excessive additions of KF (>10%) are detrimental to weld metal properties.
- The proper balance of yttrium, titanium, and potassium fluoride in the consumable can result in the control of oxygen in the weld metal to allow the formation of inclusion that can both act as hydrogen traps and nucleation sites for acicular ferrite further improving weld metal microstructure and mechanical properties.
- The addition of ferrosilicon in the consumable, approximately 1%, will allow improved weld metal characteristics through improved molten weld metal fluidity, decreased wetting angle, and the elimination of porosity.
- An optimized consumable can produce weld metal strength in the range of 88-115ksi, 20% elongation, and 35 and 60 ft-lb at -60°F and 0°F.



Spectroscopic Monitoring of Welding Arcs



Justin Chandler

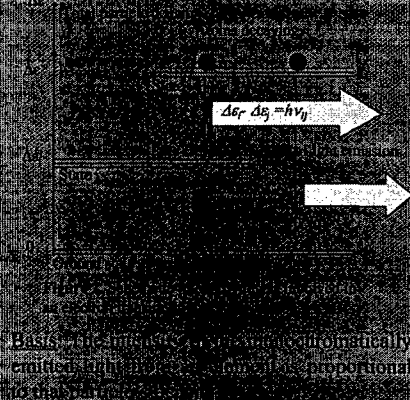
Center for Welding, Joining, and Coatings Research – Colorado School of Mines

Background

Problem: Hydrogen entrapped in weldment during deposition migrates to defects and enlarges them to form microcracks which may lead to macroscopic failure.



Figure 1. Example of hydrogen assisted cracking in a weldment.



Pickup: Hydrogen pickup in the weld metal occurs due to the presence of hydrogen in the arc. Hydrogen is introduced into the arc from moisture in the atmosphere and contaminants in the consumable.

Present: The most common way to determine the hydrogen content of a weldment is through destructive analytical techniques.

Goal: Develop a non-destructive in-situ spectroscopy process for evaluating the hydrogen content of monitored welds.

Experimental Procedure

Methodology: Welding arcs were monitored during deposition of diffusible hydrogen samples. The amount of hydrogen in the argon shielding gas was systematically varied from 0% to 3% to determine the ability to spectroscopically observe hydrogen's presence in the arc and relate it to hydrogen pickup in the weld metal.

Measurement: The diffusible hydrogen content of the weldments were determined with a gas chromatograph according to the standard AWS/ANSI A4.3-93.

Data Collection: The spectroscopy apparatus was used to amplify the light signal from the arc and collect it into a fiber optic cable. The signal was then sent to a computer within the threshold.

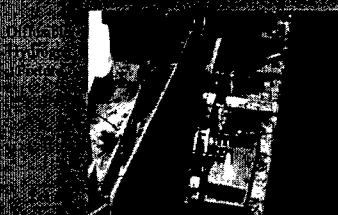


Figure 3. Photograph of the spectroscopy apparatus.

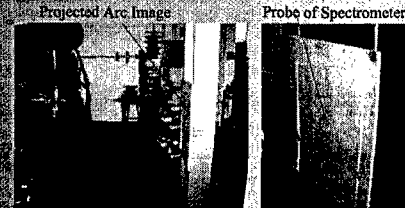


Figure 4. Photograph of arc projection and light signal collection setup.

Data Collection: An image of the arc is projected onto a screen that houses the probe of the spectrometer. Adjusting the height of the screen controls the region of the arc being monitored.

Results and Discussion

Transfer Mode: A spray metal transfer mode was required for proper ionization signal collection.

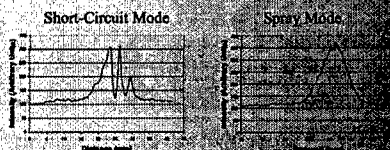


Figure 5. Comparison of spectroscopic data obtained from welding arc in short-circuit mode and spray mode.

Hydrogen Concentration: The hydrogen ionization signal is masked by iron ionization signals. Saha's equation is utilized to calculate the concentration of hydrogen ions as determined from the neutral hydrogen emission line.

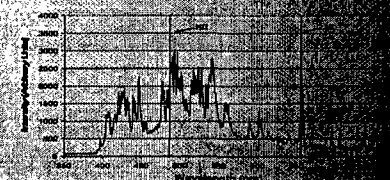


Figure 6. Spectra of GMAW arc during deposition. The hydrogen ionization signal is masked by the iron ionization signal.

The hydrogen ionization signal is masked by iron ionization signals. Saha's equation is utilized to calculate the concentration of hydrogen ions as determined from the neutral hydrogen emission line.

Concentration Calculation: Once the temperature is determined, the ionization fraction of a given element can be determined using Saha's ionization equation. The relation between ionization fraction and particle density is utilized to calculate the concentration of a given element.

Saha Ionization Equation

$$\frac{n_i}{n_a} = \frac{2}{\pi} \left(\frac{2\pi m_e}{h^2} \right)^{3/2} \frac{(kT)^{5/2}}{p_a} \frac{2q_i}{q_a} \exp\left(-\frac{eV_i}{kT}\right)$$

Ionization fraction	$\frac{n_i}{n_a}$
Temperature	T = temperature
Pressure	p = pressure
Pressure at	p_a = partition function of ion
Ion level	q_i = partition function of neutral atom
Electron mass	m_e = electron mass
Planck's constant	h = Planck's constant
Boltzmann	k = Boltzmann constant
Ionization voltage	V_i = ionization voltage
Electron charge	e = electron charge

Conclusion: Spectroscopy of a GMAW arc produced the relationship between hydrogen concentration in the arc and in the weld metal seen in the literature. The relationship appears similar to the Arrhenius Law. This result shows that the spectroscopic monitoring of a welding arc is able to predict the concentration of hydrogen in the weld metal.

Important Lessons Learnt in the Design of Consumables For Welding High Strength Steels

STEPHEN LIU

Center for Welding, Joining and Coatings Research
Colorado School of Mines, Golden CO 80401

Colorado School of Mines has built a tradition in consumables research for high strength steels during the past three decades. In the 1970's, Mines researchers investigated submerged arc welding for pipeline applications and systematically characterized the fundamental behavior of welding fluxes. They also established the relationships between flux ingredients, weld metal microstructure and weld joint mechanical properties. The knowledge gained in these studies was later applied to the development of coated electrodes for welding steels of 130-ksi yield strength. These studies established the importance of molten flux-weld pool interaction on alloying elements recovery and the non-uniform nature of weld chemical composition. The bimodal nature of weld metal inclusions were observed and related to weld pool deoxidation and weld solidification. High strength steel welding requires more stringent consumables that can deliver low diffusible hydrogen and high weld metal toughness. Consumables that result in low diffusible hydrogen, increased productivity, and enhanced weld properties are in great demand. As strength and toughness levels of the steels continue to increase, new generations of consumables must be developed. Two novel consumables design concepts are being investigated at the Colorado School of Mines for steels with strengths greater than 100-ksi yield strength. The first one is based on a duplex microstructure consisted of lath martensite and ferrite. The second one is based on low carbon, high alloy martensite.

Introduction

High strength low alloy steels containing vanadium, niobium and titanium have been in use since the 1970's with significant technical advances in plate metallurgy through the years. Development in consumables for welding these steels has been equally impressive. This paper is a comparative study of the progress in high strength steel welding accomplished in the past two decades. First, it describes the state of the understanding in HSLA steel welding in the early 1980's. Then it will review the current state of development in high strength steel welding. The discussion will contrast approaches in weld metal development in terms of microstructural control.

HSLA Steel Weld Metals at Yield Strengths < 600 MPa

Advances in HSLA steel welding have progressed to the point where weld metals of approximately 600 MPa (87 ksi) yield strengths and good toughness can readily be made, and considerable knowledge concerning the major microstructural constituent of these weld metals, acicular ferrite, has been accumulated. Many researchers (1-4) reported that the best weld metal properties are achieved in HSLA steels at yield strength levels of 600 MPa or less by eliminating most allotriomorphic or grain boundary ferrite, Widmanstätten ferrite, and bainite or martensite.

The chemical composition, thus hardenability, of these steels is such that the bainitic and martensitic transformations be avoided at nominal cooling rates. As such, the major problem becomes that of preventing the formation of grain boundary ferrite, while refining the acicular ferrite. Factors that suppress grain boundary ferrite formation and promote acicular ferrite formation are crucial to the welding of these steels.

Factors that Suppress Grain Boundary Ferrite While Promoting Acicular Ferrite

The mechanisms by which austenite decomposes in HSLA steel weld metals were established in the 1970's and 1980's. During austenite decomposition, the first product to form is grain boundary ferrite, which is unfavorable with respect to both strength and toughness. Increasing the cooling rate helps prevent grain boundary ferrite, but it may also lead to the formation of lower temperature transformation products such as bainite and martensite. Alloying element additions may also achieve the goal of minimizing the amount of grain boundary ferrite, if the right combination of elements is selected. However, excessive hardenability elements will again result in lower temperature products with inferior performance. Thus, it is essential to design a weld system with adequate weld metal composition and weld thermal cycle to minimize both high and low temperature transformation products.

Austenite Grain Size Effect

For a similar chemical composition and cooling rate, steels of large austenite grain size exhibit high hardenability, the direct result of a smaller grain surface area-to-volume ratio (indication of a low number of nucleation sites).

Consequently, less grain boundary ferrite is expected in the final microstructure of a coarse-grained austenite.

Considering the high temperatures at which grain boundary ferrite is formed, grain boundary ferrite transformation was described as a two-step process: 1) (Site saturation) nucleation at the prior austenite grain boundaries coats the boundaries with a thin film of allotriomorphic ferrite; and 2) planar diffusional growth of ferrite consumes the austenite grains (in a direction perpendicular to the austenite grain boundaries.) Liu and Olson (5) adapted the Avrami equation to describe grain boundary ferrite formation under conditions of continuous cooling:

$$X = 1 - \exp\left(-\frac{3\sqrt{t}}{d}\right) \quad (1)$$

In this equation, X is the volume fraction of grain boundary ferrite transformed, t is the cooling time from 800 to 500°C, also known as $\Delta t_{5/8}$, and d is the prior austenite grain diameter.

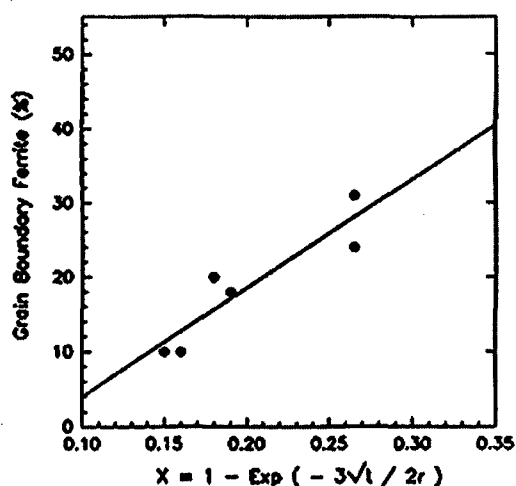


Figure 1. Calculated and measured volume fraction of grain boundary ferrite demonstrating good correlation (5).

These authors showed in Figure 1 the effect of prior austenite grain size on the amount of primary ferrite (grain boundary ferrite and sideplate ferrite) in a niobium microalloyed HSLA steel weld metal. With increasing

prior austenite grain size, the amount of primary ferrite was observed to decrease (5). Fleck, Grong, Edwards, and Matlock (6,7) also observed the same behavior; namely, that grain boundary ferrite decreased with increasing austenite grain size.

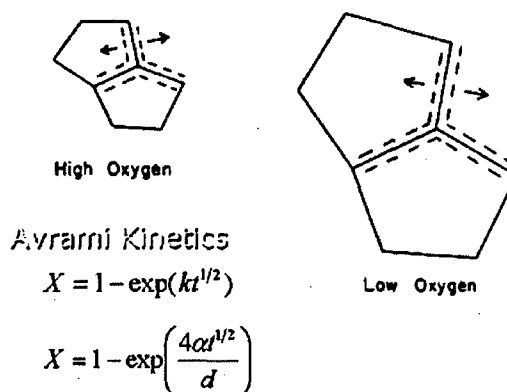


Figure 2. Schematic drawing of prior austenite grains to illustrate the effect of grain size on austenite decomposition (6,7).

The good correlation between the experimentally measured volume fraction of grain boundary ferrite and the fraction calculated by Equation 1, (see Figure 1) indicates that grain boundary ferrite formation can be predicted by overall transformation theory. Fleck et al. (7) modified Equation 1 to consider the fraction of allotriomorphic ferrite at fixed cooling time, but with varying austenite grain sizes. They suggested that austenite grain size was sensitively dependent upon oxygen content, as indicated in the schematic diagram, Figure 2. Fleck et al. (7) expressed the Avrami equation in the following form:

$$\ln(1 - X) = \frac{(-4\alpha t^{1/2})}{d} = \frac{(const)}{d} \quad (2)$$

α is the growth constant and the other variables have similar meanings as in Equation 1.

Figure 3 quantitatively illustrates this relationship between fraction of grain boundary ferrite and austenite grain size. Ferrite nucleation occurs on the austenite grain boundaries; the larger the austenite grain size, the smaller will be the volume fraction of grain boundary ferrite formed in a fixed time, as shown in Figure 3. The ability of these equations in predicting the amount of grain boundary ferrite is excellent and very comparable to the more recent and sophisticated numerical models.

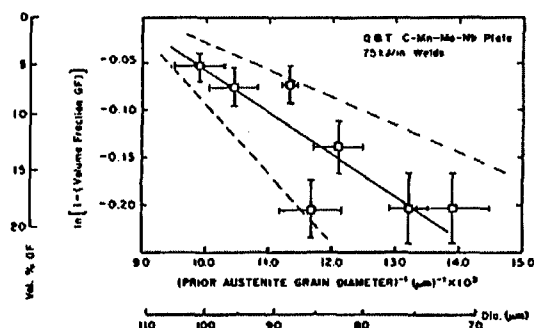


Figure 3. Calculated volume fraction of grain boundary ferrite as a function of prior austenite grain diameter (6,7).

Liu and Olson (5), Fleck, et al. (7), and Harrison and Farrar (8) correlated weld metal oxygen content, and thus, inclusion density, with austenite grain size. Oxygen-rich particles are commonly responsible for refining the austenite grain structure and promoting the formation of transformation products other than acicular ferrite. With adequate control, the amount of grain boundary ferrite can be limited to maximize intragranular products such as acicular ferrite.

Factors Affecting the Formation of Acicular Ferrite Inclusion Size Distribution & Location

Liu and Olson (5) found in niobium microalloyed steels that high oxygen weld metals contained large numbers of very fine (<0.1 μm) particles, while low oxygen welds contained large numbers of inclusions of approximately 0.3 μm in diameter. The low-oxygen (250-350 ppm) weld metals also contained the largest fraction of acicular ferrite. When the grain boundary particle densities were measured, Liu and Olson (5) found that the particle size distribution, which governed the density of inclusions in the grain boundaries, indirectly controlled the austenite grain size, as indicated in Figure 4. The difference between the total inclusion volume fraction and the fraction associated with the grain boundaries is the volume fraction of intragranular inclusions, which provide potential sites for ferrite nucleation within the grains. However, a large number of intragranular inclusions alone do not guarantee a high acicular ferrite content. Small prior austenite grains stabilized by a large number of small inclusions may also result in a large fraction of grain boundary ferrite. Thus, to possess a fine microstructure with high acicular ferrite content, the weld metal must have an adequately large prior austenite grain size and an optimal intragranular inclusion density.

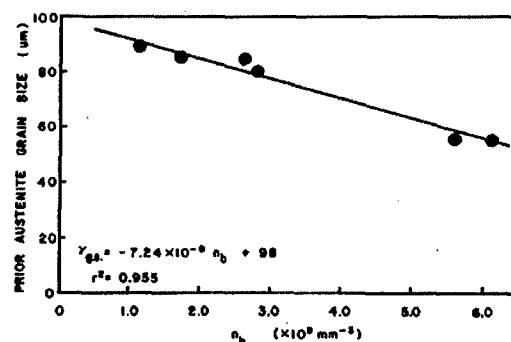


Figure 4. Prior austenite grain size as a function of number of inclusions along the grain boundary (5).

Alternate Strengthening Mechanisms for Steels with Strengths > 630 MPa (90 ksi)

As observed in the 1980's, HSLA steels can be strengthened to about 600 MPa if ferrite lath refinement was the only mechanism. For higher strengths, alternate strengthening mechanisms would be required (9). Figure 5 shows the Hall-Petch correlation (grain size strengthening) (10) for ferrite, revealing that 1.2- μm ferrite laths are required for a 600-MPa-yield strength. Figure 6 suggests that perhaps an additional 100 MPa could result from the fine niobium, vanadium, or titanium precipitates commonly present in HSLA steel base plate (Ashby-Orowan relationship). Solid solution strengthening (elastic lattice distortion) of ferrite by silicon, manganese, copper or molybdenum conceivably could add an additional 150 MPa to the strength, as indicated in Figure 7.

$$\sigma_{\text{Flow}} = \sigma_0 + k d^{-1/2} + \sum_i k_i C_i + k \frac{f^{1/2}}{X} \ln \left(\frac{X}{k_1} \right) \quad (3)$$

Equation 3 summarizes the effects of grain refinement, solid solution strengthening, and precipitation strengthening. In this equation, σ_0 is the peierls stress, k is a constant, d stands for the prior austenite grain size, k_1 and C_i are the constant and concentration for alloying element 1, respectively, X is the average diameter of the precipitates, and f is the volume fraction of the precipitates. To increase beyond the range of 480 to 550 MPa (70 to 80 ksi), a microstructure consisting of bainite or lath martensite would be required.

However, in steel weld metals, the classical precipitation or solid solution strengthening effects cannot be simply utilized. The ultrafine microalloying carbides or carbonitrides are expected to be completely altered by the welding process. Additionally, there is a large population of coarser oxide inclusions. The solid solution additions significantly increase hardenability, and promote

formation of bainite or martensite. It is generally accepted that either bainite or martensite, or both, will constitute a fraction of the microstructure in HSLA steel weld metals of yield strength levels exceeding 600 MPa (87 ksi). Here the challenge is to provide adequate toughness in these high strength weld metals, and to do so over a wide range of cooling rates.

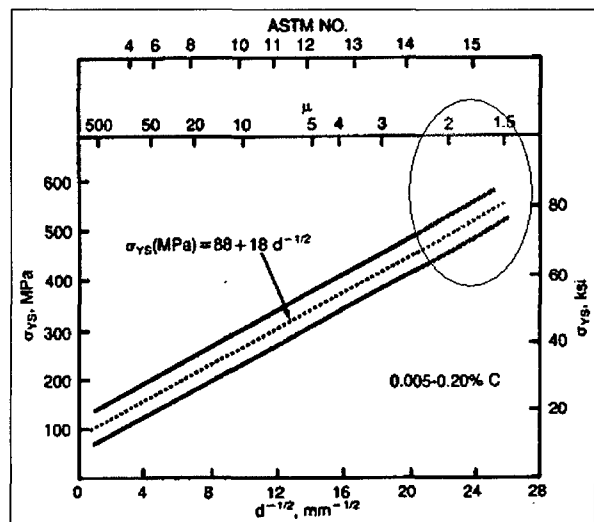


Figure 5. Hall-Petch plot to illustrate the limitation of the extent of grain refinement (10).

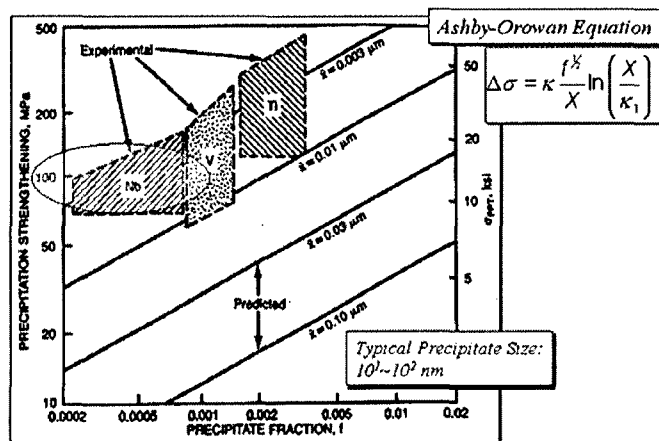


Figure 6. Precipitation effect according to the Ashby-Orowan Equation (23).

Copper, as a precipitation agent, has a strong effect on the strength and toughness, and the microstructural evolution of HSLA steel weld metals. Investigating SMAW with copper additions from 0.0 wt.pct. to 3.2 wt.pct., Es-Souni et al. (11) noticed solid solution strengthening effect at copper contents up to 0.19 wt. pct. When the copper content increased above 0.66 wt.pct., σ -copper

precipitation strengthening was evident. In addition, he also found that copper preferentially precipitated along dislocations and interphase boundaries, which agreed with Thompson's observation (12). Based upon quantitative metallography, Es-Souni (11) showed that the volume fraction of FS(A) (ferrite with aligned second phases) increased with copper content. Based on tensile and Charpy V-notch impact data, he concluded that 0.66 wt.pct. copper content was desirable for both strength and toughness of plain carbon steel weld metals. However, Krishnadev et al. (13) explored lower levels of copper contents, ranging from 0.046 wt.pct. to 0.56 wt.pct., in HSLA-100 steel weld metals that contained Ni, Cr, and Mo, and obtained a higher strength level (greater than 100 ksi (690 MPa)) and a fair Charpy V-notch toughness (40.6 ft-lb (55 J) at $-51^\circ C$ ($-60^\circ F$)). The good mechanical properties led to the conclusion that 0.5 wt.pct. copper content in the weld metal did not cause any adverse effect on the toughness.

The hardness fluctuations (Δ Hardness) on the cross-sections of the 1.0 kJ/mm weld metals was also minimized from over 100 DPH, with no Nb addition (14,15), to less than 50 DPH, with 0.03 wt.pct. Nb addition. This minimization of hardness fluctuation was attributed to the synergistic precipitation mechanism in the Cu-Nb enhanced weld metals as proposed by Ramirez and Liu (15).

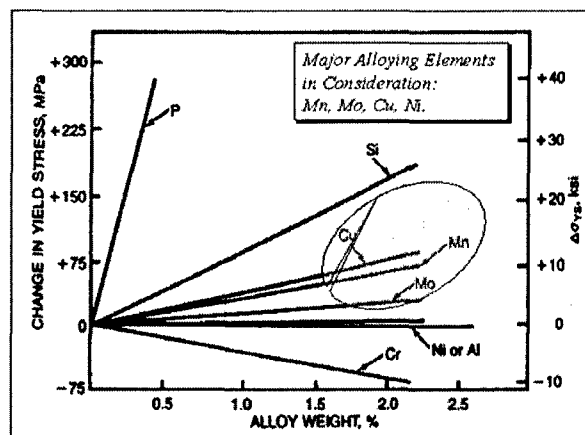


Figure 7. Solid solution effect in ferrous alloys (23).

The weld metal with a dual phase microstructure – a predominant amount of AF (around 70%) and a smaller amount of granular bainite (around 15%) offered respectable impact toughness results for high strength steels. With the AF and G.B. optimized, coarse FS(A) appeared to enhance the toughness performance by offering greater resistance to crack propagation (14).

Another dual phase microstructure that contained mainly acicular ferrite (60 vol. pct.) and martensite (30 vol. pct.) was found to exhibit good strength and acceptable toughness in single pass HSLA-100 steel weldments. (16) This microstructure resulted from the interaction of specific amounts of alloying elements (Mn, Si and Ti) with weld metal oxygen. Figure 8 shows the two dual phase microstructures in HSLA-100 steel weld metals.

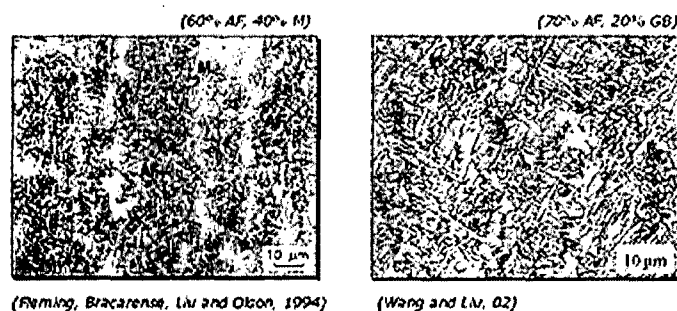


Figure 8. Duplex microstructures in high strength steel weldments, martensite-acicular ferrite and granular bainite-acicular ferrite (14,16).

Wang and Liu (14) reported that the main microstructural constituents that proportionated the required yield strength of 690 MPa (100 ksi) and impact toughness of (81 J) 60 ft-lb at -18°C (0°F), 61 J (45 ft-lb) at -35°C (-30°F), and 27 J (20 ft-lb) at -51°C (-60°F) in high strength steel welds are: granular bainite (GB), lath martensite (M), and acicular ferrite (AF). A mixture of 20 vol. pct. granular bainite and 70 vol. pct. acicular ferrite or a mixture of 40 vol. pct. lath martensite and 60 vol. pct. acicular ferrite will both provide the required properties as specified for naval applications. Ferrite with second phase aligned (FS(A)) and ferrite with second phase non-aligned (FS(NA)) make up the remaining microstructure. These microstructures are shown in Figure 8. With the GB, LM and AF optimized, coarse FS(A) laths can further improve the mechanical properties of these welds because of the reduced total interlath surface area and smaller amount of interlath carbide arrays. These combined features exhibit greater resistance to crack propagation. An optimal alloying system (in wt. pct.) for an HSLA-100 steel weld metal was reported as: 0.04 wt. pct. C, 1.30 wt. pct. Mn, 0.26 wt. pct. Si, 2.30 wt. pct. Ni, 0.40 wt. pct. Mo, 0.80 wt. pct. Cu, 0.03 wt. pct. Nb, 90 ppm N (max), and 270 ppm O.¹⁵ This composition reduced the amount of grain boundary ferrite and sideplate ferrite, but promoted the formation of acicular ferrite, bainite and martensite.

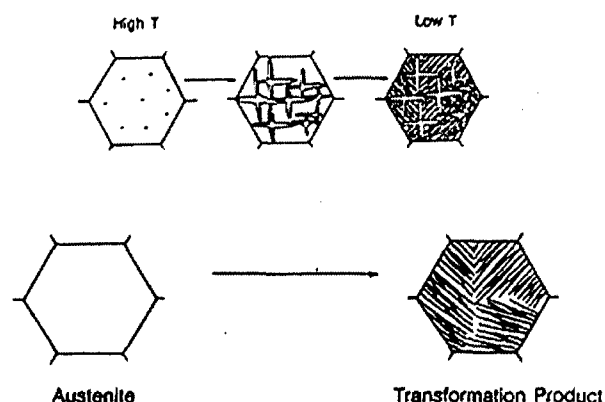


Figure 9. Schematic drawing to illustrate the toughening mechanism for high strength steel weld metal. Inclusion populations that limit prior austenite grain size and promote intragranular nucleation will break austenite grains into small packets, improving impact toughness (17,18,22).

Ramsay, et al. (17-18) studied more highly alloyed, high strength weld metals, and found that sufficient hardenability was present so that allotriomorphic or grain boundary ferrite could be avoided at conventional submerged arc welding heat inputs. They also found that small austenite grain size, fine acicular ferrite, and small packets of lath martensite would allow excellent weld metal toughness at a given strength level. Their explanation for a toughening mechanism for high strength steel weld metal is schematically illustrated in Figure 9. High oxygen content specimens underwent less grain growth because of grain boundary pinning by inclusions. Upon cooling, intragranular nucleation of acicular ferrite occurred in these welds and "subdivided" the original austenite grains into grains of a much finer "apparent austenite grain size".

Weld metals containing a mixture of low carbon lath martensite, low carbon bainite, and acicular ferrite have been reported (20-23) to be highly desirable. This mixed microstructure does not readily retransform during reheating, and thus is stable during multi-pass welding. To achieve the required high yield strength (over 700 MPa) and toughness, weld systems containing 0.05 wt.pct. carbon, high manganese (at 1.8 wt pct) and nickel (2 to 3 wt pct), medium molybdenum (0.5 to 1 wt pct), and low chromium (up to 0.5 wt pct) are typically recommended. By combining different high strength to low strength constituents in the microstructure, Liu, Wang, Bracarense, and Ramirez were able to design in the early 1990's weld metals within a relatively wide range of properties that could satisfy the high strength steel welding criteria.

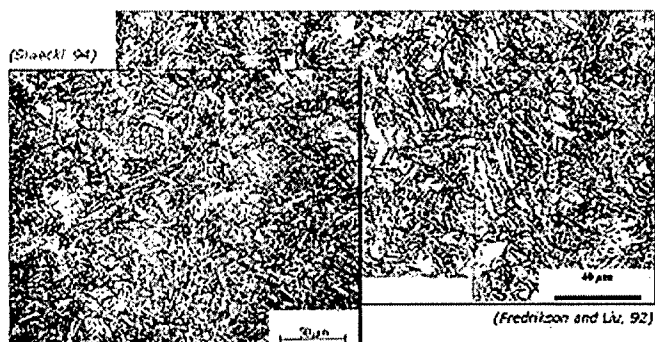


Figure 10. Bainitic and martensitic microstructure of high strength steels with 690 MPa (100 ksi) yield strength and above (23).

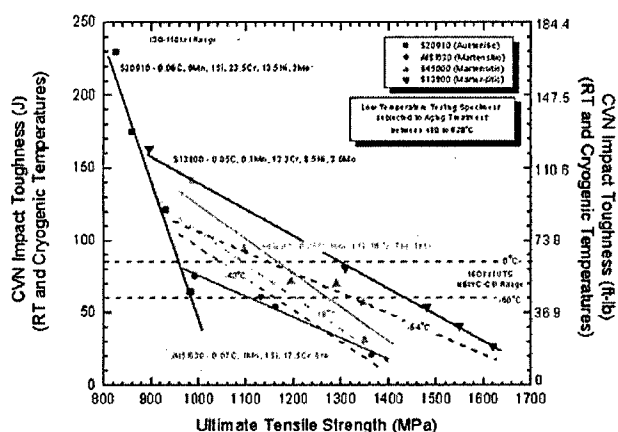


Figure 11. Supermartensitic alloys with excellent impact toughness as filler metal for welding high strength steels.

HSLA Steel Weld Metals with Yield Strengths > 690 MPa (100 ksi)

As indicated earlier, when the strength level of a steel increases beyond the 550 MPa (80 ksi) level, martensite and/or bainite are likely to be present. Figure 10 illustrates the microstructures of two steels whose yield strengths exceed the 690 MPa (100 ksi) level. However, neither steel martensite nor steel bainite is an intrinsically brittle

microconstituent. Low carbon plate martensite can be quite strong as well as tough, as demonstrated by the properties of maraging steels (19). Likewise, ultra-low carbon bainite has been shown to be quite tough (20-21). Intuitively, one might anticipate better toughness in fine martensite, where non-aligned high angle boundaries between plates would create a more tortuous crack path than that provided by the aligned boundaries in a low-

carbon bainite packet. For filler metal, supermartensitic based materials may be adequate. Figure 11 shows the impact toughness of several high chromium alloy systems. At 1000 MPa (140 ksi) tensile strength level, alloys with 0.05 wt.pct. carbon, 13 to 17 wt.pct. chromium, 7 to 8 wt.pct. nickel, and 1 to 4 wt.pct. molybdenum were able to offer greater than 110 J (80 ft.lb.) impact energy to below -20°C. These data demonstrate great potential and they should be further investigated.

Summary

Examining past and current literature on high strength steel welding, the findings of CSM on austenite grain size control and acicular ferrite formation contributed significantly to the understanding of welding HSLA steel weld metal. In the case of steels with yield strengths greater than 690 MPa (100 ksi), a different approach was proposed in the 1990's. A dual phase microstructure of martensite and acicular ferrite was designed to provide both high strength and high impact toughness. The concept of mixed microstructures was later successfully extended to granular bainite and acicular ferrite by the CSM researchers. Publications from the industry demonstrate that the dual phase microstructure concept has been transitioned to practice in the welding of steels with 840 MPa (120 ksi) strength. Based on the concept that low carbon lath martensite is not necessarily brittle, the use of super martensitic microstructure is being proposed as filler for welding higher strength steels.

Acknowledgments

The author would like to acknowledge the support of Dr. Julie Christodoulou of the Office of Naval Research. The collaboration and contribution by Dr. David Olson in steel welding research at CSM are gratefully acknowledged. My special thanks are given to Dr. Glen Edwards for his unselfish collaboration. The compilation of the supermartensitic alloys data by Dr. Fernando Martinez is greatly appreciated.

References

1. Dolby, R.E. 1976. *Factors Controlling Weld Toughness - The Present Position. Part II - Weld Metals*. 14, The Welding Inst.
2. Glover, A.G.; McGrath, J.T.; and Eaton, N.F. 1977. *Fracture Toughness of Submerged Arc Weld Metal. Proc. on Toughness Characterization and Specifications for*

HSLA and Structural Steels Conf: 143- 160, Metallurgical Society of AIME.

3. North, T.H.; Bell, H.B.; Koukabi, A.; and Craig, I. 1979. Notch Toughness of Low Oxygen Content Submerged Arc Deposits. *Welding Journal* 58 (12): 343-s to 354-S.
4. Ito, Y.; and Nakanishi, M. 1976. A Study of Charpy Impact Properties of Weld Metals with Submerged Arc Welding. *The Sumitomo Search* 1242. 13. Watanabe, I.; and Kojima, T. 1980 Effects of Titanium, Boron, and Oxygen on Notch Toughness. *J. Japan Weld. Soc.* 49: 772.
5. Liu, S. and Olson, D.L. 1986. The Role of Inclusions in Controlling HSLA Steel Weld Microstructures. *Welding Journal* 65 (6): 139-s-149-s.
6. Fleck, N.A. 111 1984. *The Effect of Filler Wire and Flux Compositions on the Microstructure and Properties of Microalloyed Steel Weld Metal*. M.S. Thesis, Golden, Colorado: Colorado School of Mines.
7. Fleck, N.A.; Grong, O.; Edwards, G.R.; and Matlock, D.K. 1986. The Role of Filler Metal Wire and Flux Composition in Submerged Arc Weld Metal Transformation Kinetics. *Welding Journal* 65 (5): 1 13-S.
8. Harrison, P.L. and Farrar, R.A. 198 1, Influence of Oxygen-Rich Inclusions on the Austenite-to- Ferrite Phase Transformations in High-Strength Low-Alloy (HSLA) Steel Weld Metals. *Journal of Materials Science* 16: 22 18.
9. Repas, P.E. 1988. Metallurgical Fundamentals for HSLA Steels. *Proc. on Microalloyed HSLA Steels Conf*: 3-14. ASM World Materials Congress.
10. Morrison, W.G. 1966. *ASTM Trans.* 59: 824-46.
11. Es-Souni, M., Beaven, P.A. and Evans, G.M., 1991, "Microstructure and mechanical properties of Cu-bearing MMA C-Mn weld metal", *WRA*, Vol. XXXVII, No. 2/3, 1991, p84-95.
12. Thompson, S.W. and Krauss, G., 1996, "Austenite Decomposition During Continuous Cooling of an HSLA-80 Plate Steel", *Metallurgical and Materials Transactions A*, Vol. 27A, June, p1557-1571.
13. Kirshnadev, M.R., Zhang, W.L., Rene, Gendron, A., Vaidy, V. and Bowker, J.T., 1995, "Influence of Composition and cleanliness of Electrodes on the Weld Metal Properties and Microstructure in Advanced Copper Precipitation Strengthened HSLA Steels", *Proceedings of the International Symposium on High Performance Steels for Structural Applications*, 30 October – 1 November, Cleveland, Ohio. P.189-196.
14. W. Wang and S. Liu, "Alloying and Microstructural Management in Developing SMAW Electrodes for HSLA-100 Steel", *Welding Journal*, 81(7), pp.132s-45s, July 2002.
15. Ramirez, E and Liu, S., and Olson, D.L., 1996, "Dual Precipitation Strengthening Effect of Copper and Niobium in High Strength Steel Weld Metal", *Materials Science and Engineering A*, A216, pp91-103, Oct.
16. D. Fleming, A.Q. Bracarense, S. Liu, and D.L. Olson, "Toward Developing a SMA Welding Electrode for HSLA-100 Grade Steel", *Welding Journal*, 75 (6), pp. 171s-183s, 1996.
17. Ramsay, C.W. 1989. *The Influence of Oxygen and Nonmetallic Inclusions on High Strength Steel Weld Metal Microstructures and Properties*. Ph.D. Thesis. Golden, Colorado: Colorado School of Mines.
18. Ramsay, C.W.; Olson, D.L.; and Matlock, D.K. 1989. The Influence of Inclusions on the Microstructure and Properties of a High Strength Steel Weld Metal. *Proc. on Recent Welding Research Conf*: ASM.
19. Kovesi, P. and Allan, G.B. 1970. Controlled Transformation and Maraging Steels. *Martensite* ed. E.R. Petty; Longman.
20. Nakasugi, N.; Matsuda, H.; and Tamehiro, K. 1983. Ultra Low Carbon Bainitic Steel for Line Pipes. *Proc. for Steel for Line Pipe and Pipeline Fittings Conf*: 90-95. The Metals Society.
21. Deb, P.; Challenger, K.D.; and Therrien, A.E. 1987. Structure-Property Correlation of SA and GMA Weldments in HY 100 Steel. *Met. Trans. A* 18: 987-999.
22. Oldland, P.T.; Ramsay, C.W.; Matlock, D.K.; and Olson, D.L. 1989. Significant Features of High Strength Steel Weld Metal Microstructures. *Welding Journal* 68 (4): 158-s-168-s.
23. S. Liu, "Welding Concerns of High Strength Steels, X-80 and Beyond," in the *Proceedings of the International Conference on the Application and Evaluation of High-Grade Linepipes in Hostile Environments*, Yokohama, Japan, November 5-8, 2002, pp. 91-108.
24. S. Liu and D.L. Olson, "Stepwise Methodology of Welding Flux Formulation: From Rutile Grade to CaO-CaF₂ Grade", in *Conf. Proc. of Molten Slags, Fluxes and Salts*, Paper 247, Stockholm and Helsinki, June 12-16, 2000.



Colorado School of Mines - CSM
Center for Welding, Joining and Coatings Research - CWJCR

High Strength Steel Welding

- ◆ HSLA Steel Weld Metals, $\sigma_y < 600$ MPa
- ◆ HSLA Steel Weld Metals, $\sigma_y > 600$ MPa
- ◆ Microstructural strengthening limits - alternate strengthening mechanisms
- ◆ New directions and concepts

Contrast Knowledge Base:
1980's & Current



Colorado School of Mines - CSM
Center for Welding, Joining and Coatings Research - CWJCR

Collaborations with GRE

- ◆ M. Marya, G.R. Edwards and S. Liu, "An Investigation on the Effects of Gases in GTA Welding of an Wrought AZ80 Magnesium Alloy," *Welding Journal*, 83(7), pp. 203s-212s, 2004.
- ◆
- ◆ J. Chandler, S. Liu, and G. Edwards, "Spectroscopic Monitoring of Hydrogen in Welding Arcs," accepted for presentation and publication in the *International Trends in Welding Research Conference Proceeding*, 2005



Colorado School of Mines - CSM
Center for Welding, Joining and Coatings Research - CWJCR

Collaborations with GRE

- ◆ D. Bucholz, S. Liu, and G. R. Edwards, "Diffusion Bonds Using Sputter Deposited Nickel-Titanium Multilayers", in Intl. Conf. Proc. on Joining of Advanced and Specialty Materials, pp. 93-100, ASM Intl., Rosemont, Illinois, October 1998.
- ◆ D. Bucholz, S. Liu and G.R. Edwards, "Diffusion Bonding of Multi-layer Metal Coatings", in Intl. Conf. Proc. on Brazing and Soldering, pp. 81-92, Albuquerque, NM, April 2000.
- ◆ S. Liu, G.R. Edwards, D.L. Olson, and M. Marya, "Laser Processing Research at the Colorado School of Mines," in Conf. Proc. of IIW Asian-Pacific Conference and WTIA Conference, Paper 62, 18pp, Melbourne, Australia, October 29-November 4, 2000.
- ◆ D.L. Olson, S. Liu and G.R. Edwards, "Materials Science of Non-Uniform Systems for Interpretation of Weld Metal Behavior, - Werkstoffkunde Nicht Einheitlicher Systeme zur Beurteilung des Schweißgutverhaltens" in "High Productivity Joining Processes - Fundamentals, Applications, Equipment - Vol. II", pp. 831-847, Shaker Verlag GmbH, Germany, ISBN 3-8265-8759-6, 2001.
- ◆ M. Marya, G.R. Edwards and S. Liu, "Interactions Between Gases and Fused Metal in Arc Welding of a Wrought AZ21 Magnesium Alloy" in Intl. Conf. on Light Materials - LIMAT 2003, Honolulu, Hawaii, November 2-4, 2003.



Colorado School of Mines - CSM
Center for Welding, Joining and Coatings Research - CWJCR

Collaborations with GRE

- ◆ D.L. Olson, S. Liu, and G.R. Edwards, "Physical Metallurgical Concerns in the Modeling of Weld Metal Transformations", in 'Mathematical Modeling of Weld Phenomena', edited by H. Cerjak and K. Easterling, Institute of Metals, Graz, Austria, pp. 89-108, 1993.
- ◆ S.K. Marya, S. Liu, D.L. Olson, and G.R. Edwards, "Underbead Hardness of Heat-Affected Zones in Steels", in Intl. Conf. Proc. on 'Materials and Manufacturing Technologies', pp. 17-24, Cluj-Napoca, Romania, May 18-21, 1994.
- ◆ S. Liu, S. D. Brandt and G.R. Edwards, "Spreading Kinetics of Reactive Filler Metal on Silicon Nitride", in Symp. Proc. on 'Welding/Joining/Coating and Surface Modification of Advanced Materials - Vol. II', IIW, pp. 315-321, Dalian, China, September 1994.
- ◆ R.P.G.M. Pieters, S. Liu and G.R. Edwards, "Laser Surface Modification of Ti-6Al-4V in a Nitrogen Atmosphere", in Conf. Proc. on Surface Performance of Titanium Alloys, TMS, pp. 87-100, Cincinnati, Ohio, October 1996.
- ◆ J.R. Schnepp, G.R. Edwards and S. Liu, "Laser Surface Modification of Ti-6Al-4V in CH₄/Ar Atmosphere", in Conf. Proc. on Surface Performance of Titanium Alloys, TMS, pp. 113-127, Cincinnati, Ohio, October 1996.
- ◆ Meier, P.R. Chidabaram, G.R. Edwards, and S. Liu, "Nucleation and Growth Kinetics of Reaction Product Formation for Copper-Titanium and Silver-Titanium Alloys on Alumina", *Journal of Materials Science*, 32, pp. 5215-5223, 1997.



Colorado School of Mines - CSM
Center for Welding, Joining and Coatings Research - CWJCR

Collaborations with GRE

- ◆ G.R. Edwards and S. Liu, "Recent Developments in the Production of Advanced High Strength Steels", *AWS/AWS-JWES, Vol. 2, pp. 142-154, 1990*.
- ◆ D.L. Olson, S. Liu, and G.R. Edwards, "Role of Solidification on HSLA Steel Weld Metal Chemistry", in 'Weldability of Materials', ASM, pp. 183-189, Detroit, Michigan, October 1990.
- ◆ G.R. Edwards and S. Liu, "Welding Technology in Japan and Korea," *ONR Far East Scientific Information Bulletin (NAVSO P-3580)* 16 (2): 81-899, 1991.
- ◆ S. Liu, G.P. Martins, D.L. Olson, and G.R. Edwards, "Modeling of Brazing Processes that use Coatings and Interlayers," *Welding Journal*, 70 (8), pp. 207s-215s, August 1991.
- ◆ D.L. Olson, G.R. Edwards, S. Liu, and D. K. Matlock, "Non-Equilibrium Behavior of Weld Metal in Flux Related Processes", *IIS/IW-1162-92*, 1992.
- ◆ D.L. Olson, G.R. Edwards, S. Liu, and D. K. Matlock, "Non-Equilibrium Behavior of Weld Metal in Flux-Related Processes", *Welding in the World*, 31 (2), pp. 142-154, 1993.
- ◆ M.Q. Johnson, G.L. Fredrickson, S. Liu, and G.R. Edwards, "Contribution to the Development for Advanced High Strength Steels", in *AWS/AWS-JWES, Vol. 2, pp. 142-154, March 1993*.



*Colorado School of Mines - CSM
Center for Welding, Joining and Coatings Research - CWJCR*

Important Lessons Learnt in the Design of Consumables For Welding High Strength Steels

S. Liu

**Center for Welding and Joining Research
Colorado School of Mines
Golden, Colorado**

**ASM International
October 2004**



Colorado School of Mines - CSM
Center for Welding, Joining and Coatings Research - CWJCR

Physical Metallurgy Approach

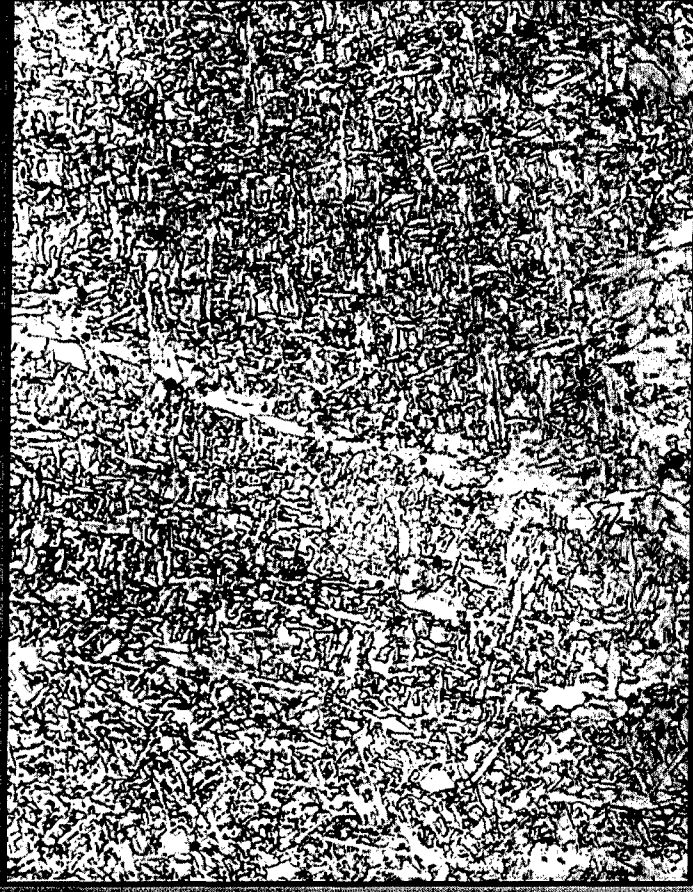
- ◆ Alloy - Chemical Composition
 - Plate, Filler, Flux
 - ◆ Processing - Thermal Conditions
 - Heat Input, Preheat, Postheat
- ⇓
- ◆ Microstructure – Essence of Material
 - ◆ Property – Performance
 - Strength, Impact, Fatigue



Colorado School of Mines - CSM
Center for Welding, Joining and Coatings Research - CWJCR

Factors that Affect Formation of Acicular Ferrite

- ◆ Alloying Content
- ◆ Weld Cooling Rate
- ◆ Nonmetallic Inclusion Population
 - Small inclusions promote fine austenite grains
 - Larger (0.3-0.4 μm) inclusions promote acicular ferrite
- ◆ Prior Austenite Grain Size





Colorado School of Mines - CSM
Center for Welding, Joining and Coatings Research - CWJCR

Austenite Grain Size Effect

- ◆ Fraction of allotriomorphic ferrite sensitive to Austenite grain surface to volume ratio,
- ◆ Overall Transformation kinetics applicable
 - Site saturation Avrami equation for planar growth:

$$X = 1 - \exp(-2S_v Gt)$$

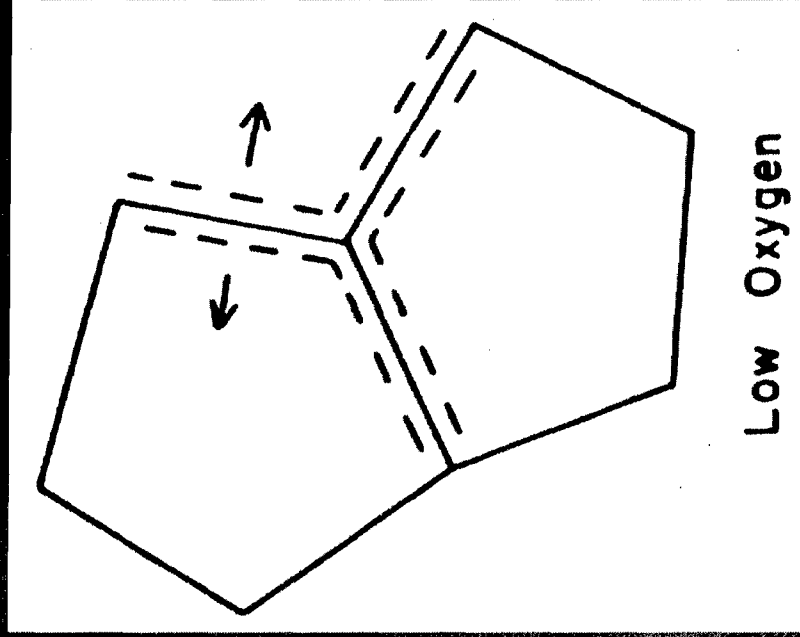
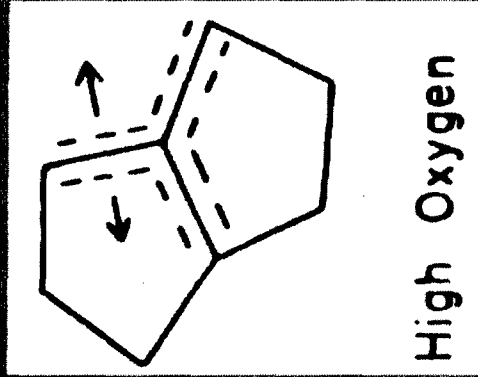
$$S_v \text{ (cylindrical grains): } \frac{2}{d}$$

$$G \propto t^{-1/2}$$

$$X = 1 - \exp\left(-\frac{\text{const}}{t}\right)$$



Colorado School of Mines - CSM
Center for Welding, Joining and Coatings Research - CWJCR

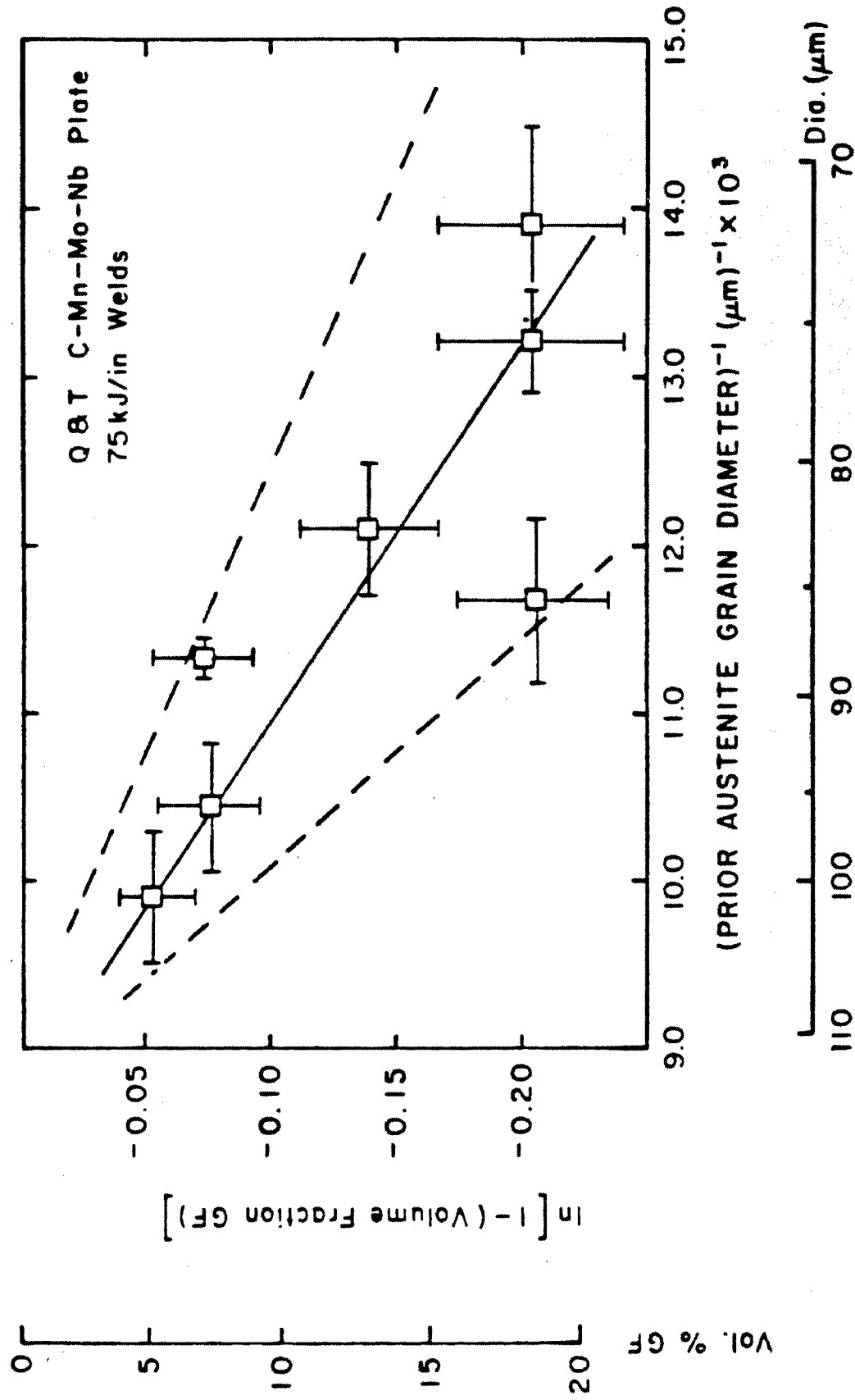


Avrami Kinetics

$$X = 1 - \exp(-kt^{1/2})$$

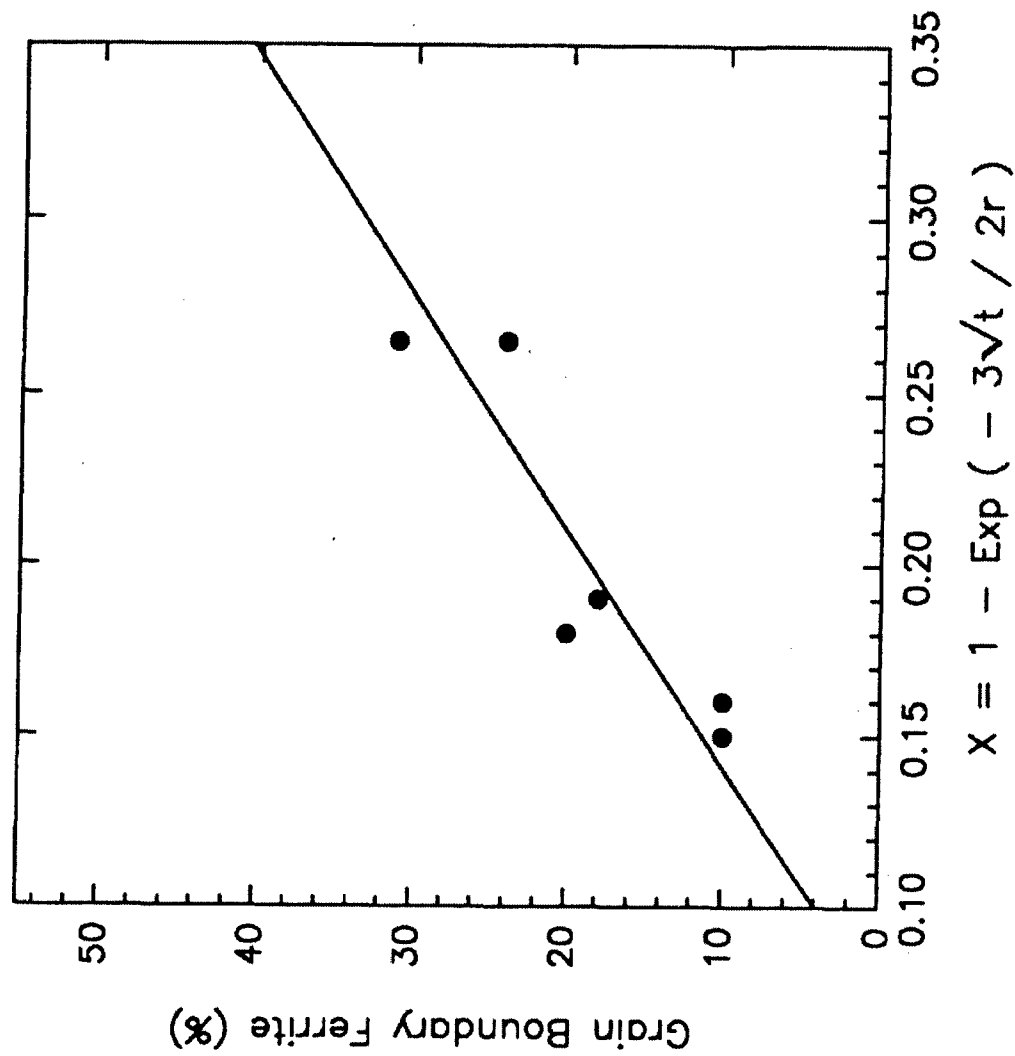
$$X = 1 - \exp\left(-\frac{4\alpha t^{1/2}}{d}\right)$$

Ref#37: Fleck, et al

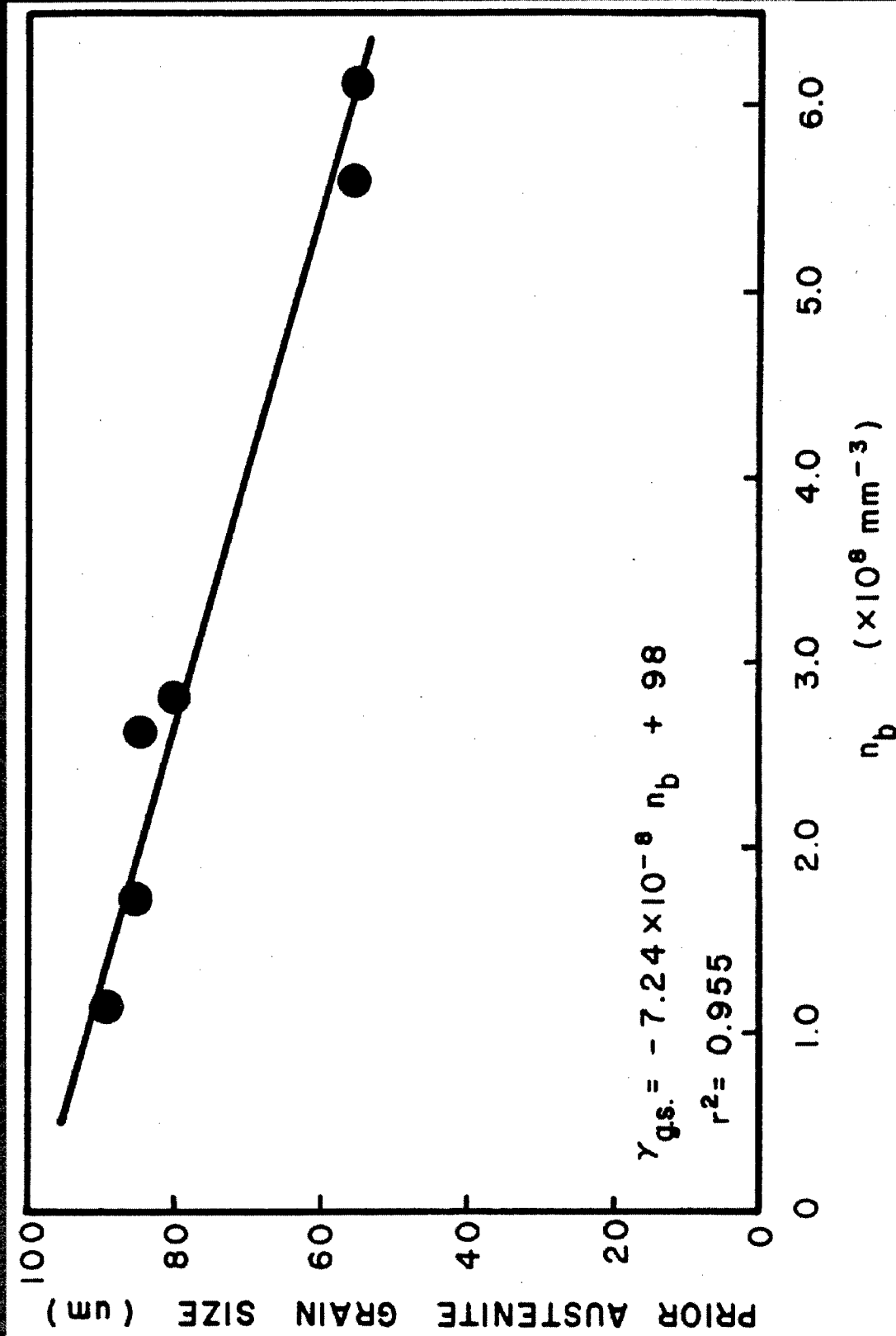




Colorado School of Mines - CSM
Center for Welding, Joining and Coatings Research - CWJCR



Ref #36: Liu and Olson



Ref #36: Liu and Olson



*Colorado School of Mines - CSM
Center for Welding, Joining and Coatings Research - CWJCR*

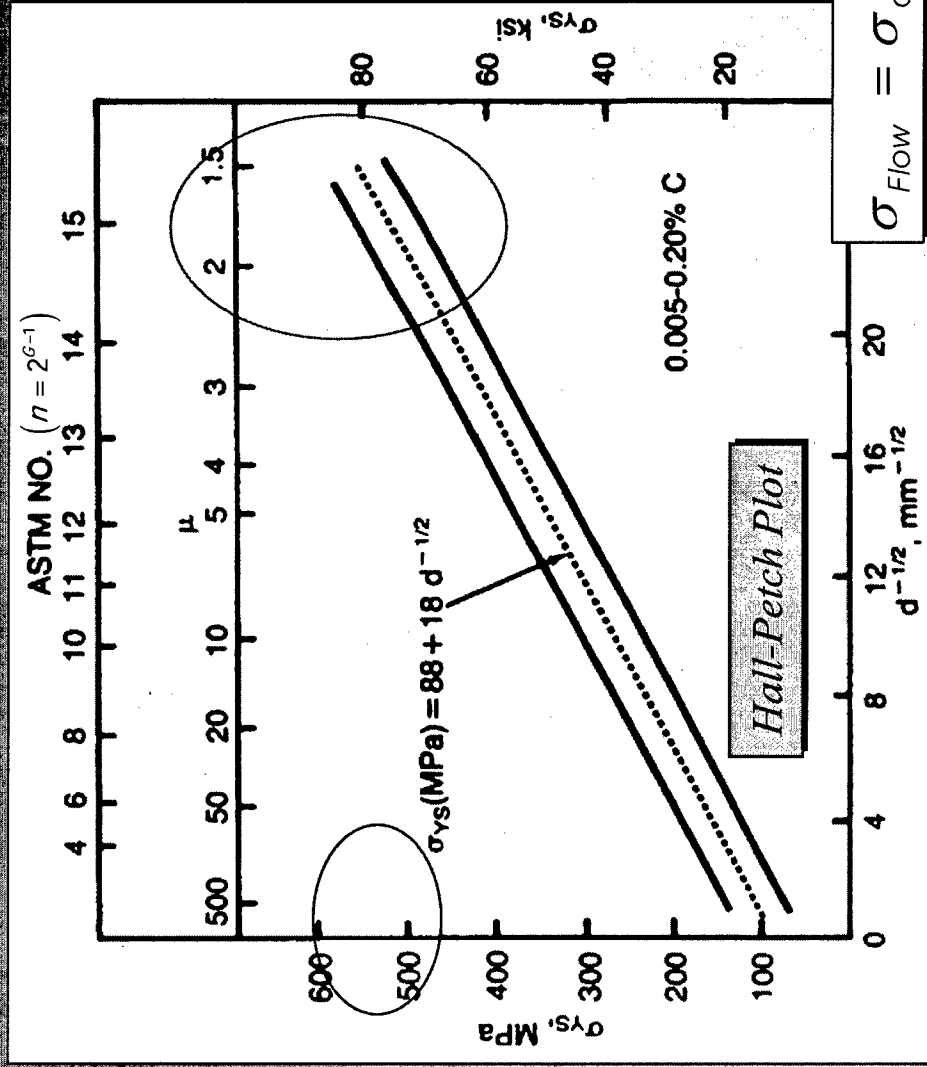
Microstructural Strengthening Limits: Alternate Strengthening Mechanisms

- ◆ Hall-Petch Strengthening
- ◆ Precipitation Strengthening
- ◆ Solid Solution Strengthening
- ◆ Microstructural Stengthening



Colorado School of Mines - CSM
Center for Welding, Joining and Coatings Research - CWJCR

Alloy Development – Strengthening Mechanisms



Further

Grain Refinement

Ferrite Grains

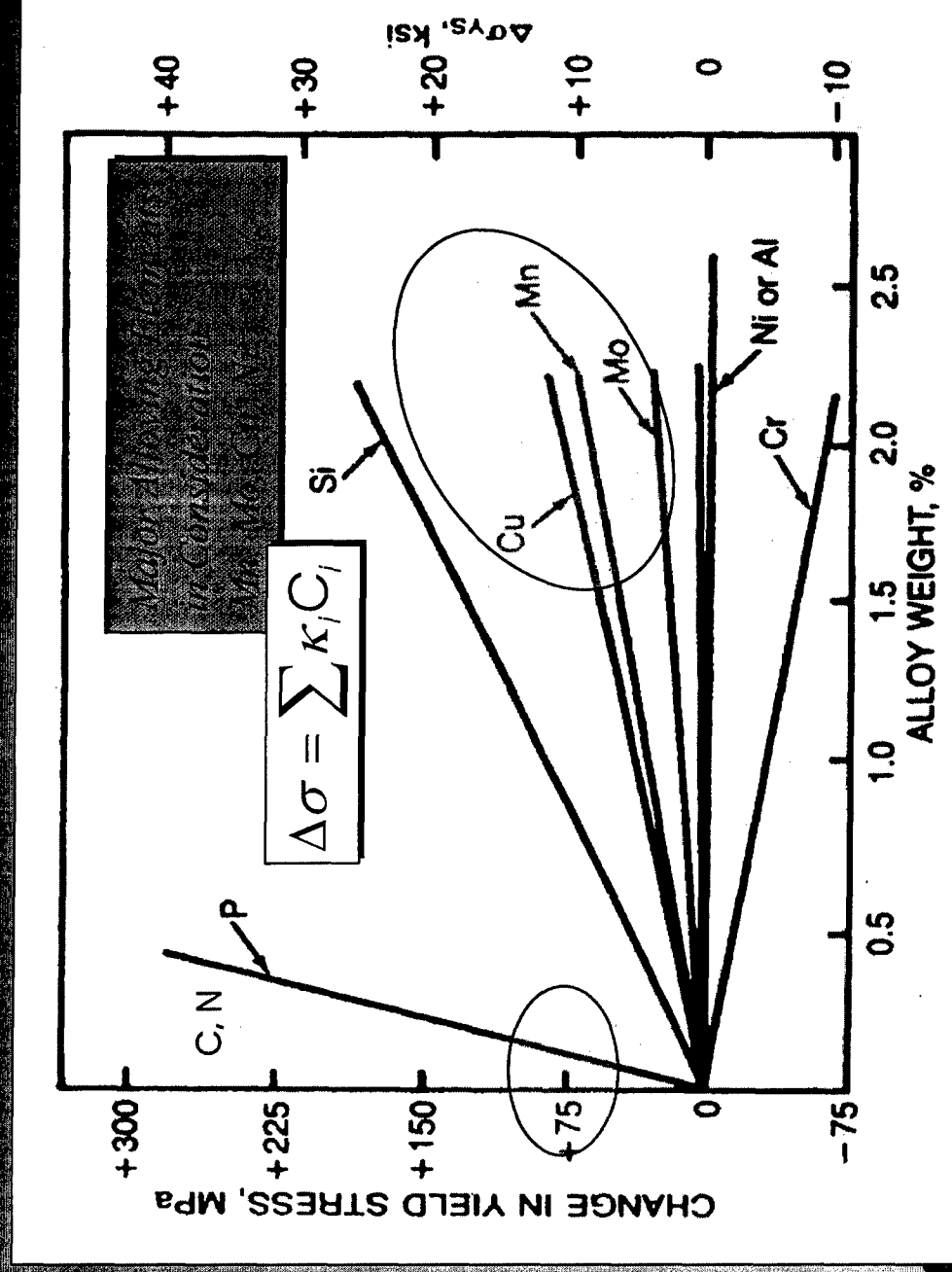
(particularly, in as-solidified condition e.g. AF) are already in 1~2 μm Range.

70/80 ksi (~500/550 MPa) seems to be the limit.



Colorado School of Mines - CSM
Center for Welding, Joining and Coatings Research - CWJCR

Alloy Development – Strengthening Mechanisms



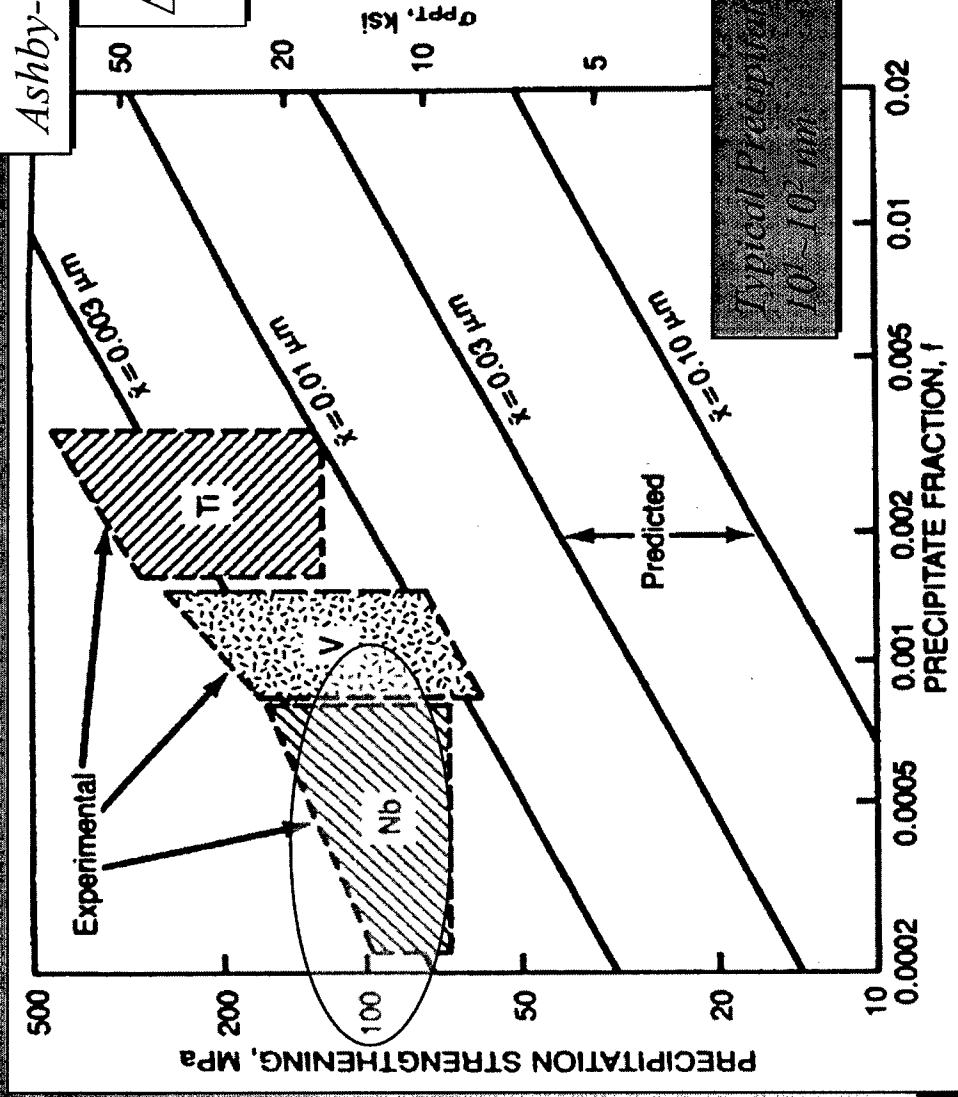


Colorado School of Mines - CSM
Center for Welding, Joining and Coatings Research - CWJCR

Alloy Development – Strengthening Mechanisms

Ashby-Orowan Equation

$$\Delta\sigma = \kappa \frac{f^{1/2}}{X} \ln \left(\frac{X}{\kappa_1} \right)$$





Colorado School of Mines - CSM
Center for Welding, Joining and Coatings Research - CWJCR

Typical Chemical Composition of HSLA-100 Steel

HSLA-100 Steel Composition (in wt%)

C	S	P	Si	Cr	Ni	Mn	Cu	Mo	Nb	Ti	Al
0.082	0.005	0.010	0.35	0.60	3.30	0.77	1.27	0.65	0.01	0.01	0.032
0.072	0.005	0.009	0.23	0.10	1.63	1.33	0.93	0.20	<0.049	0.015	0.026

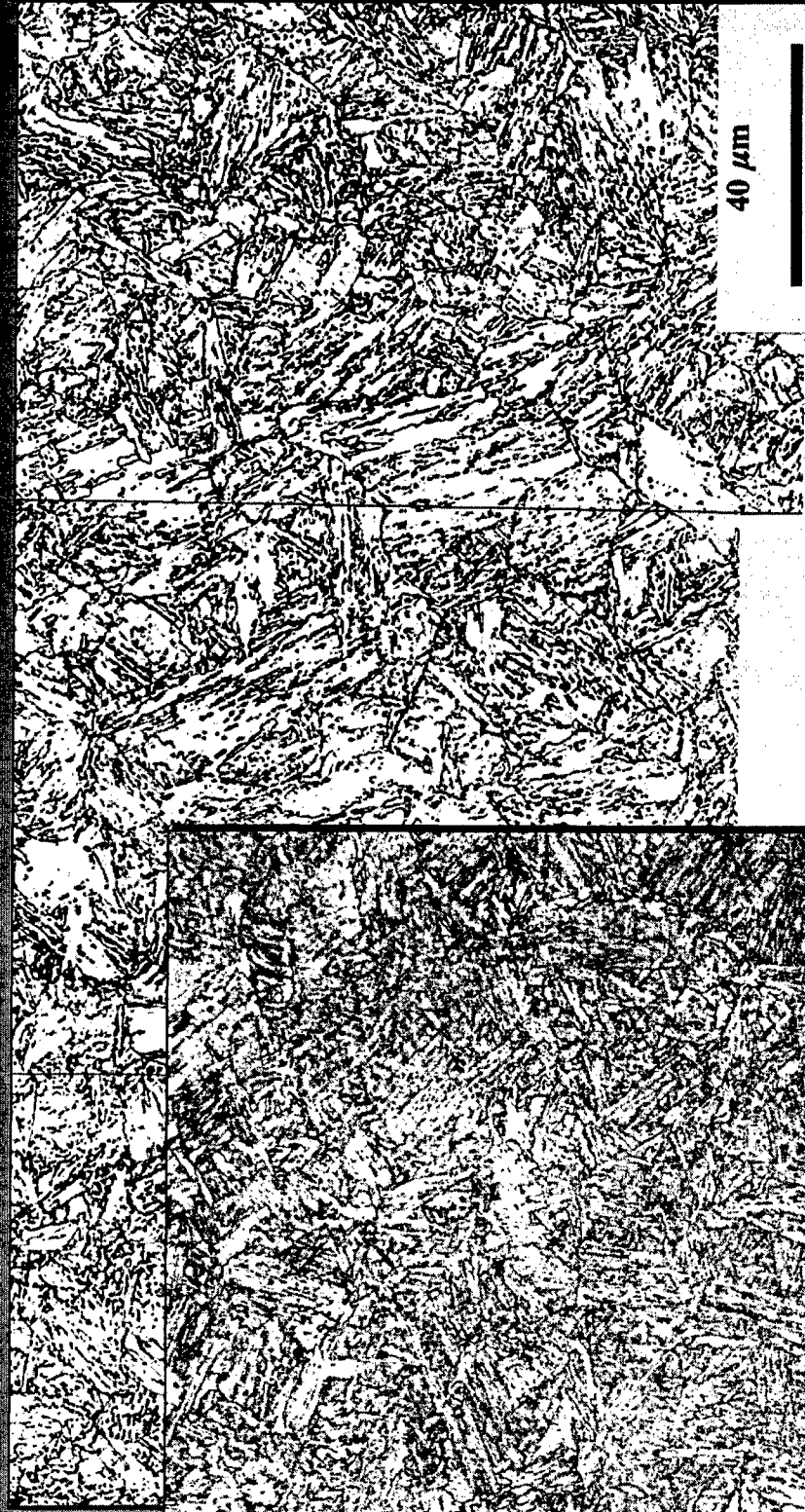
*Combination of Grain Refinement, Solid-Solution and Precipitation Strengthening, and
Microstructural Strengthening.*

*Estimate: 500 MPa (Ferritic Matrix @ 2-3 μ m Grain Size) + 140 MPa (Solid-Solution) + 90 MPa
(Precipitation Strengthening) \Rightarrow Yield Strength of 730 MPa (~104 ksi)*



Colorado School of Mines - CSM
Center for Welding, Joining and Coatings Research - CWJCR

Typical Microstructure of Q&T (1000 MPa) & HSLA-100 Steel



(Siwecki '94)





Colorado School of Mines - CSM
Center for Welding, Joining and Coatings Research - CWJCR

Potential Strengthening

◆ BASE METAL

- ◆ Microstructural refinement (*200 μm*): 500 MPa
- ◆ Fine Nb, V, Ti precipitates (*0.01 μm*): 100 MPa
- ◆ Solution strengthening (Si, Mn, Cu, Mo): 150 MPa
750 MPa

◆ WELD METAL

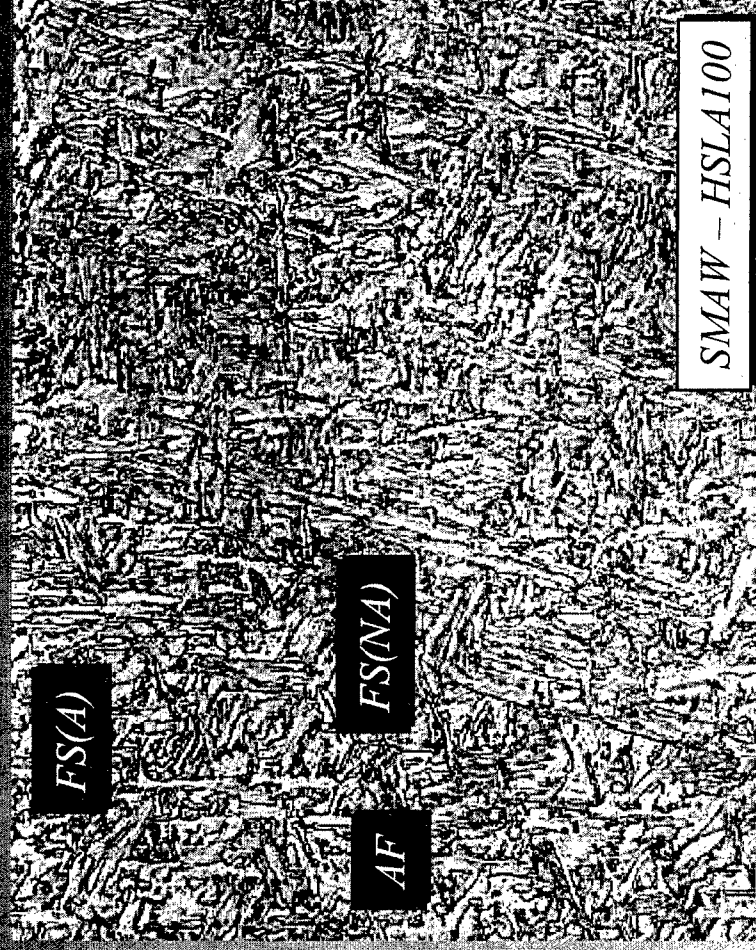
- ◆ Precipitates are coarsened, replaced by coarser oxides
- ◆ Alloying promotes bainite or martensite
- ◆ Welds with strengths in excess of 600 MPa will not be acicular ferrite based



Colorado School of Mines - CSM
Center for Welding, Joining and Coatings Research - CWJCR

HSLA Steel & Weld Metals: $\sigma_y > 600 \text{ MPa}$

- ◆ "Mixed Microstructures" Weld Metal
- ◆ Potential for Bainitic or Martensitic Weld Metals



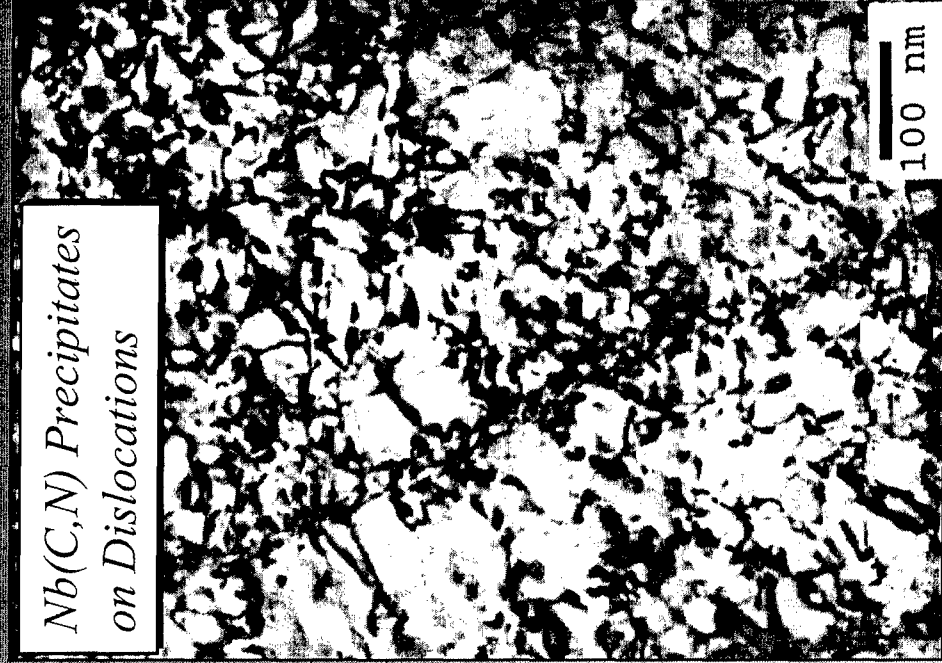
SMAW - HSLA100



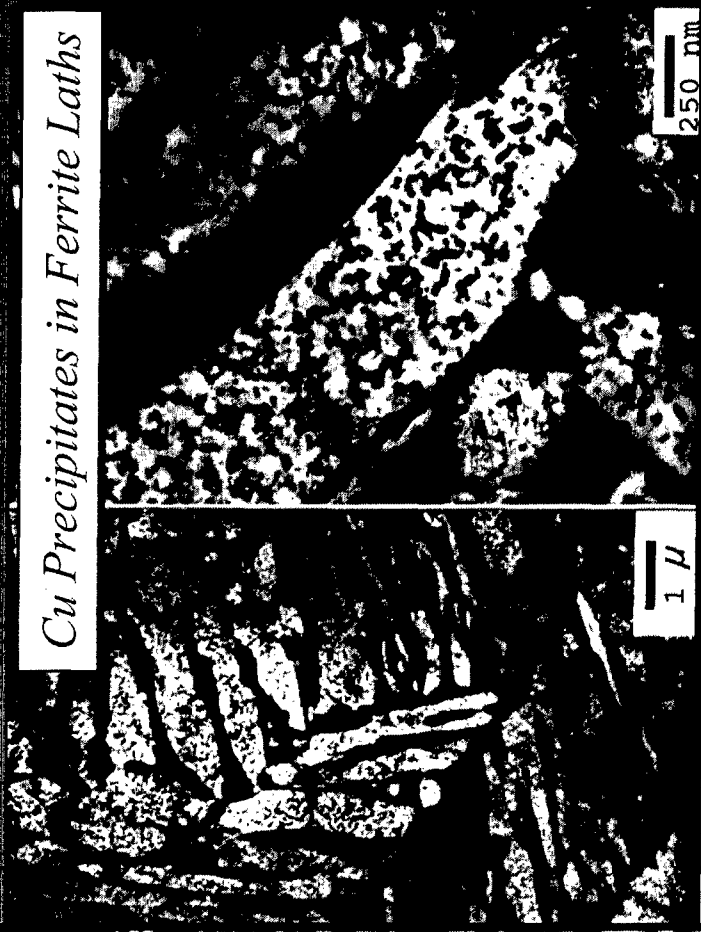
Colorado School of Mines - CSM
Center for Welding, Joining and Coatings Research - CWJCR

Evidence of Precipitation Strengthening – TEM Observation

*Nb(C,N) Precipitates
on Dislocations*



Cu Precipitates in Ferrite Laths



*Additional Benefit: Synergistic Effect of Cu-Nb
Timed Precipitation of Cu and Nb(C,N) ensures
Microstructural Stability During Reheating.*

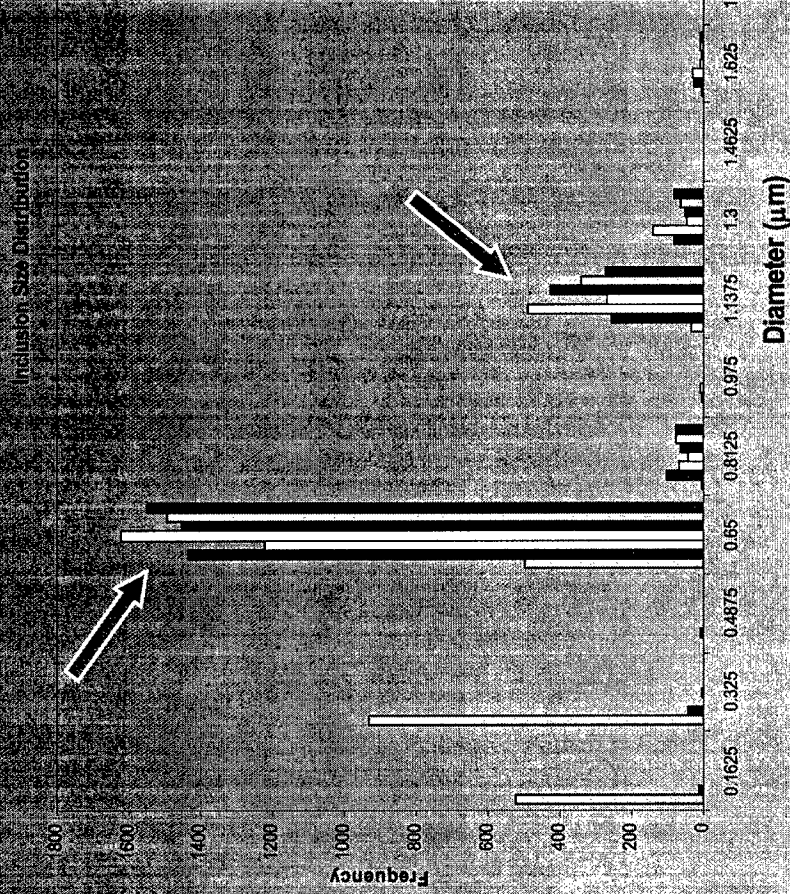
(Ramirez)



Colorado School of Mines - CSM
Center for Welding, Joining and Coatings Research - CWJCR

Inclusion Population & Roles

Bimodal Size Distribution



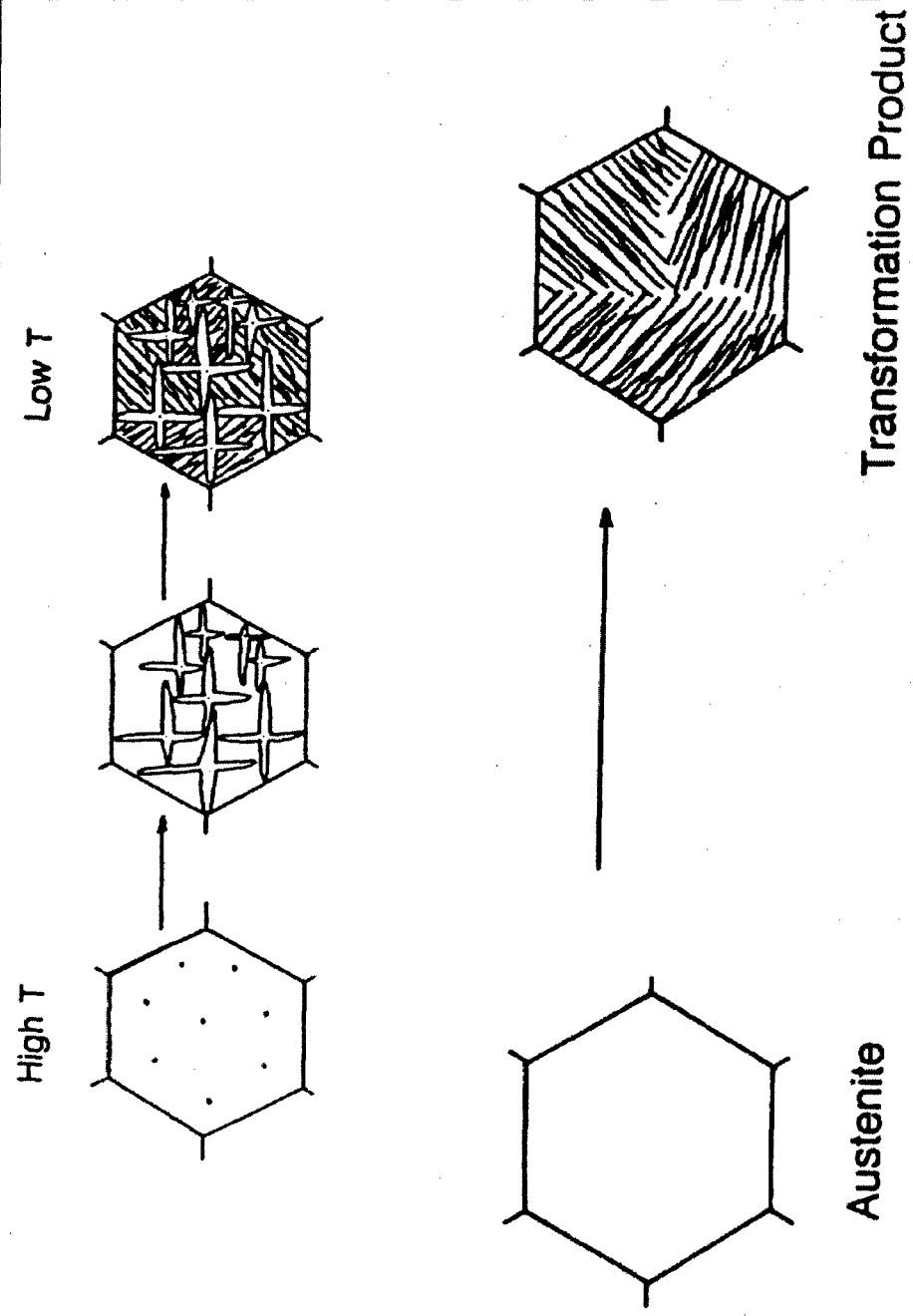
(Clasper and Liu, 2003)





Colorado School of Mines - CSM
Center for Welding, Joining and Coatings Research - CWJCR

Transformation Scheme



Ref #73: Ramsay



Colorado School of Mines - CSM
Center for Welding, Joining and Coatings Research - CWJCR

"Mixed Microstructure" Weld Metals

- ◆ Combinations of:
 - ◆ Low carbon lath martensite
 - ◆ Low carbon bainite
 - ◆ Acicular ferrite

- ◆ Compositions of:

- ◆ 2 – 5 w/o Ni
- ◆ 0.5 – 1 w/o Mo
- ◆ 0.5 – 1 w/o Cr

- ◆ Example Properties:

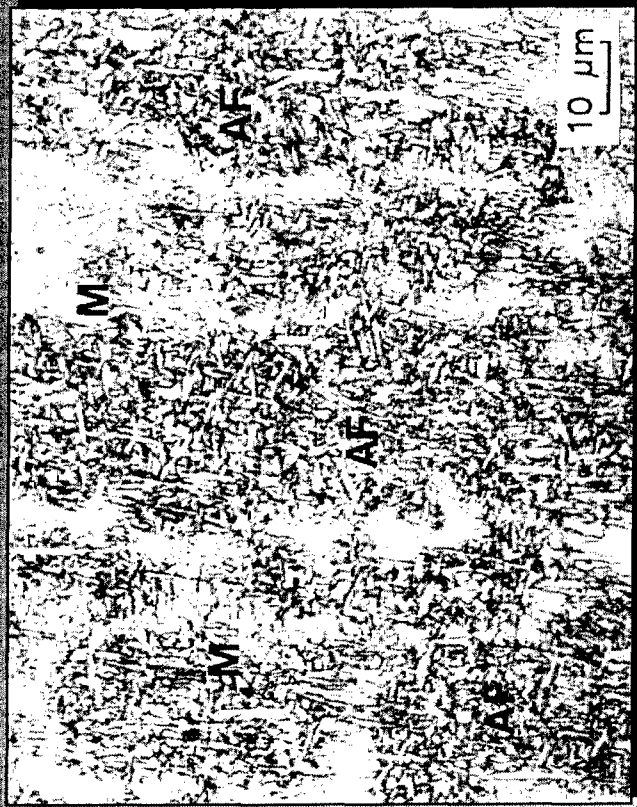
<u>Process</u>	<u>Researchers</u>	<u>YS (MPa)</u>	<u>Toughness</u>
SAW	Svensson & Bhadesia	760	CVN(-51°C): 70 J
SAW	Oldland, et al	900	50% FATT: -100°C
◆ Fine Austenite Grains May Be Desirable (Higher weld metal oxygen)			



Colorado School of Mines - CSM
Center for Welding, Joining and Coatings Research - CWJCR

Weld Metal Microstructure of Optimal Impact Toughness: HSLA-100 Steel

(60% AF, 40% M)



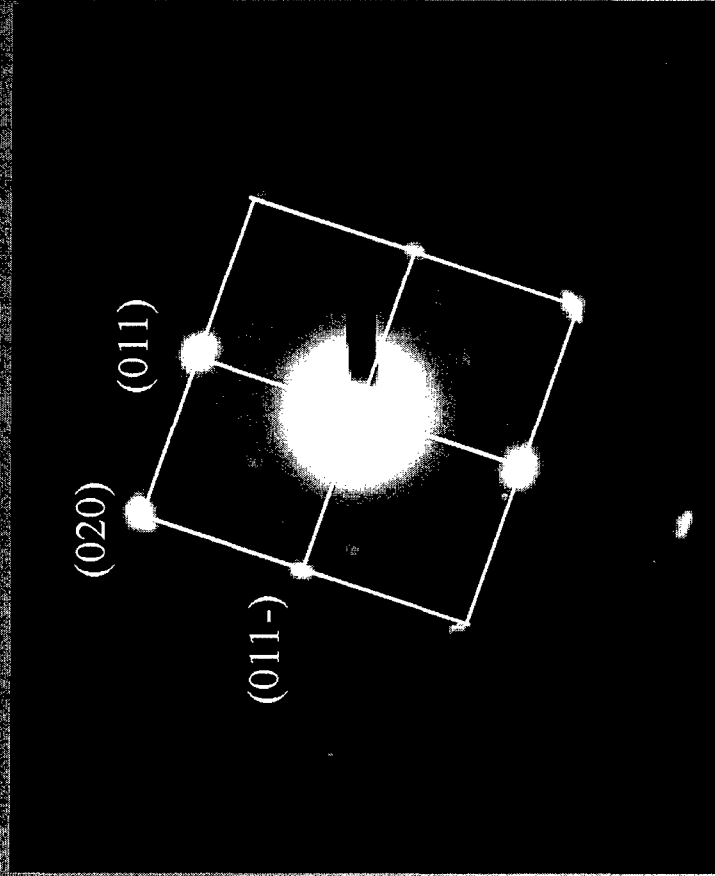
(Fleming, Bracarense, Liu and Olson, 1994)

(W)

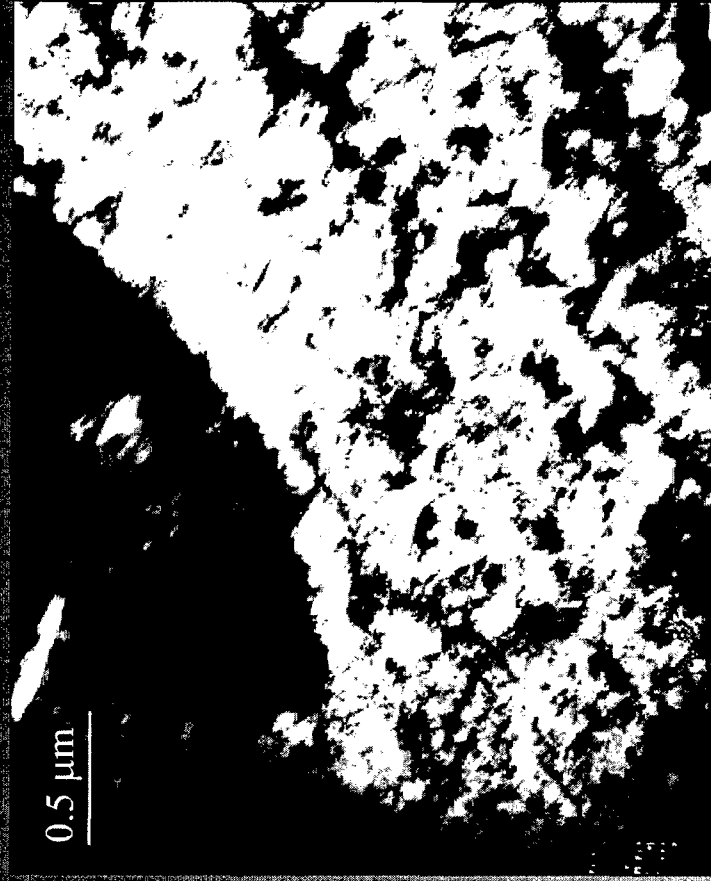


Colorado School of Mines - CSM
Center for Welding, Joining and Coatings Research - CWJCR

SAD Patterns: Granular Bainite



Diffraction Pattern of Dispersed
Phase resembled that of α -Ferrite
and Low C Martensite



Bright Field Image of Granular Bainite

Granular
Bainite



Colorado School of Mines - CSM
Center for Welding, Joining and Coatings Research - CWJCR

Mechanical Properties of the Optimized HSLA-100 Steel Weld Metal

CVN Results		Yield Strength at RT (ksi/MPa)
Testing Temperature (°F/°C)	Impact Toughness (ft-lb/J)	
76/24.4	142/193	90/621
0/-17.8	118/160	
-30/-34.4	100/136	
-60/-51.1	85/115	
-90/-67.8	61/83	
		Note: Requirements for High Strength Steel Welding
0°F	65/88	
-30°F	45/61	
-60°F		

Undermatched
Condition



Colorado School of Mines - CSM
Center for Welding, Joining and Coatings Research - CWJCR

X-120 Steel Weld Metal

- ◆ "Dual Phase" Microstructure
 - 5 to 15% Acicular Ferrite
 - 50 to 85% Lath Martensite
 - 10 to 25% Degenerated Upper Bainite (FS(A))
- ◆ Weld Chemical Composition
 - 0.06C, 1.8Mn, 0.57Si, 2.7Ni, 0.22Cr, 0.57Mo, 0.18Cu, 0.014Zr
 - Pcm = 0.265 to 0.295
- ◆ Charpy Property
 - 150J (106 ft-lb) @ -50°C

(Bangaru, Fairchild, Macia, Koo, and Ozekcin, 2004
International Pipeline Technology Conference Proceedings)



Colorado School of Mines - CSM
Center for Welding, Joining and Coatings Research - CWJCR

Potential HSLA Steel Weld Metals

- ◆ High Strength Martensitic Microstructures can Be Tough:

Alloy 18Ni (200)	<u>YS (MPa)</u>	<u>$K_{IC} \left(\frac{MPa\sqrt{m}}{m} \right)$</u>
Maraged	1400	110

- ◆ High Strength Bainitic Microstructures can Be Tough:

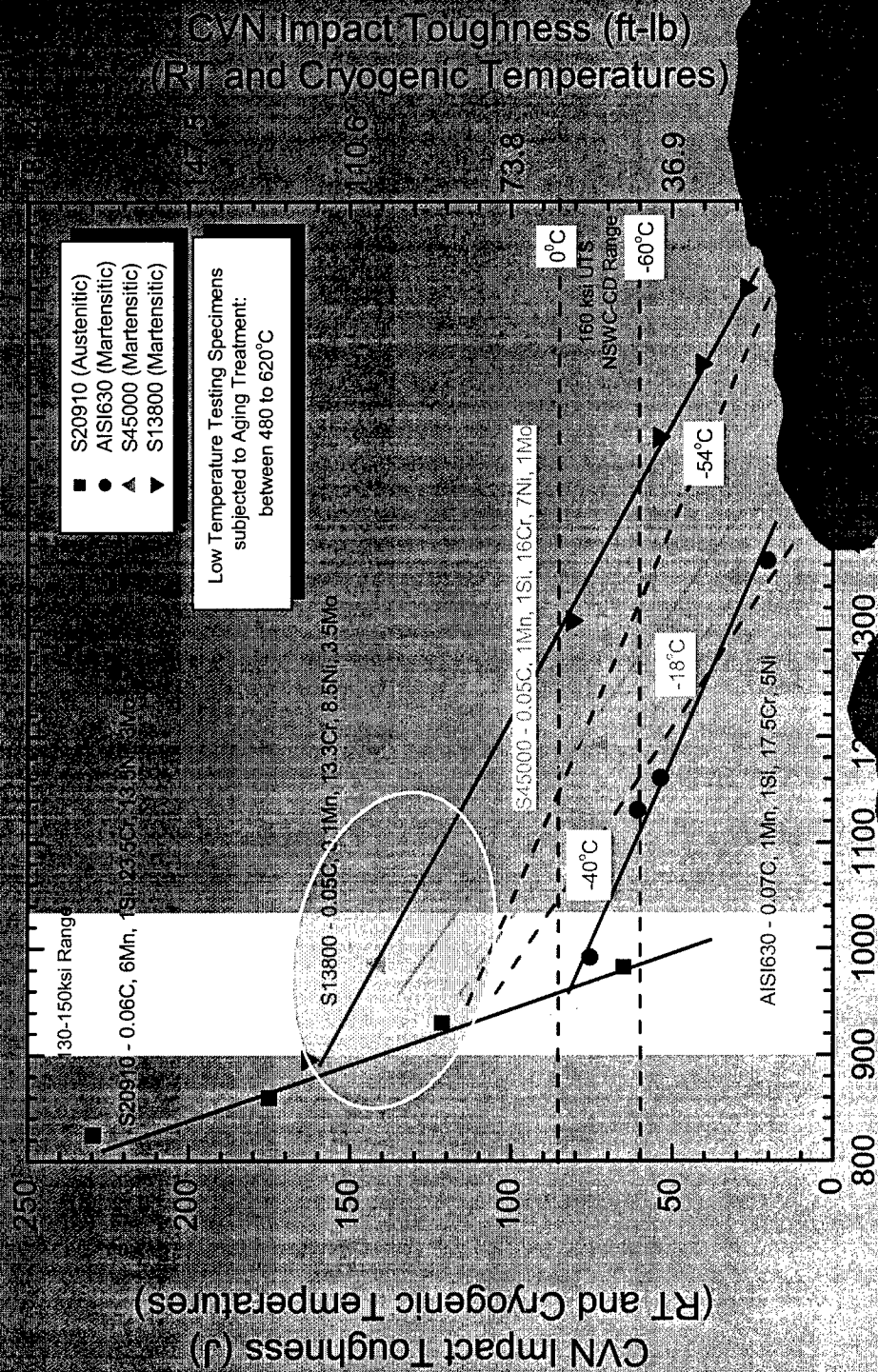
ULCB #6	<u>YS (MPa)</u>	<u>USE (J)</u>	<u>50% FATT (°C)</u>
	834	115	-48

Ref: Garcia, Lis and De Ardo
ISS Conference Proceedings



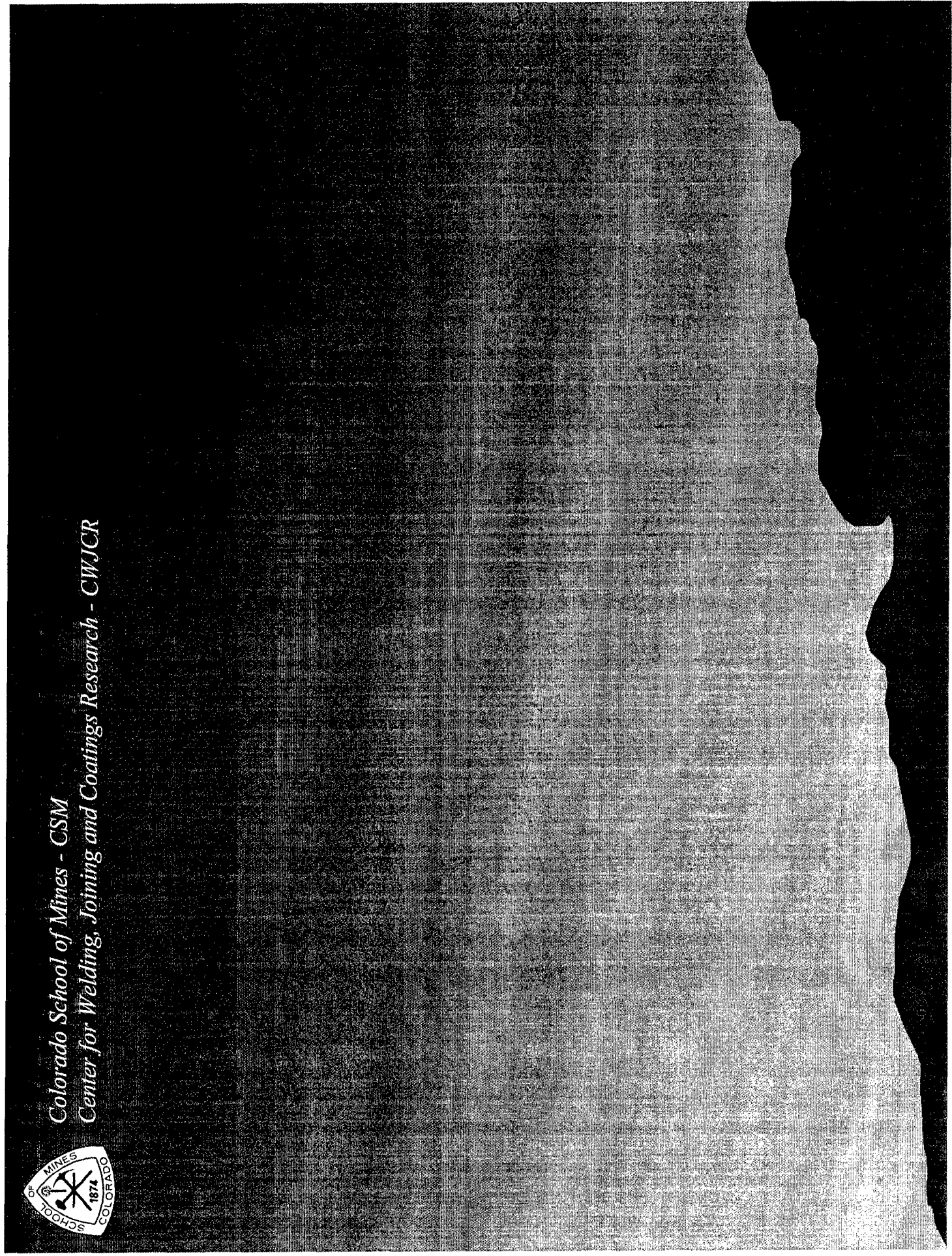
Colorado School of Mines - CSM
Center for Welding, Joining and Coatings Research - CWJCR

Design Weld Metal Tolerant to Process Fluctuations





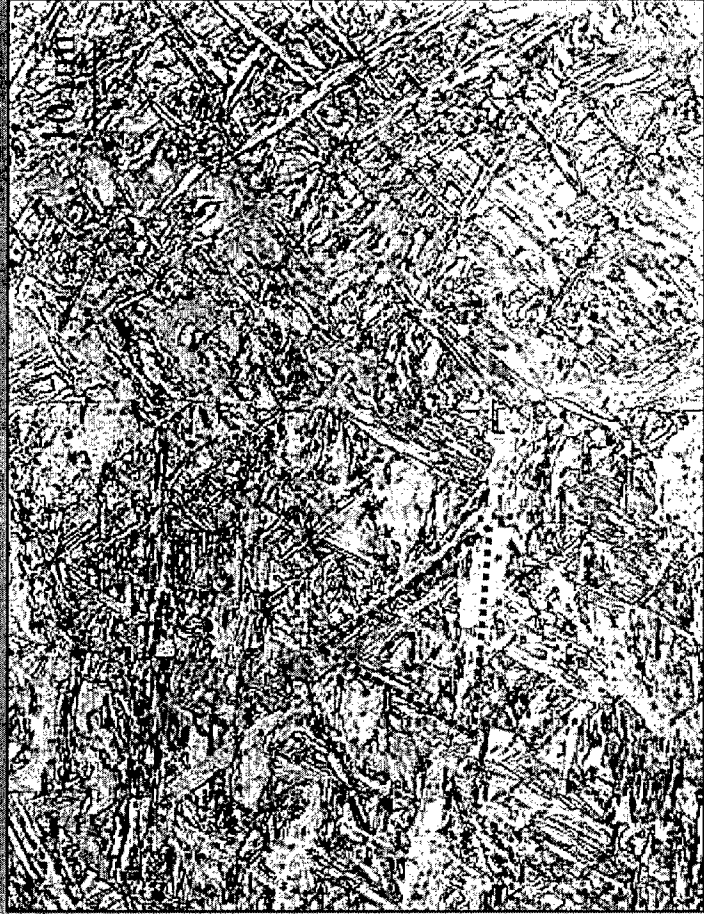
*Colorado School of Mines - CSM
Center for Welding, Joining and Coatings Research - CWJCR*





Colorado School of Mines - CSM
Center for Welding, Joining and Coatings Research - CWJCR

Lath Martensite: Sub-Lath Microstructure

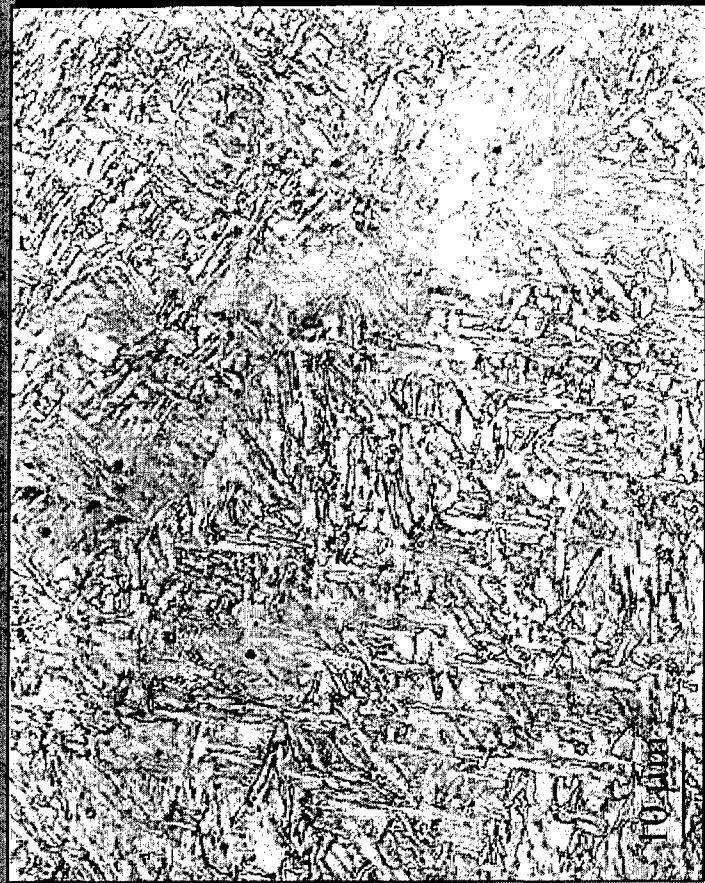


Does the Sub-Lath Spacing change with Carbon Content?
Does the Sub-Lath Spacing affect the Mechanical Properties?



Colorado School of Mines - CSM
Center for Welding, Joining and Coatings Research - CWJCR

Ferrite with Second Phase: Sub-Lath Microstructure



Ferrite Laths with High
Aspect Ratio



*Colorado School of Mines - CSM
Center for Welding, Joining and Coatings Research - CWJCR*

Acicular Ferrite: Sub-Lath microstructure

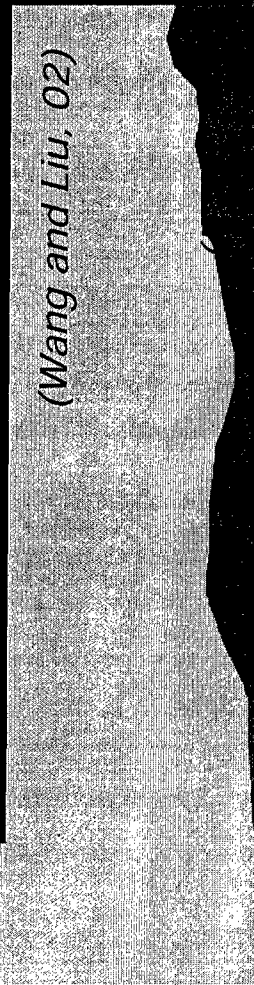


*Sub-Laths maintain
Basket-Weave Aspect*



Colorado School of Mines - CSM
Center for Welding, Joining and Coatings Research - CWJCR

"Dispersed" Phase: Granular Bainite



Spectroscopic Monitoring of Hydrogen in Welding Arcs

J. Chandler, G. Edwards, and S. Liu

Colorado School of Mines,
Center for Welding, Joining and Coatings Research
George S. Ansell Department of Metallurgical & Materials Engineering
Golden, Colorado, 80401, USA

Abstract

The focus of this work was to investigate the applicability of arc spectroscopy as a non-destructive method of hydrogen determination in gas metal arc welding (GMAW) of HSLA steel. A spectrometer active in the wavelength range of 200 – 850 nm was utilized to measure the intensity of hydrogen and argon emission lines in the arc. Determination of arc temperature and hydrogen concentration was performed using the ion-neutral line ratio method and the Saha equation. While the methodology is not new, much of the arc-emission spectroscopy work in literature has been performed on gas tungsten arc welding (GTAW) processes. Arc spectroscopy of GMAW processes required methods to account for metal transfer modes and the increased presence of iron vapor in the welding arc as compared to GTAW processes.

Varying amounts of hydrogen and moisture were added to the shielding gas and then correlated to the hydrogen content of the deposited weld metal measured using gas chromatography. A Sievert's Law type of relationship was found to exist between hydrogen spectroscopically detected in the welding arc and hydrogen content in the weld metal. Thus, spectroscopic monitoring of a GMAW process during deposition can be utilized to monitor the hydrogen activity in the arc and signal the operator when unacceptable diffusible hydrogen levels result.

Introduction

Hydrogen is a likely contaminant in arc welding processes, originating from moisture in the atmosphere or shielding gas, as well as contamination on the consumable or workpiece. The deleterious effects of hydrogen on high strength steel have been well documented [1-21]. Current methods of quantifying diffusible hydrogen require destruction of the weld sample and outgassing of hydrogen from the weld sample. Because of the lengthy time required for hydrogen diffusion and collection, current methods can only report diffusible hydrogen measurements long after welding has been completed. Thus, a method of non-intrusive, real-time monitoring of weldment hydrogen was pursued in this research. Emission spectroscopy

was chosen as the method of arc monitoring due to its real-time and non-intrusive nature during data collection. Hydrogen content of the weldments was measured and correlated to the light data emitted during deposition.

Experimental Procedure

Arc Generation System

A two-part welding arc study was conducted to investigate the capabilities of the spectroscopy system using a Miller Nirvana welding power source - a 60M series CC/CV power supply and an ER70S-3 grade electrode with 0.045-inch (1.14 mm) diameter. In this study, shielding gas composition, i.e. hydrogen and H₂O additions in argon, was the primary focus.

Light Collection Setup

In order to make measurements of the light emitted from a welding arc, an apparatus was devised to magnify the arc and collect data from small, discrete regions of the arc. A schematic diagram of the equipment can be seen in Figure 1. A shield constructed of sheet steel was placed next to the arc. In addition, a high temperature polymer shield was placed between the steel shield and the lens/filter assembly. The two shields served to limit the amount of light traveling to the spectrometer and to protect the lens and filters from errant sparks and spatters emitted from the welding process. A 30 mm double convex polymer lens was used to magnify the arc. Neutral density filters were utilized during this research to attenuate the light signal emitted from the arc. The probe of the spectrometer was placed into a hole drilled into the center of an adjustable and articulating projection screen. Thus, studies could be made of the light emitted from the various regions in the arc.

The welding process was performed on A36 steel diffusible hydrogen samples, in accordance with the standard AWS/ANSI A4.3-93: *Standard Methods for Determination of the Diffusible Hydrogen Content of Martensitic, Bainitic, and Ferritic Steel Weld Metal Produced by Arc Welding* [22].

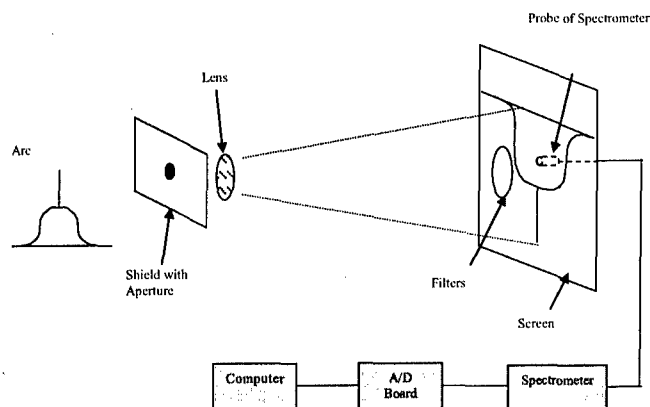


Figure 1. Schematic representation of spectroscopic data collection setup.

The probe of the spectrometer used in this research is shown in Figure 2. Within the probe was a collimating lens 5 millimeters in diameter. Light data were transmitted to the spectrometer via a fiber optic cable. Once it reached the spectrometer, the light was dispersed by a fixed grating and shone across a linear CCD array detector, which contained 2048 elements reactive to light in the wavelength range of 200 nanometers to 850 nanometers. Resolution in the spectrometer - Model S2000 manufactured by Ocean Optics, Inc. was about 0.5 nanometers. Information read by the spectrometer was converted by an analog-to-digital converter and then collected by a customized LabView-based software application. Data was acquired every 100 milliseconds and stored on disk for later processing.

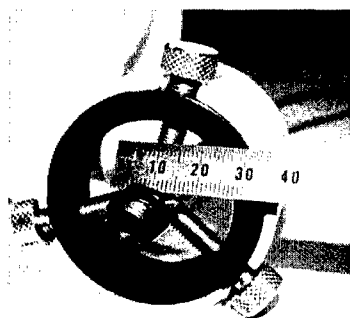


Figure 2. Photograph of spectrometer probe used in this research. Divisions on ruler in photograph are millimeters.

Spectroscopic Calculations

Spectroscopic data obtained from the welding processes were used to calculate the arc temperatures and the concentrations of the different species in the welding arcs. The raw data was pre-smoothed to allow for easier processing. To reconcile the fact that two-dimensional spectroscopic data were obtained from a three-dimensional object, the arc, the Abel inversion was used. This operation converts the line emission coefficient into the radial emission coefficient.

To fit a function to the data, a Mathcad operation was performed that fitted a cubic spline curve to the data. Using the radial emission coefficient as described earlier, the temperature of the arc was determined as functions of the arc radius using the ion-neutral line ratio method. This method utilizes the measured ratio of the particle density of an element in its neutral state to that of an ion of the same element.

Since argon constituted the major volume fraction of the shielding gases used in this research, the argon lines were used to calculate the temperature of the arc, in particular, the neutral argon line at 696.5 nanometers and the argon ionization line at 476.4 nanometers. The main advantage of this method is that the intensity of the spectral lines need only be measured on the same scale. Since this method relies on the ratio of the spectral lines to one another, readings on an absolute scale are not required. As disadvantage, Matsushita found this method to predict temperatures higher than those determined by the off-axis peaking method [23]. In addition, the noise in the spectrometer tends to cause the temperature readings to flatten out as the radial distance increases. In other words, the outer periphery of the arc seems to assume unnaturally high temperatures that should be disregarded.

The concentration of the elements present in the welding arc was calculated using the ratio of the spectral intensity of the neutral species of a particular element to the spectral intensity of neutral argon. Radial emission coefficients of the elements of interest were placed in the equation along with the temperatures calculated by the ion-neutral line ratio method. With these substitutions, particle density ratios with respect to neutral argon were obtained. The Saha equation was employed to find ionization fractions using the determined temperature.

RESULTS AND DISCUSSION

Hydrogen Additions to Argon Shielding Gas

Hydrogen additions to argon in the amounts of 220-ppm, 1-vol. percent, and 3-vol. percent were used in the experiments. The goal of this part of the study was to analyze the effect of the additions on the hydrogen content in the weldments and to test the ability of the spectroscopic system to observe hydrogen in the arc.

The relationship between diffusible hydrogen content of steel weldments and hydrogen additions to an argon shielding gas can be observed in Figure 3. As the hydrogen content of the shielding gas is increased, the diffusible hydrogen content of the weldments deposited under the shielding gases increased proportionally to the square root of the amount of hydrogen in the shielding gas. A regression line with a power of one-half is superimposed on the graphic for reference. This behavior is similar to that predicted by Sievert's law, suggesting that absorption of diatomic hydrogen plays a strong role in the total amount of hydrogen absorbed during welding. If hydrogen absorption in the weld pool were to occur only from

monatomic hydrogen, the relationship would be expected to exhibit a linear behavior, as calculated by Gedeon [19].

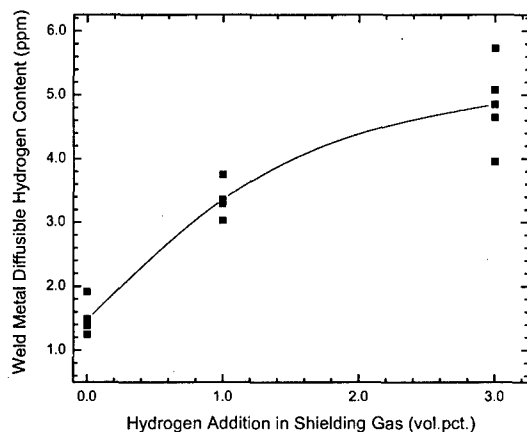


Figure 3. Relationship between diffusible hydrogen content of steel weldments and hydrogen content in an argon shielding gas.

In order to determine the concentration of constituents in the arc, the temperature had to be known. The temperature calculated with the ion-neutral line ratio method was inserted into the Saha equation to determine the ionization fractions of hydrogen and argon in the arc. Concentration calculations were performed at every 0.25 millimeters from the center of the arc out to 3.25 millimeters. Because of occasional inaccuracies in the temperature determined with the ion-neutral line ratio method, hydrogen concentration profiles were affected. Consequently, it was decided that a summation of the hydrogen concentrations at the various radii within the arc would best correlate with the hydrogen content in the weldments. In this manner, any point-to-point variations in the profile would be averaged out in the final concentration value. Measurements beyond 3.25 millimeters were not considered because readings beyond that radius would most likely be spurious noise and not true signals from the arc.

The calculated temperatures for GMAW processes with 220-ppm hydrogen additions can be seen in Figure 4. It is seen that the largest gradients occurred at the 6-mm scan height (measured from the surface of the weld pool towards the electrode tip) due to its relatively small width. Temperature profiles at 4 and 2 mm exhibited less severe gradients of temperature, due to the increased width of the arc close to the workpiece. The high temperatures at each scan height were calculated to be at the center axis of the arc, decreasing in value from approximately 25,500K at 6 mm to 22,500 K at 2 mm. This arc temperature distribution is similar to that reported by an earlier researcher [1]. The temperature values calculated in this research were somewhat higher than the temperatures calculated by White [26] in GMAW processes. However, temperatures calculated by White [26] were done so using the Boltzmann-plot method and with additions of oxygen to the shielding gas as well [26].

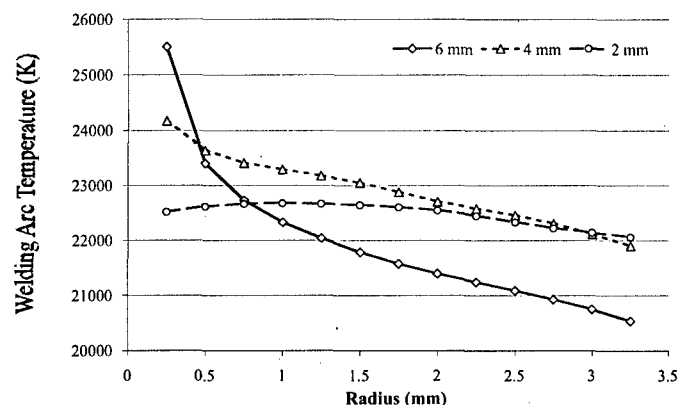


Figure 4. Temperature profiles at indicated heights (from the surface of the weld pool) for a GMAW process with 220 ppm hydrogen addition in argon shielding gas.

The relationship between the summation of hydrogen observed in the arc out to 3.25 mm radius and the diffusible hydrogen content of the weldments can be seen in Figure 5. A linear correlation exists between the summed hydrogen contents in the arc and diffusible hydrogen in the weldments. Though the relationship is not an exact correlation, it is sufficient proof that spectroscopy can be used as a diagnostic tool for determination of hydrogen concentration in the arc. With this tool, a welding manufacturer can pinpoint the level of unacceptable level of hydrogen content in the weldment by means of arc-observed hydrogen concentration. During fabrication of a structure, detection of this particular amount of hydrogen in the arc would serve as a warning sign that the deposited weldment may be prone to HAC. In this manner, the time and expense associated with destructive testing of diffusible hydrogen analysis may be reduced or avoided altogether. Before final application to a fabrication process, similar sets of tests as was performed in this research should be done with the conditions that would be present at the time of welding. Specifically, data from GMAW processes that use argon-carbon dioxide or other shielding gas mixtures should be collected for correlation and the relationship incorporated into the hydrogen detection procedure.

Hydrogen concentration profiles for GMAW processes with 1 and 3-percent hydrogen additions at 6 mm above the workpiece can be seen in Figure 6. These hydrogen concentration profiles exhibited a trend opposite that of previous researchers, generally increasing from the center of the arc outward. This trend can be attributed to the high temperatures found at the center of the arc, regions of highest energy density. As discussed earlier, the concentrations of the constituents in the arc were calculated by computing a ratio of the first and second ionized argon to neutral argon and using the Saha equation. Examining the ionization behavior of argon as a function of temperature, shown in Figure 7, it can be seen

that second ionization of argon begins to occur rapidly in the temperature range of the maximum temperatures calculated. For each second ionized argon atom in the arc, two electrons result and exert a significant influence near the center axis of the arc. Their influence, however, diminishes as the arc radius increases. As the temperature decreases with increasing radius, the argon present tends to consist mainly of first ionized argon and neutral argon.

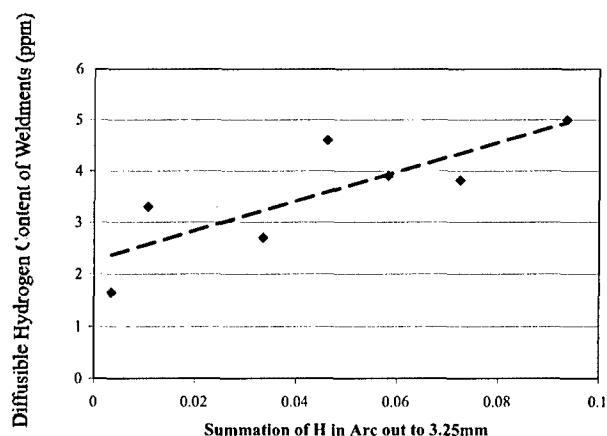


Figure 5. Relationship between diffusible hydrogen concentration of weldments and the summations of hydrogen concentration in the welding arc out to 3.25 millimeters arc radius.

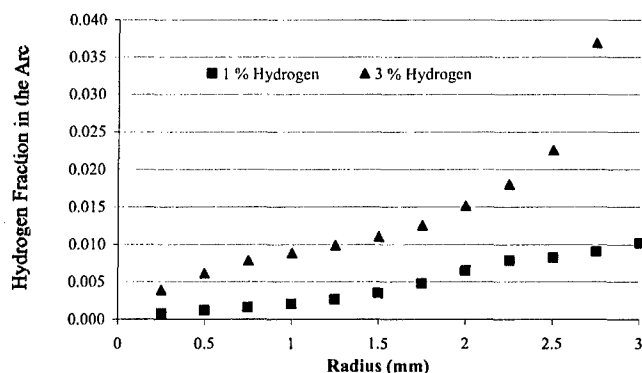


Figure 6. Hydrogen concentration profiles across welding arcs with indicated hydrogen additions to argon shielding gas.

Though the relationship shown in Figure 6 has not been reported in the literature before, it should be noted that the temperatures reported in this research are higher than those previously reported as a result of both the particular range of temperatures and the shielding gas. For instance, an increase in temperature from 15,000 to 17,000 K would not have as significant an effect as a change in temperature from 22,000 to 24,000 K, even though both differences are 2,000 K. That particular temperature range is critical only because argon is the primary constituent of the shielding gas. Another gas

would have its own particular ionization behavior in that temperature range.

In previous spectroscopic research of hydrogen in GTAW processes, it was postulated that hydrogen reaches a peak concentration near the cathode because of the diffusion behavior of monatomic hydrogen, reactions with other species in the arc, and variation of hydrogen mass transport due to the temperature and pressure gradients [27]. The hydrogen concentration profiles calculated in this research suggests that the overwhelming presence of electrons in the core of the arc serve to displace hydrogen to the outer regions of the arc. The high temperature in the center of the arc causes a rapid expansion of the shielding gas that imparts kinetic energy to the particles in the arc. For a given kinetic energy, a smaller particle will experience a greater velocity than a relatively larger one. As such, the hydrogen particles would move more quickly than the argon particles in the arc. Thus, it is not unreasonable to observe an increase in hydrogen content with increased distance from the center of the arc.

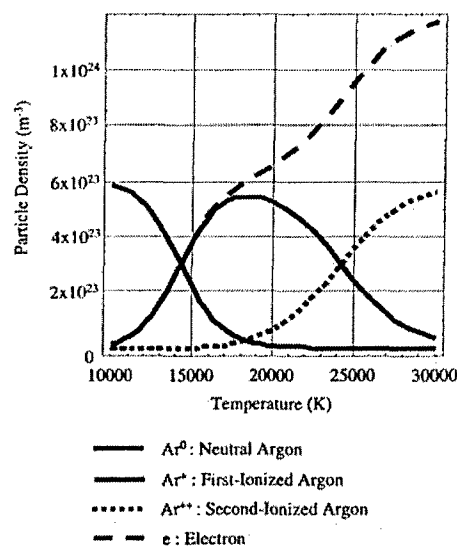


Figure 7. Ionization behavior of argon as function of temperature. (Initial particle density of 6.02×10^{23} particles per cubic meter) [8].

Another distinguishing factor in the center of the arc is the presence of molten metal droplets traveling from the electrode to the weld pool. Calculations by Mundra, et. al [17] showed that molten iron droplets absorb as much as 12 ppm hydrogen while traversing the arc. In this research, most welding was performed primarily in spray mode, which would allow for maximum surface contact with the arc atmosphere and could have led to appreciable hydrogen absorption by the metal droplets on their journey to the weld pool.

Moisture Additions to Argon Shielding Gas

A study was undertaken to test the ability of the spectroscopy system to observe hydrogen in the arc resulting from moisture

in the shielding gas. The impetus for this phase of research lies in the potential application of spectroscopy to a shipyard fabrication environment. Humidity in the atmosphere results in moisture in the shielding gas, which results in hydrogen in the weldment. Savage, et. al. [28] found that moisture additions in a shielding gas are more potent than hydrogen additions with regards to hydrogen content of the weldment. Special argon shielding gas mixtures containing hydrogen and moisture additions for 220-ppm concentration, with a ± 3 -pct. variance according to manufacturer's specifications, were used in these experiments.

As expected, weldments made with the moisture-addition shielding gas exhibited considerable porosity. It was believed that the porosity was due to the moisture itself and not any instabilities in the arc that may have been caused by the additions to the shielding gas. Spray metal transfer mode was achieved in all welding. No porosity was evident in weldments made with the 220-ppm hydrogen addition shielding gas. This observation would suggest that the moisture engendered a considerable amount of hydrogen in the weldment. Low hydrogen levels in a weldment would likely be in solution in the weld metal. Only when hydrogen levels exceed saturation in the weld metal would one expect to see porosity. Diffusible hydrogen levels in weldments made with both shielding gas mixtures were very low, often times not evolving detectable amounts of hydrogen to register on the gas chromatograph.

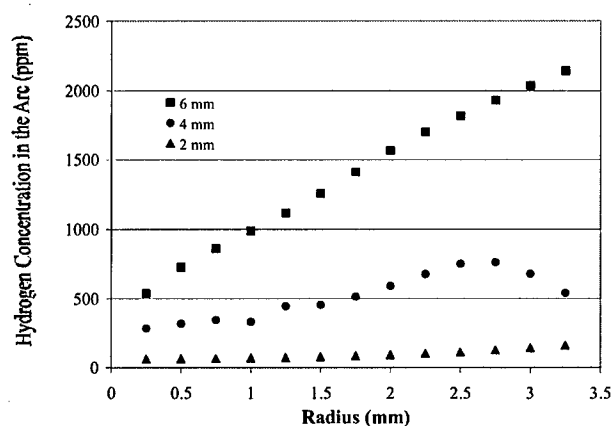


Figure 8. Hydrogen concentration profiles at indicated heights in GMAW processes with 220 ppm moisture additions in argon shielding gas.

When sufficient hydrogen is collected, the diffusible hydrogen levels were found to be 1.2 mL of hydrogen /100 g of weld metal for the moisture-addition shielding gas and 1.5 mL of hydrogen /100 g of weld metal for the 220-ppm hydrogen addition shielding gas. This was not a significant difference considering the drastic difference in weldment quality. However, the porosity of the moisture-addition weldments may be the reason for the low levels. Hydrogen in the molten weld metal exists in monatomic form until saturation. Once pores form, monatomic hydrogen is likely to leave the weld

metal to recombine in the energetically favorable diatomic form. As outlined in the AWS diffusible hydrogen standard [22], the weldments are quenched immediately after welding to retard hydrogen mobility. Upon degassing, it is entirely possible that hydrogen in the weld metal diffused into the pores instead of evolving from the sample. Once in diatomic form, hydrogen mobility in iron is severely limited. Thus, it is not necessarily a contradiction that the weldments made with the moisture-addition shielding gas exhibited lower diffusible hydrogen levels. In fact, weldments made with the moisture-addition shielding gas did contain higher levels of residual hydrogen, suggesting that the moisture additions in the shielding gas were indeed more potent than hydrogen additions with regards to weldment hydrogen content.

The spectroscopy system was able to detect hydrogen in the welding arcs resulting from moisture additions. Hydrogen concentration in the welding arcs with moisture additions followed the same general pattern as outlined in the previous section, i.e. increasing with increasing radius. The earlier discussion regarding the hydrogen concentration profiles is also valid in this case. High temperatures at the center of the arc cause an increase in the concentration of ionized argon, and thus, the concentration of electrons. A profile of the hydrogen concentration of GMAW processes with moisture additions to the shielding gas can be seen in Figure 8. The hydrogen concentrations shown further support the premise that moisture is a more potent means of hydrogen generation in the arc than hydrogen additions. A profile of the hydrogen concentration of GMAW processes with 220-ppm hydrogen additions can be seen in Figure 9.

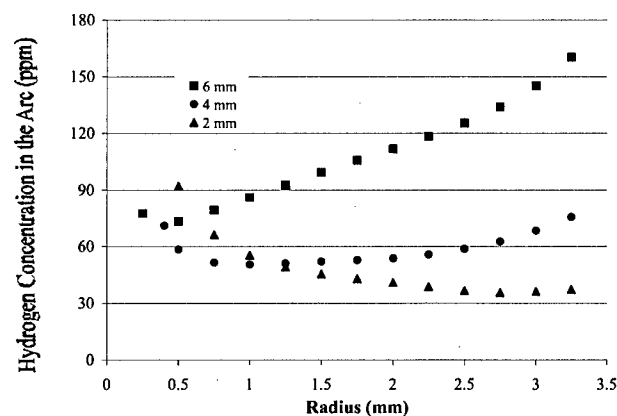


Figure 9. Hydrogen concentration profiles at indicated heights in GMAW processes with 220-ppm hydrogen additions in argon shielding gas.

Comparing the graphs, it can be observed that the concentration of hydrogen due to moisture is much greater than the hydrogen due to hydrogen additions, much greater, in fact. Both conditions follow the same trend of greater hydrogen concentration higher in the arc, but the maximum concentration of hydrogen resulting from the moisture

additions is a magnitude greater than that of the hydrogen additions.

CONCLUSIONS

1. The relationship between hydrogen additions to argon shielding gas and the diffusible hydrogen content of steel weldments produced by a GMAW process resembles a Sievert's Law type of relationship.
2. Calculations made using emission spectroscopy of a GMAW process was found to be a reliable indicator of the diffusible hydrogen content of a steel weldment.
3. The spectroscopy setup used in this research was able to detect hydrogen in the arc due to moisture in the argon shielding gas and rust on a steel wire consumable.
4. Moisture additions were found to be more potent in causing hydrogen in a steel weldment than hydrogen additions of the same concentration in argon shielding gas.

ACKNOWLEDGEMENTS

The authors gratefully acknowledge the funding and support of Dr. Julie Christodoulou of the U.S. Office of Naval Research.

REFERENCES

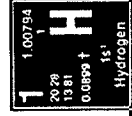
1. N. Bailey, F.R. Coe, T.G. Gooch, P.H.M. Hart, N. Jenkins, and R.J. Pargeter. Welding Steels without Hydrogen Cracking – 2nd Edition. ASM International: Abington, UK, 1973.
2. B.A. Graville, "Cold Cracking in Welds in HSLA Steels." Welding of HSLA (Microalloyed) Structural Steels – Proceedings of an International Conference November 1976 – Rome, Italy. Eds. A.B. Rothwell and J. Malcolm Gray. American Society for Metals, 1978, 85-101.
3. T. Boellinghaus, H. Hoffmeister, and C. Schubert. Proceedings of the 4th International Conference on Trends in Welding Research – Gatlinburg, TN, June 1995. ASM International.
4. C. Zapffe and C. Sims: *Transactions of the AIME*, 1941, vol. 145, pp. 225-261.
5. G.G. Hancock and H.H. Johnson: *Transactions of the TMS/AIME*, 1965, vol. 236, pp. 513-516.
6. J.P. Hirth: *Metallurgical Transactions A*, 1980, vol. 11A, pp. 861-890.
7. D.G. Westlake: *Transactions of the ASM*, 1969, vol. 62, pp. 1000-1060.
8. S. Gahr, M.L. Grossbeck, and H.K. Birnbaum: *Acta Metallurgica*, 1977, vol. 25, pp. 125-133.
9. N.J. Petch: *Philosophy Magazine*, 1956, vol. 1, pp. 331-337.
10. S.P. Lynch. "Hydrogen Embrittlement of Steels: A Review of Mechanistic Aspects." Hydrogen Management for Welding Applications – Proceedings of International Workshop, October 6-8, 1998, Ottawa, Canada. Eds. J.E.M Braid, C.V. Hyatt, D.L. Olson, and G.N. Vigilante. Ottawa: CANMET, 1999. 53-64.
11. R. Thomson: *Journal of Materials Science*, 1978, vol. 13, pp. 128-142.
12. G.W. Simmons, P.S. Pao, and R.P. Wei: *Metallurgical Transactions A*, 1978, vol. 9A, pp. 1147-1158.
13. A.R. Troiano. "The Role of Hydrogen and Other Interstitials in the Mechanical Behavior of Metals." Hydrogen Damage. Ed. C.D. Beachem. Ohio: ASM, 1977, 151-177.
14. R.A. Oriani. "A Mechanistic Theory of Hydrogen Embrittlement of Steels." Hydrogen Damage. Ed. C.D. Beachem. Ohio: ASM, 1977, 301-310.
15. C.D. Beachem: *Metallurgical Transactions*, 1972, vol. 3, pp. 437-451.
16. T.A. Palmer and T. DebRoy: *Welding Journal*, July 1996, vol. 75, pp. 197s-207s.
17. K. Mundra, J.M. Blackburn, and T. Debroy: *Science and Technology of Welding and Joining*, 1997, vol. 2, no. 4, pp. 174-184.
18. D.G. Howden and D.R. Milner: *British Welding Journal*, June 1963, pp. 304-316.
19. S.A. Gedeon and T.W. Eagar: *Welding Journal*, July 1990, vol. 69, pp. 264s-271s.
20. H. Li and T.H. North, "Hydrogen Absorption and Hydrogen Cracking in High Strength Weld Metal." Key Engineering Materials Vols. 69 & 70. Eds. D. L. Olson and T. H. North. Trans Tech Publications, 1992, 95-112.
21. S.A. Gedeon, "Hydrogen Assisted Cracking of High Strength Steel Welds," Doctoral Thesis at Massachusetts Institute of Technology, May 1987.
22. American Welding Society: AWS A4.3-93.
23. M. Matsushita, "Clarification of Hydrogen Reduction Mechanisms in Steel Weld Metal by Means of Fluoride Additions in Welding Flux," Doctoral Thesis at the Colorado School of Mines, September 2001.
24. M. Kobayashi and T. Suga, "A Method for the Spectral Temperature Measurement of a Welding Arc." Arc Physics and Weld Pool Behaviour – International Conference Proceedings, London, May 8-10 1979. Ed. W. Lucas. Abington: The Welding Institute, 1980, 25-37.
25. D. R. White, "In Process Measurement of Hydrogen in Welding." Technical Manuscript M-86/15, USA-CERL, September 1986.
26. K. Hiraoka: *Welding International*, 1998, vol. 12, pp. 186-194.
27. W.F. Savage, E.F. Nippes, and E.I. Husa: *Welding Journal*, 1982, vol. 61, pp. 233s-242s.



Colorado School of Mines - CSM
Center for Welding, Joining and Coatings Research - CWJCR
Golden, Colorado 80401, U.S.A.

Spectroscopic Monitoring of Hydrogen in Welding Arcs

J. Chandler, S. Liu, and G. Edwards



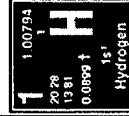
Trends in Welding Research Conference
Pine Mountain, Georgia - May 2005



Colorado School of Mines - CSM
Center for Welding, Joining and Coatings Research - CWJCR
Golden, Colorado 80401, U.S.A.

Acknowledgments

■ The authors gratefully acknowledge the support received from Dr. Julie Christodoulou of the Office of Naval Research

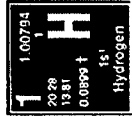




Colorado School of Mines - CSM
Center for Welding, Joining and Coatings Research – CWJCR
Golden, Colorado 80401, U.S.A.

Presentation Outline

- Hydrogen Management Strategy
- Arc Emission Spectroscopy
- Arc Temperature and Hydrogen Concentration Calculation
- Effect of Hydrogen and Moisture Additions, and Rusty Wire on Weld Metal Hydrogen
- Conclusions





Colorado School of Mines - CSM
Center for Welding, Joining and Coatings Research – CWJCR
Golden, Colorado 80401, U.S.A.

Hydrogen Management Strategy

- Control Strategy I : Elimination from Materials and Shielding Gas
- Control Strategy II – Elimination from the Arc Plasma
- Control Strategy III – Elimination from Metal Droplets during Transfer
- Control Strategy IV – Rendering Hydrogen Immobile by Trapping





Colorado School of Mines - CSM
Center for Welding, Joining and Coatings Research – CWJCR
Golden, Colorado 80401, U.S.A.

Hydrogen Management Strategy

■ Arc control

- P_{H_2} Reduction

 - Fluoride additions

- Spectroscopic monitoring

■ Weld metal control

- Hydrogen Trapping

 - Y, Nd, Ce Additions

- Microstructural Optimization

 - Duplex AF-GB/AF-M Microstructure





Colorado School of Mines - CSM
Center for Welding, Joining and Coatings Research – CWJCR
Golden, Colorado 80401, U.S.A.

Specific Objectives – Arc Emission Spectroscopy

- Non-intrusive and non-destructive assessment of hydrogen content in steel weldments
- Real-time, in-situ method of determining hydrogen content in steel weldments
- Increase reliability of qualification procedure of welded structures
- Measure wavelength and intensity of light emitted from welding arc
- Perform analysis to determine temperature and concentration

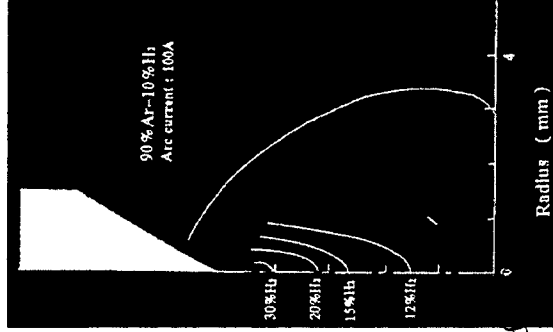
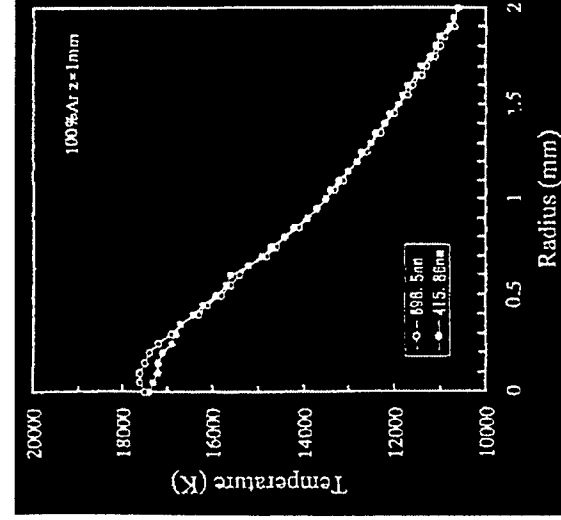
1	1.00794	H
2029	1381	0.0899 ±
		1s ¹
		Hydrogen



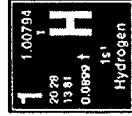
Colorado School of Mines - CSM
Center for Welding, Joining and Coatings Research - CWJCR
Golden, Colorado 80401, U.S.A.

Prior Work – Spectroscopic Measurements of Hydrogen

- Performed primarily on GTAW
- Temperature and concentration determinations



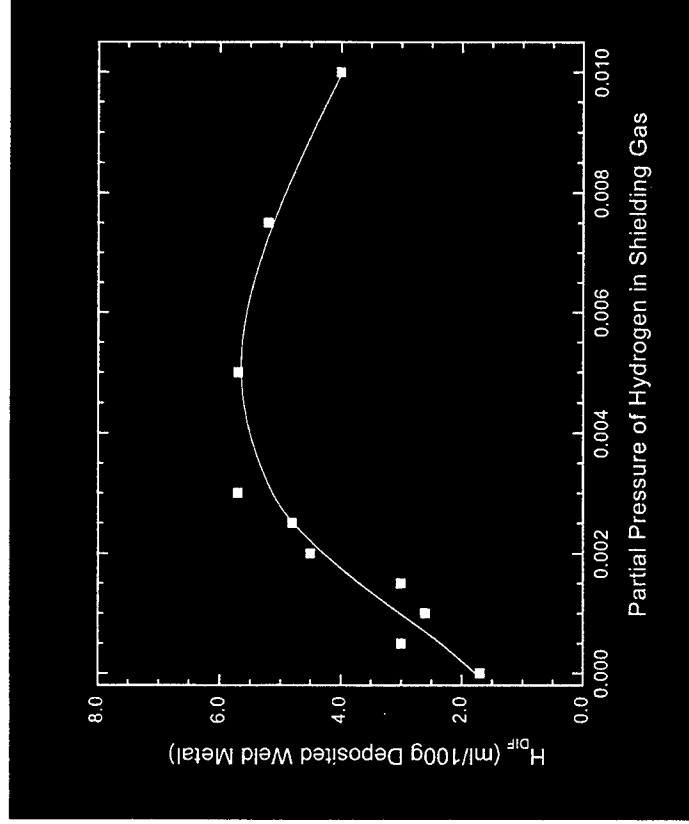
(Hiraoka, 97-98)



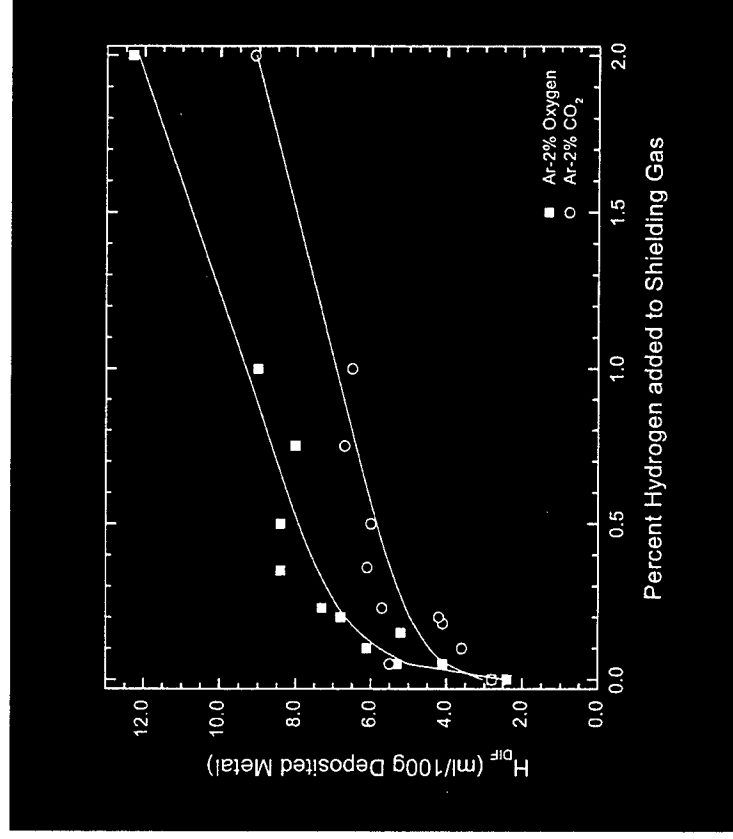


Colorado School of Mines - CSM
Center for Welding, Joining and Coatings Research - CWJCR
Golden, Colorado 80401, U.S.A.

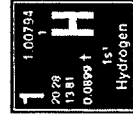
Prior Work – Spectroscopic Measurements of Hydrogen



(White and Leckie, 86)



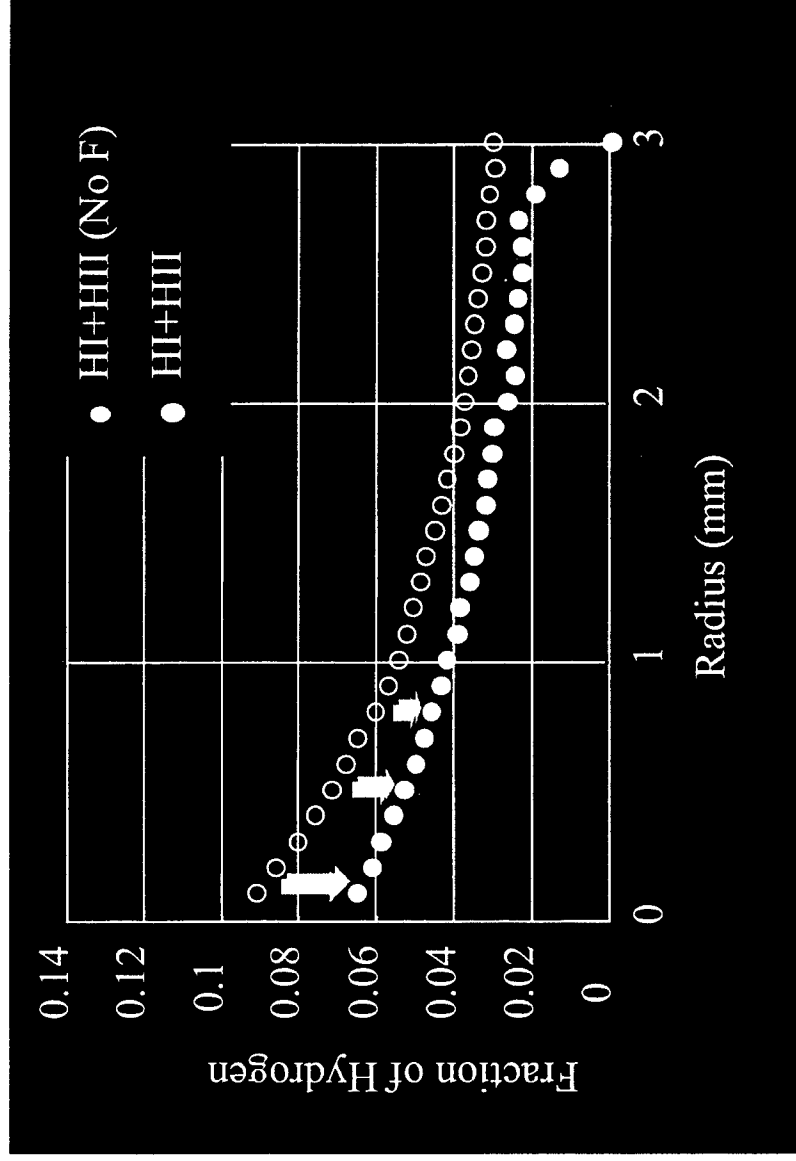
(Gideon and Eager, 86)



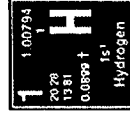


Colorado School of Mines - CSM
Center for Welding, Joining and Coatings Research - CWJCR
Golden, Colorado 80401, U.S.A.

Prior Work – Spectroscopic Measurements of Hydrogen



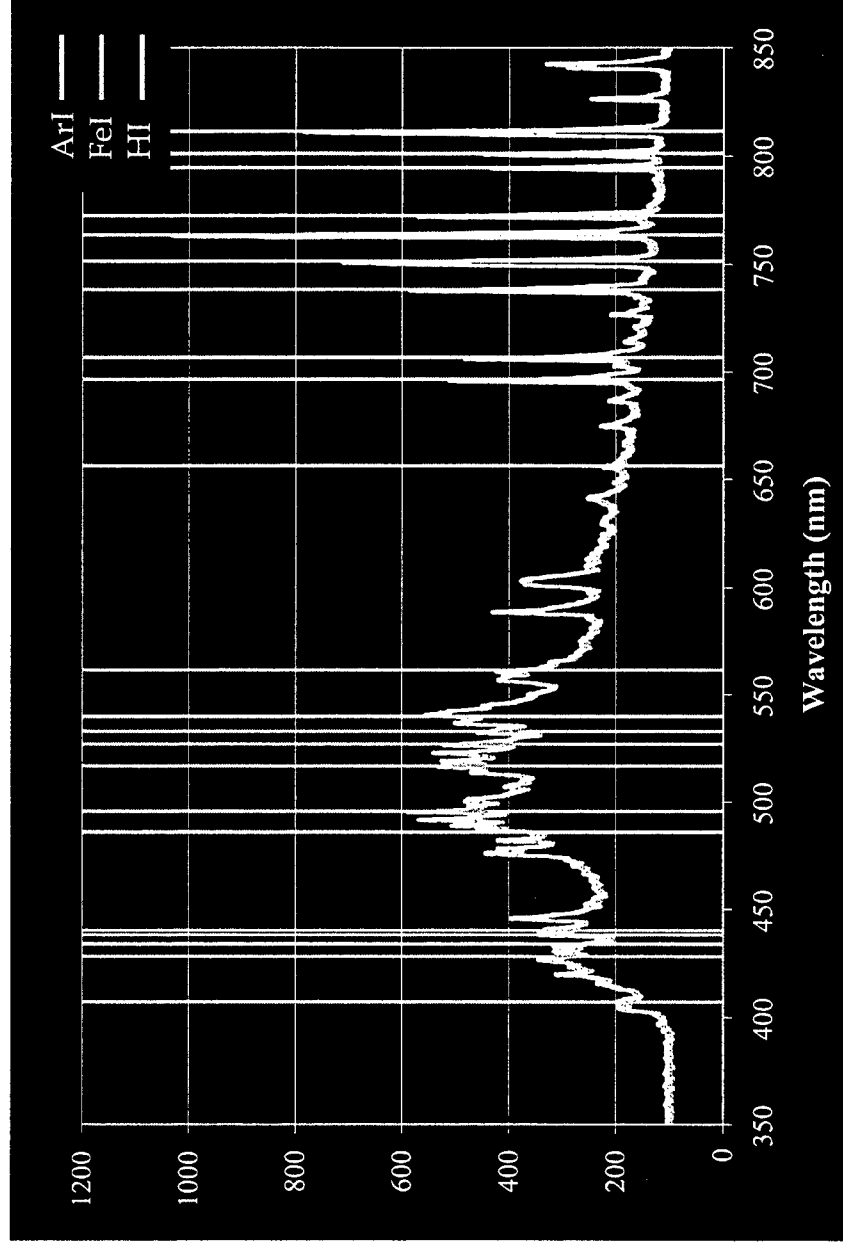
(Matsushita and Liu, 98,01)





Colorado School of Mines - CSM
 Center for Welding, Joining and Coatings Research – CWJCR
 Golden, Colorado 80401, U.S.A.

Typical Ar-Fe-H Emission Spectra



1	1.00794	¹ H
20.28	1381	
0.0099	†	1s ¹
		Hydrogen

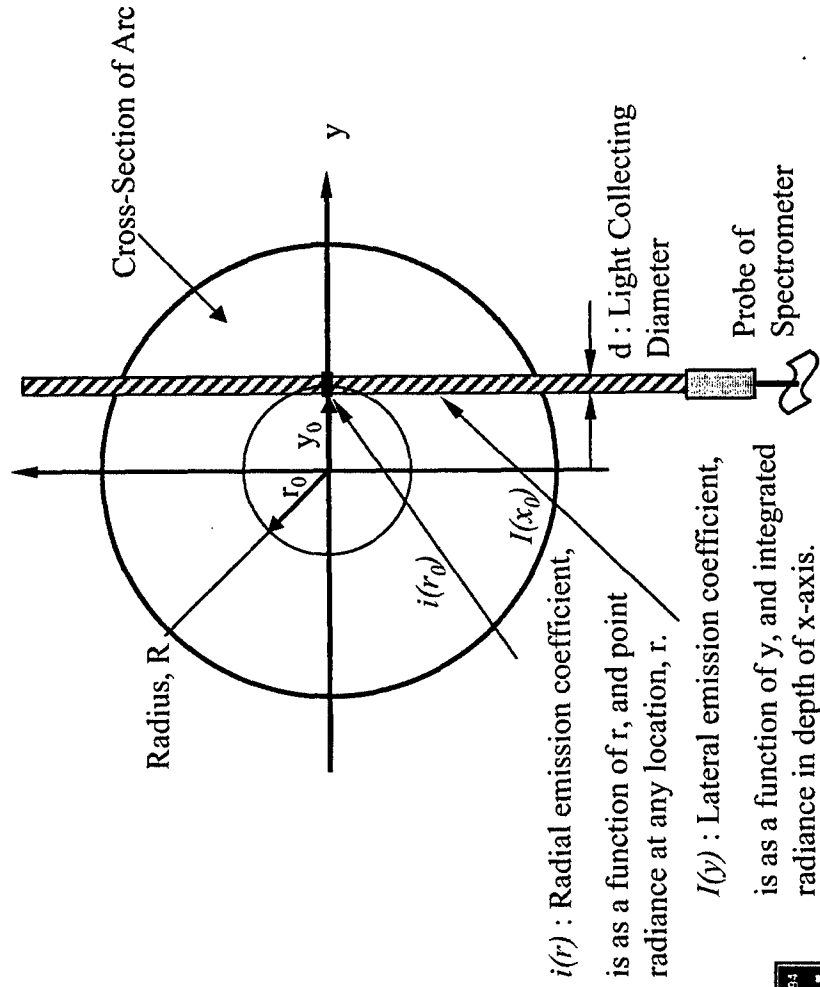
Element	Ionization Stage	Wavelength (nm)
Argon	I	696.5
	II	476.4
Hydrogen	I	656.2



Data Processing - Abel Inversion

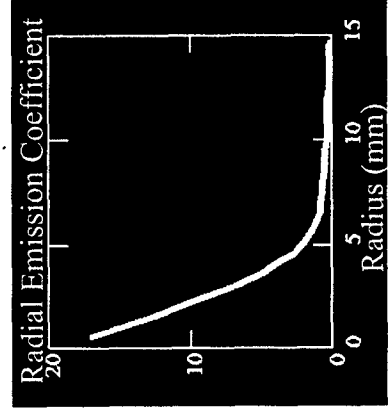
Radial emission coefficient

- Light emission intensity as function of radius in arc



$$i(r) = -\frac{1}{\pi} \int_r^R \frac{dI(x)}{(x^2 - r^2)^{1/2}} dx$$

i = radial emission coefficient
 R = outside radius or arc
 r = radius of arc
 $dI(x)/dx$ = first derivative of function of line emission coefficient
 x = lateral distance

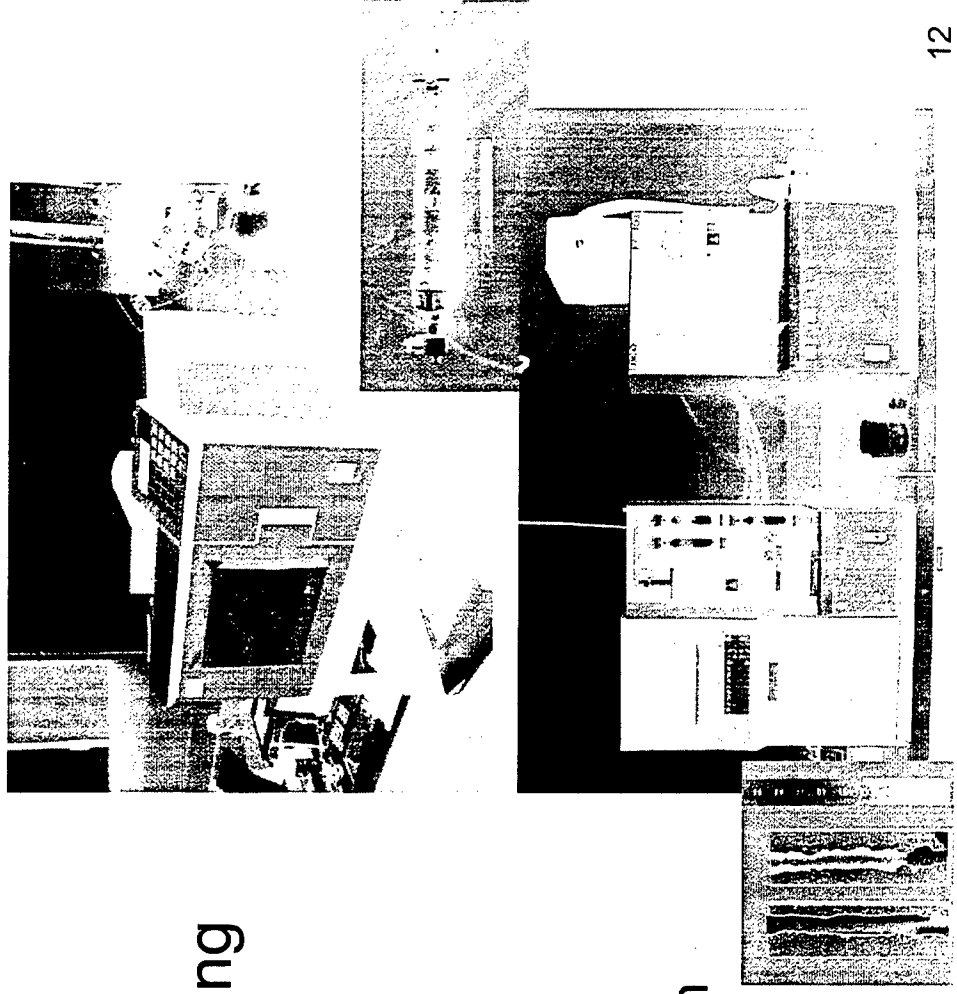




Colorado School of Mines - CSM
Center for Welding, Joining and Coatings Research - CWJCR
Golden, Colorado 80401, U.S.A.

Diffusible & Residual Hydrogen Measurement

- Diffusible hydrogen measured according to AWS/ANSI A4.3-93 using gas chromatography
- Residual hydrogen measured using Leco interstitial analyzers
 - Weldments milled down
 - Chips used for hydrogen analysis





Colorado School of Mines - CSM
Center for Welding, Joining and Coatings Research – CWJCR
Golden, Colorado 80401, U.S.A.

Temperature Calculation

■ Boltzmann-plot
method

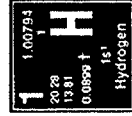
$$\frac{i_j^0}{i_j^0} = \frac{A_j^0 g_j^0 v_j^0}{A_j^0 g_j^0 v_j^0} \exp \left(- \frac{\Delta \varepsilon_j^0 - \Delta \varepsilon_j^0}{kT} \right)$$

■ Off-axis peaking
method

$$\frac{i_j^0(T)}{i_j^0(T^*)} = \frac{\delta_0(T) q_0(T^*)}{\delta_0(T^*) q_0(T)} \exp \left(\frac{\Delta \varepsilon_j^0}{k} \left(\frac{1}{T} - \frac{1}{T^*} \right) \right)$$

■ Ion-Neutral Line
Ratio Method

$$\frac{i^+}{i^0} = \frac{A^+ v^+ g^+ q^0}{A^0 v^0 g^0 q^+} \frac{\delta^+}{\delta^0} \exp \left(- \frac{\Delta \varepsilon^+ - \Delta \varepsilon^0}{kT} \right)$$





Colorado School of Mines - CSM
Center for Welding, Joining and Coatings Research – CWJCR
Golden, Colorado 80401, U.S.A.

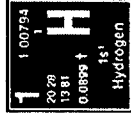
Temperature Calculation

■ Temperature from Ion-Neutral Line Ratio Method and Saha Equation

– Ion-Neutral : Intensity of ArI line at 696.5 nm and ArII line at 476.4 nm

$$\frac{\alpha}{1-\alpha} = \frac{\delta^+}{\delta_0}$$

■ Ionization fraction in Saha and particle density ratio in Ion-Neutral Line Ratio Equation





Colorado School of Mines - CSM
Center for Welding, Joining and Coatings Research – CWJCR
Golden, Colorado 80401, U.S.A.

Saha Ionization Equation

$$\frac{\alpha^2}{1 - \alpha^2} \frac{p}{p_o} = \left(\frac{2m_e}{h^2} \right)^{\frac{3}{2}} \frac{(kT)^{\frac{5}{2}}}{p_o} \frac{2q_+}{q_o} \exp \left(-\frac{eV_i}{kT} \right)$$

α = ionization fraction

T = temperature

p = pressure

q_+ = partition function of ion

p_o = pressure at sea level

q_o = partition function of neutral atom

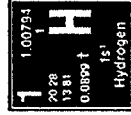
m_e = electron mass

V_i = ionization voltage

h = Planck's constant

e = electron charge

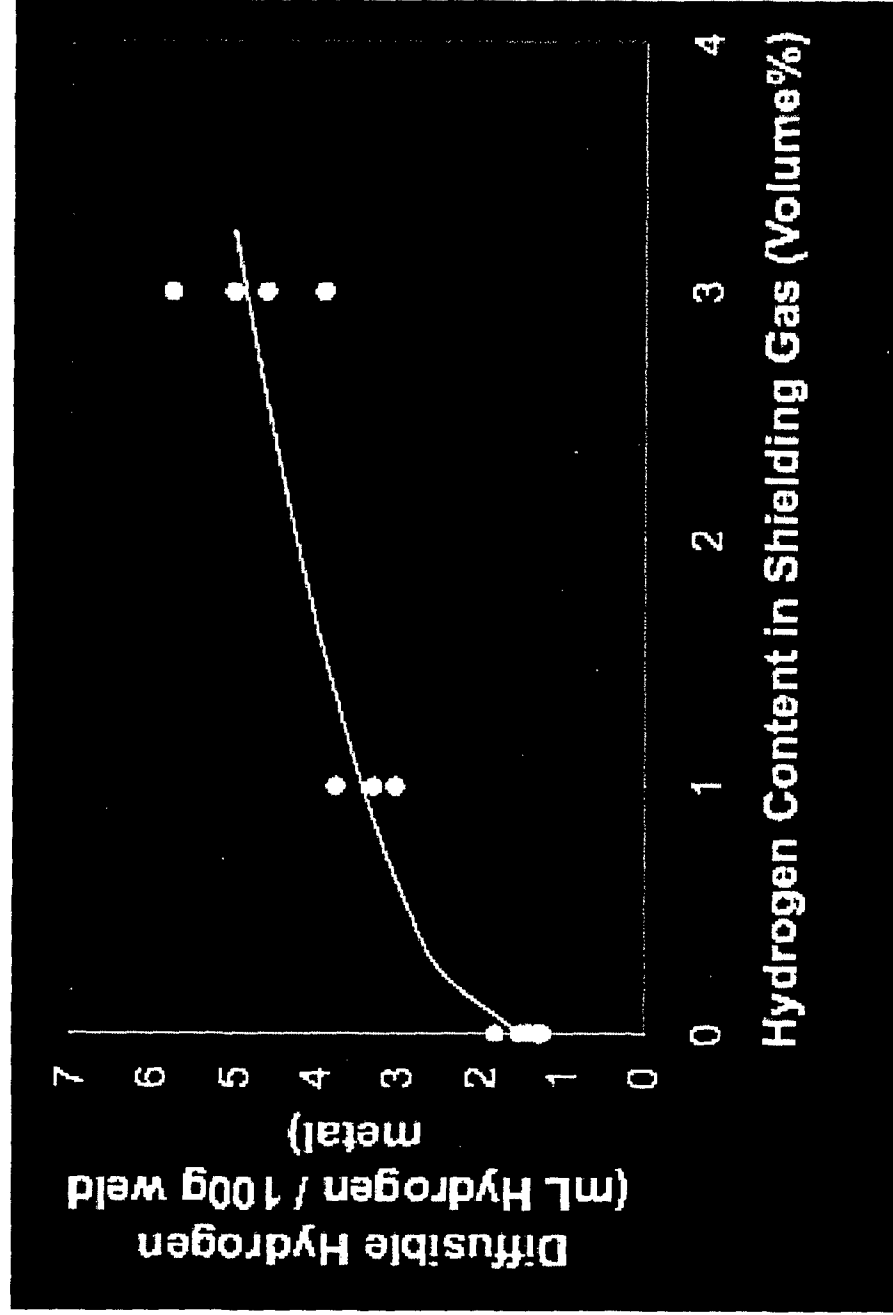
k = Boltzmann constant



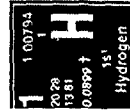


Colorado School of Mines - CSM
Center for Welding, Joining and Coatings Research - CWJCR
Golden, Colorado 80401, U.S.A.

Hydrogen Additions – Diffusible Hydrogen



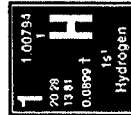
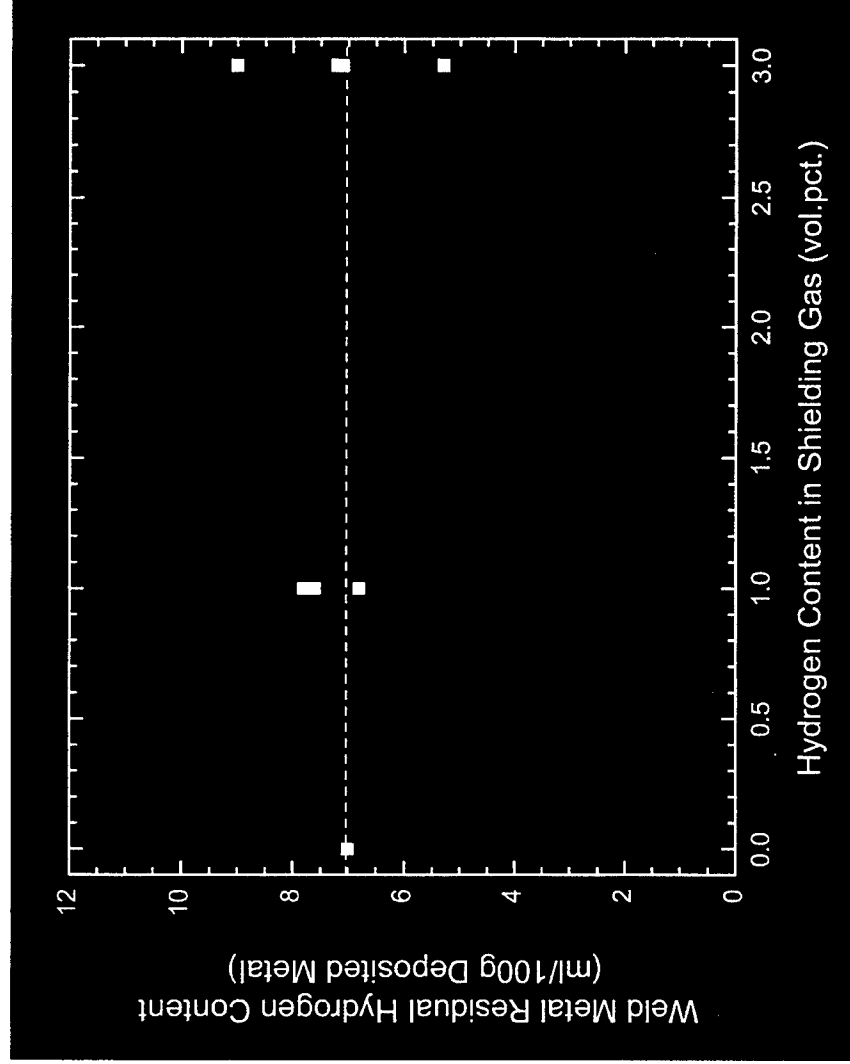
Similar trend observed
by Gideon and Eager (1987)





Colorado School of Mines - CSM
Center for Welding, Joining and Coatings Research - CWJCR
Golden, Colorado 80401, U.S.A.

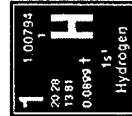
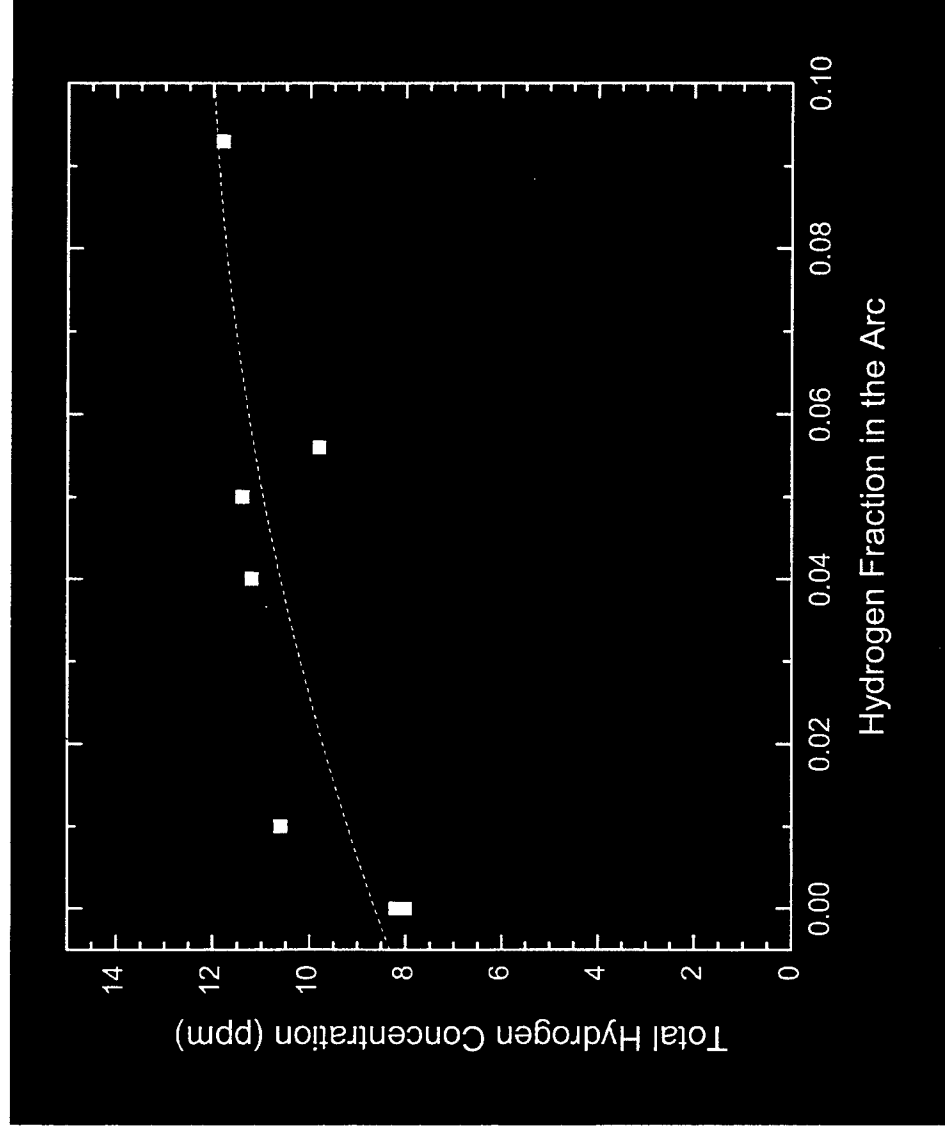
Hydrogen Additions – Residual Hydrogen





Colorado School of Mines - CSM
Center for Welding, Joining and Coatings Research - CWJCR
Golden, Colorado 80401, U.S.A.

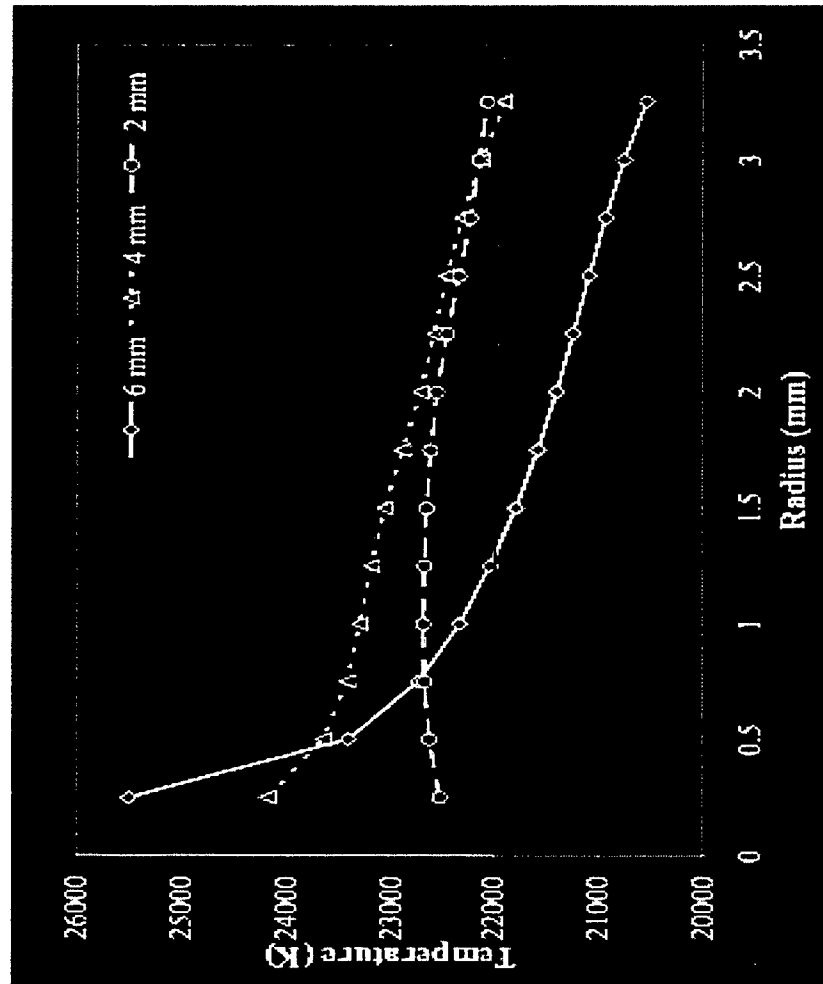
Hydrogen Relationship



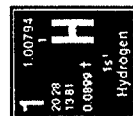


Colorado School of Mines - CSM
Center for Welding, Joining and Coatings Research - CWJCR
Golden, Colorado 80401, U.S.A.

Hydrogen Additions - Temperature



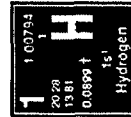
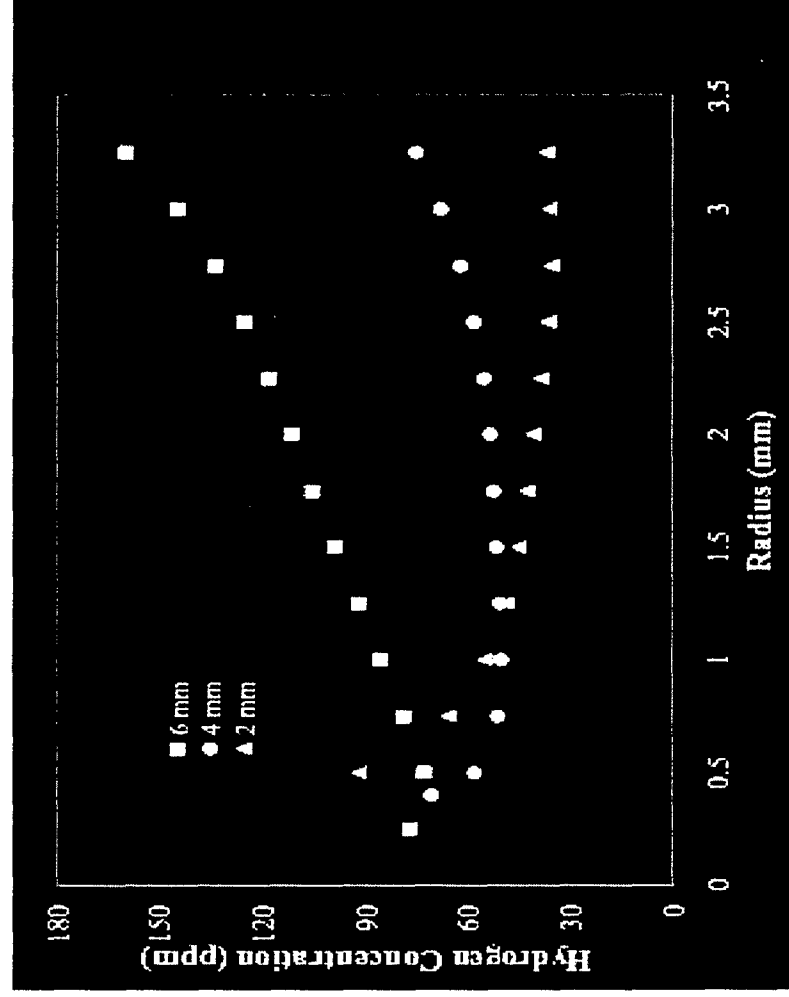
White and Leckie
determined Arc
Temperature between
14000-22000K (1986)





Colorado School of Mines - CSM
Center for Welding, Joining and Coatings Research - CWJCR
Golden, Colorado 80401, U.S.A.

Hydrogen Additions - Profile



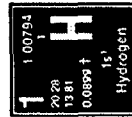
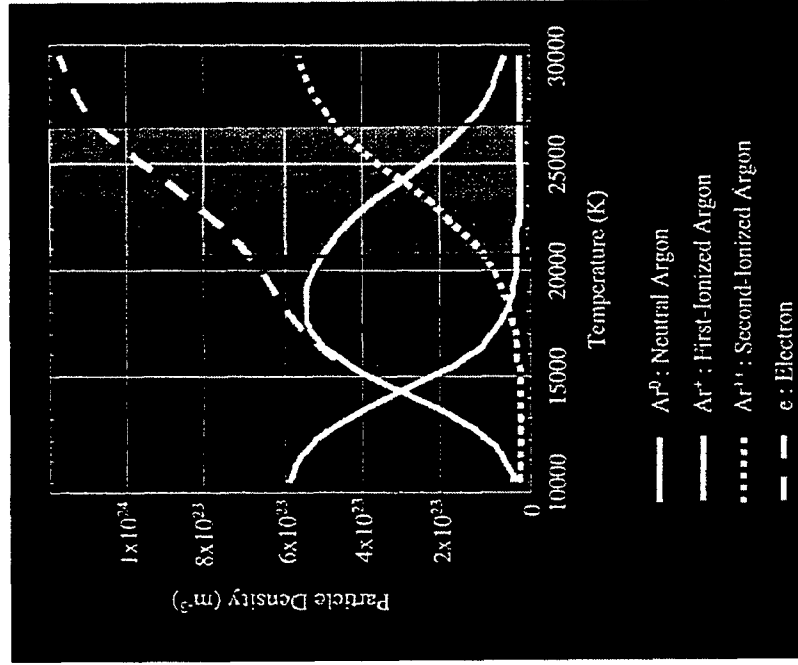


Colorado School of Mines - CSM
Center for Welding, Joining and Coatings Research - CWJCR
Golden, Colorado 80401, U.S.A.

Concentration Determination

- Ratio of each constituent species to neutral argon

$$C_{[M_1]} = \frac{R^0_{[M_1]} + R^+_{[M_1]} + R^{++}_{[M_1]}}{1 + R^+_{[Ar]} + R^{++}_{[Ar]} + R^0_{[M_1]} + R^+_{[M_1]} + R^{++}_{[M_1]} + \dots + R^{++}_{[e]}}$$

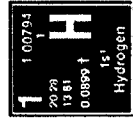
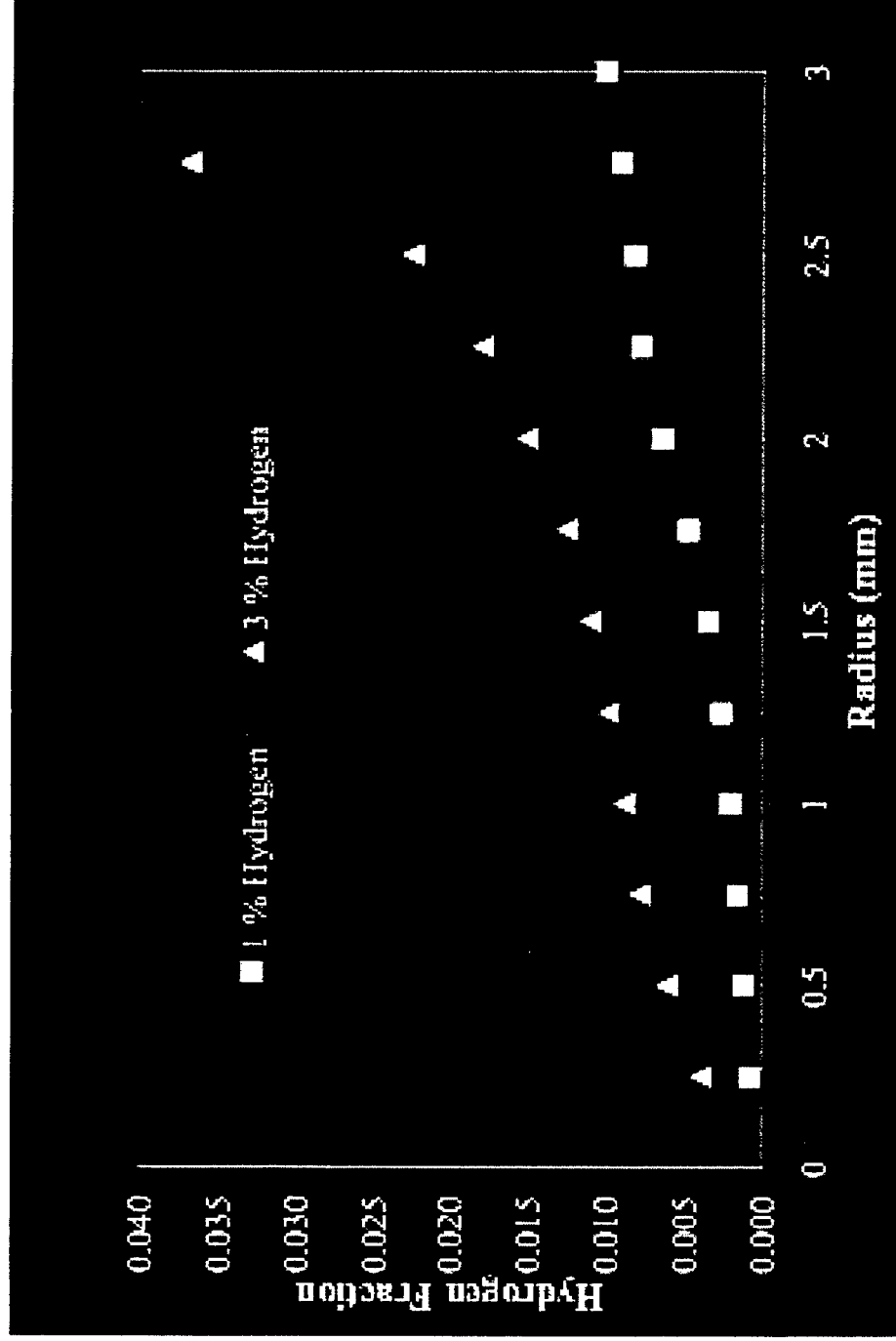


(Matsushita, 2001)



Colorado School of Mines - CSM
Center for Welding, Joining and Coatings Research - CWJCR
Golden, Colorado 80401, U.S.A.

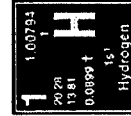
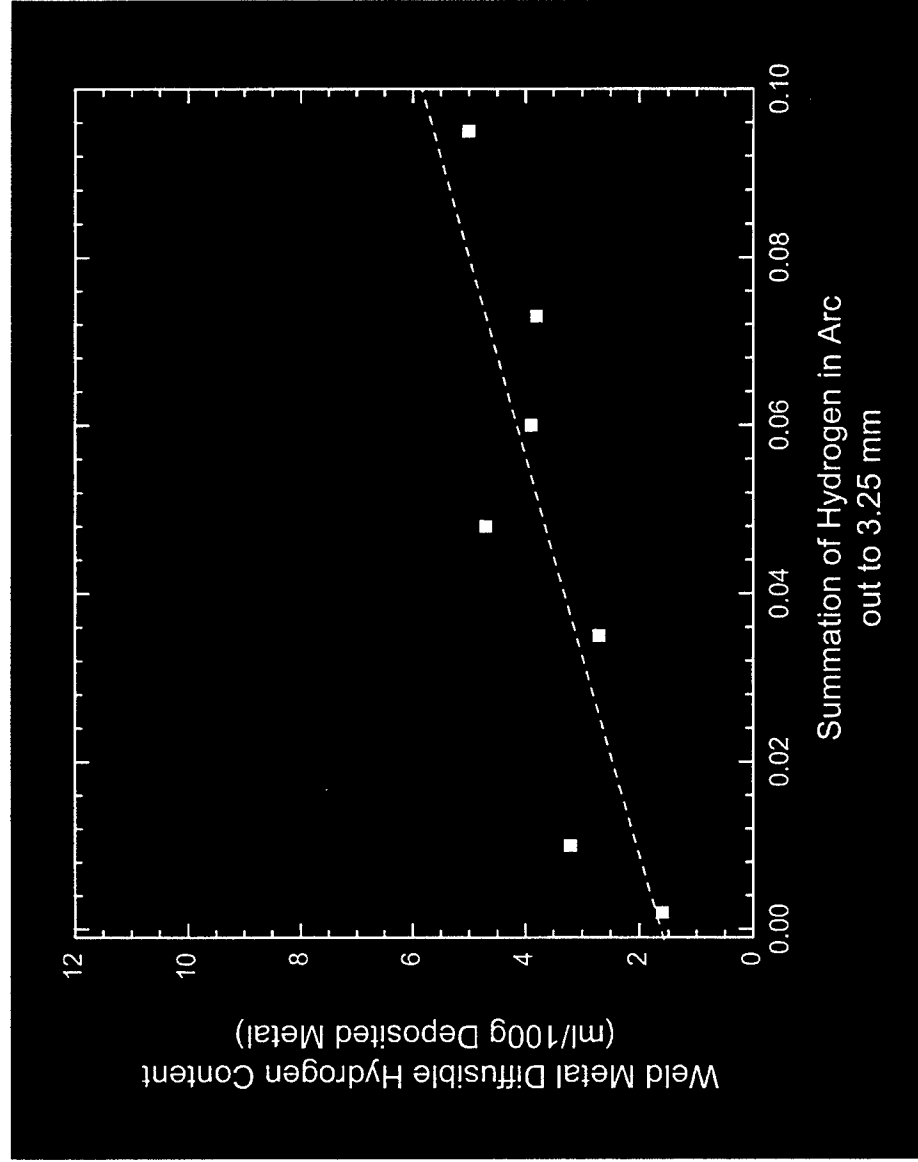
Hydrogen Additions - Profile





Colorado School of Mines - CSM
Center for Welding, Joining and Coatings Research -- CWJCR
Golden, Colorado 80401, U.S.A.

Hydrogen Additions - Summation

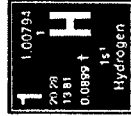
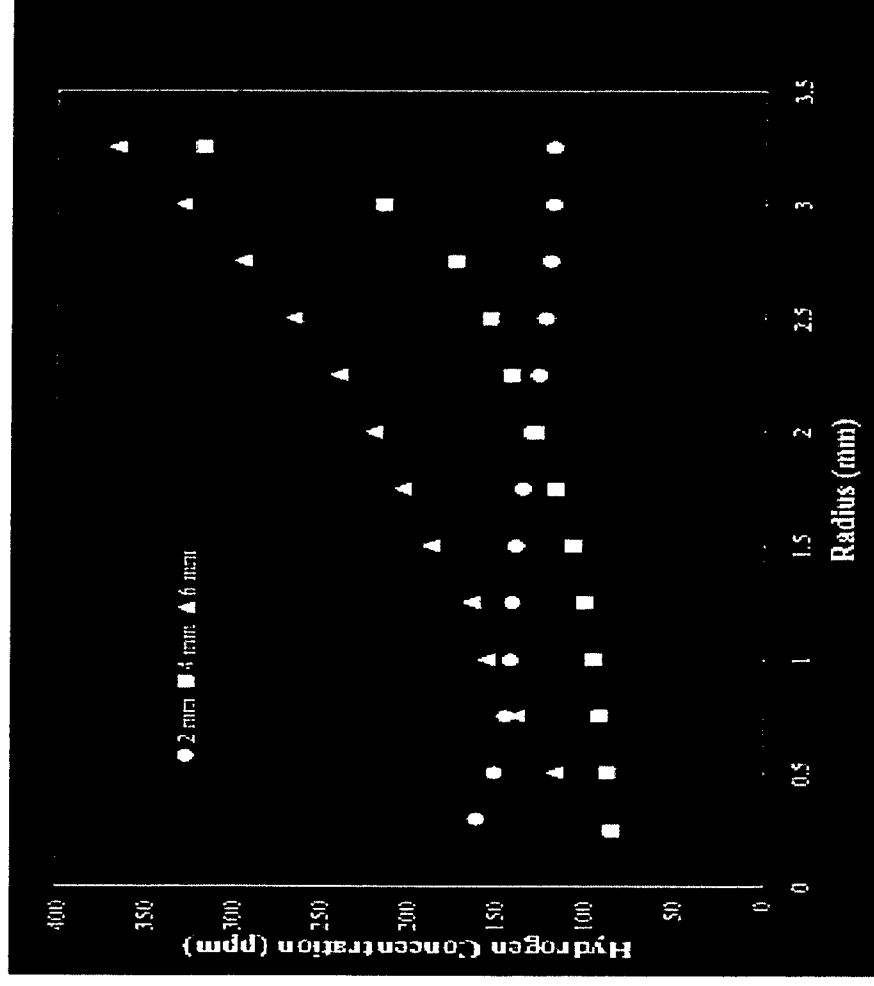




Colorado School of Mines - CSM
Center for Welding, Joining and Coatings Research - CWJCR
Golden, Colorado 80401, U.S.A.

Rusty Consumable - Profile

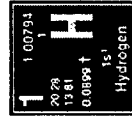
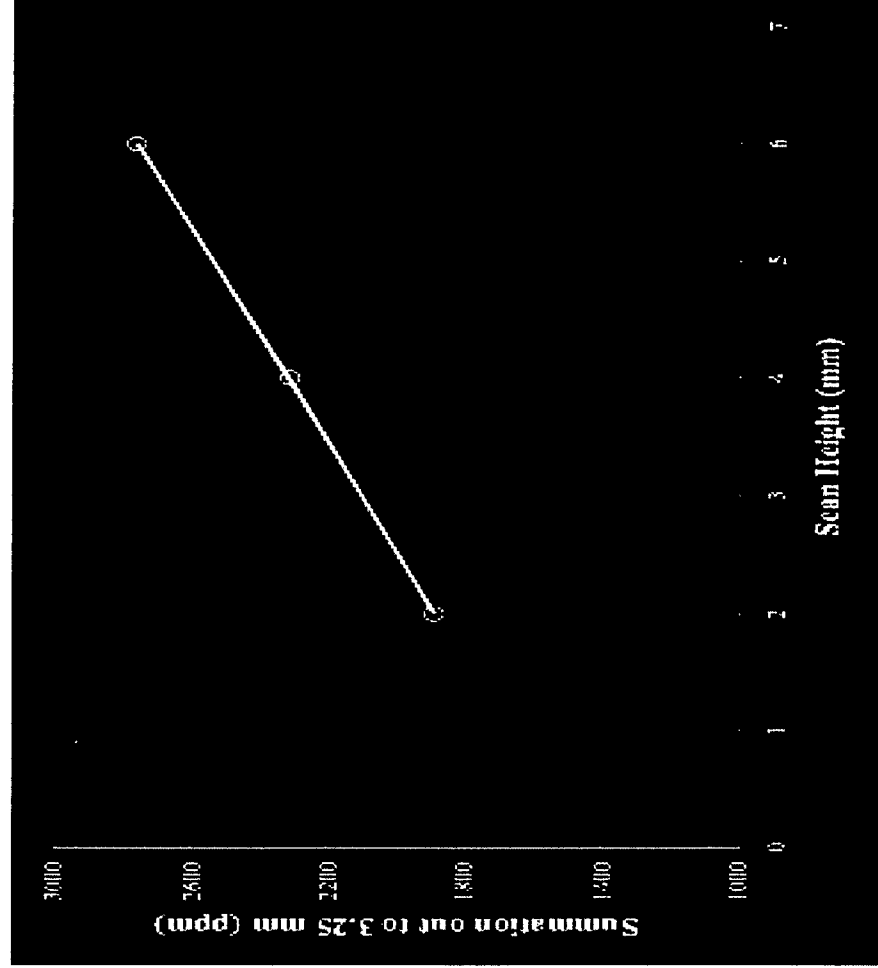
- Exposed to 33°C and 85% relative humidity for four days to simulate possible conditions in fabrication setting





Colorado School of Mines - CSM
Center for Welding, Joining and Coatings Research - CWJCR
Golden, Colorado 80401, U.S.A.

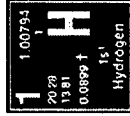
Rusty Consumable - Summation





Conclusions

- A Sievert's Law type of relationship exists between hydrogen additions to shielding gas and diffusible hydrogen levels in weldments
- Emission spectroscopy can be used to reliably determine the concentration of hydrogen in the arc (originated from hydrogen and moisture additions)
- Moisture additions were found to be more potent in causing hydrogen in a steel weldment than equivalent additions of hydrogen.



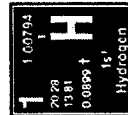


Colorado School of Mines - CSM
Center for Welding, Joining and Coatings Research – CWJCR
Golden, Colorado 80401, U.S.A.

Thank you for your attention. Questions?



*Colorado School of Mines - CSM
Center for Welding, Joining and Coatings Research – CWJCR
Golden, Colorado 80401, U.S.A.*



OMAE2005-67444

MICROSTRUCTURAL DESIGN FOR HIGH STRENGTH STEEL WELDS: THE CONCEPT OF DUPLEX MICROSTRUCTURE

Stephen Liu

Center for Welding, Joining and Coatings Research
Dept. of Metallurgical & Materials Engineering
Colorado School of Mines
Golden, CO 80401, U.S.A.

ABSTRACT

In the past three decades, Colorado School of Mines researchers have investigated flux-related welding processes for pipeline applications and systematically characterized the fundamental behavior of welding fluxes. They also established the relationships between flux ingredients, weld metal microstructure, and weld joint mechanical properties. These studies clarified for high strength steel welds the importance of the bimodal nature of weld metal inclusions, related to weld metal transformations. As strength and toughness levels of the steels continue to increase, new generations of consumables must be developed. Two novel consumables design concepts are being investigated at the CSM. The first one is based on a duplex microstructure consisted of lath martensite and ferrite, and the second is based on low carbon, high alloy martensite.

INTRODUCTION

Nowadays, steels of strength levels between 400 and 550 MPa (80 and 100 ksi) can be found in many large-scale engineering projects, including offshore structures, and on land and offshore pipelines. The challenge is to produce weld deposits of "matching" mechanical properties to the base metal. Since grain refinement through alloying can increase both strength (Hall-Petch relationship) and toughness of a weld metal, an appropriate alloying strategy becomes critical to promote a desirable microstructural distribution that will meet the specification requirements. Alloying additions such as manganese, nickel, chromium, and molybdenum play important roles in elevating the strength of these weld deposits (solid solution strengthening). Other elements such as niobium, vanadium, and titanium are added in micro-quantities for grain size control and precipitation

strengthening. The effect of interstitials such as N, O, S, and H must also be controlled. Typical microstructures can vary from almost exclusively acicular ferrite, in the case of steels with strengths around 500 and 600 MPa (72 and 81 ksi), to a mixed ferrite/martensite or ferrite/bainite microstructure, in the case of steels of strength above 690 MPa (100 ksi).

HIGH STRENGTH STEEL REQUIREMENTS

Structural steels with yield strength below 483 MPa (70 ksi) are generally based on a ferritic microstructure and mostly weldable. One of the controlling factors of impact toughness is carbon content, typically reduced to around or below 0.05 wt. pct. Titanium, known for its ability in promoting acicular ferrite formation is also optimized, at around 200 ppm level¹⁻⁴. Copper additions are common to promote both solid-solution and ϵ -Cu precipitation strengthening⁵⁻⁹. Thermo-mechanical controlled processing (TMCP) and accelerated cooling (AC) result in more uniform and fine-grained microstructure. These processing conditions also affect the precipitation of microalloying elements, e.g. Nb(C,N)⁹, that further restrict ferrite grain growth contributing to both strength increase (to beyond 70-ksi level) and enhanced impact toughness. A steel with 0.04 wt. pct. C, 1.48 wt. pct. Mn, 0.2 wt. pct. Mo, 0.07 wt. pct. Nb, and 0.02 wt. pct. Ti exhibits good tensile properties: 540 MPa (almost 80 ksi) yield strength and 634 MPa (92 ksi) and great toughness values: 347 J (Charpy V-notch - CVN) and 7099 J (Battelle Drop Weight - DWTT) at -5°C¹⁰.

Alloy design strategies for higher strength steels, greater than 80 ksi (550 MPa) yield strength, show that to go beyond the range of 480 to 550 MPa (70 to 80 ksi), a microstructure consisting of bainite or lath martensite would be required. Figure 1 shows typical microstructures of an

HSLA-100 steel¹¹. Note the predominately bainitic microstructure, with long laths and, carbides layers (resolved or unresolved under light microscope) dispersed in between. This fine microstructure proportions the steel with high strength and high impact toughness.



Figure 1. Typical HSLA-100 type steel microstructure observed under light microscope¹¹.

DUPLEX WELD MICROSTRUCTURAL DESIGN THROUGH INCLUSIONS

It is well established that inclusion size control is important in the development of an optimized microstructure for structural steel welds. For instance, if there is a large density of small inclusions in the weld metal, the prior austenite grain boundaries are likely pinned and prevented from growth, thus resulting in a large number of small grains with a large grain boundary area. Small austenite grains offer small intragranular volume for transformation; grain boundary ferrite and ferrite with second phases that nucleate from the grain boundaries grow into the grain to consume a major fraction of the intragranular volume. Incapable of effectively pinning the austenite grain boundaries, larger inclusions are collected inside each austenite grain. These particles act as nucleation sites for acicular ferrite formation. The optimal condition to develop a high amount of acicular ferrite is to have a large population of inclusions with diameter greater than 0.4 microns and an adequate density of smaller inclusions randomly distributed throughout the weld metal^{11,13,15,20-22}. This type of distribution would allow for the pinning of prior austenite grains, but still with a sufficiently large grain size so that the intragranular inclusions can nucleate acicular ferrite before the impingement of high-temperature austenite decomposition products. Subsequent cooling of the weld leads to the formation of ferrite with second phases, aligned and unaligned (FS(A) and FS(NA)), martensite (M), martensite-carbide (MC), and other minor constituents. These lower-temperature transformation products will be embedded in an acicular ferrite matrix. By manipulating the amount of each of these phases and the ratio between the major phases, the resulting welds can assume a large range of mechanical properties. As example, a weld with high acicular ferrite and low martensite will exhibit lower strength but higher impact

toughness than one that contains lower acicular ferrite but higher martensite.

The duplex microstructure appears to best suit the high strength steel base metal. This concept was first presented by Ramsay and Olson^{12,13} to describe the microstructure observed in HY-130 steel weld metals. They reported welds with two distinct microstructures: one with a mixture of lathy phases and acicular ferrite stars, and the other with almost exclusively lathy phases such as FS and martensite. Additionally, they also observed inclusion populations with bimodal size distribution in the welds. They proposed that depending on the inclusion population (size and spatial) distribution, austenite grain size might vary. Large austenite grain size with few intragranular inclusions would result in a microstructure of FS(A), FS(NA), and M. Proper amounts of fine inclusions that held the austenite grain boundaries and larger inclusions located inside the austenite grains that nucleated acicular ferrite stars formed a duplex microstructure as shown in Figure 2.

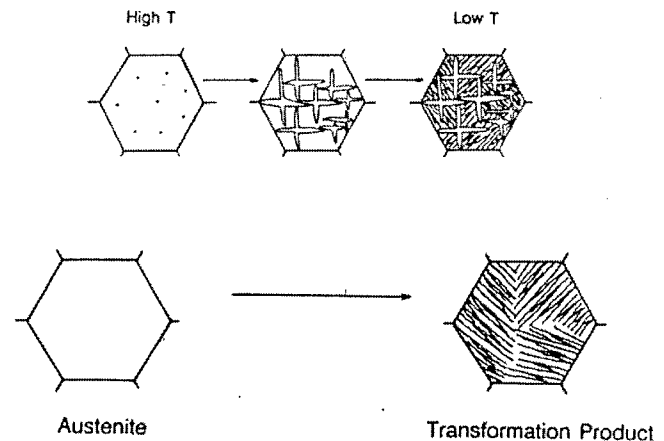


Figure 2. Schematic drawings showing the strong influence of inclusions on the phases that result in high strength steel welds¹²⁻¹³.

Control of inclusion characteristics depends on the alloying and the oxygen content in the weld. At the designed oxygen content, weld specimens undergo limited grain growth because of grain boundary pinning by inclusions. Upon further cooling, intragranular nucleation of acicular ferrite occurs and subdivide the original austenite grains into volumes of a much finer "apparent austenite grain size"¹²⁻¹³. The carbon auto-tempered lath martensite and ferrite form in the interior of these apparent grains. This duplex microstructure of martensite and acicular ferrite was designed to provide both high strength and high impact toughness. Examples of inclusion size distribution in high strength steel welds can be seen in Figure 3 below.

Duplex microstructure was also reported by Bracarense, Fleming, Liu, and Olson¹¹ as shown in Figure 4.

Streaks of martensite can be seen distributed in the acicular ferritic matrix.

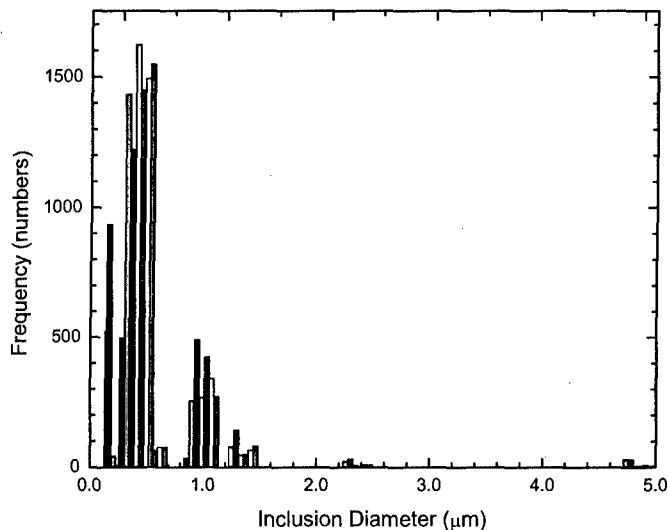


Figure 3. Inclusion size distribution in high strength steel welds illustrating the bimodal size distribution¹⁴.



Figure 4. Duplex microstructure – martensite and acicular ferrite – as observed by Bracarense and Fleming in HSLA-100 steel welds¹¹.

By combining different high strength to low strength constituents, i.e. a mixture of low carbon lath martensite, low carbon bainite, and acicular ferrite in the microstructure, a relatively wide range of properties can be obtained to satisfy the high strength steel welding criteria. Following the works of Ramsay and Olson¹²⁻¹³, Bracarense, Fleming, Liu and Olson¹¹, Wang and Liu¹⁵ extended the concept of duplex microstructure to steel welds of 110 to 120 ksi (760 to 830 MPa) strength levels. These welds contained granular bainite and acicular ferrite, Figure 5.

A mixture of 20 vol. pct. granular bainite and 70 vol. pct. acicular ferrite¹⁴ or a mixture of 40 vol. pct. lath martensite and 60 vol. pct. acicular ferrite¹¹ will both provide yield strengths of 690 MPa (100 ksi) and impact toughness

values of (81 J) 60 ft-lb at -18°C (0°F), 61 J (45 ft-lb) at -35°C (-30°F), and 27 J (20 ft-lb) at -51°C (-60°F)¹⁴. Ferrite with second phase aligned (FS(A)) and ferrite with second phase non-aligned (FS(NA)) make up the remaining microstructure. An optimal alloying system (in wt. pct.) for a 100 ksi (690 MPa) strength level was reported as: 0.04 wt. pct. C, 1.30 wt. pct. Mn, 0.26 wt. pct. Si, 2.30 wt. pct. Ni, 0.40 wt. pct. Mo, 0.80 wt. pct. Cu, 0.03 wt. pct. Nb, 90 ppm N (max), and 270 ppm O.¹⁴ This composition reduced the amount of grain boundary ferrite and sideplate ferrite, but promoted the formation of acicular ferrite, bainite and martensite.

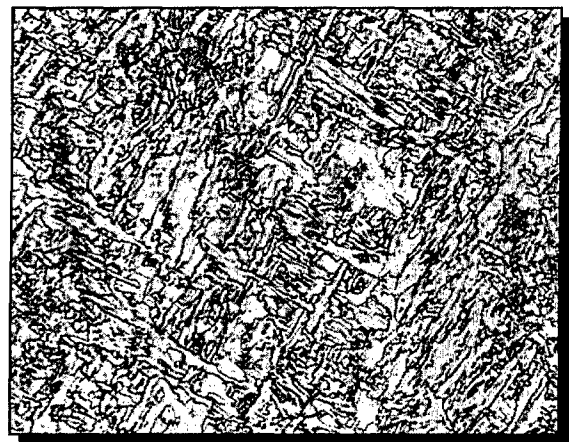


Figure 5. Duplex microstructure – granular bainite and acicular ferrite – as observed by Wang and Liu in steel welds of strength above 100 ksi (690 MPa)¹⁴.

Granular bainite is dispersed in the matrix of acicular ferrite, as shown in Figure 5. Its optical morphology under light microscope resembles blocky ferrite, except for the less developed boundary. The electron diffraction pattern of the dispersed phase resembled that of the body-centered cubic, α -ferrite, Figure 6. Higher magnification examination of the granular bainite revealed a population of small dark islands, Figure 7a, identified as retained austenite using electron diffraction techniques in dark field TEM, Figures 7b and 8 (SAD pattern). Thus, the dispersed phase was actually an α -ferrite type matrix with retained austenite islands. Since low carbon martensite crystal has an electron diffraction pattern that is basically the same as that of ferrite, and that no cementite was found, the dispersed phase fits the description of granular bainite¹⁴.

A sample weld composition that met both strength and impact toughness requirements for above 100 ksi strength welds is shown in Table I below. Note the low carbon content and the balance of solid-solution elements, precipitation strengthening elements, and inclusion formers.

Recent publications by Bangalu, Fairchild et al.¹⁶ demonstrate that the duplex microstructure concept has been transitioned to practice in the welding of steels with 830 MPa (120 ksi) strength. The duplex microstructure refers to acicular

ferrite (between 5 and 15%) and lath martensite (between 50 to 85%)¹⁵. As discussed earlier, the larger amount of lath martensite with respect to acicular ferrite in the weld increased the strength level. Aside from the two major phases, degenerated upper bainite (FS(A)) can also be found. The weld composition that met Charpy property of 150J (106 ft-lb) at -50°C is 0.06% C, 1.8% Mn, 0.57% Si, 2.7% Ni, 0.22% Cr, 0.57% Mo, 0.18% Cu, and 0.014% Zr¹⁵. The P_{CM} of the alloy varied between 0.265 and 0.295¹⁶.

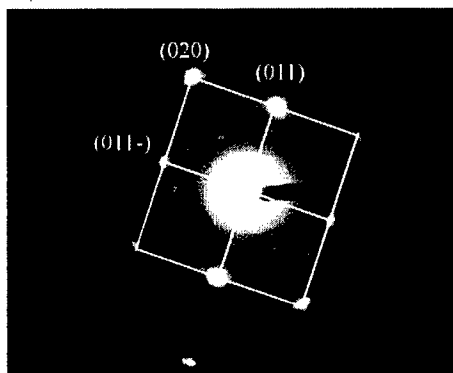


Figure 6. Selected area diffraction (SAD) of the dispersed phase identifying that the matrix is a BCC α -Fe¹⁴.

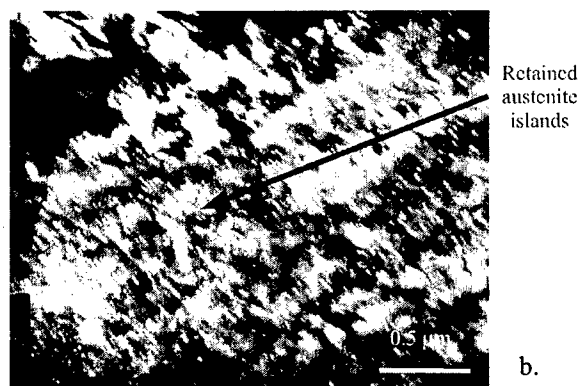


Figure 7. a. TEM micrographs of the granular bainite (the dispersed phase), b. Dark-field image showing the dispersed phase with islands of retained austenite¹⁴.

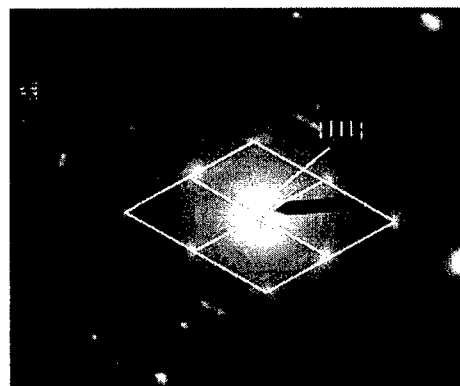


Figure 8. SAD of the fine precipitates in the dispersed phase identifying that those are retained austenite islands¹⁴.

Table I. Sample composition that met both strength and impact toughness requirements for above 100 ksi strength welds¹⁴.

C	Mn	Si	Ni	Mo	Ti (ppm)	N (ppm)	O (ppm)
0.045	1.31	0.26	1.52 - 2.30	0.28 - 0.54	180 - 240	90	270 - 300
	Cu	P	S	V	Cr	Nb	
	0.80	0.012	0.004	0.009	0.03	0.03	

ALTERNATE APPROACH FOR HIGH STRENGTH STEEL WELDING: LOW CARBON MARTENSITE WELD METAL

Neither steel martensite nor steel bainite is an intrinsically brittle microconstituent. In fact, low carbon plate martensite can be quite strong as well as tough. Likewise, ultra-low carbon bainite has been shown to be quite tough. Intuitively, one might anticipate better toughness in fine martensite, where non-aligned high angle boundaries between plates would create a more tortuous crack path than that provided by the aligned boundaries in a low-carbon bainite packet. For filler metal, supermartensitic-based materials may be adequate to provide excellent impact toughness as filler metal for welding high strength steels¹⁹. Figure 9 shows a photomicrograph of a low carbon martensitic stainless steel weld metal. It is the view of the author that this microstructure will provide sufficient strength and impact toughness to match the high strength structural steels.

Figure 10 summarizes the tensile and impact properties of several high alloy steels. While the impact properties of the austenitic steel decreases rapidly with increasing ultimate tensile strength, the decreases observed in the martensitic steels were far more gradual. In the range of 120 to 150 ksi (830 to 1030 MPa) tensile strength, all three martensitic stainless steels exhibited low temperature impact properties much superior to those specified by the U.S. Navy. Impact toughness around 100 ft-lb (115 J) can be obtained. It is very likely that when used as filler metals, these martensitic stainless steels will still perform well to meet the high

requirements. The great potential of these alloys should be further investigated.

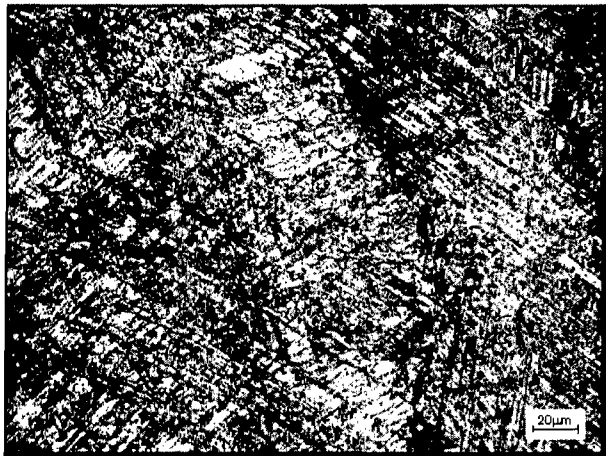


Figure 9. Photomicrograph of a low carbon, martensitic stainless steel weld metal¹⁷⁻¹⁸.

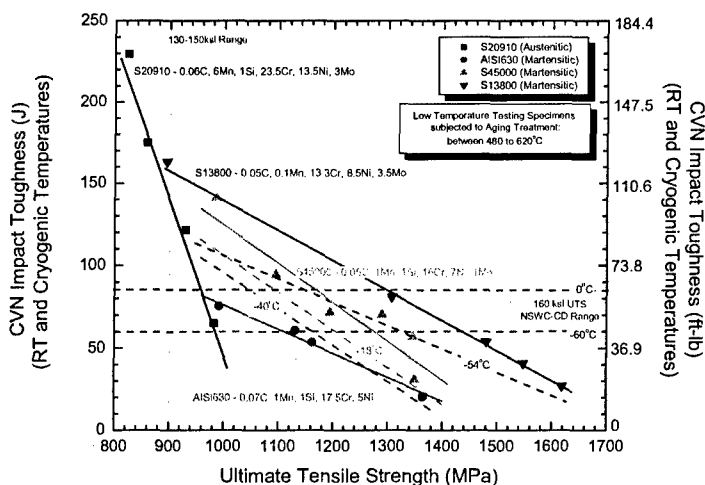


Figure 10. Summary of tensile and impact properties of several high austenitic and martensitic stainless steels. Impact toughness around 100 ft-lb (115 J) can be obtained¹⁷⁻¹⁸.

CURRENT CONSUMABLE CHALLENGES

Based on current understanding of welding metallurgy, it can be safely concluded that consumables for higher strength pipeline steels can be developed. Two novel consumables design concepts are being investigated at the CSM. The first one is based on a duplex microstructure consisted of lath martensite and ferrite, and the second is based on low carbon, high alloy martensite. By manipulating the inclusion population and the duplex microstructure that results, a respectable combination of strength and impact properties can be obtained. Low carbon, high alloyed martensite steels are known to possess excellent strength and

impact properties. These alloys should be investigated regarding their ability to serve as filler alloys for high strength steels.

CONCLUSIONS

The major conclusions of this paper can be summarized in the following:

- A dispersed phase, often unresolved under light microscope, is actually granular bainite with small retained-austenite islands dispersed in a BCC-iron matrix.
- Steel weld metals with a predominately AF microstructure matrix and considerable amount of GB or M exhibit respectable strength and impact toughness. The AF phase provides the toughness and GB and M give the strength.
- With the AF and GB optimized, coarse FS(A) appeared to further enhance the toughness performance by offering greater resistance to crack propagation.
- Supermartensitic-based alloys should be investigated regarding their ability to serve as filler metals for high strength steel welding.

ACKNOWLEDGMENTS

The author acknowledges the support of US-ONR and The Lincoln Electric Company for their support in the development of this research program.

REFERENCES

- Johnson, M.Q., 1996, "Microstructure-Property Relationships in Titanium-Bearing High Strength Multipass Shielded Metal Arc Welding", Ph.D. thesis, Colorado School of Mines.
- Evans, G.M., 1992, "The effect of titanium on the microstructure and properties of C-Mn all-weld metal deposits", WRA, Vol. XXXVIII, No. 8/9, p13-21.
- Evans, G.M., 1996, "Microstructure and Properties of Ferritic Steel Welds Containing Ti and B", *Welding Journal*, Vol. 75, (8), p251-260s.
- Oh, D.W., Olson, D. L. and Frost, R.H., 1990, "The Influence of Boron and Titanium on low-Carbon Steel Weld Metal", *Welding Journal*, 69 (4), 151s-158s.
- Es-Souni, M., Beaven, P.A. and Evans, G.M., 1991, "Microstructure and mechanical properties of Cu-bearing MMA C-Mn weld metal", WRA, Vol. XXXVII, No. 2/3, 1991, p84-95.
- Kirshnadev, M.R., Zhang, W.L., Rene, Gendron, A., Vaidy, V. and Bowker, J.T., 1995, "Influence of Composition and cleanliness of Electrodes on the Weld Metal Properties and Microstructure in Advanced Copper Precipitation Strengthened HSLA Steels", *Proceedings of the International Symposium on High Performance Steels for Structural Applications*, 30 October - 1 November, Cleveland, Ohio. p189-196.

7. Hannerz, N.E., 1987, "Review on the Influence of Copper Content on Weld Metal Properties", IIW doc. IX-1487-87.
8. Thompson, S. W., 1993, "Austenite Transformation Behavior and Fracture Performance of Low-Carbon, Copper-containing Steels with Bainitic Microstructures", Research report in CSM.
9. Ramirez, E and Liu, S., and Olson, D.L., 1996, "Dual Precipitation Strengthening Effect of Copper and Niobium in High Strength Steel Weld Metal", Materials Science and Engineering A, A216, p91-103, Oct.
10. L.E. Collins, M. Kostic, T. Lawrence, R. Mackenzie, and N. Townley, "High Strength Linepipe: Current and Future Production," Proc. of International Pipeline Conference 2000, ASME, V. I, pp. 185-191, 2000.
11. Flemming, D. A., Barcarene, A. Q., Liu, S., and Olson, D.L., 1996, "Toward Developing a SMA Welding Electrode for HSLA-100 Grade Steel", Welding Journal, June, p171s-183s.
12. P.T. Oldland, C.W. Ramsay, D. K. Matlock, and D.L. Olson, "Significant Features of High Strength Steel Weld Metal Microstructures", Welding Journal 68 (4), 158s-168s (1989), addition 68 (6), pp. 252s (1989).
13. C.W. Ramsay, D.L. Olson, and D.K. Matlock, "The Influence of Inclusions on the Microstructures and Properties of a High Strength Steel Weld Metal", Proc. Gatlinburg International Conference on "Recent Trends in Welding Research", May 14-18, 1989, pp. 763-768, Metals Park, Ohio (1990).
14. C. Clasper – *M.S. October 2004* – "Consumables for High Strength Steel Welding with Optimized REM and Fluoride Additions".
15. W. Wang and S. Liu, "Alloying and Microstructural Management in Developing SMAW Electrodes for HSLA-100 Steel", Welding Journal, 81(7), pp.132s-45s, 2002.
16. Bangaru, Fairchild, Macia, Koo, and Ozekcin, "Microstructural Aspects of High Strength Steel Pipelines Girth Welds", Proc. International Pipeline Technology Conference, pp. 789-808, Ostend, Belgium, May 2004.
17. F. Martinez Diez – *Ph.D. Thesis, August 2004* – "Development of Compressive Residual Stress in Structural Steel Weld Toes by means of Weld Metal Phase Transformations".
18. F. Martinez – *M.Eng. Thesis, September 2004* – "The Effect of Carbon Content and Second Phase Particles on the Toughness of a Martensitic Steel Weld Metal".
19. Fernando Martinez Private communication in 2004.
20. S. Liu and D.L. Olson, "The Role of Inclusions in Controlling HSLA Steel Weld Microstructures", Welding Journal, 65 (6), pp. 139s-150s, June 1986.
21. S. Liu, "Measurement and Identification of Weld Metal Inclusions", in 'Metallography and Interpretation of Weld Microstructures', edited by J. McCall, D. Olson and I. LeMay, IMS/ASM, AWS, pp. 87-131, Denver, Colorado, June 1987.
22. S. Liu and D.L. Olson, "The Influence of Inclusion Chemical Composition on Weld Metal Microstructure", ASM Journal of Materials for Energy Systems, 9 (3), pp. 237-251, October 1987.

GTAW of Titanium Using Flux-cored Wire with Magnesium Fluoride

Kook-soo Bang¹, Greg Chirieleison², and Stephen Liu²

1 Division of Advanced Materials Science and Engineering,

Pukyong National University, Pusan, 608-739, Korea

ksbang@pknu.ac.kr

2 Center for Welding, Joining and Coatings Research,

Colorado School of Mines, Golden, CO 80401, USA

gchirieleison@haynesintl.com

sliu@mines.edu

Abstract

Grade 2 Ti-CP was gas tungsten arc welded using flux-cored wires and flux pastes that contained various MgF_2 contents. The effects of MgF_2 on bead morphology, chemical composition, and hardness of weld bead were investigated and interpreted. With an increase of MgF_2 content in the flux paste, depth-to-width ratio of weld bead increased gradually with little variation in interstitial element contents and hardness. Weld bead made with cold flux-cored wire feed showed even deeper and narrower bead, indicating the greater effectiveness of wire feed than flux paste on weld penetration. While the 50% MgF_2 flux-cored wire produced complete slag coverage and smooth weld bead surface, 85% MgF_2 wire resulted in incomplete slag coverage and rough weld surface. Arc spectroscopy revealed that the 50% MgF_2 flux-cored wire produced plasma spectrum with atomic and ionized titanium peaks, which is an indication of a high temperature arc and, a larger amount of flux vapors in the arc. Therefore, it is believed that deep weld penetration associated with high MgF_2 fluxes in this experiment is caused by arc constriction, resulting from the greater amount of flux vapors due to high arc temperature.

Keywords

Titanium, Flux-cored wire, MgF_2 , Weld bead morphology, Arc constriction

Introduction

The high strength, light weight, and excellent corrosion resistance possessed by titanium and titanium alloys have led to a wide and diversified range of applications in the aerospace, chemical plant, power generation, marine and other industries. The gas shielded arc welding processes are well suited for joining titanium and its alloys, provided that the gas shielding arrangement adequately protects the weld area from the atmosphere. Of these welding processes, gas tungsten arc (GTA) is currently the most commonly applied. Welds can be made autogenously or with addition of a filler wire into the arc. The GTA welding process is capable of producing high quality welds with no weld spatter. The principal disadvantages of GTAW lie in the limited thickness of material that can be welded in a single pass, poor tolerance to some material composition, low productivity, and the need of additional shielding gas. For example, under nominal currents, the weld penetrations are generally around 3mm in a single pass. For thicker welds, proper joint preparation and a filler wire are usually required and multipass welding is a general practice. At high temperatures, such as those found in a molten pool, titanium may react with nitrogen, oxygen and hydrogen, if improperly shield, to form nitrides, oxides and hydrides, which can significantly affect the mechanical properties of the welded joints. Even after solidification and cooling to close to ambient temperature, titanium still exhibits high solubility for the three gases. A possible contamination of the weld is indicated by a gold or straw color of the nitride/oxide film. Blue color film indicates a high level of contamination, rendering the weld unacceptable. Therefore, trailing shield and backside

shielding are typical when welding titanium. However, the bulky equipment makes the process unwieldy in structural fabrication.

A novel variant of the GTAW process, activating flux or A-TIG, has recently become available, which offers the potential for overcoming the principal limitations of GTAW, namely its poor penetration and its sensitivity to material composition. This simple process variant, of applying a thin coating of an activating flux to the surface of the material before welding can produce a dramatic increase in weld bead penetration. The A-TIG process was developed at the E. O. Paton Institute in the early 1960's for welding titanium.^{1,2} The principal effect of the coating appears to be the constriction of the arc. Arc constriction increases the current density at the anode root and with the increase in the arc force, a substantial increase in the penetration depth of the molten pool can be achieved. Many flux ingredients can be used to produce arc constriction and several flux formulations have been reported as being effective for particular materials.³⁻⁷ Fluorides of alkali and alkali-earth metals have been reported to constrict the arc and to increase the weld depth of penetration in titanium.^{3,4} In arc welding, however, fluxes that consist mainly of fluorides, do not provide a sufficiently stable welding process nor do they produce good welds. The behavior of fluxes is improved when fluorides are partially replaced by chlorides. In fact, the use of flux in titanium welding was exploited for submerged arc welding in the early 60's in the former Soviet Union.⁵ As the high reactivity of titanium prevents the use of oxide-based fluxes, Gurevich⁵ had concentrated on the development of a CaF_2 -based flux to which small amounts of BaCl_2 , NaCl , and NaF were added. These fluxes were reported to produce high quality welds

with no porosity and good mechanical properties. The preferred flux compositions were CaF_2 -(5-21%) BaCl_2 -(1-5%) NaCl -(0.5-1.5%) NaF . Petsch⁶ in the U.S. also concentrated on developing a CaF_2 -based flux. The composition with the best operability was CaF_2 -5% BaCl_2 -2% LiF . Hill and Choi⁷ showed that the performance of the submerged arc weld made using CaF_2 flux was comparable with that of the gas metal arc (GMA) welds. Based on this result, they claimed that contamination from the atmosphere and from the flux was not overwhelming, even in the case of no auxiliary shielding.

Recently, Liu and Faustino⁸ reported that grade 2 Ti-CP was successfully GTA welded with CaF_2 -based flux-cored (FC) filler wires. Standard GTAW equipment was used without auxiliary shielding. Both 85% CaF_2 -14% BaCl_2 -1% NaF and 70% CaF_2 -14% BaCl_2 -15% MgF_2 -1% NaF flux systems resulted in excellent slag coverage, as can be seen in Fig. 1. These fluxes produced slags that were easily removed by mechanical brushing. The effectiveness of the slag protection resulted in good bead morphology with no visible defects in the weldment even though no secondary shielding was applied. The flux with MgF_2 addition showed deeper penetration than the flux without it. Compared to other processes, two technological advantages are obvious in this welding process. First is the elimination of auxiliary shielding gas. As shown in their results,⁸ if the contamination from the CaF_2 -based flux is negligible, sound weld metal could be obtained through the slag protection without the auxiliary shielding gas. Second is the increase in weld penetration depth. Due to the active nature of the fluoride and chloride-based fluxes, an increase in weld bead penetration would be expected in the process. In this research, the effects of MgF_2 on bead

morphology, chemical composition, and hardness of weld bead were investigated. Comparison was made between GTAW with FC wire and the conventional A-TIG process.

Experimental procedures

The chemical composition of the 6mm thick titanium plate is provided in Table 1 along with ASTM specification requirement for comparison. The plate meets the chemical requirement for ASTM B265 Ti-CP (grade 2). Before welding, the plates (150x100x6mm) were ground using a grinder and then cleaned with acetone. A series of bead-on-plate GTA welding were conducted at a constant current of 180 amperes and a travel speed of 3mm s^{-1} . The arc was generated by a constant current DC power source (Hobart Cyber TIG), using a 2% thoriated tungsten electrode. Voltage varied between 13 and 15 volts depending on the flux system in use. The welding parameters used are listed in the Table 2. To precisely record the welding conditions, a current and voltage data acquisition system was used. Shielding gas was used only in the torch and no trailing gas was used. Since no welds showed full penetration, back shielding was not used. The FC wires were fed automatically during welding at a constant speed of 15mm s^{-1} . The FC wires were manufactured from a strip (12.7mm width x 0.4mm thickness) of Ti-CP (grade 2). The titanium strip was first formed to the intermediate shape of "U", and then completely filled with the flux powder. The excess powder was then carefully removed using an adjustable spatula-type scraper. Finally, the powder-filled sheath was folded into a tubular shape and drawn through successively smaller dies to the final outer diameter of 1.4mm.

Powder filling ratio was about 20%. The composition of the base flux was 85%CaF₂-14%BaCl₂-1%NaF. MgF₂ was added to partially replace CaF₂ to study the effect of MgF₂ on arc constriction and bead morphology.

For comparison, bead-on-plate A-TIG welding was also conducted with the same welding parameters. Flux pastes were applied manually with a brush. For flux pastes, powders were mixed with acetone and painted on the surface of the titanium plate before welding. Acetone evaporated within seconds leaving behind a layer of the flux on the surface.

After welding, the beads were cross-sectioned, polished, and etched to reveal fusion zone. For etching, a modified Weck's solution containing 100mL water, 2mL ethanol and 2g ammonium bifluoride was used. Fusion zone dimensions were analyzed by optical microscopy. Diamond pyramid hardness (DPH) of weld metal was measured at a load of 10kg. Chemical analyses for interstitials and iron content of weld metal were performed. Emission spectroscopy was used to characterize the plasma during welding. The radiation emitted from the central region of plasma was collected by the probe attached with a collimating lens 5mm in diameter. The light was transmitted by a fiber optic bundle to the spectrometer (Ocean Optic Inc. Model S2000) entry slit and dispersed by a fixed grating across a linear CCD array detector.

Results

As FC wire with MgF₂ resulted in deeper penetration than FC wire with no MgF₂ in the previous research, the effect of MgF₂ content on weld bead morphology was studied systematically first. Bead-on-plate welding was

performed using flux pastes with different MgF_2 content. MgF_2 was added to partially replace CaF_2 , while maintaining BaCl_2 and NaF contents constant as 14% and 1%, respectively. Fig. 2 shows typical cross section of several weld beads. Welds made with higher MgF_2 contents showed deeper, but narrower, bead. Weld bead dimensions are summarized in Table 3. While bead made with no MgF_2 showed 2.1mm depth and 9.1mm width, bead made with 85% MgF_2 showed 3.8mm depth and 7.3mm width. Fig. 3 shows the variation of depth-to-width ratio of beads as a function of MgF_2 content. As MgF_2 content increased, the ratio gradually increased. Bead made with 85% MgF_2 showed 0.52, which is two times greater than the ratio of the bead made with no MgF_2 .

As the mechanical behavior of Ti-CP welds can be altered to a great extent by the interstitial elements such as oxygen, nitrogen, and carbon in the lattice, the effect of MgF_2 content on the chemical composition and hardness of weld bead was also investigated. Table 4 lists the chemical composition and hardness of weld beads. Compared to the bead made with no MgF_2 , all other beads made with MgF_2 showed higher hydrogen content. Other than that, little differences were observed between weld beads, indicating no harmful effect of high MgF_2 content on the chemistry of weld bead. Accordingly, all weld beads showed almost identical hardness readings, 210~216 H_V . However, the values were slightly higher than that of base plate, 187 H_V . Referring to the chemical composition of the base plate shown in Table 1, this increase in hardness in the weld metals might have been caused by higher interstitial elements. However, the content of each element still meets the maximum chemical composition requirement of the base plate. Because weld metal chemical composition is not

specified in the titanium filler material specification, it is generally accepted that the weld metal must meet the maximum chemical composition requirements of the base plate for qualification.

Based on the above results, two FC wires with high MgF_2 contents, 50 and 85%, were manufactured and used for bead-on-plate welding. After welding, both weld beads were covered with a layer of dark colored slag. Fig. 4 shows a weld bead made with 50% MgF_2 before and after slag removal. Note that the slag coverage was 100%, Fig. 4 (a). Brushing was sufficient to remove the slag. Light sandblasting returned the original color of the weld bead with no indication of oxygen and nitrogen pickup, Fig. 4 (b). The weld bead exhibited smooth surface and showed no visual defects. Welds made with 85% MgF_2 , however, had incomplete slag coverage, especially along the edges of the weld beads, and the surface was also rough. Fig. 5 shows an XRD spectrum of the slag made with 50% MgF_2 . In addition to the dominant CaF_2 peaks, several unidentified peaks were observed. These unknown peaks are presumably from the complex phase or phases formed the flux ingredients. Fig. 6 shows the cross-section of a weld bead made by 50% MgF_2 FC wire. Penetration depth and width of the bead were 4.6 and 7.6mm, respectively. Compared to the dimensions of bead made by flux pastes with similar MgF_2 content, it had deeper and narrower bead. Flux paste with 60% MgF_2 showed 3.1mm depth and 8.1mm width as shown in Table 3. This indicates that FC wire is far more effective on deep penetration than flux paste. Note also the excellent wetting as manifested by the smooth tie-in between base metal and weld metal.

Table 5 shows the chemical composition and hardness of weld bead made by 50% MgF_2 FC wire. These weld beads showed higher oxygen and nitrogen contents than the base plate. However, when compared with the weld bead made using flux pastes with similar MgF_2 content (60% MgF_2), the FC wire produced similar oxygen and nitrogen contents but lower hydrogen and carbon contents. Hardness reading was 202H_v. These results indicate that FC wire is beneficial to reduce hydrogen and carbon contents in weld bead, even if little influence was observed on reducing oxygen and nitrogen contamination from atmosphere.

Discussion

Several mechanisms and explanations have been proposed to account for the effectiveness of flux composition on bead morphology and arc constriction in A-TIG. As the metal melts, a weld pool can only form if the flux is fully removed from the root of the arc column, either by evaporation or forced out by other forces that act on the weld pool. The area of the weld pool and anode spot becomes smaller when the molten flux wets the liquid weld metal better. As adhesion of a liquid to the solid substrate is in direct dependence upon the Gibbs free energy change for chemical interaction between them, Gibbs free energy change can be used as a criterion for evaluating the efficiency of fluxes or their components.⁹

Arc constriction depends on flux vapors as well. The greater the amount of flux vapors enters the arc, and the greater the extent to which they are dissociated, the more the arc will contract due to the increase of thermal conductivity of the arc. To confirm this theory, Zamkov¹⁰ calculated the amount

of dissociated vapors of single-component halide fluxes, and compared the results with experimental data such as penetration depth. Greater amounts of dissociated vapors of MgF_2 delivered deeper penetration. Another reason of arc constriction is the reduction in electrical conductivity in the peripheral region of the arc column because of electron trapping.¹¹ In the central regions of the arc, the temperature is higher than the dissociation temperature of the molecules and the gas and flux atoms are ionized to generate electrons and cations. In the cooler outer periphery of the arc column, however, most vaporized material will exist as molecules and dissociated atoms. When these species are large enough for electrons to attach to them, negatively charged particles are formed. In this case, the degree of constriction will be determined by the effectiveness of the flux vapor to combine with the electrons. Zamkov¹⁰ also argued that titanium fluoride, i.e. product of interaction between titanium and the flux, is likely the compound most able to trap electrons in the peripheral regions of the arc. Furthermore, he showed the effectiveness of MgF_2 on the formation of titanium fluoride in terms of thermodynamics. In the presence MgF_2 fluxes, the calculated equilibrium constant of the fluoride-titanium reaction was the highest. Eroshenko *et al.*¹² studied arc plasma spectra and observed TiF_n molecular bands when titanium was welded with fluxes of MgF_2 , AlF_3 and NaF . When welds were made using CaF_2 and BaF_2 , no molecular bands of titanium fluorides could be found and little improvement on penetration depth was observed. Based on these results, they concluded that the effectiveness of a flux, i.e., its capacity for increasing the penetration depth, depended on the concentration of titanium fluorides in the arc. The higher is this concentration, the more effective the flux is.

Fig. 7 (a) shows a typical plasma spectrum obtained in the experiments when welded with 50% MgF_2 FC wire. The spectrum showed that atomic and ionized argon contributed most to the arc emission. In addition, the presence of flux vapors and its dissociation products was observed. Peaks corresponding to atomic and ionized titanium, Ti I and Ti II, from the base metal and sheath material were observed. TiF_n molecular peaks were not observed in this experiment. Fig. 7 (b) shows a typical spectrum obtained when welding was performed with FC wire with no MgF_2 . Compared to Fig. 7 (a), no atomic and ionized titanium peaks were observed. This difference was also reported in other experiments. Eroshenko¹³ examined the spectral lines of titanium vapors and grouped fluoride fluxes on the basis of their effect on the Ti I and Ti II lines. The first group included fluorides of barium, lithium, and calcium. In welding with BaF_2 or LiF , the Ti I and Ti II lines were visible on the background of the continuum only at the surface of the anode, as in the case of welding without the fluorides. The second group consisted of fluorides of sodium, magnesium, and aluminum, which caused marked increases in the intensity of Ti I and Ti II lines. As increases in the intensity of the excited atoms and ions of the anode material indicate high arc temperature, and consequently large amount of vapors in the arc, the observation of Ti I and Ti II lines in the spectrum of 50% MgF_2 FC wire confirms effectiveness of MgF_2 on arc constriction. Fig. 8 shows another experimental result indicating the effectiveness of MgF_2 on arc constriction. It shows the variation of arc voltage as a function of the MgF_2 content in the flux paste. Arc voltage increased with the increase of MgF_2 content. Therefore, it is believed that deep penetration in high MgF_2 fluxes in the present experiments

was caused by arc constriction, resulting from the high temperature of the arc and greater amount of flux vapors in the arc.

The result of deeper penetration in welds made using FC wire than those with flux pastes, both containing similar MgF_2 contents, indicates that flux ingredients from the FC wires evaporated and dissociated in the arc to greater extents than the flux pastes. Moreover, droplet transfer from FC wire during welding may also enhance the penetration depth. More research is needed to clarify the contribution of metal droplet transfer in the future.

Conclusions

Grade 2 Ti-CP was gas tungsten arc welded using flux-cored wires and flux pastes with various MgF_2 contents. The effects of MgF_2 content on bead morphology, chemical composition and hardness of weld bead were investigated. Important results obtained are as follows:

(1) When bead-on-plate welding was performed using flux pastes, the depth-to-width ratios of weld beads increased gradually with increasing MgF_2 content. Weld bead made with 85% MgF_2 showed the ratio of 0.46, which is two times greater than the ratio measured in welds made without MgF_2 . All weld beads made with MgF_2 showed little differences in interstitial elements contents and hardness, indicating no harmful effect of high MgF_2 content on the chemical composition and hardness of the titanium welds.

(2) Weld beads made by FC wires showed even deeper and narrower bead with little change in oxygen and nitrogen contents and hardness of weld metal. This finding indicates that FC wires are more effective in promoting deep

penetration than the flux pastes. However, compared to the complete slag coverage and smooth surface provided by the 50% MgF_2 FC wire, incomplete slag coverage and rough surface were obtained with the 85% MgF_2 FC wire.

(3) Plasma spectrum obtained with 50% MgF_2 FC wire showed atomic and ionized titanium peaks, Ti I and Ti II, indicating high arc temperature and, consequently, large amount of flux vapors in the arc. Thus, the deep penetration in high MgF_2 flux welds in this experiment is caused by arc constriction, a result of the greater amount of flux vapors due to the higher arc temperature.

Acknowledgements

The authors are grateful to J. Chandler and F. Perez in CWJCR for their assistance in this work. Two of the authors (G. Chirieleison and S. Liu) acknowledge the support of Mr. Michael Wells of NSWC-CD and Mr. Stephen Luckowski of ARDEC.

References

- 1) S. Gurevich, V. Zamkov and N. Kushnirenko: *Avt. Svarka.*, 1965, (9), 1-4
- 2) S. Gurevich and V. Zamkov: *Avt. Svarka.*, 1966, (12), 13-16
- 3) A. Simonik: *Svar. Proiz.*, 1974, (3), 52-53
- 4) S. Gurevich, V. Zamkov and N. Kushnirenko: Proc. 2nd Int. Conf. on 'Titanium', Cambridge, USA, May, 1972
- 5) S. Gurevich: US Patent 3,551,218, December 29, 1970
- 6) H. Petsch: 'Research study to develop a submerged arc automatic welding process for fabricating butt welds in thick titanium alloy plates', US Navy Contract N00140-68-C-0148, Final report, 1968
- 7) D. Hill and C. Choi: *Weld. J.*, 1976, **55**, (6), 152s-158
- 8) S. Liu and F. Perez: 'Manufacturing titanium flux-cored arc welding electrodes – feasibility study', US Navy contract N00167-01-M-0053, Final report, 2001
- 9) B. Paton, V. Zamkov, V. Prilutsky and P. Poritsky: *Paton Weld. J.*, 2000, 5-11
- 10) V. Zamkov, V. Prilutsky and S. Gurevich: *Avt. Svarka.*, 1977, (4), 22-26
- 11) D. Howse and W. Lucas: *Sci. Technol. Weld. Joining*, 2000, **5**, (3), 189-193
- 12) L. Eroshenko, V. Zamkov, V. Meehev and V. Prilutsky: *Avt. Svarka*, 1980, (9), 23-25
- 13) L. Eroshenko, V. Zamkov, V. Meehev and V. Prilutsky: *Avt. Svarka*, 1979, (9), 33-35

List of Figure Captions

Fig. 1. Weld bead made with flux-cored wire with composition of 70%CaF₂-14%BaCl₂-15%MgF₂-1%NaF.

Fig. 2. Typical cross-section of weld beads made with flux pastes with various MgF₂ content: (a) 0 wt%; (b) 15 wt%; (c) 30 wt%; (d) 60 wt%.

Fig. 3. Variation of depth-to-width ratio of weld beads as a function of MgF₂ content.

Fig. 4. Weld bead made with 50% MgF₂ flux-cored wire: (a) before slag removal; (b) after slag removal.

Fig. 5. XRD spectrum of slag obtained from weld bead made with 50% MgF₂ flux-cored wire.

Fig. 6. Typical cross-section of weld bead made with 50% MgF₂ flux-cored wire.

Fig. 7. Arc plasma spectra when welded with flux-cored wires with (a) 50% MgF₂ and (b) no MgF₂.

Fig. 8. Variation of arc voltage as a function of MgF₂ content in flux pastes.

Table 1. Chemical composition and hardness of Ti plate and specification requirement

Material	Composition, wt%					Hardness H _V
	O	N	H	C	Fe	
Plate	0.12	0.003	0.0014	0.01	0.13	187
ASTM B265, Gr.2	0.25 max	0.03 max	0.015 max	0.10 max	0.30 max	-

Table 2. Parameters for gas tungsten arc welding

Current	180A
Voltage	13-15V
Travel speed	3mm s ⁻¹
Wire feeding rate	15mm s ⁻¹
Shielding gas type and flow rate	Argon, 0.275 l s ⁻¹
Shielding gas cup size	No. 10
Electrode type and size	3.2mm diameter, 2% thoriated
Electrode tip preparation	45 deg. included angle
Arc gap	3mm

Table 3. Results of weld bead dimensions depending on MgF₂ content

MgF ₂ content wt%	Penetration depth mm	Width mm	Depth-to-width ratio
0	2.1	9.1	0.23
15	2.3	9.1	0.25
30	2.5	9.4	0.27
60	3.1	8.1	0.38
75	3.2	7.9	0.41
85	3.8	7.3	0.52

Table 4. Interstitial elements content and hardness of weld metal made by flux pastes with various MgF_2 content

MgF_2 content wt%	Interstitial elements content, wt%				Hardness H_v
	O	N	H	C	
0	0.17	0.005	0.001	0.03	213
15	0.19	0.007	0.004	0.03	210
30	0.17	0.006	0.004	0.03	216
60	0.17	0.005	0.005	0.04	216
85	0.19	0.007	0.004	0.03	212

Table 5. Interstitial elements content and hardness of weld metal made by FC wire with 50% MgF_2

Interstitial elements content, wt%				Hardness H_v
O	N	H	C	
0.17	0.005	0.0013	0.01	202

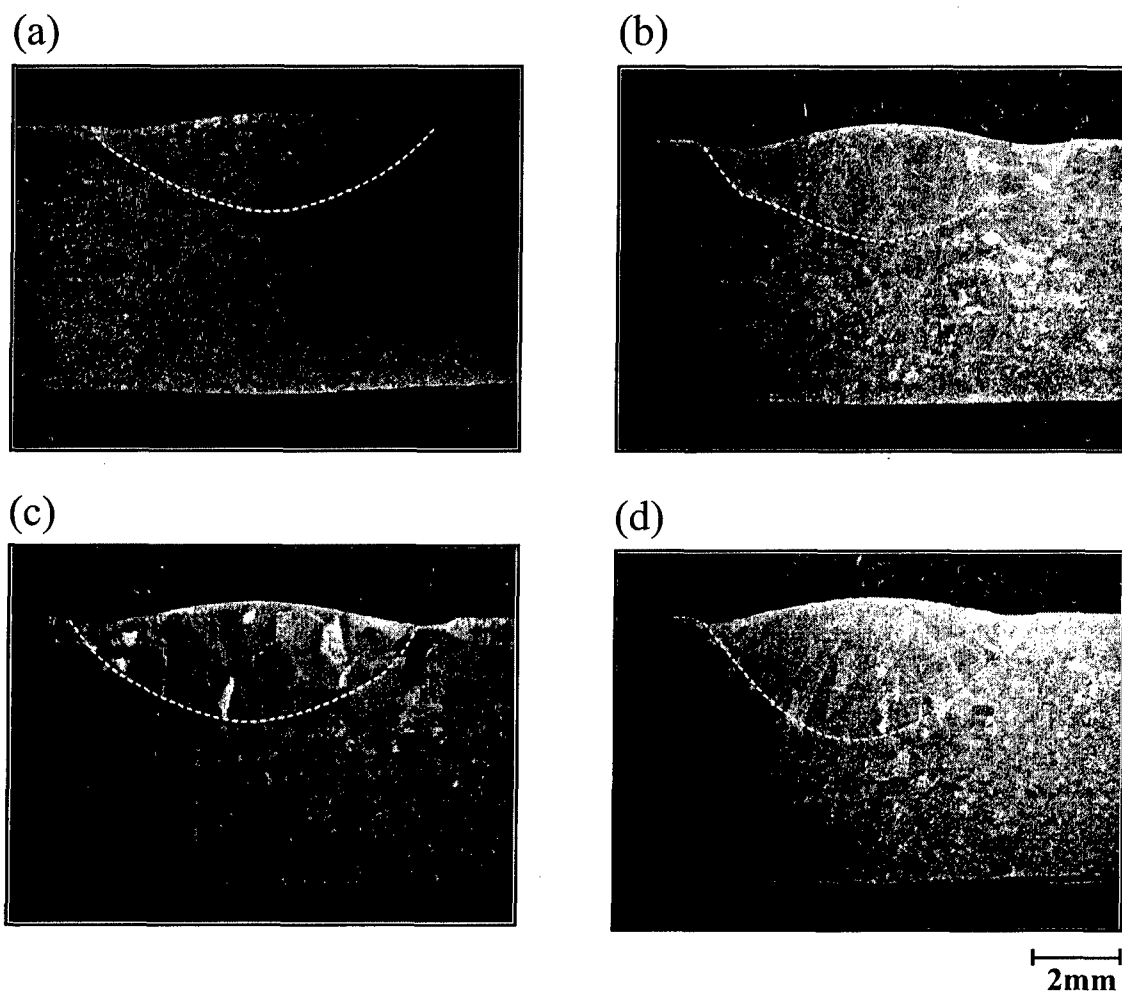


Fig. 1. Typical cross section of weld beads made by paste flux with various MgF_2 content : (a) 0 wt%; (b) 15 wt%, (c) 30 wt% (d) 60 wt%

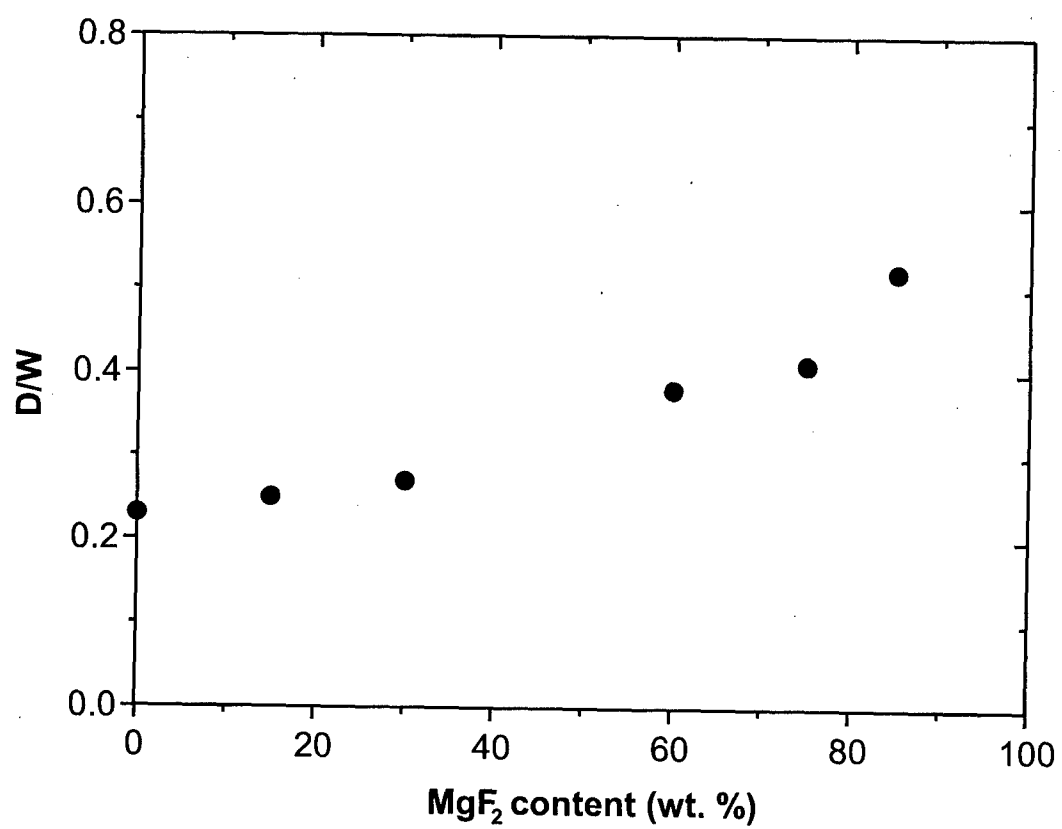
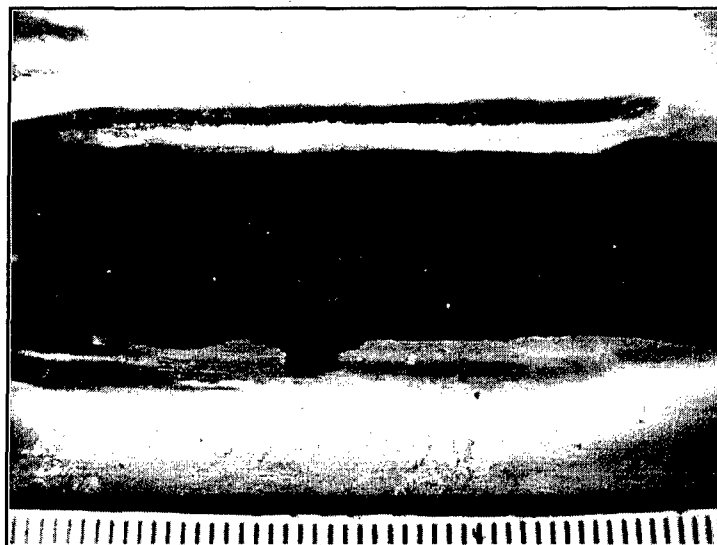
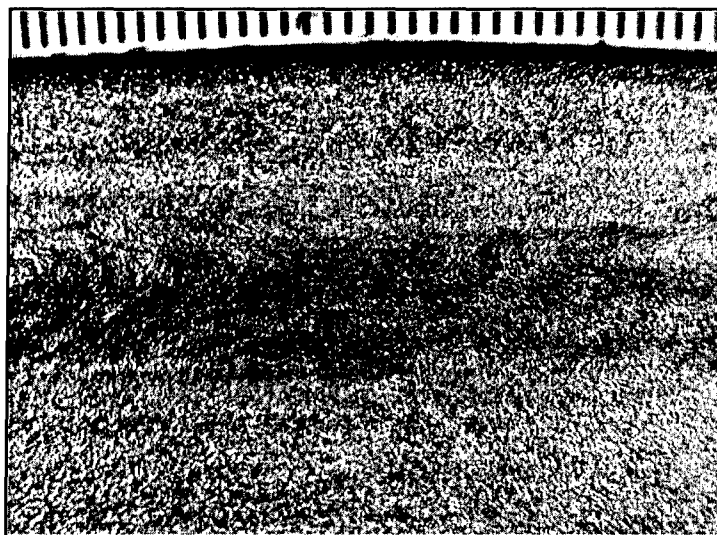


Fig. 2. Variation of depth to width ratio of weld bead as a function of MgF_2 content

(a)



(b)



**Fig. 3. Weld bead made by 50% MgF_2 flux cored wire :
(a) before slag removal; (b) after slag removal**

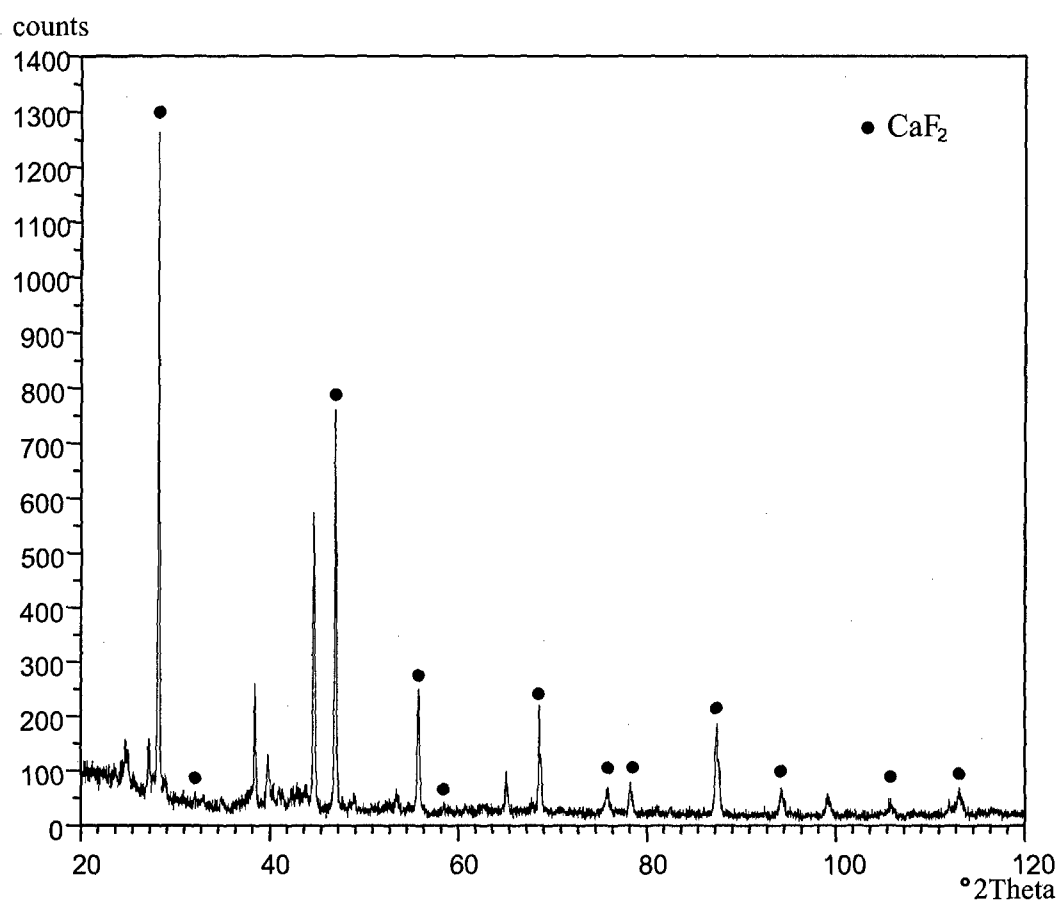
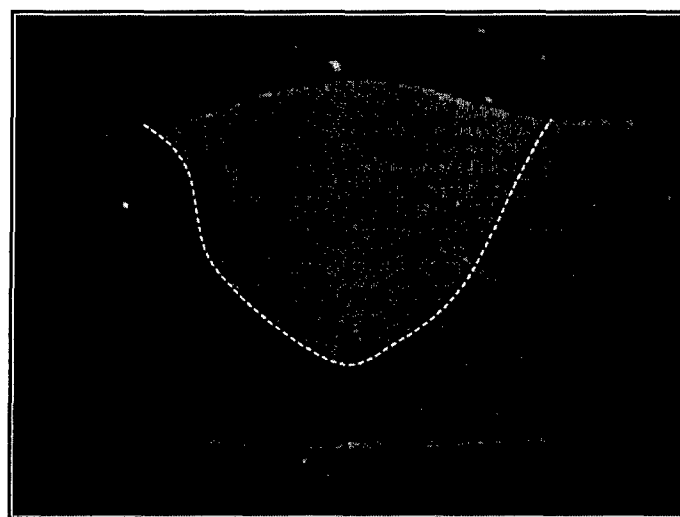


Fig. 4. XRD spectrum of slag from weld bead made by 50% MgF₂ flux cored wire



2mm

**Fig. 5. Typical cross section of weld bead made by
50% MgF_2 flux cored wire**

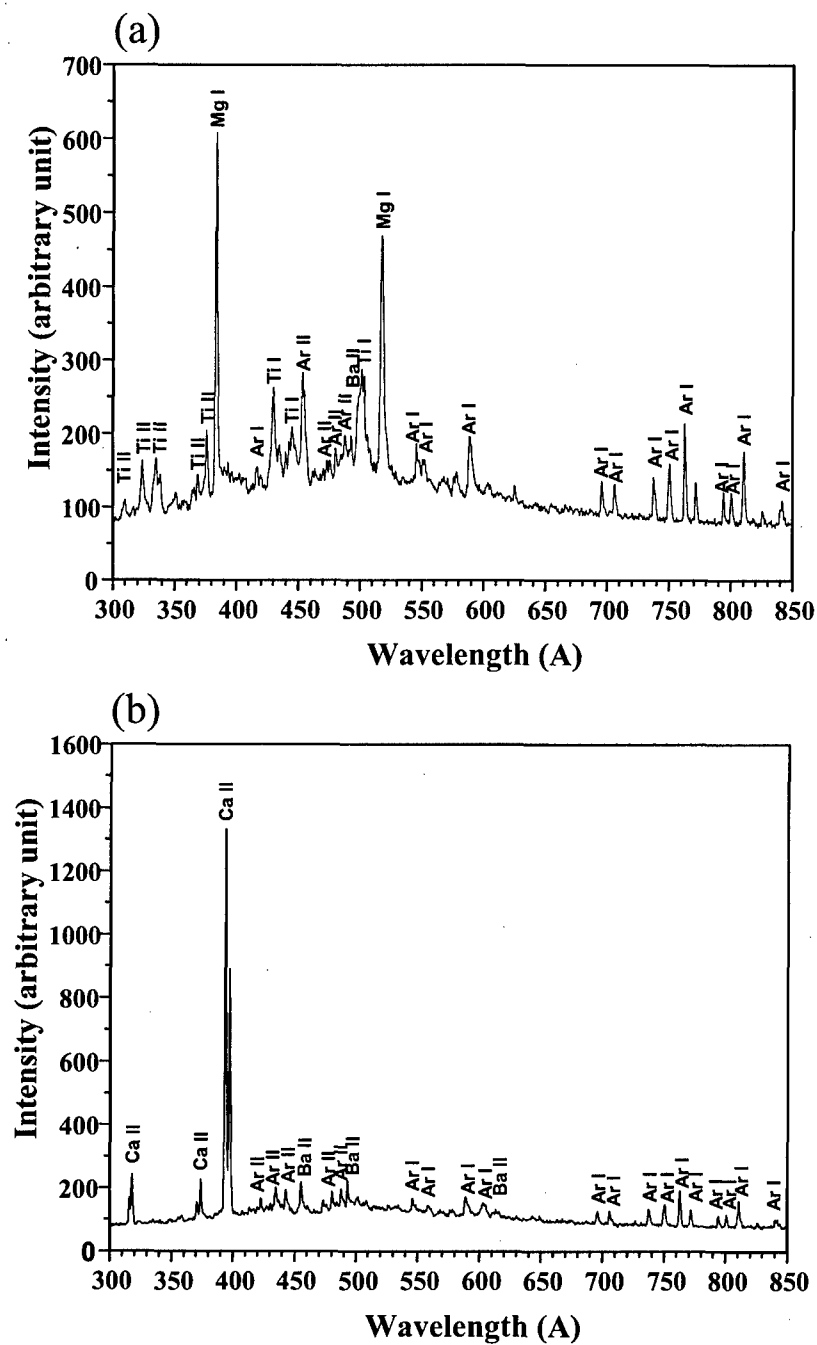


Fig. 6. Arc plasma spectra when welded with (a) 50% MgF_2 and (b) no MgF_2 flux cored wires

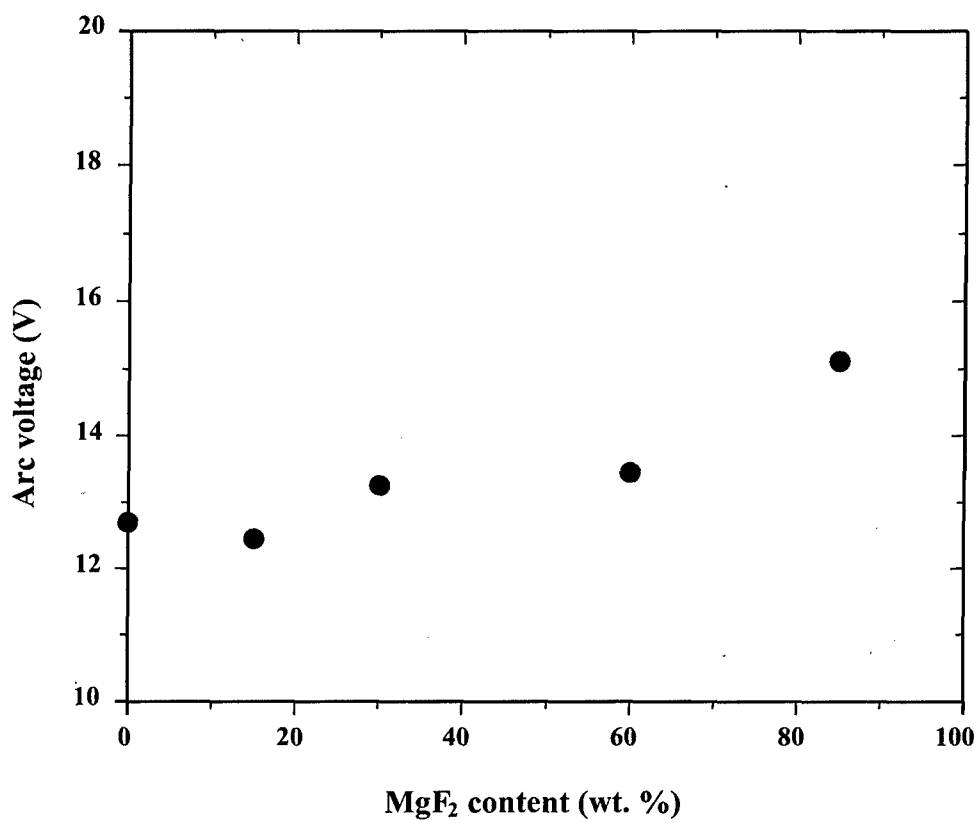


Fig. 7. Variation of arc voltage as a function of MgF₂ content in paste flux